

Université Paris Cité

Laboratoire Astroparticule et Cosmologie (APC-Paris)

École Doctorale des Sciences de la Terre et de l'Environnement
et Physique de l'Univers de Paris, ED 560

**Search for di-Higgs production and measurement of the
Higgs boson self-coupling in the final state
with a pair of b quarks and a pair of tau leptons
with the ATLAS detector at the LHC,
Perspectives on the measurement of the Higgs boson mass
and the electron-positron to ZH cross-section
at the Future Circular Collider**

Par ANG LI

Thèse de doctorat en PHYSIQUES DE L'UNIVERS
Dirigée par GREGORIO BERNARDI

Présentée et soutenue publiquement le 27 novembre 2023

Devant un jury composé de:

MME.	ALESSANDRA TONAZZO	PROFESSEUR	UNIVERSITÉ PARIS CITÉ	PRÉSIDENT DU JURY
M.	GREGORIO BERNARDI	DR	APC-PARIS	DIRECTEUR
M.	JEAN-BAPTISTE DE VIVIE DE REGIE	DR	LPSC	RAPPORTEUR
M.	ROBERTO SALERNO	DR	LLR	RAPPORTEUR
M.	EMMANUEL PEREZ	CHERCHEUR	CERN	EXAMINATEUR
MME.	ELISABETH PETIT	CR	CPPM	EXAMINATEUR

Abstract

Title: Search for di-Higgs production and measurement of the Higgs boson self-coupling in the final state with a pair of b quarks and a pair of tau leptons with the ATLAS detector at the LHC, Perspectives on the measurement of the Higgs boson mass and the electron-positron to ZH cross-section at the Future Circular Collider

Abstract: After the discovery of the Higgs boson in 2012 by the ATLAS and CMS collaborations at the Large Hadron Collider (LHC), precision measurements of the Higgs boson mass and couplings have taken center stage, serving both the validation of the Standard Model (SM) and the exploration for new physics Beyond the Standard Model (BSM).

After an introduction to the Standard Model and to the experimental apparatus and tools, the thesis describes the calibration of the b -tagging efficiency within ATLAS. The p_T^{rel} method, which uses muon-in-jets events, is employed here with the DL1r tagger for the first time. In comparing the p_T^{rel} calibration to the $t\bar{t}$ calibration, the primary method at ATLAS, a clear agreement between the two was observed.

The search for double Higgs boson (di-Higgs) production is then the major component of this thesis. This process will give access to the Higgs self-coupling and Higgs potential. This thesis utilizes ATLAS Run 2 data to investigate di-Higgs production through the $HH \rightarrow b\bar{b}\tau^+\tau^-$ decay channels.

No significant excess above the expected background from Standard Model processes is observed. For this channel, the observed (expected) upper limit for the di-Higgs production cross-section obtained in our study is 5.9 (3.1) times the SM prediction at a 95% confidence level. The Higgs self-coupling parameter, κ_λ , has an observed (expected) 95% confidential interval of $-3.2 < \kappa_\lambda < 9.1$ ($-2.5 < \kappa_\lambda < 9.2$). Moreover, the 95% confidential interval of di-Higgs to two weak bosons ($HHVV$) coupling parameter, κ_{2V} , is observed (expected) to be constrained between $-0.4 < \kappa_{2V} < 2.6$ ($-0.2 < \kappa_{2V} < 2.4$). These results are in the process of being published.

The last part of the thesis introduces the Future Circular Collider, the proposed successor to the LHC. It evaluates the physics feasibility of the FCC-ee, its electron-positron phase, to measure the Higgs mass and the ZH cross-section. By applying the recoil mass method with Z boson decays to muon or electron pairs, the Higgs mass can be measured with a precision of 4.0 MeV, and the ZH cross-section can be determined with an accuracy of 0.69%.

Keywords: ATLAS, Higgs boson, b -tagging calibration, p_T^{rel} calibration, di-Higgs, $HH \rightarrow b\bar{b}\tau^+\tau^-$, Higgs self-coupling, di-Higgs to two bosons, FCC, Higgs mass, ZH cross-section

Résumé

Titre: Recherche de la production de di-Higgs et mesure de l'auto-couplage du boson de Higgs dans l'état final d'une paire de quarks b et d'une paire de leptons tau avec le détecteur ATLAS au LHC, Perspectives sur la mesure de la masse du boson de Higgs et la section efficace de production electron-positron à ZH au Futur Collisionneur Circulaire

Résumé: Suite à la découverte du boson de Higgs en 2012 par les collaborations ATLAS et CMS au Grand collisionneur de hadrons (LHC), les mesures de précision de la masse et des couplages du boson de Higgs sont devenues primordiales, tant pour la validation du Modèle Standard (SM) que pour la recherche de nouvelles physiques au-delà du Modèle Standard (BSM).

Après une introduction au modèle standard et à l'appareillage instrumental, nous décrivons la calibration de l'identification des jets de quark b dans les événements d'ATLAS. La méthode p_T^{rel} , qui utilise des événements muon-in-jets, est utilisée pour la première fois avec l'identificateur de quarks b "DL1r". En comparant la calibration p_T^{rel} à la calibration $t\bar{t}$, méthode principale dans ATLAS, un accord probant entre les deux méthodes est observé.

La recherche de la production de deux bosons de Higgs dans l'état final ("di-Higgs") est un élément central de cette thèse. Ce processus permet de remonter au potentiel de Higgs et à son autocouplage. Cette thèse utilise les données d'ATLAS prises lors du Run 2 du LHC, pour étudier la production de di-Higgs à travers le canal de désintégration $HH \rightarrow b\bar{b}\tau^+\tau^-$.

Aucun excès significatif au-dessus du bruit de fond attendu des processus du Modèle Standard n'est observé. Pour ce canal, la limite supérieure observée (attendue) pour la section efficace de production de di-Higgs obtenue dans notre étude est de 5,9 (3,1) fois la prédiction du MS à un niveau de confiance de 95%. Le paramètre d'auto-couplage du Higgs, κ_λ , a un intervalle de confiance de 95% observé (attendu) de $-3,2 < \kappa_\lambda < 9,1$ ($-2,5 < \kappa_\lambda < 9,2$). De plus, l'intervalle de confiance à 95% du paramètre de couplage de di-Higgs à deux bosons faibles ($HHVV$), κ_{2V} , est observé (attendu) être contraint entre $-0,4 < \kappa_{2V} < 2,6$ ($-0,2 < \kappa_{2V} < 2,4$). Ces résultats sont en cours de publication.

La dernière partie de la thèse présente le Futur Collisionneur Circulaire, successeur proposé du LHC. Elle évalue la faisabilité physique du FCC-ee, sa phase électron-positron, sur les mesures de la masse du boson de Higgs et de la section efficace ZH. En utilisant la méthode de la masse de recul avec les désintégrations du boson Z en paires de muons ou d'électrons, la masse du boson de Higgs peut être mesurée avec une précision de 4,0 MeV, et la section efficace ZH peut être déterminée avec une précision de 0,69%.

Mots clés: ATLAS, boson de Higgs, étalonnage de b-tagging, étalonnage p_T^{rel} , di-Higgs, $HH \rightarrow b\bar{b}\tau^+\tau^-$, auto-couplage du Higgs, di-Higgs vers deux bosons, FCC, masse du Higgs, section efficace ZH

Résumé étendu

Suite à la découverte du boson de Higgs en 2012 par les collaborations ATLAS [1] et CMS [2] au LHC, les mesures de précision du Higgs et de ses couplages sont devenues primordiales. Ces mesures remplissent une double fonction: elles valident les prédictions du Modèle Standard (MS) et ouvrent des voies pour explorer de nouvelles physiques au-delà du Modèle Standard (BSM).

Parallèlement, le LHC a renforcé son potentiel pour sonder la nouvelle physique en augmentant à la fois l'énergie au centre de masse de ses collisions et l'intensité de ses faisceaux de protons, atteignant ainsi des luminosités intégrées plus élevées.

Dans l'anticipation de futurs progrès, la communauté de la Physique des Hautes Énergies (PHE) est en phase de planification pour la prochaine génération de collisionneurs, envisagés comme des usines à Higgs. Parmi ceux-ci, le Collisionneur Circulaire Futur (FCC) proposé par le CERN est l'un des projets les plus prometteurs.

Mes contributions comprennent des travaux sur les études de la Physique du Higgs à la fois sur ATLAS et le FCC.

Le document est organisé comme suit :

Le Chapitre 1 offre une introduction concise au Modèle Standard de la physique des particules, au mécanisme de Higgs, à la production de di-Higgs, aux modes de désintégration, au formalisme kappa, et aux paramétrisations κ_λ et κ_{2V} .

Le Chapitre 2 détaille le Grand Collisionneur de Hadrons (LHC) et le détecteur ATLAS.

Le Chapitre 3 décrit la reconstruction des objets physiques utilisés dans l'analyse ATLAS.

Le Chapitre 4 introduit la méthode p_T^{rel} , qui utilise des événements "jets-avec-muon" pour calibrer l'algorithme de "*b*-tagging" en utilisant à la fois les identificateurs de jets de *b* "MV2c10" et "DL1r". DL1r est introduit dans cette méthode et est appliqué aux données de Run 2. Une comparaison avec la calibration basée sur les événements $t\bar{t}$, la méthode principale de calibration à ATLAS, est également présentée.

Le Chapitre 5 présente l'analyse du canal $HH \rightarrow b\bar{b}\tau^+\tau^-$, mettant l'accent sur la mesure de l'intensité du signal HH , du couplage propre de Higgs (κ_λ) et du couplage $HHVV$ (κ_{2V}). Une catégorie VBF dédiée est introduite pour renforcer la sensibilité sur κ_{2V} .

Le projet du Collisionneur Circulaire Futur (FCC) discuté dans les Chapitres 6 et 7.

Le Chapitre 6 offre un aperçu du projet FCC, incluant sa chronologie et les phases de travail électron-positron et proton-proton. D'autres sujets de physique importants au FCC sont également présentés.

Le Chapitre 7 décrit mes contributions aux mesures de la masse et de la section efficace du Higgs au FCC, notamment dans le canal $e^+e^- \rightarrow ZH \rightarrow \ell^+\ell^-$. La technique de la masse de recul est employée pour extraire la masse du boson de Higgs, et un BDT est utilisé pour assurer le caractère indépendant du modèle de l'analyse de la section efficace de ZH.

Un résumé du contenu de la thèse est donné à la fin et offre des perspectives sur les développements futurs dans le domaine.

Mesure de l'efficacité d'identification du jet b avec la méthode p_T^{rel}

Dans l'expérience ATLAS au Grand Collisionneur de Hadrons, l'identification précise des jets qui proviennent des quarks b , notée b -tagging, est essentielle pour diverses analyses physiques. Ce chapitre explique le calcul de l'efficacité du b -tagging, symbolisée par ε_b , des jets contenant un muon apparié spatialement en utilisant des événements multi-jets. Ces muons proviennent principalement des désintégrations semi-leptoniques des hadrons bottom et charm. De plus, certains hadrons dans les jets de quarks légers et de gluons, lorsqu'ils sont mal interprétés comme des muons, jouent également un rôle.

En examinant l'impulsion transversale du lepton par rapport à l'axe combiné du lepton et du jet, notée par p_T^{rel} , il est possible de déduire la fraction de jets provenant des quarks b (b -jets) en utilisant un ajustement de vraisemblance. La détermination de ε_b est dérivée de l'estimation de cette fraction dans les jets qui respectent ou s'écartent des critères de b -tagging. En conséquence, les résultats sont exprimés en tant que rapport de l'efficacité trouvée dans les données par rapport à celle dans la simulation Monte Carlo. Ces rapports, appelés facteurs d'échelle, sont détaillés pour les algorithmes de b -tagging, MV2c10 et DL1r, en fonction de l'impulsion transverse du jet, pour 4 valeurs de référence. Ces valeurs de référence représentent les efficacités de b -tagging de 60%, 70%, 77% et 85%, telles que déterminées en utilisant les b -jets dans la simulation tt .

L'étalonnage basé sur MV2c10 est documenté dans Ref. [3], tandis que l'étalonnage basé sur DL1r est présenté dans cette étude pour la première fois.

L'équipe d'analyse prévoit d'appliquer la méthode p_T^{rel} sur les premières données du Run 3 et de combiner avec toutes les autres méthodes de calibration de " b -tagging" pour produire un ensemble unique de facteurs d'échelle de " b -tagging" pour l'ensemble complet des données Run 3.

Recherche de la production de di-Higgs dans l'état final $b\bar{b}\tau^+\tau^-$

Cette partie décrit l'analyse de toutes les données du Run 2 pour la production HH dans l'état final avec deux b -jets et deux leptons τ . Les données consistent en 140 fb^{-1} de collisions proton-proton enregistrées par l'expérience ATLAS à $\sqrt{s} = 13 \text{ TeV}$. Le canal $b\bar{b}\tau^+\tau^-$ présente une fraction d'embranchement significative de 7,3 % parmi les possibles canaux de désintégration des HH , avec un état final relativement propre. Étant donné que les leptons τ peuvent subir soit une désintégration leptonique (τ_{lep} : en e ou μ) soit hadronique (τ_{had} : généralement en un ou trois pions chargés avec certains pions neutres), deux sous-canaux, $b\bar{b} \tau_{\text{lep}} \tau_{\text{had}}$ et $b\bar{b} \tau_{\text{had}} \tau_{\text{had}}$, sont examinés séparément.

Bien qu'une analyse précédente pour la production HH dans l'état final $b\bar{b}\tau^+\tau^-$ en utilisant l'ensemble des données Run 2 ait été rendue publique [4], elle était uniquement optimisée pour le mode de production par fusion de gluons ("ggF"). Cette analyse avait fixé une limite supérieure observée (attendue) sur la section efficace de production HH de 140 (110) fb à un niveau de confiance de 95% (CL). Cela correspond à 4,7 (3,9) fois la prédiction du modèle standard contre l'hypothèse de fond uniquement. Sous l'hypothèse d'une production standard SM HH et de couplages, κ_λ était contraint entre $-2,7 < \kappa_\lambda < 9,5$ ($-3,1 < \kappa_\lambda < 10,2$) et κ_{2V} entre $-0,6 < \kappa_{2V} < 2,7$ ($-0,5 < \kappa_{2V} < 2,7$) à 95% CL [5]. Un résultat consolidé de l'exploration $HH \rightarrow b\bar{b}\tau^+\tau^-$, ainsi que d'autres canaux HH , sont disponibles dans [6, 7]. De plus, une interprétation dans le cadre phénoménologique "Higgs EFT (HEFT)" est fournie en [8].

Pour cette nouvelle analyse, une réoptimisation a été effectuée pour améliorer la contrainte κ_λ en introduisant une classification d'événements basée sur la masse invariante du système HH , m_{HH} , dans la région cinématique dominée par la production ggF. Ceci a également impliqué

l'amplification de la sensibilité κ_{2V} à travers l'utilisation d'une catégorie VBF dédiée. Pour assurer une distinction idéale entre le signal ggF/VBF et les processus de bruit de fond, des techniques d'analyse multivariée (MVA) ont été employées. Les sorties de cette MVA servent de discriminants dans l'ajustement.

Nous comparons les performances attendues dérivées de deux méthodologies distinctes : un ajustement construit à partir de prédictions de fond pré-ajustées (comme présenté dans la section précédente), et un ensemble de données simulées après la calibration des paramètres de nuisance aux valeurs dérivées de l'ajustement des données avec un signal nul.

Aucun excès significatif au-dessus du bruit de fond attendu des processus du Modèle Standard n'est observé.

Pour ce canal, la limite supérieure observée (attendue) pour la section efficace de production de di-Higgs obtenue dans notre étude est de 5, 9 (3, 1) fois la prédiction du MS à un niveau de confiance de 95%.

Le paramètre d'auto-couplage du Higgs, κ_λ , a un intervalle de confiance de 95% observé (attendu) de $-3, 2 < \kappa_\lambda < 9, 1$ ($-2, 5 < \kappa_\lambda < 9, 2$). De plus, l'intervalle de confiance à 95% du paramètre de couplage de di-Higgs à deux bosons faibles ($HHVV$), κ_{2V} , est observé (attendu) être contraint entre $-0, 4 < \kappa_{2V} < 2, 6$ ($-0, 2 < \kappa_{2V} < 2, 4$).

Ces résultats sont en cours de publication.

Étude de faisabilité du FCC-ee pour la mesure de la masse du boson de Higgs et de la section efficace ZH

Le projet du Futur Collisionneur Circulaire (FCC) est piloté par l'Organisation Européenne pour la Recherche Nucléaire, communément appelée CERN.

Le premier document officiel décrivant le FCC, le Rapport de Conception (CDR), a été publié en janvier 2019, comme indiqué par les références [9], [10], [11] et [12].

Le projet FCC, également connu sous le nom de programme intégré du FCC (FCC-Int), est divisé en deux étapes principales: le Collisionneur Électron-Positron du FCC (FCC-ee) et le Collisionneur Hadron-Hadron du FCC (FCC-hh).

L'étape cruciale de l'étude de faisabilité du FCC a commencé en 2021, et une revue à mi-parcours de cette étude de faisabilité est réalisée à l'automne 2023 [13]. Ceci servira de point de contrôle important pour l'avancement du projet.

Ma contribution à l'étude de faisabilité des mesures de la masse et de la section efficace du boson de Higgs au Futur Collisionneur Circulaire (FCC) est présentée ci-dessous.

Les mesures de la masse et de la section efficace du Higgs sont l'une des études de faisabilité physique les plus importantes du FCC, car elles peuvent déterminer la masse du boson de Higgs avec une précision au niveau du MeV, et mesurer les sections efficaces de production du boson de Higgs avec une précision au niveau du pour mille. La largeur du boson de Higgs, dont la prédiction théorique est de 4,1 MeV [14], peut être déterminée au niveau du pourcent. La mesure de la section efficace peut également être utilisée pour contraindre les couplages du boson de Higgs au boson Z (g_{HZZ}) comme une "bougie" standard, puis pour déterminer d'autres couplages du boson de Higgs.

Bénéficiant de l'information sur l'état initial disponible dans un collisionneur électron-positron, la technique de la masse de recul est utilisée dans cette étude, pour calculer la masse du système en recul par rapport au boson Z reconstruit, garantissant ainsi que les mesures sont indépendantes de l'information sur le boson de Higgs. Sans faire d'hypothèses sur les modes de désintégration du

boson de Higgs, la section efficace ZH peut être mesurée de manière inclusive. Toute discordance de la mesure de la section efficace ZH indiquerait que les modes de désintégration du boson de Higgs ne sont pas pleinement compris, ou qu'il existe de la nouvelle physique au-delà du Modèle Standard.

Les états finals $Z \rightarrow \mu^+ \mu^-$ et $Z \rightarrow e^+ e^-$ sont utilisés dans cette étude, car ils ont la signature expérimentale la plus claire et la meilleure résolution de masse.

Dans cette partie, la masse du boson de Higgs et les mesures de section efficace ZH indépendantes du modèle ont été étudiées en utilisant des événements di-muon et di-électron, avec la méthode de la masse de recul, sur les données simulées du FCC-ee à $\sqrt{s} = 240$ GeV. Tout d'abord, une première sélection d'événements est appliquée pour réduire les principaux bruits de fond tout en conservant l'efficacité du signal. La mesure de la section efficace se poursuit ensuite en utilisant un Arbre de Décision Boosté (ADBoosté) spécifique pour séparer davantage le signal des bruits de fond, avec un accent sur l'indépendance du mode de désintégration du Higgs. Les états finaux di-électron et di-muon sont ajustés simultanément pour extraire la section efficace ZH avec une précision relative de 0,69 %. Au lieu de l'ADBoosté, l'analyse de la masse du boson de Higgs utilise une exigence cinématique supplémentaire pour réduire le bruit de fond: la masse du boson de Higgs est mesurée en ajustant directement la distribution de la masse de recul, après avoir imposé une sélection supplémentaire sur l'angle du vecteur impulsion de l'énergie manquante ($\cos(\theta_{\text{miss}})$). Les distributions de la masse de recul sont modélisées analytiquement et sont injectées dans un ajustement de vraisemblance maximale pour extraire l'incertitude sur la masse. En catégorisant les leptons selon leur angle polaire, la sensibilité est augmentée et une incertitude combinée de 4,0 MeV est obtenue en incluant les systématiques dominantes. Plusieurs incertitudes systématiques ont été évaluées et ont été trouvées presque négligeables pour la mesure de la section efficace, mais impactant l'incertitude sur la masse du boson de Higgs au niveau de 30 %. Un ensemble exhaustif d'exigences expérimentales est discuté, du point de vue de la machine et du détecteur, et la conclusion est que la performance du suivi et la détermination de l'énergie du centre de masse sont les éléments les plus cruciaux. Ils doivent être contrôlés précisément pour atteindre la précision finale que les statistiques qui seront livrées par le FCC-ee promettent.

Contribution de l'auteur

Pour p_T^{rel} , j'ai travaillé à adapter le code pour le tagger DL1r; auparavant, il ne fonctionnait que sur MV2c10. J'ai contribué à l'extrapolation semi-leptonique des données Run2 pour les taggers MV2c10 et DL1r et reproduit l'intégralité de l'étude sur la base de DL1r.

En ce qui concerne les systématiques, la plupart d'entre elles sont héritées du tagger MV2c10. Cependant, les systématiques "Fraction de Fragmentation des B-hadrons" et "extrapolation semi-leptonique" ont été redérivées.

En ce qui concerne $HH \rightarrow b\bar{b}\tau^+\tau^-$, mon travail a été concentré principalement sur l'optimisation du BDT et les études d'ajustement du canal LepHad pour améliorer les attentes μ_{HH} , μ_{ggF} , μ_{VBF} , κ_λ , et κ_{2V} . Les BDT ont été entraînés dans les régions de signal ggF low- m_{HH} , ggF high- m_{HH} , et VBF dédiées pour séparer le signal des bruits de fond. J'ai également mis en œuvre le BDT ggF/VBF pour définir les régions de signal enrichies en ggF et en VBF. La région de signal VBF a été introduite dans cette analyse. Je contribue également de manière significative au logiciel d'analyse.

La partie FCC, elle a été principalement réalisée par moi, Gregorio Bernardi et Jan Eysermans. Cette analyse a été construite de zéro par moi sous la supervision de Gregorio, ce qui signifie que j'ai travaillé sur tous les aspects depuis les étapes initiales jusqu'à maintenant.

Table of Contents

Abstract	3
Résumé	5
Résumé étendu	7
Table of Contents	11
Introduction	17
I Standard Model and Higgs Physics	19
1 Theoretical framework	21
1.1 Standard Model in a nutshell	22
1.1.1 Electroweak sector	23
1.1.2 Sector of Strong Interactions	26
1.2 Higgs Physics	27
1.2.1 The Brout-Englert-Higgs mechanism	27
1.2.2 The fermion Yukawa couplings	29
1.2.3 Higgs boson production mechanism at the LHC	30
1.2.4 Higgs decay mode	31
1.3 Di-Higgs theory framework	33
1.3.1 Di-Higgs mechanism	33
1.3.2 SM Higgs boson pair production at the LHC	34
1.3.3 Di-Higgs decay channels	34
1.3.4 Kappa Parameters	35
1.3.5 HH cross-section Parametrisation	36
1.3.5.1 ggF HH parametrisation	36
1.3.5.2 VBF HH parametrisation	38
II Higgs Physics at ATLAS	41
2 The LHC and the ATLAS detector	43
2.1 The Large Hadron Collider	44
2.1.1 Luminosity at LHC	45
2.1.2 Production and Acceleration of Particles at LHC	47
2.1.3 Main Experiments on the LHC Ring	48
2.2 An Overview of the ATLAS Detector	49
2.2.1 ATLAS Coordinate System and Associated Definitions	51
2.2.2 The ATLAS Magnet Systems	52
2.2.3 The ATLAS Inner Detector	53
2.2.3.1 Pixel	55
2.2.3.2 SemiConductor Tracker	56
2.2.3.3 Transition Radiation Tracker	56
2.2.4 ATLAS Calorimeters	56
2.2.4.1 Electromagnetic Calorimeter	57

2.2.4.2	Hadronic Calorimeter	58
2.2.5	ATLAS Muon Spectrometer	60
2.2.6	ATLAS Data Trigger and Acquisition System	60
3	Object Reconstruction and Identification within the ATLAS Detector	63
3.1	Reconstruction of Primary Vertices and Particle Tracks	65
3.2	Electron in the ATLAS Detector	68
3.2.1	Electron Reconstruction	68
3.2.2	Criteria for Electron Identification and Isolation	70
3.2.3	Calibration of Electron Data	72
3.3	Muon at ATLAS	73
3.3.1	Muon Reconstruction	74
3.3.2	Criteria for the Isolation and Identification of Muon Candidates	74
3.4	Tau Leptons at ATLAS	77
3.5	Jets in the ATLAS Detector	78
3.5.1	anti- k_t Algorithm for Jet Reconstruction	78
3.5.2	Particle Flow and EMTopo Reconstruction Approaches	80
3.5.3	Flavour Tagging	81
3.6	Missing Transverse Energy	84
4	Measuring the b-jet identification efficiency with the p_T^{rel} method	87
4.1	Introduction	89
4.2	Data used for the Calibration	90
4.2.1	Trigger Criteria	90
4.2.2	Event Simulation Methodology	90
4.3	Event and Object Selection	92
4.3.1	Jet Selection Criteria	92
4.3.2	Muon Selection Criteria	92
4.3.3	Event Selection Criteria	93
4.4	The p_T^{rel} Methodology	93
4.4.1	Template construction	94
4.4.1.1	b -jet template	94
4.4.1.2	c -jet template	95
4.4.1.3	$light$ -jet template	95
4.4.1.4	Template Fit	96
4.5	Extrapolation to inclusive b -jets	98
4.6	Systematic Uncertainties	102
4.6.1	Experimental Uncertainties	103
4.6.1.1	Muon reconstruction and identification	103
4.6.1.2	Lepton momentum scale and resolution	103
4.6.1.3	Jet vertex tagger efficiency	103
4.6.1.4	Jet energy scale	103
4.6.1.5	Jet energy resolution	104
4.6.2	Modelling Uncertainties	104
4.6.2.1	Muon Origin	104
4.6.2.2	Muon p^*	104
4.6.2.3	Fake muons	105
4.6.2.4	Gluon Splitting	105
4.6.2.5	B-hadrons Fragmentation Fraction	106
4.6.2.6	Semileptonic-to-inclusive extrapolation	106
4.7	Results	107

5	Search for di-Higgs production in the $b\bar{b}\tau^+\tau^-$ final state	111
5.1	Data and Monte Carlo samples	113
5.1.1	Signal samples	114
5.2	Event Selection	118
5.2.1	Trigger selection	119
5.2.1.1	$\tau_{\text{lep}}\tau_{\text{had}}$	119
5.2.1.2	$\tau_{\text{had}}\tau_{\text{had}}$	120
5.2.2	Event selection	121
5.2.2.1	$\tau_{\text{lep}}\tau_{\text{had}}$	121
5.2.2.2	$\tau_{\text{had}}\tau_{\text{had}}$	122
5.2.3	Event categorisation	123
5.2.4	$Z + HF$ control region	129
5.3	Background modelling	133
5.4	Multi-Variables Analysis	133
5.4.1	Optimisation Strategy	134
5.4.1.1	Input Variables Optimisation	134
5.4.1.2	Hyperparameters Optimisation	135
5.4.2	ggF/VBF BDT	136
5.4.2.1	Selection of input variables	136
5.4.2.2	Optimization of hyperparameters	137
5.4.2.3	Selection of working point	143
5.4.3	Signal Region BDT	145
5.4.3.1	Optimization of hyperparameters	145
5.4.3.2	Input variable selection	146
5.4.3.3	BDT score distributions in different folds	146
5.5	Statistical interpretation	153
5.5.1	Statistical model	153
5.5.2	Fit setup	154
5.5.3	Binning	155
5.5.4	Blinding strategy	156
5.6	Results	157
5.6.1	Fit results	157
5.6.1.1	$\tau_{\text{had}}\tau_{\text{had}}$	157
5.6.1.2	$\tau_{\text{lep}}\tau_{\text{had}}$	165
5.6.1.3	Combined fit	174
5.6.2	Limits and scans	181
5.6.2.1	$\tau_{\text{had}}\tau_{\text{had}}$	181
5.6.2.2	$\tau_{\text{lep}}\tau_{\text{had}}$	181
5.6.2.3	Combined Limits	183
5.7	Conclusion	186

III Higgs Physics beyond LHC 189

6	The Future Circular Collider	191
6.1	Introduction of FCC project	192
6.1.1	Future Colliders	192
6.1.2	The Future Circular Collider	193
6.2	FCC Integrated program	194
6.2.1	FCC-ee	194
6.2.2	FCC-hh	194
6.3	Higgs Physics at Future Circular Colliders	194

6.3.1	Higgs-Electron Yukawa coupling	195
6.3.2	Trilinear Higgs self-coupling	195
7	Higgs mass and cross-section measurements at the Future Circular Collider	197
7.1	Introduction to ZH recoil analysis	199
7.2	"Recoil mass" method	200
7.3	IDEA	202
7.3.1	Muon and electron performance	203
7.4	Monte-Carlo samples	203
7.4.1	Event generators	204
7.5	Event Selection	208
7.5.1	Preselection Requirements	208
7.5.2	Kinematic Requirements	208
7.5.3	Basic and Baseline selections	209
7.5.4	Event yields and requirement flow	209
7.6	Higgs mass measurement	212
7.6.1	Event categorization	212
7.6.2	Signal modeling	213
7.6.3	Background modeling	215
7.6.4	Results	215
7.6.5	Auxiliary fit configurations	217
7.7	ZH Cross-section measurement	219
7.7.1	Boosted Decision Tree	221
7.7.1.1	Training samples	221
7.7.1.2	Input variables	222
7.7.1.3	Hyper-parameters	223
7.7.1.4	BDT performance	223
7.7.2	Fitting Strategy	227
7.7.2.1	Fit on recoil mass distribution (m_{recoil})	227
7.7.2.2	Fit on BDT score distribution	229
7.7.3	Conclusion	231
7.8	Sources of systematic uncertainties	231
7.8.1	Beam Energy Spread (BES)	232
7.8.2	Initial State Radiation (ISR)	233
7.8.2.1	ISR treatment in WHIZARD	233
7.8.2.2	Comparison with KKMC	234
7.8.3	Center-of-mass (COM)	235
7.8.4	Lepton momentum scale (LEPSCALE)	236
7.8.5	Lepton momentum resolution (LEPRES)	237
7.8.6	Final State Radiation (FSR)	237
7.8.7	Signal modeling (SIGM)	237
7.8.8	Background modeling (BKGM)	237
7.9	Experimental requirements	237
7.10	Conclusion	238
	Conclusion	241
	Appendix	245
A	Spurious Signal Test for di-Higgs production in the $b\bar{b}\gamma\gamma$ final state	245
A.1	Smoothing the di-photon background	245
A.1.1	Gaussian Process Regression	246

A.1.1.1	1 GeV and 4 GeV binning result	246
A.1.2	4-to-1GeV refill method (or equivalently RGFR method)	246
A.1.2.1	Fit Function	246
A.1.2.2	Histogram refilling	250
A.1.2.3	Final RGFR (4-to-1 GeV) smoothing strategy	251
A.2	Spurious Signal Test	253
A.2.1	Test of Original Data	253
A.2.2	Test of the distribution obtained with the RGFR (4-to-1 GeV) method	253
A.3	Conclusion	257
B	Background studies for di-Higgs production in the $b\bar{b}\tau^+\tau^-$ final state	259
B.1	Background modelling	259
B.1.1	Fake- τ backgrounds in the $\tau_{\text{lep}}\tau_{\text{had}}$ channel	259
B.1.2	Multijet with fake- τ in the $\tau_{\text{had}}\tau_{\text{had}}$ channel	266
B.1.3	$t\bar{t}$ with fake- τ_{had} in the $\tau_{\text{had}}\tau_{\text{had}}$ channel with scale-factor method	271
B.2	Complementary Results	272
B.2.1	Limits and scans compare with the previous results	272
B.2.1.1	$\tau_{\text{had}}\tau_{\text{had}}$: Comparison with previous analysis	272
B.2.1.2	$\tau_{\text{lep}}\tau_{\text{had}}$: Comparison with previous analysis	273
B.2.1.3	Combined: Comparison with previous analysis	274
B.2.2	Additional fit checks	275
B.2.2.1	Alternative post-fit plots for the HadHad channel	275
B.2.2.2	Alternative post-fit plots for the LepHad channel	279
B.2.2.3	Alternative post-fit plots for the Combined fit	280
B.2.3	Compatibility tests	280
B.2.3.1	Compatibility across different channels	281
B.2.3.2	Compatibility across different analysis regions and channels	281
B.2.3.3	Compatibility with previous Run-2 result	282
C	Detailed points of the Higgs analyses at the Future Circular Collider	285
C.1	Event selection plots	285
C.2	Recoil mass fits	288
C.3	BDT input variables	289
C.4	BDT hyper-parameters	292
	Bibliography	293
	List of Figures	303
	List of Tables	315
	Acknowledgement	319

Introduction

Following the discovery of the Higgs boson in 2012 by the ATLAS [1] and CMS [2] collaborations at the LHC, precision measurements of the Higgs and its couplings have become paramount. These measurements serve a dual purpose: they validate the predictions of the Standard Model (SM) and provide avenues to explore potential new physics Beyond the Standard Model (BSM).

Simultaneously, the LHC has been enhancing its potential to probe new physics by increasing both the centre-of-mass energy of its collisions and the intensity of its proton beams, thereby achieving higher integrated luminosities.

In anticipation of future advancements, the High Energy Physics (HEP) community is in the planning stages for the next generation of colliders, envisioned first as a Higgs factory. Among these, the Future Circular Collider (FCC) proposed by CERN is one of the most promising projects.

My contributions include work on Higgs Physics studies at both ATLAS and the FCC.

Chapter 1 provides a concise introduction to the Standard Model of particle physics, the Higgs mechanism, di-Higgs production, decay modes, the kappa framework, and the κ_λ and κ_{2V} parametrizations.

In Chapters 2, 3, 4, and 5, the physics of the ATLAS experiment is discussed.

Chapter 2 details the Large Hadron Collider (LHC) and the ATLAS detector.

Chapter 3 outlines the reconstruction of the physics objects utilized in the ATLAS analysis.

Chapter 4 introduces the p_T^{rel} method, which employs muon-in-jet events to calibrate the b -tagging algorithm using both MV2c10 and DL1r taggers. The DL1r tagger is introduced in this method and is applied to Run 2 data. A comparison with the $t\bar{t}$ based calibration, the primary calibration method at ATLAS, is also presented.

Chapter 5 discusses the analysis of the $HH \rightarrow b\bar{b}\tau^+\tau^-$ channel, emphasizing the measurement of the HH signal strength, Higgs self-coupling (κ_λ), and the $HHVV$ coupling (κ_{2V}), where $Z = W, Z$. A dedicated VBF category is introduced to enhance κ_{2V} sensitivity.

The Future Circular Collider (FCC) project is the focus of Chapters 6 and 7.

Chapter 6 offers an overview of the FCC project, including its timeline and both the electron-positron and proton-proton working phases. Other important physics topics at the FCC are also highlighted.

Chapter 7 describes my contributions to the Higgs mass and cross-section measurements at the FCC, particularly in the $e^+e^- \rightarrow ZH \rightarrow \ell^+\ell^-$ channel. The recoil mass technique is employed to extract the Higgs mass, and a BDT is trained to insure the model-independent of ZH cross-section analysis.

A summary of the content of the thesis will be given in the end and offers insights into future prospects in the field.

Part I

Standard Model and Higgs Physics

Theoretical framework

1.1	Standard Model in a nutshell	22
1.1.1	Electroweak sector	23
1.1.2	Sector of Strong Interactions	26
1.2	Higgs Physics	27
1.2.1	The Brout-Englert-Higgs mechanism	27
1.2.2	The fermion Yukawa couplings	29
1.2.3	Higgs boson production mechanism at the LHC	30
1.2.4	Higgs decay mode	31
1.3	Di-Higgs theory framework	33
1.3.1	Di-Higgs mechanism	33
1.3.2	SM Higgs boson pair production at the LHC	34
1.3.3	Di-Higgs decay channels	34
1.3.4	Kappa Parameters	35
1.3.5	HH cross-section Parametrisation	36
1.3.5.1	ggF HH parametrisation	36
1.3.5.2	VBF HH parametrisation	38

This chapter is dedicated to the theoretical framework of the thesis. The Standard Model (SM) of particle physics is introduced in Section 1.1. The Higgs boson, which is the focus of this thesis, is discussed in Section 1.2. The di-Higgs production mechanism is presented in Section 1.3.

1.1 Standard Model in a nutshell

The Standard Model (SM) is considered a landmark achievement in the field of particle physics, providing a comprehensive understanding of fundamental particles and their interactions. Since its inception, the SM has been the subject for multiple Nobel Prizes, awarded to those who have made significant contributions to its establishment.

In 1967, a revolutionary perspective on leptons was introduced by Steven Weinberg in his article titled "A Model of Leptons" [15]. This seminal work laid the foundation for the theory of electroweak unification. As a result, the 1979 Nobel Prize in Physics was equally awarded to Steven Weinberg, Abdus Salam, and Sheldon Lee Glashow for their pioneering work in this field.

A significant milestone was reached in 1983 when the discovery of W and Z bosons was announced by CERN, based on data from the Underground Area 1 (UA1) and confirmed by the Underground Area 2 (UA2) experiments. Carlo Rubbia and Simon van der Meer, who led the accelerator team and UA1 experiment, were awarded the Nobel Prize in Physics in 1984.

In 1964, the Ω^- baryon, composed of three strange quarks with parallel spins, was discovered [16]. This configuration, based on the known quantum status, which would typically be forbidden by the Pauli exclusion principle, suggested that quarks must possess an additional SU(3) degree of freedom to form an anti-symmetry state. This additional degree of freedom was incorporated into the Quantum Chromodynamics (QCD) theory by Harald Fritzsch, Heinrich Leutwyler, and Murray Gell-Mann in 1973 [17].

The theoretical discovery of the Higgs mechanism by Peter Higgs, François Englert and Robert Brout in 1964, for which they were awarded the Nobel Prize in 2013, has been instrumental in enhancing our understanding of the origin of mass of fundamental particles.

The foundation of the Higgs mechanism is first introduced in [18–22]. The existence of the Higgs mechanism was confirmed by joint data from the ATLAS [1] and CMS [2] experiments at the Large Hadron Collider (LHC) in 2012.

The SM, depicted in Figure 1.1, is a theory of $SU(3) \times SU(2) \times U(1)$ symmetry, where $SU(2) \times U(1)$ constitutes the electroweak part and SU(3) describes the strong interaction. These aspects will be discussed in Subsection 1.1.1 and 1.1.2 respectively.

In the electroweak (EW) unification, three families of fermions, electron (e), muon (μ), and tau (τ), along with their corresponding neutrinos, are introduced. It is a chiral theory, implying that particles behave differently based on their chirality. The left-handed neutrino and charged lepton form an isospin doublet $(\nu_e, e)_L$, while the right-handed charged lepton is a singlet e_R . In EW, there are four bosons, three of which are massive bosons (W^+ , W^- and Z), while the photon (γ) is massless. The Higgs boson, described in the next section 1.2, is the only scalar particle in the SM. It gives mass to all matter (fermions) and W^\pm/Z gauge bosons through spontaneous symmetry breaking. Three families of quarks, sorted by flavor, each forming an isospin doublet (u, d) , (c, s) , and (t, b) , also participate in EW interactions.

The strong interaction is based on a SU(3) symmetry, with quarks assigned three different color states (red, blue, and green), and eight massless gluons (generators of SU(3)) mediating the interaction between colors.

The Lagrangian of the SM can be decomposed into the Electroweak (EW), Quantum Chromodynamics (QCD), and Higgs terms:

$$\mathcal{L}_{\text{SM}} = \mathcal{L}_{\text{EW}} + \mathcal{L}_{\text{QCD}} + \mathcal{L}_{\text{Higgs}} \quad (1.1.1)$$

The \mathcal{L}_{EW} term describes the electromagnetic and weak forces. It includes the dynamics of the W^\pm ,

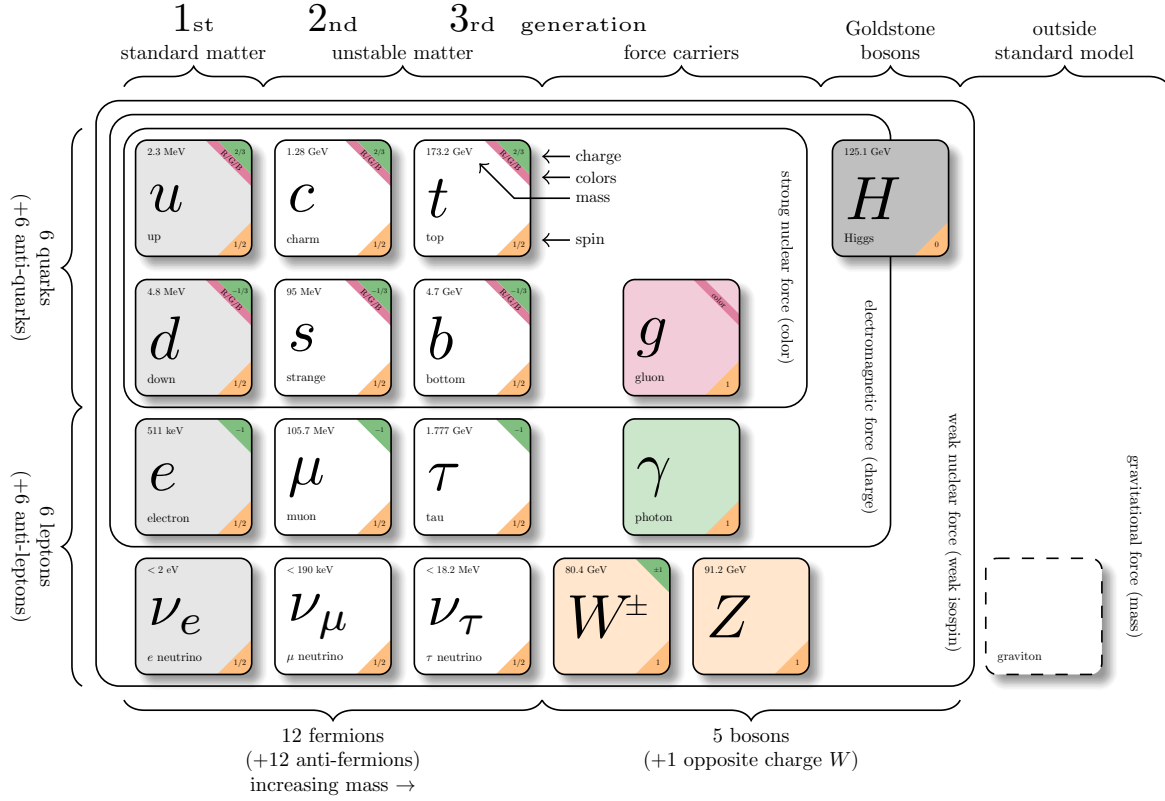


Figure 1.1: Standard Model from: texample.net/tikz/examples/model-physics/

Z , and γ gauge bosons, as well as their interactions with the fermions (quarks and leptons).

The \mathcal{L}_{QCD} term describes the strong force, including the dynamics of the gluons and their interactions with the quarks.

The $\mathcal{L}_{\text{Higgs}}$ term describes the dynamics of the Higgs boson and its interactions with the other particles. This term is responsible for generating the masses of the fermions and the W^\pm and Z gauge bosons through the Higgs mechanism.

1.1.1 Electroweak sector

The formalization of electroweak unification, is the theory explaining the interplay between electromagnetic and weak interactions, and could be derived from the work of Sheldon Glashow, Steven Weinberg, and Abdus Salam [15, 23, 24]. This theory, frequently referenced as the GWS model, pivots around the $SU(2)_L \times U(1)_Y$ local gauge symmetry.

Within the context of electroweak unification, two categories of weak interactions are identified: charged current and neutral current interactions. The charged W^\pm bosons mediate charged current interactions, which include processes such as β decays. Conversely, the neutral Z boson and photon (γ) is the mediator of neutral current interactions.

The flavor-changing processes are exclusive to charged current interactions, facilitated by W^\pm bosons. This arises from the discrepancy between the weak interaction eigenstates, which dictate the strengths of interactions, and the mass eigenstates, which govern the behavior of particles during free propagation. The Cabibbo-Kobayashi-Maskawa (CKM) matrix, Ref. [25, 26], for quarks and the Pontecorvo-Maki-Nakagawa-Sakata (PMNS) matrix, Ref. [27–29], for leptons provide the

transformation between these two sets of states.

Contrastingly, the Glashow-Iliopoulos-Maiani (GIM) mechanism, Ref. [30], in the Standard Model significantly suppresses flavor-changing neutral currents (FCNCs). This mechanism ensures the conservation of flavor in neutral current interactions, which are mediated by the Z boson.

Observations from numerous experiments have established a profound connection between the weak interaction and the chirality of particles. Particles are differentiated into left- and right-handed categories. For massless (or ultra-relativistic i.e., $E \gg m$) particles, the notion of chirality converges with helicity - the sign of the projection of the spin vector onto the momentum vector of the particle. The weak charged current interaction, involving a W boson, has been found to connect left-handed particles with right-handed antiparticles. The assemblage of left-handed fermions forms weak isospin 1/2 doublets, such as:

$$\begin{pmatrix} \nu_e \\ e^- \end{pmatrix}_L, \quad \begin{pmatrix} u \\ d \end{pmatrix}_L, \quad (1.1.2)$$

By contrast, right-handed particles emerge as singlets.

$$(e^-)_R, \quad (1.1.3)$$

The weak interaction mechanic has been observed to maintain the weak isospin (T) and the weak hypercharge (Y). These quantities are linked to the electric charge (Q) via the Gell-Mann-Nishijima formula [31, 32]:

$$Y = 2(Q - T_3), \quad (1.1.4)$$

where T_3 denotes the third component of the weak isospin.

In Noether's theorem, the existence of two gauge symmetries in the Lagrangian integral imply the conservation of the quantities Y and T to the electroweak unification [33, 34]. The $SU(2)$ transformation, underpinning the weak charged current interaction, involves a weak isospin rotation given by

$$\psi(x) \rightarrow \psi'(x) = e^{ig\alpha(x) \cdot \mathbf{T}} \psi(x), \quad (1.1.5)$$

In this formulation, g represents the W boson coupling constant, $\alpha(x) = (\alpha_1(x), \alpha_2(x), \alpha_3(x))$ is a triad of real parameters. And, in the fundamental representation, $\mathbf{T} = \boldsymbol{\sigma}/2$, where $\boldsymbol{\sigma} = (\sigma_1, \sigma_2, \sigma_3)$ symbolizes the vector of Pauli matrices. The requirement of local gauge invariance mandates the introduction of three gauge fields, W_μ^k , with $k = 1, 2, 3$, symbolizing three gauge bosons, labeled as W^1 , W^2 , and W^3 . Owing to the fact that the three generators (\mathbf{T}) of $SU(2)$ are 2×2 matrices, the wavefunction ψ should incorporate two components. Hence, $\psi(x)$ becomes a complex scalar of $SU(2)$, typically termed as the weak isospin doublet

$$\psi(x) = \begin{pmatrix} \psi_1(x) \\ \psi_2(x) \end{pmatrix}, \quad (1.1.6)$$

where both $(\psi_1(x), \psi_2(x))$ are elements of \mathbb{C}^2 .

Furthermore, the weak charged current interaction's unique property of coupling different fermions, arising from observed flavour violation, necessitates that the weak isospin doublet be composed of different flavours. These flavours differ by a single unit in terms of electric charge, given that the interaction mediator is a W^\pm boson. This leads to the instance of $\psi(x) = (\nu_e(x), e^-(x))$ and implies that the gauge transformation from Equation (1.1.5) should be confined to left-handed particles and right-handed antiparticles to remain in concordance with experimental observations. Hence, the

notation $SU(2)_L$ is employed, given that right-handed particles and left-handed antiparticles are embedded in singlets with $T = 0$, meaning they are unaffected by the $SU(2)$ transformation and do not couple to the W boson.

The charged current can be represented as a linear combination of W_μ^1 and W_μ^2 , which are associated with the W^\pm bosons. However, the Z boson, which couples to both left- and right-handed particles, cannot be equivalent to the W^3 boson of the $SU(2)_L$ local gauge symmetry. The same claim holds true for the photon. The GSW model substitutes the $U(1)$ gauge symmetry from QED with the $U(1)_Y$ symmetry, incorporating the hypercharge transformation represented by a local phase change:

$$\psi(x) \rightarrow \psi'(x) = e^{i\beta(x)Y} \psi(x), \quad (1.1.7)$$

where $\beta(x)$ is a real parameter. A field denoted as B_μ is associated with the $U(1)_Y$ symmetry.

The resultant Lagrangian of the EW interaction, in the context of massless particles, is as follows:

$$\mathcal{L}_{EW} = i\bar{\psi}\not{D}\psi - \frac{1}{4}W_{\mu\nu}^a W_a^{\mu\nu} - \frac{1}{4}B_{\mu\nu}B^{\mu\nu}, \quad (1.1.8)$$

where

$$D_\mu = \partial_\mu + igW_\mu^a T^a + \frac{i}{2}g'B_\mu Y, \quad (1.1.9)$$

$$W_{\mu\nu}^a = \partial_\mu W_\nu^a - \partial_\nu W_\mu^a - g\varepsilon^{abc}W_\mu^b W_\nu^c, \quad (1.1.10)$$

$$B_{\mu\nu} = \partial_\mu B_\nu - \partial_\nu B_\mu, \quad (1.1.11)$$

ε^{abc} symbolizes the totally antisymmetric tensor and $a = 1, 2, 3$.

The collective impact of $SU(2)_L \times U(1)_Y$ suggests that the four gauge fields W_μ^1 , W_μ^2 , W_μ^3 , and B_μ characterize the electroweak interaction. One can demonstrate that a rotation of these fields, as exhibited in Equation (1.1.12), facilitates an electromagnetic-like interaction for the fermions. This interaction influences both left-handed and right-handed spinors, with the coupling proportional to the charge with the A_μ field. Consequently, this field is interpreted as the photon. The W^\pm bosons are associated with charged currents that involve only left-handed particles. The Z bosons, associated with neutral currents couples to both left-handed and right-handed particles. In this theoretical model, all four mediator bosons are massless.

$$\begin{pmatrix} W_\mu^+ \\ W_\mu^- \\ Z_\mu \\ A_\mu \end{pmatrix} = \begin{pmatrix} 1/\sqrt{2} & -1/\sqrt{2} & 0 & 0 \\ 1/\sqrt{2} & 1/\sqrt{2} & 0 & 0 \\ 0 & 0 & \cos(\theta_W) & -\sin(\theta_W) \\ 0 & 0 & \sin(\theta_W) & \cos(\theta_W) \end{pmatrix} \begin{pmatrix} W_\mu^1 \\ W_\mu^2 \\ W_\mu^3 \\ B_\mu \end{pmatrix}, \quad (1.1.12)$$

Here, θ_W signifies the weak mixing angle, also referred to as the Weinberg angle, and is measured to be approximately $\theta_W \approx 30^\circ$ [35]. It relates to the electromagnetic coupling constant (e , the charge of the electron) via the equation:

$$e = g \sin(\theta_W) = g' \cos(\theta_W). \quad (1.1.13)$$

In this equation, g and g' denote the coupling constants of the $SU(2)_L$ and $U(1)_Y$ local gauge transformations, respectively.

The electroweak unification retains its validity at high energies where the B_μ and W_μ^a bosons can be considered massless, as otherwise the theory's renormalization would be compromised [34]. However, at low energy, the electroweak symmetry undergoes spontaneous breaking, resulting in a

disconnection between the weak and electromagnetic forces. The carriers of the weak interaction, Z and W bosons, acquire masses while the photon, the electromagnetic carrier, remains massless. This phenomenon is termed the Higgs mechanism, detailed in the Section 1.2.

1.1.2 Sector of Strong Interactions

Quantum chromodynamics (QCD) is a non-abelian gauge theory that provides a detailed account of the strong interaction. Developed in the aftermath of the quark model, it is built upon an $SU(3)$ gauge symmetry associated with the conservation of colour charge (red, green, blue) during strong interaction processes. The associated local $SU(3)_C$ phase transformation is given by [34, 36]

$$\psi(x) \rightarrow \psi'(x) = e^{ig_S \alpha(x) \cdot \mathbf{T}} \psi(x), \quad (1.1.14)$$

where g_S is the strong interaction coupling constant, \mathbf{T} are the eight generators of the $SU(3)$ symmetry group associated with the Gell-Mann matrices by $T^a = \lambda^a/2$ ($a = 1, \dots, 8$) in the fundamental representation, and $\alpha^a(x)$ are eight functions of the spacetime coordinate x . Given that $SU(3)$ is represented by 3×3 matrices, the wavefunction ψ now incorporates the 3 colour charge degrees of freedom. The transformation from Equation (1.1.14) can be seen as a rotation in colour space, where the axis of rotation varies for each point in spacetime.

The QCD Lagrangian for quarks with mass m_q can be expressed as follows:

$$\mathcal{L}_{\text{QCD}} = -\frac{1}{4} G_{\mu\nu}^a G_a^{\mu\nu} + \sum_q \bar{\psi}_{qj} (i\not{D} - m_q \delta_{jk}) \psi_{qk}, \quad (1.1.15)$$

with

$$D_\mu = \partial_\mu \delta_{jk} + ig_S (T_a^a)_{jk}, \quad (1.1.16)$$

$$G_{\mu\nu}^a = \partial_\mu A_\nu^a - \partial_\nu A_\mu^a + g_S f^{abc} A_\mu^b A_\nu^c, \quad (1.1.17)$$

where ψ_{qk} is the Dirac spinor associated with the quark q , k represents its colour charge, δ_{jk} enforces colour charge conservation during free quark propagation (implied in Equation (1.1.15)), D_μ is the covariant derivative, A^a are the gluon fields, and f^{abc} symbolizes the structure constant of the $SU(3)$ group, with a, b, c representing different colour states of the gluons. Consequently, only quarks possessing a colour charge can interact through the strong force via the exchange of gluons.

The term $G_{\mu\nu}^a G_a^{\mu\nu}$ is the kinetic term of gluons. When expanded with the definition of $G_{\mu\nu}^a$ from Equation (1.1.17), three terms materialize in the $G_{\mu\nu}^a G_a^{\mu\nu}$ product. These correspond to the free propagation of gluons, the three-gluon self-interaction vertex, and the four-gluon interaction vertex (trilinear and quartic self interactions).

Therefore, the eight gluons are massless particles carrying a colour charge. At short distances (equivalently, high energies $E \gg \Lambda_{\text{QCD}} \approx 200 \text{ MeV}$), quark-gluon interactions diminish, allowing the particles to be considered asymptotically free: this is the perturbative regime. In this regime, predictions from the QCD Lagrangian in Equation (1.1.15) can be handled with a perturbative approach, referred to as perturbative QCD (pQCD). However, at lower energies, parton interactions significantly increase, precluding the use of pQCD as the coupling becomes substantial: this phenomenon is termed quark and gluon confinement. Consequently, quarks are never observed in isolation but are confined within hadrons (either mesons or baryons composed of two or three valence quarks and/or antiquarks), forming colourless combinations. Here, the potential energy between quarks is proportional to their separation distance. As this distance grows, the potential energy eventually matches the quark-antiquark (and gluons) production threshold, triggering the creation of a pair and the formation of new hadrons via combination with initial quarks. This combination process, referred to as hadronization, explains why jets, rather than single hadron particles, are observed at colliders, as high-energy hadrons fragment into less energetic hadrons, creating a collimated stream.

1.2 Higgs Physics

The validity of the electroweak theory, as well as the electroweak Lagrangian depicted in Equation (1.1.8), rests on the assumption of massless mediator particles. This condition maintains the gauge invariance; any violation of it would disrupt the theory's renormalization. Hence, the masses of the W^\pm and Z bosons necessitate an alternative mechanism for explanation. Analogously, the measured masses of the remaining elementary particles, namely all fermions, are inconsistent with the gauge invariance property of the electroweak Lagrangian.

One theoretical proposition to address this challenge came in the form of the *Brout-Englert-Higgs mechanism* [18–22], proposed in 1964. This theory advocates for the spontaneous breaking of the $SU(3)_C \times SU(2)_L \times U(1)_Y$ symmetry group, transitioning it into $SU(3)_C \times U(1)_Q$. This transition imparts mass to the weak bosons, while the photon, associated with the $U(1)_Q$ group symmetry, retains its massless characteristic. Additionally, the Brout-Englert-Higgs mechanism explains the origin of fermion masses through the Yukawa interaction between the fermions and the Higgs field. This theory has been subjected to experimental validation and ongoing study at CERN's Large Hadron Collider (LHC). Here, the ATLAS and CMS experiments confirmed the existence of a particle with a mass of 125 GeV, exhibiting properties consistent with the expected Higgs boson, thereby substantiating the credibility of the Higgs mechanism theory.

1.2.1 The Brout-Englert-Higgs mechanism

Incorporating the Brout-Englert-Higgs (BEH) mechanism into the Standard Model (SM) requires the inclusion of a scalar Higgs term into the SM Lagrangian. This term is written as:

$$\mathcal{L}_{\text{Higgs}} = (D^\mu \phi)^\dagger (D_\mu \phi) - V(\phi), \quad (1.2.1)$$

Here, ϕ refers to a complex scalar (Higgs) field of 2-dimensions which can be mathematically expressed as:

$$\phi = \begin{pmatrix} \phi^+ \\ \phi_0 \end{pmatrix} = \frac{1}{\sqrt{2}} \begin{pmatrix} \phi_1 + i\phi_2 \\ \phi_3 + i\phi_4 \end{pmatrix}, \quad (1.2.2)$$

The term $(D^\mu \phi)^\dagger (D_\mu \phi)$ is the kinetic element of the Lagrangian and the D_μ denotes the covariant derivative defined in Equation (1.1.9). Furthermore, $V(\phi)$ represents the Higgs potential and it can be defined as:

$$V(\phi) = \mu^2 \phi^\dagger \phi + \lambda (\phi^\dagger \phi)^2 = \mu^2 |\phi|^2 + \lambda |\phi|^4, \quad (1.2.3)$$

where two constant real numbers are denoted by μ^2 and λ (μ can be complex). Here, μ^2 acts as a mass-type term while λ describes the quartic self-interaction among the scalar fields.

For the field ϕ , the lowest energy state corresponds to the vacuum state which is also the minimum of the potential $V(\phi)$. To ensure an energetically bounded from below theory, in other words, a finite minimum for the potential, λ must hold a positive value while μ^2 can be either positive or negative, affecting the potential's shape as depicted in Figure 1.2. If $\mu^2 \geq 0$, the potential $V(\phi)$ possesses a single minimum at $\phi = 0$. However, if $\mu^2 < 0$, $\phi = 0$ is not a minimum and the potential has an infinite number of minima corresponding to:

$$|\phi|^2 = -\frac{\mu^2}{2\lambda} = \frac{v^2}{2}, \quad (1.2.4)$$

In the above equation, v refers to the vacuum expectation value, or denoted as vev .

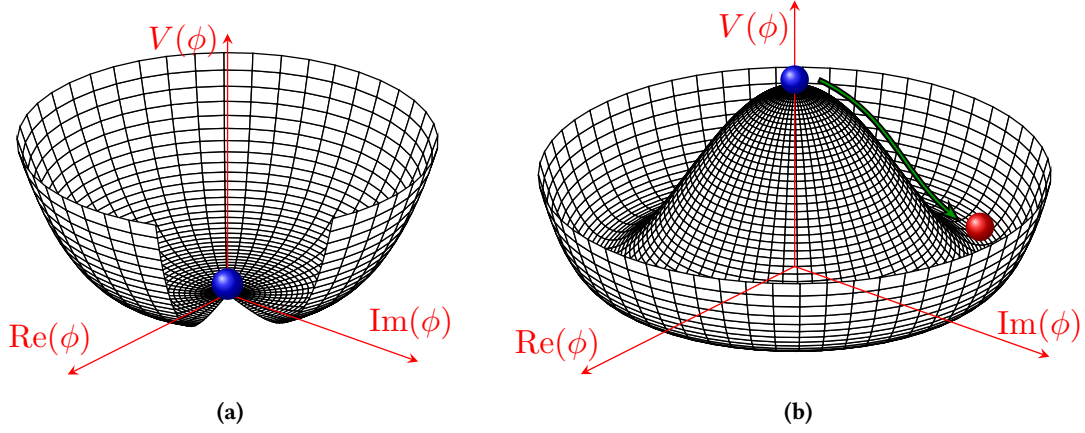


Figure 1.2: Higgs potential $V(\phi) = \mu^2 |\phi|^2 + \lambda |\phi|^4$ with $\lambda > 0$ and either (a) $\mu^2 \geq 0$ or (b) $\mu^2 < 0$ (Adapted from Refs. [37, 38]).

The following basis can express the chosen vacuum state ϕ_0 :

$$\phi_0 = \frac{1}{\sqrt{2}} \begin{pmatrix} 0 \\ v \end{pmatrix}. \quad (1.2.5)$$

The Higgs field around its ground state can be expanded as:

$$\phi(x) = \frac{1}{\sqrt{2}} \begin{pmatrix} 0 \\ v + h(x) \end{pmatrix}, \quad (1.2.6)$$

where $h(x)$ is a real scalar field.

Upon inserting the specified field into the kinetic term from Equation (1.2.1), kinetic terms that are linked to the W , Z bosons and photons are identified. These kinetic terms facilitate the derivation of their corresponding masses as posited by the BEH mechanism, resulting in the following relationships [39]:

$$m_W = \frac{gv}{2}, \quad m_Z = \frac{\sqrt{g'^2 + g^2}v}{2}, \quad m_\gamma = 0, \quad \frac{m_W}{m_Z} = \cos(\theta_W), \quad (1.2.7)$$

where $v \approx 246 \text{ GeV}$ is determined through muon decays. The anticipated absence of a kinetic term for the field A_μ is indeed observed, corresponding to the photon's predicted masslessness.

Furthermore, remaining terms in the expansion of the covariant derivative that are dependent on the Higgs scalar field $h(x)$ outline the interaction between the Higgs and gauge bosons:

$$\mathcal{L}_{V VH} = \frac{2m_W^2}{v} W_\mu^+ W^{-\mu} h(x) + \frac{2m_Z^2}{v} Z_\mu Z^\mu h(x), \quad (1.2.8)$$

$$\mathcal{L}_{V V H H} = \frac{2m_W^2}{v^2} W_\mu^+ W^{-\mu} h^2(x) + \frac{2m_Z^2}{v^2} Z_\mu Z^\mu h^2(x). \quad (1.2.9)$$

Furthering the analysis by injecting the field expansion into the potential $V(\phi)$, the Higgs Lagrangian can be reframed to consider only terms involving h :

$$\mathcal{L}_H = \mu^2 h^2 - \lambda v h^3 - \frac{\lambda}{4} h^4 = \frac{1}{2} m_H^2 h^2 - \sqrt{\frac{\lambda}{2}} m_H h^3 - \frac{\lambda}{4} h^4, \quad (1.2.10)$$

From which the Higgs mass can be written as

$$m_H = \sqrt{2}|\mu| = \sqrt{2\lambda}v. \quad (1.2.11)$$

The mass of the Higgs boson is neither constrained nor predicted by the Higgs mechanism theory, thus requiring experimental determination. The approximate value for λ is 0.13, as determined from $m_H = 125$ GeV and $v = 246$ GeV. [39].

The interaction vertices corresponding to the terms discovered in the \mathcal{L}_H , \mathcal{L}_{VVH} and \mathcal{L}_{VVHH} Lagrangians are depicted in Figure 1.3, along with their interaction coupling factors. The coupling factors are all shown to be proportional to the square of the masses of the Higgs boson or vector bosons ($V = W, Z$).

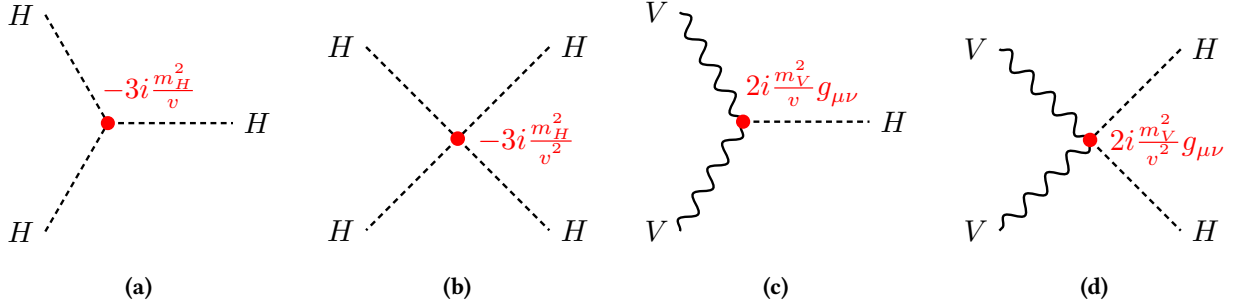


Figure 1.3: Depictions of the leading order interaction vertices of the Higgs as predicted by the Brout-Englert-Higgs mechanism. (a) Trilinear and (b) quartic Higgs self-coupling respectively as predicted by the h^3 and h^4 terms of the \mathcal{L}_H Lagrangian. (c) and (d) delineate the Higgs interaction with the vector boson ($V = W, Z$) in the \mathcal{L}_{VVH} and \mathcal{L}_{VVHH} Lagrangians. The coupling factors values (displayed in red) are derived from the Lagrangians themselves, while their signs are referenced from Ref. [40].

1.2.2 The fermion Yukawa couplings

The Brout-Englert-Higgs (BEH) mechanism provides an explanation for the mass of the W and Z bosons, yet it fails to account for the masses of fermions. To address this issue, the Yukawa interaction Lagrangian is introduced:

$$\mathcal{L}_{\text{Yukawa}} = -y_f(\bar{\psi}_L\phi\psi_R + \bar{\psi}_R\phi^\dagger\psi_L), \quad (1.2.12)$$

Here, y_f denotes the Yukawa coupling of the fermion f , ψ_R and ψ_L represent the singlet right-handed and doublet left-handed fermion isospin, and ϕ corresponds to the Higgs complex scalar field. In the case of an electron, for example, $\psi_R = e_R$ and $\psi_L = (\nu_e, e)_L$. If we incorporate the Higgs field expansion from Equation (1.2.6) into the Lagrangian, we obtain:

$$\mathcal{L}_e = -\frac{y_e v}{\sqrt{2}}(\bar{e}_L e_R + \bar{e}_R e_L) - \frac{y_e h}{\sqrt{2}}(\bar{e}_L e_R + \bar{e}_R e_L). \quad (1.2.13)$$

The Yukawa coupling of the electron (y_e) is not predefined, rather, it is derived from the first term's multiplicative factor as the electron's mass (m_e), while the second term is indicative of the Higgs boson's coupling (g_{eeH}) with the electron:

$$m_e = \frac{y_e v}{\sqrt{2}}. \quad (1.2.14)$$

Thus, the lepton's coupling with the Higgs is proportional to its mass, a mechanism that holds true for quarks as well. This Higgs-to-fermion interaction vertex is illustrated in Figure 1.4.

The preceding formalism exclusively explains the masses of the doublet's lower component, meaning only the charged leptons and the masses of the down-type quarks are justified. To provide a rationale for the mass of the up-type quarks, one needs to introduce the Hermitian conjugate of the Higgs field, ϕ^c :

$$\phi^c = -i\sigma_2\phi^* = -\frac{1}{\sqrt{2}} \begin{pmatrix} v + h \\ 0 \end{pmatrix}. \quad (1.2.15)$$

Employing the conjugate Higgs field, we obtain transformation properties analogous to those of the Higgs field, thereby explaining the up-type quarks' masses.

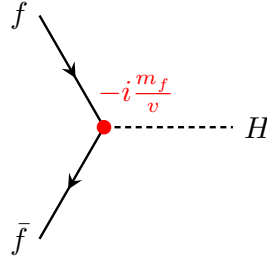


Figure 1.4: Leading order fermion couplings to the Higgs and interaction vertex factor as predicted by the Yukawa theory.

1.2.3 Higgs boson production mechanism at the LHC

Higgs boson production mode in Hadron Colliders and Lepton Colliders are different. The Higgs boson production mechanism at Lepton Colliders will be discussed in Section 7.1. And the Higgs boson production mechanism at Hadron Colliders will be discussed in this section.

The main Higgs production modes at LHC are the gluon-gluon fusion (ggF) process (Figure 1.6a), vector-boson fusion (VBF) process (Figure 1.6b), production associated with a vector boson (VH) process (Figure 1.6c), and top-quark associated production ($t\bar{t}H$) process (Figure 1.6d), the single top quark associated (tHq) mode (Figure 1.6e). The Higgs boson production cross-sections as a function of the centre-of-mass-energy (\sqrt{s}) for a Higgs mass $m_H = 125$ GeV is shown in Section 1.2.3.

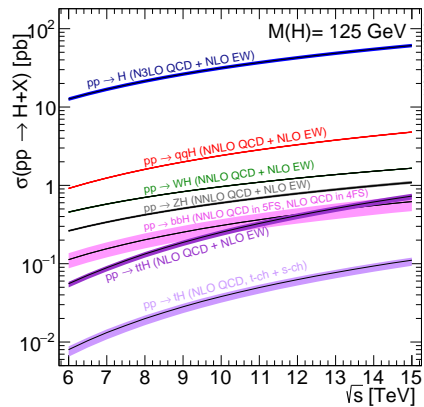


Figure 1.5: Higgs boson production cross-sections as a function of the centre-of-mass-energy (\sqrt{s}) for a Higgs mass $m_H = 125$ GeV. The tH production cross-section accounts for t -channel and s -channel only (no tWH production). (Adapted from Refs. [41, 42]).

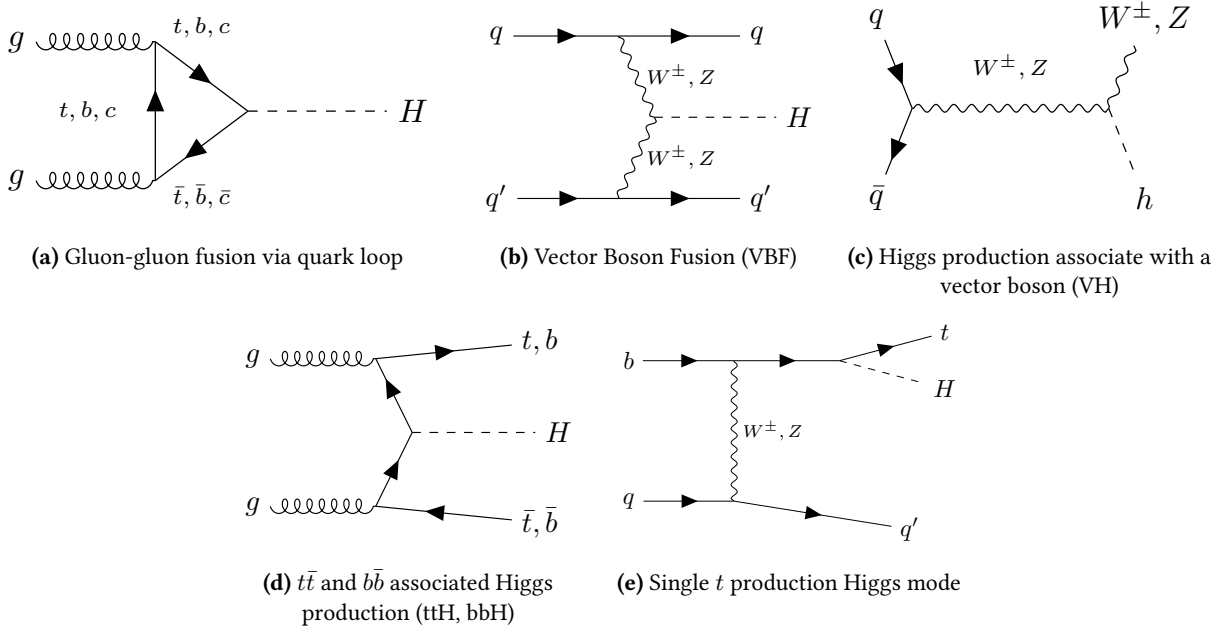


Figure 1.6: Leading order Feynman diagrams contribution to the Higgs boson production at LHC. Different Higgs boson production modes at the Large Hadron Collider (LHC) for a Higgs mass $m_H = 125$ GeV: (a) gluon fusion (ggF), (b) Vector Boson Fusion (VBF), (c) Higgs production associated with a vector boson (VH), (d) Higgs production associated with $t\bar{t}$ (ttH), (e) Higgs production associated with single t .

The predicted cross-sections of these main production processes and their associated uncertainties are listed in Table 1.1. Gluon-gluon fusion is the dominant production mode with a total cross-section of 48.6 pb at 13 TeV, followed by vector-boson fusion with a cross-section of 3.78 pb. The cross-sections of the other production modes are much smaller, with a cross-section of 1.37 pb for WH , 0.88 pb for ZH , 0.50 pb for $t\bar{t}H$. The total cross-section of all the production modes is 55.1 pb at 13 TeV.

Table 1.1: The Standard Model Higgs boson production cross-sections for $m_H = 125$ GeV in pp collisions at $\sqrt{s} = 13$ TeV. Adapted from Ref. [14].

	$\sqrt{s} = 13$ TeV
ggF	$48.6^{+5.6\%}_{-7.4\%}$
VBF	$3.78^{+2.1\%}_{-2.1\%}$
WH	$1.37^{+2.0\%}_{-2.0\%}$
ZH	$0.88^{+4.1\%}_{-3.5\%}$
ttH	$0.50^{+6.8\%}_{-9.9\%}$
Total	55.1

1.2.4 Higgs decay mode

As explained in Section 1.2.1 and Section 1.2.2, the Higgs boson exhibits a direct interaction with all massive particles present in the Standard Model (SM), including the W^\pm , Z boson, and leptons. Moreover, the Higgs boson also interacts with massless particles (gluons and photons). However, these interactions are mediated by loops of heavier particles, predominantly top quarks or W bosons.

Figure 1.7 depicts the various decay modes of the Higgs boson. Figure 1.7a illustrates the decay of the Higgs boson into a bottom quark pair ($b\bar{b}$), effectively demonstrating its interaction mechanism

Table 1.2: The branching ratios and the relative uncertainty for an SM Higgs boson with $m_H = 125$ GeV, Adapted from Reference [14].

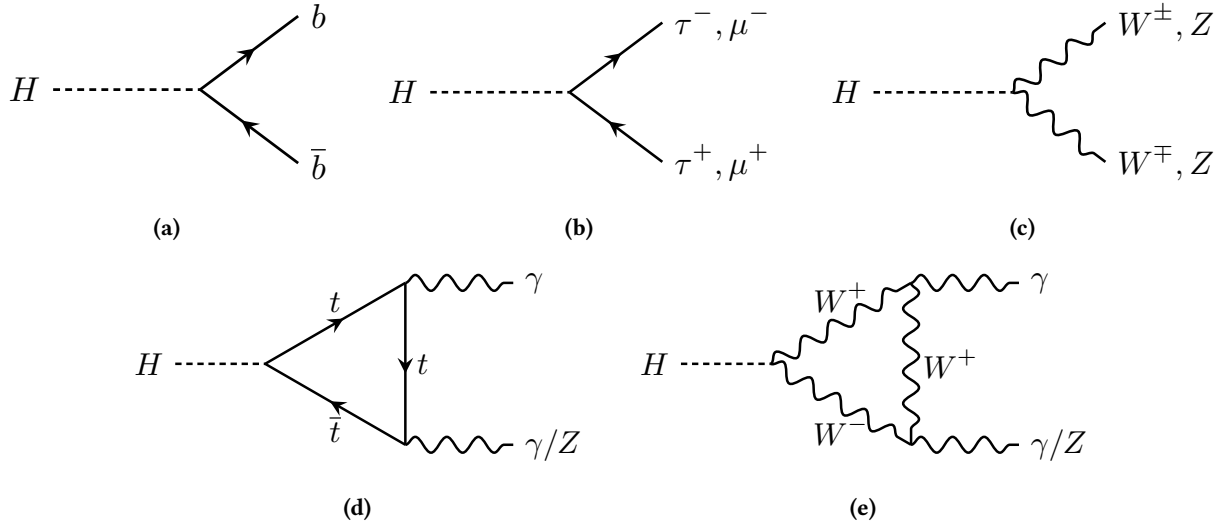
Decay channel	Branching ratio	Relative uncertainty
$H \rightarrow b\bar{b}$	5.82×10^{-1}	$+1.2\% / -1.3\%$
$H \rightarrow W^+W^-$	2.14×10^{-1}	$\pm 1.5\%$
$H \rightarrow \tau^+\tau^-$	6.27×10^{-2}	$\pm 1.6\%$
$H \rightarrow ZZ$	2.62×10^{-2}	$\pm 1.5\%$
$H \rightarrow c\bar{c}$	2.89×10^{-2}	$+5.5\% / -2.0\%$
$H \rightarrow \gamma\gamma$	2.27×10^{-3}	2.1%
$H \rightarrow Z\gamma$	1.53×10^{-3}	$\pm 5.8\%$
$H \rightarrow \mu^+\mu^-$	2.18×10^{-4}	$\pm 1.7\%$

with fermions. A similar depiction of interaction with massive particles is portrayed in Figure 1.7b, where the Higgs boson decays into a pair of leptons.

On the other hand, Figure 1.7c offers a visualization of the Higgs boson decay into a pair of gauge bosons, emphasizing the interactions of the Higgs with other bosonic particles within the SM.

Lastly, Figures 1.7d and 1.7e display the indirect decay process of the Higgs boson into two photons via fermion loop and boson loop respectively, highlighting the indirect interaction mechanism of the Higgs boson with massless particles.

Each of these decay modes presents critical insights into the branching ratios of the Higgs boson and the associated uncertainties, especially within different mass regions centered around 125 GeV.

**Figure 1.7:** Feynman diagrams representing various decay modes of the Higgs boson: (a) Higgs decay into a pair of b quarks, (b) Higgs decay into a pair of leptons, (c) Higgs decay into a pair of gauge bosons, (d) Higgs decay into two photons via fermion loop, (e) Higgs decay into two photons via boson loop.

The theoretical calculation of the Higgs branching ratio, depicted as a function of the Higgs mass in Figure 1.8. This plot is further broken down for a specific Higgs mass of 125 GeV in Table 1.2, presenting the theoretical predictions with $\sqrt{s} = 13$ TeV.

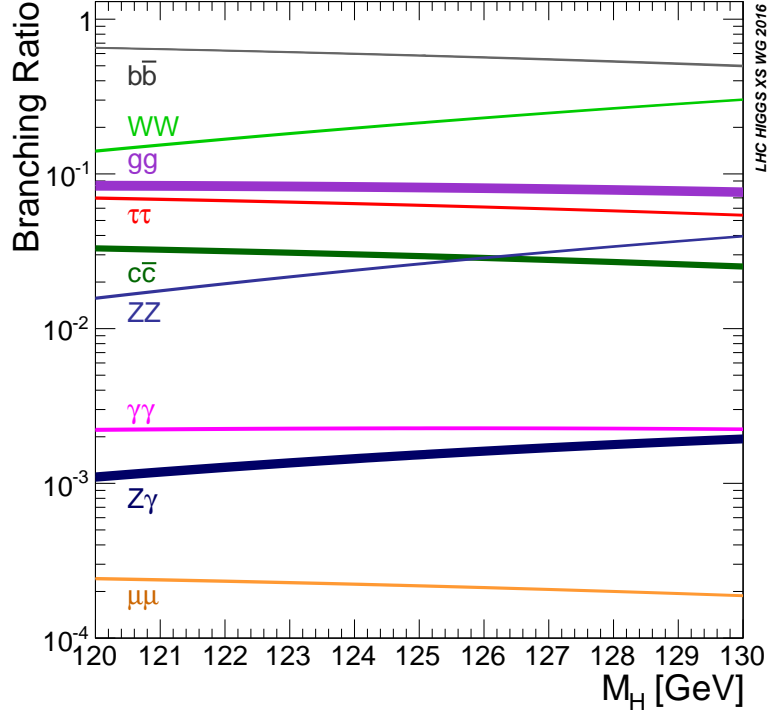


Figure 1.8: Higgs boson branching ratios and their uncertainties for different mass ranges around 125 GeV (Adapted from Refs. [41, 42]).

1.3 Di-Higgs theory framework

Ever since the landmark discovery of the Higgs boson at the Large Hadron Collider (LHC) in the year 2012, an essential goal for both the ATLAS and CMS collaborations has been to delve deeper into the intricacies of its properties and associated couplings. A significant step towards the comprehension of the electroweak symmetry breaking mechanism lies in manifesting evidence of the self-coupling of the Higgs boson (λ_{HHH}). This feature holds a direct correlation to the contour of the Higgs potential. Realizing this objective can be effectively achieved through the evaluation of the production of Higgs boson pairs (HH), thereby contributing to the understanding of this unique particle.

1.3.1 Di-Higgs mechanism

Reconsidering the Higgs potential Lagrangian as presented in Equation (1.2.10), it can be generalized and reformulated as follows:

$$\mathcal{L}_H = \frac{1}{2}m_H^2 h^2 + \lambda_3 h^3 + \lambda_4 h^4, \quad (1.3.1)$$

where λ_3 and λ_4 are the trilinear and quartic Higgs parameters, respectively.

Within the context of the Standard Model (SM), the self-couplings can be expressed as:

$$\lambda_3^{SM} = \frac{m_H^2}{2v}, \quad (1.3.2)$$

$$\lambda_4^{SM} = \frac{m_H^2}{8v^2}. \quad (1.3.3)$$

As discussed in Section 1.2.1, the Higgs boson has a crucial role in the mass generation of SM particles. As the Higgs boson itself possesses mass, which is generated by itself.

And the di-Higgs processes provides give us the access to a deeper understanding of the Higgs self-coupling mechanism, and the shape of the Higgs potential.

1.3.2 SM Higgs boson pair production at the LHC

In the Standard Model (SM), di-Higgs events are dominantly produced via the gluon-gluon fusion (ggF) processes at the LHC, involving both the Yukawa coupling to top quarks and the Higgs boson self-coupling. Figure 1.9 shows the leading-order (LO) ggF HH production Feynman diagrams, i.e. the so-called box and triangle diagrams. These two diagrams interfere destructively, leading to a small HH cross-section, namely $\sigma_{\text{ggF},HH}^{SM} = 31.05 \pm 3\%$ (PDF+ α_s) $^{+6\%}_{-23\%}$ (Scale + m_{top}) fb, calculated at next-to-next-to-leading-order (NNLO) accuracy in the finite top-quark mass approximation for $m_H = 125$ GeV and $\sqrt{s} = 13$ TeV [43, 44]. The HH cross-section is 3 orders of magnitude smaller than the dominant single Higgs boson production [45].

The second most dominant mode to produce a Higgs boson pair in the SM is vector-boson fusion (VBF), with an even smaller cross-section of $\sigma_{\text{VBF},HH}^{SM} = 1.726 \pm 2.1\%$ (PDF+ α_s) $^{+0.03\%}_{-0.04\%}$ (Scale) fb at $\sqrt{s} = 13$ TeV [43]. The three tree-level diagrams for VBF HH production are shown in Figure 1.10.

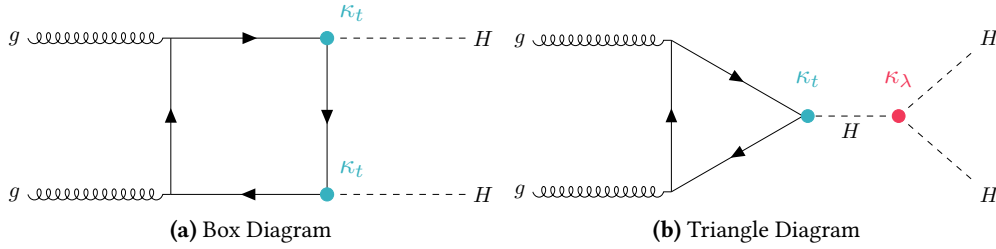


Figure 1.9: Leading-order Feynman diagrams of the ggF Higgs boson pair production in the Standard Model through the Higgs-top quark Yukawa interactions parameter, defined as $\kappa_t \equiv y_t/y_t^{SM}$ (a) and the Higgs boson self-coupling parameter, defined as $\kappa_\lambda \equiv \lambda_{HHH}/\lambda_{HHH}^{SM}$ (b).

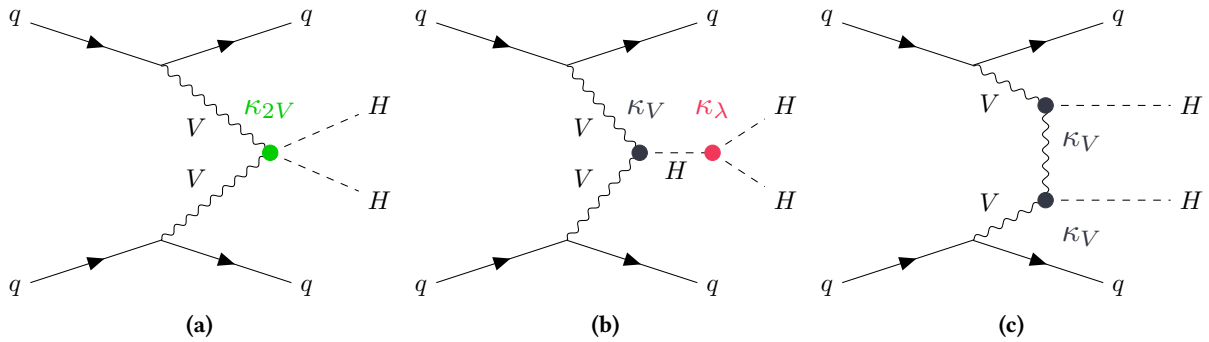


Figure 1.10: Tree-level Feynman diagrams for the VBF HH production mode. The vertices denoted by κ_{2V} , κ_V and κ_λ represent the $VVHH$, VVH and HHH couplings, respectively.

1.3.3 Di-Higgs decay channels

This dissertation is focused on the exploration of HH production via the $b\bar{b}\tau^+\tau^-$ decay channel (Chapter 5). As indicated in Table 1.2, there are numerous potential final states for Higgs decays. The branching ratios for some of the most frequently investigated search channels are presented in Figure 1.11.

	bb	WW	$\tau\tau$	ZZ	$\gamma\gamma$
bb	34%				
WW	25%	4.6%			
$\tau\tau$	7.3%	2.7%	0.39%		
ZZ	3.1%	1.1%	0.33%	0.069%	
$\gamma\gamma$	0.26%	0.10%	0.028%	0.012%	0.0005%

Figure 1.11: Di-Higgs decay branching ratios.

Given the small cross-section of HH production, the leading search channels typically involve at least one Higgs decaying to b -quarks ($H \rightarrow b\bar{b}$) in the final state. Three channels, namely $HH \rightarrow b\bar{b}b\bar{b}$, $HH \rightarrow b\bar{b}\tau^+\tau^-$, and $HH \rightarrow b\bar{b}\gamma\gamma$, dominate the sensitivity to the HH search. These channels exhibit a broad range in branching ratios, $HH \rightarrow b\bar{b}b\bar{b}$ at 34%, $HH \rightarrow b\bar{b}\tau^+\tau^-$ at 7.3%, and $HH \rightarrow b\bar{b}\gamma\gamma$ at 0.26%.

While a large branching ratio facilitates improved HH signal statistics, achieving robust analysis sensitivity necessitates a balance between high statistics and low background rates. The signal is examined for its production rate and the Higgs self-coupling parameter κ_λ .

During my Ph.D., I have contributed to the ATLAS di-Higgs search in both the $HH \rightarrow b\bar{b}\tau^+\tau^-$ (as described in Chapter 5) and to the $HH \rightarrow b\bar{b}\gamma\gamma$ (Chapter A, and [46]).

Previously, ATLAS has published the following di-Higgs searches: ATLAS: $HH \rightarrow b\bar{b}\tau^+\tau^-$ [4, 47], $HH \rightarrow b\bar{b}\gamma\gamma$ [46, 47], and $HH \rightarrow b\bar{b}b\bar{b}$ [48–50]

1.3.4 Kappa Parameters

κ_λ and κ_{2V} are the two most commonly used parameters to parametrize the Higgs boson self-coupling (trilinear HHH) and the $HHVV$ coupling, respectively. The κ_λ parameter is defined as the ratio of the Higgs boson self-coupling to its SM value, shown in Equation (1.3.4), while the κ_{2V} parameter is defined as the ratio of the $HHVV$ coupling to its SM value, shown in Equation (1.3.5).

$$\kappa_\lambda = \frac{\lambda_3}{\lambda_3^{SM}} \quad (1.3.4)$$

$$\kappa_{2V} = \frac{\lambda_{VVHH}}{\lambda_{VVHH}^{SM}} \quad (1.3.5)$$

where V refers to the vector bosons W or Z . The strength of the coupling is different for each vector boson as shown in Figure 1.3d. Both λ_{ZZHH} and λ_{WWHH} are modified using same κ_{2V} .

The Higgs to top quark coupling and Higgs to vector boson coupling are also modified by a parameter κ_t and κ_V , defined the same way as the ratio of the Higgs boson coupling to top quarks or vector boson to its SM value, shown in Equation (1.3.6) and (1.3.7).

$$\kappa_t = \frac{y_t}{y_t^{SM}} \quad (1.3.6)$$

where y_t is the top quark Yukawa coupling strength.

$$\kappa_V = \frac{g_{HVV}}{g_{HVV}^{SM}} \quad (1.3.7)$$

where g_{HVV} is the Higgs to vector boson coupling strength.

For the case of the SM, the κ_λ , κ_t , κ_V and κ_{2V} parameters are equal to 1. Any deviation from this value would indicate a BSM scenario.

1.3.5 HH cross-section Parametrisation

HH production via ggF and VBF modes depends fundamentally on κ_λ , κ_t , κ_V and κ_{2V} coupling parameters. Given the higher cross-section, the ggF production mode gives the strongest handle on κ_λ , while the VBF topology has a unique sensitivity to κ_{2V} because the ggF process does not involve the $VVHH$ interaction. In the SM, the Feynman diagrams in Figure 1.10a and Figure 1.10c interfere destructively. However, if κ_{2V} deviates from its SM value, the cross-section is significantly enhanced and the event kinematics provide stronger momenta [51].

The complete simulation of HH samples with a fine grid in the $(\kappa_\lambda, \kappa_{2V})$ plane is computationally expensive. To overcome this limitation, a representative number of MC simulation samples for selected coupling values are produced as described in Section 5.1.1, and a sample combination technique is employed to model the signal hypothesis across the coupling parameter space.

The process of combining a few samples in such a way as to cover the entire parameter space of coupling constants is based on exploiting the underlying mathematics of the differential cross-section formula.

1.3.5.1 ggF HH parametrisation

As shown by the triangle and box diagrams in Figure 1.9 contributing to the ggF HH production, only the two coupling parameters κ_λ and κ_t are involved. The differential ggF cross-section can be expressed as:

$$\begin{aligned} \frac{d\sigma(\kappa_\lambda, \kappa_t)}{dm_{HH}} &= |A(\kappa_t, \kappa_\lambda)|^2 \\ &= |\kappa_\lambda \kappa_t M_\Delta(m_{HH}) + \kappa_t^2 M_\square(m_{HH})|^2 \end{aligned} \quad (1.3.8)$$

$$\begin{aligned} &= \kappa_\lambda^2 \kappa_t^2 |M_\Delta(m_{HH})|^2 \\ &\quad + \kappa_\lambda \kappa_t^3 [M_\Delta^*(m_{HH}) M_\square(m_{HH}) + M_\square^*(m_{HH}) M_\Delta(m_{HH})] \\ &\quad + \kappa_t^4 |M_\square|^2 \end{aligned} \quad (1.3.9)$$

$$= \kappa_\lambda^2 \kappa_t^2 a_1(m_{HH}) + \kappa_\lambda \kappa_t^3 a_2(m_{HH}) + \kappa_t^4 a_3(m_{HH}), \quad (1.3.10)$$

where the M_{Δ} and M_{\square} terms represent the triangle and box diagrams respectively.

Setting κ_t to its SM prediction ($\kappa_t = 1$), Equation (1.3.10) is simplified to an equation quadratically dependent on the κ_{λ} coupling value:

$$\frac{d\sigma(\kappa_{\lambda})}{dm_{HH}} = \kappa_{\lambda}^2 a_1(m_{HH}) + \kappa_{\lambda} a_2(m_{HH}) + a_3(m_{HH}). \quad (1.3.11)$$

In Equation (1.3.11), the a_i matrix element expansion values have a dependence on m_{HH} , which is not trivially derivable as an analytic function. Instead, for a given κ_{λ} , its cross-section in each m_{HH} bin can be mathematically determined by solving a set of linear equations for a_1 , a_2 , and a_3 , using three different cross-section values (in the same m_{HH} bin) for three different κ_{λ} values. Samples with $\kappa_{\lambda} = 0, 1$ and 20 are used as a basis, with each sample consisting of over 10 million truth-level events simulated using POWHEG BOX v2 (without parton showering) in m_{HH} bins of 10 GeV with a bin range of 200 to 1000 GeV. These samples have no decays or requirements and are common to all HH analyses. In practice, the cross-section values of these three basis samples are represented by the yields from MC simulation, binned by their true m_{HH} . Once the a_i values are obtained, event weights for every κ_{λ} value can be derived for one of the simulated samples (e.g. the SM sample), by taking the ratio between the true m_{HH} distributions of the target coupling and the SM. By applying these weights to the SM sample, one obtains a reweighted sample for the targeted κ_{λ} value. The linear combination is validated with a MC sample generated with $\kappa_{\lambda} = 10$. In order to obtain a reweighted distribution at reconstruction-level, the truth m_{HH} value is stored in the SM sample, and the weights are applied to the events remaining after reconstruction and selection. The reweighting procedure is only used to determine the signal shapes, with the results normalised to their theoretical predictions [52]. While Equation (1.3.11) should hold for any variable, m_{HH} is selected due to the assumption that acceptance times efficiency only depends on m_{HH} , and was checked to be about right for ggF HH . The rest of the kinematics is assumed to vary coherently with the truth m_{HH} distributions.

This reweighting approach based on truth- m_{HH} weights has some limitations, since it does not allow to build an analysis which varies continuously in κ_{λ} (or κ_t , or both). Instead, one can probe only one fixed value of the coupling at a time. To overcome this limitation and to allow the analysis to be described by a parametric likelihood in κ_{λ} , the expected number of events and the discriminant distributions are obtained by a linear combination of samples, obtained from Eq. (1.3.10) with linear coefficients that are expressed as functions of $(\kappa_{\lambda}, \kappa_t)$ at reconstruction level. The basis of the linear combination is composed by the SM MC sample and two other samples (namely $\kappa_{\lambda} = 0$ and $\kappa_{\lambda} = 20$) that are obtained using the reweighting procedure from the SM sample, as explained previously.

$$\begin{aligned} \text{sample}(\kappa_{\lambda}, \kappa_t) = \kappa_t^2 & \left[\left(\kappa_t^2 + \frac{\kappa_{\lambda}^2}{20} - \frac{399}{380} \kappa_{\lambda} \kappa_t \right) \text{sample}(0, 1) \right. \\ & + \left(\frac{40}{38} \kappa_{\lambda} \kappa_t - \frac{2}{38} \kappa_{\lambda}^2 \right) \text{sample}(1, 1) \\ & \left. + \left(\frac{\kappa_{\lambda}^2 - \kappa_{\lambda} \kappa_t}{380} \right) \text{sample}(20, 1) \right]. \end{aligned} \quad (1.3.12)$$

Given a set of $\kappa_{\lambda}, \kappa_t$ values the signal distribution and yield are obtained by the sum of the signal distributions and yields of the three samples of the basis. In practice, the basis samples are run through reconstruction and selection (or alternatively the SM sample, after passing the analysis selections, is reweighted to the other κ_{λ} basis samples), then the signal component in the likelihood is described by three signal sub-components which are evaluated by the distribution and yield of

the three samples of the basis. Each component contributes to the signal likelihood with a weight that scales with the linear coefficient function of $(\kappa_\lambda, \kappa_t)$ as in Eq. (1.3.12).

1.3.5.2 VBF HH parametrisation

The VBF HH production dependence on κ_λ , κ_V and κ_{2V} coupling parameters is modelled in a similar manner to the ggF mode, but with no truth reweighting. The kinematics of the VBF mode involves both the Higgs pair and the two VBF jets generated by the hadronisation of the two quarks that participate in the hard scattering. Given this topology, the reweighting approach is discarded, since it is not trivial to establish a limited number of variables that can fully describe the VBF HH kinematics. Instead, a linear combination of the existing VBF HH MC samples allows to parametrise the VBF HH signals as a function of the three coupling parameters κ_λ , κ_V and κ_{2V} , and is performed directly after reconstruction and selection, in order to generate the distribution of any variable for the desired κ_λ , κ_V and κ_{2V} values as described in the following.

As shown in Figure 1.10, the total amplitude for HH production via VBF at LO is given by the sum of three diagrams, scaling with $\kappa_\lambda\kappa_V$, κ_{2V} and κ_V^2 respectively:

$$\mathcal{A}_{VBF}(\kappa_\lambda, \kappa_{2V}, \kappa_V) = A_1 \cdot \kappa_\lambda\kappa_V + A_2 \cdot \kappa_{2V} + A_3 \cdot \kappa_V^2, \quad (1.3.13)$$

where A_1 , A_2 and A_3 represent the normalisation coefficients for each diagram. Hence, the differential cross-section $\frac{d\sigma_{VBF}}{d\Phi}$ (where $d\Phi$ represents the infinitesimal phase space element) can be expressed as a function of the three coupling parameters affecting the VBF HH production as follows:

$$\frac{d\sigma_{VBF}}{d\Phi}(\kappa_\lambda, \kappa_{2V}, \kappa_V) \propto |\mathcal{A}_{VBF}(\kappa_\lambda, \kappa_{2V}, \kappa_V)|^2 \quad (1.3.14)$$

$$= |A_1 \cdot \kappa_\lambda\kappa_V + A_2 \cdot \kappa_{2V} + A_3 \cdot \kappa_V^2|^2 \quad (1.3.15)$$

$$= |A_1|^2 \cdot \kappa_\lambda^2\kappa_V^2 + |A_2|^2 \cdot \kappa_{2V}^2 + |A_3|^2 \cdot \kappa_V^4 \\ + (A_1A_2^* + A_1^*A_2) \cdot \kappa_\lambda\kappa_V\kappa_{2V} \\ + (A_1A_3^* + A_1^*A_3) \cdot \kappa_\lambda\kappa_V^3 + (A_2A_3^* + A_2^*A_3) \cdot \kappa_{2V}\kappa_V^2 \quad (1.3.16)$$

$$= x_1 \cdot \kappa_\lambda^2\kappa_V^2 + x_2 \cdot \kappa_{2V}^2 + x_3 \cdot \kappa_V^4 + x_4 \cdot \kappa_\lambda\kappa_V\kappa_{2V} \\ + x_5 \cdot \kappa_\lambda\kappa_V^3 + x_6 \cdot \kappa_{2V}\kappa_V^2. \quad (1.3.17)$$

The differential VBF HH cross-section can be written as a polynomial of the coupling parameters κ_λ , κ_{2V} and κ_V , whose coefficients are identified by the x_i terms, with $i = 1, 2, \dots, 6$. The following expression holds for the differential cross-section of the generic variable Φ for SM VBF HH events:

$$\begin{pmatrix} 9 & 1 & 1 & 3 & 3 & 1 \\ 1 & & & 1 & 1 & \\ \frac{1}{4} & 1 & 1 & \frac{1}{2} & \frac{1}{2} & 1 \\ 1 & 4 & 1 & 2 & 1 & 2 \\ 0 & 0 & 1 & 0 & 0 & 0 \\ 1 & 100 & 1 & 10 & 1 & 10 \\ 1 & 1 & 1 & 1 & 1 & 1 \end{pmatrix} \times \begin{pmatrix} x_1 \\ x_2 \\ x_3 \\ x_4 \\ x_5 \\ x_6 \end{pmatrix} = \begin{pmatrix} \frac{d\sigma_{VBF}}{d\Phi}(3, 1, 1) \\ \frac{d\sigma_{VBF}}{d\Phi}\left(\frac{1}{2}, 1, 1\right) \\ \frac{d\sigma_{VBF}}{d\Phi}(1, 2, 1) \\ \frac{d\sigma_{VBF}}{d\Phi}(0, 0, 1) \\ \frac{d\sigma_{VBF}}{d\Phi}(1, 10, 1) \\ \frac{d\sigma_{VBF}}{d\Phi}(1, 1, 1) \end{pmatrix}. \quad (1.3.18)$$

This suggests the possibility of solving a system of linear equations, whose unknowns are represented by the x_i terms, while the constant term is identified with the distribution of any variable Φ (correctly normalized using the predicted cross-section) extracted from an available VBF HH MC sample, simulated with a determined variation of the coupling values. Given the six unknowns x_i , six VBF HH reference samples, generated with different values of the couplings κ_λ , κ_{2V} and κ_V , are needed.

By inverting the 6×6 coefficient matrix of the system of linear equations, one can obtain an expression of the x_i variables in terms of the known $d\sigma_{VBF}/d\Phi(\kappa_{2V}, \kappa_\lambda, \kappa_V)$ distributions, extracted using the six basis samples. Finally, plugging the solutions for the x_i variables in Eq. (1.3.17), yields the distribution of any variable Φ for VBF HH events, simulated with any variation of the couplings κ_λ , κ_{2V} and κ_V in form of linear combinations of six reference samples, whose linear coefficients appear as functions of the probed κ_{2V} , κ_λ and κ_V values.

This procedure results in a natural parametrisation of VBF HH events in the $(\kappa_\lambda, \kappa_{2V})$ plane (by fixing $\kappa_V = 1$), once a basis is chosen. The potential choices of basis are constrained by the available VBF HH MC samples, summarised in Table 5.2, and can be optimised depending on the desired effect for signal generation. The basis chosen for the VBF HH parametrisation was shown to be able to model the VBF HH kinematics across a large parameter space, reaching κ_{2V} , κ_λ and κ_V values well beyond the SM [53]:

$$\begin{aligned} \frac{d\sigma_{VBF}}{d\Phi}(\kappa_{2V}, \kappa_\lambda, \kappa_V) = & \left[\left(\frac{\kappa_{2V}^2}{5} - \frac{\kappa_{2V}\kappa_V^2}{5} - \frac{\kappa_{2V}\kappa_V\kappa_\lambda}{10} + \frac{\kappa_V^3\kappa_\lambda}{10} \right) \times \frac{d\sigma_{VBF}}{d\Phi}(3, 1, 1) \right. \\ & + \left(\frac{4\kappa_{2V}^2}{5} - \frac{4\kappa_{2V}\kappa_V^2}{5} - \frac{12\kappa_{2V}\kappa_V\kappa_\lambda}{5} + \frac{12\kappa_V^3\kappa_\lambda}{5} \right) \times \frac{d\sigma_{VBF}}{d\Phi}\left(\frac{1}{2}, 1, 1\right) \\ & + \left(-\frac{5\kappa_{2V}\kappa_V^2}{4} + \frac{5\kappa_{2V}\kappa_V\kappa_\lambda}{4} + \frac{\kappa_V^3\kappa_\lambda}{8} - \frac{\kappa_V^2\kappa_\lambda^2}{8} \right) \times \frac{d\sigma_{VBF}}{d\Phi}(1, 2, 1) \\ & + \left(-\kappa_{2V}\kappa_V^2 + \kappa_{2V}\kappa_V\kappa_\lambda + \kappa_V^4 - \kappa_V^3\kappa_\lambda \right) \times \frac{d\sigma_{VBF}}{d\Phi}(0, 0, 1) \\ & + \left(\frac{\kappa_{2V}\kappa_V^2}{36} - \frac{\kappa_{2V}\kappa_V\kappa_\lambda}{36} - \frac{\kappa_V^3\kappa_\lambda}{72} + \frac{\kappa_V^2\kappa_\lambda^2}{72} \right) \times \frac{d\sigma_{VBF}}{d\Phi}(1, 10, 1) \\ & \left. + \left(-\kappa_{2V}^2 + \frac{29\kappa_{2V}\kappa_V^2}{9} + \frac{5\kappa_{2V}\kappa_V\kappa_\lambda}{18} - \frac{29\kappa_V^3\kappa_\lambda}{18} + \frac{\kappa_V^2\kappa_\lambda^2}{9} \right) \times \frac{d\sigma_{VBF}}{d\Phi}(1, 1, 1) \right]. \end{aligned} \quad (1.3.19)$$

Part II

Higgs Physics at ATLAS

The LHC and the ATLAS detector

2.1	The Large Hadron Collider	44
2.1.1	Luminosity at LHC	45
2.1.2	Production and Acceleration of Particles at LHC	47
2.1.3	Main Experiments on the LHC Ring	48
2.2	An Overview of the ATLAS Detector	49
2.2.1	ATLAS Coordinate System and Associated Definitions	51
2.2.2	The ATLAS Magnet Systems	52
2.2.3	The ATLAS Inner Detector	53
	2.2.3.1 Pixel	55
	2.2.3.2 SemiConductor Tracker	56
	2.2.3.3 Transition Radiation Tracker	56
2.2.4	ATLAS Calorimeters	56
	2.2.4.1 Electromagnetic Calorimeter	57
	2.2.4.2 Hadronic Calorimeter	58
2.2.5	ATLAS Muon Spectrometer	60
2.2.6	ATLAS Data Trigger and Acquisition System	60

Situated around the border of Switzerland and France, the Large Hadron Collider (LHC) extends 27 km in circumference, constituting the highest energy particle collider with a capacity to produce collisions at 13.6 TeV in the center of mass energy, \sqrt{s} . It holds four main experiments, namely, ATLAS, LHCb, ALICE, and CMS. The goals of these experiments lie in deciphering the characteristics of elementary particles to enhance our understanding of the universe. By initiating proton collisions at sufficiently high energies, the discovery of new particles becomes feasible.

The ATLAS detector employs meticulously engineered subsystems to determine the attributes of these particles along with their interactions. The current chapter delivers a synopsis of the LHC, outlining the fundamental geometry and salient design philosophies underpinning the ATLAS experiment.

2.1 The Large Hadron Collider

The Large Hadron Collider (LHC) [54–57] currently represents the most advanced technology in the field of particle accelerators. This monumental circular hadron accelerator is situated an average of 100 meters below the Earth’s surface, intersecting the border between Switzerland and France.

As elaborated in Figure 2.1, the fundamental operation of the LHC involves accelerating bunches of protons into two separate beams, each travelling in the opposite direction. These beams attain velocities close to the speed of light ($99.9999991\% \times c$), allowing them to circulate the accelerator ring more than 11,000 times within a single second.

The LHC was designed to achieve a maximum center of mass energy $\sqrt{s} = 14$ TeV, implying an energy of 7 TeV for each individual beam. However, during Run 2, the operational energy was $\sqrt{s} = 13$ TeV, whereas during Run 3, it is increased to 13.6 TeV. Proton collisions are happening at four specific collision points within the accelerator, locations where the detectors for ATLAS, CMS, LHCb, and ALICE are installed, with the interval between collisions being 25 ns.

Additionally, the LHC is capable of accelerating lead ions (Pb^{82+}), achieving a nucleon-nucleon center of mass energy $\sqrt{s_{NN}} = 5.02$ TeV.

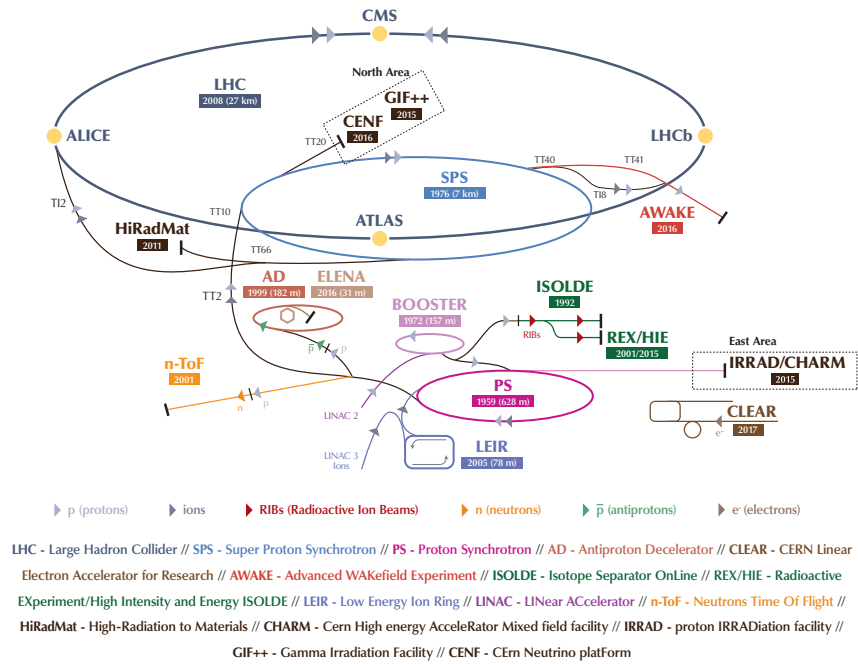


Figure 2.1: Schematic representation of the LHC’s configuration. Notably, the physical proximity between the ALICE, ATLAS, and LHCb detectors is closer than illustrated in this diagram (adapted from Ref. [58]).

Constructed between the years 1998 and 2008, the Large Hadron Collider (LHC) was developed as the successor to the Large Electron-Positron (LEP), utilizing the identical tunnel that was built for the LEP.

The LHC initiated operations on the 10th of September 2008. Regrettably, a catastrophic quench happened on the 18th of September resulting in severe damage to some of its magnets. Consequently, the first run (Run 1) of the LHC, was postponed. It started in 2009 and finished in 2012. During this period, the LHC operated at $\sqrt{s} = 7$ and 8 TeV. Subsequently, the collider underwent its first long shutdown (LS1) for two years. This period was used to carry out repairs and upgrades on various detectors that had their performances impaired by radiation.

During the period from 2015 to 2018, data acquisition was carried out at an energy level of $\sqrt{s} = 13$ TeV, constituting the second running period (Run 2). This phase was followed by a shutdown phase referred to as Long Shutdown 2 (LS2). The initiation of the third running period, Run 3, was marked on the 5th of July 2022. This phase reached a record-breaking energy level of $\sqrt{s} = 13.6$ TeV. My role in this phase involved active participation in various data acquisition and testing processes as an Inner Detector (ID) Desk shifter, tasked with monitoring the status of the sub-detector.

2.1.1 Luminosity at LHC

The particle accelerator's instantaneous luminosity (\mathcal{L}) is essentially the count of particle crossings in a unit area within a unit time. It plays a significant role in determining the cross-section (σ) of a specific interaction process and the frequency of such events (dN/dt), following the relation:

$$\mathcal{L} \times \sigma = \frac{dN}{dt} \quad (2.1.1)$$

The cross-section, expressed in cm^2 , is the apparent surface of the object colliding, the expected number of produced events being $N = \Sigma \times \mathcal{L}$. It is influenced by the type of physics process being examined, and the energy involved in the collisions, as certain resonances can be observed or suppressed. Typically, it is expressed in barns (b), where $1 \text{ b} = 10^{-24} \text{ cm}^2$. Luminosity \mathcal{L} is commonly expressed in $\text{cm}^{-2}\text{s}^{-1}$ or $\text{fb}^{-1}\text{s}^{-1}$.

The accelerator and its settings intrinsically determine the instantaneous luminosity. In a circular collider with round and identical beams, the luminosity can be presented as follows, based on Reference [59]:

$$\mathcal{L} = \frac{N_b^2 n_b f_r \gamma_r}{4\pi \varepsilon_n \beta^*} F. \quad (2.1.2)$$

N_b stands for the number of particles in each bunch, and in the case of a typical Large Hadron Collider (LHC)-injected bunch, it contains $N_b = 1.15 \times 10^{11}$ protons. The number of bunches for each beam is represented by n_b , with $n_b = 2808$ being the standard for the LHC¹.

The revolution frequency is equal to $f_r = 11245$ Hz. The relativistic gamma factor, γ_r , is approximately 7000. Normalized transverse beam emittance is denoted by ε_n and is $\varepsilon_n = 3.75 \mu\text{m}$.

The beta function at the collision point, denoted by β^* , is associated with the focusing of the bunches and is given by $\beta^* = 0.55$ m. Finally, the geometric luminosity reduction factor, F , is used to account for non heads-on collisions. It equals $F = 0.84$ for the LHC, as the bunches collide at a crossing angle of $\theta_c = 285 \mu\text{rad}$ to prevent collisions outside the nominal interaction points. Using the RMS bunch length ($\sigma_z = 7.55$ cm) and transverse bunch width ($\sigma^* = 16.7 \mu\text{m}$), this parameter can be calculated [59, 62]:

$$F = \left[1 + \left(\frac{\sigma_z}{\sigma^*} \tan \left(\frac{\theta_c}{2} \right) \right)^2 \right]^{-\frac{1}{2}} \approx \left[1 + \left(\frac{\sigma_z \theta_c}{2\sigma^*} \right)^2 \right]^{-\frac{1}{2}}, \quad (2.1.3)$$

The luminosity can be reduced by small crossing angle or by increasing the transverse distance between the beams to limit the number of interactions per bunch crossing.

¹The Batch Compression Merging and Splitting (BCMS) system, introduced in 2016, enables a reduction in beam size while maintaining the same proton count per bunch [60, 61]. This increased the LHC's instantaneous luminosity by 20%, but reduced the bunch count to 2556 from the previous 2808.

The concept of integrated luminosity, denoted by \mathcal{L}_{int} , is another commonly used measure. This quantity, integrated over a predefined time period (T), represents the integration of the instantaneous luminosity, as defined by:

$$\mathcal{L}_{\text{int}} = \int_0^T \mathcal{L}(t) dt. \quad (2.1.4)$$

Examining the data from Run 1, at $\sqrt{s} = 7$ and 8 GeV, ATLAS and CMS have recorded 25 fb^{-1} of high-quality data that is eligible for physics analysis, given the assured operational state of the critical detector components [63]. In Run 2, both experiments accumulated 139 fb^{-1} each, illustrated for ATLAS in Figure 2.2. Projections for Run 3 estimate a collection of approximately 300 fb^{-1} of data per experiment.

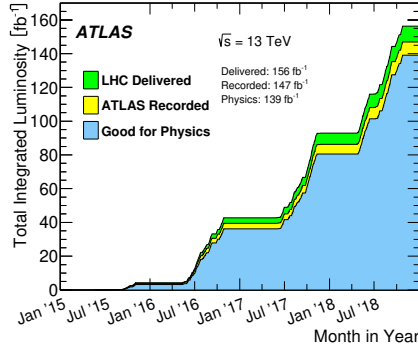


Figure 2.2: The LHC and ATLAS integrated luminosity evolution over time for the full Run 2 (taken from Ref. [63]).

At $\sqrt{s} = 13 \text{ TeV}$, the inelastic collision cross-section of pp is estimated to be nearly $\sigma_{\text{inel}} \approx 70 \text{ mb}$ [64], indicating the propensity for multiple pp collisions per bunch crossing. Such coinciding interactions are labeled as *in-time pile-up*. During the second run (Run 2) of the LHC, the mean number of interactions per bunch crossing (μ) oscillated between 13 and 38, with an average of 33.3 interactions per bunch crossing encapsulating all data recording periods of Run 2. This is visualized in the context of ATLAS in Figure 2.3.

The design of detectors, characterized by high granularity, allows for the differentiation of the numerous interaction vertices and their corresponding particle generation. Additionally, μ is observed to demonstrate a gradual reduction over time. This trend can be attributed to the attrition of protons in the bunches due to repeated collisions. Consequently, the instantaneous luminosity follows a downward trajectory primarily due to these collisions until the beams are eventually dumped (usually after several hours) and replaced. This diminishing luminosity can be approximated as a first order model [59]:

$$\mathcal{L}(t) = \frac{\mathcal{L}_0}{(1 + t/\tau_{\text{nuclear}})^2}, \quad (2.1.5)$$

where $\mathcal{L}_0 = 10^{34} \text{ cm}^{-2}\text{s}^{-1}$ is the peak luminosity and $\tau_{\text{nuclear}} \approx 50 \text{ h}$ represents the decay time of the bunch intensity caused by proton collision losses. However, minor loss influences, such as emittance blow up, transverse expansion of the beam size, sporadic collisions with remaining gas atoms, etc., necessitate consideration, implying that the practical lifespan of the beam is approximately 15 hours for the LHC.

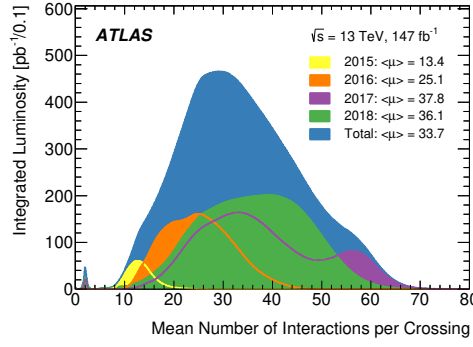


Figure 2.3: ATLAS luminosity-weighted distribution of the mean number (μ) of interactions per bunch crossing for the full Run 2 (taken from Ref. [63]).

2.1.2 Production and Acceleration of Particles at LHC

The generation of protons for the LHC involves a process wherein hydrogen atoms are stripped of their electrons by a robust electric field [56]. These protons are initially accelerated to 50 MeV using a linear accelerator, known as Linac 2. They are then injected in a series of circular accelerators of increasing sizes and escalating accelerating power. The initial stage of acceleration takes place inside the Proton Synchrotron Booster (PSB or "Booster" in Figure 2.1), where they attain a kinetic energy of 1.4 GeV. Subsequently, inside the Proton Synchrotron (PS), this energy is boosted to 25 GeV, and further boosted to 450 GeV by the Super Proton Synchrotron (SPS). Finally, these protons are injected into the LHC, in both clockwise and anticlockwise directions, and accelerated to their nominal energy of 6.5 TeV for Run 2 over a span of 20 minutes.

In the case of Run 3, the acceleration chain differs slightly. Linac 2 is substituted with a newer linear accelerator, Linac 4, resulting in varying acceleration energies: 160 MeV in Linac 4, 2 GeV in PSB, 25 GeV in PS, 450 GeV in SPS, and 6.8 TeV in the LHC.

Protons are transported in beam pipes, maintained at an ultra-high vacuum to prevent beam losses due to beam-gas interactions. This necessitates that the local pressure stays below 10^{-5} Pa. At the interaction points, experimental requirements dictate even lower pressures, down to 2×10^{-9} Pa, to minimize background interference from beam-gas interactions [65].

The LHC is a complex assembly of straight sections for accelerating, and curved sections for bending trajectories and focusing charged particles (protons or ions), facilitated by electric and magnetic fields, respectively:

The acceleration process in the LHC is carried out by radio-frequency (RF) cavities, which additionally establish the bunch structure of the beam. This procedure is such that it only facilitates particle acceleration when the electric field aligns appropriately during the RF cycle. Notably, each beam in the LHC uses eight superconducting RF cavities that incrementally enhance the proton's energy by 485 keV at every turn until they reach their nominal energy. After this stage, the RFs merely compensate for the proton energy loss per turn.

In parallel to this, the manipulation of bunch trajectories is achieved via 1232 superconducting dipole magnets, each extending to 15 meters in length and operating at a temperature of 1.9 K. These magnets generate a magnetic field of 8.3 T and are constructed out of Nb-Ti. The creation of such potent magnetic fields required extensive development efforts. These dipole magnets are also equipped with sextupole, octupole, and decapole magnets, which serve to rectify minor imperfections in the magnetic field at their extremities.

Moreover, beam focusing is conducted by 78 superconducting quadrupoles, also fabricated from Nb-Ti. They play a crucial role in sustaining the particles within a restricted beam by compressing

it either vertically or horizontally, depending on the orientation of the four poles of the magnets.

In addition to these, the LHC incorporates what are termed insertion magnets, which come into play when particles are entering the detectors. These magnets substantially compress the bunches, which consequently elevates the luminosity.

Finally, the LHC employs approximately 3800 single apertures and 1000 twin aperture corrector magnets which are utilized for orbital corrections, showcasing the complexity and precision of this large-scale experimental setup.

To achieve the high center of mass energy at the LHC, it is crucial to accelerate relatively heavier particles, such as protons or heavy ions (like lead ions). This is because, compared to lighter particles like electrons, these heavier particles have substantially lower energy loss in curved trajectories due to synchrotron radiation.

For an ultra-relativistic particle of charge q , mass m , and energy E that is kept constant inside a circular accelerator, the instantaneous power loss due to synchrotron radiation is described by:

$$P = \frac{c}{6\pi\epsilon_0} \cdot \frac{E^4}{\rho^2} \cdot \frac{q^2}{(mc^2)^4}, \quad (2.1.6)$$

where ρ represents the curvature radius and ϵ_0 is the vacuum permittivity.

Equation (2.1.6) is a specialized form of the relativistic Larmor equation [66, 67]. From this equation, we deduce that the energy loss (U_0) for a particle per turn is:

$$U_0 = \frac{1}{3\epsilon_0} \cdot \frac{E^4}{\rho} \cdot \frac{q^2}{(mc^2)^4}. \quad (2.1.7)$$

As protons are nearly 2000 times heavier than electrons, the energy loss due to synchrotron radiation is considerably mitigated for protons.

2.1.3 Main Experiments on the LHC Ring

The LHC facilitates the operation of four primary detectors, depicted in Figure 2.1.

The ATLAS (A Toroidal LHC ApparatuS) experiment is one of the two general-purpose detectors at the LHC [68–70]. It is engaged in exploration of the Standard Model and precise measurements ranging from studies on Higgs boson properties to the search for new physics beyond the Standard Model (BSM), including super-symmetry (SUSY) and dark matter candidates search. The ATLAS detector, being the largest detector ever designed for a particle collider (46 meters long, 25 meters in diameter and weighting 7000 tonnes), possesses a cylindrical shape and uses large toroidal magnets to generate the magnetic field in the outer part of the detector for muon tracking. The tracking part of the detector is confined within a solenoid magnet. A workforce comprising over 5500 individuals from 245 institutions across 42 countries collaboratively contributes to the ATLAS experiment.

The Compact Muon Solenoid (CMS) represents the other general-purpose detector at the LHC with physics objectives akin to ATLAS [71–73]. Despite being a “compact” detector (21 meters long, 15 meters in diameter and weighting 12 500 tonnes), CMS has a strong solenoidal magnetic field of 3.8 T.

The difference in technologies and design between ATLAS and CMS validates measurements conducted by one or the other experiment, thereby reducing potential bias. Combining the measurements from these two experiments bolsters precision and enables tighter constraints on SM and BSM theories. The CMS experiment involves over 5500 participants from approximately 241 universities and institutes in 54 countries.

The Large Hadron Collider beauty (LHCb) differs from the other LHC detectors, being an asymmetric one-sided forward detector (21 meters long, 10 meters high, 13 meters wide and weighting 5600 tonnes) [74–76]. Its unique design aims to examine the asymmetry between matter and anti-matter, focusing on bottom (beauty) and charm hadrons decays primarily produced in forward and backward regions, close to the beam axis. LHCb is designed to carry out extremely precise flavour physics measurements and CP violation studies. The LHCb collaboration comprises approximately 1600 persons from 20 countries.

Finally, the A Large Ion Collider Experiment (ALICE) detector is optimized for examining heavy-ion (lead-ion) collisions, particularly the properties of the quark-gluon plasma formed in these collisions [77–79]. Such measurements emulate what possibly existed shortly after the Big Bang, before the recombination of quark-gluon into familiar hadrons like protons and neutrons. Thus, ALICE probes the quantum chromodynamics (QCD) theory and quark confinement. Like ATLAS and CMS, ALICE is a cylindrical detector (26 meters long, 16 meters in diameter and weighting 10 000 tonnes). The ALICE collaboration consists of over 2000 members from 174 institutes in 40 countries.

2.2 An Overview of the ATLAS Detector

As depicted in Figure 2.4, the ATLAS detector [68–70] possesses a cylindrical configuration and encompasses multiple concentric sub-detectors, each contributing towards the precise calculation of energy, momentum, and particle trajectories [80, 81]. The *barrel*, positioned centrally within the cylinder, is complemented by the *end-caps* that reside on either extremity, collectively ensuring particle detection.

The subsequent sections provide an in-depth analysis of the following sequentially arranged sub-detectors, listed in order of proximity to the interaction point:

- **Inner Detector (ID):** Positioned closest to the beam-pipe, the ID plays a pivotal role in the accurate reconstruction of charged particles' trajectories, inclusive of electrons, protons, and charged pions. The ID's magnetic field facilitates this by bending their trajectories, enabling the accurate measurement of momentum and impact parameters. Such data allows for the discrimination of positive and negative charges and aids in primary and secondary vertex reconstruction, essential for identifying pp collisions of interest, rejecting pile-up, and enabling flavour-tagging algorithms.
- **Electromagnetic (ECAL) and Hadronic (HCAL) Calorimeters:** These calorimeters are designed to measure energies and directions of electromagnetic particles (e.g., electrons, positrons, photons) and hadrons (e.g., protons, neutrons, pions).
- **Muon Spectrometer (MS):** This sub-detector is tasked with identifying and measuring the momenta of muons, as these particles can traverse all other sub-detectors.

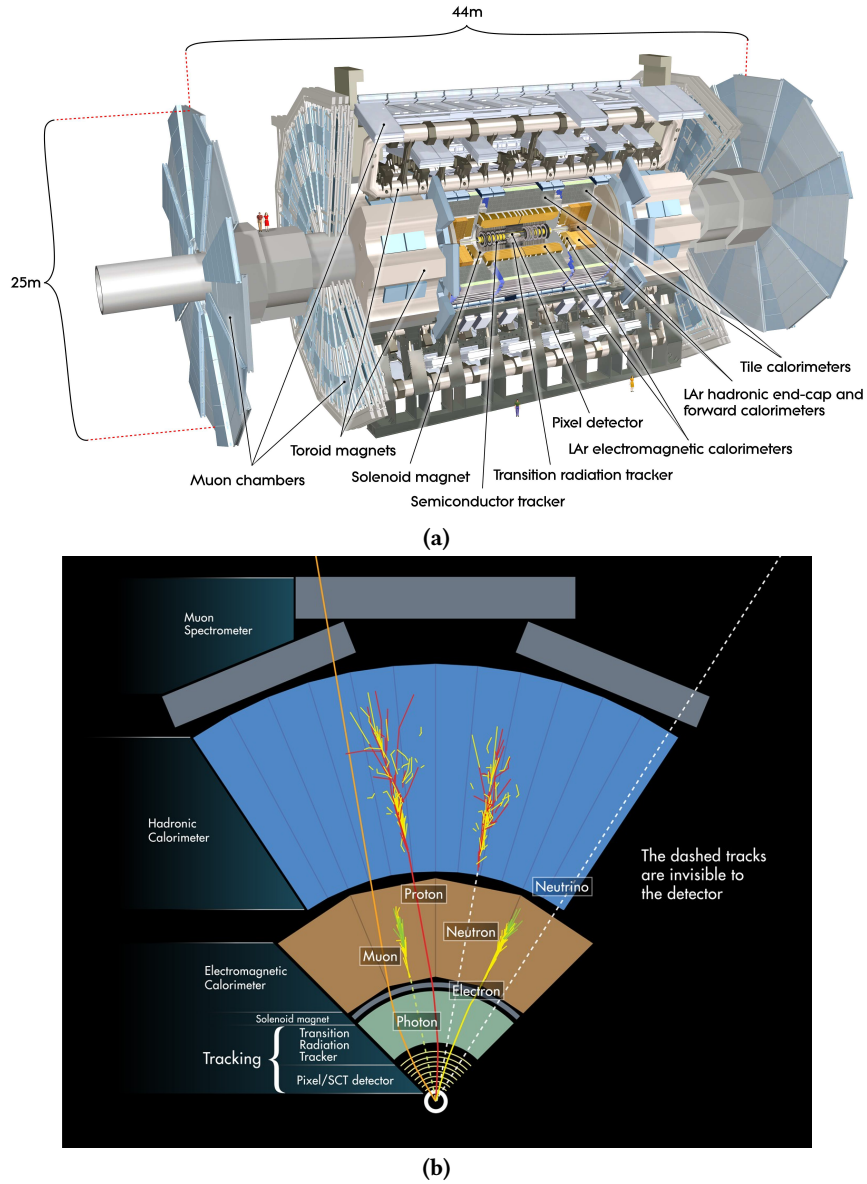


Figure 2.4: (a) Schematic of the ATLAS detector and (b) Transverse cut-away view of the detector. The bending of the trajectories for charged particles is a result of the magnetic field within the ATLAS (Referenced from [80, 81]).

2.2.1 ATLAS Coordinate System and Associated Definitions

ATLAS employs a right-handed coordinate system, with its origin set at the nominal interaction point (IP) situated at the center of the detector, as illustrated in Figure 2.5. The beam pipe aligns with the z -axis. The x -axis projects from the IP towards the center of the LHC ring, while the y -axis points upwards. Typically, the transverse plane is denoted as the x - y plane. Any plane that includes the z -axis is termed a longitudinal plane. Within the transverse plane, cylindrical coordinates (r, ϕ) are used, where $\phi \in [-\pi, \pi)$ denotes the azimuthal angle about the z -axis. The angle, which establishes its relation with the beam axis, is represented as $\theta \in [0, \pi]$ and is called the polar angle.

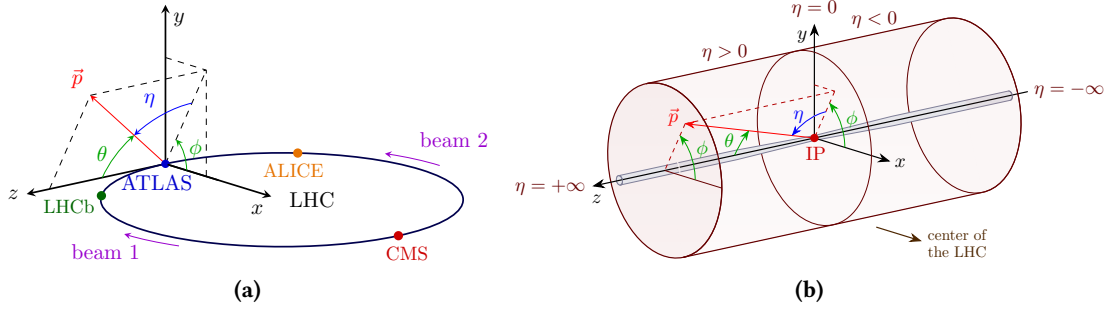


Figure 2.5: An illustration of the coordinate system of the LHC and the ATLAS detector. Adapted from Ref. [37].

Consider a particle characterized by the four-momentum (E, \mathbf{p}) , where E represents its energy and $\mathbf{p} = (p_x, p_y, p_z)$ its momentum. The momentum components p_x , p_y , and p_z correspond to the momentum projections on the x , y , and z axes, respectively. The particle's transverse momentum, p_T , is obtained by projecting its momentum onto the transverse plane: $\mathbf{p}_T = p_x \mathbf{e}_x + p_y \mathbf{e}_y$, where \mathbf{e}_x and \mathbf{e}_y are the normalized vectors of the x and y axes, respectively. The relationships between the transverse momentum norm p_T and the \mathbf{p} components are:

$$p_T = \sqrt{p_x^2 + p_y^2} = |\mathbf{p}| \sin(\theta) \quad (2.2.1)$$

$$p_x = p_T \cos(\phi) = |\mathbf{p}| \sin(\theta) \cos(\phi) \quad (2.2.2)$$

$$p_y = p_T \sin(\phi) = |\mathbf{p}| \sin(\theta) \sin(\phi) \quad (2.2.3)$$

$$p_z = \frac{p_T}{\tan(\theta)} = |\mathbf{p}| \cos(\theta). \quad (2.2.4)$$

In hadron colliders, the longitudinal momentum of the colliding partons is unknown, but momentum conservation always applies in the transverse plane. Hence, the transverse momentum is a more valuable measure than the momentum itself. Conversely, in a Lepton collider, where the initial state is known, momentum can be considered over transverse momentum.

The rapidity of a particle is given by:

$$y = \frac{1}{2} \ln \left(\frac{E + p_z}{E - p_z} \right) = \tanh^{-1} \left(\frac{p_z}{E} \right). \quad (2.2.5)$$

The difference of rapidity remains invariant under Lorentz transformation along the Z -axis, making it independent of the boost along this axis.

For ultra-relativistic particles, particularly under the approximation of a massless particle ($E \gg m$), the particle's rapidity, y , approaches its pseudorapidity, η . Pseudorapidity, favored in ATLAS over the polar angle θ , is defined as:

$$\eta = -\ln \left[\tan \left(\frac{\theta}{2} \right) \right]. \quad (2.2.6)$$

A graphical depiction of the pseudorapidity values against the polar angle is shown in Figure 2.6. It's important to note that, in the transverse plane, $\eta = 0$, and along the beam axis, η approaches $\pm\infty$.

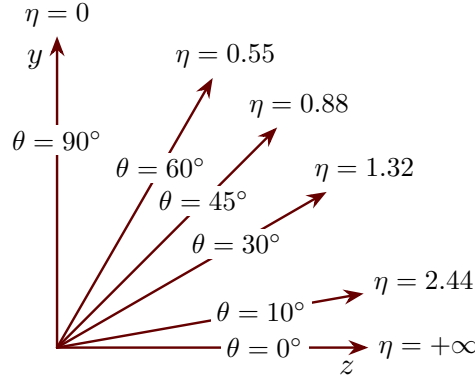


Figure 2.6: The correlation between pseudorapidity η and specific values of the polar angle θ . Adapted from Ref. [37].

The angular separation between two particles, which remains unchanged under Lorentz transformations along the z -axis, is expressed as:

$$\Delta R = \sqrt{(\Delta y)^2 + (\Delta \phi)^2} \underset{\text{massless particle}}{\approx} \sqrt{(\Delta \eta)^2 + (\Delta \phi)^2}. \quad (2.2.7)$$

2.2.2 The ATLAS Magnet Systems

Magnetic fields play an indispensable role in particle detectors. When a particle of charge q with a velocity \mathbf{v} moves within electric and magnetic fields \mathbf{E} and \mathbf{B} , it undergoes the Lorentz force (\mathbf{F}) as defined by:

$$\mathbf{F} = q(\mathbf{E} + \mathbf{v} \times \mathbf{B}). \quad (2.2.8)$$

The trajectory of the particle, primarily influenced by its momentum-to-charge ratio (p/q), bends in the presence of a magnetic field, facilitating the measurement of its charge.

Within ATLAS, a distinctive hybrid magnet system [68] is implemented. Central to this system is an axial magnetic field of magnitude 2 T, created by a solenoid, that envelops the inner detector, producing a magnetic field aligned with the beam axis in the tracking segment of the detector. The external part of the detector benefits from a toroidal magnetic field generated by the barrel and endcap toroids, which yield magnetic fields of 3.9 T and 4.1 T, respectively. This renders the magnetic field within ATLAS non-uniform. Liquid helium is the cooling agent of choice for these magnets.

The central solenoid, a cylinder characterized by specific dimensions, has its magnetic field generated by a current of 7.73 kA, cooled to 4.5 K. To optimize calorimeter performance, meticulous design considerations were applied to the solenoid, ensuring minimal material thickness preceding the calorimeter. As a consequence, for normally incident particles, the solenoid assembly contributes approximately 0.66 radiation lengths. The radiation length (X_0) is the mean distance over which a high-energy electron loses all but $1/e$ of its energy through bremsstrahlung. The steel of

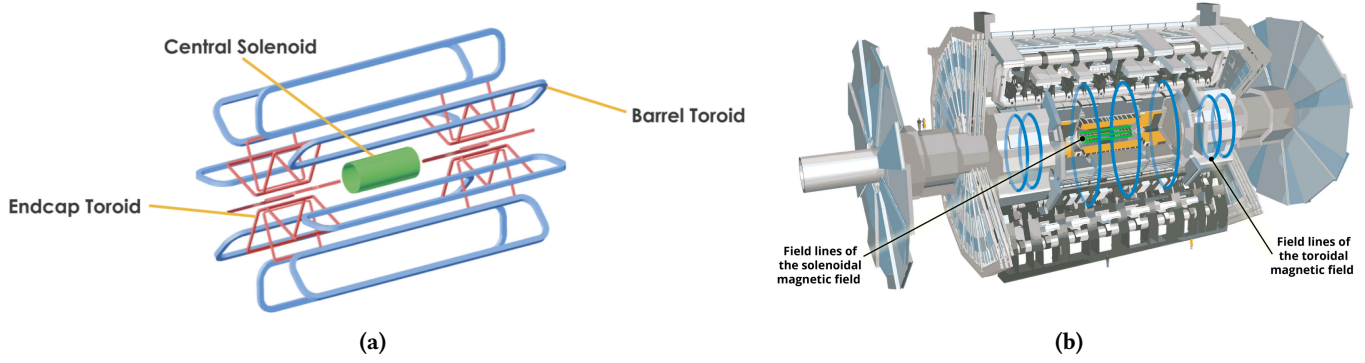


Figure 2.7: (a) Illustrations of the solenoid, barrel, and endcap toroid magnets. (b) The generated magnetic field lines: the solenoid induces a field parallel to the beam axis within the tracker (depicted by the straight green lines), whereas the toroidal magnets produce the rotating field (blue lines). The barrel toroid magnets account for the broader central field lines, and the smaller outer ones result from the combined influence of the endcap magnet field and the barrel toroid. (Adapted from Refs. [82, 83]).

the hadronic calorimeter structure returns the magnetic field flux. A noteworthy feature is the precipitous decline of the solenoidal magnetic field towards the extremities of the inner detector, as illustrated in Figure 2.8.

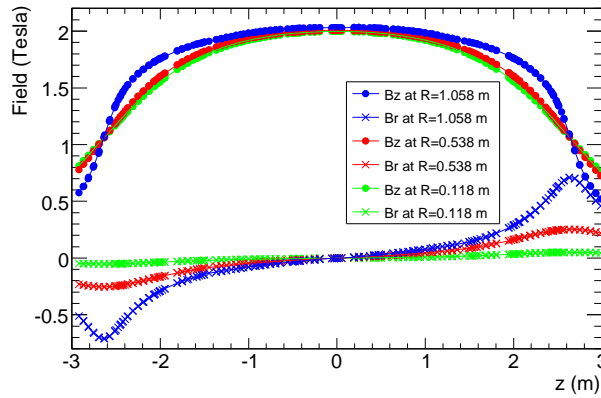


Figure 2.8: Dependence of the radial (B_r) and axial (B_z) magnetic field components on radial (R) and longitudinal (z) coordinates within the inner detector cavity (source: Ref. [68]).

Functioning in the cylindrical volume around the calorimeters and in both endcaps, the barrel toroid features eight distinct stainless-steel coils. Cooled to 4.6 K, they maintain a "racetrack-shape" with a circulating current of 20.5 kA. The sizable Lorentz forces engendered per coil are approximated at 1400 tonnes [68].

To support the muon spectrometer system in the endcap region, the endcap toroids are employed. To ameliorate the uniformity and ensure overlap of their magnetic fields with that of the barrel, they are oriented at an angle of 22.5° relative to the barrel toroid.

2.2.3 The ATLAS Inner Detector

The ATLAS Inner Detector (ID) [84], depicted in Figure 2.9, covers a region defined by $|\eta| < 2.5$. This detector integrates three sub-detectors: the pixel detector, the Semi-Conductor Tracker (SCT), and the Transition Radiation Tracker (TRT). Figure 2.9c illustrates the arrangement of these sub-detectors: in the barrel region, they form concentric cylinders about the beam axis, and in the endcaps, they are organized into disks oriented perpendicularly to the beam axis.

Within the ID, a 2 T solenoidal magnetic field bends the trajectory of charged particles, enabling their identification and momentum measurement [68]. Specifically, the ID provides electron identification for $|\eta| < 2.0$ within the energy range of 0.5 GeV to 150 GeV, augmenting data acquired from the calorimeters. The original design specifications (TDR, [84]) stipulate a momentum resolution for the ID is given by [85]:

$$\sigma\left(\frac{1}{p_T}\right) = A \oplus \frac{B}{p_T \sqrt{\sin(\theta)}} = \left(0.00036 \oplus \frac{0.0013}{p_T [\text{GeV}] \sqrt{\sin(\theta)}}\right) \text{GeV}^{-1}, \quad (2.2.9)$$

where A is indicative of the intrinsic error on track parameters, and B denotes the error from multiple scattering.

With its detailed segmentation into cells, the ID possesses the capability to reconstruct and differentiate all collisions resulting from pile-up events. This design facilitates the reconstruction of both primary and secondary vertices for charged particle tracks with transverse momenta greater than 0.5 GeV.

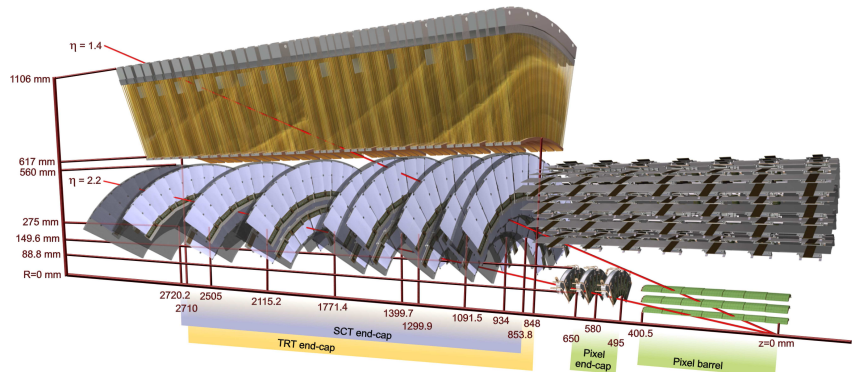
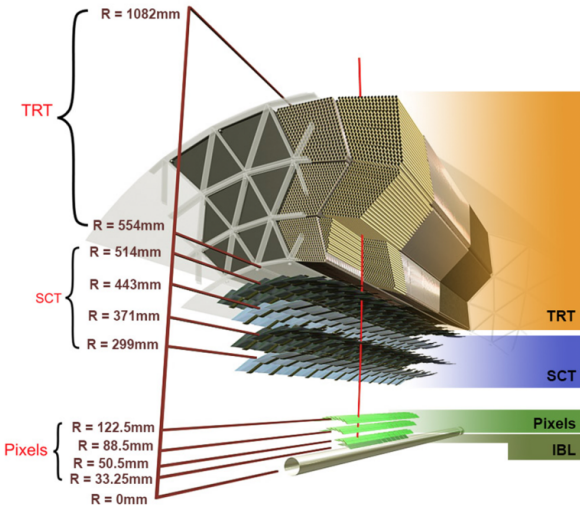
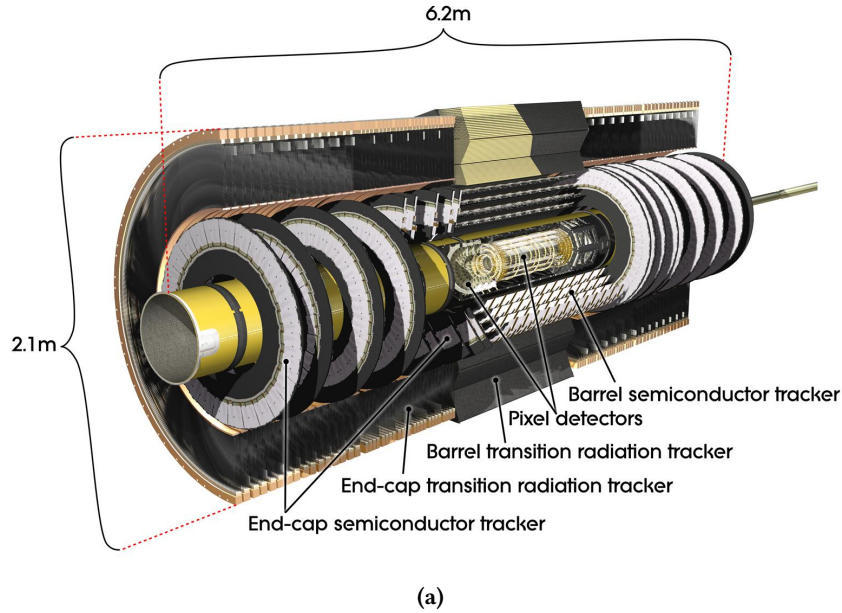


Figure 2.9: (a) The three-dimensional structure of the ATLAS inner detector. (b) Transverse and (c) longitudinal representations of the ATLAS inner detector. The Insertable B-Layer (IBL) is displayed only in the transverse view (referenced from Refs. [68, 86, 87]).

In crafting the ID layout, careful consideration was given to strike a balance between performance metrics and the thickness of the three sub-detectors. This was essential to ensure that the momentum and energy resolutions of the calorimeter remained uncompromised due to multiple scattering effects. The ID is also optimized to tolerate high irradiation conditions. Its maximum radiation length limited to $2.5 X_0$ in the forward area, as highlighted in Figure 2.10.

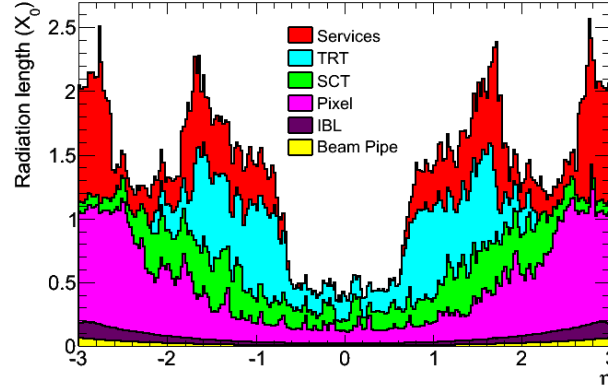


Figure 2.10: Variation of radiation length (X_0) with η for the distinct components of the inner detector (adapted from Ref. [88]).

2.2.3.1 Pixel

Situated nearest to the ATLAS beam-pipe, the pixel detector consists of four high granularity silicon layers segmented in both ϕ and z dimensions. These layers house a total of 92 million pixels: the Insertable B-Layer (IBL) and three other pixel layers named b -layer, layer 1, and layer 2. To ensure optimal performance, the temperature of the silicon cells is regulated to remain under 0°C .

Charged particles that pass through the sensor cells, typical of those found at the LHC and identified as nearly minimum-ionizing particles (MIP)[89], deposit energy by ionizing the silicon. The ionization results in the formation of electron-hole pairs, with an energy requisite of 3.6 eV for silicon. Under the influence of the electric field produced by the reverse bias voltage applied to the module electrodes, these pairs drift through the sensor. The consequent analogue signal is then captured by the electrodes, digitized, and read via a chip. Conversely, the sensor may suffer radiation damage due to non-ionizing interactions initiated by heavier particles and nuclei. Such interactions can cause a silicon atom to be displaced from its lattice position, creating a Frenkel pair (a silicon interstitial site and a residual vacancy). This disruption negatively affects MIP detection, as it diminishes signal collection efficiency and enhances sensor leakage current.

The IBL, positioned as the innermost layer of the pixel detector at a radius of 3.3 centimeters from the beam axis, provides coverage for $|\eta| < 3$. Introduced during the prolonged shut down between Run1 and Run2, it was strategically placed between the pre-existing pixel detector layers and a newly installed, smaller radius beam-pipe. Among its numerous enhancements, the IBL improves the differentiation of b -jets from gluon and light quark-originated jets, increasing the track impact parameter resolutions by about 40% for tracks with $p_T < 1\text{ GeV}$. It encompasses approximately 12 million silicon cell pixels, each measuring $50 \times 250\text{ }\mu\text{m}^2$, and employs two distinct sensor technologies: n^+ -in- n planar sensors [90] and 3D n^+ -in- p sensors [91]. These cells are built to endure the projected conditions for the end of Run 3, which include a fluence of $5 \times 10^{15}\text{ n}_{\text{eq}}\text{ cm}^{-2}$ and peak luminosity on the order of $10^{34}\text{ cm}^{-2}\text{ s}^{-1}$. The IBL's granularity enables it to achieve transverse hit spatial resolutions of $10\text{ }\mu\text{m}$ and $66.5\text{ }\mu\text{m}$ in the transverse (r - ϕ) and longitudinal (z) dimensions, respectively.

The b -layer, layer 1, and layer 2 are positioned at distances of 5.1, 8.9, and 12.3 centimeters from the beam pipe axis, respectively [68, 88]. These layers comprise silicon cells with dimensions of $50 \times 400 \mu\text{m}^2$. Each layer has transverse hit spatial resolutions of $10 \mu\text{m}$ and $115 \mu\text{m}$ for the transverse (r - ϕ) and longitudinal (z) dimensions of the barrel. The disk feature resolutions of $10 \mu\text{m}$ and $115 \mu\text{m}$ in the transverse (r - ϕ) and radial (R) dimensions.

2.2.3.2 SemiConductor Tracker

Positioned surrounding the pixel detector, the SemiConductor Tracker (SCT) represents a precision silicon microstrip detector [68, 92]. A depiction of the SCT can be observed in Figure 2.9. The main function of this tracker is the reconstruction of tracks associated with charged particles. This is accomplished utilizing 4088 silicon sensor modules of the p^+ -on- n type. Additionally, it provides significant contributions to measurements concerning the transverse momenta of these particles.

The SCT architecture comprises four cylindrical barrel layers situated within the region $|\eta| < 1.4$. The intrinsic accuracies per module for these layers are $17 \mu\text{m}$ in the transverse (r - ϕ) direction and $580 \mu\text{m}$ in the longitudinal (z) direction. Conversely, each endcap, spanning the region $1.4 < |\eta| < 2.5$, incorporates 8 planar discs. These discs yield resolutions of $17 \mu\text{m}$ in the transverse (r - ϕ) direction and $580 \mu\text{m}$ in the radial (R) orientation.

To maintain its functionality and integrity, the sensors of SCT are cooled to an approximate temperature of -7°C utilizing the C_3F_8 fluid.

2.2.3.3 Transition Radiation Tracker

Occupying the outermost layer of the inner detector, the Transition Radiation Tracker (TRT) functions as a straw-tube tracker [68, 93, 94]. The design of the TRT encompasses drift tubes with a 4-millimeter diameter. These tubes are imbued with a gaseous blend, comprising 70% Xe, 27% CO_2 , and 3% O_2 . At the core of each tube is a slender tungsten wire, measuring $31 \mu\text{m}$ in diameter, which serves as a small proportional counter. It functions to accumulate charges when a voltage approximating 1.5 kV is implemented across the straw wall and the tungsten wire.

Upon the intrusion of a charged particle into the TRT, ionization of the resident active gas within the straws occurs. After this process, the liberated electrons are directed towards the tungsten wire. Owing to the high voltage, these electrons undergo amplification, culminating in the generation of an identifiable current signal.

In terms of its construction, the barrel domain of the TRT, spanning a range $|\eta| < 1$, integrates 52,544 straw tubes. Each tube, extending 1.5 meters in length, is aligned parallel to the beam axis. The internal wires are divided electrically to facilitate the reading of charges from both straw ends. Conversely, the endcaps of the TRT, enveloping the range $1 < |\eta| < 2$, incorporate radial straws of 0.4 meters in length, which are oriented perpendicular to the beam direction. A total of 122,880 straws is included in each endcap, with charge readout conducted at the outer terminus of straws.

2.2.4 ATLAS Calorimeters

The ATLAS detector features its calorimeter system, illustrated in Figure 2.11, succeeding the inner detector and enveloping the region $|\eta| < 4.9$. The calorimeter subsystem is divided into two main sections: the barrel and the endcap calorimeters. Within these segments, further differentiation is observed with the electromagnetic calorimeter (ECAL) constituting the inner layer and the hadronic calorimeter (HCAL) forming the outer layer.

Calorimeters are engineered to fully absorb and quantify the energy of an array of particles resulting from proton-proton collisions except muons and neutrinos. This design ensures these particles deposit their entire energy and terminate their motion within the detector's confines. Structurally, each calorimeter integrates alternating layers of inactive and active materials. The former, a high-density absorbing substrate, arrests incoming particles, while the latter actively quantifies the energy of the particles.

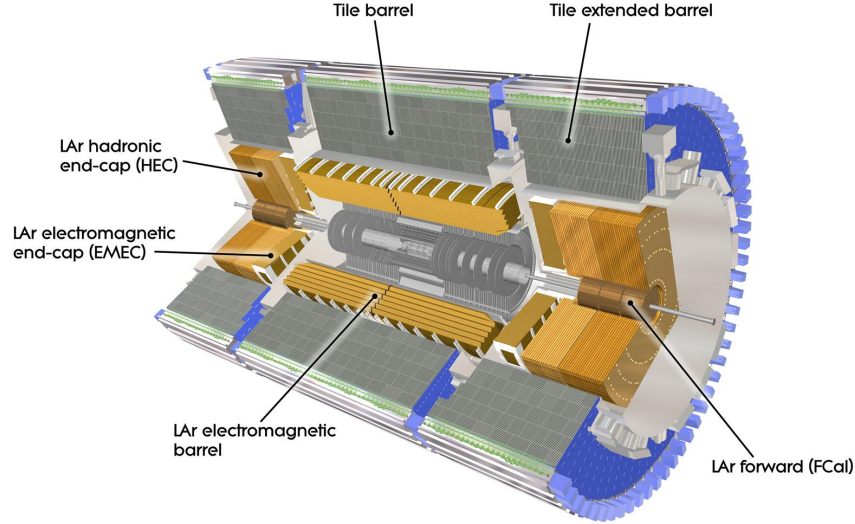


Figure 2.11: Illustrative depiction of the ATLAS calorimeter delineating both the electromagnetic and hadronic calorimeters (sourced from Refs. [68, 95]).

2.2.4.1 Electromagnetic Calorimeter

Designed with an accordion geometry, the electromagnetic calorimeter (ECAL) [68, 96] utilizes a lead-liquid argon (LAr) sampling approach, depicted in Figure 2.12. The ECAL comprises a central barrel calorimeter ($|\eta| < 1.475$) and two electromagnetic endcap calorimeters (EMEC) situated in the endcaps ($1.375 < |\eta| < 3.2$). The transition region, characterized by $1.37 < |\eta| < 1.52$, possesses significant material preceding the initial calorimeter layer, as shown in Figure 2.10. Instrumentation in this region includes scintillators positioned between the barrel and endcap cryostats, extending to $|\eta| = 1.63$. The ECAL serves to determine the energy and trajectory of electromagnetic showers.

Liquid Argon (LAr) was selected as the active medium due to its intrinsic linear response, stability over time, and inherent radiation tolerance. Mechanical strength is imparted to the lead absorber plates by adhering two stainless-steel sheets, each 0.2 mm thick. Within the barrel, these lead plates have a thickness of 1.53 mm for $|\eta| < 0.8$ and 1.13 mm for $|\eta| > 0.8$, with variations in lead thickness at $|\eta| = 0.8$ aiming to maintain a consistent sampling fraction as $|\eta|$ escalates. The sampling fraction is defined as the ratio of the energy deposited in the active medium to the total energy of the particle. In the endcap calorimeters, the plates are 1.7 mm thick for $|\eta| < 2.5$ and 2.2 mm thick for $|\eta| > 2.5$. The readout electrodes are situated in the gaps separating the absorbers.

The unique accordion design ensures full azimuthal (ϕ) coverage, optimizing particle interactions with the absorber and active layers, while also facilitating rapid signal extraction from at the front or at the rear of the electrodes. Thickness variations in the barrel calorimeter range from $22X_0$ to $33X_0$ based on increasing $|\eta|$, while the endcap calorimeters go from $24X_0$ to $38X_0$. As demonstrated in Figure 2.12, the accordion waves in the barrel are oriented axially and align with φ . To maintain a uniform liquid-argon gap, the folding angles of these waves adjust with radius. Conversely, in

the endcaps, waves align with the radial direction and are oriented axially. Similarly, the amplitude of the wave and the folding angles of both absorbers and electrodes change with the radius. Such design intricacies yield consistent performance in terms of both linearity and resolution across ϕ .

As highlighted in Figure 2.12, the barrel calorimeter features three layers: front, middle, and back. A LAr pre-sampler layer precedes the front layer in the region $|\eta| < 1.8$ to quantify energy losses of electrons and photons before the calorimeter. Thicknesses in the barrel and endcaps for this layer are 1.1 cm and 0.5 cm, respectively. The front layer possesses an optimized granularity along $|\eta|$, with a depth of $4.3X_0$ designed to distinguish neutral pions (π^0) that decay into two photons from individual photons. The middle layer, having a depth of $16X_0$, captures the majority of the shower energy, while the back layer at a $2X_0$ depth mainly measures shower tails but also aids in approximating energy escaping beyond the ECAL.

The relative energy resolution of the ECAL can be represented as

$$\frac{\sigma(E)}{E} = \frac{a}{\sqrt{E}} \oplus \frac{b}{E} \oplus c, \quad (2.2.10)$$

where the *sampling term* a pertains to stochastic fluctuations during calorimeter shower development. Simulations and prior test-beam measurements agree well in this context. The *noise term* b accounts for electronic disturbances. Lastly, the *constant term* c includes contributions unaffected by energy variations, such as radiation damage and detector non-uniformities. The dependence of these parameters on η and the particle energy varies. High-energy particles predominantly experience the effects of the constant term, while the sampling term is predominant at moderate energy levels, and the noise term is prevalent at lower energies. The designed values for the sampling and constant terms are respectively $a = 10\%$ and $c = 0.7\%$, with the noise term determined as $b = 350 \times \cosh(\eta)$ MeV for a cluster of 3×7 cluster in the barrel, given an average interaction count per bunch crossing $\mu = 25$ [97]. To reconstruct the EM clusters, the EM calorimeter is divided into a grid of $N_\eta \times N_\phi$ towers of size $\eta \times \phi = 0.025 \times 0.025$.

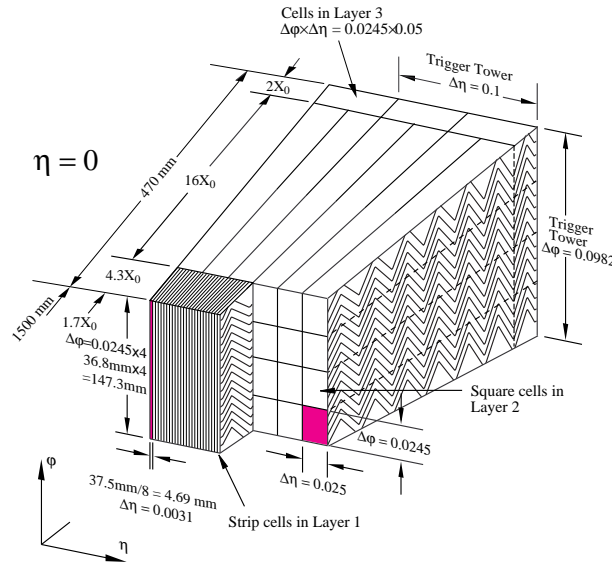


Figure 2.12: Illustration of a barrel module. The granularity in η and ϕ of the cells across the three layers, in conjunction with the trigger towers, is displayed (source: Ref. [68]).

2.2.4.2 Hadronic Calorimeter

The hadronic calorimeter (HCAL) plays a crucial role in measuring the energy of hadrons such as protons, neutrons, and pions, which fail to deposit their full energy in the electromagnetic

calorimeter (ECAL) [68]. Positioned around the ECAL, the HCAL is sectioned into three distinct regions: the central barrel hadronic calorimeter, Tile Calorimeter (TileCal), covering $|\eta| < 1.7$, the Hadronic Endcap Calorimeters (HEC) in the span of $1.5 < |\eta| < 3.2$, and the LAr hadronic Forward Calorimeter (FCal) that caters to the $3.1 < |\eta| < 4.9$ range.

Constructed with steel as its absorber and plastic scintillator as the active medium, the TileCal is designed to measure the energy of incoming particles. Upon encountering the steel layers, these particles initiate a cascade of secondary particles. Subsequently, the plastic scintillators generate photons, which are translated into an electric current by a photomultiplier. This current's magnitude aligns with the energy of the initiating particle. Comprising 420,000 plastic scintillator tiles and 9,500 photomultipliers, the TileCal, with a radial depth of $7.4X_0$, consists of a central barrel and two extended barrels, as illustrated in Figure 2.11. With 64 distinct modules in total, the structure is depicted in Figure 2.13, ensuring full coverage in the ϕ direction. Every tile in the calorimeter is oriented perpendicular to the beam axis and spans radially.

Located posterior to the electromagnetic calorimeter endcaps (EMEC), the hadronic endcap calorimeters (HEC) feature a copper/liquid argon combination for absorber and active material, respectively. The HEC consists of two cylindrical wheels for each endcap, designed with an overlap with the forward calorimeter. Every wheel, aligned perpendicular to the beam axis, boasts a diameter of 4 meters and is built from 32 wedge-shaped modules, all identical in design.

Situated adjacent to the beam axis, the LAr hadronic forward calorimeter (FCal) resides beside the endcap calorimeters. This proximity ensures minimal energy losses in gaps between calorimeter systems and largely shields the muon spectrometer from most background radiation. The FCal hosts three modules per endcap, with one electromagnetic module (FCal1) followed by two hadronic ones (FCal2 and FCal3). Copper serves as the absorber for FCal1, while tungsten is the chosen material for FCal2 and FCal3, aiming to contain and limit the lateral dispersion of hadronic showers.

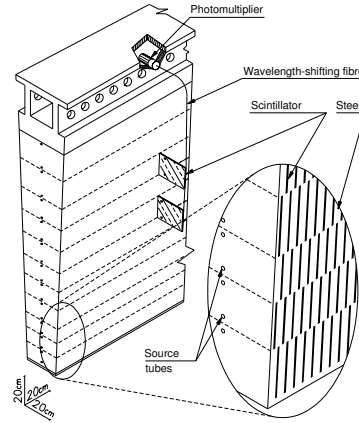


Figure 2.13: A schematic of the hadronic tile calorimeter module, showcasing the components of the optical readout, including tiles, fibers, and photomultipliers. Adapted from Ref. [68].

When merging readings from the TileCal or HEC with those from the electromagnetic calorimeters for hadronic particle assessments, the jet energy resolution achieved is [68]:

$$\frac{\sigma(E)}{E} \approx \frac{50\%}{\sqrt{E}} \oplus 3\%, \quad (2.2.11)$$

Contrastingly, the energy resolution for the FCal is noted as:

$$\frac{\sigma(E)}{E} \approx \frac{100\%}{\sqrt{E}} \oplus 10\%. \quad (2.2.12)$$

2.2.5 ATLAS Muon Spectrometer

Due to their higher mass compared to electrons, muons experience reduced energy radiation via the bremsstrahlung effect. Consequently, they often traverse the inner detector and calorimeters with minimal energy loss.

The muon spectrometer (MS) [68], encircling the calorimeters, is partitioned into two regions: the barrel spectrometer, covering $|\eta| < 1.2$, and the endcap spectrometers for $1 < |\eta| < 2.7$. A triggering mechanism for muons is designed for the region $|\eta| < 2.4$. The spectrometer is capable of independently determining the direction, electric charge, and momentum of muons with energies exceeding 3 GeV by observing their trajectory's curvature. For energies below 3 GeV, energy loss within the calorimeter can inhibit this standalone measurement, necessitating the inclusion of track information from the inner detector. A notable characteristic of the MS is its excellent charge identification.

Muons are bent in the R - z plane as the toroidal magnetic field is orthogonal to the muon's trajectory in the r - ϕ plane. This orientation minimizes resolution degradation due to multiple scattering during muon passage through the MS layers.

The MS integrates several distinct detectors as depicted in Figure 2.14. The Monitored Drift Tubes (MDT), consisting of three to eight layers of drift tubes, measure track curves spanning $|\eta| < 2.7$ and achieve an average resolution of $80\ \mu\text{m}$ per tube, translating to a chamber precision of approximately $35\ \mu\text{m}$. The Cathode Strip Chambers (CSC), crucial for high-precision coordinate measurement in the detector's forward section, are utilized predominantly in the innermost tracking layer of the forward region ($2 < |\eta| < 2.7$) due to heightened rate capability and time resolution. The Resistive Plate Chambers (RPC), located in concentric cylinders and spanning $|\eta| < 1.05$, serve triggering functions and furnish a secondary coordinate measurement. The Thin Gap Chambers (TGC) are installed in the forward region ($1.05 < |\eta| < 2.4$) and play roles in triggering, providing an auxiliary coordinate measurement to complement the data from the MDT chambers.

The MS's transverse momentum resolution performance fluctuates between 3% and 12%, correlating to p_T values in the range 10 GeV to 1 TeV.

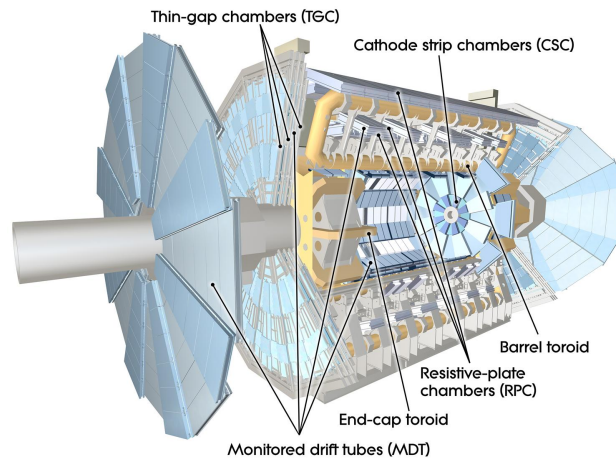


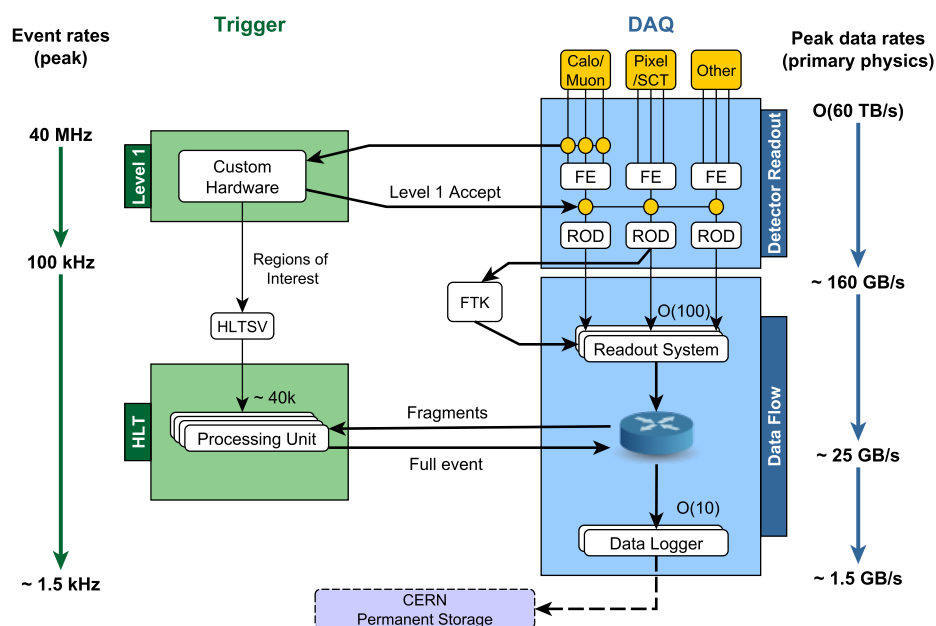
Figure 2.14: Representation of the Muon Spectrometer (Source: Ref. [98]).

2.2.6 ATLAS Data Trigger and Acquisition System

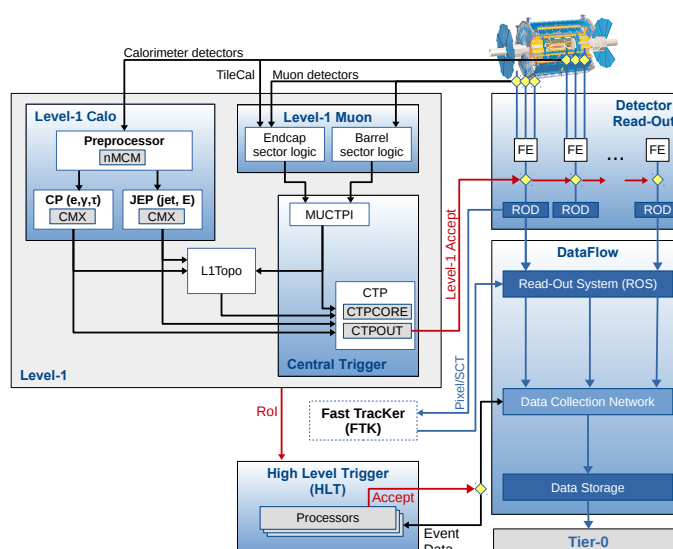
Every second, 1.7 billion proton-proton collisions happen in the ATLAS interaction region [99]. Recording such vast data would necessitate an impractical storage capacity of 60 million megabytes per second. From a physics perspective, only a few of these collisions hold significance, with the

majority being simply elastic or low-energy inelastic collisions. The Trigger and Data Acquisition (TDAQ) system, illustrated in Figure 2.15, is responsible for identifying and retaining events of potential physics relevance [100, 101]. The TDAQ operates based on input derived from various sections of the detector.

For Run 1, the TDAQ employed a tri-stage system, consisting of the level 1 (L1), level 2 (L2) triggers, and the event filter. However, in response to the elevated instantaneous luminosity in Run 2 and Run 3, the TDAQ system was modified to incorporate just two decision-making levels: the L1 trigger and a high-level trigger (HLT). The L1 trigger, embedded within the ATLAS detector, is a hardware-based system that makes decisions grounded on raw data from a segment of information emanating from the calorimeters and the muon spectrometer, primarily seeking characteristic concurrent signals. A decision by the L1 trigger is reached within a brief span of 2.5 microseconds post-event, during which the event details are temporarily stored in a buffer. This L1 decision effectively slashes the data rate from 40 MHz to 100 kHz, thereby shortlisting merely 100,000 events per second. Events that gain acceptance at this level undergo further scrutiny by the HLT, which further diminishes the data rate to a manageable 1.5 kHz. This rate represents the collection of events earmarked for subsequent offline Physics analyses. With access to around 40,000 CPU cores, the HLT reaches its verdict in 200 microseconds, employing comprehensive detector information and adhering to stringent selection criteria via reconstruction algorithms, akin to those used offline.



(a)



(b)

Figure 2.15: The Trigger and Data Acquisition (TDAQ) mechanism employed by ATLAS during Run 2. (a) displays anticipated peak rates and bandwidths across each component, whereas (b) shows into the intricacies of the Level 1 (L1) trigger system (sourced from Ref. [101]).

CHAPTER 3

Object Reconstruction and Identification within the ATLAS Detector

3.1	Reconstruction of Primary Vertices and Particle Tracks	65
3.2	Electron in the ATLAS Detector	68
3.2.1	Electron Reconstruction	68
3.2.2	Criteria for Electron Identification and Isolation	70
3.2.3	Calibration of Electron Data	72
3.3	Muon at ATLAS	73
3.3.1	Muon Reconstruction	74
3.3.2	Criteria for the Isolation and Identification of Muon Candidates	74
3.4	Tau Leptons at ATLAS	77
3.5	Jets in the ATLAS Detector	78
3.5.1	anti- k_t Algorithm for Jet Reconstruction	78
3.5.2	Particle Flow and EMTopo Reconstruction Approaches	80
3.5.3	Flavour Tagging	81
3.6	Missing Transverse Energy	84

Events, once recorded, are subject to offline algorithms specifically designed for the reconstruction and identification of events. Through the combination of measurements from sub-detectors, it becomes feasible to perform the calibration, identification, and reconstruction of physics objects or particles, such as tracks, vertices, leptons, missing transverse energy, photons, jets, and more. The current chapter provides a description of this complex process, which is uniformly applied to both event simulations and data.

An example of this process is the reconstruction of an electron, demonstrated in Figure 3.1. To reconstruct the track of electron, direction, and momenta, it is essential to combine hit measurements from the tracking segment of the detector. Subsequently, this information is paired with measurements from the electromagnetic calorimeter to determine its energy.

It is vital to clarify the concepts of efficiency and rejection, as these two notions dominate the entirety of this chapter. The efficiency of identification (represented by ε) refers to the proportion of a particular number before and after the application of a selection, such as the number of jets of certain kind. The b -tagging efficiency (ε_b) in a b -tagging algorithm can be mathematically expressed as:

$$\varepsilon_b = \frac{N_{b\text{-jet}}^{\text{tagged}}}{N_{b\text{-jet}}^{\text{total}}} = \frac{N_{b\text{-jet}}^{\text{tagged}}}{N_{b\text{-jet}}^{\text{tagged}} + N_{b\text{-jet}}^{\text{untagged}}}. \quad (3.0.1)$$

The rejection ratio for a selection is defined as $1/\varepsilon$. For instance, a c -jet rejection of 100 in a b -tagging algorithm indicates that only one out of 100 authentic c -jets will be b -tagged. Thus, a higher c - and light-jet rejection corresponds to a superior b -tagging algorithm for a given efficiency,

as it will exclusively select b -jets while rejecting c - and light-jets.

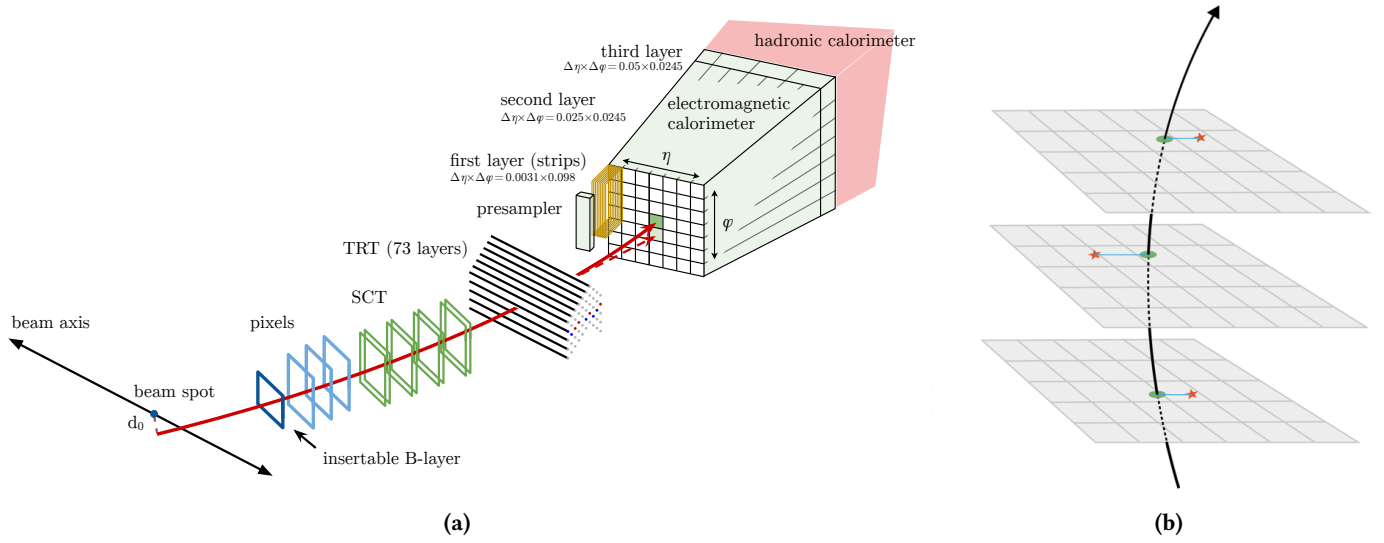


Figure 3.1: (a) A diagram showing the path of an electron (depicted by the red solid line) through the ATLAS detector, including its passage through the tracking system and the electromagnetic calorimeter where it releases its energy. The dashed red line portrays the path of a photon generated by the interaction of electron with the tracking system material. (b) An illustration of a charged particle traversing sub-detector planes, with red stars marking hit measurements in the layers, black arrows for fitted tracks, green dots for reconstructed track intersections, and blue lines for the distance between each layer's track and hit (Adapted from Refs. [87, 102]).

3.1 Reconstruction of Primary Vertices and Particle Tracks

Charge particle track reconstruction holds paramount importance across various physics analyses [103, 104]. Crucially, discerning primary (PV) from secondary (SV) vertices is instrumental in distinguishing between light- and c -jets and b -jets. Given the relative long lifetime of b -hadrons (approximately $\tau \approx 1.5$ ps) [105], their consequential flight distance ($\gamma c\tau$) ranges from $450 \mu\text{m}$ to several millimeters contingent on their relativistic factor. This results in the decay of b -hadrons into distinct particles, culminating in the formation of a secondary vertex, a signature feature of the b -jet, as illustrated in Figure 3.2b.

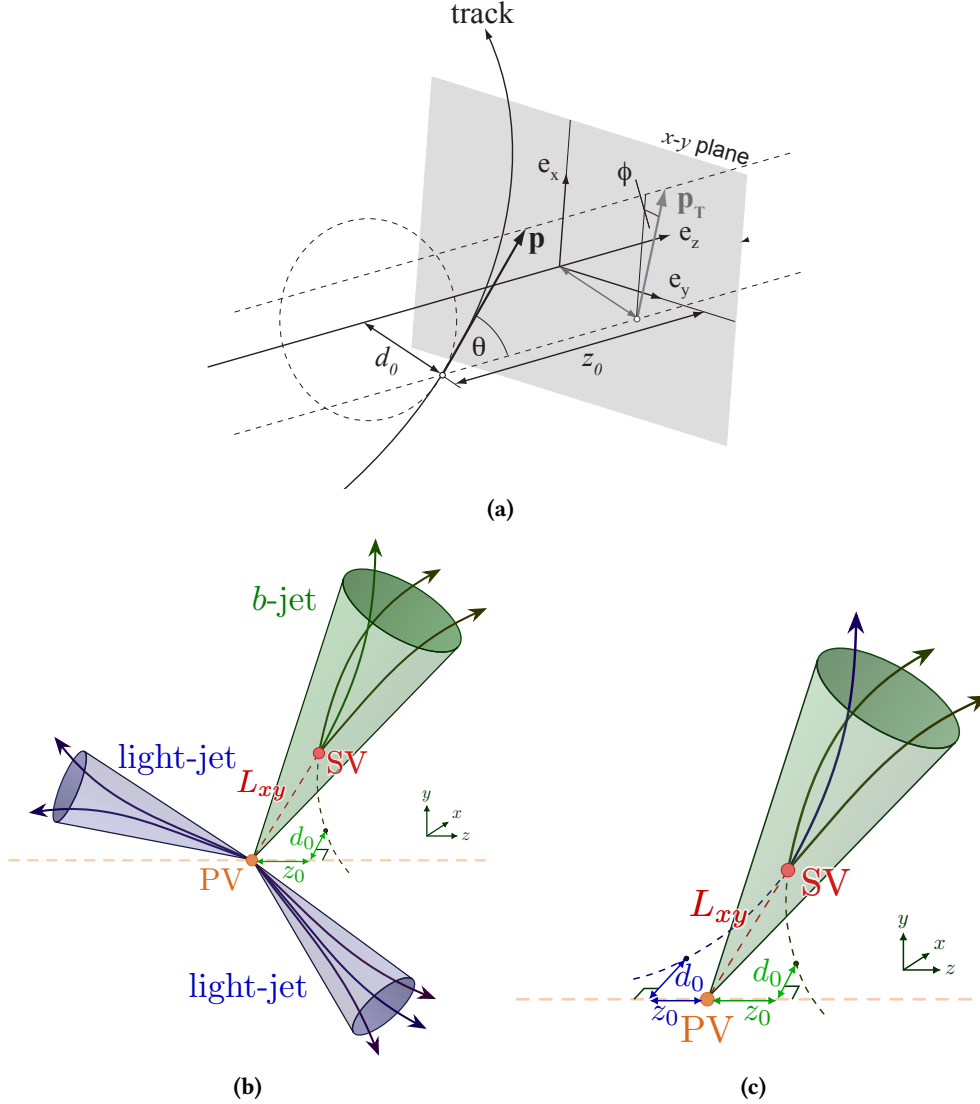


Figure 3.2: (a) Schematic representation of the track helix parameters ATLAS utilizes for comprehensive track description. (b) Comparative schematic of Light- and b -jet tracks. Light-jets originate at the primary vertex (PV) while b -hadrons generate a secondary vertex (SV) distanced from the primary vertex. Tracks associated with b -jets are typified by pronounced longitudinal (z_0) and transverse (d_0) impact parameters. (c) Depiction of the longitudinal and transverse impact parameters related to two varied tracks (blue and green) from a b -jet (sourced from Refs. [37, 106]).

Charged particles within the ATLAS inner detector are governed by helicoidal trajectories due to the influence of the solenoidal magnetic field. Such trajectories can be comprehensively described using five helical parameters: $d_0, z_0, \theta, \phi, q/p$ [104, 106], as depicted in Figure 3.2. The point where the track comes closest in transverse approach to the beam axis is designated as the perigee.

The transverse impact parameter (d_0) represents the transverse distance between the beam axis and the perigee. The distance, longitudinally, between the transverse plane ($x-y$)—which contains ei-

ther the nominal interaction point or the primary vertex depending on the context—and the perigee is defined by the longitudinal impact parameter (z_0). The azimuthal angle of the direction of track at its perigee is characterized by the track azimuthal angle (ϕ). Meanwhile, the track polar angle (θ) indicates the polar angle of the track’s direction at its perigee. Due to the solenoidal magnetic and the field strength of 2 T, measuring the sagitta (curvature) of the track, the charge-momentum ratio (q/p) can be deduced.

An *inside-out* method is employed by ATLAS for track reconstruction, meaning that the information from the inner subdetectors (pixel detector and SCT) is utilized first, followed by the outer TRT data. The reconstruction process initiates with clusters being assembled from the raw measurements of inner detector. Clusters are utilized to perform three-dimensional measurements, reconstructing the point—referred to as *space-point*—through which the charged particle passed the active material of inner detector.

After the reconstruction of space-points, a track-seeding process is initiated. This involves the formation of triplets of space-points, which are considered seeds, either from the pixel or SCT subdetectors, that are consistent with a charged particle track’s origin. To minimize combinatorics, *search roads* are established to find the remaining detector through the estimated seed trajectory.

Track candidates are subsequently formulated by radially extending the seeds using the Kalman filter [107], which identifies both outward and inward adjacent clusters, refining the trajectory in the process. Any overlaps between track candidates are addressed through an ambiguity resolution step. The ranking of track candidates is based on specific criteria, including the track fit χ^2 , the transverse momentum, and the number of clusters associated with the track.

For quality control, a minimum of seven hit clusters is required for a track, taking into account hits from the silicon tracker and SCT, with no more than two shared clusters per track. The track is then extended to the TRT, with the Kalman filter used again to initiate a search from the position estimation of the track candidate within the TRT volume. If the extension is deemed successful, the TRT hits are appended to the tracks, and a global χ^2 fit is applied again.

It should be noted that seeds not meeting track-finding requirements undergo a check for calorimeter compatibility. If a seed falls within a calorimeter’s region of interest (ROI), the track procedure is repeated, allowing for an additional track “kink”. This method, known as *bremsstrahlung recovery*, enhances the reconstruction efficiency of electrons.

While the inside-out procedure is efficient for reconstructing tracks from primary pp interactions, it may fail for particles produced further from the beam-pipe. To address this, an *outside-in* method is employed, which prioritizes TRT data before utilizing pixel and SCT information.

The efficiency of track reconstruction for charged particles inside jets in simulated dijet events is illustrated in Figure 3.3.

In Figure 3.4, the enhancements in the resolution of both the transverse and longitudinal impact parameters from Run 1 to Run 2 are depicted. These improvements are attributed to the integration of the Insertable B-Layer (IBL) within the inner detector during Run 2.

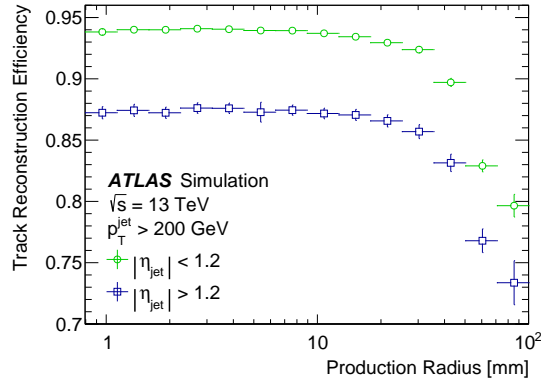


Figure 3.3: Efficiency of track reconstruction for charged primary particles within jets having $|\eta| < 1.2$ ($|\eta| > 1.2$) plotted against the production radius in simulated dijet MC events (sourced from Ref. [103]).

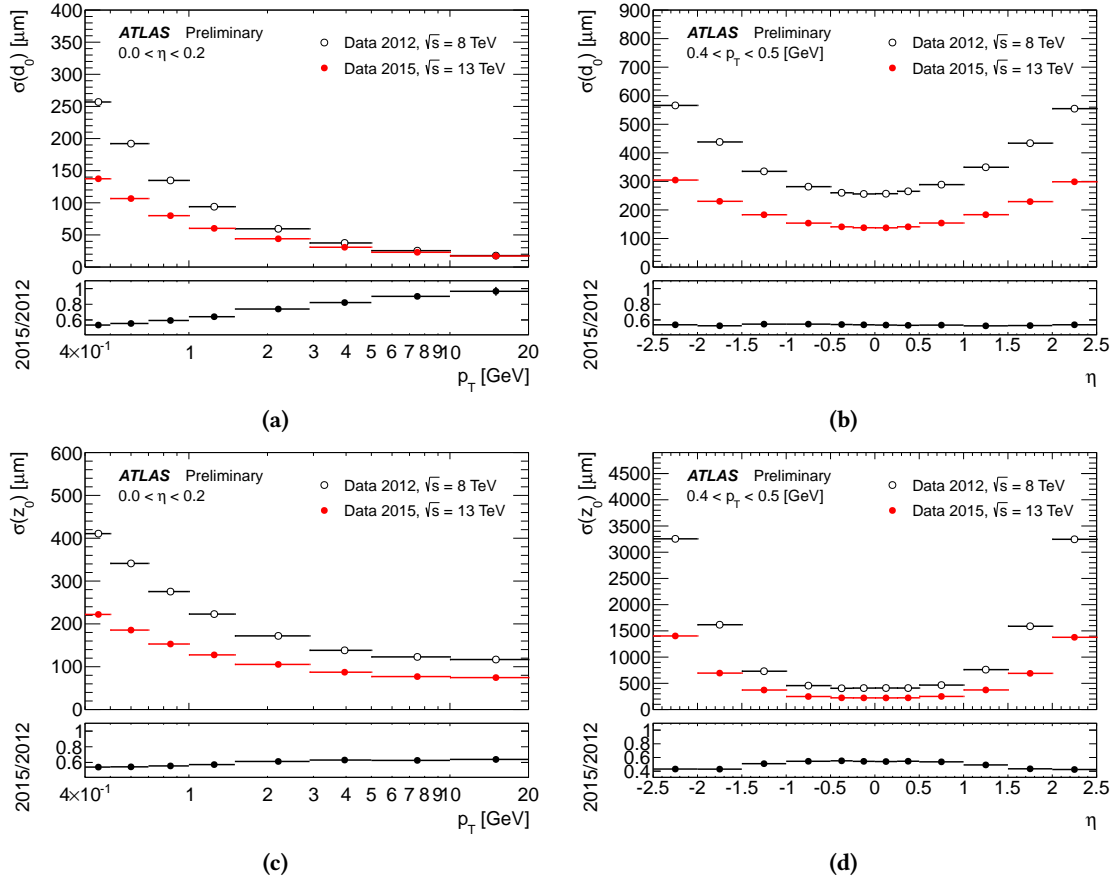


Figure 3.4: Spatial resolution (σ) comparison for the transverse (d_0) and longitudinal (z_0) impact parameters between Run 1 (2012, $\sqrt{s} = 8$ TeV) and Run 2 (2015, $\sqrt{s} = 13$ TeV) datasets, plotted as a function of (a), (c) p_T within $0 < \eta < 0.2$, and (b), (d) η for the range $0.4 < p_T < 0.5$ GeV. The observed improvements can be associated with the Run 2 integration of the Insertable B-Layer (IBL) in the inner detector (source: Ref. [108]).

3.2 Electron in the ATLAS Detector

When electrons traverse the ATLAS detector, they are identified by the tracks they imprint within the inner detector and their energy deposition in the electromagnetic (EM) calorimeter [109–111], as illustrated in Figure 3.1. The preliminary step involves the reconstruction of the electromagnetic shower associated with the electron candidate. Subsequently, data from both the calorimeter and the inner detector are coordinated within the $\eta \times \phi$ phase space to facilitate electron identification. The process finishes with the calibration of the detected electron.

3.2.1 Electron Reconstruction

Prior to 2017, the reconstruction of electromagnetic showers employed a *sliding-window* algorithm, resulting in clusters of fixed size [112]. However, post-2017, ATLAS adopted the *dynamical topological cell clustering* method (often abbreviated as topo-cluster) [109–111, 113]. This new method creates clusters with a variable size. The dynamic topo-cluster algorithm addresses the primary limitation of the sliding-window algorithm by effectively recovering energy from bremsstrahlung photons and photon conversions. Importantly, its performance regarding energy response linearity and pile-up stability remains comparable to its predecessor.

The working principle of the topo-cluster algorithm is as follows:

The algorithm initiates by iteratively generating *proto-clusters* from both electromagnetic and hadronic calorimeters. This is done using predefined noise thresholds. The cell responsible for initiating the cluster must satisfy the condition:

$$\zeta_{\text{cell}}^{\text{EM}} = \frac{E_{\text{cell}}^{\text{EM}}}{\sigma_{\text{noise,cell}}^{\text{EM}}}, \zeta_{\text{cell}}^{\text{EM}} > n_{\text{seed}}, n_{\text{seed}} = 4 \text{ as default} \quad (3.2.1)$$

where $E_{\text{cell}}^{\text{EM}}$ represents the net energy in the calorimeter cell after accounting for and subtracting an expected average contribution of the noise, including electronic and pile-up noise. Due to noise subtraction, $E_{\text{cell}}^{\text{EM}}$ can occasionally have a negative value. Meanwhile, $\sigma_{\text{noise,cell}}^{\text{EM}}$ denotes the anticipated cell noise, which factors in all recognized sources of noise, primarily from electronics and pile-up.

The following condition is imposed: $\zeta_{\text{cell}}^{\text{EM}} > n_{\text{seed}}, n_{\text{seed}} = 4$ as default where n_{seed} is the minimum number of cells required to initiate a proto-cluster.

All neighboring cells satisfying $|\zeta_{\text{cell}}^{\text{EM}}| > 2$ are incorporated into the proto-cluster. Each such cell then acts as a seed cell, repeating the process. If a common cell is shared by two proto-clusters, they are merged. This approach is resilient to energy biases since it utilizes $|\zeta_{\text{cell}}^{\text{EM}}|$, ensuring that even negative energy cells are considered, preventing proto-cluster energy overestimation. Subsequently, a "crown" made up of the nearest neighbor cells is annexed to the proto-clusters, regardless of their significance. If multiple local maxima are identified, the proto-cluster is partitioned into individual clusters.

To pre-select potential electron clusters, the EM fraction (f_{EM}) is defined as:

$$f_{\text{EM}} = \frac{E_{L1} + E_{L2} + E_{L3} + w(E_{E4} + E_{\text{PS}})}{E_{\text{clus}}}, \quad w = \begin{cases} 1 & \text{if } 1.37 < |\eta| < 1.63 \\ 0 & \text{otherwise} \end{cases} \quad (3.2.2)$$

Where E_{Lx} indicates the energy in the calorimeter's layer x . The term $E_{E4} + E_{\text{PS}}$ is considered only for clusters in the transition region, as electron energy deposition in the pre-sampler and scintillator layers is significant.

Considering that electrons deposit a majority of their energy in the electromagnetic calorimeter, f_{EM} values are expected to be proximate to 1. Therefore, electron candidate clusters are typically mandated to have $f_{\text{EM}} > 0.5$. This criterion has shown to effectively eliminate about 60% of pile-up clusters without hampering the true electron topo-clusters selection, as illustrated in Figure 3.5. Additionally, only clusters with an EM energy surpassing 400 MeV are deemed suitable.

The properties of the proto-cluster, such as its energy, momentum, and center of gravity, are ascertained by weighted sums, factoring in each cell's energy and their geometrical weight within the proto-cluster [113].

EM clusters that meet the loose shower shape regarding energy leakage in the hadronic calorimeter and energy distribution in η are used to define the region of interest (ROI) where standard track reconstruction is performed. Tracks are subsequently paired with the EM clusters based on stringent criteria in η and ϕ .

Superclusters are derived in two phases: EM topo-clusters are scrutinized as potential seed cluster candidates, and neighboring EM topo-clusters to these seeds are labeled as *satellites*. These satellites, which can arise due to the bremsstrahlung effect, are integrated into the supercluster if they meet specific requirements.

Finally, the supercluster undergoes calibration by pairing tracks similarly to the EM topo-clusters. This results in the formation of the corresponding electron object intended for analysis. Figure 3.6 showcases the reconstruction efficiencies during various electron reconstruction stages as a function of transverse energy.

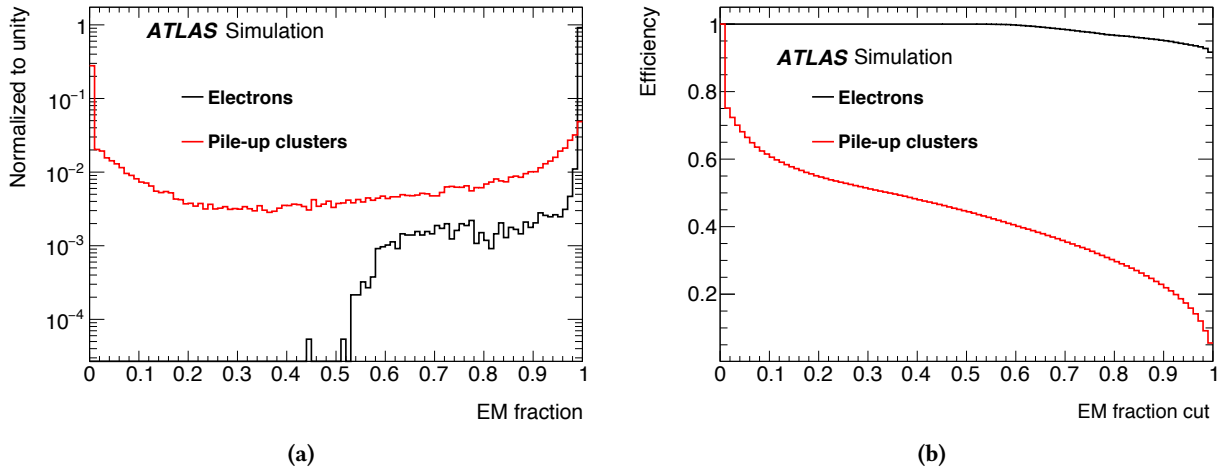


Figure 3.5: (a) Distribution of the EM fraction (f_{EM}) and (b) reconstruction efficiency as a function of the f_{EM} selection requirement for simulated true electron (black) and pile-up (red) clusters (taken from Ref. [109]).

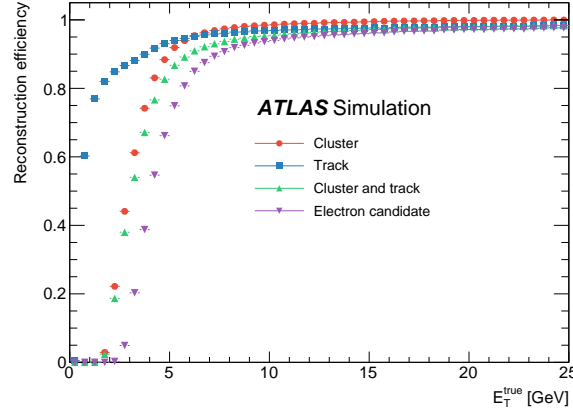


Figure 3.6: Reconstruction efficiencies for cluster, track, cluster and track, and electron as a function of the generated electron E_T (taken from Ref. [109]).

3.2.2 Criteria for Electron Identification and Isolation

Following the reconstruction process, criteria are established to enhance the purity of selected electrons, subsequently leading to the rejection of inauthentic electrons [109–111]. Discriminating variables, employed to assess electron quality, can be categorized into several groups: lateral, longitudinal shower development profiles, electron tracking, and the compatibility of track-cluster association. Notably, some discriminant variables encompass the transverse impact parameter (d_0) of the track, its significance ($|d_0/\sigma(d_0)|$), hit count, the energy deposition variables in the lateral shower for the η and ϕ directions, lateral width, longitudinal shower shape, energy leakage in the hadronic calorimeter, and the E/p ratio.

In the ATLAS framework, three electron quality criteria or working points, namely *LHTight*, *LHMedium*, and *LHLoose*, are delineated. Here, "LH" is an abbreviation for likelihood. Utilizing the probability density functions of the discriminant variables (typically encompassing 13 variables), this likelihood is segregated into 9 bins for η and 12 for E_T . A unique outcome, d_L , represents the likelihood's discriminant. The working points correlate with three diminishing fixed values of the LH discriminant d_L . Consequently, the resultant identification efficiencies for electrons with $E_T = 40$ GeV are 80%, 88%, and 93% for *LHTight*, *LHMedium*, and *LHLoose* working points respectively, as depicted in Figure 3.7.

Electrons can be separated into *prompt* and *non-prompt* types. While *prompt* electrons originate directly from the primary collision, *non-prompt* electrons, which are not necessarily isolated, are emitted, for instance, during the semi-leptonic decay of heavy hadrons (such as in the case of an electron associating within a jet). It is crucial to highlight that *non-prompt* electrons are not rejected via the quality criteria since they are genuine electrons. The isolation criteria can be fundamentally gauged through energy deposits within the calorimeter surrounding the electron (termed *calorimeter isolation*) or via tracks of proximate charged particles (*track isolation*). A combination of both the calorimeter and track isolation criteria can also be employed.

ATLAS stipulates distinct working points for both calorimeter and track isolation, shown in Table 3.1. These points can either target an explicit efficiency value (under the *Gradient WP*) or can be anchored on fixed cutoffs on the isolation variables (e.g., *HighPtCaloOnly*, *Loose*, and *Tight* WPs). The efficiency corresponding to the diverse isolation working points is illustrated in Figure 3.8. Depending on the event topology targeted, each physics analysis necessitates unique isolation criteria. As such, isolating becomes a balance between efficaciously identifying prompt electrons, whether isolated or originating in high-activity surroundings, and proficiently excluding electrons resulting from heavy-flavour decays or light hadrons misidentified as electrons.

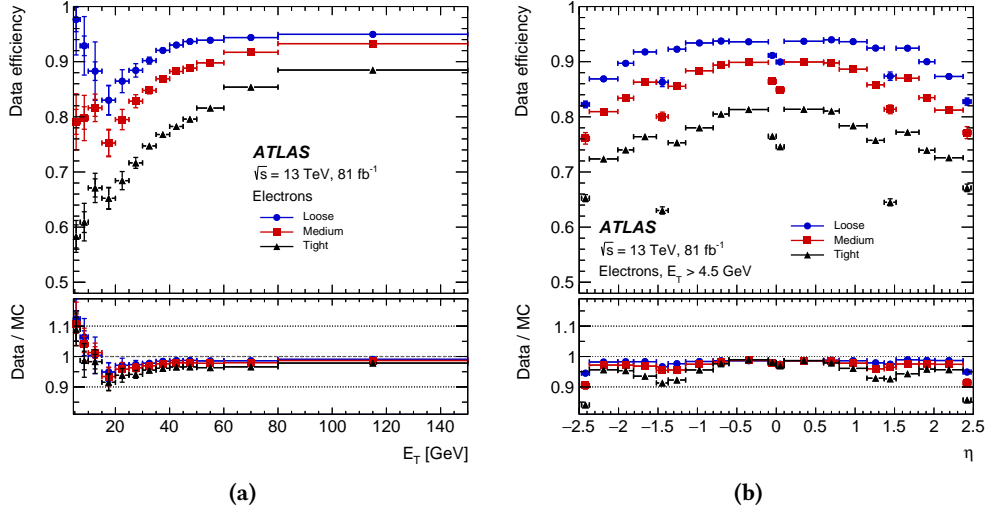


Figure 3.7: Electron identification efficiency in $Z \rightarrow e^+e^-$ events in data as a function of (a) E_T and (b) η for the Loose, Medium and Tight operating points. For both plots, the bottom panel shows the data-to-simulation ratios (taken from Ref. [109]).

For calorimeter-based isolation, the energy enveloping the electromagnetic shower, symbolized as E_T^{coneXX} , is ascertained using a cone $\Delta R = XX/100$ centered on the electron cluster barycenter. By illustration, for $XX = 20$, $\Delta R = 0.2$ and consequently E_T^{cone20} is measured. This is achieved by subtracting the summation of core EM shower energy, the transverse energy dispersing beyond the core, and pile-up contributions from the total energy encapsulated within the cone [109].

For track-based isolation, the transverse momentum, represented as $p_T^{\text{varconeXX}}$, is deduced by summing the transverse momenta of chosen tracks within a cone centralized around the electron track, excluding those tracks directly matched to the electron. Here, the cone possesses a variable radius ΔR , as articulated in Equation (3.2.3). Only those tracks that satisfy certain criteria are considered: they must exhibit $p_T > 1$ GeV, bear $|\eta| < 2.5$, possess a minimum of 7 silicon hits (from Pixel+SCT subdetectors), and exhibit a loose association with the vertex. This implies they must either have been utilized in the primary vertex fit or should adhere to $|z_0| \sin(\theta) < 3$ mm, with z_0 representing the longitudinal distance of impact parameter from the primary vertex.

$$\Delta R = \min \left(\frac{10}{p_T [\text{GeV}]}, \Delta R_{\text{max}} \right), \quad (3.2.3)$$

It's beneficial to use track isolation due to the significantly finer granularity of the tracker, which permits the construction of narrower cones. On the contrary, for calorimeter-based isolation, it's challenging to fabricate cones possessing radii considerably smaller than $\Delta R = 0.2$, given to the finite granularity of the calorimeter.

Working point	Calorimeter isolation	Track isolation
Gradient	$\epsilon = 0.1143 \times p_T + 92.14\%$ (with E_T^{cone20})	$\epsilon = 0.1143 \times p_T + 92.14\%$ (with $p_T^{\text{varcone20}}$)
HighPtCaloOnly	$E_T^{\text{cone20}} < \max(0.015 \times p_T, 3.5 \text{ GeV})$	-
Loose	$E_T^{\text{cone20}}/p_T < 0.20$	$p_T^{\text{varcone20}}/p_T < 0.15$
Tight	$E_T^{\text{cone20}}/p_T < 0.06$	$p_T^{\text{varcone20}}/p_T < 0.06$

Table 3.1: Electron isolation working points and isolation efficiency ϵ definitions. In the Gradient working point definition, the unit of p_T is GeV. For all working points, a cone size of $\Delta R = 0.2$ for calorimeter and $\Delta R_{\text{max}} = 0.2$ for track isolations has been used. The HighPtCaloOnly WP is only based on calorimeter isolation while the other WPs require both calorimeter and tracks isolation criteria. (taken from Ref. [109]).

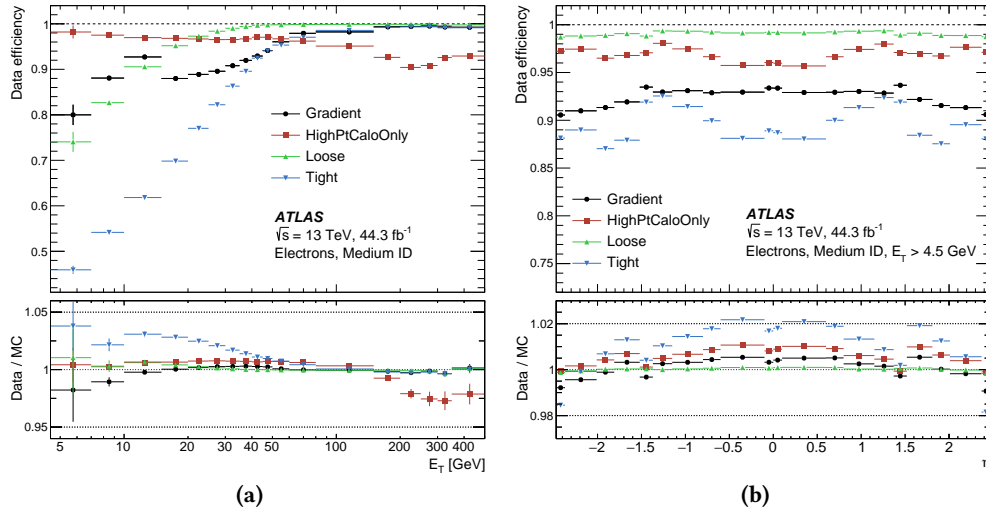


Figure 3.8: Efficiency of the different isolation working points for electrons passing the Medium identification criterion in inclusive $Z \rightarrow e^+e^-$ events as a function (a) E_T and (b) η . The bottom panel shows the ratio of the efficiencies measured in data and in MC simulations (taken from Ref. [109]).

3.2.3 Calibration of Electron Data

Once the reconstruction of electrons is completed, their calibration is achieved using a multivariate analysis (MVA) regression algorithm applied on data and on simulation [109]. A regression algorithm is a machine learning mechanism that utilizes input variables to predict certain output variables. For example, corrections for a particle's energy and transverse momentum are determined using these output variables. Such algorithms play a pivotal role in calibrating particles, like electrons, by enhancing resolution, minimizing biases, and offering other advancements.

The MVA regression algorithm is trained on simulated samples that comprise single electrons without pile-up. The phase space is categorized based on regions of $(|\eta|, E_T)$. In this context, the MVA is designed to evaluate the electron's energy based on the energy deposited in the calorimeter. The input variables include: energy deposited in the calorimeter, energy observed in the pre-sampler, the energy ratio between the first and second layers (E_{L1}/E_{L2}) of the EM calorimeter, the η of the impact point of shower in the calorimeter, and the angular distances in η and ϕ from the impact point of the shower to the nearest center of cell in the second layer of the calorimeter. In the transitional region between the barrel and endcap calorimeters, specifically in the range $1.4 < |\eta| < 1.6$, the extensive material before the first active layer of calorimeter negatively impacts electron energy resolution. To counteract this, the MVA regression algorithm incorporates information from a cell type scintillators. In this zone, the energy (E_{L4}) observed in the scintillator cells and the positional difference between the cluster and the center of scintillator cell are added to the input variables.

Subsequently, an energy correction is exclusively applied to the datasets to adjust for possible detector miscalibrations and the energy reconstruction process's imperfections. This correction is ascertained through a template technique using $Z \rightarrow e^+e^-$ events. The method involves contrasting the e^+e^- system's invariant mass distribution in datasets and simulations to derive the energy correction [109–111]. An analogous method has been used to establish energy correction for b -jets.

In practice, the energy scale correction is executed on the data, while the resolution correction is applied to the simulation:

$$E^{\text{data corrected}} = E^{\text{data}} / (1 + \alpha), \quad \left(\frac{\sigma_E}{E} \right)^{\text{MC corrected}} = \left(\frac{\sigma_E}{E} \right)^{\text{MC}} \oplus c, \quad (3.2.4)$$

Here, α denotes the energy scale factor, and c represents the constant resolution factor. Typically, these corrections are derived in η -bins corresponding to different sections of the ATLAS calorime-

ter. Since different technologies are employed, the calorimeter's energy response is anticipated to fluctuate with η . Both the energy scale factor and the constant resolution factor are assessed annually to account for the LAr temperature fluctuations and the rising instantaneous luminosity influencing the required corrections. Figure 3.9 illustrates measurements for the α and c corrections along with a comparative analysis of the invariant mass distribution between datasets and simulations post their respective corrections.

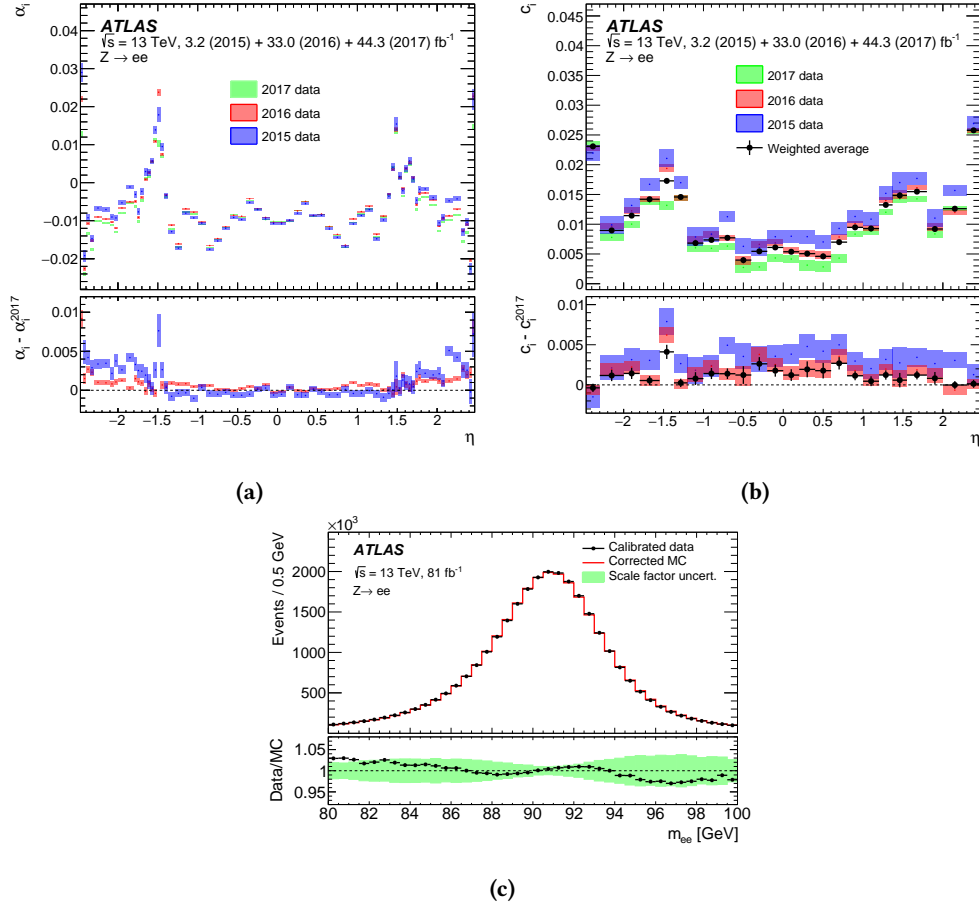


Figure 3.9: (a) Depiction of energy scale factors, α , and (b) the additional constant term, c , as functions of η . The shaded areas represent statistical uncertainties. For (a) and (b), the bottom panels demonstrate the disparities between values measured during a particular data-acquisition period and those measured using 2017 data. (c) This contrasts the invariant mass distribution, m_{ee} , of the selected $Z \rightarrow e^+e^-$ candidates between data and simulation after applying calibration and resolution corrections to the data and simulation, respectively. The total event count in the simulation is scaled to match the data. The uncertainty band in the bottom plot indicates the impact of variations in the calibration and resolution correction factors (adapted from Ref. [109]).

3.3 Muon at ATLAS

To reconstruct muon candidates, a combination of information from the inner detector (ID) and the muon spectrometer (MS) is utilized [114, 115]. Initially, muon candidate tracks are reconstructed within the muon spectrometer. Subsequently, data from both the MS and the ID are integrated, facilitating muon identification.

3.3.1 Muon Reconstruction

Within the r - z plane, the muon spectrometer measures the deviation in the trajectories of muons resulting from the toroidal magnetic field. Since the trajectories of the muons are linear in the r - ϕ plane, the primary step in track reconstruction within the MS is the recognition of short linear track segments from hits in distinct MS stations, components of the sub-detectors. The Hough transform is employed for this identification, as it aids in discerning point patterns in an image [116]. These segments are subsequently merged into track candidates, applying a relaxed pointing constraint anchored on the IP. This assumes optimal parabolic trajectories within the bending plane, which is an initial order approximation.

The muon trajectory undergoes a χ^2 fit throughout the entire muon spectrometer, considering potential interactions between the muon and detectors. While acquiring the muon trajectory from this global fit, any outlier hits are omitted. Meanwhile, hits present along the trajectory but not previously associated with a track are incorporated. The trajectory fitting process is then reiterated with this updated track information. When tracks overlap significantly regarding hits, higher-quality tracks are retained to address this ambiguity. A notable exception exists for identical tracks in two stations, which don't share hits in a third station. This exception aids in enhancing the reconstruction efficiency of boosted low-mass di-muon systems. Ultimately, a third trajectory fitting occurs, applying a relaxed constraint on the interaction point while also accounting for energy dissipation linked to the calorimeters. The p_T of the muon candidate at the interaction site is extrapolated based on this fit.

The concluding phase involves muon reconstruction, leveraging detector data. Following methodologies are used to reconstruct muons.

Combined (CB) muons are derived by integrating MS and ID tracks, conducting a joint track fit anchored on hits within these two subdetectors while factoring in energy depletion in the calorimeters. The MS track might be updated during this fit, allowing for a possible repetition of the entire track fitting process. For $|\eta| > 2.5$, MS tracks are merged with short track segments from the pixel and SCT detectors, designating these muons as silicon associated forward (SiF) muons.

Using an Inside-out (IO) combined muons approach, a supplementary inside-out algorithm is employed. ID tracks are extrapolated to the MS, seeking a minimum of three loosely-aligned hits in the MS. The ID tracks, energy depletion in the calorimeters, and MS hits are then merged into a track fit. MS reconstructed tracks are not used, improving efficiency in regions with limited MS coverage or for low- p_T muons.

The Muon spectrometer extrapolated (ME) muons approach is used when a muon MS track doesn't correspond with an ID track. Parameters are projected onto the beamline, categorizing it as a ME muon, extending muon reconstruction beyond the ID acceptance domain.

For Segment-tagged (ST) muons, an extrapolated ID track is aligned with the MS, necessitating a stringent angular condition. The ID track is then deemed a muon candidate, and parameters are extracted from this fit.

Lastly, Calorimeter-tagged (CT) muons are identified by projecting tracks through the calorimeters to locate energy deposits consistent with a MIP. These deposits enable the tagging of the ID track as a muon, deriving the muon's parameters from this track. Only tracks with a significant p_T are evaluated, reducing background interference.

3.3.2 Criteria for the Isolation and Identification of Muon Candidates

High-quality muon candidates must be properly identified upon reconstruction. The identification process is specific to the analysis and relies on the particular topology of the events that are being

targeted [114, 115].

ATLAS has implemented several working points to facilitate the identification of muons and to differentiate prompt muons from non-prompt muons. Non-prompt muons can be categorized into those originating from semi-leptonic decays of light hadrons and those arising from heavy flavour hadrons decays.

The working points for identification are designed to reject muons originating from the in-flight decays of light hadrons, as these often exhibit lower track quality. This is a result of the change in trajectory that occurs from in-flight decay within the detector. Such muons are often characterized by a "kink" in the reconstructed track, a deviation caused by the momentum carried away by an undetected neutrino. Consequently, it is anticipated that the fit quality of the resultant combined track will be suboptimal, leading to incompatibility between the momentum measurements in the Inner Detector (ID) and Muon Spectrometer (MS).

On the other hand, bottom and charm hadrons tend to produce muons with good quality. These can be separated from prompt muons by applying isolation requirements and evaluating the distance to the primary vertex, given that prompt muons are typically expected to originate from the primary vertex (PV).

Three identification working points, namely *Loose*, *Medium*, and *Tight*, are defined by ATLAS to enable progressively stricter selections. The Loose working point is optimized for reconstructing the decay of the Higgs boson into 4 muons ($H \rightarrow ZZ^* \rightarrow 4\mu$), possessing high signal efficiency suitable for that channel due to the favorable signal-to-background ratio. The Medium working point offers a balanced efficiency and background rejection, serving a broad array of analyses. The Tight working point provides the highest purity, albeit at a minor loss in prompt muon efficiency, and is recommended for analyses constrained by non-prompt muon background. Two additional working points for extreme phase space regions have also been introduced: the *High- p_T* and *Low- p_T* working points, targeting muons with specific momentum ranges.

A summary of the efficiency and misidentification rates for prompt and non-prompt muons across the various working points can be found in Table 3.2 and Figure 3.10.

Identification is further based on specific requirements concerning the number of hits in the MS and ID subdetectors. Discriminating criteria include the q/p compatibility ($\sigma^{\text{comp.}}(q/p)$) for combined (CB) and inside-out (IO) muons, as described by:

$$\sigma^{\text{comp.}}(q/p) = \frac{|q/p_{\text{ID}} - q/p_{\text{MS}}|}{\sqrt{\sigma^2(q/p_{\text{ID}}) + \sigma^2(q/p_{\text{MS}})}} \quad (3.3.1)$$

Where q/p_{ID} and q/p_{MS} are measurements of the charge-to-momentum ratio in the ID and MS, respectively. Additionally, the absolute difference between the ID and MS p_T measurements (ρ') serves as another relevant criterion:

$$\rho' = \frac{|p_{T,\text{ID}} - p_{T,\text{MS}}|}{p_{T,\text{CB}}}, \quad (3.3.2)$$

The Tight and Medium working points accept only CB and IO muons, and details on the identification requirements for various working points are documented in Reference [114].

For the vertex association of a muon candidate, the transverse impact parameter significance is constrained by the relation: $|d_0|/\sigma(d_0) < 3$. Additionally, to ensure compatibility with the reconstructed primary vertex, the requirement is $|z_0| \sin(\theta) < 0.5$ mm.

Muon isolation follows a similar principle as electron isolation. The proximity of activities sur-

	$3 < p_T \text{ [GeV]} < 5$		$5 < p_T \text{ [GeV]} < 20$		$20 < p_T \text{ [GeV]} < 100$		$p_T > 100 \text{ GeV}$	
Working point	$\epsilon_\mu \text{ [%]}$	$\epsilon_{\text{had}} \text{ [%]}$	$\epsilon_\mu \text{ [%]}$	$\epsilon_{\text{had}} \text{ [%]}$	$\epsilon_\mu \text{ [%]}$	$\epsilon_{\text{had}} \text{ [%]}$	$\epsilon_\mu \text{ [%]}$	$\epsilon_{\text{had}} \text{ [%]}$
<i>Loose</i>	90	1.17	98	1.06	99	0.25	98	0.12
<i>Medium</i>	70	0.63	97	0.85	97	0.17	97	0.07
<i>Tight</i>	36	0.15	90	0.38	93	0.12	93	0.04
<i>Low-p_T (cut-based)</i>	86	0.82	95	0.71	97	0.17	97	0.07
<i>Low-p_T (multivariate)</i>	88	0.73	96	0.66	97	0.17	97	0.07
<i>High-p_T</i>	45	0.34	79	0.60	80	0.13	80	0.05

Table 3.2: Prompt-muon efficiencies (ϵ_μ) and light-hadron misidentification rates (ϵ_{had}) for different identification working points, assessed on a $t\bar{t}$ MC sample across various p_T -regions within $|\eta| < 2.5$. The Tight working point inherently does not select muons with $p_T < 4 \text{ GeV}$, evident in the $3 < p_T < 5 \text{ GeV}$ region. The provided statistical uncertainties are substantially smaller than the reported final digit (adapted from Ref. [114]).

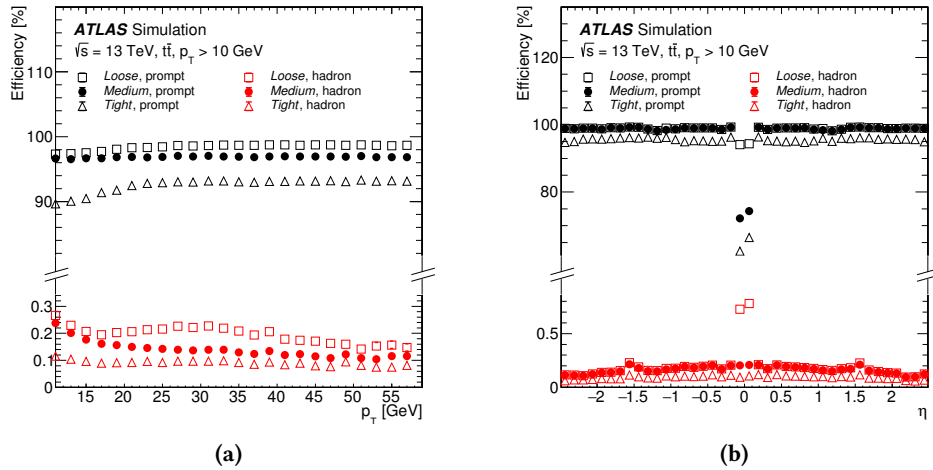


Figure 3.10: Efficiency functions based on (a) p_T and (b) η for the Loose, Medium, and Tight identification WP in simulated $t\bar{t}$ events for tracks with $p_T > 10 \text{ GeV}$, differentiated between prompt muons and muons from hadron decays (source: Ref. [114]).

Isolation WP	Definition	Track p_T requirement
$PflowLoose^*$ $PflowTight^*$	$(p_T^{varcone30} + 0.4 \cdot E_T^{neflow20}) < 0.16 \cdot p_T^\mu$ $(p_T^{varcone30} + 0.4 \cdot E_T^{neflow20}) < 0.045 \cdot p_T^\mu$	$p_T > 500 \text{ MeV}$
$Loose^*$ $Tight^*$	$p_T^{varcone30} < 0.15 \cdot p_T^\mu, E_T^{topocone20} < 0.3 \cdot p_T^\mu$ $p_T^{varcone30} < 0.04 \cdot p_T^\mu, E_T^{topocone20} < 0.15 \cdot p_T^\mu$	$p_T > 1 \text{ GeV}$
$HighPtTrackOnly$ $TightTrackOnly^*$	$p_T^{cone20} < 1.25 \text{ GeV}$ $p_T^{varcone30} < 0.06 \cdot p_T^\mu$	$p_T > 1 \text{ GeV}$
$PLBDTLoose (PLBDTTight)$	$p_T^{varcone30} < \max(1.8 \text{ GeV}, 0.15 \cdot p_T^\mu)$ BDT cut to mimic $TightTrackOnly$ ($Tight$) efficiency	$p_T > 1 \text{ GeV}$

Table 3.3: Muon isolation working point definitions. The utilized criteria are listed in the second column, while the third column presents the minimum track p_T requirement. The working points indicated with “*” are available in two versions: one using $p_T^{varcone30}$ (i.e., variable ΔR cone) and the other utilizing p_T^{cone20} (i.e., fixed ΔR cone) for $p_T > 50 \text{ GeV}$ (based on Ref. [114]).

rounding them can distinguish prompt muons from non-prompt ones. Both a track-based isolation and a calorimeter-based isolation variables are introduced.

For the track-based isolation variable, akin to the electron (detailed in Section 3.2), a variable size radius cone is set as $\Delta R = \min(10 \text{ GeV}/p_T, \Delta R_{\max})$, where p_T represents the muon’s transverse momentum and $\Delta R_{\max} = 0.3$. The transverse momentum surrounding the muon, represented as $p_T^{varcone30}$, is computed as the scalar sum of the transverse momenta of tracks (excluding the muon track) with $p_T > 1 \text{ GeV}$. This variable is ideal for configurations expecting close proximity of jets or other leptons to an energetic muon. Some isolation working points utilize a fixed radius cone of $\Delta R = 0.2$ with associated transverse momenta denoted as p_T^{cone20} .

Calorimeter-based isolation employs the variable $E_T^{topocone20}$. This variable corresponds to the sum of the transverse energy from the topological cell clusters within a $\Delta R = 0.2$ radius around the extrapolated calorimeter position of muon, subtracting the energy deposition of muon. The $E_T^{topocone20}$ is noise-corrected, analogous to treatments for electrons and jets.

	$3 < p_T [\text{GeV}] < 5$		$5 < p_T [\text{GeV}] < 20$		$20 < p_T [\text{GeV}] < 100$		$p_T > 100 \text{ GeV}$	
Working point	$\epsilon_\mu [\%]$	$\epsilon_{\text{HF}} [\%]$	$\epsilon_\mu [\%]$	$\epsilon_{\text{HF}} [\%]$	$\epsilon_\mu [\%]$	$\epsilon_{\text{HF}} [\%]$	$\epsilon_\mu [\%]$	$\epsilon_{\text{HF}} [\%]$
<i>Loose</i>	63	14.3	86	7.2	97	6.1	99	12.7
<i>Tight</i>	53	11.9	70	4.2	89	1.0	98	1.6
<i>PflowLoose</i>	62	12.9	86	6.8	97	5.0	99	9.1
<i>PflowTight</i>	45	8.5	63	3.1	87	0.9	97	0.8
<i>HighPtTrackOnly</i>	92	35.9	92	17.2	92	4.5	92	0.6
<i>TightTrackOnly</i>	80	19.9	81	7.0	94	3.2	99	3.3
<i>PLBDTLoose</i>	81	17.4	83	5.1	93	1.3	98	1.7
<i>PLBDTTight</i>	57	9.6	69	2.7	87	0.5	98	1.7

Table 3.4: Isolation working point efficiencies for prompt muons (ϵ_μ) and muons originating from bottom and charm semileptonic decays (ϵ_{HF}) assessed in a $t\bar{t}$ MC sample for tracks within different p_T -regions that satisfy the Medium identification and vertex association criteria. The studied isolation working points pertain to variants with a constant cone size of $\Delta R = 0.2$ for $p_T > 50 \text{ GeV}$. The statistical uncertainties are notably smaller than the last reported digit (adapted from Ref. [114]).

3.4 Tau Leptons at ATLAS

Tau leptons, with a mean lifetime of 290.3 fs [117], undergo decay prior to reaching the ATLAS detector. Their decay can be either leptonically ($\tau \rightarrow l\nu_l\nu_\tau, l = e, \mu$) or hadronically ($\tau \rightarrow \nu_\tau + \text{hadrons}$). Leptonic decays account for about 34% of all tau decays, yielding isolated electrons or muons along with neutrinos which lead to a momentum imbalance in the transverse plane (refer to

Section 3.6). Meanwhile, hadronic decays represent 66% and are further split into 1-prong (72%) and 3-prong (22%) categories. In 68% of hadronic decays, at least one neutral pion is present.

Within the ATLAS detector, hadronic tau decays are perceived as jets, formed using the anti- k_t $R = 0.4$ clustering algorithm, elaborated further in Section 3.5.1. For these jets, the conditions set are $p_T > 10$ GeV, $|\eta| < 2.5$, and they should include either one or three charged tracks in a $\Delta R = 0.2$ cone around the jet's axis [118]. The neutrinos produced from the decay of hadronic tau leptons are excluded from reconstruction, thus the ensemble of visible decay constituents is denoted as $\tau_{\text{had-vis}}$.

For the discrimination against jets that originate from quarks and gluons, ATLAS has transitioned from utilizing a boosted decision tree (BDT) methodology [119] to a more recent recurrent neural network (RNN) based technique [120]. Figure 3.11 illustrates the contrast in background rejection relative to tau identification efficiency between the RNN and BDT algorithms, where the RNN showcases better performance.

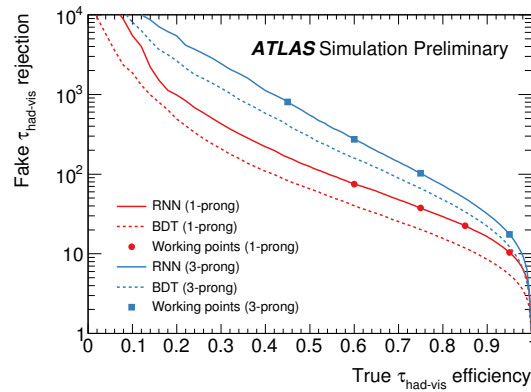


Figure 3.11: Depending on the genuine $\tau_{\text{had-vis}}$ efficiency, this showcases the rejection of quark and gluon jets falsely identified as hadronic τ -decays (designated as fake $\tau_{\text{had-vis}}$). The RNN-based (solid line) and BDT-based (dotted line) identification techniques are represented by the 1-prong (in red) and 3-prong (in blue) ROC curves. The markers align with the four pre-established working points: *Tight*, *Medium*, *Loose*, and *Very loose*, which sequentially depict increased signal selection efficiencies (sourced from Ref. [120]).

3.5 Jets in the ATLAS Detector

In the detector, a jet appears as a collimated spray of hadrons, originating from the hadronization of a parton, which may be a quark or a gluon. Calibration of these jets is subsequently performed to account for a range of effects. The reconstruction of jets in ATLAS incorporates information both from the calorimeter and the inner detector.

3.5.1 anti- k_t Algorithm for Jet Reconstruction

Jets in the ATLAS detector are reconstructed using 3D topological clusters (topo-clusters). A comprehensive description of topo-cluster reconstruction can be found in Section 3.2.1. For each event, an "origin correction" is applied to every topo-cluster to account for the position of the primary vertex. This is based on its depth within the calorimeter and its pseudorapidity, ensuring they align with the origin of the ATLAS detector.

The anti- k_t clustering algorithm [121], an infrared and collinear safe algorithm, is employed to successively merge the topo-clusters. For jets with high transverse momentum, this algorithm forms a cone with certain circular radius in the η - ϕ plane.

Association between clusters is achieved by calculating the distance (d_{ij}) between two clusters i and j and the distance (d_{iB}) between cluster i and the beam B . The mathematical representations for these are:

$$d_{ij} = \min \left(\frac{1}{p_{T,i}^2}, \frac{1}{p_{T,j}^2} \right) \frac{\Delta R_{ij}^2}{R^2}, \quad (3.5.1)$$

$$d_{iB} = \frac{1}{p_{T,i}^2}, \quad (3.5.2)$$

Here, R denotes the radius parameter which dictates the final size of the jets, while $\Delta R_{i,j}$ is the angular distance between the clusters, and $p_{T,i}$ and $p_{T,j}$ represent the transverse momentum of the clusters i and j respectively.

For every cluster i , the association process is as follows:

- Both d_{iB} and the minimal distance d_{ij} across all clusters j are computed.
 - If the minimal distance is d_{ij} , clusters i and j are merged into a new cluster.
 - If the minimal distance is d_{iB} , cluster i is recognized as a jet and is excluded from the cluster list.
- This method is repetitively applied to the updated cluster list until no clusters remain.

Uncalibrated physical jet properties (such as direction, energy, and transverse momentum) are derived similarly to electron reconstruction through weighted sums. A thorough calibration chain is then applied to jets.

Depending on the chosen value of R , jets are categorized as either small- R or large- R , corresponding to radii $R = 0.4$ and $R = 1.0$ in ATLAS. Figure 3.12 illustrates the reconstruction of large- R jets in the y - ϕ plane.

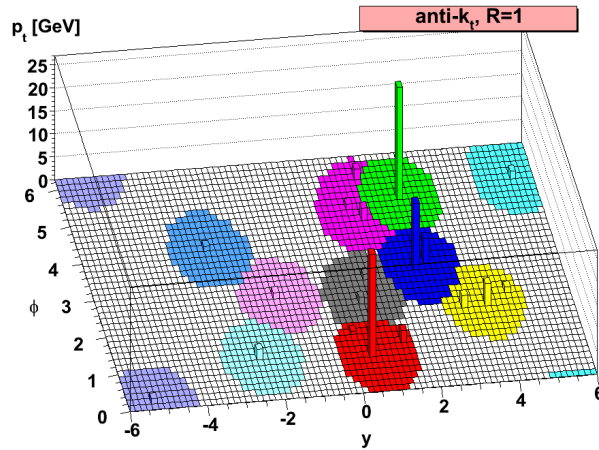


Figure 3.12: Reconstruction of Large- R jets ($R = 1.0$) using the anti- k_t algorithm, displaying circular cones in the η - ϕ plane (sourced from Ref. [121]).

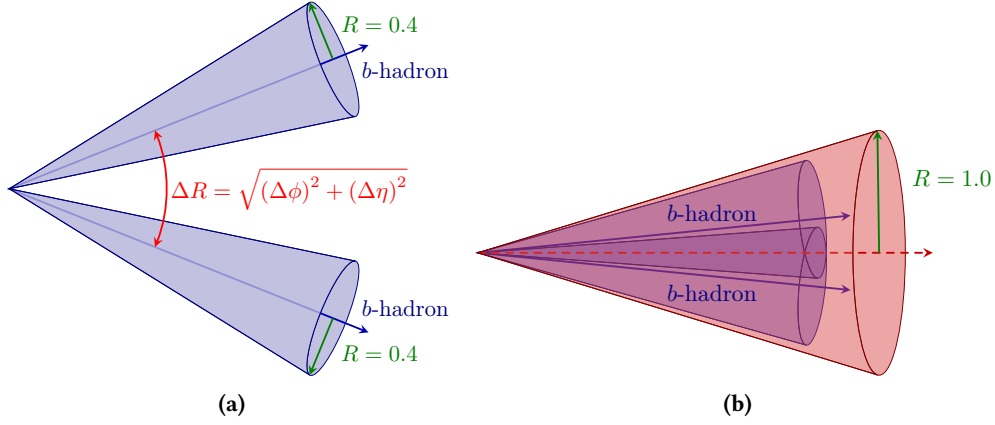


Figure 3.13: $H \rightarrow b\bar{b}$ decay depictions: (a) shows resolved topology and (b) showcases boosted topology. Events are either reconstructed with small-R jets ($R = 0.4$) or a large-R jet ($R = 1.0$). The angular separation between the b-hadrons is given by: $\Delta R(b, b) \approx \frac{2m_H}{p_T^H}$.

3.5.2 Particle Flow and EMTopo Reconstruction Approaches

Jets with a reduced radius, designated as small-R jets, possess a radius parameter $R = 0.4$. For energy reconstruction of these jets, multiple algorithms can be utilized, detailed subsequently. To improve features such as energy reconstruction and jet directionality, these jets undergo a calibration process.

In 2021, the inputs to jet algorithm in ATLAS transitioned from the electromagnetic topological (EMTopo) to the particle flow (PFlow) jets [122–124].

The EMTopo technique relies exclusively on calorimeter information. In this method, jets are reconstructed based on topo-clusters calibrated at the electromagnetic (EM) energy scale [125]. The EM scale measures energy depositions from electromagnetic showers after adjustments for pile-up and electronic noise.

In contrast, the PFlow method integrates data from both the inner detector and the calorimeter, enabling a more comprehensive reconstruction of the event's energy flow. The energy registered in the calorimeter from charged entities gets deducted from the registered EM energy-scaled topo-clusters and is substituted with the momentum of tracks associated with those topo-clusters. The adoption of PFlow-jets introduces numerous enhancements. Notably, these include heightened reconstruction efficiency and enhanced jet energy and angular resolutions. Additionally, they offer superior suppression of pile-up contamination relative to EMTopo-jets, which is further discussed in the ensuing sections.

For a charged pion situated at the detector's center, the energy resolution of the calorimeter and the inverse transverse momentum resolution of the tracker are represented by [122]:

$$\frac{\sigma(E)}{E} = \frac{50\%}{\sqrt{E}} \oplus 3.4\% \oplus \frac{1\%}{E}, \quad \sigma\left(\frac{1}{p_T}\right) = 0.036\% \oplus \frac{1.3\%}{p_T}, \quad (3.5.3)$$

Here, both E and p_T are in GeV units. Consequently, for low-energy charged particles, the tracker offers a resolution notably superior to the calorimeter. Furthermore, the trajectory of these low-energy charged particles might be excessively diverted by the magnetic field, making them fall outside the jet cone by the time of reaching the calorimeter. With PFlow jets, leveraging their perigee coordinate ensures they align with the calorimeter topo-cluster, thereby getting factored into consideration. Additionally, due to its advanced granularity, the tracker's angular resolution surpasses that of the calorimeter. This is complemented by an enhanced capability for pile-up discrimination, facilitated by vertex reconstructions using the inner detector.

3.5.3 Flavour Tagging

The process of identifying jets initiated by heavy flavour b - and c -hadrons is pivotal for examining the decay patterns of Higgs into pairs of b or c quarks. This identification is facilitated by the utilization of flavour tagging algorithms, which are elaborated upon in this subsection.

For Monte Carlo (MC) simulations, a jet's truth flavour is determined as follows: A jet receives a b -label if a b -hadron, possessing $p_T > 5$ GeV, is located within a cone of fixed radius, $\Delta R = 0.3$, centered on the jet axis. In the absence of such a b -hadron, a search is conducted for a c -hadron (with $p_T > 5$ GeV) in an analogous manner and if one is found, the jet is labelled as c . If neither b nor c -hadrons are found, but τ -lepton is found, the jet is τ -labelled. Otherwise, the jet is designated as light-flavoured.

During the reconstruction phase, tagging algorithms for b and c are employed. Historically, ATLAS utilized a boosted decision tree (BDT) [126] algorithm known as the MV2c10 tagger [127, 128]. However, a transition has been made to a more recent flavour tagging approach based on a deep neural network (DNN) named the DL1r tagger [128–133].

To improve the performance of the b -tagging algorithm, an ensemble of low-level taggers are employed. These taggers provide input variables for the high-level MV2c10 and DL1r taggers, as illustrated in Figure 3.14.

- **IP3D** [127]: This log-likelihood ratio (LLR) discriminants utilizes the track impact parameters. Tracks associated with jets are categorized based on their compatibility with the primary vertex. IP3D incorporates both transverse and longitudinal impact parameter significances, thereby accounting for the correlations between these parameters. Computations are made for LLR discriminations between b - and light-flavour jets, as well as b -jets from c -jets and c -jets from light-flavour jets.
- **SV1** [134]: This algorithm is designed to detect and reconstruct secondary vertices within jets. Initially, two-track vertices are identified. These vertices are then merged into multi-track vertices when spatially proximate. To circumvent track ambiguities, each track is linked to the vertex exhibiting the lowest track-vertex association χ^2 . The algorithm then conducts a track cleaning for each vertex. Tracks with the highest χ^2 are iteratively eliminated until the vertex achieves a satisfactory χ^2 and an invariant mass below 6 GeV. Vertices surpassing this value are discarded. Additionally, SV1 enables the exclusion of tracks likely originating from other long-lived particle decays or interactions. The output comprises 8 discriminating variables tied to the secondary vertex.
- **JetFitter** [135]: This tagger aspires to reconstruct the decay chain of b - and c -hadrons by searching for two vertices aligning from the primary vertex. The variables computed by JetFitter echo those of the SV1 tagger.
- **RNNIP** [136]: Deploying a recurrent neural network (RNN), this tagger processes a sequence of track variables, making it responsive to their correlations. This is pivotal since the IP3D approach presupposes independent computation of per-track flavour conditional likelihood, which is not always valid. Consequently, RNNIP amplifies the differentiation between b -, c -, light- and τ -jets vis-à-vis IP3D. The output consists of 4 probability variables denoting the likelihoods of jets being classified into specific categories.

The high-level taggers MV2c10 and DL1r utilize output variables, detailed in Table 3.5, from the aforementioned low-level taggers. Owing to the exclusive use of the more discriminative RNNIP tagger by DL1r, it surpasses MV2c10 in rejecting c - and light-jets, a fact corroborated by Figure 3.15.

The MV2c10 operates as a BDT classifier, allocating scores to jets within the range of -1 to 1. A

score nearing 1 typically indicates the tagger's inclination to recognize the jet as a b -jet.

Conversely, the DL1r tagger offers three probabilities for jets: p_b , p_c , and p_{light} , which represent the likelihoods of the jets being b -, c -, and light-jets, respectively. For the purpose of b -tagging, these probabilities are synthesized into a single discriminative variable as follows:

$$\mathcal{D}_{DL1r} = \log \left(\frac{p_b}{f_c \times p_c + (1 - f_c) \times p_{\text{light}}} \right), \quad (3.5.4)$$

Here, the factor $f_c = 0.018$ determines the emphasis on c -jet rejection and aligns with the c -jet fraction from the training dataset, having been fine-tuned for the DL1r discriminant. A discriminant tailored for c -tagging can be derived by interchanging “ b ” and “ c ” in Equation (3.5.4).

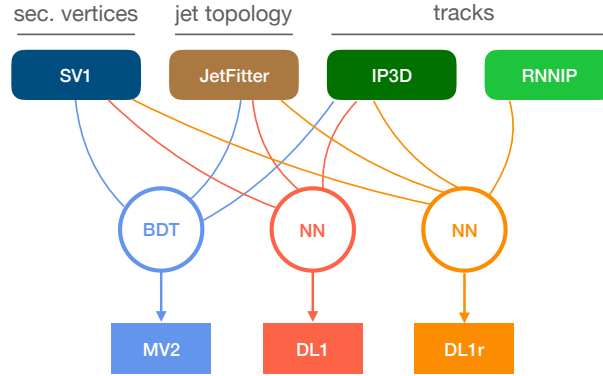


Figure 3.14: Low level taggers used by the MV2, DL1 and DL1r tagger (taken from Ref. [129]).

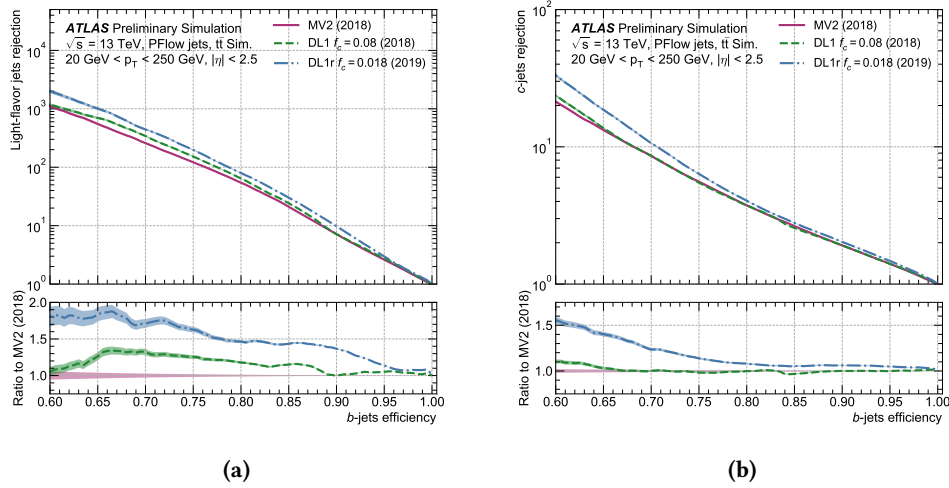


Figure 3.15: Comparison of ROC curves for the 2018 recommended versions of MV2 and DL1, the 2019 DL1r optimization, evaluated on a simulated dataset of $t\bar{t}$ events. The MV2c10 and DL1 algorithms do not use the RNNIP input variables, while the DL1r algorithm does. (a),(b): Performance on PFlow small-R jets with $20 < p_T < 250$ GeV and $|\eta| < 2.5$. The shaded bands represent statistical uncertainty (Adapted from Refs. [130, 131]).

Input	Variable	Description
Kinematics	p_T	Jet p_T
	η	Jet $ \eta $
IP3D	$\log(P_b/P_{\text{light}})$	Likelihood ratio between the b -jet and light-flavour jet hypotheses
	$\log(P_b/P_c)$	Likelihood ratio between the b - and c -jet hypotheses
	$\log(P_c/P_{\text{light}})$	Likelihood ratio between the c -jet and light-flavour jet hypotheses
SV1	$m(\text{SV})$	Invariant mass of tracks at the secondary vertex assuming pion mass
	$f_E(\text{SV})$	Energy fraction of the tracks associated with the secondary vertex
	$N_{\text{TrkAtVtx}}(\text{SV})$	Number of tracks used in the secondary vertex
	$N_{2\text{TrkVtx}}(\text{SV})$	Number of two-track vertex candidates
	$L_{xy}(\text{SV})$	Transverse distance between the primary and secondary vertex
	$L_{xyz}(\text{SV})$	Distance between the primary and the secondary vertex
	$S_{xyz}(\text{SV})$	Distance between the primary and the secondary vertex divided by its uncertainty
	$\Delta R(\mathbf{p}_{\text{jet}}, \mathbf{p}_{\text{vtx}})(\text{SV})$	ΔR between the jet axis and the direction of the secondary vertex relative to the primary vertex.
JETFITTER	$m(\text{JF})$	Invariant mass of tracks from displaced vertices
	$f_E(\text{JF})$	Energy fraction of the tracks associated with the displaced vertices
	$\Delta R(\mathbf{p}_{\text{jet}}, \mathbf{p}_{\text{vtx}})(\text{JF})$	ΔR between the jet axis and the vectorial sum of momenta of all tracks attached to displaced vertices
	$S_{xyz}(\text{JF})$	Significance of the average distance between PV and displaced vertices
	$N_{\text{TrkAtVtx}}(\text{JF})$	Number of tracks from multi-prong displaced vertices
	$N_{2\text{TrkVtx}}(\text{JF})$	Number of two-track vertex candidates (prior to decay chain fit)
	$N_{1\text{-trk vertices}}(\text{JF})$	Number of single-prong displaced vertices
	$N_{\geq 2\text{-trk vertices}}(\text{JF})$	Number of multi-prong displaced vertices
JETFITTER c -tagging (DL1r tagger only)	$L_{xyz}(2^{\text{nd}}/3^{\text{rd}}\text{vtx})(\text{JF})$	Distance of 2^{nd} or 3^{rd} vertex from PV
	$L_{xy}(2^{\text{nd}}/3^{\text{rd}}\text{vtx})(\text{JF})$	Transverse displacement of the 2^{nd} or 3^{rd} vertex
	$m_{\text{Trk}}(2^{\text{nd}}/3^{\text{rd}}\text{vtx})(\text{JF})$	Invariant mass of tracks associated with 2^{nd} or 3^{rd} vertex
	$E_{\text{Trk}}(2^{\text{nd}}/3^{\text{rd}}\text{vtx})(\text{JF})$	Energy fraction of the tracks associated with 2^{nd} or 3^{rd} vertex
	$f_E(2^{\text{nd}}/3^{\text{rd}}\text{vtx})(\text{JF})$	Fraction of charged jet energy in 2^{nd} or 3^{rd} vertex
	$N_{\text{TrkAtVtx}}(2^{\text{nd}}/3^{\text{rd}}\text{vtx})(\text{JF})$	Number of tracks associated with 2^{nd} or 3^{rd} vertex
	$Y_{\text{trk}}^{\text{min}}, Y_{\text{trk}}^{\text{max}}, Y_{\text{trk}}^{\text{avg}}(2^{\text{nd}}/3^{\text{rd}}\text{vtx})(\text{JF})$	Min., max. and avg. track rapidity of tracks at 2^{nd} or 3^{rd} vertex
RNNIP (DL1r tagger only)	P_b	b -jet probability
	P_c	c -jet probability
	P_τ	hadronic τ -jet probability
	P_{light}	light-jet probability

Table 3.5: Input variables for the MV2c10 and DL1r algorithms. Only the DL1r algorithm uses the JETFITTER c -tagging and RNNIP variables (adapted from Ref. [128]).

3.6 Missing Transverse Energy

The collider multipurpose detectors are unable to directly detect neutral weakly interacting particles such as neutrinos or potential dark matter particles because they depart the detector without leaving a detectable trace. Nevertheless, their presence in a collision can be deduced from imbalances in the transverse momentum. According to the conservation of momentum, the vector sum of transverse momenta of all participating particles should be zero, given that the partons within the protons possess negligible transverse momentum prior to collisions. Thus, the vector sum of the transverse momenta of these undetectable particles can be evaluated as the negative vector sum of all detected ones. This vector sum is termed the missing transverse momentum vector. Its magnitude can either be defined as the missing transverse energy (E_T^{miss}) or momentum (p_T^{miss}), contingent on its derivation from the calorimeter energy deposits or the ID track momenta. If only charged particles are considered, as in the latter case, then the track-based transverse missing momentum (p_T^{miss}) is generally favored over the calorimeter-based missing transverse energy (E_T^{miss}).

It is significant to highlight that prior to a collision, the exact longitudinal momentum of the parton is undetermined, as every parton carries only a fragment of the proton's momentum. Consequently, only the conservation of the transverse momentum becomes a useful metric.

The E_T^{miss} is ascertained by integrating the data from the calorimeters and the muon spectrometer with all the robust entities such as electrons, muons, hadronic taus, photons, and jets [124, 137, 138]. Any supplementary reconstructed signals not linked with a detected physic object contribute to what is termed the E_T^{miss} "soft term", symbolized as $E_T^{\text{miss,soft}}$. The total missing energy in direction $u = x, y$ can be determined as:

$$E_u^{\text{miss}} = - \left(\sum_{i \in \{\text{hard objects}\}} p_{u,i} + \sum_{i \in \{\text{soft signal}\}} p_{u,i} \right), \quad (3.6.1)$$

$$E_u^{\text{miss}} = E_u^{\text{miss,e}} + E_u^{\text{miss,\mu}} + E_u^{\text{miss,\tau}_{\text{had}}} + E_u^{\text{miss,\gamma}} + E_u^{\text{miss,jets}} + E_u^{\text{miss,soft}}, \quad (3.6.2)$$

Here, $p_{u,i}$ is the u component of the momentum of calibrated objects from the calorimeter and tracking or the soft signal from the calorimeter, and $E_u^{\text{miss,obj}} = -p_{u,\text{obj}}$ represents the negative transverse momentum component for each object along the u -axis. The complete transverse missing energy can be calculated as:

$$\mathbf{E}_T^{\text{miss}} = (E_x^{\text{miss}}, E_y^{\text{miss}}, 0), \quad (3.6.3)$$

$$E_T^{\text{miss}} = |\mathbf{E}_T^{\text{miss}}| = \sqrt{(E_x^{\text{miss}})^2 + (E_y^{\text{miss}})^2}, \quad (3.6.4)$$

$$\phi^{\text{miss}} = \tan^{-1} \left(\frac{E_y^{\text{miss}}}{E_x^{\text{miss}}} \right). \quad (3.6.5)$$

In order to avoid double counting, objects are considered in the subsequent order: muons, electrons, photons, hadronic taus, and lastly, jets.

For soft terms, they can be determined either through track-based soft terms (TST) or calorimeter-based soft terms (CST). While the former are deduced from ID tracks not associated with physics objects and primarily arise from low momentum tracks, the latter are calculated from energy deposits in calorimeter cells. This latter approach effectively accounts for both neutral and charged aspects of soft terms, albeit being more prone to pile-up contamination. Thus, the TST approach is preferred for the soft-term computation.

In conclusion, the overall E_T^{miss} resolution is influenced by the individual object resolutions, with the JER contribution being the primary determinant. The RMS width of the E_u^{miss} , $u = x, y$ escalates as $\text{RMS}(E_u^{\text{miss}}) \propto \sqrt{E_u^{\text{miss}}}$.

The representation in Figure 3.16 contrasts the E_T^{miss} distributions in $Z \rightarrow \mu^+\mu^-$ events (where no missing transverse energy is anticipated) when reconstructed with EMTopo and PFlow jets, indicating a higher accuracy with PFlow jets. It further elucidates that PFlow jets in $Z \rightarrow e^+e^-$ events deliver a superior RMS resolution.

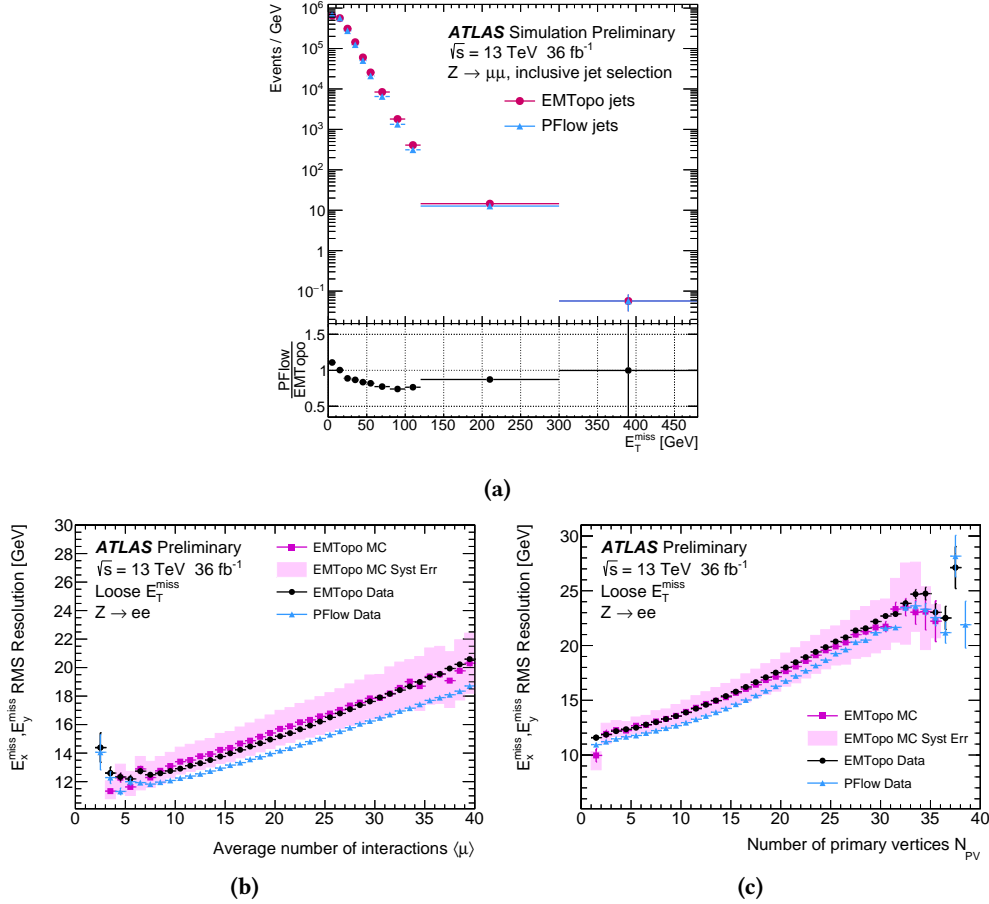


Figure 3.16: (a) Illustration of the E_T^{miss} distributions for $Z \rightarrow \mu^+\mu^-$ simulations using a specialized event selection and the Loose E_T^{miss} working point with EMTopo and PFlow jets. The RMS resolution derived from combined distributions of E_x^{miss} and E_y^{miss} is presented in relation to (b) the count of inelastic collisions per bunch crossing (μ) and (c) the primary vertex count per bunch crossing (N_{PV}). Analysis conducted using the Loose E_T^{miss} working point for datasets comprising EMTopo jets (circular marker) and PFlow jets (triangular marker) as well as MC simulation with EMTopo jets (square marker) in the $Z \rightarrow e^+e^-$ event selection (Adapted from Ref. [124]).

Measuring the b -jet identification efficiency with the p_T^{rel} method

4.1	Introduction	89
4.2	Data used for the Calibration	90
4.2.1	Trigger Criteria	90
4.2.2	Event Simulation Methodology	90
4.3	Event and Object Selection	92
4.3.1	Jet Selection Criteria	92
4.3.2	Muon Selection Criteria	92
4.3.3	Event Selection Criteria	93
4.4	The p_T^{rel} Methodology	93
4.4.1	Template construction	94
4.4.1.1	b -jet template	94
4.4.1.2	c -jet template	95
4.4.1.3	light-jet template	95
4.4.1.4	Template Fit	96
4.5	Extrapolation to inclusive b -jets	98
4.6	Systematic Uncertainties	102
4.6.1	Experimental Uncertainties	103
4.6.1.1	Muon reconstruction and identification	103
4.6.1.2	Lepton momentum scale and resolution	103
4.6.1.3	Jet vertex tagger efficiency	103
4.6.1.4	Jet energy scale	103
4.6.1.5	Jet energy resolution	104
4.6.2	Modelling Uncertainties	104
4.6.2.1	Muon Origin	104
4.6.2.2	Muon p^*	104
4.6.2.3	Fake muons	105
4.6.2.4	Gluon Splitting	105
4.6.2.5	B-hadrons Fragmentation Fraction	106
4.6.2.6	Semileptonic-to-inclusive extrapolation	106
4.7	Results	107

In the ATLAS experiment at the Large Hadron Collider, accurately identifying jets that originate from b -quarks, denoted as b -tagging, is essential for various physics analyses. This chapter explains the computation of the b -tagging efficiency, symbolized as ε_b , of jets containing spatially-matched muon using multi-jet events. These muons primarily arise from the semileptonic decays of both bottom and charm hadrons. In addition, certain hadrons in light quark and gluon jets, when misinterpreted as muons, also play a role.

By examining the transverse momentum of the lepton relative to the combined axis of the lepton

and jet, denoted by p_T^{rel} , it is possible to deduce the fraction of jets originating from b -quarks (b -jets) using a profile-likelihood fit. The determination of ε_b is derived from estimating this fraction in jets that either adhere to or deviate from the b -tagging criteria. As a result, the findings are expressed as the ratio of efficiency found in data to that in the Monte Carlo simulation. These ratios, termed scale factors, are detailed for the b -tagging algorithms, MV2c10 and DL1r, in reference to the transverse momentum of jet across four unique benchmarks. These benchmarks represent b -tagging efficiencies of 60%, 70%, 77%, and 85%, as determined using b -jets in the $t\bar{t}$ simulation.

The MV2c10 based calibration is documented in Ref. [3], while the DL1r based calibration is presented in this study for the first time.

This chapter begins with an introduction to the p_T^{rel} method in Section 4.1. This is followed by a description of the data and simulation samples used in the study in Section 4.2. The event selection criteria are detailed in Section 4.3, while the specifics of the p_T^{rel} method are elucidated in Section 4.4. The systematic uncertainties are discussed in Section 4.6 and the results are presented in Section 4.7.

4.1 Introduction

The ATLAS experiment heavily utilizes the b -tagging process for the identification of jets containing b -hadrons. This is fundamental for numerous investigations and measurements, including precision measurements in the top quark sector [139], evaluations of Higgs couplings [140], and various explorations beyond the Standard Model. Summaries of flavour-tagging undertakings during Run 1 and Run 2 of the ATLAS experiment are presented in Ref. [141, 142].

The large semi-leptonic branching ratio of b -hadrons coupled with the significant cross-section of $b\bar{b}$ events allows this study to calibrate the b -tagging efficiency with multi-jet events. This is achieved by employing a muon kinematic variable, independent of b -tagging algorithms. The calibration does not only depend on $t\bar{t}$ events, offering alternative measurements that benefit various analyses, such as the $Br(t \rightarrow b)$ measurement. Combining it with other measurements offers increased precision. Moreover, this calibration technique necessitates a smaller integrated luminosity compared to calibrations based on $t\bar{t}$, positioning it as a pivotal calibration during the initial data acquisition phase.

This study investigates into the calibration of the b -tagging algorithm, both MV2c10 and DL1r taggers are used, the details of these two algorithms can be found in Section 3.5.3.

Although the principal calibration technique for b -jets at ATLAS is based on $t\bar{t}$ events, as described in Ref. [142], an orthogonal sample comprising muons matched to jets in multi-jet events can also be used, referred to as the *muon-based* calibration. This muon-based method may offer enhanced precision, particularly in the low p_T region, and can validate results from the baseline calibration.

Because of their greater mass compared to hadrons containing only charm or light quarks, the decay products of b -hadrons possess higher energy. This characteristic imparts greater momentum to the final state particles in the rest frame of the decay hadron, referred to as p^* .

The p_T^{rel} variable, equivalent to the transverse momentum p_T of lepton relative to the combined lepton and jet axis three-vector, is strongly correlated with p^* . The p_T^{rel} method, described in Section 4.4, harnesses the distinctive power of p_T^{rel} distribution to determine the fraction of b -flavour jets.

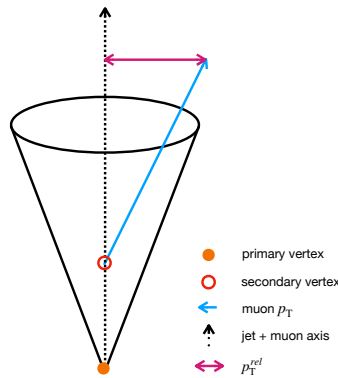


Figure 4.1: A diagrammatic representation depicting a jet cone (in black) with an embedded b -hadron decaying semi-leptonically at a secondary vertex (in green). The resulting muon and its momentum, projected transverse to the jet+muon axis, is illustrated as the p_T^{rel} . (Taken from Ref. [3].)

By employing a profile-likelihood fit, this study aligns the predicted p_T^{rel} templates for b and c -jets, sourced from Monte Carlo (MC) muon-filtered dijet samples, against the p_T^{rel} distribution of a data

set of jets satisfying the b -tagging criteria. From this, the b -tagging efficiency is derived as:

$$\varepsilon_b = \frac{N_b^{\text{tagged}}}{N_b^{\text{tagged}} + N_b^{\text{untagged}}} \quad (4.1.1)$$

Where N_b^{tagged} and N_b^{untagged} refer to the numbers of b -jets that meet and fail the b -tagging criteria, respectively.

This investigation sheds light on the key selections for objects and events, the generation of p_T^{rel} templates, fitting methodologies, and systematics considerations, leading to a comprehensive understanding of the b -tagging calibration process in the ATLAS experiment.

4.2 Data used for the Calibration

For the calibration discussed in this chapter, a region enriched with semileptonic b -hadron decays was investigated. Events were chosen based on muon-in-jet triggers, followed by applying moderate kinematic requirements on jets and muons.

4.2.1 Trigger Criteria

Events wherein a muon correlates spatially with a jet, both satisfying specific p_T thresholds, are selected by muon-in-jet triggers. These triggers aim to select multi-jet events with a high fraction of semileptonic b -decays. The spatial correlation is determined within a cone defined by $\Delta R = \sqrt{\Delta\eta^2 + \Delta\phi^2} < 0.5$ surrounding the jet's axis. Here, η refers to the pseudorapidity, and ϕ is the azimuthal angle perpendicular to the beam axis. Furthermore, $|\Delta z| < 2$ mm is required, where $|\Delta z|$ represents the nearest approach distance along the beam axis from the muon track to the main vertex.

Owing to the rapidly decreasing jet p_T spectrum and the substantial cross-section of multi-jet events, only a subset of events that meet the muon-in-jet trigger criteria are documented. The proportion documented, governed by the trigger pre-scale factor, differs across each muon-in-jet trigger configuration. To augment the number of obtainable events, diverse muon-in-jet triggers are employed. Each is associated with a distinct jet p_T bin to ensure comprehensive efficiency over the entire jet p_T spectrum. The trigger motivations entirely dictate the binning boundaries. A limitation is set at 200 GeV due to the diminished distinguishing capacity of the p_T^{rel} technique.

For this study, the muon-in-jet triggers from 2015 were disregarded. Consequently, only events from 2016, 2017, and 2018 were considered. The effective luminosities accumulated by each trigger prior to the selection process during these years are outlined in Table 4.2 and Table 4.3. Notably, the provided thresholds pertain to pre-calibration online values. The post-calibration thresholds, established from bootstrapped trigger turn-on curves, determined the binning selection as highlighted earlier.

The total effective luminosity used for this calibration amounts to 6.8 fb^{-1} .

4.2.2 Event Simulation Methodology

The analysis uses both data and simulated events sets produced in the FTAG3 format. Within the explored phase space of this analysis, multi-jet events dominate, whereas other processes, including electroweak processes, offer minimal contribution due to their smaller cross-section relative to the QCD multi-jet.

Table 4.1: List of trigger identifiers used in this research for each year alongside their respective jet p_T thresholds.

Jet p_T Threshold [GeV]	Trigger name
2016	
15	HLT_mu4_j15_bperf_split_dr05_dz02
25	HLT_mu4_j25_bperf_split_dr05_dz02
35	HLT_mu4_j35_bperf_split_dr05_dz02
55	HLT_mu4_j55_bperf_split_dr05_dz02
85	HLT_mu6_j85_bperf_split_dr05_dz02
110	HLT_mu6_j110_bperf_split_dr05_dz02
150	HLT_mu6_j150_bperf_split_dr05_dz02
2017	
15	HLT_mu4_j15_boffperf_split_dr05_dz02
25	HLT_mu4_j25_boffperf_split_dr05_dz02
35	HLT_mu4_j35_boffperf_split_dr05_dz02 HLT_mu4_j15_gsc35_boffperf_split_dr05_dz02
55	HLT_mu4_j35_gsc55_boffperf_split_dr05_dz02
85	HLT_mu6_j60_gsc85_boffperf_split_dr05_dz02
110	HLT_mu6_j60_gsc110_boffperf_split_dr05_dz02
150	HLT_mu6_j110_gsc150_boffperf_split_dr05_dz02 HLT_mu6_j110_gsc150_bperf_split_dr05_dz02
2018	
15	HLT_mu4_j15_boffperf_split_dr05_dz02
25	HLT_mu4_j25_boffperf_split_dr05_dz02
35	HLT_mu4_j35_boffperf_split_dr05_dz02 HLT_mu4_j15_gsc35_boffperf_split_dr05_dz02
55	HLT_mu4_j35_gsc55_boffperf_split_dr05_dz02 HLT_mu4_j45_gsc55_boffperf_split_dr05_dz02
85	HLT_mu6_j60_gsc85_boffperf_split_dr05_dz02
110	HLT_mu6_j60_gsc110_boffperf_split_dr05_dz02 HLT_mu6_j85_gsc110_boffperf_split_dr05_dz02
150	HLT_mu6_j110_gsc150_boffperf_split_dr05_dz02 HLT_mu6_j110_gsc150_bperf_split_dr05_dz02

Table 4.2: Details of p_T^{jet} bins and relevant thresholds for triggers during 2016 and 2017.

Jet p_T Bin	Jet p_T Threshold	Muon p_T Threshold	Effective Luminosity	
			2016	2017
[20 GeV, 30 GeV], [30 GeV, 40 GeV]	15 GeV	4 GeV	6.48 pb ⁻¹	4.23 pb ⁻¹
[40 GeV, 50 GeV]	25 GeV	4 GeV	7.40 pb ⁻¹	5.05 pb ⁻¹
[50 GeV, 70 GeV]	35 GeV	4 GeV	9.34 pb ⁻¹	6.68 pb ⁻¹
[70 GeV, 90 GeV], [90 GeV, 110 GeV]	55 GeV	4 GeV	56.63 pb ⁻¹	16.68 pb ⁻¹
[110 GeV, 140 GeV]	85 GeV	6 GeV	380.36 pb ⁻¹	175.88 pb ⁻¹
[140 GeV, 170 GeV]	110 GeV	6 GeV	695.38 pb ⁻¹	386.93 pb ⁻¹
[170 GeV, 200 GeV]	150 GeV	6 GeV	2133.05 pb ⁻¹	1263.04 pb ⁻¹

Table 4.3: Details of p_T^{jet} bins and relevant thresholds for triggers during 2018.

Jet p_T Bin	Jet p_T Threshold	Muon p_T Threshold	Effective Luminosity
			2018
[20 GeV, 30 GeV], [30 GeV, 40 GeV]	15 GeV	4 GeV	4.15 pb ⁻¹
[40 GeV, 50 GeV]	25 GeV	4 GeV	4.79 pb ⁻¹
[50 GeV, 70 GeV], [70 GeV, 90 GeV], [90 GeV, 110 GeV]	35 GeV	4 GeV	5.92 pb ⁻¹
[110 GeV, 140 GeV], [140 GeV, 170 GeV]	85 GeV	6 GeV	211.23 pb ⁻¹
[170 GeV, 200 GeV]	150 GeV	6 GeV	1379.23 pb ⁻¹

b - and c -jet p_T^{rel} templates are developed using a PYTHIA8(v.243p4) dijet muon-filtered MC sample. This particular sample was formulated utilizing the A14 Pythia8 tune combined with the NNPDF23LO PDF set[143][144]. The sample is segmented into multiple p_T^{jet} segments to ensure adequate statistics throughout the p_T^{jet} range.

A muon filter is applied at the generator stage, such that events with only post-generator muons are excluded from this set. This increases the proportion of heavy versus light flavour jets in the filtered set. While muons in heavy flavour jets are primarily generated during the generator stage, muons in light flavour jets, such as in-flight decays, can emerge post-generation and subsequently fail the filter. For each year (2016, 2017, and 2018), three distinct MC sample sets are utilized, aligning with the observed pileup distributions in the collected data.

Moreover, an unfiltered dijet PYTHIA8 NNPDF23LO sample has been deployed. This unfiltered sample does not exhibit the muon-filtering bias, making it suitable for determining the predicted relative fractions of b , c , and *light* jets in each p_T^{jet} bin. It is also employed for computing the simulated b -tagging efficiency. Separate MC sets for 2016, 2017, and 2018 were used.

The EVTGEN(v.1.7.0) simulation tool [145] was harnessed to simulate the b -hadrons decay branching fractions and decays. All MC sets underwent simulation with the comprehensive ATLAS detector simulation using the GEANT4 4 toolkit [146]. Additional interaction impacts (pileup) were incorporated by overlaying minimum bias events simulated by PYTHIA8.

4.3 Event and Object Selection

4.3.1 Jet Selection Criteria

EMTopo Jets are formed from clusters of calorimeter cells linked by topology, while PFlow jets are formed from clusters of calorimeter cells and tracks, see Section 3.5.2. The clusters are merged into jets using the anti- k_t algorithm where R is set to 0.4 [147]. All jets are subject to criteria where $|\eta| < 2.5$ and $p_T > 20$ GeV. Moreover, a criterion known as the Tight (Medium) Working point of the "Jet Vertex Tagger" (JVT) for DL1r (MV2c10) discriminant is essential. This criterion substantially reduces pileup jets by a factor ranging from 10 to 100, depending on the jet p_T , while keeping about 92% of genuine hard scattering collisions [148]. The JVT is derived using two crucial variables: the corrected Jet Vertex Fraction (corrJVF) and R_{pT} , where R_{pT} represents the scale sum ratio of the p_T of tracks with hard-scatter vertex of a jet to the fully adjusted jet p_T . An adjustment is made to the simulated events to align with the JVT efficiency.

4.3.2 Muon Selection Criteria

For the identification of semileptonic b -decays and the minimization of light jets, the presence of at least one muon surpassing a specific muon p_T threshold within an event is necessary. Owing to the fact that muons within high-energy jets exhibit a steeper p_T spectrum, the threshold for muon p_T is influenced by the jet p_T bin in question. The thresholds are presented in Table 4.4. An increase in light jets at high p_T^{jet} is observed with basic muon p_T requirements. In contrast, adaptable muon p_T requires moderate the prevalence of light jets in such bins. Notably, the proportion of c -jets remains consistent. The adaptable requirement is marginally reduced the MC yields of high p_T^{jet} for both b and c -jets. However, considering that the templates for b and c are constructed by combining jets from all p_T^{jet} bins, the statistical viability of the template is still satisfactory.

A jet and a muon should be spatially matched within a $\Delta R < 0.4$ cone. Further, the muons must satisfy $|\eta| < 2.5$, $d_0 < 2$ mm, and $|z_0 \cdot \sin \theta| < 4$ mm. Corrections are applied to the simulated events to align with the efficiency measurements observed during dedicated calibration analyses.

Table 4.4: Selection parameters for muon-jet samples.

Jet Selections	$p_T > 20 \text{ GeV}$ $ \eta \leq 2.5$ JVT Tight (Medium) WP for DL1r (MV2c10) tagger
Muon Selections	$ \eta \leq 2.5$ $ d_0 < 2 \text{ mm}$ $ z_0 \cdot \sin \theta < 4 \text{ mm}$ Tight Quality
Muon p_T Requirement	5 GeV (if $p_T^{\text{Jet}} < 40 \text{ GeV}$) 6 GeV (if $40 < p_T^{\text{Jet}} < 90 \text{ GeV}$) 8 GeV (if $p_T^{\text{Jet}} > 90 \text{ GeV}$)
Muon-Jet Matching	$\Delta R < 0.4$

4.3.3 Event Selection Criteria

Efficiency extraction for b -tagging occurs in the b -enhanced region. The definition of this region is based on the tendency of b -quarks to predominantly manifest in pairs in pp collisions. This implies that if a jet in an event is marked as a b -jet, there is an elevated probability of another b -jet being present in that event. The following sequence outlines the approach to enhance the b -jet purity and to determine the "tag" jet:

- At least one jet is identified as a b -jet by the DL1r or MV2c10 algorithm at the 85% working point.
 - If multiple candidate b -jets are identified, preferentially choose the jet without a matched muon
 - If multiple non-matched muon jets are tagged or all tagged jets contain muons, a random selection process determines the tag b -jet from the candidate pool.
- Remove the tag b -jet to avoid bias and perform the analysis using the remaining jets.

This enhancement procedure is applied to the data selected for the measurement and to the unfitted MC used to obtain the simulation efficiency.

A $light$ -enhanced region is identified by applying the identical trigger selections and necessitating that all event jets fail the 85% working point DL1r or MV2c10 requirement. This region is primarily composed of light-jets and is statistically distinct from the events designated for the b -tagging efficiency measurement.

4.4 The p_T^{rel} Methodology

To determine the b -tagging efficiency, ε_b , using Equation 4.1.1, two essential quantities are required. The first is N_b^{tagged} , which represents the number of b -jets identified by the chosen algorithm. The second is N_b^{fail} , indicating the b -jets not identified. Within simulations, the number of b -jets either meeting or not meeting the b -tagging criteria can be extracted from the truth record. However, in the case of data, these quantities must be evaluated separately for every b -tagging operation point (OP) of interest.

The template fit method, utilizing p_T^{rel} as the distinguishing factor, is employed to determine the normalizations of b -flavour jets and, subsequently, the b -tagging efficiency from the data in the b -enhanced region. We derive templates for b -, c -, and light jets. The τ -jets have not been included in this analysis due to the minimal cross-section of the $Z \rightarrow \tau^+ \tau^-$ production. Moreover, cascade

b -decays via τ (such as $b \rightarrow \tau \rightarrow \mu$) have minimal impact on the p_T^{rel} template given the minor mass variance between τ and μ . Taking into account that both data and MC distributions have a p_T^{jet} dependency, templates are produced using identical p_T^{jet} binning to that of the data.

4.4.1 Template construction

Heavy flavour jet (b -jets and c -jets) templates for the p_T^{rel} spectrum are produced using muon-filtered MC samples. These are detailed in Section 4.2. The event selection outlined in Section 4.3 is exempted, as there is no observed correlation with the event selection in these heavy flavour templates. Additionally, by omitting the event selection, statistical uncertainties are minimized.

4.4.1.1 b -jet template

Variations in the b -jet template are observed across distinct p_T^{jet} bins, depicted in Figure 4.2a.

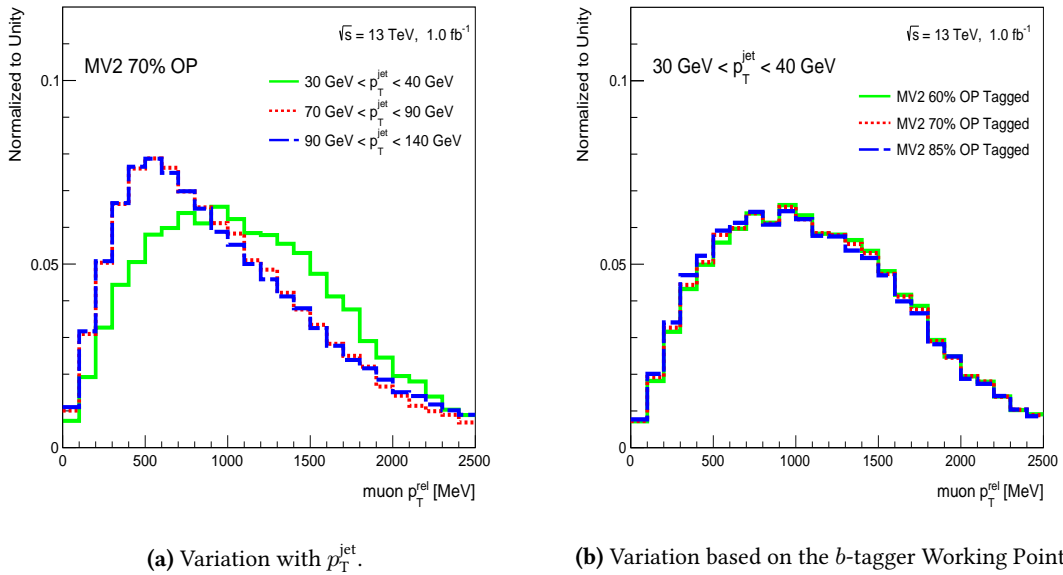


Figure 4.2: (a) Displays the b -jet distributions for three distinctive p_T^{jet} bins. (b) contrasts the b -jet distributions for four distinct MV2 OPs. (From Ref. [3])

Due to the variations observed, the b -jet distributions are extracted individually for each jet p_T bin. The differences arise from the relative contributions of direct (for instance, $B^0 \rightarrow \mu^\pm + \nu_\mu + X$) and cascade ($B^0 \rightarrow D^0 + X \rightarrow \mu^\pm + \nu_\mu + X$) decays. The cascade decay fraction, computed from the MC simulation, increases from 25% to 50% as jet p_T is increases from 30 GeV to 200 GeV.

The p_T^{rel} distributions for direct and cascade b -hadron decays are shown in Figure 4.3. The direct decay template exhibits a steeper spectrum compared to the cascade decay, where the muon results from a charm hadron. Hence, in p_T^{jet} bins with a greater direct decay proportion than the cascade, the resulting p_T^{rel} template demonstrates a sharper spectrum.

Two main factors influence the proportion of direct versus cascade decays in any given p_T^{jet} bin: the required muon p_T and the energy absent from semileptonic decays. Muons from direct semileptonic decays exhibit higher energy levels, making them more favourable to meet specific muon p_T thresholds. This amplifies the fraction of direct b -hadron decays. Therefore, in cases of direct decay, the neutrino also possesses greater energy, leading the reconstructed jet p_T to predominantly shift towards lower p_T compared to cascade b -hadron decays. The effect previously mentioned grows proportionally with jet p_T . Consequently, the lowest p_T^{jet} slice manifests a sharper p_T^{rel} spectrum.

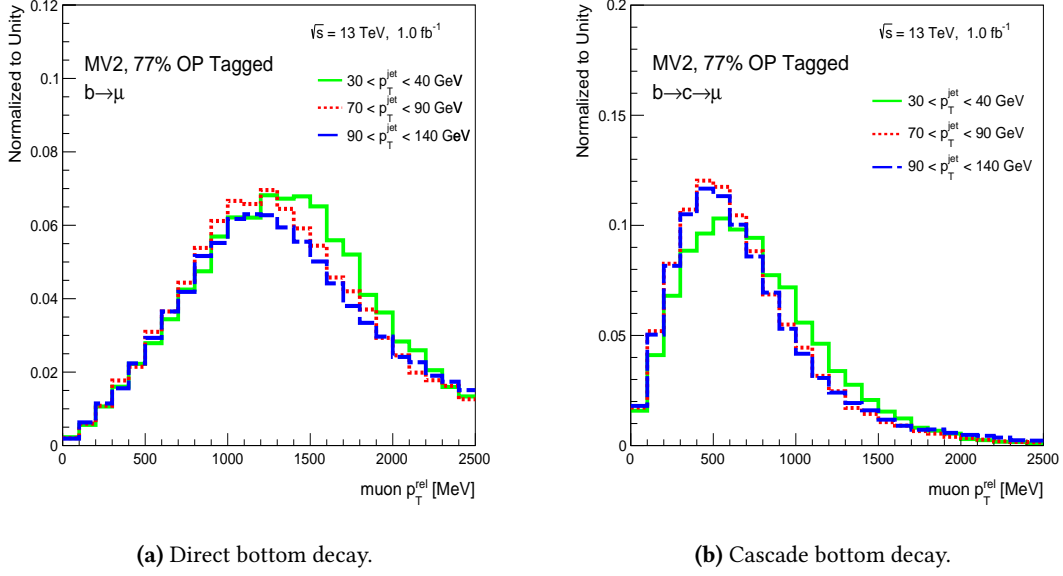


Figure 4.3: (a) p_T^{rel} distributions for muons originating from direct bottom hadron decays across three separate jet p_T^{jet} bins. (b) p_T^{rel} distributions for muons originating from cascade bottom hadron decays across three separate jet p_T^{jet} bins. (From Ref. [3])

This is attributed to the reduced likelihood of cascade decays in this slice to meet the muon p_T prerequisite, resulting in a bin primarily populated by direct decays. In higher jet p_T bins, the direct b -hadron decays produce energetic neutrinos, leading to a reduction in the direct b -hadron fraction. Additionally, minor variations in the b -jet template shapes are observed based on the imposed MV2 b -tagging prerequisite, as illustrated in Figure 4.2b. This outcome aligns with expectations since MV2 is determined using boost and impact parameter displacement data, potentially influencing the jet axis. The same behavior should also be observed for DL1r. The p_T^{rel} distribution for tagged (fail) b -jet is employed to quantify the b -jets in the corresponding tagged (fail) data set.

4.4.1.2 c -jet template

Analogously to the b -jet template, individual c -jet templates are generated for each p_T^{jet} bin. Minor variations in the c -jet templates are observed based on the p_T^{jet} , these variations are predominantly attributed to statistical inconsistencies.

Direct c decays, exemplified by $D^0 \rightarrow \pi^- + \mu^+ + \nu_\mu$, exhibit a harder spectrum than cascade decays like $D^0 \rightarrow K^-/\pi^- \rightarrow \mu^- + X$. The influence of direct versus cascade decays in the context of c -decays is less pronounced than in b -decays. This is due to the infrequent occurrence of charm cascade decays that meet the selection criteria. Moreover, intermediate particles in this context are often kaons or pions, which are not anticipated to decay within the inner detector, leading to a negligible cascade impact on the c -jet template.

4.4.1.3 light-jet template

A data-driven approach is employed to derive the *light-jet* template, primarily due to two constraints:

- The unfiltered simulation provides an insufficient number of *light-jets* that are spatially aligned with muons.
- The muon-filtered simulation yields a *light-jet* purity that is less than ideal. This discrepancy

can be attributed to the application of the muon-in-jet filter at the generator phase.

The extraction of the *light*-jet template is performed using data events present in the *light-enhanced region*. To account for the contamination from heavy flavour jets (both b - and c -jets) within the *light*-jet sample, an estimation is conducted utilizing data during the fitting process.

The prediction for the *light*-jet, represented as N_i^{light} for each bin i in the p_T^{rel} distribution, is expressed as:

$$N_i^{\text{light}} = N_i^{\text{data-l-enhanced}} - k_b \cdot \hat{N}_i^b - k_{\text{non-}b} \cdot \hat{N}_i^c, \quad (4.4.1)$$

where:

- $N_i^{\text{data-l-enhanced}}$ corresponds to the events sourced from the light-enhanced domain.
- \hat{N}_i^b and \hat{N}_i^c denote the predicted contamination from the b -jet and charm-jet respectively.
- k_b and $k_{\text{non-}b}$ are applied corrections to the normalization of b -jets and non- b -jets.

4.4.1.4 Template Fit

In Figure 4.4, the normalized p_T^{rel} distributions are presented within a singular p_T^{jet} bin for three distinct jet flavours. A more rigid p_T^{rel} spectrum is evident in the b -template compared to both c - and *light*-jet templates.

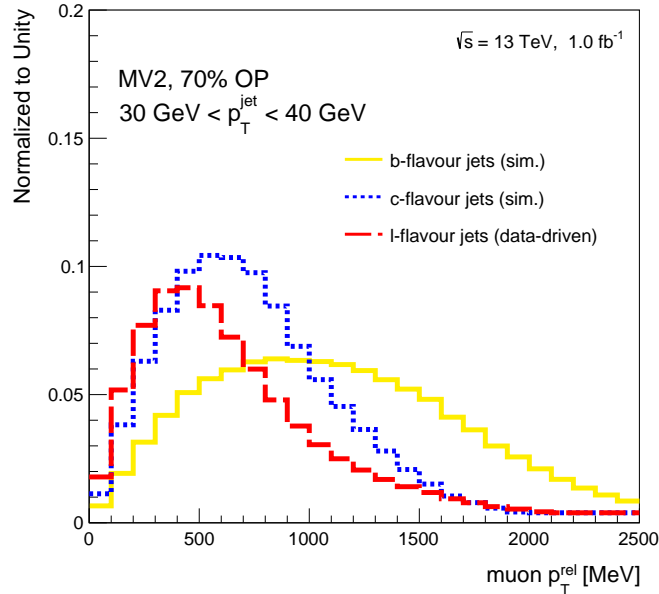


Figure 4.4: Spectra of Muon p_T^{rel} for the b -, c - and *light*-jet templates are depicted in yellow, blue, and red colors, respectively. Simulations generate the heavy flavour templates, while a data-driven method extracts the *light*-jet template. (From Ref. [3])

To the tagged and fail data distributions, a binned profile likelihood fit is executed using the b -, c -, and *light*-flavour templates, as shown in Figure 4.6. Each p_T^{jet} bin undergoes an independent fit.

From the data fit, three parameters emerge:

- The scale factor for b -tagging efficiency, represented as SF_b ,
- The normalization factor for b -jets, k_b ,

➤ The normalization factor for both c - and light-jets, $k_{\text{non-}b}$.

The prediction of tagged region is given by

$$N_{\text{tagged}} = \text{SF}_b \cdot k_b \cdot N_b^{\text{tagged}} + k_{\text{non-}b} \cdot (N_{\text{charm}}^{\text{tagged}} + N_{\text{light}}^{\text{tagged}}), \quad (4.4.2)$$

whereas the prediction of fail region is

$$N_{\text{fail}} = \frac{1 - \text{SF}_b \cdot \varepsilon_b^{\text{MC}}}{1 - \varepsilon_b^{\text{MC}}} \cdot k_b \cdot N_b^{\text{fail}} + k_{\text{non-}b} \cdot (N_{\text{charm}}^{\text{fail}} + N_{\text{light}}^{\text{fail}}), \quad (4.4.3)$$

with $N^{\text{tagged/fail}}$ representing the event numbers in the tagged/fail region. Additionally, the numbers of b -jets, c -jets, and light-jets predicted in the simulation for the tagged region are represented as $N_b^{\text{tagged/fail}}$, $N_{\text{charm}}^{\text{tagged/fail}}$, and $N_{\text{light}}^{\text{tagged/fail}}$, respectively.

Systematic uncertainties contribute to the fit as nuisance parameters θ in a Gaussian term, detailed in Section 4.6. This incorporation ensures that potential distortions in the templates due to systematic uncertainties are accounted for. Jets that have either passed or failed the b -tagging requirement are depicted in a pre-fit plot in Figure 4.5. In this plot, the different jet flavour fractions matched to the simulation predictions.

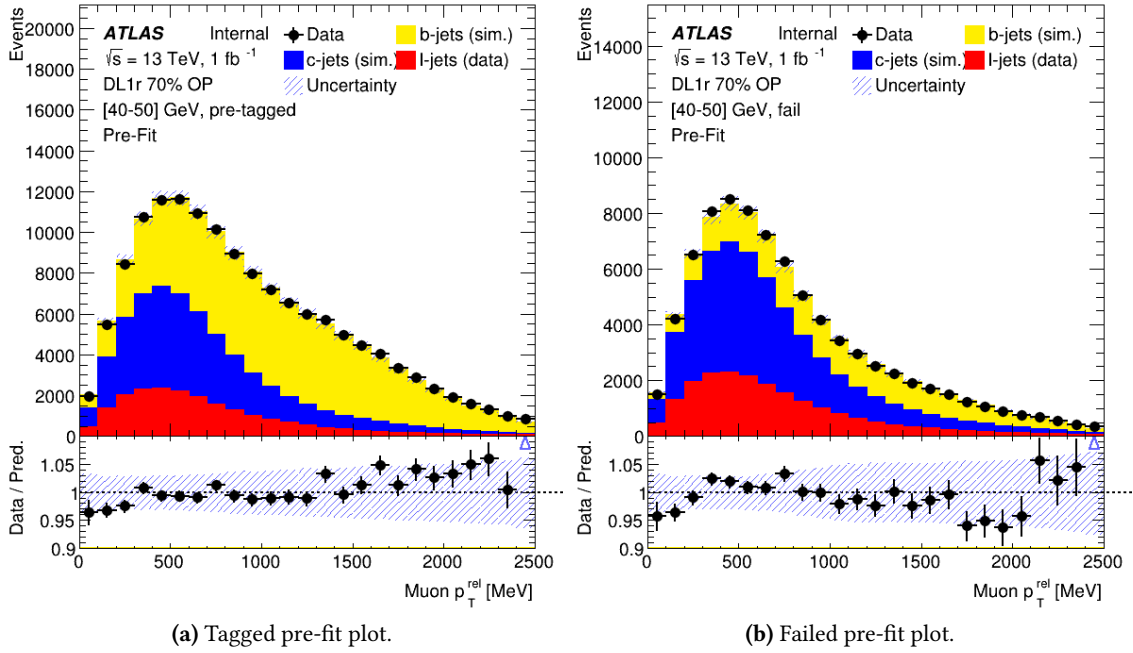


Figure 4.5: (a) The pre-fit distribution is b -tagged by DL1r at $\varepsilon_b^{\text{nom}} = 70\%$. (b) The pre-fit distribution presents jets failed the tagging criterion. Data is in black, and templates appear as a stack. Both systematic and statistical uncertainties are included in the uncertainty band.

The fit results of the b -tagged p_T^{rel} distribution and the failed region are respectively illustrated in Figure 4.6a and Figure 4.6b. The fitting process omits the overflow bin. Due to the long tails in the p_T^{rel} distribution data, this overflow bin becomes statistically significant. However, this tail arises from reconstruction and detector effects. p_T^{rel} values exceeding half the b -hadron mass are non-physical, and such effects do not find an accurate representation in MC. As a result, the p_T^{rel} range of the templates is restricted to 0-2.5 GeV.

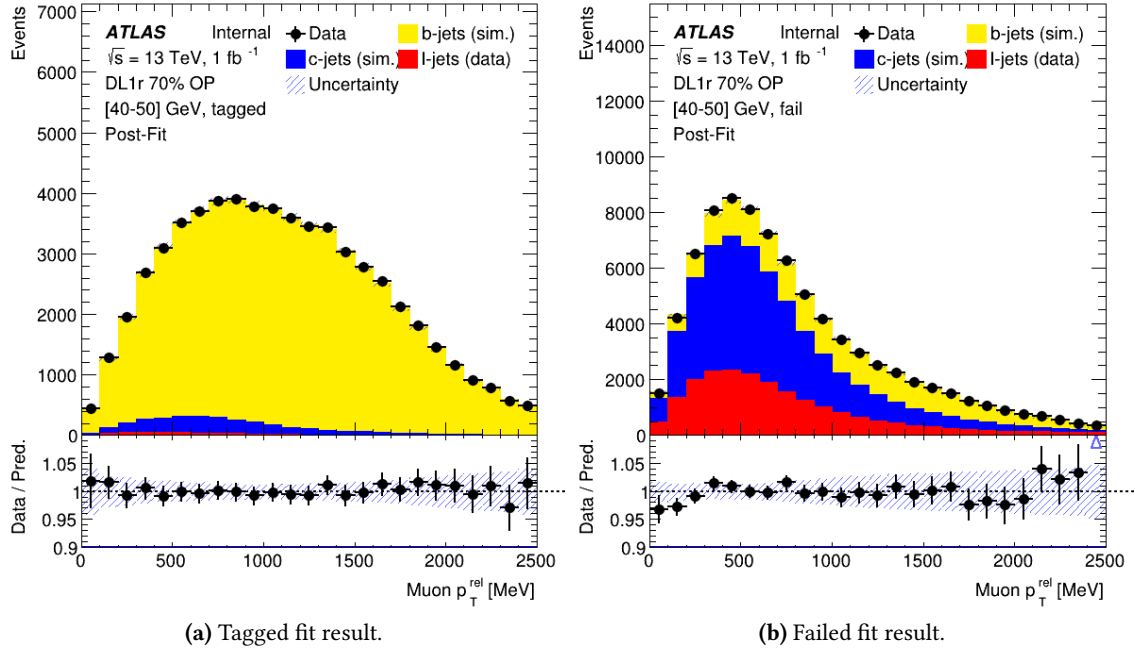


Figure 4.6: (a) The post-fit distribution is b -tagged by DL1r at $\varepsilon_b^{\text{nom}} = 70\%$. (b) The post-fit distribution of jets that did not meet the tagging criterion. Black represents data, with templates forming a stack. The band of uncertainty includes both systematic and statistical uncertainties.

4.5 Extrapolation to inclusive b -jets

The p_T^{rel} method serves as a tool for calibrating the b -tagging efficiency in jets that originate from semileptonic b -hadron decays. The question arises, however, regarding the reliability of the derived scale factor when applied to inclusive sample of b -hadron decays. To address this, it is essential to conduct an analysis to identify any potential systematic uncertainties. Previous work during Run 1 yielded consistency within 4% systematic uncertainty [141].

The intrinsic attributes of semileptonic and hadronic decays differ, particularly in the number of charged particles produced at the secondary vertex. Moreover, semileptonic jets must contain a high-momentum, well-reconstructed muon to meet selection criteria. Experimental data (as depicted in the left plots of Figure 4.7) reveal that b -jets from hadronic decays with low momentum show a 10% reduction in b -tagging efficiency compared to semileptonic jets. This efficiency gap narrows and eventually vanishes when the jet p_T exceeds 60 GeV.

The inefficiency in the identification of b -tagged jets arises primarily from the incorrect reconstruction of low-momentum particles originating from the secondary vertex. As demonstrated in Figure 4.7, the application of a momentum correction to semileptonic jets does not restore the efficiency ratio between the two cases under investigation. This adjustment entails the summation of the muon momentum to the existing jet momentum and the subtraction of energy deposits from the muon calorimeter. While this procedure results in a transition of the jet from a low transverse momentum region to a high transverse momentum region, it fails to serve as an improved proxy for the b -hadron. Nevertheless, if the simulation faithfully captures the discrepancies between the two scenarios, the scale factor determined via the p_T^{rel} method may be extended to inclusive cases.

To quantify the uncertainty in the semileptonic-to-inclusive extrapolation, scale factors for b -tagging efficiency were derived. These were evaluated for jets having a muon within a distance of $\Delta R < 0.4$, as well as for those jets that do not satisfy this criterion. Utilizing the tag-and-probe methodology, these scale factors were evaluated based on a high-purity sample of b -jets from dileptonic $t\bar{t}$ events. The data set used for this exercise encompasses an integrated luminosity of 138.9 fb^{-1} , gathered over the entire Run 2 period of the LHC.

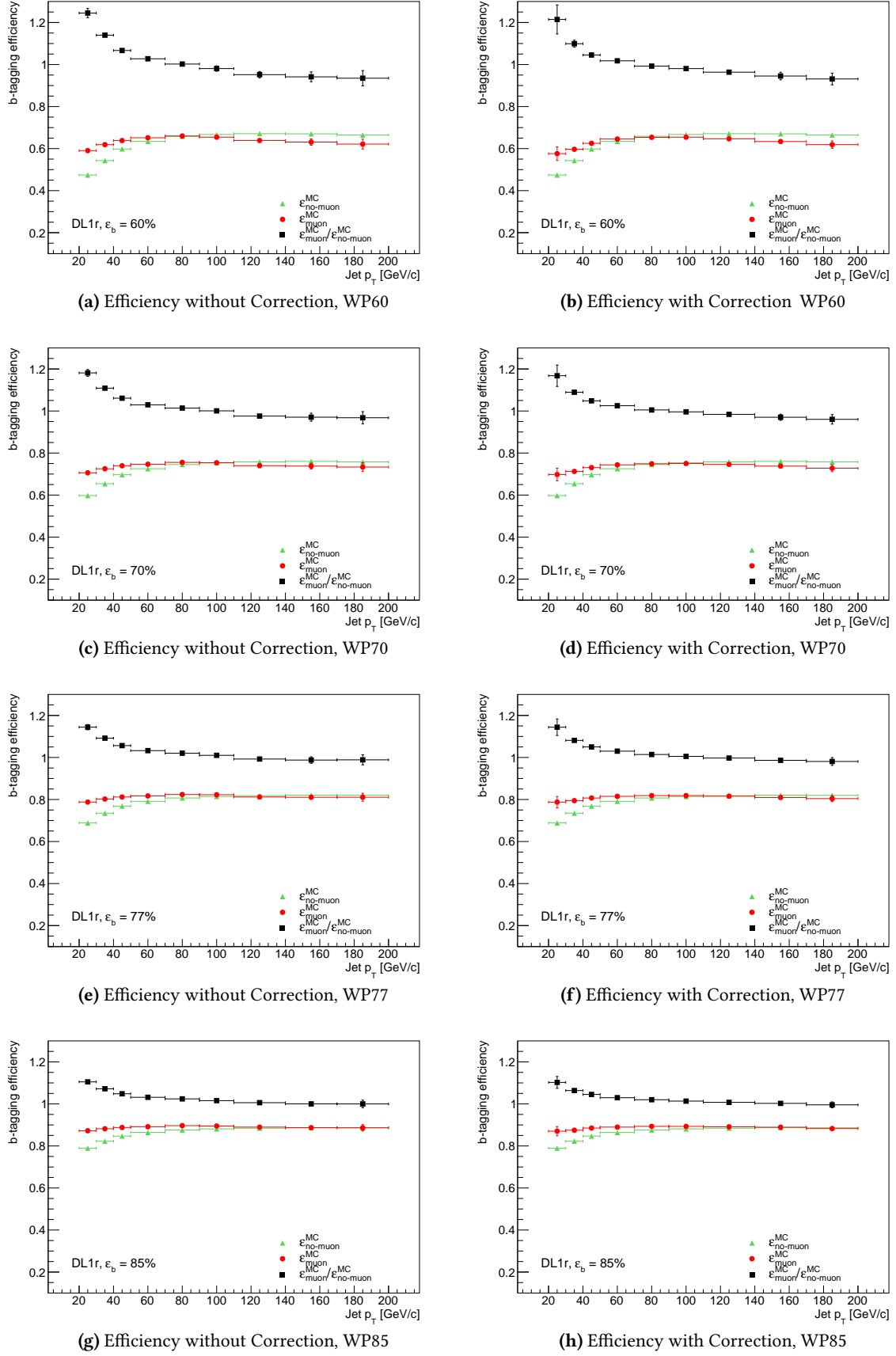


Figure 4.7: A comparative analysis of simulated b -tagging efficiency as a function of jet transverse momentum (p_T). The efficiency for jets containing muons is depicted by the red curve, while the green curve represents jets devoid of muons. The black curve illustrates the ratio of these efficiencies. The plot on the right incorporates a semileptonic correction to the jet momentum.

The criteria defining the signal region are as follows:

- One prompt electron of $p_T > 27$ GeV and $|\eta| < 2.47$, excluding the $1.37 < |\eta| < 1.52$ region
- One prompt muon of $p_T > 27$ GeV and $|\eta| < 2.4$
- Opposite electric charge between the prompt electron and the prompt muon
- Two jets of $p_T > 20$ GeV and $|\eta| < 2.5$, when $20 \text{ GeV} < p_T < 120 \text{ GeV}$,
- JVT *Medium* (default) for EMTopo jets
 1. if $|\eta| < 2.4$, JVT > 0.59 ,
 2. if $2.4 < |\eta| < 2.5$, JVT > 0.11
- JVT *Tight* (default) for PFlow jets
 1. Two jets of $p_T > 20$ GeV and $|\eta| < 2.4$, when $20 \text{ GeV} < p_T < 60 \text{ GeV}$, JVT > 0.5 ,
- At least one b -tagged jet at the 85% working point of the MV2c10 tagger
- Invariant mass of prompt muon and electron $M_{e\mu} > 15$ GeV

Based on Monte Carlo simulations, it has been inferred that the defined signal region contains 93% of the $t\bar{t} \rightarrow e\mu + 2j$ events. The main sources of background, contributing to 7% of the events in the signal region, are single-top and diboson productions. Contributions from the production of W and Z bosons in association with jets or top-quark pairs are minimal, amounting to only 0.4%. A satisfactory level of agreement is observed between the collected data and the simulation across all kinematic distributions.

In the application of the tag-and-probe methodology, a jet b -tagged at the 85% level serves as the tag, while the other jet functions as the probe to measure b -tagging efficiency. In instances where both jets in the event are b -tagged at the 85% level, each jet is utilized as a probe. The simulated b -tagging efficiency is calculated using Monte Carlo truth information as expressed in Equation 4.5.1.

$$\varepsilon_b^{sim} = \frac{N_{\text{truth-b}}^{\text{pass}}}{N_{\text{truth-b}}} \quad (4.5.1)$$

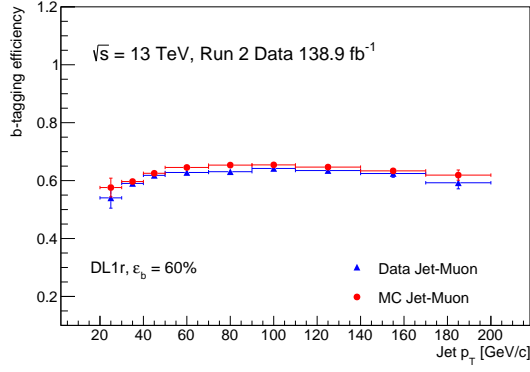
The same quantity is computed for data events, as indicated in Equation 4.5.3. The initial step involves subtracting the background contribution, detailed in Equation 4.5.2, followed by corrections based on the number of probe jets originating from b -quarks and the mis-tag rate as estimated from the $t\bar{t}$ simulation.

$$\varepsilon_b^{uncorr} = \frac{N_{\text{data}}^{\text{pass}} - N_{\text{bkg}}^{\text{pass}}}{N_{\text{data}} - N_{\text{bkg}}} \quad (4.5.2)$$

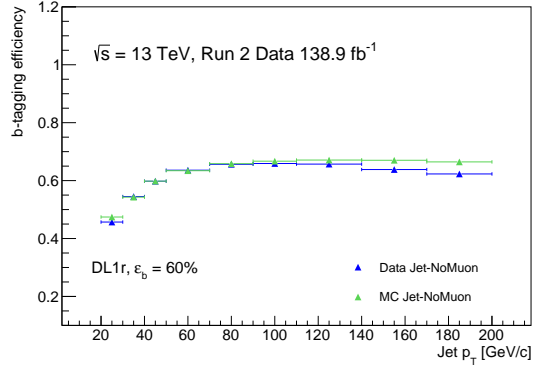
$$\varepsilon_b^{\text{data}} = \frac{\varepsilon_b^{uncorr} - (1 - f_b^{t\bar{t}}) \cdot \varepsilon_{\text{non-b}}^{t\bar{t}}}{f_b^{t\bar{t}}} \quad (4.5.3)$$

The derived scale factors, both in the semileptonic and hadronic cases, appear to be consistent with unity across all jet p_T bins. Their ratio also shows this consistency. Figure 4.8 illustrates the comparison between the b -tagging efficiency in data and simulated events.

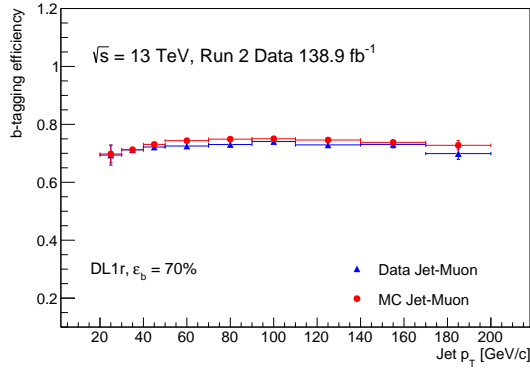
Figure 4.9 presents the ratio of scale factors for jets, distinguishing between those containing muons and those without, at all working point. The uniformity of this ratio serves as an indicator of the simulation's accuracy in replicating the diverse decay topologies of all b -hadrons, whether semileptonic or hadronic. A constant function has been employed to fit the distribution of the scale



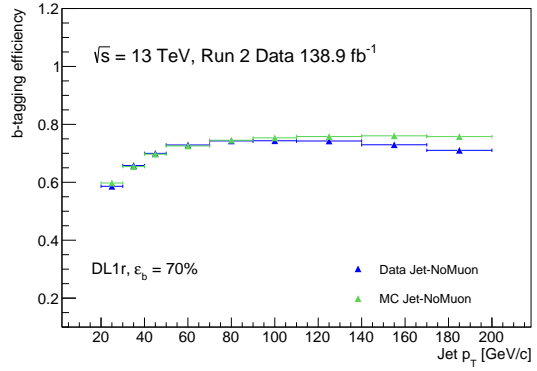
(a) Efficiency for Jets Containing Muons, WP60



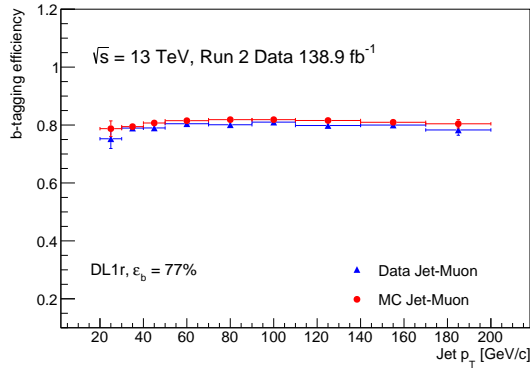
(b) Efficiency for Jets Without Muons, WP60



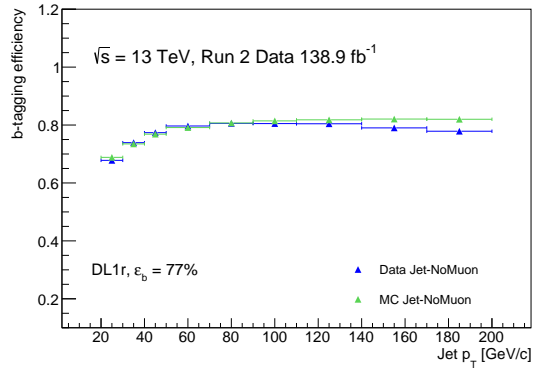
(c) Efficiency for Jets Containing Muons, WP70



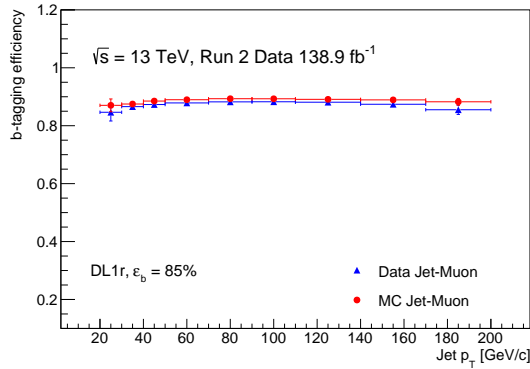
(d) Efficiency for Jets Without Muons, WP70



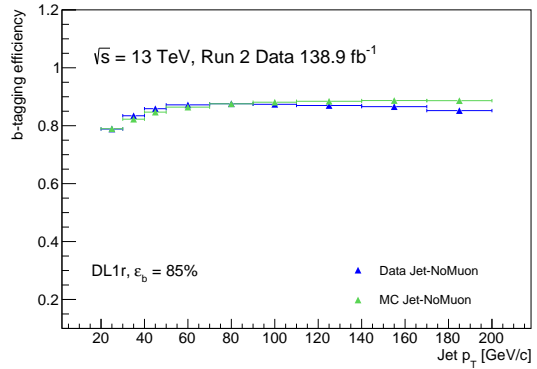
(e) Efficiency for Jets Containing Muons, WP77



(f) Efficiency for Jets Without Muons, WP77



(g) Efficiency for Jets Containing Muons, WP85



(h) Efficiency for Jets Without Muons, WP85

Figure 4.8: Comparative analysis of b -tagging efficiency, both in data and simulation, as a function of jet transverse momentum (p_T). The left plot illustrates efficiency for jets that contain muons, while the right plot focuses on jets that are devoid of muons.

factor ratio as a function of jet p_T . The fit outcome aligns closely with unity across all b -tagging working points. The uncertainty associated with the constant value obtained from the fit is considered as the systematic uncertainty for extrapolating from semileptonic to inclusive b -jets in the p_T^{rel} calibration.

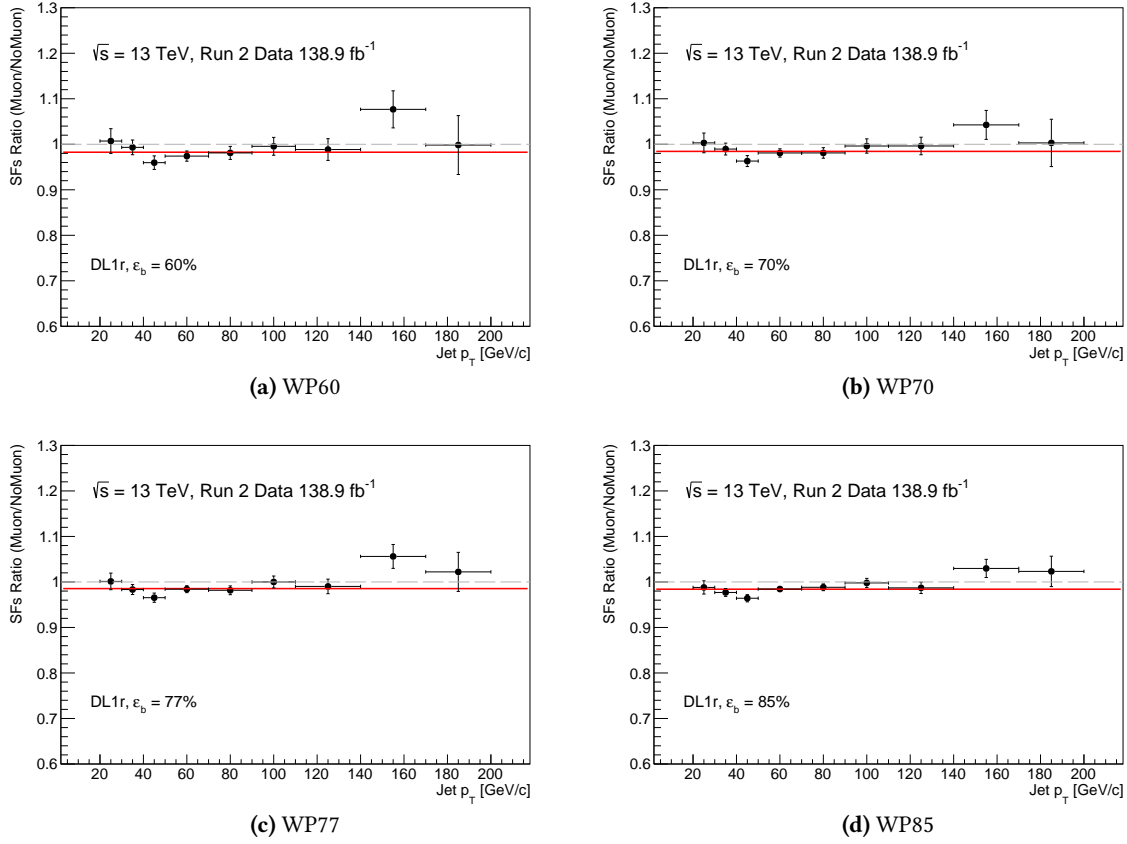


Figure 4.9: Ratio between the b -tagging efficiency scale factor of jet with and without muons for the 60, 70, 77 and 85% working point as function of jet p_T bins.

4.6 Systematic Uncertainties

The calibration employs simulated events to derive p_T^{rel} templates associated with various jet flavours. Consequently, any discrepancies in the simulation can impact the resultant b -tagging scale factors. Systematic uncertainties can be categorized into two main groups: those associated with experimental procedures and those related to the physics modelling of di-jet events, as well as the production and decay of heavy hadrons.

Experimental uncertainties arise from the identification and reconstruction of physics entities. Modelling uncertainties, on the other hand, are related to the theoretical framework adopted for the Monte Carlo (MC) simulations.

In the subsequent sections, an overview of the systematic uncertainty sources is delineated.

Several uncertainties are evaluated by varying the originating effect within 1σ . The deviation from the primary outcome is regarded as the systematic uncertainty. For certain sources where only a single variation exists, this deviation is symmetrically adjusted.

The majority of systematic variations are incorporated into the profile likelihood-fit as Gaussian-distributed nuisance parameters. Such an approach facilitates the constraining of uncertainties using data while also leveraging correlations with other parameters in the fitting model. The only

exception is the uncertainty linked to the scale-factors extrapolation towards a comprehensive b -jet sample. This uncertainty is subsequently detailed and is combined in quadrature with the uncertainty deduced from the profile-likelihood fit.

4.6.1 Experimental Uncertainties

4.6.1.1 Muon reconstruction and identification

In this analysis, the efficiencies for both the reconstruction and identification of muons are ascertained from data events. Using the tag-and-probe method on $Z \rightarrow \mu\mu$, $W \rightarrow \mu\nu$, and $J/\Psi \rightarrow \mu\mu$ events, scale factors are derived and subsequently applied to the simulated event samples. Detailed insights into the method can be found in [149, 150], and the approach taken in this study adheres to the established guidelines.

4.6.1.2 Lepton momentum scale and resolution

Discrepancies may exist in the precision of the muon momentum scale and resolution when comparing simulated events with data. To validate the simulation, reconstructed distributions of the $Z \rightarrow \mu\mu$ and $J/\Psi \rightarrow \mu\mu$ masses are examined using methodologies akin to those described in [149, 151]. Adjustments to the momentum scale and resolution are exclusively made to the simulated events. The uncertainties associated with the momentum scale and resolution of muons from both the inner detector and the muon spectrometer are acknowledged and independently adjusted.

4.6.1.3 Jet vertex tagger efficiency

The efficiency with which jets pass the Medium Working Point JVT selection is not consistent between simulated events and the data observed. To address these inconsistencies, scale factors derived from the tag-and-probe measurements involving $Z \rightarrow \mu\mu$ and supplementary jets are applied to the simulated events [152]. The verification of JVT efficiency scale factors takes into account uncertainties arising from a 20% estimation error related to the residual contamination of pile-up jets post pile-up suppression. Additionally, the scale factor adjustments incorporate a systematic uncertainty evaluated by employing various generators in the MC simulation for the Z +jets events.

4.6.1.4 Jet energy scale

The Jet Energy Scale (JES) and its associated uncertainty are determined using test-beam data, collision data, and simulations. Data acquired at $\sqrt{s} = 13$ TeV are instrumental in calibrating the lingering uncertainty on the JES [153]. Events featuring a vector boson complemented by additional jets assist in the calibration of jets in the central region. For calibrating forward jets, di-jet events are employed, while multi-jet events cater to the calibration of high transverse momentum jets. Subsequently, these measurements are combined and decorrelated, resulting in a set of 30 eigen-vectors contingent on the jet p_T and η .

These 30 Nuisance Parameters (NPs) are classified as follows:

- 15 NPs result from the in-situ calibration uncertainty.
- 4 NPs stem from the uncertainty linked to the pile-up components.
- 6 NPs account for the η intercalibration uncertainty.

- 2 NPs are due to uncertainties concerning the flavour composition of jets and their response variances.
- 1 NP is attributed to the punch-through¹ modelling uncertainty.
- 1 NP encapsulates the uncertainty for high- p_T jets.

4.6.1.5 Jet energy resolution

The Jet Energy Resolution (JER) is determined using data events characterized by $Z \rightarrow \ell\ell$ or a photon, complemented by an additional jet. This evaluation employs in-situ techniques, mirroring those presented in [154]. Within the simulated dijet events, the JER is gauged across diverse jet p_T and η categories, drawing upon the particle truth information.

During the simulation process, the reconstructed jets are paired with particle truth jets, provided they are contained within a $\Delta R < 0.3$ cone. The energy of these matched jets is compared with the particle truth jet energies and the results are incorporated into a histogram. Employing a Gaussian function, these histograms are fitted, centering around the peak of the distribution. The width of the Gaussian, denoted as σ , represents the simulated JER. Examination of this simulated JER extends across distinct jet η and p_T bins. In every η bin, JER values across various p_T bins undergo fitting using a calorimeter response function. This approach ensures interpolation of the measured JER across all p_T categories. For alignment with the JER observed in data, the energy of the jets from the simulation is smeared. The uncertainty associated with JER is defined by 8 Nuisance Parameters (NPs).

4.6.2 Modelling Uncertainties

In this analysis, the uncertainties related to physics modelling have been systematically categorized based on their relevance to either muons or jets.

4.6.2.1 Muon Origin

In this analysis, the muons being analyzed are derived from both direct $b \rightarrow \mu + X$ decays and cascade $b \rightarrow c \rightarrow \mu + X$ decays. The branching fraction for the direct decay of b -hadrons has been determined to be $BR(b \rightarrow \mu X) = 10.86 \pm 0.16$ [141, 155]. The uncertainty associated with this measurement, expressed as a percentage, is employed to adjust the *in-situ* direct decay fraction incorporated into the bottom template. Variations in both upward and downward directions are conducted, with the differential outcome being recognized as the systematic uncertainty linked to the decay of b -hadrons.

4.6.2.2 Muon p^*

The momentum of the muon in the b -hadron rest frame, denoted as p^* , is integral to this measurement. We evaluated the p^* spectrum of truth muons within the b -hadron rest frame using ATLAS simulation and compared the results with the findings from DELPHI [156], as presented in Figure 13 of [156]. The DELPHI analysis derived the p^* spectrum from a set of $e\bar{e} \rightarrow b\bar{b}$ events in which one b -hadron decayed following the pattern $b \rightarrow X\ell\bar{\nu}$. As illustrated in Figure 4.10, there are noticeable deviations in the low p^* domain. These discrepancies could be attributed to the stringent kinematic requirements applied to the muons and b -hadrons in the ATLAS simulation. In the ATLAS simulation truth record, a lower limit of 5 GeV is applied for b -hadrons, while a 4 GeV

¹An event wherein a jet constituent traverses the entirety of the calorimeter without depositing all its energy.

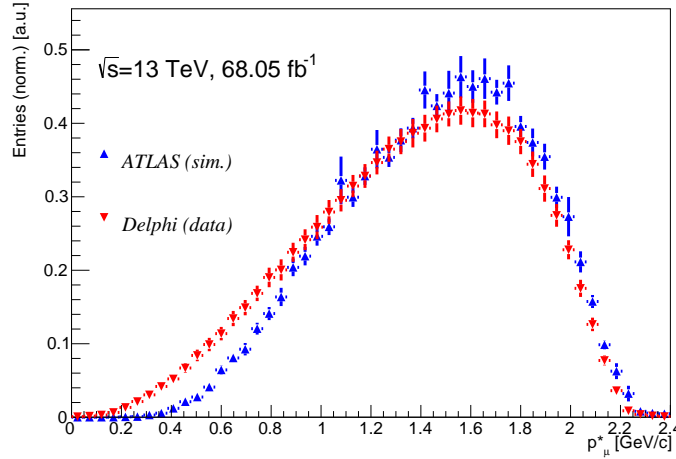


Figure 4.10: Comparison of the p^* spectrum between the ATLAS simulated data and results from DELPHI [156].
(From Ref. [3])

limit is set for the muons. In contrast, the DELPHI unfolded spectrum includes softer b -hadrons and muons, thereby providing a more detailed representation of the low p^* domain. The lower bounds for lepton momentum in the DELPHI spectrum are 2.5 GeV for muons and 3 GeV for electrons. Given the limited scope of our knowledge, a nuisance parameter (NP) is formulated, taking the DELPHI distribution as a reference and adjusting it within its defined uncertainty.

4.6.2.3 Fake muons

In the effort to minimize the influence of "fake" muons—particularly those originating from decay-in-flight processes of pions or kaons produced muon reconstruction quality criteria have been adopted in the analysis. However, despite these strict standards, it's still possible for misidentified particles or decay-in-flight muons to meet the selection criteria.

An inherent challenge exists in the Monte Carlo (MC) simulation. Due to the muon filter applied in the simulation, it tends to underestimate the frequency of these fake muons. Recognizing this limitation, we have undertaken a strategy to estimate the potential effects of these extra fake muons. Specifically, in the simulation, jets containing a fake muon were reweighted, effectively doubling their count. This approach serves to amplify the possible impact of fake muons. The consequences of this adjustment were then tracked through to the derived scale factors, offering an enhanced understanding of the systematics associated with fake muons.

4.6.2.4 Gluon Splitting

Gluon decays with high energy can give rise to jets containing multiple heavy-flavour hadrons within the jet cone. This phenomenon, often termed as gluon-splitting into quarks, stands apart from jets that emanate from single b -quark decays. These gluon-splitting jets exhibit unique characteristics: they have a distinctive tagging efficiency, they demonstrate a varying likelihood of containing a muon, and they exhibit a specific p_T^{rel} distribution. As such, how these jets are modelled holds implications for the measurement.

The frequency of gluon-splitting occurrence is tied to the transverse momentum of the jet (p_T^{jet}). Specifically, as p_T^{jet} climbs, so too does the rate of gluon-splitting. Further analysis indicates that magnifying the gluon-splitting fraction by a factor of 2.5 leads to a better alignment of the bottom template with the data, improving overall data-to-MC agreement. This observation lends support to

the notion that the ATLAS simulation might be undershooting the actual gluon-splitting fraction.

In an ideal scenario, the gluon-splitting component would be derived directly from data. However, given the intricacies involved, generating a gluon-splitting component that offers bin-by-bin statistical precision on par with other templates proves challenging. As a workaround, a methodical systematic uncertainty has been employed. In this approach, the gluon-splitting fraction undergoes a scaling - increased and decreased by a factor of 2 within the p_T^{jet} window of 20-70 GeV. Outside this range, a scaling factor of 4 is applied.

4.6.2.5 B-hadrons Fragmentation Fraction

The accuracy of this measurement is intrinsically tied to the modeling of the final state particles within the b -hadron rest-frame. Variations in mass among different b -hadrons, as detailed in Table 4.5, can influence the p_T^{rel} distribution, especially if their prevalence is not accurately represented. Consequently, in this study, the ratios of hadrons (B^0 , B^+ , B_s , b -baryons) emanating from the fragmentation process are acknowledged as a source of systematic uncertainty.

Hadron	Mass [MeV]	Mean lifetime 10^{-12}s	Decay into $l\nu_l + X$
B^\pm	5279.34 ± 0.12	1.638 ± 0.004	$10.99 \pm 0.28 \%$
B^0	5279.65 ± 0.12	1.519 ± 0.004	$10.33 \pm 0.28 \%$
B_s^0	5366.88 ± 0.14	1.515 ± 0.004	$9.6 \pm 0.8\%$
b -baryon (λ_b^0)	5619.60 ± 0.17	1.471 ± 0.009	$10.9 \pm 2.2\%$

Table 4.5: Mass, mean lifetime, and decay rate into $l\nu_l + X$ decay of the different b -hadrons as cited in Ref. [155].

The reliability of this modeling hinges on the precision of the measured fractions. For the current measurement, fragmentation fractions are grounded on the HFAG's estimates [157]. To gauge the systematic uncertainty, events were adjusted to align with the flavor fractions delineated by the CDF collaboration [158]. The simulation and inclusive measurements is provided in Table 4.6.

Table 4.6: Fractions of b -hadrons as generated in simulated Z^0 -decays, inclusive assessments executed at CDF [158], Compared to the mean value proposed by the HFAG [157] (CDF, LHCb and LEP). The concluding column reveals values derived using the ATLAS muon filtered di-jets simulation, using DL1r tagger.

Hadron Fraction	Z^0 -decays (MC)	Tevatron	HFAG-combination	ATLAS muon-filtered MC
B^+ fraction	0.410 ± 0.007	0.350 ± 0.020	0.406 ± 0.005	0.449
B^0 fraction	0.410 ± 0.007	0.350 ± 0.020	0.406 ± 0.005	0.417
B_s^0 fraction	0.100 ± 0.008	0.100 ± 0.010	0.105 ± 0.005	0.087
b -baryon fraction	0.080 ± 0.010	0.199 ± 0.044	0.083 ± 0.010	0.046

The energy partitioning during the fragmentation process sees the initial b -quark's energy being allocated to the resultant hadrons. An up-down variation of 5% in the energy fraction X_b conveyed to the b -hadron offers a conservative estimation of the systematic uncertainty, given the restricted comprehension of the hadronization process.

4.6.2.6 Semileptonic-to-inclusive extrapolation

For the calibration of p_T^{rel} , it is imperative that a muon exists within the jet cone. This occurrence is typically seen for semileptonically decaying b -hadrons. Nevertheless, the tagging efficiency for this sample is not the same as the inclusive b -tagging efficiency. Provided this discrepancy is accurately represented in the simulation, its effects will nullify during the computation of the data-to-MC SFs. Previous ATLAS data indicates that potential biases arising from modeling disparities between semileptonic and inclusive decays are minimal.

A measurement, dependent on the jet p_T , was conducted on a $t\bar{t}$ event set. The assessment involved a comparison of SFs in both hadronic and leptonic top decays. It was determined that this uncertainty is independent of the jet p_T . The description of the entire process is provided in the previous Section 4.5.

4.7 Results

The calibration terminates at p_T^{jet} of 140 GeV due to superior precision in this region. Challenges primarily arise from the gluon splitting modeling in MC.

The calculation of the b -tagging efficiency, as outlined in Section 4.4, is achieved by conducting a template fit on both tagged and untagged p_T^{rel} distributions. This process is replicated across all jet p_T bins, specifically for the four operational points of DL1r algorithm. The resultant p_T^{jet} dependent b -tagging efficiency, ε_b , for the DL1r algorithm at nominal efficiencies of $\varepsilon_b^{\text{nom}} = 85\%, 77\%, 70\%$, and 60% is illustrated in Figure 4.11. A division of the two efficiencies on the left yields the scale factors on the right, inclusive of their associated uncertainties. Notably, the scale factors exhibit general alignment with unity, yet pronounced discrepancies are evident in the lower p_T^{jet} bins, specifically for the stricter working points of $\varepsilon_b^{\text{nom}} = 60\%$ and 70% .

In Figure 4.12, the scale factors for b -tagging efficiency are contrasted against the results from $t\bar{t}$ calibrations², which is the main calibration method at ATLAS. This comparison underscores that the calibration method discussed herein offers reduced uncertainty in the p_T^{jet} range from 20 to 40 GeV across all operational points.

The analyses team is planning apply the p_T^{rel} method on early Run 3 data and to combine with all other b -tagging calibration methods to produce a single set of b -tagging scale factors for the full Run 3 dataset.

²<http://atlas.web.cern.ch/Atlas/GROUPS/PHYSICS/PLOTS/FTAG-2021-001/>

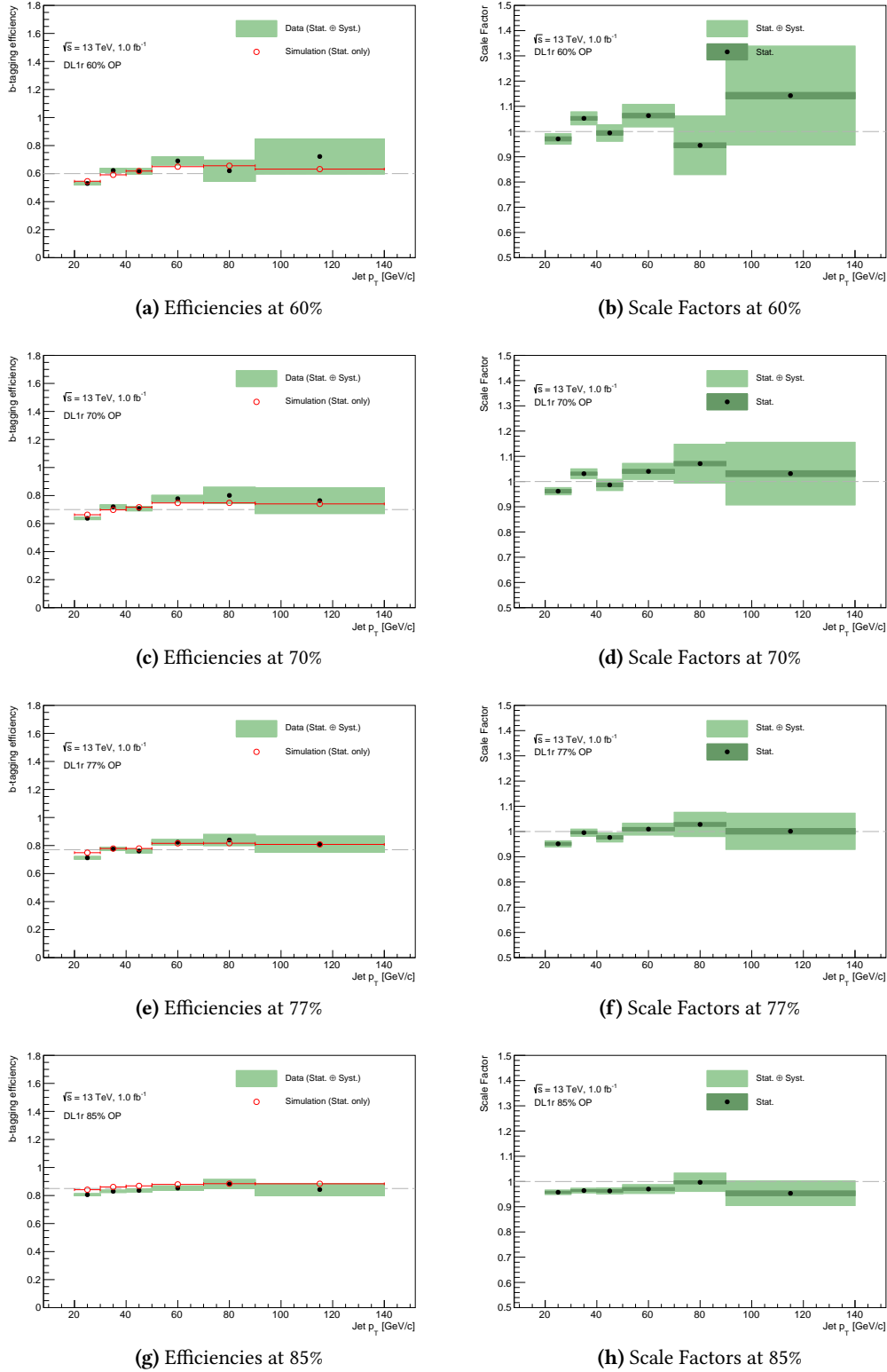
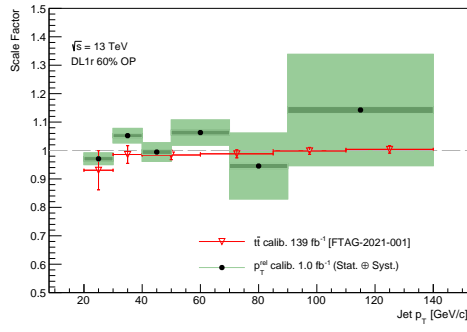
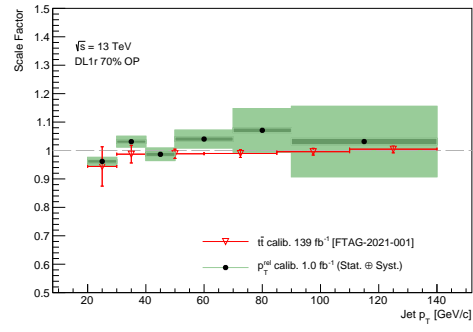


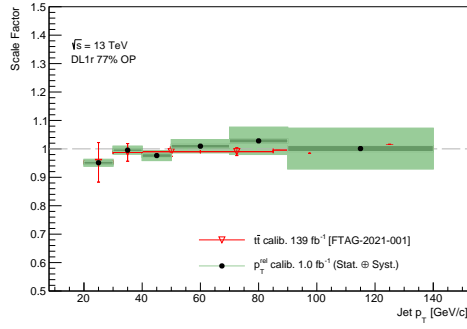
Figure 4.11: Jet p_T dependent efficiencies (left) and scale factors (right) determined through the p_T^{rel} technique for the DL1r algorithm at nominal efficiencies of $\varepsilon_b^{\text{nom}} = 60\%$, 70% , 77% , and 85% in sequence from top to bottom. The MC predictions are displayed in red, with data symbolized by black dots. The green bands convey both statistical and systematic uncertainties.



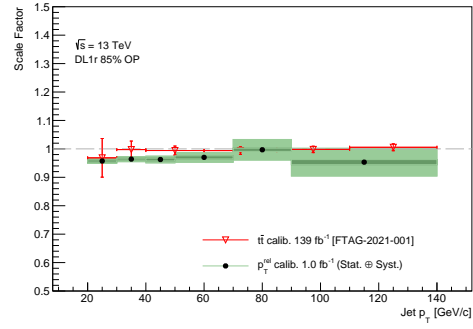
(a) Scale Factors at 60%



(b) Scale Factors at 70%



(c) Scale Factors at 77%



(d) Scale Factors at 85%

Figure 4.12: Comparative analysis between p_T^{rel} b -tagging efficiency scale factors (represented by a black marker and accompanied by a green uncertainty band) and $t\bar{t}$ likelihood-based method scale factors (shown in red).

Search for di-Higgs production in the $b\bar{b}\tau^+\tau^-$ final state

5.1	Data and Monte Carlo samples	113
5.1.1	Signal samples	114
5.2	Event Selection	118
5.2.1	Trigger selection	119
5.2.1.1	$\tau_{\text{lep}}\tau_{\text{had}}$	119
5.2.1.2	$\tau_{\text{had}}\tau_{\text{had}}$	120
5.2.2	Event selection	121
5.2.2.1	$\tau_{\text{lep}}\tau_{\text{had}}$	121
5.2.2.2	$\tau_{\text{had}}\tau_{\text{had}}$	122
5.2.3	Event categorisation	123
5.2.4	$Z + HF$ control region	129
5.3	Background modelling	133
5.4	Multi-Variables Analysis	133
5.4.1	Optimisation Strategy	134
5.4.1.1	Input Variables Optimisation	134
5.4.1.2	Hyperparameters Optimisation	135
5.4.2	ggF/VBF BDT	136
5.4.2.1	Selection of input variables	136
5.4.2.2	Optimization of hyperparameters	137
5.4.2.3	Selection of working point	143
5.4.3	Signal Region BDT	145
5.4.3.1	Optimization of hyperparameters	145
5.4.3.2	Input variable selection	146
5.4.3.3	BDT score distributions in different folds	146
5.5	Statistical interpretation	153
5.5.1	Statistical model	153
5.5.2	Fit setup	154
5.5.3	Binning	155
5.5.4	Blinding strategy	156
5.6	Results	157
5.6.1	Fit results	157
5.6.1.1	$\tau_{\text{had}}\tau_{\text{had}}$	157
5.6.1.2	$\tau_{\text{lep}}\tau_{\text{had}}$	165
5.6.1.3	Combined fit	174
5.6.2	Limits and scans	181
5.6.2.1	$\tau_{\text{had}}\tau_{\text{had}}$	181
5.6.2.2	$\tau_{\text{lep}}\tau_{\text{had}}$	181
5.6.2.3	Combined Limits	183
5.7	Conclusion	186

This chapter outlines the Legacy Run 2 analysis for HH production in the final state with two b -jets and two τ leptons. The data consists of 140 fb^{-1} of proton-proton collision data from the ATLAS experiment at $\sqrt{s} = 13 \text{ TeV}$. The $b\bar{b}\tau^+\tau^-$ channel exhibits a significant branching fraction of 7.3% among the possible HH decay channels, complemented by a relatively clean final state. Given that τ leptons can undergo either leptonic (τ_{lep} : into e or μ) or hadronic (τ_{had} : usually into one or three charged pions with some neutral pions) decay, two sub-channels, $b\bar{b} \tau_{\text{lep}} \tau_{\text{had}}$ and $b\bar{b} \tau_{\text{had}} \tau_{\text{had}}$, are examined.

While a previous analysis for HH production in the $b\bar{b}\tau^+\tau^-$ final state using the full Run 2 dataset was made public [4], it was solely optimised for the gluon-gluon fusion (ggF) production mode. This analysis placed an observed (expected) upper limit on the HH production cross-section of 140 (110) fb at a 95% confidence level (CL). This translated to 4.7 (3.9) times the standard model (SM) prediction against the background-only hypothesis. Under the assumption of SM HH production and couplings, κ_λ was constrained between $-2.7 < \kappa_\lambda < 9.5$ ($-3.1 < \kappa_\lambda < 10.2$) and κ_{2V} between $-0.6 < \kappa_{2V} < 2.7$ ($-0.5 < \kappa_{2V} < 2.7$) at 95% CL [5]. A consolidated outcome of the $HH \rightarrow b\bar{b}\tau^+\tau^-$ exploration, along with other HH channels, is available in [6, 7]. Additionally, an interpretation within the framework of Higgs EFT (HEFT) was provided [8].

For this new round of analysis, documented in this chapter, re-optimisation was conducted to enhance the κ_λ constraint by introducing an event classification based on the invariant mass of the HH system, m_{HH} , in the ggF region. The process also involved constraining the κ_{2V} sensitivity through the creation of a dedicated Vector Boson Fusion (VBF) region. To ensure an ideal distinction between the ggF/VBF signal and background processes, multivariate analysis (MVA) techniques were employed. The outputs of these MVAs are used to derive the ggF and VBF enriched regions. MVAs are also used to discriminate between the signal and background processes in the ggF and VBF regions, and the outputs are used as the conclusive discriminants in the fit.

The structure of this chapter is the following:

Section 5.1 introduces the data and Monte Carlo (MC) simulation samples utilised in the study. Event selection methodologies are articulated in Sections 5.2. Section 5.3 provides a succinct overview of the background modelling strategy, inherited from the prior analysis, supported by validation plots. The MVA approach for every sub-channel is elaborated in Section 5.4. Discussions on statistical interpretation are in Sections 5.5. Results are presented in Section 5.6.

5.1 Data and Monte Carlo samples

The ATLAS detector at the LHC collected proton-proton collision data with a centre-of-mass energy of $\sqrt{s} = 13$ TeV from 2015 to 2018 (Full Run 2). This data corresponds to an integrated luminosity of $\mathcal{L} = 140.1 \pm 1.2 \text{ fb}^{-1}$ [159]. Only data events in which the relevant components of the ATLAS detector were operational, as defined by the ATLAS Good-Run-List (GRL), were considered for this analysis.

To model the SM background production, and SM-like HH signal production, MC simulated events were employed. These events underwent the full ATLAS detector simulation [160], which is based on GEANT4 [146]. By overlaying each hard-scatter event with minimum-bias events, the impacts of pile-up from both the same and neighbouring bunch crossings were taken into account. These minimum-bias events were simulated leveraging the soft quantum chromodynamics (QCD) processes from PYTHIA 8.186 [161]. This used a parameter set, known as the A3 tune [162], in conjunction with the NNPDF2.3LO [144] parton distribution functions (PDFs). In the modeling of bottom and charm hadron decays across all simulated event samples, the EVTGEN program [145] was employed, with the exception of events generated by SHERPA [163]. In the latter case, the built-in model of the generator for bottom- and charm-hadron decay was utilized. The simulated events were subject to identical reconstruction algorithms as the actual data.

All sample sets that incorporated an SM Higgs boson had its mass set to 125 GeV. This consistent mass value was also adopted during the determination of the Higgs boson decay branching fractions and while computing the cross-sections for single-Higgs-boson and SM HH production. Except where explicitly stated otherwise, the order of the calculation of the cross-section is in relation to the expansion in the strong coupling constant (α_s). A list of event samples deployed for simulating signal and background processes can be found in Table 5.1.

Table 5.1: Generators used to simulate the signal and background processes. If not otherwise specified, the order of the cross-section calculation refers to the expansion in the strong coupling constant (α_s). The acronyms ME, PS and UE are used for matrix element, parton shower and underlying event, respectively. Details of the simulation of the signal and background samples are described in the text. (†) The NNLO(QCD)+NLO(EW) cross-section calculation for the $pp \rightarrow ZH$ process already includes the $gg \rightarrow ZH$ contribution. The $qq \rightarrow ZH$ process is normalised to the NNLO(QCD)+NLO(EW) cross-section for the $pp \rightarrow ZH$ process, after subtracting the $gg \rightarrow ZH$ contribution.

Process	ME generator	ME QCD order	ME PDF	PS and hadronisation	UE model tune	Cross-section order
Signal						
$gg \rightarrow HH$ (ggF with $\kappa_\lambda = 1, 10$)	POWHEG BOX v2	NLO	PDF4LHC15NLO	PYTHIA 8.244	A14	NNLO FTApprox
$qq \rightarrow qqHH$ (VBF with varied $\kappa_\lambda, \kappa_{2V}, \kappa_V$)	MADGRAPH5_AMC@NLO 2.7.3	LO	NNPDF3.0NLO	PYTHIA 8.244	A14	N ³ LO(QCD)
Top-quark						
$t\bar{t}$	POWHEG BOX v2	NLO	NNPDF3.0NLO	PYTHIA 8.230	A14	NNLO+NNLL
t -channel	POWHEG BOX v2	NLO	NNPDF3.0NLO	PYTHIA 8.230	A14	NLO
s -channel	POWHEG BOX v2	NLO	NNPDF3.0NLO	PYTHIA 8.230	A14	NLO
Wt	POWHEG BOX v2	NLO	NNPDF3.0NLO	PYTHIA 8.230	A14	NLO
$t\bar{t}Z$	SHERPA 2.2.1	NLO	NNPDF3.0NNLO	SHERPA 2.2.1	Default	NLO
$t\bar{t}W$	SHERPA 2.2.8	NLO	NNPDF3.0NNLO	SHERPA 2.2.8	Default	NLO
Vector boson + jets						
W/Z +jets	SHERPA 2.2.11	NLO (≤ 2 jets) LO (3,4,5 jets)	NNPDF3.0NNLO	SHERPA 2.2.11	Default	NNLO
Diboson						
WW, WZ, ZZ	SHERPA 2.2.1	NLO (≤ 1 jet) LO (2,3 jets)	NNPDF3.0NNLO	SHERPA 2.2.1	Default	NLO
Single Higgs boson						
ggF	POWHEG BOX v2	NNLO	NNPDF3.0NLO	PYTHIA 8.212	AZNLO	N ³ LO(QCD)+NLO(EW)
VBF	POWHEG BOX v2	NLO	NNPDF3.0NLO	PYTHIA 8.212	AZNLO	NNLO(QCD)+NLO(EW)
$qq \rightarrow WH$	POWHEG BOX v2	NLO	NNPDF3.0NLO	PYTHIA 8.212	AZNLO	NNLO(QCD)+NLO(EW)
$qq \rightarrow ZH$	POWHEG BOX v2	NLO	NNPDF3.0NLO	PYTHIA 8.212	AZNLO	NNLO(QCD)+NLO(EW) ^(†)
$gg \rightarrow ZH$	POWHEG BOX v2	NLO	NNPDF3.0NLO	PYTHIA 8.212	AZNLO	NLO+NLL
$t\bar{t}H$	POWHEG BOX v2	NLO	NNPDF3.0NLO	PYTHIA 8.230	A14	NLO

5.1.1 Signal samples

The HH signal production simulation incorporates both the ggF and VBF processes.

The SM ($\kappa_\lambda = 1$) and BSM ($\kappa_\lambda = 10$) ggF HH signal samples were produced using the POWHEG BOX v2 generator [164], at a next-to-leading order (NLO) precision, considering finite top-quark mass. For these simulations, the PDF4LHC15_NLO_30_PDFAS PDF set was chosen, which corresponds to code 90400 in the LHAPDF database [165] [166]. Further steps of the simulation, including parton showers and hadronisation, were executed with PYTHIA 8.244 [161], utilizing the A14 tune [167, 168] along with the NNPDF2.3LO PDF set. An illustration of the m_{HH} distribution for the aforementioned nominal ggF HH signal samples within the $\tau_{\text{had}}\tau_{\text{had}}$ channel for κ_λ values of 1 and 10, as produced at the parton level, is showcased in Figure 5.1. This graph underscores the significant insights offered by this kinematic variable, especially in relation to the analysis categorization, further elaborated upon in Section 5.2.3.

For ggF HH events in the interval $\kappa_\lambda \in [-20, 20]$, the common HH κ_λ reweighting tool can be employed to obtain varying κ_λ values. This tool furnishes per-event weights based on the desired κ_λ value and the truth m_{HH} . An explanation of the κ_λ reweighting approach for the ggF HH sample is available in Section 1.3.5.

The standard normalization for the SM process employs the SM ggF di-Higgs cross-section, denoted as $\sigma_{\text{ggF}} = 31.05$ fb, as calculated at NNLO FTApprox [169]. It is further multiplied by the $b\bar{b}\tau^+\tau^-$ branching ratio: $\sigma_{\text{ggF}} \times \mathcal{B}(b\bar{b}\tau^+\tau^-) = 31.05 \text{ fb} \times 0.0730562561 = 2.268\,396\,7$ fb. The normalization for the BSM process originates from a 2nd order Polynomial function in terms of κ_λ [52].

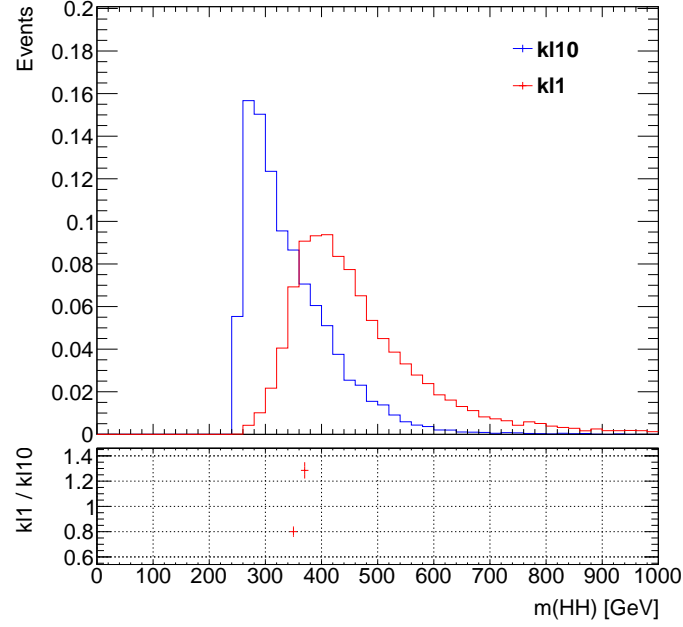


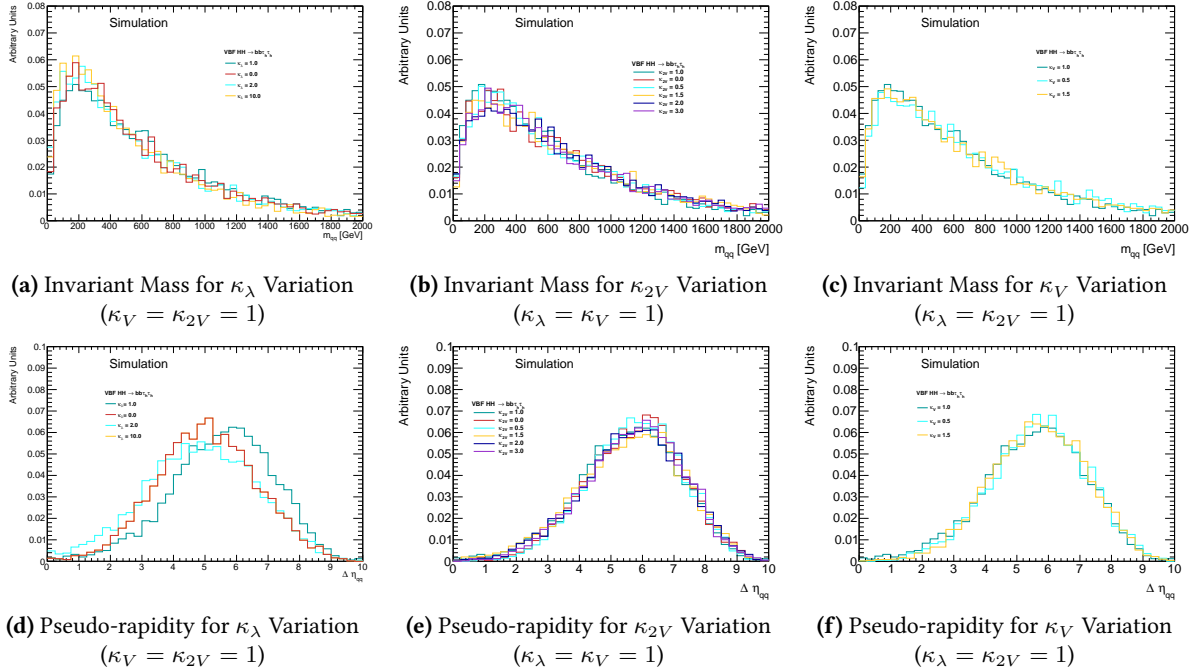
Figure 5.1: Parton level invariant mass distribution of the HH system m_{HH} , for the nominal ggF HH signal samples in the $\tau_{\text{had}}\tau_{\text{had}}$ channel with varied $\kappa_\lambda = 1, 10$ values overlaid.

To evaluate the uncertainty related to parton showering, alternative ggF signal samples, for κ_λ values of 1 and 10, were produced utilizing the POWHEG BOX v2 generator [164] at NLO. This was further interfaced with HERWIG 7 [170, 171].

Regarding **VBF HH** production, nominal VBF signal samples were generated at LO through the MADGRAPH5_AMC@NLO 2.7.3 [172] generator in conjunction with the NNPDF3.0NLO [173] PDF set. The process of parton showering and hadronization was executed using PYTHIA 8.244 paired with the A14 tune and the NNPDF2.3LO PDF set. VBF samples were created for various coupling parameter values (κ_λ , κ_{2V} , and κ_V) as displayed in Table 5.2. In this context, the SM case corresponds to $\kappa_\lambda = \kappa_V = \kappa_{2V} = 1$. A set of (κ_λ , κ_{2V} , κ_V) values was employed to produce distributions for a refined κ_{2V} granularity. These chosen basis samples reside in the region anticipated for analysis sensitivity, which helps in minimizing the statistical uncertainties that may arise during reweighting. Selected distributions from these nominal samples at the parton level are illustrated in Figures 5.2 and 5.3. These plots represent the $\tau_{\text{had}}\tau_{\text{had}}$ and $\tau_{\text{lep}}\tau_{\text{had}}$ channels, focusing on the highest m_{jj} pair. Observably, the invariant mass distribution for the VBF jets system remains consistent regardless of the coupling variations. Likewise, the pseudo-rapidity difference distributions between two VBF jets persist unchanged across different couplings. Nonetheless, the pseudo-rapidity difference remains a unique characteristic of VBF jets, enabling an effective differentiation between ggF and VBF HH processes. Another prospective way is probing the extended kinematic region at high m_{HH} , especially when κ_{2V} diverges from its SM benchmark [51], as depicted in Figure 5.4. An in-depth overview of the κ_{2V} and κ_V parameterization for the VBF HH samples is provided in Section 1.3.5.

Table 5.2: κ_λ , κ_{2V} and κ_V coupling parameter values considered for the nominal VBF HH samples generation.

κ_λ	κ_{2V}	κ_V
1	1	1
1	0	1
1	0.5	1
1	1.5	1
1	2	1
1	3	1
0	1	1
2	1	1
10	1	1
1	1	0.5
1	1	1.5
0	0	1
-5	1	0.5

**Figure 5.2:** Parton-level distributions of the nominal VBF HH signal sample showing (top row) the invariant mass and (bottom row) the pseudo-rapidity separation of the VBF jet system in the $\tau_{\text{had}}\tau_{\text{had}}$ channel. Each plot varies one coupling (κ_λ , κ_{2V} , or κ_V) according to the settings detailed in Table 5.2, while the other two couplings are fixed to their Standard Model values. Distributions have been normalized to unity.

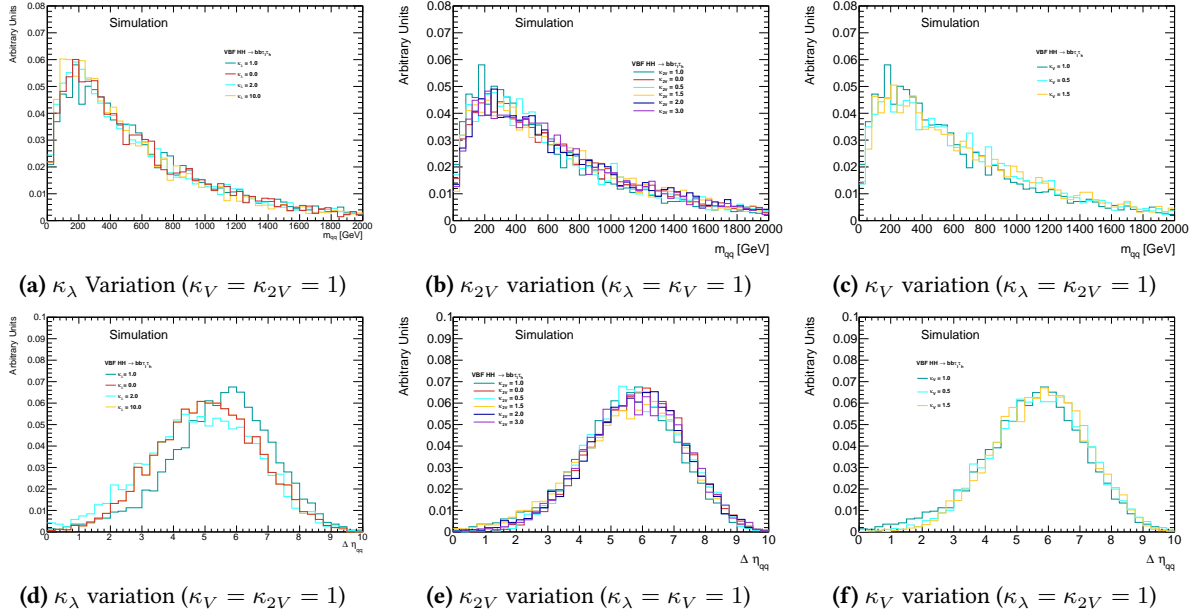


Figure 5.3: Parton level plots for the nominal VBF HH signal sample showing the invariant mass distribution and the pseudo-rapidity separation of the VBF jets system in the $\tau_{\text{lep}}\tau_{\text{had}}$ channel. For each plot κ_λ , κ_{2V} and κ_V are varied respectively as shown in Table 5.2 while the other two couplings are set to their SM prediction. The distributions are normalised to unity.

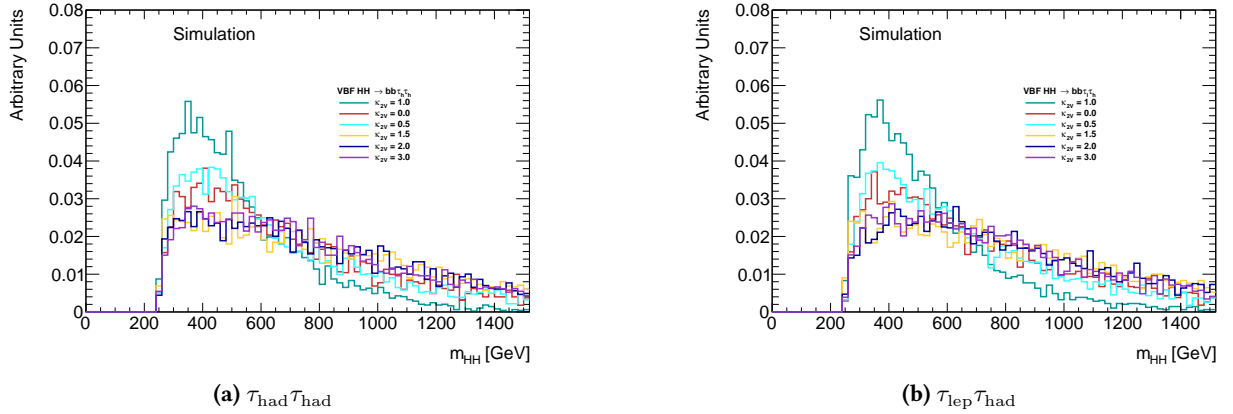


Figure 5.4: Nominal VBF HH signal sample plots for various κ_{2V} values at parton level. m_{HH} distributions are shown in the $\tau_{\text{had}}\tau_{\text{had}}$ (Figure 5.4a) and $\tau_{\text{lep}}\tau_{\text{had}}$ (Figure 5.4b) channels. For each plot κ_λ , κ_{2V} , and κ_V are varied respectively as shown in Table 5.2 while the other two couplings are set to their SM prediction. The distributions are normalised to unity.

For the standard model (SM) process, the normalization is determined by the SM VBF HH cross-section, represented as $\sigma_{\text{VBF}} = 1.726$ fb. This is derived at next-to-next-to-next-to-leading order (N^3LO) in QCD, considering the scenario where no partonic exchange occurs between the two protons [174]. The resultant value is further multiplied by the $b\bar{b}\tau^+\tau^-$ branching ratio: $\sigma_{\text{VBF}} \times \mathcal{B}(b\bar{b}\tau^+\tau^-) = 1.726 \text{ fb} \times 0.07306 = 0.1261 \text{ fb}$. For the beyond standard model (BSM) processes, normalization is based on a 2nd order polynomial function in terms of κ_{2V} [52]. The initial step in this process involves utilizing the generator cross-sections at LO, paired with κ_{2V} variations scaled to N3LO using the SM k-factor. Subsequently, a 2nd order polynomial fit is applied to these derived values.

To account for the variations in parton shower, alternative VBF signal samples were produced for three distinct coupling values, as detailed in Table 5.3. These alternative samples were generated at LO through the MADGRAPH5_AMC@NLO 2.7.3 [172] generator, combined with the NNPDF3.0NLO [173] PDF set. The generation process was subsequently interfaced with HERWIG

7 [170, 171].

Table 5.3: κ_λ , κ_{2V} and κ_V coupling parameter values considered for the alternative VBF HH samples generation.

κ_λ	κ_{2V}	κ_V
1	1	1
1	0	1
10	1	1

5.2 Event Selection

The presented analysis is partitioned into two distinct sub-channels, as characterized by the di- τ decay mode, illustrated in Figure 5.5. The $b\bar{b}\tau_{\text{had}}\tau_{\text{had}}$ sub-channel focuses on events characterized by two oppositely charged $\tau_{\text{had-vis}}$ candidates accompanied by two b -jets. Conversely, the $b\bar{b}\tau_{\text{lep}}\tau_{\text{had}}$ sub-channel targets events which include either an electron or muon, an oppositely charged $\tau_{\text{had-vis}}$, and a pair of b -jets. This sub-channel is further divided based on the employed trigger. In both cases, the two b -jets are required to satisfy the 77% efficiency criterion.

For the $b\bar{b}\tau_{\text{lep}}\tau_{\text{had}}$ sub-channel, the configurations for single-lepton triggers (SLT) and lepton-plus- $\tau_{\text{had-vis}}$ triggers (LTT) are employed. The $b\bar{b}\tau_{\text{had}}\tau_{\text{had}}$ sub-channel uses a combination of single- $\tau_{\text{had-vis}}$ triggers (STT) and di- $\tau_{\text{had-vis}}$ triggers (DTT). Further details provided in Section 5.2.2.1 and Section 5.2.2.2 respectively.

Each sub-channel has its events classified into either ggF or VBF signal regions (SRs), employing specialized BDTs for this purpose. The ggF regions are further stratified into low- and high-mass SRs, contingent on the invariant mass of the HH system for individual events. This distinction is made utilizing a threshold value of 350 GeV, as delineated in Figure 5.5.

A specific control region, termed the $Z + HF$ CR, has been established to facilitate the determination of the background normalization. This background corresponds to scenarios where a Z boson is produced in association with one or multiple jets that originate from heavy-flavour quarks, denoted as the $Z + HF$ background. Employing $b\bar{b}\ell\ell$ triggers and a specific event selection protocol, the $m_{\ell\ell}$ shape emerges as parameter of interest.

Subsequent sections provide a concise overview of the trigger mechanisms harnessed for each sub-channel. Additionally, enhanced attention is directed towards elucidating the revamped event categorization (see Section 5.2.3). Furthermore, the refinement in the definition of the $Z + HF$ CR's domain (Section 5.2.4) is highlighted, particularly in relation to the previous round of the analysis [4].

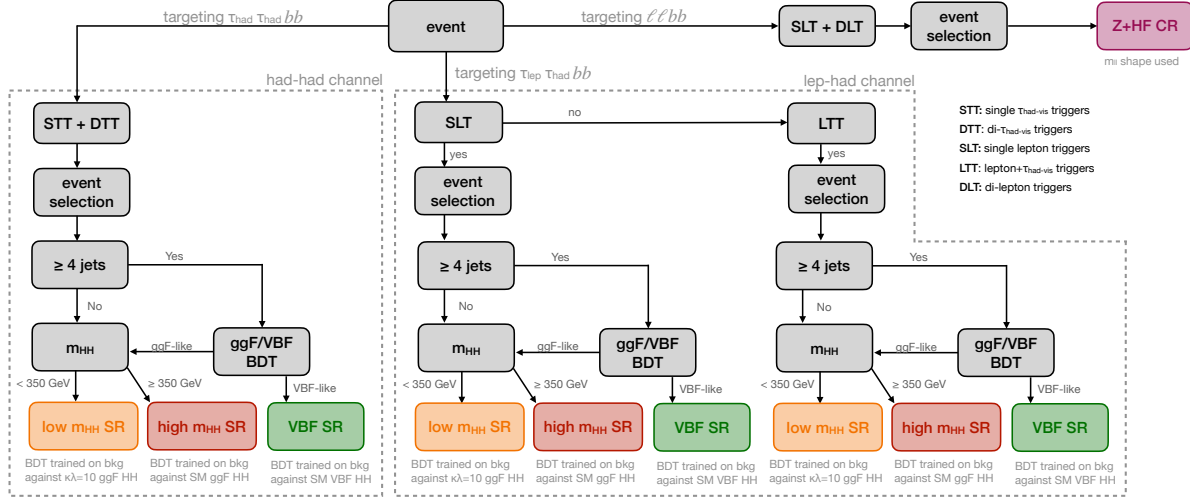


Figure 5.5: Sketch depicting the analysis strategy starting with the triggers and event selection for the $b\bar{b} \tau_{\text{had}} \tau_{\text{had}}$ and $b\bar{b} \tau_{\text{lep}} \tau_{\text{had}}$ sub-channels, followed by a BDT approach defining the orthogonality between ggF and VBF signal regions. The ggF signal region is subsequently split based on a m_{HH} requirement of 350 GeV to improve the sensitivity of enhanced κ_λ . Furthermore, a control region ($Z + H F$) is defined based on various single- and di-lepton triggers and event selection with the $m_{\ell\ell}$ shape used as parameter of interest.

5.2.1 Trigger selection

The trigger selection has not changed since the previous round of the analysis.

5.2.1.1 $\tau_{\text{lep}} \tau_{\text{had}}$

In the $\tau_{\text{lep}} \tau_{\text{had}}$ sub-channel, events were recorded using single-lepton triggers (SLTs) and lepton-plus- $\tau_{\text{had-vis}}$ triggers (LTTs). SLTs set an E_T threshold between 24 GeV and 26 GeV for HLT reconstructed electrons, and a p_T range of 20 GeV to 26 GeV for HLT reconstructed muons, depending on the data-taking period. For LTTs, the criteria include an electron with $p_T > 17$ GeV or a muon with $p_T > 14$ GeV paired with a $\tau_{\text{had-vis}}$ having $p_T > 25$ GeV at the HLT.

Special conditions are in place for LTTs recording events with $\tau_{\text{had-vis}} p_T < 35$ GeV. These involve L1 trigger specifications like an extra jet having $E_T > 25$ GeV or two jets each with $E_T > 12$ GeV. Moreover, a unique filtering process ensures that if one type of electron-plus- $\tau_{\text{had-vis}}$ trigger fails to select an event, another can. Events selected due to a muon presence must also meet the $|\eta| < 2.5$ criterion.

There are set proximity requirements between offline and HLT objects: $\Delta R = 0.07$ for electrons, $\Delta R = 0.1$ for muons, and $\Delta R = 0.2$ for $\tau_{\text{had-vis}}$. Also, there are specific p_T requirements for offline objects, ensuring they are above their HLT counterparts by 1 GeV for leptons, 5 GeV for $\tau_{\text{had-vis}}$, and 80 GeV or 45 GeV for jets, contingent on their L1-trigger E_T thresholds.

To guarantee no overlap between SLT and LTT event categories, events satisfying the offline SLT lepton p_T criteria are exempted from LTT, leading to two distinct analysis categories.

The triggers employed and their offline p_T prerequisites are detailed in Table 5.4 and 5.5.

Table 5.4: SLTs used in the $\tau_{\text{lep}}\tau_{\text{had}}$ sub-channel, along with the trigger-dependent offline p_T thresholds, for each year/period.

Single Lepton Triggers (SLT)					
Period	Single Electron Triggers (SET)	e p_T [GeV]	Single Muon Triggers (SMT)	μ p_T [GeV]	Leading (Sub-leading) jet p_T [GeV]
2015	HLT_e24_lhmedium_L1EM20VH()	25	HLT_mu20_iloose_L1MU15	21	45 (20)
	HLT_e60_lhmedium		HLT_mu50		
	HLT_e120_lhloose				
2016 & 2017 & 2018	HLT_e26_lhtight_nod0_ivarloose	27	HLT_mu26_ivarmedium	27	45 (20)
	HLT_e60_lhmedium_nod0		HLT_mu50		
	HLT_e140_lhloose_nod0				

Table 5.5: LTTs used in the $\tau_{\text{lep}}\tau_{\text{had}}$ sub-channel, along with the trigger-dependent offline p_T thresholds, for each year/period. These triggers are checked when the event fails the SLTs. When an OR of multiple triggers is used in the electron channel, the 4J12 trigger is prioritized due to lower jet p_T thresholds. This means that other triggers are checked if and only if 4J12 doesn't fire. The offline selection is adjusted accordingly. For 2017 and 2018, different MTTs are used for two different regions defined by $30 \text{ GeV} < p_T^\tau \leq 40 \text{ GeV}$ and $p_T^\tau > 40 \text{ GeV}$.

Lepton Tau Triggers (LTT)				
Period	Electron Tau Triggers (ETT)	e p_T [GeV]	τ_{had} p_T [GeV]	Leading (Sub-leading) jet p_T [GeV]
15-16 A	e17_tau25	18	30	80 (20)
16 B-	e17_ivarloose_tau25	18	30	80 (20)
17	e17_ivarloose_tau25_4J12 OR e17_ivarloose_tau25	18	30	if pass 4J12: 45 (45) else: 80 (20)
18 B-	e17_ivarloose_tau25_EF_4J12 OR e17_ivarloose_tau25_EF	18	30	if pass 4J12: 45 (45) else: 80 (20)
18 K-	e17_ivarloose_tau25_EF_4J12 OR e17_ivarloose_tau25_RNN_4J12 OR e17_ivarloose_tau25_EF OR e17_ivarloose_tau25_RNN	18	30	if pass 4J12: 45 (45) else: 80 (20)
Period	Muon Tau Triggers (MTT)	μ p_T [GeV]	τ_{had} p_T [GeV]	Leading (Sub-leading) jet p_T [GeV]
15-16 A	mu14_tau25	15	30	80 (20)
16 B-	mu14_ivarloose_tau25	15	30	80 (20)
17	mu14_ivarloose_tau25_3J12	15	(30,40]	45 (45)
	mu14_ivarloose_tau35	15	40	45 (20)
18 B-	mu14_ivarloose_tau25_EF_3J12	15	(30,40]	45 (45)
	mu14_ivarloose_tau35_EF	15	40	45 (20)
18 K-	(mu14_ivarloose_tau25_EF_3J12 OR mu14_ivarloose_tau25_RNN_3J12)	15	(30,40]	45 (45)
	(mu14_ivarloose_tau35_EF OR mu14_ivarloose_tau35_RNN)	15	40	45 (20)

5.2.1.2 $\tau_{\text{had}}\tau_{\text{had}}$

In the $\tau_{\text{had}}\tau_{\text{had}}$ sub-channel, events are registered through the synergy of single- $\tau_{\text{had-vis}}$ triggers (STTs) and di- $\tau_{\text{had-vis}}$ triggers (DTTs). For the STTs, events that feature at least one $\tau_{\text{had-vis}}$ at the HLT with a p_T range from 80 GeV to 160 GeV are considered, with the specific range contingent upon the data-collection period. On the other hand, DTTs are employed to pick out events that have, at a minimum, a pair of $\tau_{\text{had-vis}}$ objects identified at the HLT. The leading $\tau_{\text{had-vis}}$ has a threshold p_T of 35 GeV whereas its sub-leading counterpart possesses a threshold of 25 GeV. Notably, the leading $\tau_{\text{had-vis}}$ is distinguished by having the highest p_T in the event, with the second-highest being the sub-leading $\tau_{\text{had-vis}}$.

Beginning from the 2016 data-taking period, supplementary conditions were incorporated at the L1 trigger stage to reduce the DTT rates. In the 2016 data-taking period, the presence of an additional jet with $E_T > 25$ GeV was required. In the subsequent periods of 2017 and 2018, a specific condition was applied based on the offline jets: if two offline jets exhibited $p_T > 45$ GeV, then a trigger necessitating two extra jets with $E_T > 12$ GeV (and $|\eta| < 2.3$) at L1 was invoked. Alternatively, a distinct trigger was activated which demanded a single jet with $E_T > 25$ GeV and a constraint for $\tau_{\text{had-vis}}$ to be mapped within $\Delta R = 2.8$ of each other.

To isolate events close to trigger efficiency plateaux, where efficiencies are accurately depicted, offline $\tau_{\text{had-vis}}$ objects are required to lie within a $\Delta R = 0.2$ radius of the respective HLT $\tau_{\text{had-vis}}$ entities. Additionally, a baseline offline p_T condition is instituted for both $\tau_{\text{had-vis}}$ and jets. For the STTs, this offline p_T restriction for the $\tau_{\text{had-vis}}$ oscillates between 100 GeV and 180 GeV. For the DTTs, the limits stand at 40 GeV for the leading and 30 GeV for the sub-leading $\tau_{\text{had-vis}}$. Further offline conditions for the DTTs specify either the presence of two supplementary jets with $p_T > 45$ GeV or one jet with $p_T > 80$ GeV, accompanied by the $\tau_{\text{had-vis}}$ objects mapped within $\Delta R = 2.5$ of one another. If events are acknowledged by both the STTs and DTTs, the offline prerequisites aligned with the STTs are enforced. Conclusively, all events that fulfill the $\tau_{\text{had}}\tau_{\text{had}}$ event criteria are aggregated for joint analysis.

Refer to Table 5.6 for an overview of the triggers employed.

Table 5.6: Triggers used for data taking in the $\tau_{\text{had}}\tau_{\text{had}}$ channel.

Period	Trigger
Single-$\tau_{\text{had-vis}}$ triggers (STT)	
15 – 16 A	HLT_tau80_medium1_tracktwo_L1TAU60
16 B – 16 D3	HLT_tau125_medium1_tracktwo
16 D4 – 17 B4	HLT_tau160_medium1_tracktwo
17 B5 – 17 end	HLT_tau160_medium1_tracktwo_L1TAU100
18 –	HLT_tau160_medium1_tracktwoEF_L1TAU100
18 K –	HLT_tau160_mediumRNN_tracktwoMVA_L1TAU100
Di-$\tau_{\text{had-vis}}$ triggers (DTT)	
15	HLT_tau35_medium1_tracktwo_tau25_medium1_tracktwo_L1TAU20IM_2TAU12IM
16 – 17 B4	HLT_tau35_medium1_tracktwo_tau25_medium1_tracktwo
17	HLT_tau35_medium1_tracktwo_tau25_medium1_tracktwo_L1TAU20IM_2TAU12IM_4J12
17 B5 – 17 end	HLT_tau35_medium1_tracktwo_tau25_medium1_tracktwo_L1DR-TAU20ITAU12I-J25
18 –	HLT_tau35_medium1_tracktwoEF_tau25_medium1_tracktwoEF_L1TAU20IM_2TAU12IM_4J12.0ETA23
18 –	HLT_tau35_medium1_tracktwoEF_tau25_medium1_tracktwoEF_L1DR-TAU20ITAU12I-J25
18 K –	HLT_tau35_mediumRNN_tracktwoMVA_tau25_mediumRNN_tracktwoMVA_L1TAU20IM_2TAU12IM_4J12.0ETA23
18 K –	HLT_tau35_mediumRNN_tracktwoMVA_tau25_mediumRNN_tracktwoMVA_L1DR-TAU20ITAU12I-J25

5.2.2 Event selection

5.2.2.1 $\tau_{\text{lep}}\tau_{\text{had}}$

For the $\tau_{\text{lep}}\tau_{\text{had}}$ categories, following the trigger-based criteria detailed in Section 5.2.1, it is necessary to have precisely one "loose" electron or "loose" muon, an oppositely charged $\tau_{\text{had-vis}}$, and two b -tagged jets. The selected electron (muon) should meet a tight (medium) identification criterion with efficiencies of roughly 80% (97%). Events are mandated to meet the condition $m_{\tau\tau}^{\text{MMC}} > 60$ GeV [175], where $m_{\tau\tau}^{\text{MMC}}$ is calculated using the four-momenta of the electron or muon, the $\tau_{\text{had-vis}}$, and the p_T^{miss} . The invariant mass of the b -tagged jet pair (m_{bb}) must be under 150 GeV. This restriction helps reduce $t\bar{t}$ background and assists in defining a $t\bar{t}$ -rich area, crucial for the estimation of $t\bar{t}$ backgrounds as explained in Section 5.3. The SLT category specifies a $\tau_{\text{had-vis}}$ with $p_T > 20$ GeV and $|\eta| < 2.3$. For the LTT category, a $\tau_{\text{had-vis}}$ is needed with $p_T > 30$ GeV, or a

greater value if mandated by the trigger, and $|\eta| < 2.3$. In both categories, the primary (secondary) b -tagged jet must exhibit $p_T > 45$ (20) GeV, taking into account any trigger-based requirements.

An overview of the event selection for the $\tau_{\text{lep}}\tau_{\text{had}}$ signal region categories is highlighted in Table 5.7.

5.2.2.2 $\tau_{\text{had}}\tau_{\text{had}}$

Beyond the trigger criteria elaborated in Section 5.2.1, supplementary selection measures are established to define the signal region in the $\tau_{\text{had}}\tau_{\text{had}}$ sub-channel. Events are expected to contain exactly two τ -leptons, each meeting the ‘loose’ identification criteria and having opposite-sign charges. The presence of at least two jets is necessary, of which exactly two should be b -tagged, with the DL1r 77% working point. Events with additional leptons, be they electrons or muons, are rejected. Also, the two b -jets should have a $p_T > 45$ GeV and $p_T > 20$ GeV. The invariant mass of the τ -lepton pair, labeled as $m_{\tau\tau}^{\text{MMC}}$, is determined using the four-momenta of the $\tau_{\text{had-vis}}$ and the $\mathbf{p}_T^{\text{miss}}$. This determination utilizes the Missing Mass Calculator (MMC) [175], working on the assumption that the $\mathbf{p}_T^{\text{miss}}$ is purely from the neutrinos in the τ -lepton decay sequence. To ward off interference from low-mass Drell-Yan scenarios, a value of $m_{\tau\tau}^{\text{MMC}}$ greater than 60 GeV is required.

A detailed breakdown of the event selection for the $\tau_{\text{had}}\tau_{\text{had}}$ signal region category is displayed in Table 5.7.

Table 5.7: Summary of the event selections, shown separately for events that are selected by different triggers. In cases where pairs of reconstructed objects of the same type are required, thresholds for the (sub-)leading p_T object are given outside (within) parentheses where different event selection thresholds are applied. When the selection depends on the year of data-taking, the possible values of the requirements are separated by commas, except for the jet selection in the LTT and DTT triggers, which use multiple selection criteria as described in Section 5.2. The trigger p_T thresholds shown are applied to the offline physics objects that are matched to the corresponding trigger objects.

$\tau_{\text{had}}\tau_{\text{had}}$ category		$\tau_{\text{lep}}\tau_{\text{had}}$ categories	
STT	DTT	SLT	LTT
e/μ selection			
No loose e/μ		Exactly one loose e/μ	
		e (μ) must be tight (medium and have $ \eta < 2.5$)	
		$p_{\text{T}}^e > 25, 27 \text{ GeV}$	$18 \text{ GeV} < p_{\text{T}}^e < \text{SLT requirement}$
		$p_{\text{T}}^\mu > 21, 27 \text{ GeV}$	$15 \text{ GeV} < p_{\text{T}}^\mu < \text{SLT requirement}$
$\tau_{\text{had-vis}}$ selection			
Two loose $\tau_{\text{had-vis}}$		One loose $\tau_{\text{had-vis}}$	
		$ \eta < 2.3$	
$p_{\text{T}} > 100, 140, 180 \text{ (25) GeV}$	$p_{\text{T}} > 40 \text{ (30) GeV}$	$p_{\text{T}} > 30 \text{ GeV}$	
Jet selection			
≥ 2 jets with $ \eta < 2.5$			
Leading jet $p_{\text{T}} > 45 \text{ GeV}$	Trigger dependent	Leading jet $p_{\text{T}} > 45 \text{ GeV}$	Trigger dependent
Event-level selection			
Trigger requirements passed			
Collision vertex reconstructed			
$m_{\tau\tau}^{\text{MMC}} > 60 \text{ GeV}$			
Opposite-sign electric charges of $e/\mu/\tau_{\text{had-vis}}$ and $\tau_{\text{had-vis}}$			
Exactly two b -tagged jets			
$m_{bb} < 150 \text{ GeV}$			

5.2.3 Event categorisation

The events in this study, after satisfying all selection criteria, are sorted into three distinct categories, as depicted in Figure 5.6. This segmentation results in three signal regions for each sub-channel ($\tau_{\text{had}}\tau_{\text{had}}$, $\tau_{\text{lep}}\tau_{\text{had}}$ SLT and $\tau_{\text{lep}}\tau_{\text{had}}$ LTT). Events within these regions are used in the fitting of the MVA discriminant distributions, further detailed in Section 5.5.

Events with at least four jets undergo classification using a ggF/VBF BDT classifier, detailed in Section 5.4.2. This classifier is designed to optimally distinguish events originating from ggF from those arising from VBF mechanisms. Events below a specific ggF/VBF BDT threshold are considered VBF-like and are allocated to the VBF-enriched signal region. Conversely, events with fewer than four jets or those passing the ggF/VBF BDT criterion are identified as ggF-like. These events are further categorized based on the invariant mass of the di-Higgs system, m_{HH} . The low-mass ggF signal is defined for values $m_{HH} < 350$ GeV, targeting BSM signals with distinct κ_λ values prevalent in this region. Events characterized by $m_{HH} > 350$ GeV are placed into the high-mass ggF region, intended for SM-like scenarios. The decision for the 350 GeV threshold was strategic, emphasizing precision constraints on κ_λ . This ensures a sizable sample in the low-mass region while maintaining the ability to identify SM-like HH signals. Furthermore, this threshold coincides with the peak destructive interference between the two ggF LO Feynman diagrams.

For each signal region, a distinct BDT classifier is applied, with training conducted using different HH signal hypotheses to effectively distinguish HH signal events from the background. The VBF region BDT training uses the standard model VBF HH signal, while the high- m_{HH} region employs the SM ggF HH signal. The low- m_{HH} region, in contrast, uses the ggF $\kappa_\lambda = 10$ HH signal, which is particularly prominent there. A thorough exploration of MVA optimization, input variable enumeration, and hyperparameter considerations can be found in Section 5.4. In-depth MVA training evaluations and fit result discussions, especially highlighted in Sections 5.6.2,

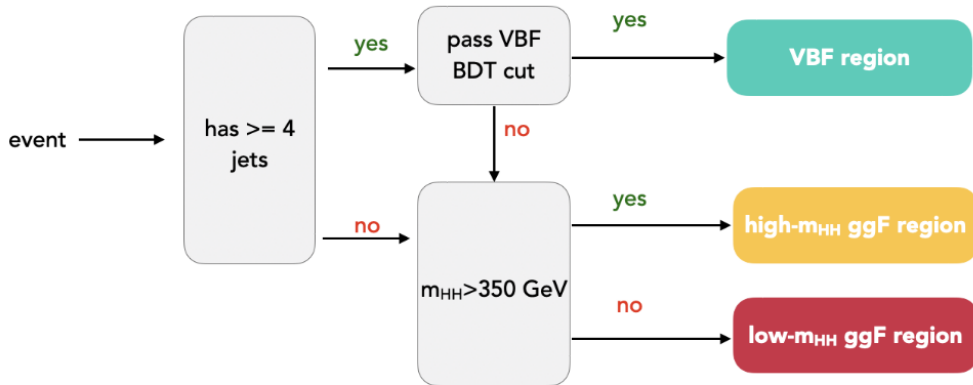


Figure 5.6: Event categorisation into low- m_{HH} ggF, high- m_{HH} ggF and VBF signal regions.

Table 5.8 presents the event yields following the application of the $bb\tau_{\text{had}}\tau_{\text{had}}$ event selection criteria.

Figure 5.7 illustrates the signal acceptance multiplied by efficiency for the ggF HH process as a function of κ_λ in $\tau_{\text{had}}\tau_{\text{had}}$, $\tau_{\text{lep}}\tau_{\text{had}}$ SLT and $\tau_{\text{lep}}\tau_{\text{had}}$ LTT channels. For the VBF HH process, the relevant plots are Figures 5.8 and 5.9, showing dependencies on κ_λ and κ_{2V} . When adjusting any of the coupling parameters, others are maintained at their Standard Model (SM) values.

For shape comparisons of the m_{HH} distribution considering different κ_λ values, Figures 5.10a and 5.10b focus on the VBF HH process within $\tau_{\text{had}}\tau_{\text{had}}$ and $\tau_{\text{lep}}\tau_{\text{had}}$ SLT ggF Signal Regions (SRs). These figures provide insight into the behavior of acceptance multiplied by efficiency for the VBF HH as influenced by κ_λ . The initial bin in Figure 5.10a aligns with the 350 GeV ggF

Table 5.8: Pre-fit event yields in the $b\bar{b}\tau_{\text{had}}\tau_{\text{had}}$ signal regions. Here, Zttjj represents the processes as $Z \rightarrow \tau\tau + jj$, whereas Zjj represents $Z \rightarrow ee/\mu\mu + jj$. Inclusive SR refers to inclusiveness in m_{HH} .

Sample	low- m_{HH} ggF SR	high- m_{HH} ggF SR	VBF SR	Inclusive SR
hhttbbVBFSM	0.008	0.047	0.113	0.168
hhttbb	0.592	4.413	0.433	5.438
Fake	301.462	629.561	387.584	1307.291
ttbarSFFF	119.939	115.711	126.495	362.145
ttbarSFFT	189.567	296.163	220.023	705.753
ttbarSFTF	356.086	609.538	477.961	1443.711
ttbar	713.678	1945.410	948.479	3607.567
stopWt	35.202	138.617	67.325	241.144
stopt	3.381	20.353	7.715	31.365
stops	0.333	0.944	0.402	1.679
Zbb	0.000	0.495	0.153	0.761
Zbc	0.000	0.035	0.002	0.039
Zbl	0.027	0.065	0.026	0.118
Zcc	0.000	0.002	0.043	0.045
Zttbb	252.897	568.479	107.346	928.722
Zttbc	21.269	50.442	11.399	83.101
Zttbl	13.941	31.072	7.948	52.961
Zttcc	19.380	40.068	10.231	69.655
Zttcl	6.100	15.585	4.583	26.249
Zttl	0.614	5.680	1.179	7.264
Wtt	14.468	31.979	11.129	56.976
W	0.804	0.000	0.600	1.914
VBFHtautau	0.163	1.115	0.395	1.673
ggFHtautau	2.344	9.605	2.198	14.148
qqZHtautau	1.570	3.694	0.299	5.563
ggZHtautau	0.543	1.610	0.352	2.505
WHtautau	0.135	0.205	0.078	0.418
qqZHbb	3.307	6.645	0.433	10.385
ggZHbb	1.119	3.018	0.407	4.543
WHbb	0.039	0.094	0.032	0.165
WW	0.102	0.385	1.473	1.960
WZ	1.934	4.371	2.663	8.968
ZZ	11.097	17.029	3.593	31.666
ttW	1.759	6.270	5.765	13.794
ttZ	5.011	18.628	8.895	32.533
ttH	5.500	18.613	10.882	34.995
bkg sum	2083.779	4591.481	387.584	9091.774
data	1997	4165	2218	8380

mass categorization. A nuanced dependency of the VBF signal m_{HH} distribution on κ_λ , especially within the ggF low and high- m_{HH} regions, reflects the dip pattern evident in Figure 5.8.

Figures 5.10c and 5.10d present the ggF/VBF BDT score distributions for the VBF HH process, including different κ_λ values across the inclusive $\tau_{\text{had}}\tau_{\text{had}}$ and $\tau_{\text{lep}}\tau_{\text{had}}$ SLT SRs. In the $\tau_{\text{had}}\tau_{\text{had}}$ ($\tau_{\text{lep}}\tau_{\text{had}}$ SLT) channel, the event categorization threshold is -0.11 (-0.13), marking events beyond this as ggF-like, the rest as VBF-like. Particularly in Figure 5.10b, the VBF SM process scores the lowest, which aligns with expectations due to the training data for the ggF/VBF BDT. The peak acceptance times efficiency for the VBF HH regarding κ_λ is at $\kappa_\lambda=1$, as shown in Figure 5.8a.

Lastly, Figure 5.11 offers shape comparisons for the m_{HH} distribution related to the ggF HH process. This is when different κ_λ values are close to the peak of interference within the $\tau_{\text{had}}\tau_{\text{had}}$ SRs.

The acceptance times efficiency of the SM ggF and VBF HH signals across all analysis categories for the $\tau_{\text{had}}\tau_{\text{had}}$, $\tau_{\text{lep}}\tau_{\text{had}}$ SLT, and $\tau_{\text{lep}}\tau_{\text{had}}$ LTT channels are presented in Table 5.9. Minor discrepancies might be observed in the VBF SM values compared to those in Figure 5.8 at $\kappa_\lambda=1$. These discrepancies arise from the fact that the polynomial fit for the VBF HH cross-section, as

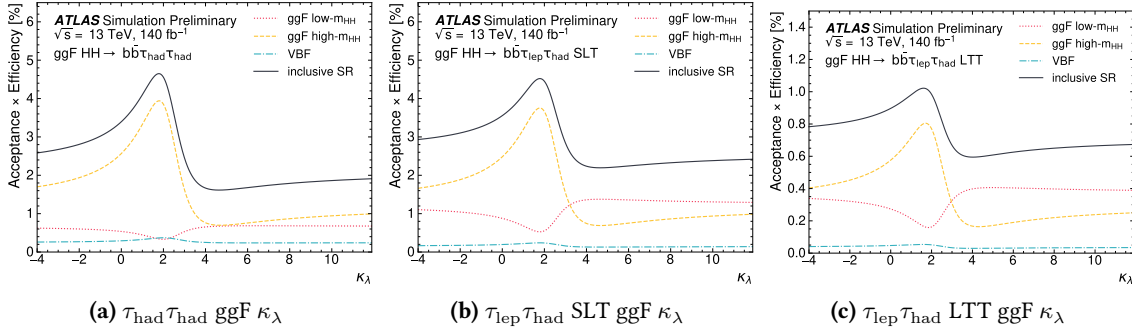


Figure 5.7: Selection efficiency for the ggF HH signal across various analysis categories. The efficiency is plotted against the coupling parameter κ_λ for the channels: $\tau_{\text{had}}\tau_{\text{had}}$ (a), $\tau_{\text{lep}}\tau_{\text{had}}$ SLT (b), and $\tau_{\text{lep}}\tau_{\text{had}}$ LTT (c).

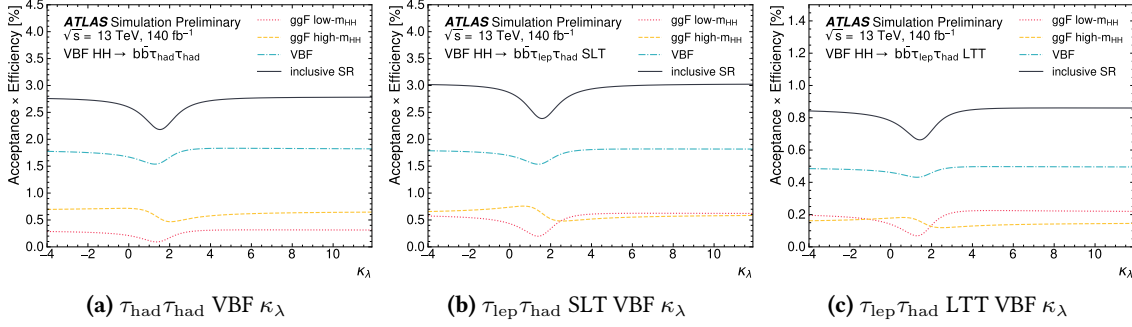


Figure 5.8: Selection efficiency for the VBF HH signal across various analysis categories. The efficiency is plotted against the coupling parameter κ_λ for the channels: $\tau_{\text{had}}\tau_{\text{had}}$ (a), $\tau_{\text{lep}}\tau_{\text{had}}$ SLT (b), and $\tau_{\text{lep}}\tau_{\text{had}}$ LTT (c).

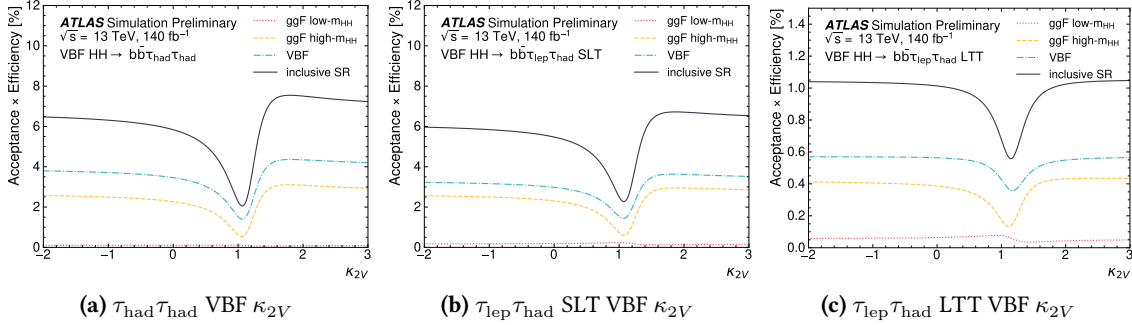


Figure 5.9: Selection efficiency for the VBF HH signal across various analysis categories. The efficiency is depicted in relation to the coupling parameter κ_{2V} for channels: $\tau_{\text{had}}\tau_{\text{had}}$ (a), $\tau_{\text{lep}}\tau_{\text{had}}$ SLT (b), and $\tau_{\text{lep}}\tau_{\text{had}}$ LTT (c).

a function of κ_λ , does not perfectly match the most accurate theoretical computation of the SM cross-section. Similarly, a mismatch is observed for κ_{2V} , leading to variations in the values at $\kappa_\lambda = 1$ between Figures 5.8 and 5.9.

Table 5.9: Acceptance times efficiency of the SM ggF and VBF HH signals in all analysis categories.

Channel	Process	low- m_{HH} ggF SR	high- m_{HH} ggF SR	VBF SR
$\tau_{\text{had}}\tau_{\text{had}}$	ggF SM	0.45%	3.33%	0.33%
$\tau_{\text{had}}\tau_{\text{had}}$	VBF SM	0.11%	0.64%	1.56%
$\tau_{\text{lep}}\tau_{\text{had}}$ SLT	ggF SM	0.68%	3.19%	0.22%
$\tau_{\text{lep}}\tau_{\text{had}}$ SLT	VBF SM	0.25%	0.74%	1.57%
$\tau_{\text{lep}}\tau_{\text{had}}$ LTT	ggF SM	0.21%	0.72%	0.05%
$\tau_{\text{lep}}\tau_{\text{had}}$ LTT	VBF SM	0.08%	0.18%	0.44%

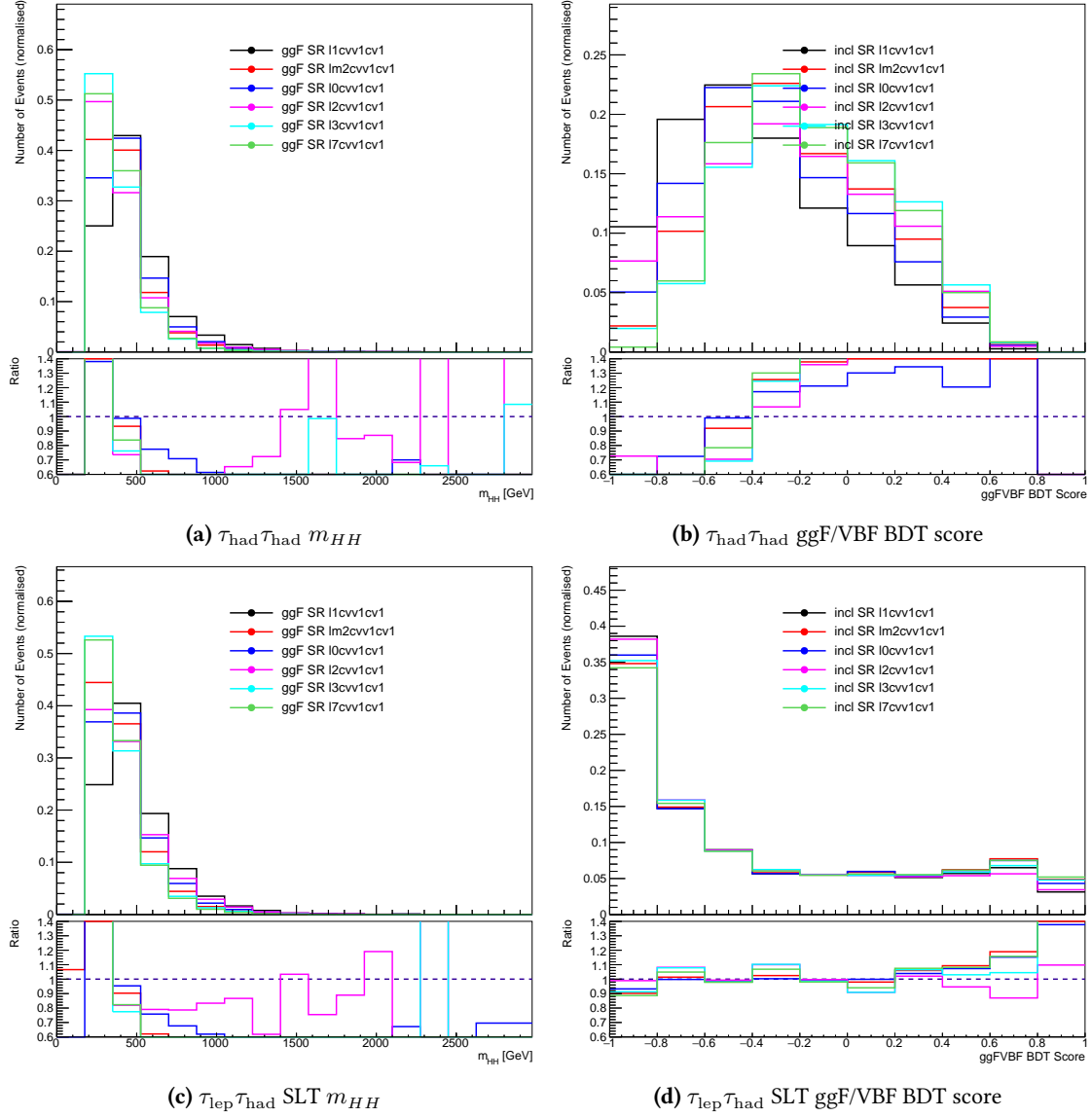


Figure 5.10: Comparisons of the m_{HH} shape for the VBF HH process across various κ_λ values in the $\tau_{\text{had}}\tau_{\text{had}}$ (a) and $\tau_{\text{lep}}\tau_{\text{had}}$ ggF SRs (c). Furthermore, the distributions of the ggF/VBF BDT scores for the VBF HH process across different κ_λ values in the inclusive SR are shown for $\tau_{\text{had}}\tau_{\text{had}}$ (b) and $\tau_{\text{lep}}\tau_{\text{had}}$ (d). The nominal values for the event categorization in ggF/VBF are set at -0.11 and -0.13 for $\tau_{\text{had}}\tau_{\text{had}}$ and $\tau_{\text{lep}}\tau_{\text{had}}$ channels, respectively.

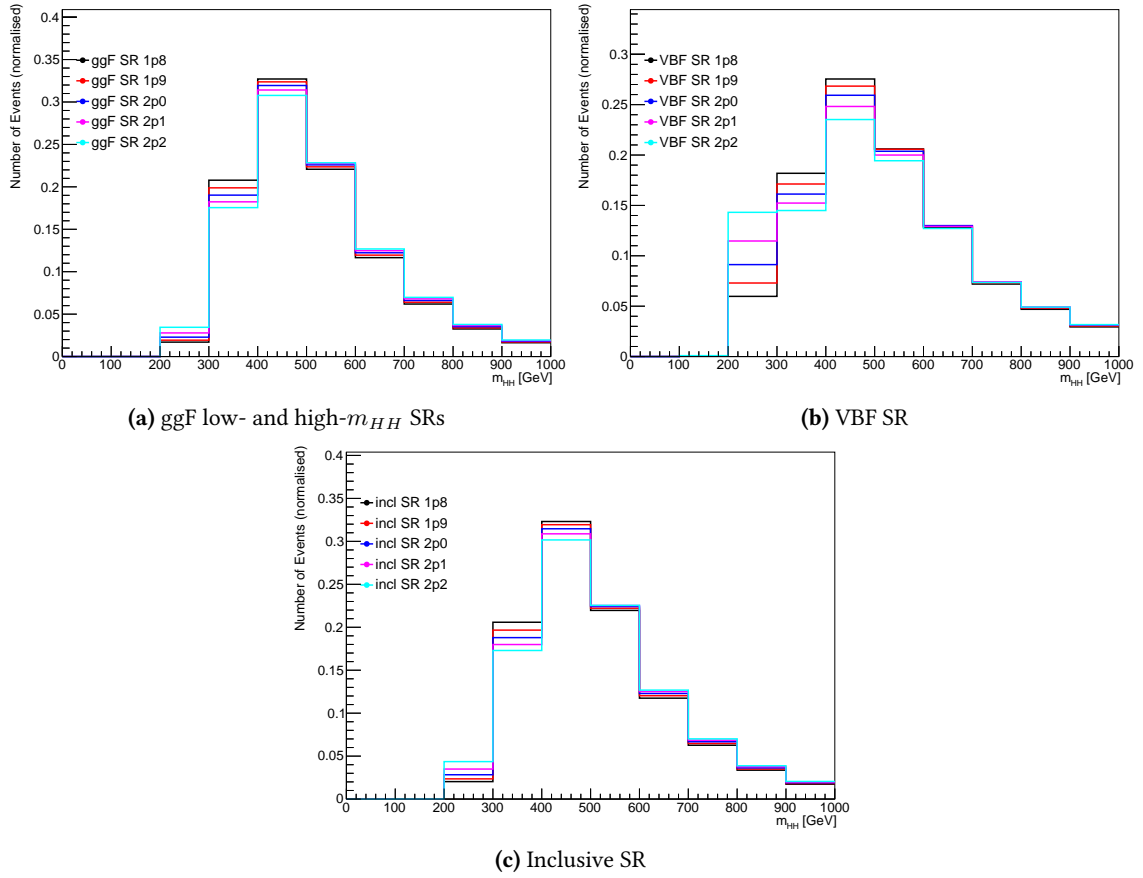


Figure 5.11: Comparisons of the m_{HH} shape for the ggF HH process at various κ_λ values near the interference maximum. This is observed in the $\tau_{\text{had}}\tau_{\text{had}}$ channel (a) for the ggF low- and high- m_{HH} SRs, (b) the VBF SR, and (c) the inclusive SR.

Table 5.10: Pre-fit event yields in the di-Higgs $bb\tau_{\text{lep}}\tau_{\text{had}}$ SLT signal region for the data, background and signal. Here, Zttjj represents the processes as $Z \rightarrow \tau\tau + jj$, whereas Zjj represents $Z \rightarrow ee/\mu\mu + jj$. Inclusive SR refers to inclusiveness in m_{HH} .

Sample	low- m_{HH} ggF SR	high- m_{HH} ggF SR	VBF SR	Inclusive SR
hhttbbVBFSM	0.0194	0.0586	0.1236	0.2016
hhttbb	0.9804	4.6055	0.3185	5.9044
Fake	20197.125	11437.782	2707.953	34342.860
ttbar	30491.313	26371.939	4640.861	61504.113
stopWt	1313.267	1595.587	152.202	3061.056
stopt	258.053	279.119	60.814	597.985
stops	24.342	13.025	0.949	38.316
Zbb	414.253	171.418	36.471	622.142
Zbc	37.173	15.508	2.710	55.375
Zbl	24.265	15.234	2.547	41.715
Zcc	38.052	16.395	4.886	57.839
Zcl	12.895	7.086	1.284	21.255
Zl	16.660	3.517	0.908	21.084
Zttbb	714.964	309.024	61.668	1085.657
Zttbc	59.477	29.221	4.653	93.352
Zttbl	40.440	20.605	3.671	64.716
Zttcc	64.894	26.215	5.296	96.393
Zttcl	21.310	12.444	2.711	36.416
Zttl	7.902	3.067	0.595	11.039
Wtt	8.024	3.688	-	11.286
W	23.979	42.749	4.437	69.420
VBFHtautau	0.392	0.788	0.240	1.420
ggFHtautau	6.371	9.652	1.108	17.132
qqZHtautau	4.242	4.024	0.235	8.501
ggZHtautau	0.888	1.828	0.173	2.889
WHtautau	0.338	0.331	0.050	0.719
qqZHbb	8.920	8.392	0.461	17.773
ggZHbb	1.781	3.807	0.456	6.043
WHbb	2.995	3.738	0.222	6.954
WW	4.126	7.060	2.529	13.635
WZ	26.248	27.643	4.578	58.469
ZZ	50.842	29.213	3.244	83.299
ttW	47.110	61.613	11.298	120.021
ttZ	47.480	53.032	11.082	111.593
ttH	41.559	44.347	8.014	93.921
bkg sum	54020.305	40636.981	7739.248	102391.922
data	53094	38203	7159	98456

Table 5.10 and 5.11 display the event yields following the application of the $bb\tau_{\text{lep}}\tau_{\text{had}}$ SLT and LTT event selections, respectively.

Table 5.11: Pre-fit event yields in the di-Higgs $bb\tau_{\text{lep}}\tau_{\text{had}}$ LTT signal region for signal, data and background. Here, Zttjj represents the processes as $Z \rightarrow \tau\tau + jj$, whereas Zjj represents $Z \rightarrow ee/\mu\mu + jj$. Inclusive SR means inclusiveness in m_{HH} .

Sample	low- m_{HH} ggF SR	high- m_{HH} ggF SR	VBF SR	Inclusive SR
hhttbbVBFsM	0.006	0.014	0.034	0.054
hhttbb	0.308	1.032	0.075	1.415
Fake	1150.569	484.121	149.085	1783.429
ttbar	2421.024	1337.964	352.585	4111.572
stopWt	79.363	78.813	8.073	166.249
stopt	7.175	16.409	2.295	25.878
stops	1.114	0.507	0.085	1.706
Zbb	22.252	7.983	2.135	32.362
Zbc	2.479	0.918	0.199	3.575
Zbl	1.719	0.565	0.146	2.355
Zcc	3.420	0.728	-	4.224
Zcl	1.031	0.463	0.003	1.526
Zl	0.208	-	7.442	7.634
Zttbb	222.673	79.963	21.384	324.020
Zttbc	18.091	8.323	1.535	27.950
Zttbl	12.038	5.324	1.381	17.894
Zttcc	18.201	7.542	2.428	28.171
Zttcl	5.579	3.107	0.636	9.280
Zttl	4.215	0.983	-	4.851
Wtt	0.643	2.062	-	2.394
W	0.672	-	-	0.861
VBFHtautau	0.093	0.195	0.059	0.347
ggFHtautau	1.826	2.207	0.327	4.360
qqZHtautau	1.074	1.017	0.068	2.159
ggZHtautau	0.273	0.418	0.046	0.738
WHtautau	0.076	0.075	0.016	0.166
qqZHbb	2.340	1.384	0.100	3.824
ggZHbb	0.500	0.720	0.084	1.305
WHbb	0.087	0.063	0.015	0.166
WW	-	0.247	-	0.247
WZ	1.842	0.964	0.548	3.302
ZZ	10.742	5.171	0.607	16.504
ttW	4.012	3.149	0.828	7.986
ttZ	5.746	3.980	1.029	10.755
ttH	6.135	3.642	0.769	10.546
bkg sum	4007.633	2059.249	554.076	6619.166
data	3908	1840	453	6201

5.2.4 $Z + HF$ control region

The Z boson production with heavy flavour (b, c) jets cross-section is known to be not well predicted by the SHERPA MC. Consequently, these processes are calibrated to data within a specific control region. Given that jet production remains unaffected by the decay mode of the Z boson, decays into $Z \rightarrow \mu^+\mu^-/e^+e^-$ combined with heavy flavour jets are chosen. This ensures a high-quality sample that does not overlap with signal region selections, enabling its inclusion in the final fit for determining the $Z + HF$ normalization using data.

The phase space of the $Z + HF$ control region exhibits a significant difference when compared to those of the signal region. In the signal regions, there is a preference for τ -leptons possessing higher p_T , and additionally, a leading b -jet p_T is imposed with a threshold of 45 GeV. Consequently, the signal regions manifest a generally steeper $V p_T$ spectrum compared to the $Z + HF$ control regions.

To minimize the dependency on the uncertainties associated with phase-space extrapolation between the SR and CR, modifications were made to the CR requirements to more closely align with

the SR requirements. Events within the defined control region are selected based on the following criteria:

- Events selected with $b\bar{b}\ell\ell$ trigger selection using single-lepton and di-lepton triggers;
- Exactly two muons or two electrons with opposite-sign charges;
- Exactly two b -tagged jets (using DL1r tagger and 77% working point);
- $75 \text{ GeV} < m_{\ell\ell} < 110 \text{ GeV}$ (select Z mass peak);
- $m_{bb} < 40 \text{ GeV}$ or $m_{bb} > 210 \text{ GeV}$ (to veto Higgs mass peak and to ensure orthogonality to $b\bar{b}\ell\ell$ signal region);
- leading b -jet $p_T > 45 \text{ GeV}$;
- lepton $p_T > 40 \text{ GeV}$.

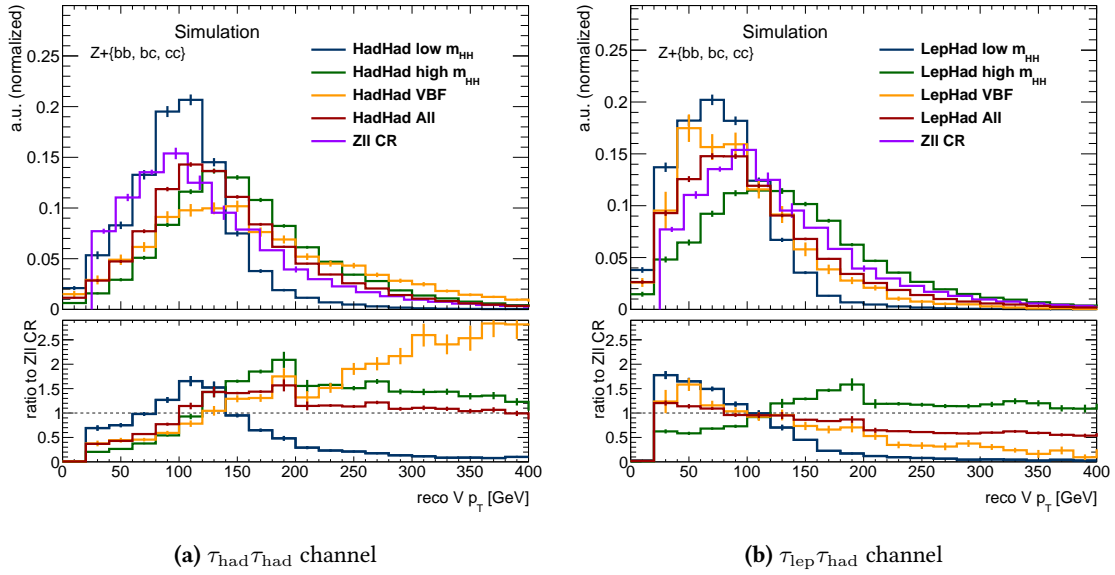


Figure 5.12: Comparison of $V p_T$ shapes between the various SRs and the Z CR for both $\tau_{\text{had}}\tau_{\text{had}}$ (a) and $\tau_{\text{lep}}\tau_{\text{had}}$ (b) channels.

The normalisation factor for $Z + HF$ of 1.20 ± 0.05 is obtained from the fit to the $Z + HF$ control region.,

The pre-fit normalisation factors μ_{Z+HF} for the $Z + HF$ ($Z + (bb, bc, cc)$) components in the $Z + HF$ control region are derived as depicted in Equation (5.2.2). These factors are determined through the subsequent ratio.

$$\mu_{Z+HF} = \frac{(\text{data} - (\text{sum of backgrounds}) + (Z(ee, \mu\mu) + HF) + (Z(\tau\tau) + HF))}{(Z(ee, \mu\mu) + HF) + (Z(\tau\tau) + HF)}. \quad (5.2.1)$$

Table 5.12 presents the event yields with the normalisation factor extracted according Equation (5.2.1), and explicitly demonstrated in Equation (5.2.2).

$$\mu_{Z+HF} = \frac{(21458 - 18596.707 + 10837.434 + 1.309)}{(10837.434 + 1.309)} \approx 1.26 \quad (5.2.2)$$

A dedicated shape uncertainty is introduced to address the $V p_T$ mismodelling, visible in figures such as Figure 5.13d. This uncertainty is determined by the complete difference between the data and the standard MC prediction across bins of the reconstructed $V p_T$. This process is illustrated in Figure 5.14.

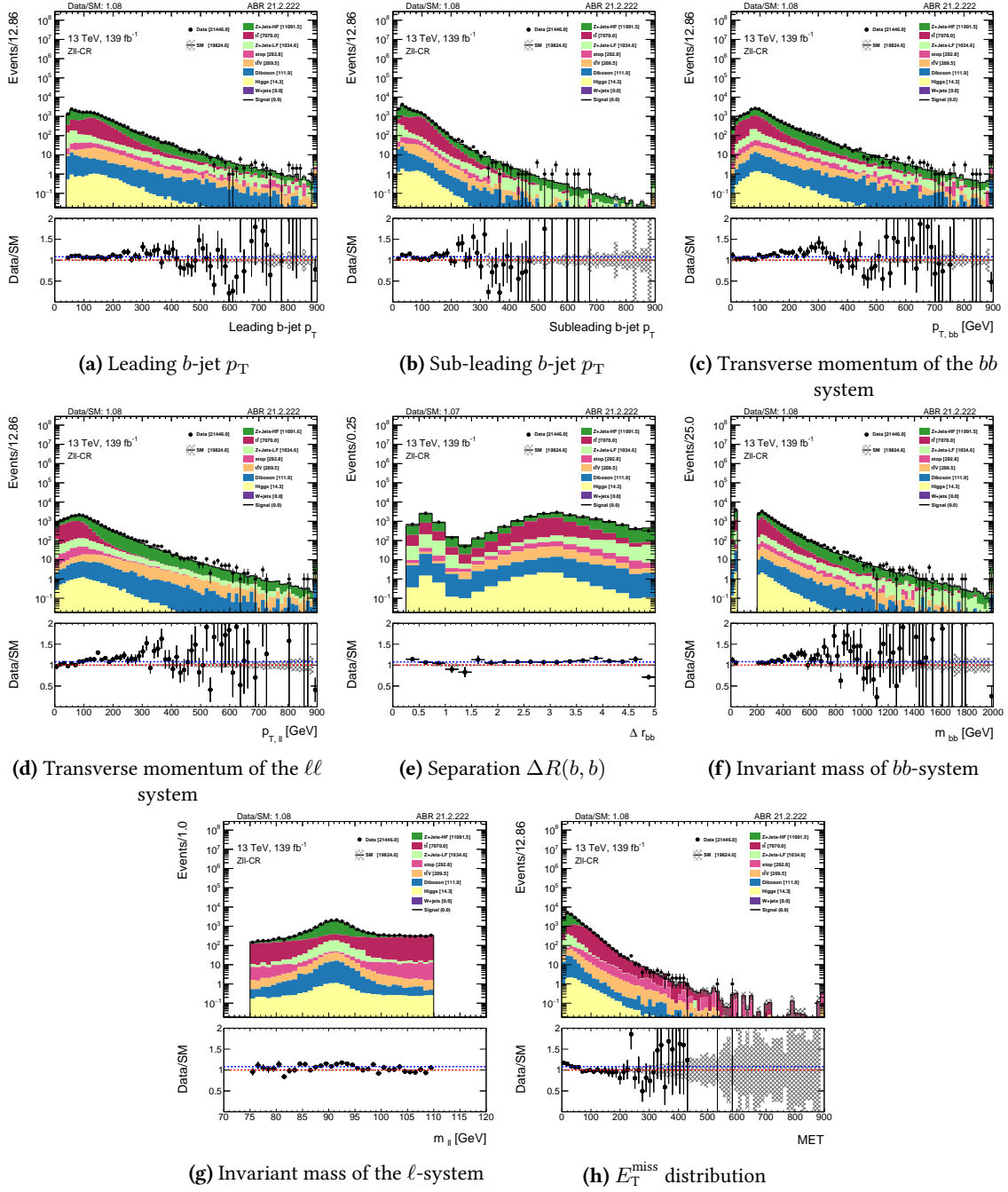
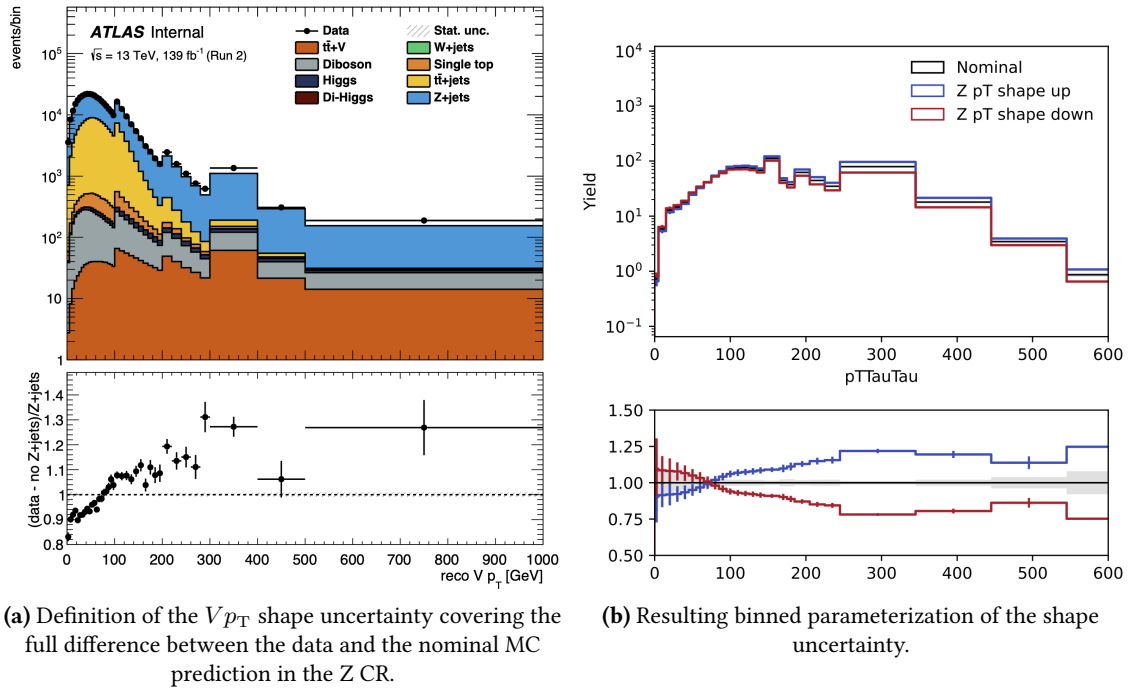


Figure 5.13: $Z + HF$ CR Data/MC comparison. Each subfigure shows different variable.

This variable aligns closely with the reconstructed V p_T , which is precisely measured in the CR.

Table 5.12: Pre-fit event yields obtained from the $Z + HF$ control region. Only contributions > 0.1 are shown.

data	21458	
ttH	8.2053	± 0.0905
ggZHbb	1.8215	± 0.0270
qqZHbb	3.9163	± 0.0491
ttV	207.8556	± 1.2159
Ztbb	1.0585	± 0.2369
W	1.0484	± 0.5271
ZZ	55.3968	± 1.5553
WZ	49.2535	± 1.4850
other Diboson	21.3449	± 0.6644
Zl	158.3162	± 26.4240
Zbc	694.2620	± 8.2900
Zbl	522.1541	± 8.3366
Zcc	646.5807	± 10.8511
Zbb	8556.9188	± 28.9223
Zcl	259.2019	± 7.8166
ttbar	7129.0727	± 16.8742
stopWt	278.9754	± 6.0295
stopt	0.7225	± 0.1843
Total Bkgd	18596.7070	± 0.2511
Data/MC	1.1539	

**Figure 5.14:** Investigations on the Vp_T shape uncertainty in the Z CR.

5.3 Background modelling

The methods for background estimation echo those employed in the previous round of analysis for both channels, as detailed in [4]. The simulation event samples model all background processes, with the exception of those involving fake- τ_{had} . These particular processes are modeled using data-driven techniques.

For the $\tau_{\text{lep}}\tau_{\text{had}}$ channel, the backgrounds from fake- τ_{had} arising from $t\bar{t}$ and multi-jet processes are deduced using an inclusive fake-factor method. This is delineated further in Section B.1.1. Meanwhile, in the $\tau_{\text{had}}\tau_{\text{had}}$ channel, the multi-jet background is determined using a data-driven fake-factor method (see Section B.1.2). The $t\bar{t}$ background with fake- τ_{had} uses a different method: a scale-factor approach. Here, scale factors extracted from data are applied to amend the MC prediction, with details in Section B.1.3.

Due to complexities in the $\tau_{\text{had}}\tau_{\text{had}}$ channel, individual estimation techniques are essential for multi-jet and $t\bar{t}$ processes. Complications arise from the presence of HLT τ_{had} identification and the requirement for at least one loose τ_{had} in the derivation skim. Despite higher uncertainties compared to a joint approach, this does not impact the analysis outcome due to the statistical constraints of Run 2. Furthermore, given the limited contribution of the fake- τ_{had} background in sensitive analysis bins, this technique is seen as more cautious.

Regarding the $t\bar{t}$ with true- τ_{had} and $Z+HF$ templates, while they are sourced from MC predictions, their normalizations are data-derived. This is covered in Section 5.5. Events where electrons or muons are mistaken for τ_{had} objects are a minor background concern, primarily originating from the $t\bar{t}$ production. These are predicted via simulation, and are bundled with the $t\bar{t}$ events that contain true- τ_{had} objects.

5.4 Multi-Variables Analysis

In this section, I will present my work on the Boosted Decision Tree (BDT) Optimization for the $HH \rightarrow b\bar{b}\tau^+\tau^-$ analysis.

The Boosted Decision Tree (BDT) is a machine learning algorithm that has been widely used in high energy physics since its introduction in 2005 [176]. As a supervised learning algorithm, BDT combines the strengths of decision trees with the boosting technique, enhancing the performance and accuracy of the model.

In this study, The TMVA package [177] is used for the BDT training and optimization. A Machine Learning Tool Kit wrapped around TMVA is made by the analysis group and is used to perform the BDT training and optimization.

There are two types of classification BDTs used in this analysis, one is used to sort events into ggF or VBF enriched regions, and the second type server to separate signal events from background events in each of the ggF and VBF enriched region.

A ggF vs. VBF BDT is trained to define the specific ggF and VBF signal region and separate the ggF and VBF events. Two different ggF BDTs are trained to separate the ggF events vs. all backgrounds in the ggF signal region but in the low- m_{HH} and high- m_{HH} regions separately. A VBF BDT is trained to separate the VBF events vs. all backgrounds in the VBF signal region.

Considering the fact that there are three channels in this analysis, $\tau_{\text{had}}\tau_{\text{had}}$, $\tau_{\text{lep}}\tau_{\text{had}}$ SLT, and $\tau_{\text{lep}}\tau_{\text{had}}$ LTT, and four different BDTs in each channel (ggF vs. VBF, ggF low- m_{HH} , ggF high- m_{HH} , and VBF), and we are using 3-fold cross validation, there are 36 BDTs in total.

To maximize the sensitivity of the analysis, the events are categorized into different signal regions

(SR).

First, events which failed the VBF jets candidate selection are categorized into the ggF-enriched signal region. The events which have two more jets on top of the two b-jets from the Higgs decay ($H \rightarrow b\bar{b}$) are called event which has VBF-jet candidates. Then the events are classified into different categories based on the BDT output of the ggF vs. VBF BDT, if the BDT output is smaller than certain BDT score, working point (WP), the event is categorized as VBF-enriched SR, otherwise it is again categorized as ggF-enriched SR.

Within the ggF-enriched SR, the events are further categorized into low- m_{HH} and high- m_{HH} regions depending on if $m_{HH} > 350\text{GeV}$, or not.

This section will focus on the $\tau_{\text{lep}}\tau_{\text{had}}$ SLT channel and give the results of all channels in the end.

5.4.1 Optimisation Strategy

In this study, a consistent optimization strategy is applied to all the Boosted Decision Trees (BDTs), which is carried out in two distinct steps. The first step is the optimization of the BDT input variables, which is accomplished by sequentially incorporating each variable into the optimization process. The second step involves the optimization of the BDT hyperparameters, achieved through the application of the grid search method.

5.4.1.1 Input Variables Optimisation

To initialize the input variables for the optimisation, a set of variables (baseline input variables) is selected based on physics motivation and the expected discrimination power. This set comprises m_{HH} , m_{bb} , $m_{\tau\tau}^{\text{MMC}}$, $\Delta R(b, b)$ and $\Delta R(\tau, \text{lep})$ ($\Delta R(\tau, \tau)$ for $\tau_{\text{had}}\tau_{\text{had}}$ channel), which is used mostly in the $\tau_{\text{lep}}\tau_{\text{had}}$ channel. A complementary set of variables is chosen based on their separation power, which is defined as the difference between the signal and background distributions.

The input variables optimisation is performed by sequentially incorporating each variable into the optimisation process. The optimisation process start with the baseline input variables, and then add one variable at a time from the complementary list to the input variables list.

At epoch 0, the baseline input variables are used to train the BDT, and binned significance was calculated to evaluate the performance of the BDT. At epoch 1, on top of the baseline input variables, one variable from the complementary list is added to the input variables list, and the BDT is re-trained with the new input variables list. Let's suppose there are N variables in the complementary list, N BDT training are performed at epoch 1, each with one variable from the complementary list added to the baseline input variables list. The binned significance is calculated for each BDT, and the variable that gives the highest binned significance is selected to go to the next epoch. At epoch 2, on top of the baseline input variables and the variable selected at epoch 1, N-1 BDT training are performed at epoch 2, each with one variable from the complementary list added to the baseline input variables list and the variable selected at epoch 1. And the variable that gives the highest binned significance is selected to go to the next epoch. The process is repeated until all the variables in the complementary list are added to the input variables list. We choose the epoch that gives the highest binned significance as the final input variables list.

The optimisation process is illustrated in Figure 5.15.

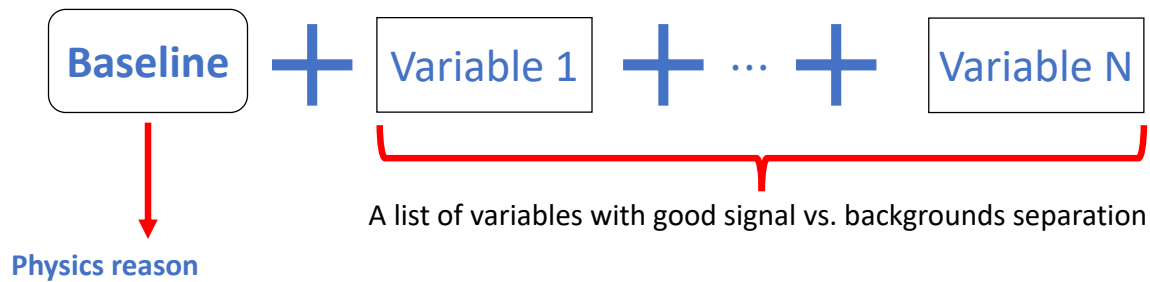


Figure 5.15: Input variables optimisation strategy.

5.4.1.2 Hyperparameters Optimisation

Using the optimised input variables list, the hyperparameters optimisation is performed by applying the grid search method using regression. Any number of hyperparameters can be optimised in this way, and the optimisation is performed by scanning the hyperparameters space and evaluating the performance of the BDT with each set of hyperparameters. But in this study, only the number of trees and the maximum depth of the trees are optimised. The rest of the hyperparameters are set to the default values. We in the past tried to change the other hyperparameters, but the performance of the BDT did not change significantly.

The hyperparameters optimisation is performed by scanning the number of trees from 100 to 1000, and the maximum depth of the trees from 2 to 10, with a step size of 1, to restrict these two hyperparameters to a reasonable range. The hyperparameters combination that gives the highest binned significance is selected as the final hyperparameters.

The hyperparameters optimisation is illustrated in Figure 5.16. The hyperparameters are set into fixed value when training. The fixed values are shown in table 5.13

Table 5.13: Training hyperparameters that are fixed during training.

Hyperparameter	value
MinNodeSize	1%
BoostType	Grad
Shrinkage	0.2
IgnoreNegWeightsInTraining	True

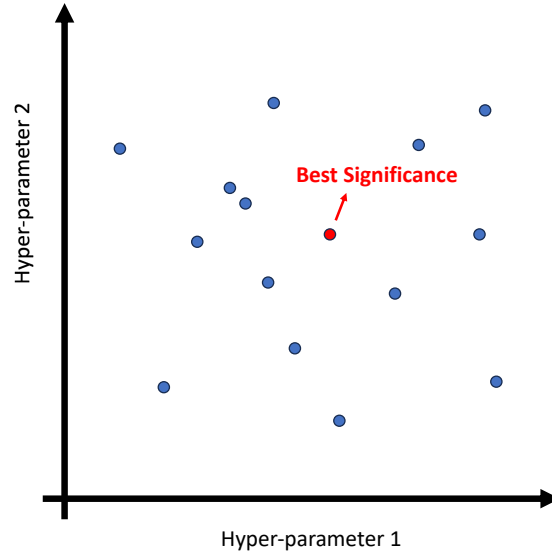


Figure 5.16: Hyperparameters optimisation strategy.

5.4.2 ggF/VBF BDT

The aim of the classification ggF vs. VBF BDT is to improve the κ_{2V} constraint by creating a dedicated category for VBF events. Since the κ_{2V} vertex is only present in the VBF events, while the κ_λ is present in both ggF and VBF events as explained in Section 1.3, a specific VBF-enriched region will improve the κ_{2V} sensitivity significantly

It is trained to separate the ggF and VBF events to further define the ggF and VBF signal region on top of the 4-jets requirement.

The optimisation procedure follows the principle described in subsection 5.4.1

5.4.2.1 Selection of input variables

This BDT is trained with 7 variables including event shape variables such as Fox-Wolfram moments [178], effective mass, and centrality. Furthermore, it also includes VBF-specific variables. Unlike the other BDTs in this study, the ggF/VBF BDT at $\tau_{\text{lep}}\tau_{\text{had}}$ SLT input variable optimisation starts with two input variables, m_{jj}^{VBF} and $\Delta\eta_{jj}^{\text{VBF}}$, as baseline, then end-up with 7 input variables.

The training is performed on the 4-jets region, since events which failed the 4-jets requirement are classified into the ggF-enriched region, thus irrelevant to the functionality of the ggF/VBF BDT.

A 3-fold training is performed for the ggF/VBF BDT. We have conducted a study on the improvement each variable provides, as depicted in Figure 5.17, where the baseline represents m_{jj}^{VBF} and $\Delta\eta_{jj}^{\text{VBF}}$. The primary improvements come from $\text{cent}(\tau\tau jj)$, $\Delta R_{jj}^{\text{VBF}}$, VBF $\eta_0 \times \eta_1$, $\text{mEff}(\tau\tau jj)$, $\text{fwm0}(\tau\tau jj)$. Table 5.14 provides a detailed description of these variables. Figure 5.18 illustrates the separation between ggF and VBF HH events for the input variables used in the ggF/VBF training in the $\tau_{\text{lep}}\tau_{\text{had}}$ SLT channel. Furthermore, the pre-fit distributions for the input MVA variables that are used in the $\tau_{\text{lep}}\tau_{\text{had}}$ SLT ggF/VBF BDT are shown in Figure 5.19, after the ggF/VBF categorisation.

The complementary list for the input variable optimisation is chosen to have a good separation

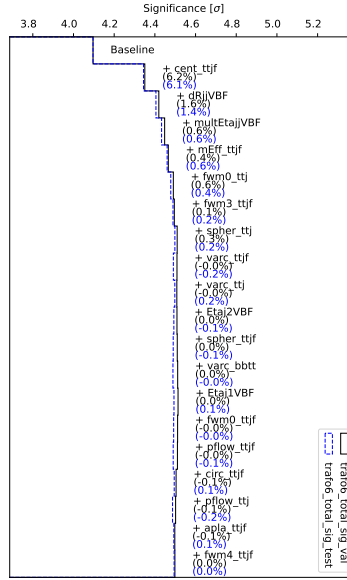


Figure 5.17: Level of improvement of the trafo6 [179] binned significance obtained by adding one variable after another, where m_{jj}^{VBF} and $\Delta\eta_{jj}^{\text{VBF}}$ are considered as baseline.

Table 5.14: Input variables used for the ggF-VBF BDT training in the $\tau_{\text{lep}}\tau_{\text{had}}$ SLT channel.

Variable	Description
m_{jj}^{VBF}	Invariant mass of the VBF jet system
$\Delta\eta_{jj}^{\text{VBF}}$	The $\Delta\eta$ between the two VBF jets
$\text{cent}(\tau\tau jjf)$	Centrality, taking into account the τ -lepton pair and central and forward jets
$\Delta R_{jj}^{\text{VBF}}$	The ΔR of the VBF jet system
$\text{VBF } \eta_0 \times \eta_1$	Product of the pseudorapidities of the leading and sub-leading VBF jets
$\text{mEff}(\tau\tau jjf)$	Effective mass, taking into account the τ -lepton pair and central and forward jets
$\text{fwm0}(\tau\tau jj)$	⁰ order Fox-Wolfram moment, taking into account the τ -lepton pair and central jets

between ggF and VBF SM events, as shown in Figure 5.18.

The BDT is trained with SM ggF and SM VBF samples as signal and background respectively. This BDT has also a good discrimination power between ggF and VBF even if the parameters (κ_λ and κ_{2V}) are not at their SM values, as can be seen in Figure 5.18.

The data/MC comparison plots are shown in Figure 5.19.

The following figures show a representative set of the pre-fit MVA input variable distributions in each of the $\tau_{\text{lep}}\tau_{\text{had}}$ SLT signal regions. In all the plots, the background is adjusted using scale factors obtained from a full fit to data. Figure 5.20 shows how key variables are modelled in the three signal regions, whereas Figure 5.21 shows new variables introduced for the signal-background BDT in each region. Finally, Figure 5.22 displays the BDT used to categorize ggF and VBF signal regions and in this case, only events with at least four jets are considered.

5.4.2.2 Optimization of hyperparameters

A 2-D scan was performed by using the various range of maximum depth of the decision tree (MaxDepth) and the number of trees (NTrees) in order to find the optimal combination of hyperparameters. NTrees and MaxDepth were allowed to vary from 100 to 1000 and from 2 to 10,

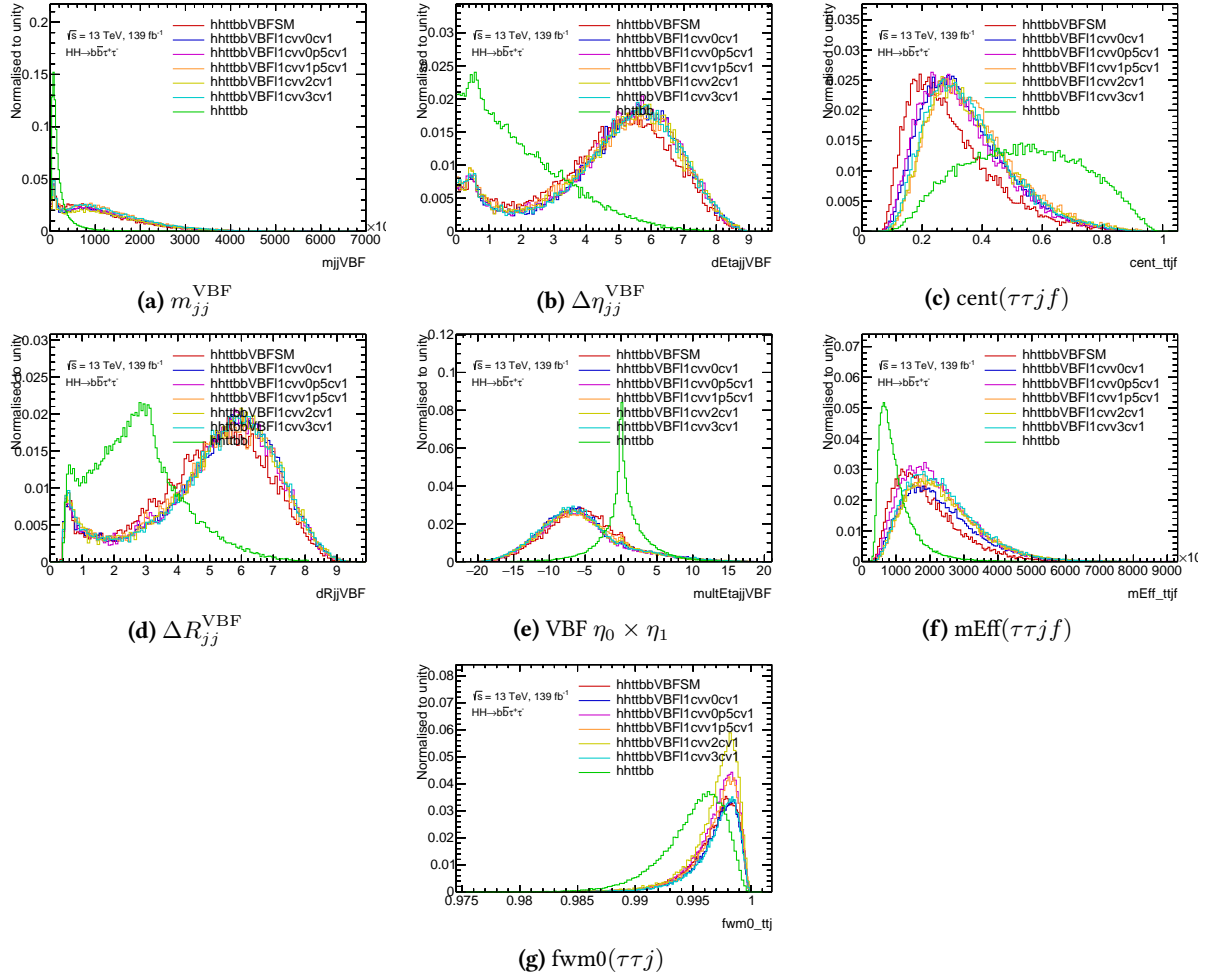


Figure 5.18: Distributions of ggF/VBF BDT input variables in the $\tau_{lep}\tau_{had}$ SLT channel showing the separation between the ggF HH events (in green) and the SM VBF HH events (in red). BSM VBF HH processes are also included in these plots although they are not used in the training.

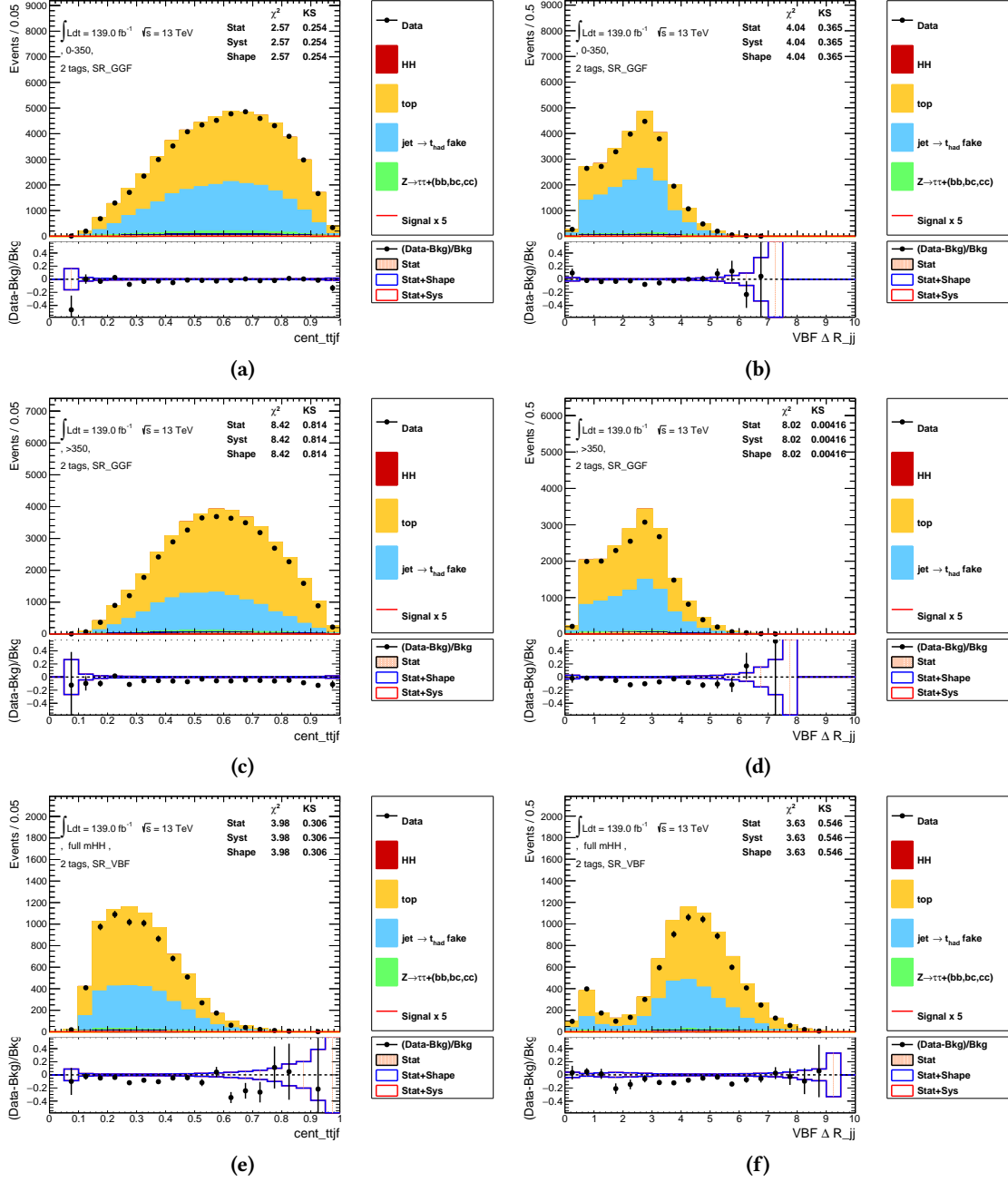


Figure 5.19: Pre-fit distributions input MVA variables in the $\tau_{lep}\tau_{had}$ SLT channel for the ggF/VBF BDT in the low- m_{HH} ggF SR (a)-(b), high- m_{HH} ggF SR (c)-(d), and VBF SR (e)-(f) regions.

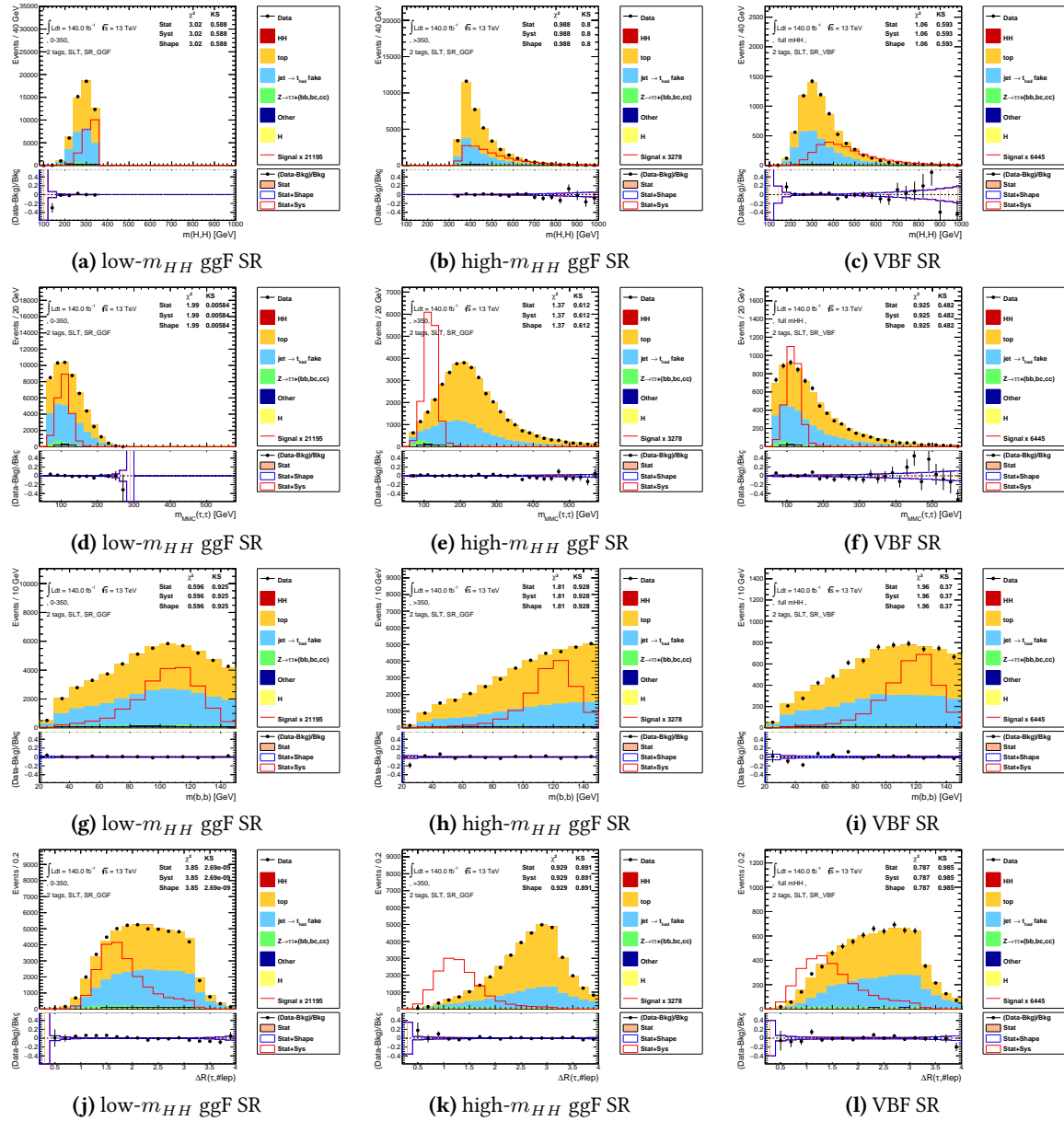


Figure 5.20: Representative set of pre-fit MVA input variable distributions in the $\tau_{lep}\tau_{had}$ SLT SRs.

respectively, as shown in Figure 5.23. The binned significance was employed to evaluate the BDT model's performance in the training region. The optimal combination was found to be: NTrees = 126 and MaxDepth = 4. Further details can be found in Table 5.15.

Table 5.15: Training hyperparameters chosen for the ggF/VBF BDT in the $\tau_{lep}\tau_{had}$ SLT channel.

Hyperparameter	value
NTrees	126
MaxDepth	4
MinNodeSize	1%
BoostType	Grad
Shrinkage	0.2
IgnoreNegWeightsInTraining	True

The BDT response in training, validation, and test samples and the final BDT response obtained is

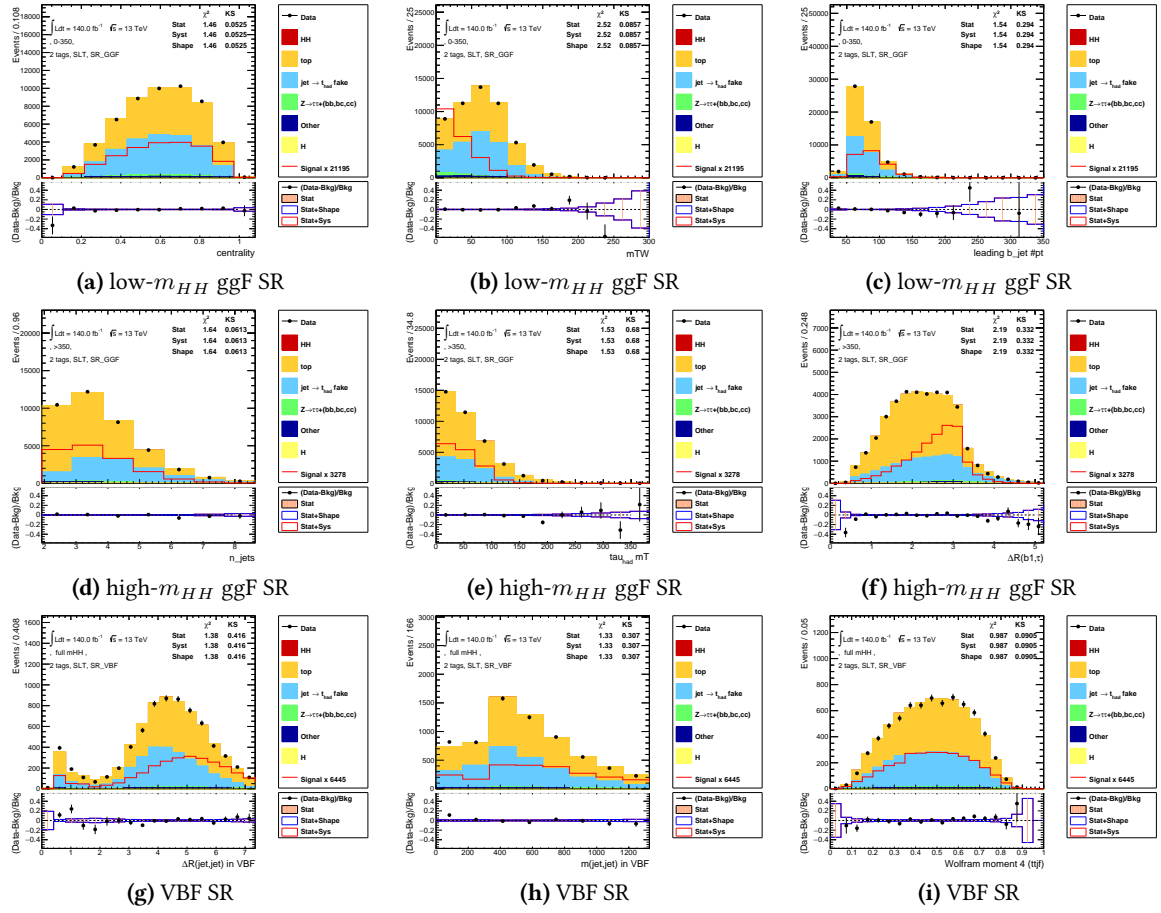


Figure 5.21: Representative set of pre-fit MVA input variable distributions in the $\tau_{lep}\tau_{had}$ SLT SRs.

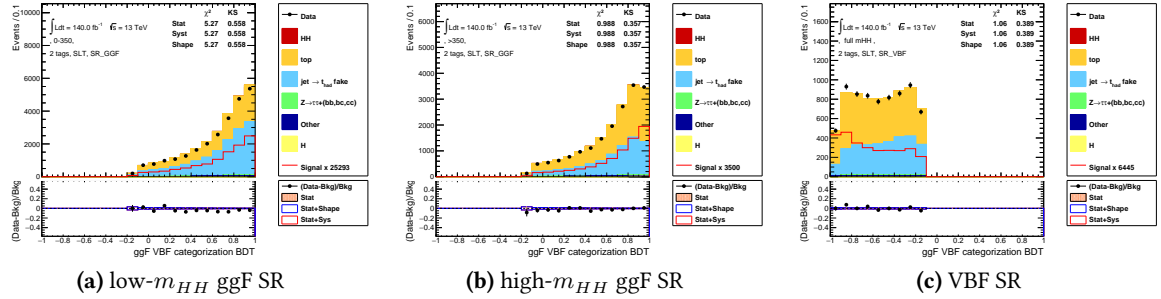


Figure 5.22: Categorisation BDT variable distributions in the $\tau_{lep}\tau_{had}$ SLT SRs.

illustrated in Figure 5.24.

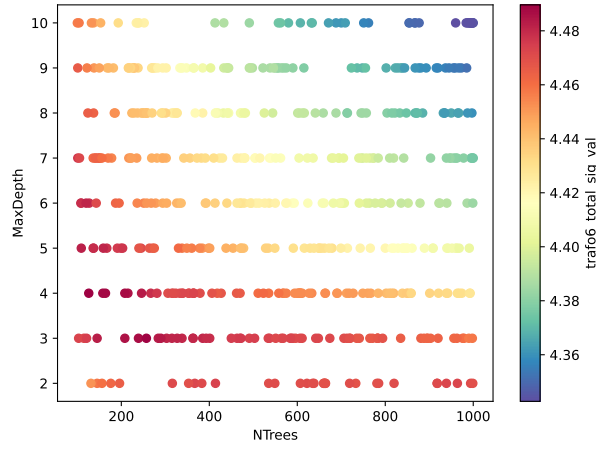
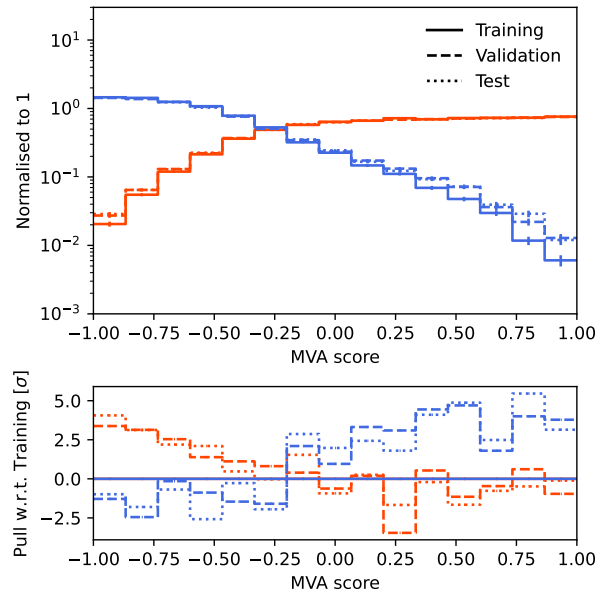
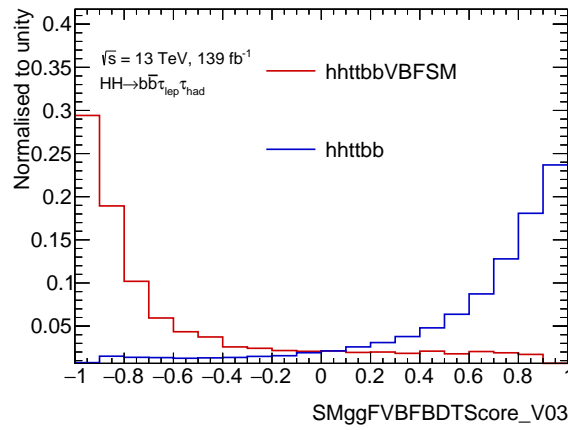


Figure 5.23: Hyperparameters optimisation for the ggF/VBF BDT in the $\tau_{lep}\tau_{had}$ SLT channel. The optimal point is found at $texttt{NTrees} = 126$ and $MaxDepth = 4$.



(a) ggF/VBF BDT score in training, validation and test samples in the $\tau_{lep}\tau_{had}$ SLT channel



(b) ggF/VBF BDT score outputs in the $\tau_{lep}\tau_{had}$ SLT channel.

Figure 5.24: ggF/VBF BDT scores for training, validation and test samples and output scores in the $\tau_{lep}\tau_{had}$ SLT channel

5.4.2.3 Selection of working point

In order to properly define the ggF and VBF enriched regions, it is necessary to define a working point that is dependent on the BDT score, i.e. a requirement on the BDT score. This working point is a threshold that is used to determine whether an event is classified as ggF- or VBF-like based on its BDT score. By setting an appropriate threshold, we can ensure that events are properly assigned to their respective regions, and thus improve the accuracy of our analysis. This threshold must be determined, taking into account the trade-off between the efficiency and purity of the selected events.

The working point is chosen to maximize the VBF efficiency times purity as a starting point, where this choice was found to improve the κ_{2V} constraint while at the same time not degrading the κ_λ constraint and the μ_{HH} limit.

Only the study on $\tau_{\text{lep}}\tau_{\text{had}}$ SLT is shown here, the other channels are done in the same manner. Figure 5.25 shows the final result of the ggF/VBF working point scan, and the $\tau_{\text{lep}}\tau_{\text{had}}$ SLT channel is using -0.13 as the default working point for event categorisation.

The scanning process is executed across the ggF/VBF BDT score (WP) within a range from -0.99 to 0.99 , with a step of 0.01 . For each point within this range, several parameters are calculated: the 95% confidence level (CL) intervals for κ_λ and κ_{2V} , as well as the limits for μ_{HH} , μ_{ggF} , and μ_{VBF} .

The performance of the WP selection is subsequently evaluated by examining the allowed ranges of κ_λ and κ_{2V} , as well as the limits on μ_{HH} , μ_{VBF} , and μ_{ggF} .

The smallest differences between the upper and lower limits of κ_λ , μ_{HH} , and μ_{ggF} are observed at WP values of -0.99 or -0.98 . These values correspond to the scenario in which the VBF category is almost absent.

Conversely, the smallest differences between the upper and lower limits of κ_{2V} and μ_{VBF} are located at WP = -0.09 and 0.48 respectively. However, these points lie within a plateau region where the value variations in response to changes in WP are not significant.

But removing the VBF category is not a viable option, as it would result in a significant loss of sensitivity for the κ_{2V} and μ_{VBF} . The WP = -0.13 is chosen as the default working point for event categorisation in the $\tau_{\text{lep}}\tau_{\text{had}}$ SLT channel as it is the point where the VBF efficiency times purity is maximised from TMVA output.

WP	μ_{HH}	μ_{ggF}	μ_{VBF}	κ_λ	κ_{2V}
Default (-0.13)	5.13	5.19	118.51	$[-4.22, 11.32]$	$[-0.63, 2.81]$
-0.99 (best κ_λ)	4.96	5.04	328.83	$[-4.04, 11.08]$	$[-0.79, 2.93]$
0.09 (best κ_{2V})	5.17	5.23	117.40	$[-4.25, 11.37]$	$[-0.60, 2.79]$
0.48 (best μ_{VBF})	5.33	5.40	114.07	$[-4.35, 11.50]$	$[-0.74, 2.92]$

Table 5.16: κ_{2V} , κ_λ as well as the limits on μ_{HH} , μ_{VBF} and μ_{ggF} values for various parameters across different WP points. The fit is performed on the validation dataset to avoid biasing the results.

To further validate if training the SR BDTs on specific ggF/VBF categories improves the sensitivity of the analysis, or change the tendency of the WP scan. WP = -0.13 , -0.8 and 0.7 are chosen as the representative points to confirm this.

SR BDTs trained on inclusive dataset has better performance. Therefore, the WP = -0.13 is chosen as the default working point for event categorisation in the $\tau_{\text{lep}}\tau_{\text{had}}$ SLT channel. And the SR BDTs are trained on the inclusive dataset.

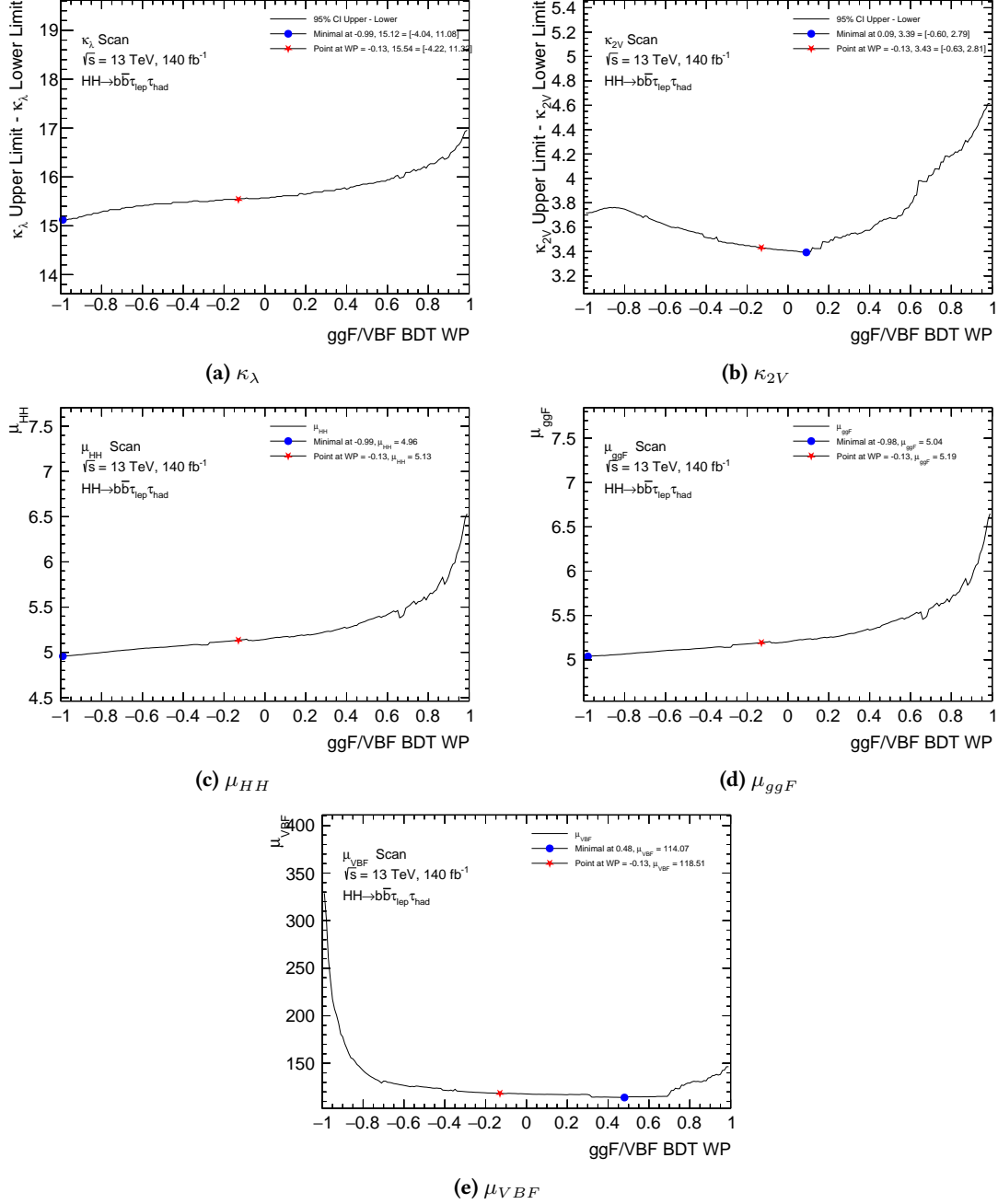


Figure 5.25: Constraints on κ_{2V} , κ_λ as well as the limits on μ_{HH} , μ_{VBF} and μ_{ggF} as a function of the ggF-VBF separation BDT working point. The same signal vs. sum of backgrounds BDT has been used to evaluate the performance for each of the scan points.

WP	μ_{HH}	μ_{ggF}	μ_{VBF}	κ_λ	κ_{2V}
−0.13 inclusive	5.13	5.19	118.51	[−4.22, 11.32]	[−0.63, 2.81]
−0.13 region	5.24	5.30	118.59	[−4.25, 11.34]	[−0.63, 2.82]
−0.8 inclusive	5.00	5.06	142.41	[−4.11, 11.17]	[−0.79, 2.96]
−0.8 region	4.96	5.02	142.36	[−4.10, 11.17]	[−0.79, 2.97]
0.7 inclusive	5.51	5.58	117.77	[−4.46, 11.64]	[−0.92, 3.10]
0.7 region	5.55	5.63	117.80	[−4.47, 11.64]	[−0.92, 3.10]

Table 5.17: κ_{2V} , κ_λ as well as the limits on μ_{HH} , μ_{VBF} and μ_{ggF} values for various parameters across different WP points. The fit is performed on the validation dataset to avoid biasing the results. Inclusive: SR BDT trained on events without ggF/VBF categorisation. Region: SR BDT trained on events with ggF/VBF categorisation.

5.4.3 Signal Region BDT

All $\tau_{had}\tau_{had}$, $\tau_{lep}\tau_{had}$ SLT and $\tau_{lep}\tau_{had}$ LTT channels follow a harmonized approach. Two separate sets of BDTs are trained, one for each m_{HH} ggF region, where the low- m_{HH} region BDT is trained on the ggF $\kappa_\lambda = 10$ signal events, while the ggF SM signal sample is used in the high- m_{HH} region. Alternative training strategies such as an inclusive BDT have been tried as well, but the BDT with m_{HH} categorization overall performed better. While the VBF BDT classifier was trained specifically to distinguish VBF HH events from the combined background events in the VBF region.

The hyperparameters and input variables for each SR BDTs were chosen separately and will be shown below. The obtained BDT scores are then fitted using the profile likelihood fit to obtain the final results, which are discussed in Section 5.6.

5.4.3.1 Optimization of hyperparameters

The hyperparameter optimization closely follows Section 5.4.1.2. A 2-D scan was performed by using the various range of maximum depth of the decision tree (MaxDepth) and the number of trees (NTrees) in order to find the optimal combination of hyperparameters. NTrees and MaxDepth were allowed to vary from 100 to 1000 and from 2 to 10 respectively. Figure 5.26 shows the dependence of this performance measure on NTrees and MaxDepth for the three sets of BDTs. The hyperparameters maximizing the validation significance were selected. They are listed on Table 5.18.

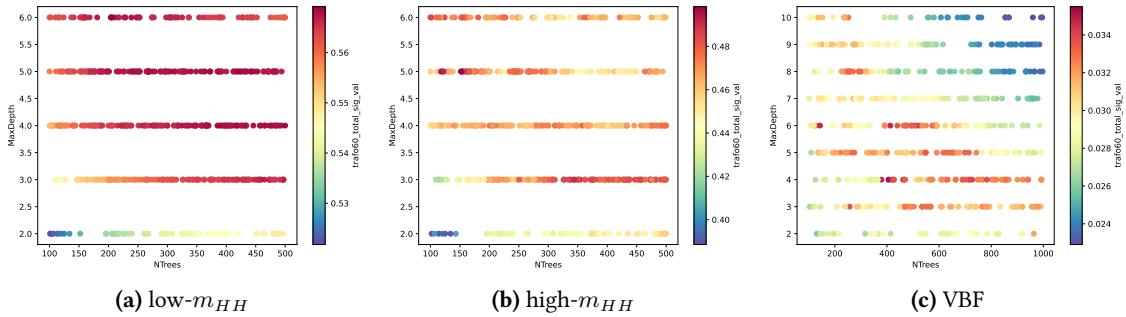


Figure 5.26: BDT hyperparameter optimisation in the $\tau_{lep}\tau_{had}$ SLT channel. Dependence of the validation significance on the number of trees (NTrees) and the maximum allowed depth of each tree (MaxDepth).

Table 5.18: Training hyperparameters chosen for the BDTs used in the three $\tau_{\text{lep}}\tau_{\text{had}}$ analysis categories.

Hyperparameter	low- m_{HH} ggF SR	high- m_{HH} ggF SR	VBF SR
NTrees	421	152	406
MaxDepth	5	5	4
MinNodeSize	1%	1%	1%
BoostType	Grad	Grad	Grad
Shrinkage	0.2	0.2	0.2
IgnoreNegWeightsInTraining	True	True	True

5.4.3.2 Input variable selection

The selection of input variables uses the strategy outlined in Section 5.4.1.1. Figures 5.27 and 5.28 show the validation significance computed for a binning requiring at least 1 expected background events per bin. The final selections of input variables for the three sets of BDTs are summarized in Tables 5.19–5.21.

Figure 5.31 shows a representative set of the pre-fit MVA input variable distributions in each of the $\tau_{\text{lep}}\tau_{\text{had}}$ signal regions.

Table 5.19: Input variables used for the low- m_{HH} ggF BDT training in the $\tau_{\text{lep}}\tau_{\text{had}}$ SLT channel.

Variable	Description
Input Variables for Low-m_{HH} ggF BDT Training	
m_{HH}	Invariant mass of the HH system, reconstructed from the τ -lepton pair and b -tagged jet pair
m_{bb}	Invariant mass of the b -tagged jet pair system
$m_{\tau\tau}^{\text{MMC}}$	Invariant mass of the τ -lepton pair system, calculated using the MMC
$\Delta R(b, b)$	The ΔR between the two b -tagged jets
$\Delta R(\tau\text{lep})$	The ΔR between the two τ -lepton pair system
m_{T}^W	The transverse mass of the reconstructed W boson
$\cos(b\bar{b})^{\text{helicity}}$	The angle of two b -jets with respect to the Higgs rest frame
$p_{\text{T}}(\tau)$	Transverse momentum of the τ s
$\Delta\phi(\tau\tau, E_{\text{T}}^{\text{miss}})$	The $\Delta\phi$ between the τ -lepton pair system and missing transverse energy
$E_{\text{T}}^{\text{miss}}$	The missing transverse momentum of the event
n_jets	Number of jets in the event
$p_{\text{T}}(b_0)$	Transverse momentum of the leading b -tagged jet
T_1	Topness, as defined in Ref. [180] assuming $\sigma_t = 5 \text{ GeV}$ and $\sigma_W = 5 \text{ GeV}$.
$p_{\text{T}}(HH)$	Transverse momentum of the HH system
$\Delta R(b_1, \tau_1)$	The ΔR between the sub-leading b -tagged jet and lepton
$\Delta R(b_1, \tau_0)$	The ΔR between the sub-leading b -tagged jet and τ
$\Delta R(b_0, \tau_0)$	The ΔR between the leading b -tagged jet and τ
$p_{\text{T}}(\text{lep})$	Transverse momentum of the leptons

5.4.3.3 BDT score distributions in different folds

Figure 5.29 shows the BDT score distributions for the fully optimized sets of BDT discriminants in the three SRs, separately for the training, validation, and testing folds. The binning is constructed with the trafo60 algorithm explained in Section 5.5.3, requiring at least 1.0 expected background events in each bin and a MC statistical uncertainty on the background estimate of at most 20%. In each case, the signal sample used during training is used in the binning definition.

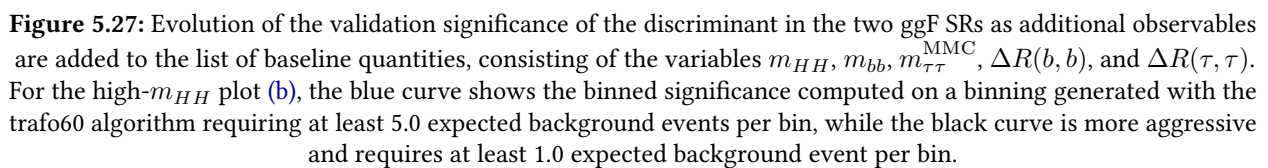
Table 5.20: Input variables used for the high- m_{HH} ggF BDT training in the $\tau_{\text{lep}}\tau_{\text{had}}$ SLT channel.

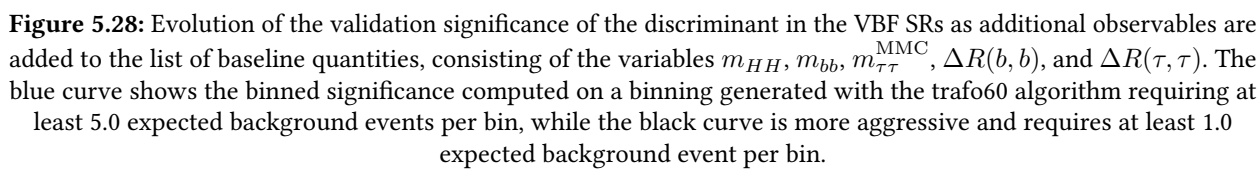
Variable	Description
Input Variables for high-m_{HH} ggF BDT Training	
m_{HH}	Invariant mass of the HH system, reconstructed from the τ -lepton pair and b -tagged jet pair
m_{bb}	Invariant mass of the b -tagged jet pair system
$m_{\tau\tau}^{\text{MMC}}$	Invariant mass of the τ -lepton pair system, calculated using the MMC
$\Delta R(b, b)$	The ΔR between the two b -tagged jets
$\Delta R(\tau\text{lep})$	The ΔR between the two τ -lepton pair system
m_T^W	The transverse mass of the reconstructed W boson
$\cos(b\bar{b})^{\text{helicity}}$	The angle of two b -jets with respect to the Higgs rest frame
H_T	Total hadronic transverse energy in the event, perpendicular to the beamline
$\text{quant}b_0$	b -tagging quantile of leading b -tagged jet
T_1	Topness, as defined in Ref. [180]
$\text{quant}b_1$	b -tagging quantile of sub-leading b -tagged jet
$p_T(\tau)$	Transverse momentum of the τ s
$\Delta R(b_1, \tau_0)$	The ΔR between the sub-leading b -tagged jet and τ
$\Delta\phi(\tau\tau, E_T^{\text{miss}})$	The $\Delta\phi$ between the τ -lepton pair system and missing transverse energy
$p_T(\text{lep})$	Transverse momentum of the leptons
$m_T(\tau)$	Transverse mass of the τ s
$p_T(b_1)$	Transverse momentum of the sub-leading b -tagged jet

Table 5.21: Input variables used for the VBF BDT training in the $\tau_{\text{lep}}\tau_{\text{had}}$ SLT channel.

Variable	Description
Input Variables for high-m_{HH} ggF BDT Training	
m_{HH}	Invariant mass of the HH system, reconstructed from the τ -lepton pair and b -tagged jet pair
m_{bb}	Invariant mass of the b -tagged jet pair system
$m_{\tau\tau}^{\text{MMC}}$	Invariant mass of the τ -lepton pair system, calculated using the MMC
$\Delta R(b, b)$	The ΔR between the two b -tagged jets
$\Delta R(\tau\text{lep})$	The ΔR between the two τ -lepton pair system
m_{jj}^{VBF}	Invariant mass of the VBF jet system
$\text{fwm0}(\tau\tau jj)$	0 order Fox-Wolfram moment, taking into account the τ -lepton pair and central and forward jets
H_T	Total hadronic transverse energy in the event, perpendicular to the beamline
$\Delta R_{jj}^{\text{VBF}}$	The ΔR of the VBF jet system
$\text{mEff}(\tau\tau jj)$	Effective mass, taking into account the τ -lepton pair and central and forward jets
$\text{fwm4}(\tau\tau jj)$	4 order Fox-Wolfram moment, taking into account the τ -lepton pair and central and forward jets
$\text{fwm2}(\tau\tau jj)$	2 order Fox-Wolfram moment, taking into account the τ -lepton pair and central and forward jets
$\Delta\eta^{HH}$	The $\Delta\eta$ between the two Higgs bosons
$\Delta\eta_{jj}^{\text{VBF}}$	The $\Delta\eta$ between the two VBF jets
$\text{pflow}(\tau\tau jj)$	Planar flow, taking into account the τ -lepton pair and central and forward jets

Figure 5.30 shows the data/MC comparison for the pre-fit BDT score distributions in the $\tau_{\text{lep}}\tau_{\text{had}}$ SRs, which are blinded in the most sensitive bins when training BDTs, as described in Section 5.5.4. The choice of binning is discussed in Section 5.5.3.





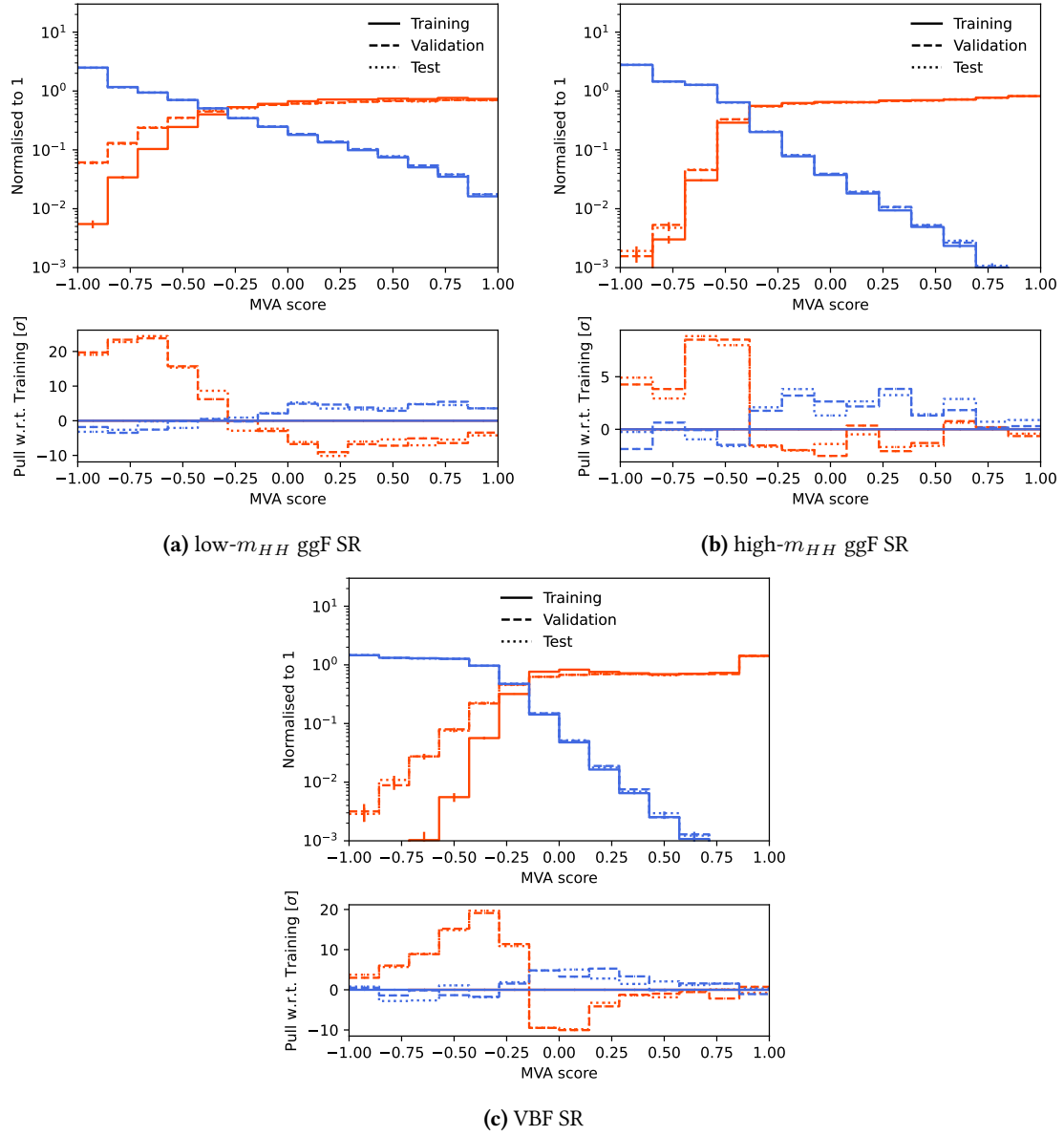


Figure 5.29: Binned distributions of the trained BDT discriminants in each $\tau_{lep}\tau_{had}$ signal region, shown for the signal used during training (red) and the sum of all SM backgrounds (blue). The distributions are shown separately for the training, validation, and test data sets.

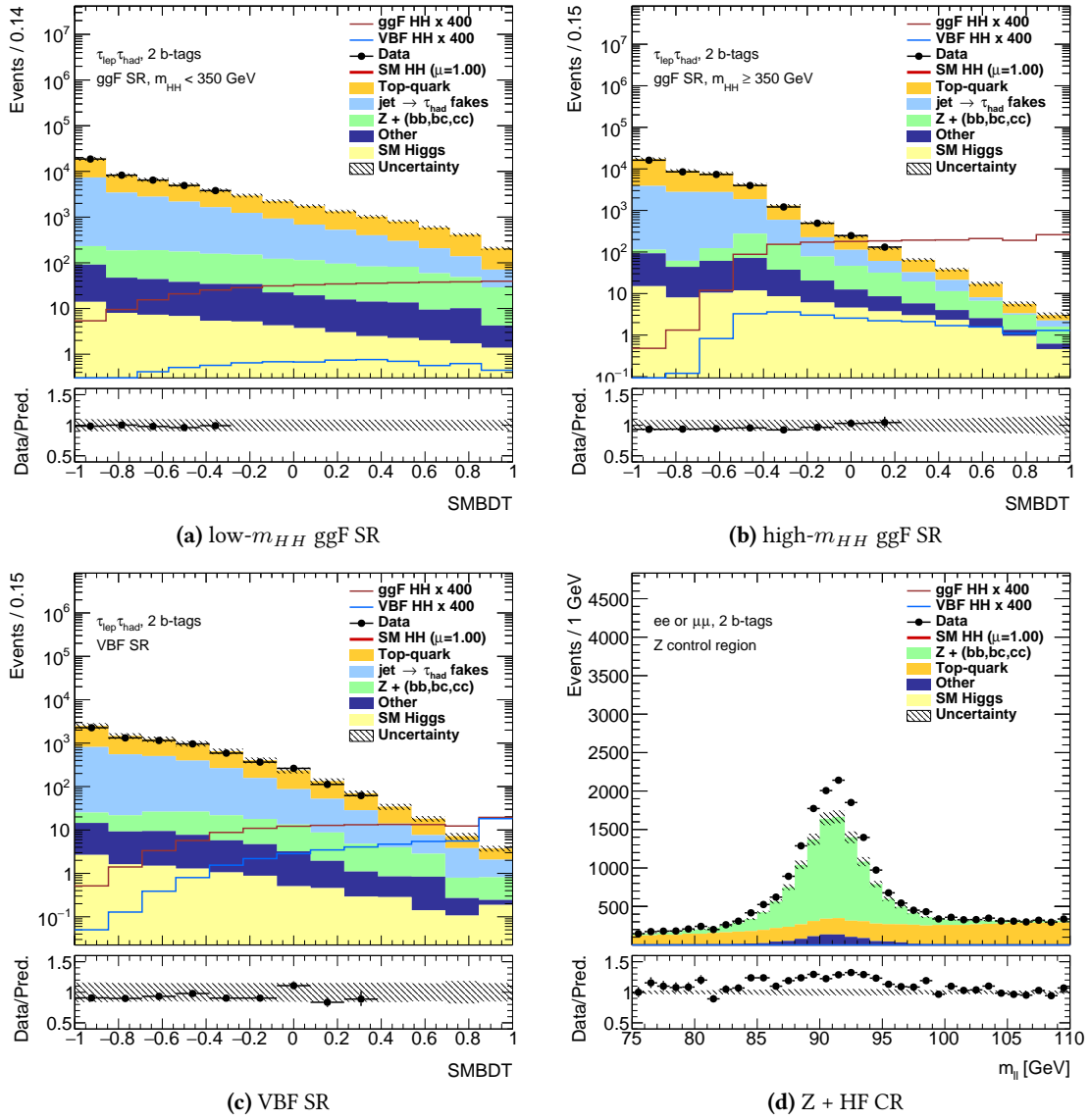


Figure 5.30: Pre-fit BDT score distributions in the $\tau_{lep}\tau_{had}$ SLT regions ((a)-(c)) and pre-fit m_{ll} distribution in the $Z + HF$ control region ((d)).

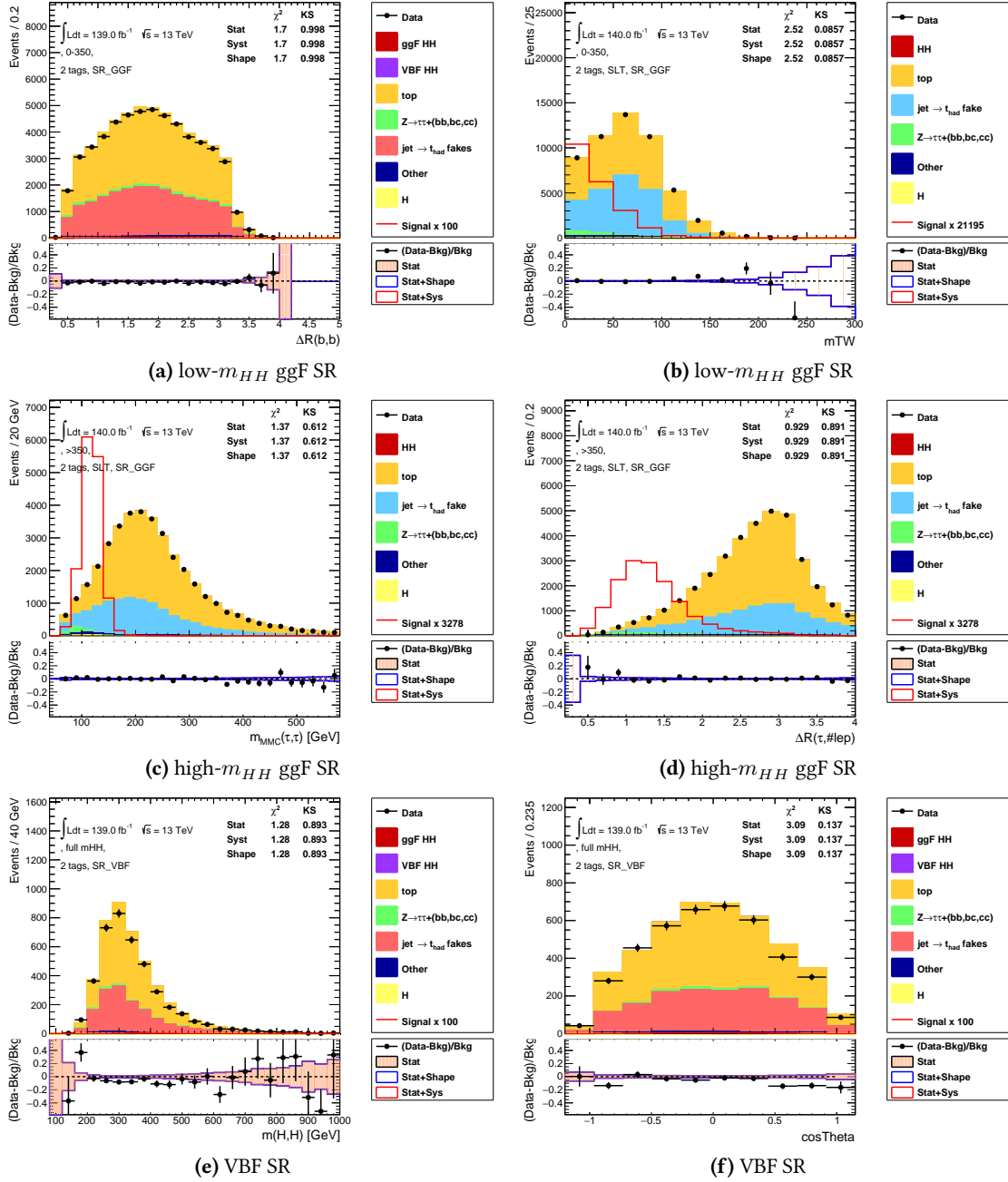


Figure 5.31: Pre-fit distributions of the input variables used in the $\tau_{\text{lep}}\tau_{\text{had}}$ SLT channel for the low- m_{HH} ggF SR ((a)-(b)), high- m_{HH} ggF SR ((c)-(d)), and VBF SR ((e)-(f)) regions.

5.5 Statistical interpretation

The results from the $HH \rightarrow b\bar{b}\tau^+\tau^-$ analysis are derived by performing a simultaneous binned maximum-likelihood fit on the MVA output distributions across both $\tau_{\text{had}}\tau_{\text{had}}$ and $\tau_{\text{lep}}\tau_{\text{had}}$ event categories, as detailed in Sections 5.2.3 and 5.4. Additionally, a fit is applied to the m_{ll} distribution within the $Z + HF$ CR.

5.5.1 Statistical model

Given the analysis, the likelihood function is expressed as:

$$\mathcal{L}(\boldsymbol{\mu}, \boldsymbol{\theta}; \text{data}) = \prod_{c=1}^{N_{\text{cats}}} \mathcal{L}_c(\boldsymbol{\mu}, \boldsymbol{\theta}; \text{data}) \prod_{k \in \text{constraint NPs}} f_k(\theta_k) \quad (5.5.1)$$

In the above equation, $\boldsymbol{\mu}$ and $\boldsymbol{\theta}$ represent the vectors for the parameters of interest (POIs) and the nuisance parameters (NPs), respectively. N_{cats} denotes the total number of analysis categories, and \mathcal{L}_c symbolizes the likelihood function associated with category c . There are certain types of NPs that are influenced by the external constraints represented by f_k .

The POIs are the parameters we aim to measure. Examples include the signal strength, represented as μ , and coupling parameters such as κ_λ and κ_{2V} . Within the fit model, there are nuisance parameters (NPs). Some of these NPs are derived solely from the data, and they are termed as "unconstrained". Conversely, there are parameters that rely on auxiliary measurements in addition to the data. These are classified as "constrained" and serve to quantify the influence of systematic uncertainties in the measurement. An in-depth discussion on the NPs involved in the $HH \rightarrow b\bar{b}\tau^+\tau^-$ analysis fit is available in Section 5.5.2.

For every category, the likelihood adopts in bins. It takes the form of a product of Poisson distributions, where each corresponds to an analysis bin:

$$\mathcal{L}_c(\boldsymbol{\mu}, \boldsymbol{\theta}; \text{data}) = \prod_{i=1}^{n_{\text{bins}}} P(\sum_s N_{H_s}^{c,i}(\boldsymbol{\mu}) + \sum_b N_{B_b}^{c,i}, n_i) \quad (5.5.2)$$

Here, n_i designates the observed number of data events per bin. Meanwhile, the expression $\sum_s N_{H_s}^{c,i}(\boldsymbol{\mu}) + \sum_b N_{B_b}^{c,i}$ indicates the sum of signal and background yields.

The measurement of the POIs employs a statistical test based on the profile likelihood ratio:

$$\Lambda(\mu) = \frac{L(\mu, \hat{\hat{\boldsymbol{\theta}}}(\mu))}{L(\hat{\mu}, \hat{\boldsymbol{\theta}})} \quad (5.5.3)$$

In the numerator of the ratio, the NPs assume their profiled values, $\hat{\hat{\boldsymbol{\theta}}}$, which bring the likelihood function to its conditional maximization for given POIs, μ . For the denominator, both the POIs and NPs align with their optimal values, $\hat{\mu}$ and $\hat{\boldsymbol{\theta}}$, ensuring the unconditional maximization of the likelihood. In the asymptotic regime, in which the likelihood is approximately Gaussian, the value of $-2 \ln \Lambda(\mu)$ follows a χ^2 distribution with a number of degrees of freedom (d.o.f) equal to the dimensionality of the vector μ .

In the absence of signal, upper limits on the HH signal strength, μ_{HH} , i.e. on the di-Higgs production rate, get established at the 95% CL. This is achieved following the CL_s prescription and using the asymptotic formulation. The considered test statistic, \tilde{q}_μ , is defined as:

$$\tilde{q}_\mu = \begin{cases} -2 \ln \frac{\mathcal{L}(\mu, \hat{\boldsymbol{\theta}}(\mu))}{\mathcal{L}(0, \hat{\boldsymbol{\theta}}(0))} & \hat{\mu} < 0, \\ -2 \ln \frac{\mathcal{L}(\mu, \hat{\boldsymbol{\theta}}(\mu))}{\mathcal{L}(\hat{\mu}, \hat{\boldsymbol{\theta}})} & 0 \leq \hat{\mu} \leq \mu, \\ 0 & \hat{\mu} > \mu. \end{cases} \quad (5.5.4)$$

5.5.2 Fit setup

The profile likelihood fit, executed in a binned manner, is concurrently applied to the MVA scores across all analysis regions. This is coupled with the m_{ll} distribution within the $Z + HF$ CR. A summary of these processes can be found in Table 5.22.

Table 5.22: Regions entering the fit and fitted observable in each analysis region and channel.

	low- m_{HH} SR	high- m_{HH} SR	VBF SR	Inclusive
$\tau_{\text{had}}\tau_{\text{had}}$	BDT score	BDT score	BDT score	–
$\tau_{\text{lep}}\tau_{\text{had}}$ SLT	BDT score	BDT score	BDT score	–
$\tau_{\text{lep}}\tau_{\text{had}}$ LTT	BDT score	BDT score	BDT score	–
$Z + HF$ CR	–	–	–	m_{ll}

The primary POI in the Standard Model fits is the HH signal strength, denoted as μ_{HH} . This strength is measured as the ratio of the combined ggF and VBF input signal cross-section, expressed as $31.05 + 1.73$ fb, multiplied by the branching ratio (BR). Additionally, separate fits are executed considering two distinct parameters of interest, namely μ_{ggF} and μ_{VBF} . These parameters represent the HH signal strength for ggF and VBF respectively, with each associated with its individual normalization factor (NF).

In the fitting process, the normalization of the $t\bar{t}$ and $Z + HF$ jets backgrounds are freely floating in the fit and are determined from data. The uncertainties in relative acceptance between the signal regions (SRs) and control regions (CR) influence these normalizations in the SRs that are part of the fit.

Regarding the likelihood scans for κ_λ and κ_{2V} , the distribution of the MVA scores is parametrized according to κ_λ and κ_{2V} . This is achieved by generating three ggF and 6 VBF signal templates. More details on this parametrization can be found in Section 1.3.5. The analysis workspaces undergo modifications to establish correlations among the signal samples via the new parameters κ_λ and κ_{2V} . Using the linear combination approach, as presented in Section 1.3.5, the signals are merged to derive signal distributions for diverse κ_λ and κ_{2V} values. Within the fitting framework, the cross-sections and BRs of single-Higgs production are adjusted in accordance with κ_λ .

Every source of systematic uncertainty highlighted is treated as nuisance parameters (NPs) during the profile likelihood fitting. The effect of each NP is split into two components: normalisation and shape, which correspond to the uncertainties of the same names discussed earlier. The fit templates incorporate shape uncertainties via alternative histograms. For normalisation uncertainties, they are integrated either as flat priors (in the case of "floating" templates) or Gaussian priors.

Subsequently, the NP correlations across all fitting regions are enumerated as follows:

- All experimental uncertainties are correlated across all fit regions
- Cross-section and acceptance uncertainties on the MC estimated backgrounds and on signal are also correlated

- Floating $t\bar{t}$ and $Z + HF$ normalisations are correlated across all fit regions
- Relative acceptance uncertainties on the normalisation of $t\bar{t}$ and $Z + HF$, which are determined from data in the fit, are correlated with the shape variations from the same source of uncertainty are correlated between the $\tau_{\text{had}}\tau_{\text{had}}$ and $\tau_{\text{lep}}\tau_{\text{had}}$ channels. The main exception from the rule is the shape uncertainties due to generator comparison for $Z + HF$ in the CR which is kept uncorrelated to extrapolation and shape uncertainties in the SR in order to avoid propagating the observed constrain likely due to a fluctuation in the alternative sample distribution.
- Uncertainties on the data-driven backgrounds are not correlated

Prior to their inclusion in the fit model, the NPs are subjected to various procedures. These encompass symmetrization, refinement, and pruning. On symmetrization:

- One-sided experimental and modelling systematics are symmetrized
- Experimental systematics resulting in same-sided variations are also symmetrized, using the average of up and down variations. This is done to fix under-constraints from same-sided variations

The systematic variations can also be smoothed to mitigate potential instabilities during the likelihood minimization, which emerge due to statistical fluctuations present in the templates. Smoothing is implemented for 4-vector-based CP variations; however, they are not applied to weight CP variations. A variety of algorithms are available for this smoothing process. The default approach incorporates an iterative rebinning technique for the systematic variations until a predetermined number of local extreme is attained. Typically, two extreme are utilized, corresponding to systematic variations which are monotonic in the fitted variable.

Furthermore, pruning is employed on all systematics, aiming to accelerate the fitting procedure and to reduce instabilities resulting from minor systematics that mainly introduce noise with negligible effect on analysis sensitivity. Pruning is applied distinctly to the normalization and shape implications of a systematic uncertainty. The criteria for pruning are as follows:

- the normalisation effect of a systematic uncertainty is pruned away if the difference between the nominal and systematic yield is less than 0.5%
- the shape effect of a systematic uncertainty is pruned away if the variation between the nominal and the systematic templates is less than 0.5% in all bins
- normalisation or shape effects of a systematic are pruned away if the variation is one-sided (for example because one side is below the 0.5% threshold)
- the shape systematics having up and down variations on the same side are pruned away based on a χ^2 test; if the χ^2 value between up and down variation is smaller than the χ^2 between nominal and up/down variation (only applied to the smoothed systematics)

Moreover, Monte Carlo (MC) statistical uncertainties are incorporated as NPs, using Poissonian priors. The name of these NPs reflect the signal region (SR) and the associated bin number.

5.5.3 Binning

The construction of the MVA output score distributions involves an initial process of very fine binning, which subsequently undergoes a rebinning process to create fit templates. The primary objectives of this process are to reduce the number of bins, while retaining the expected sensitivity, and maintaining the stability of the fit and validity of the asymptotic approximation. Both $\tau_{\text{lep}}\tau_{\text{had}}$ and $\tau_{\text{had}}\tau_{\text{had}}$ channels utilize the same rebinning algorithm, referred to as Trafo60, which is elaborated upon below.

The BDT score histograms are initially constructed with 2090 bins, utilizing a non-uniform binning approach. The distribution of scores ranges from -1 to 0.990 with a bin width of 10^{-3} (accounting 1990 bins). A more precise width of 10^{-4} is adopted from 0.990 to 1 , accounting for 100 bins, which correspond to the scores most signal-like. The rebinning process commences with these intricately binned histograms. Bins are subsequently merged in an iterative manner, starting from the MVA bins that are most indicative of a signal, until specific criteria are met.

To transform the BDT output histograms, the following generic function can be employed:

$$Z(I[k, l]) = Z(z_s, n_s(I[k, l]), N_s, z_b, n_b(I[k, l]), N_b), \quad (5.5.5)$$

where:

- $I[k, l]$ represents an interval of histograms that includes the bins from bin k to bin l .
- N_s and N_b denote the aggregate number of signal and background events in the histogram, respectively.
- $n_s(I[k, l])$ and $n_b(I[k, l])$ signify the total signal and background events within the interval $I[k, l]$.
- The parameters z_s and z_b serve to adjust the algorithm.

In this analysis, the function previously discussed is expressed as:

$$Z = z_s \frac{n_s}{N_s} + z_b \frac{n_b}{N_b}, \quad (5.5.6)$$

where the pair $(z_s, z_b) = (10, 5)$ is the selected configuration for the BDT across all analysis regions. The choice of a larger z_s relative to z_b is motivated by the intention to refine binning within regions of the BDT output score that exhibit a high signal-to-background ratio.

Initiating from the right most bin of the original histogram (representing high-BDT score), the interval $I[k, \text{last}]$ is progressively expanded by integrating one bin at a time, moving from the rightmost bin inwards. The Z value is recalculated with every such step. Upon reaching a condition where $Z(I[k_0, \text{last}]) > 1$, the entire span of bins within the interval $I[k_0, \text{last}]$ is merged into a single bin. The term "last" in this context references the furthest right bin of the original histogram during the initial iteration. With the culmination of every iteration, the label "last" is reassigned to the rightmost bin, excluding bins newly created in prior iteration.

Subsequent to each iteration, two supplementary criteria are incorporated, and the above-described process is reiterated until both are met:

- The Monte Carlo (MC) statistical uncertainty associated with the cumulative backgrounds of each bin must be below 20%.
- Each bin must have an expected background event count exceeding 3.

5.5.4 Blinding strategy

When choosing the analysis strategy and training BDTs, the analysis is designed blinded to avoid measurement bias. All the pre-fit plots of the MVA output score distributions are blinded in the most sensitive region. In both channels and all analysis categories, the distributions are blinded from right to left in the region containing 85% of the total signal.

When applying the final fitting studies, the analysis is unblinded.

5.6 Results

In Section 5.5, the model is validated through multiple stages. While the simultaneous fit is applied across all analysis regions, individual fits are also performed for both the $\tau_{\text{had}}\tau_{\text{had}}$ and $\tau_{\text{lep}}\tau_{\text{had}}$ channels. The fit engages with the Asimov dataset as well as actual data. For the real data fitting process, the signal strength is assigned a value of zero.

5.6.1 Fit results

5.6.1.1 $\tau_{\text{had}}\tau_{\text{had}}$

In the $\tau_{\text{had}}\tau_{\text{had}}$ fit, three signal regions are included: low- m_{HH} ggF, high- m_{HH} ggF, and VBF, along with the $Z + HF$ control region. It is important to note that the normalizations of the $t\bar{t}$ and $Z + HF$ backgrounds are determined as free-floating nuisance parameters (NPs).

Signal strengths derived from fitting the data under different signal hypotheses are presented in Table 5.23. These values align with the Standard Model (SM) predictions within a one sigma level.

Table 5.23: Signal strengths observed from data fitting in the $\tau_{\text{had}}\tau_{\text{had}}$ channel under varied signal hypotheses. The uncertainties encompass both statistical and systematic aspects. The designation 1D indicates a single parameter consideration, whereas 2D denotes a simultaneous fit of two signal strengths.

Signal Hypothesis	Signal Strength
μ_{HH}	-0.36 ± 1.35
μ_{ggH} 1D	-0.36 ± 1.35
μ_{VBF} 1D	-17 ± 35
μ_{ggH} 2D	-0.28 ± 1.38
μ_{VBF} 2D	-11 ± 37

Figures 5.32 to 5.35 illustrate the comparison of NP pulls from a fit conducted on the data with the signal strength set to 0 (used during unblinding) and an unconditional fit to data for the inclusive signal strength.

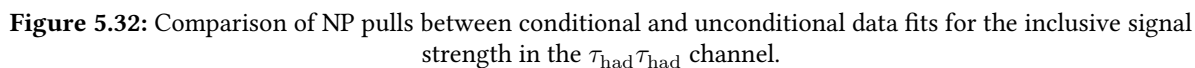
Given that the best value for the signal strength closely aligns with 0, only minor differences are observed in the nuisance parameters of the two fits to data.

Figure 5.36 presents a comparison of nuisance parameter (NP) rankings for the fits conducted on both data and the Asimov dataset under the hypothesis of inclusive signal strength.

The primary uncertainties influencing the determination of signal strength include the uncertainty in the single Higgs plus heavy flavour production, the combined HH cross-section uncertainty of the renormalization scheme and the top-quark mass scheme, and the Monte Carlo (MC) statistical uncertainties in the higher BDT bins in the high m_{HH} region. Notable consistency is observed between the expected and observed NP rankings, with the most significant change attributed to the signal cross-section uncertainties, which are ranked lower in the data fit due to the negative best-fit signal strength. It is also important to highlight that these factors are considerably smaller than the statistical uncertainty of the data on the result, which is anticipated to be 1.3.

Figure 5.37 displays the correlations for highly correlated NPs from the $\tau_{\text{had}}\tau_{\text{had}}$ fit to both the Asimov dataset and the data. The correlations for the MC statistical uncertainty NPs are excluded. The level of NP correlation observed is similar in both fit configurations.

Figure 5.38 shows the post-fit distributions of the fitted variables in the four regions. The rationale behind the choice of binning is discussed in Section 5.5.3. Due to the negative signal strength, signal templates are omitted.



The post-fit distribution of other input variables is depicted in Figures 5.39 and 5.40. These plots are generated by extrapolating the nuisance parameters from the data fit, excluding the gamma parameters.

ATLAS Internal

— Parameter
* Blinded NP

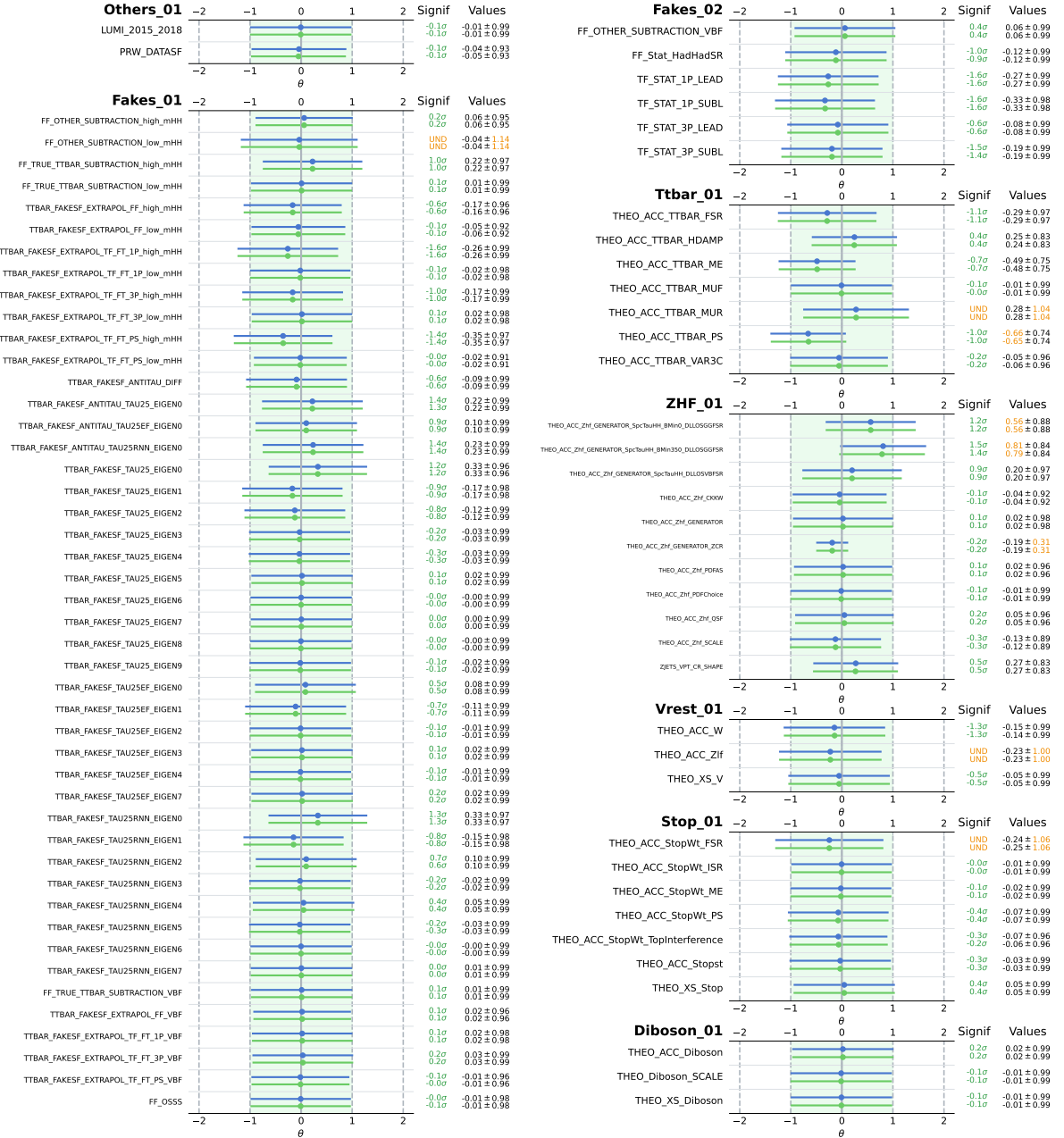
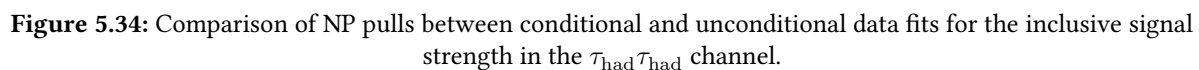


Figure 5.33: Comparison of NP pulls between conditional and unconditional data fits for the inclusive signal strength in the $\tau_{\text{had}}\tau_{\text{had}}$ channel.



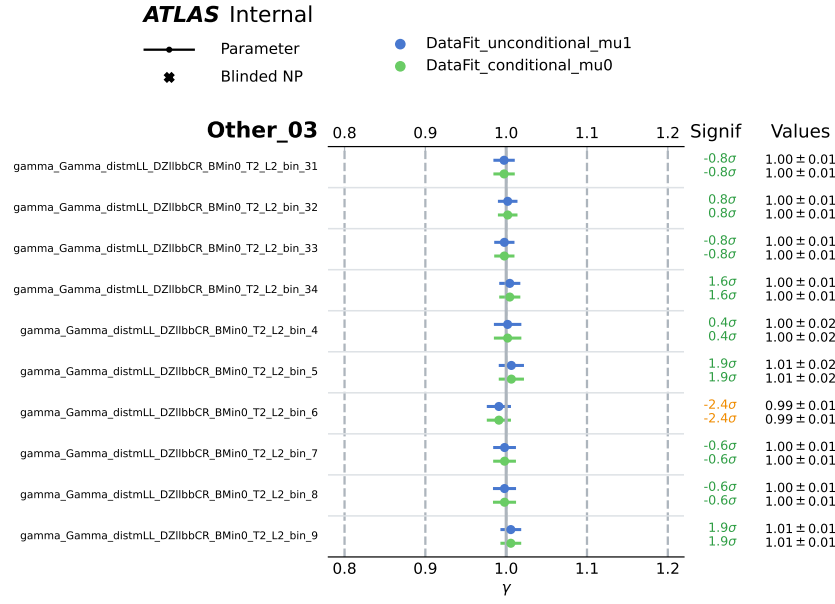


Figure 5.35: Comparison of NP pulls between conditional and unconditional data fits for the inclusive signal strength in the $\tau_{\text{had}}\tau_{\text{had}}$ channel.

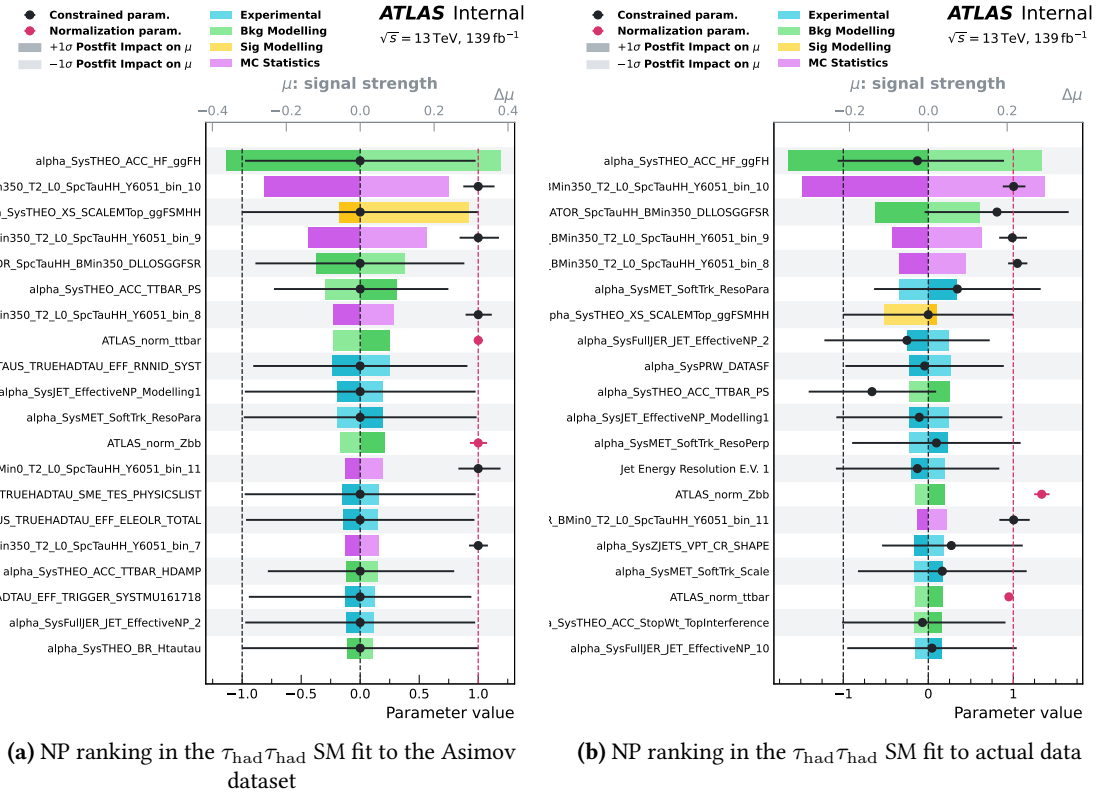


Figure 5.36: NP ranking for the $\tau_{\text{had}}\tau_{\text{had}}$ SM fit (μ_{HH} hypothesis) to the Asimov dataset (Figure (a)) and to actual data (Figure (b)).

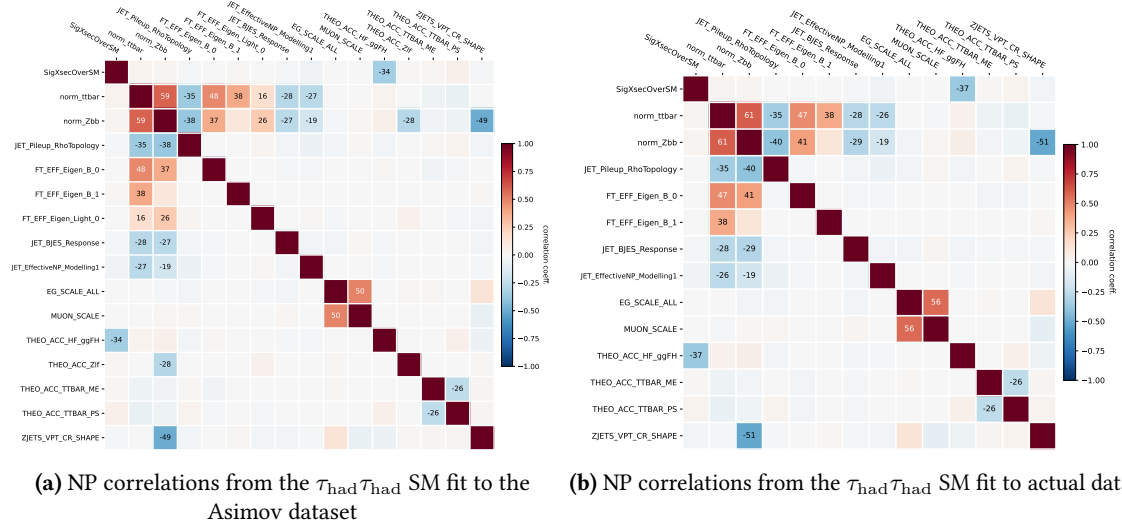


Figure 5.37: NP correlations from the $\tau_{had}\tau_{had}$ SM fit to the Asimov dataset in Figure (a) and to actual data in Figure (b). MC statistical uncertainties are not included in the correlations.

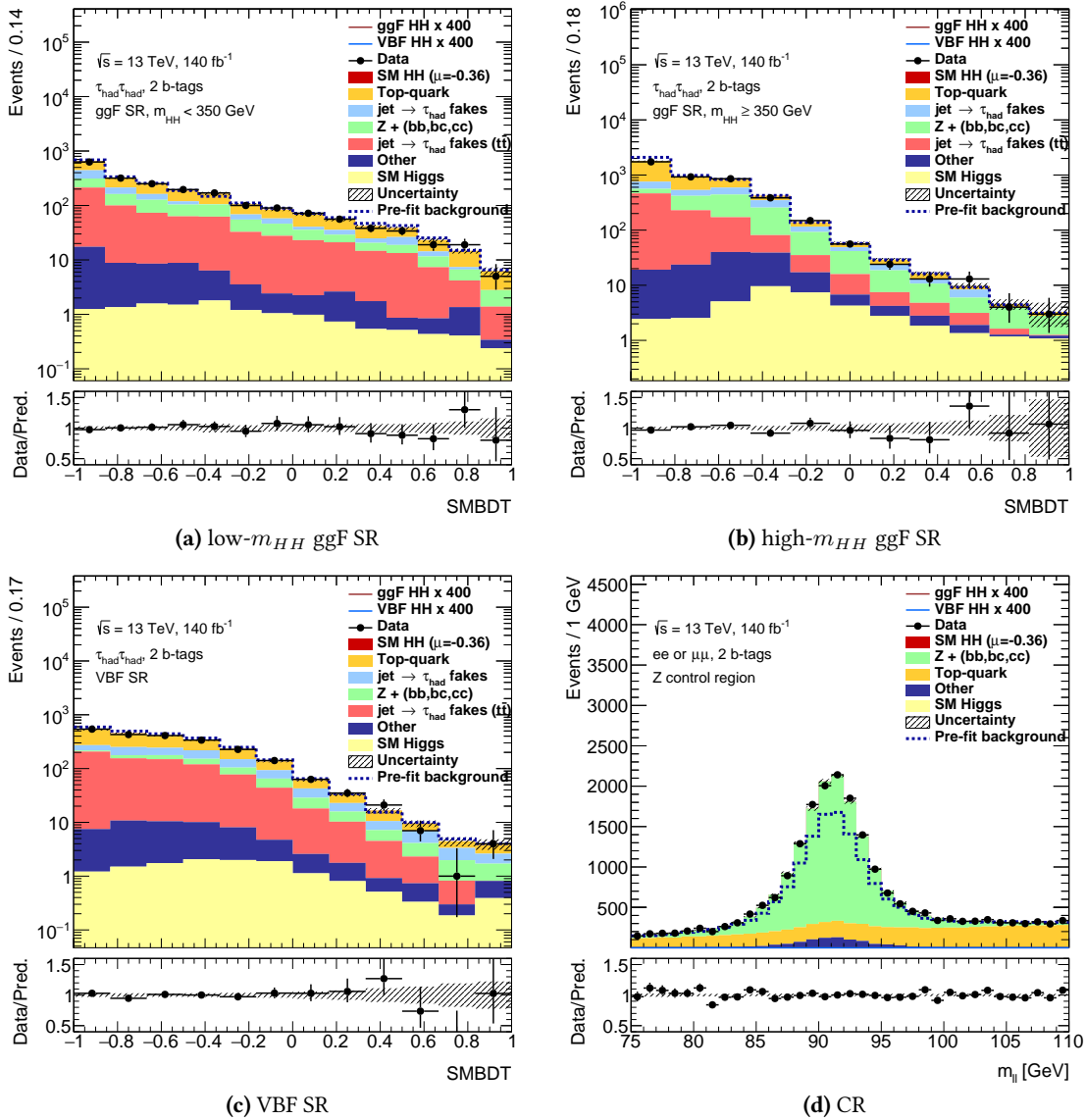


Figure 5.38: Post-fit BDT score distributions in the $\tau_{had}\tau_{had}$ signal regions. Due to the negative signal strength, the signal templates are not shown. The definition of the uncertainty band needs clarification.

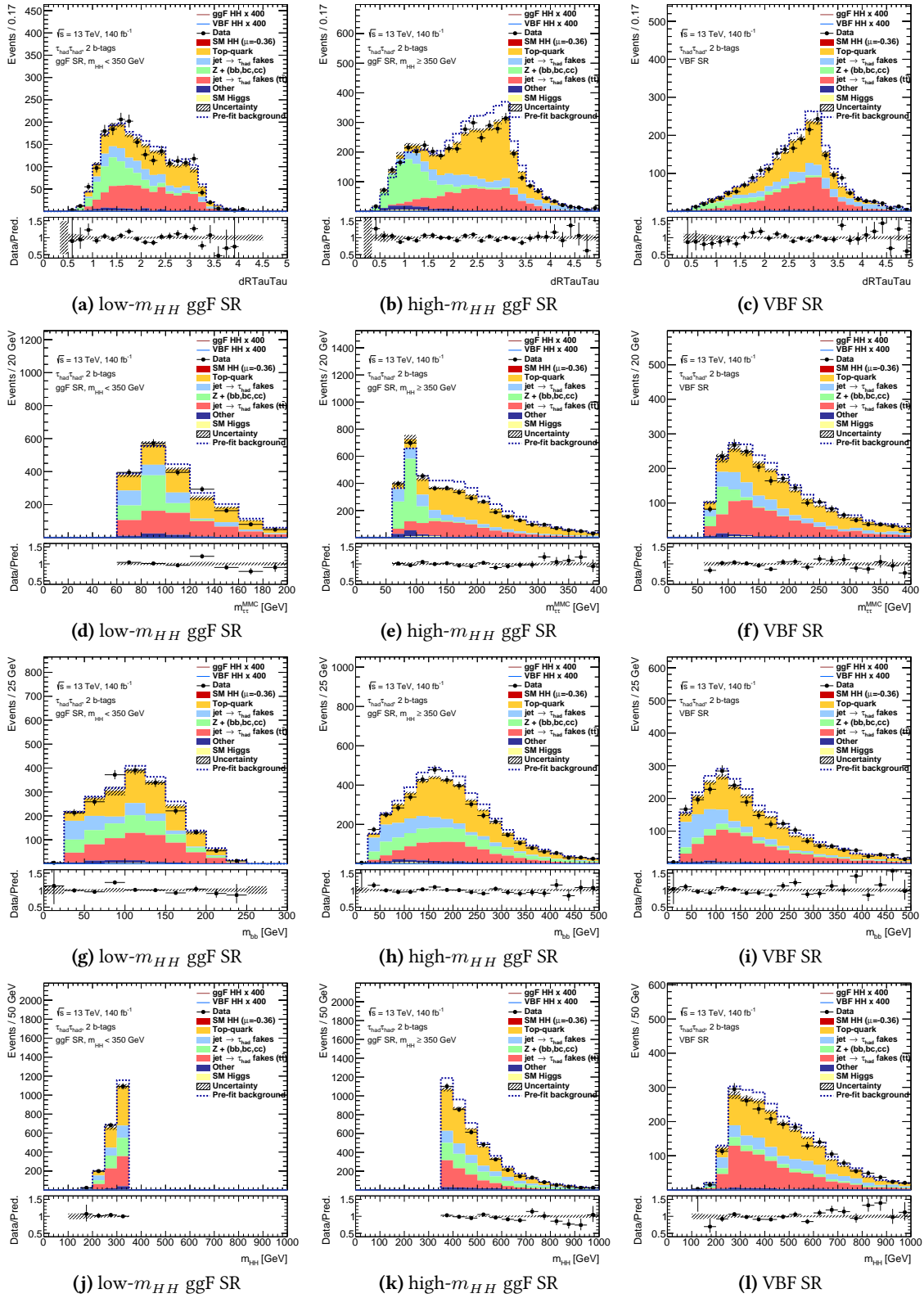


Figure 5.39: Post-fit distributions of key variables in the $\tau_{\text{had}}\tau_{\text{had}}$ channel signal regions. Due to the negative signal strength, the signal templates are not shown.

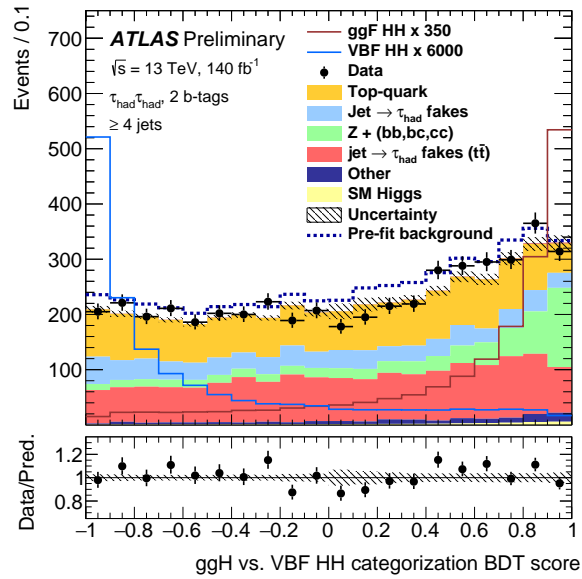


Figure 5.40: Post-fit distribution of the ggF/VBF classification BDT score in the $\tau_{\text{had}}\tau_{\text{had}}$ channel. The categorisation BDT is only shown for events with at least four jets, representing a subset of the ggH SRs. Due to the negative signal strength, the signal templates are not shown.

5.6.1.2 $\tau_{\text{lep}}\tau_{\text{had}}$

In the $\tau_{\text{lep}}\tau_{\text{had}}$ channel, the analysis includes data from three signal regions for both SLT and LTT channels: low- m_{HH} ggF, high- m_{HH} ggF, and VBF. Additionally, the $Z + HF$ control region is incorporated into all fits. Similar to the $\tau_{\text{had}}\tau_{\text{had}}$ channel, the normalizations of the $t\bar{t}$ and $Z + HF$ backgrounds are treated as free-floating nuisance parameters (NPs).

Fits are executed separately for both SLT and LTT regions, including the control region, as well as for the combination of the two selections. The focus of this subsection is primarily on the combined $\tau_{\text{lep}}\tau_{\text{had}}$ fit. It is noteworthy that the sensitivity of the LTT channel is approximately half that of the SLT channel.

Table 5.24 details the best-fit signal strengths for the SLT, LTT, and $\tau_{\text{lep}}\tau_{\text{had}}$ channels, derived from fitting the data under various signal hypotheses. A slight excess in the inclusive signal strength is primarily observed in the high- m_{HH} ggF SR of the SLT analysis; the significance of this excess is 2.7 standard deviations from the background-only hypothesis, increasing to 2.8 standard deviations when combined with the LTT analysis. The expected significances are 0.39 and 0.42, respectively. Respect to the SM, this excess holds a significance of 2.3 standard deviations.

When considering the VBF production, a slight excess is primarily observed in the LTT channel. The significance of this excess in a standalone fit to the LTT channel is 2.39 standard deviations from the background-only hypothesis. In a combined fit to the $\tau_{\text{lep}}\tau_{\text{had}}$ channel, this excess has a significance of 1.35 standard deviations.

Table 5.24: Observed signal strength when fitting data in the SLT, LTT and $\tau_{\text{lep}}\tau_{\text{had}}$ channel under different signal hypothesis. The uncertainty includes both statistical and systematic components. 1D indicates that only that parameter is considered, while 2D implies simultaneous fit of two signal strengths.

signal hypothesis	SLT	LTT	$\tau_{\text{lep}}\tau_{\text{had}}$
μ_{HH}	7.8 ± 3.6	2.6 ± 8.1	7.7 ± 3.4
μ_{ggH} 1D	7.9 ± 3.7	1.5 ± 7.9	7.6 ± 3.4
μ_{VBF} 1D	24 ± 63	373 ± 183	85 ± 69
μ_{ggH} 2D	7.9 ± 3.7	-3.1 ± 7.9	7.1 ± 3.4
μ_{VBF} 2D	1 ± 59	394 ± 190	54 ± 66

Figures 5.41 to 5.44 depict the comparison of NP pulls for a fit to data in the $\tau_{\text{lep}}\tau_{\text{had}}$ channel and the SLT and LTT regions individually.

Overall, few pulled or over-constrained nuisance parameters are observed, especially considering those already present in the CR-only fit. In these cases, the two individual channels generally concur in the direction of the constrain/pull, predominantly driven by the SLT regions.

Figure 5.45 compares the NP ranking for the fit to data and to the Asimov dataset in the inclusive signal strength hypothesis for the $\tau_{\text{lep}}\tau_{\text{had}}$ combination.

The primary uncertainties impacting the signal strength determination include the uncertainty on the modeling of single top production, single Higgs plus heavy flavor production, the combined HH cross-section uncertainty of the renormalization scheme and the top-quark mass scheme, and the Monte Carlo (MC) statistical uncertainties on the higher BDT bins in the high m_{HH} region. It is significant to note that these factors are substantially smaller than the statistical uncertainty on the data, expected to be 2.00. The main difference in ranking between the expected and observed results is the increased importance of signal-related uncertainties, attributable to the larger best-fit signal strength.

Figure 5.46 displays the correlations for highly correlated NPs from the $\tau_{\text{lep}}\tau_{\text{had}}$ fit to both the Asimov dataset and the data. Correlations for the MC statistical uncertainty NPs are excluded. A similar level of NP correlation is observed in both fit configurations for the majority of NPs.

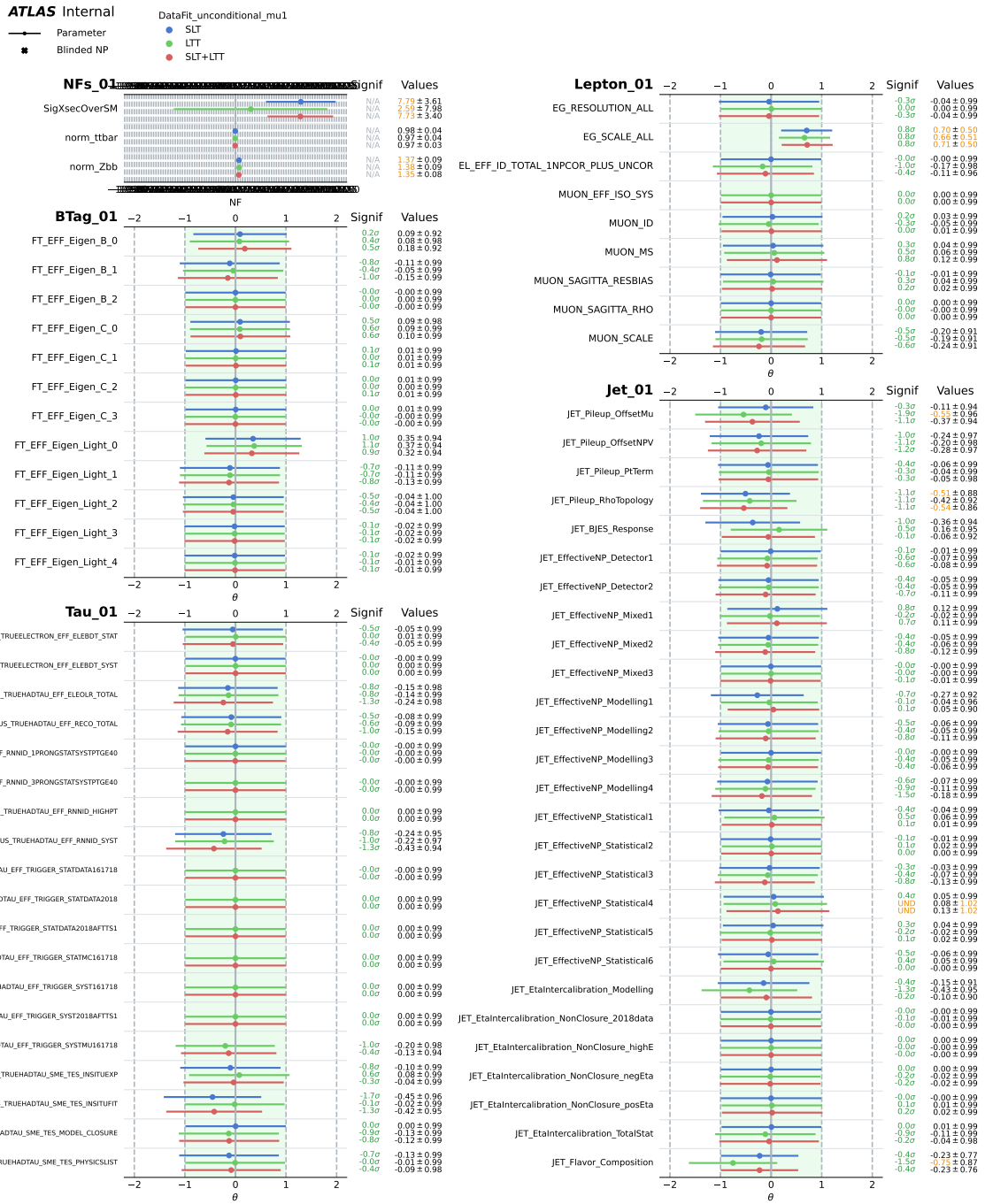


Figure 5.41: NP pulls comparison for the unconditional fit to data for the $\tau_{lep}\tau_{had}$ channel and the SLT and LTT channels individually.

Figure 5.47 shows the data/prediction comparison for the post-fit BDT score distributions in the $\tau_{lep}\tau_{had}$ SRs. The choice of the binning is discussed in Section 5.5.3; In the post-fit plots, the signal is included in the stack of histograms and the ratio, the uncertainty band is drawn on the background stack only. The same version of plots with the signal excluded from the stack and the ratio pad can be found in Appendix B.2.2.2. The CR agreement is not shown, since this is identical to the one from the $\tau_{had}\tau_{had}$ standalone fit.

Figure 5.47 presents the data/prediction comparison for the post-fit BDT score distributions in the $\tau_{lep}\tau_{had}$ SRs. The rationale behind the choice of binning is discussed in Section 5.5.3. In the post-fit plots, the signal is included in the stack of histograms and the ratio, with the uncertainty band drawn only on the background stack.

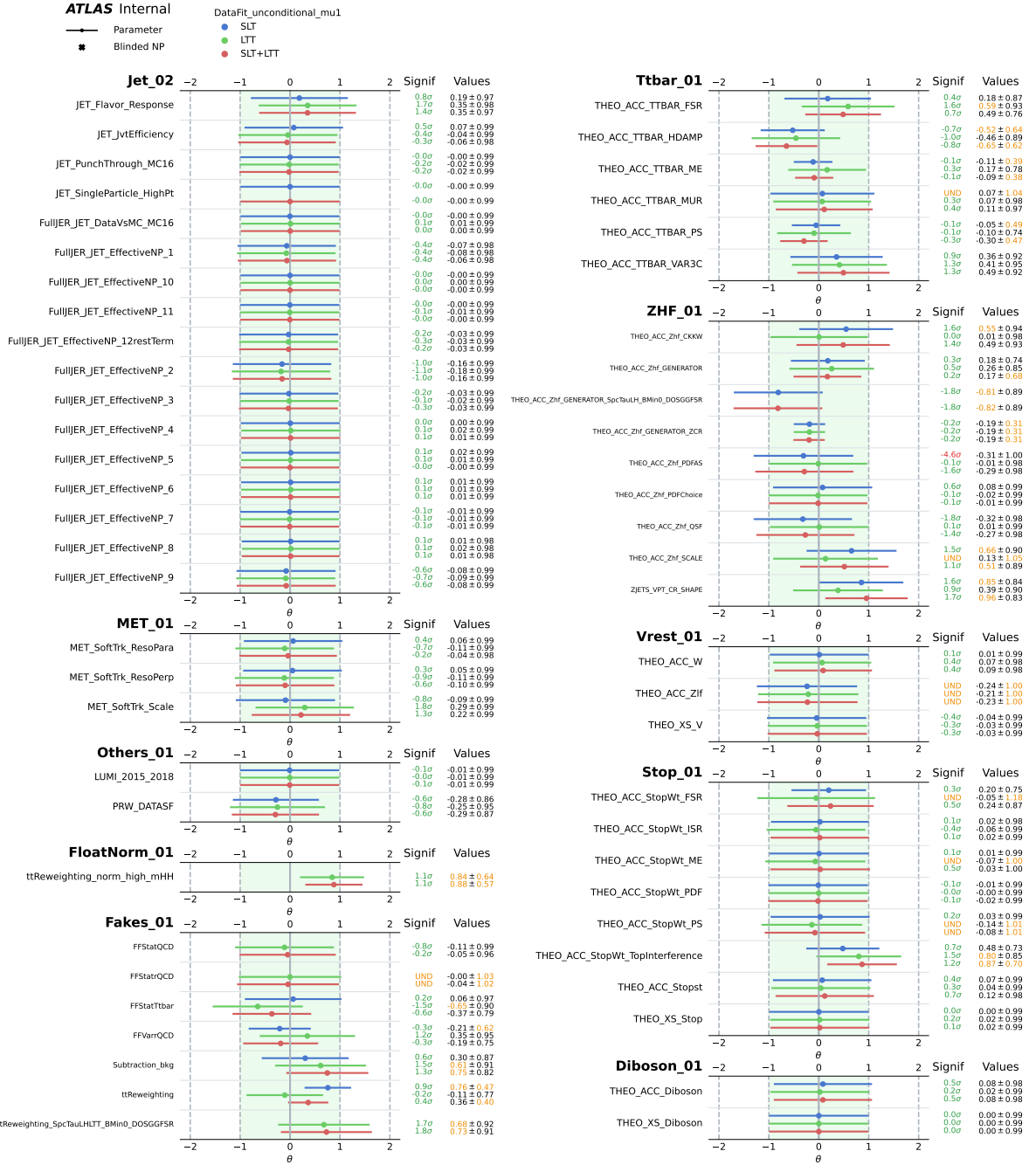
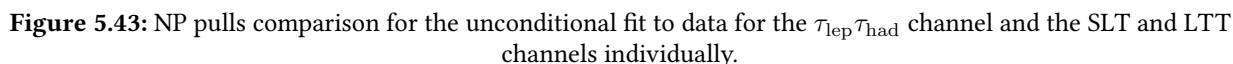
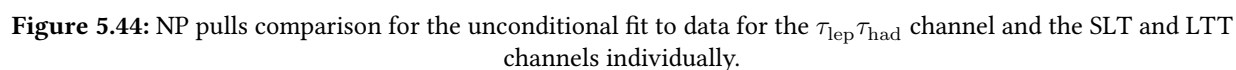


Figure 5.42: NP pulls comparison for the unconditional fit to data for the $\tau_{lep}\tau_{had}$ channel and the SLT and LTT channels individually.

The post-fit distribution of other input variables is illustrated in Figures 5.48, 5.49, and 5.50; these plots are obtained by extrapolating the nuisance parameters from the data fit, excluding the gamma parameters.





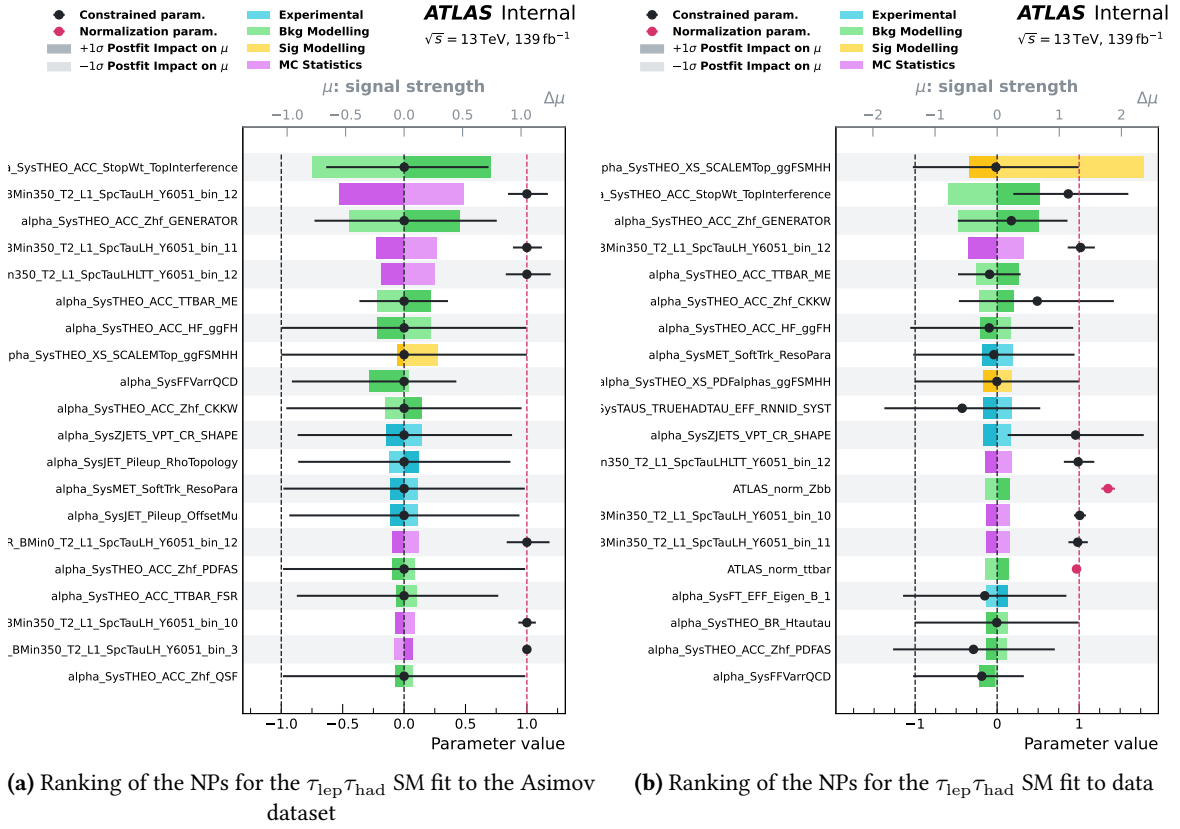


Figure 5.45: Ranking of the NPs for the $\tau_{lep}\tau_{had}$ SM fit (μ_{HH} hypothesis) to the Asimov dataset in Figure (a) and to data in Figure (b).

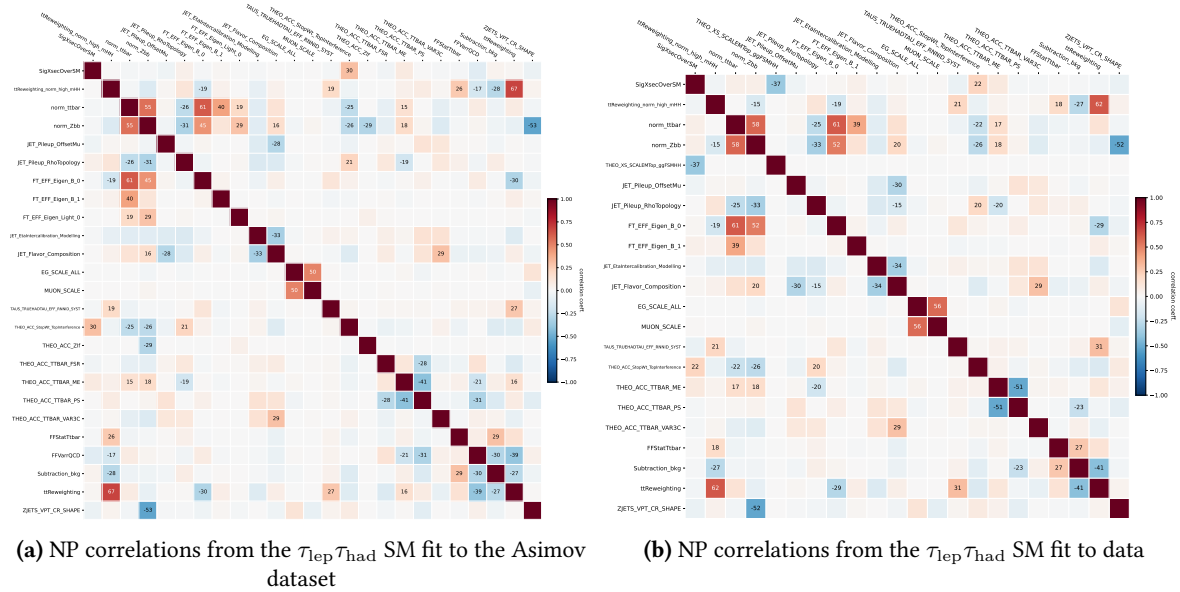


Figure 5.46: NP correlations from the $\tau_{lep}\tau_{had}$ SM fit to the Asimov dataset in Figure (a) and to data in Figure (b). MC statistical uncertainties are not included in the correlations.

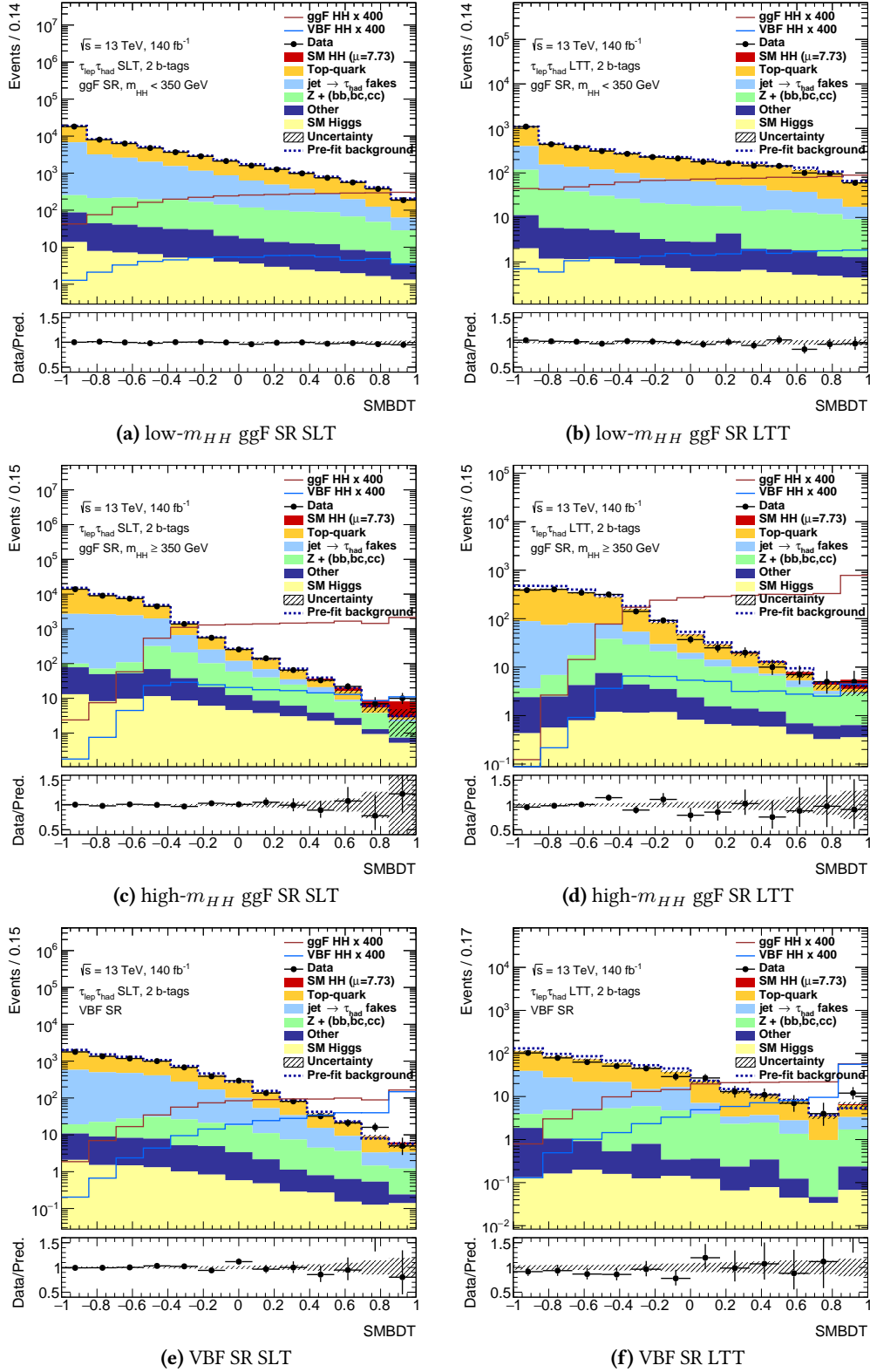


Figure 5.47: Post-fit BDT score distributions in the $\tau_{lep}\tau_{had}$ signal regions. The result of the inclusive signal strength fit is used to produce these distributions.

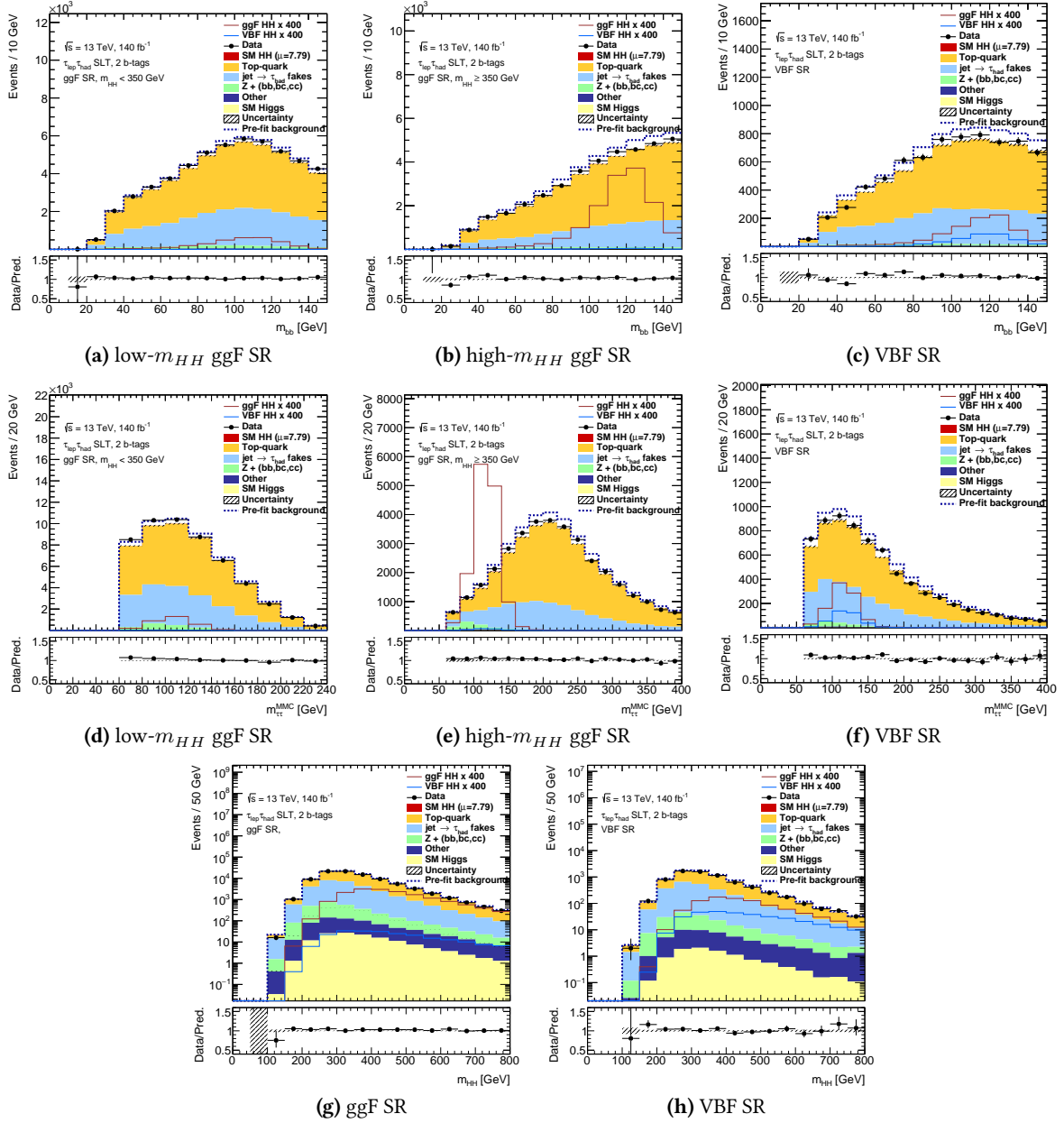


Figure 5.48: Post-fit data/MC distributions of key variables in the SLT signal regions. The results are obtained by applying the SLT fit results to the SLT signal region.

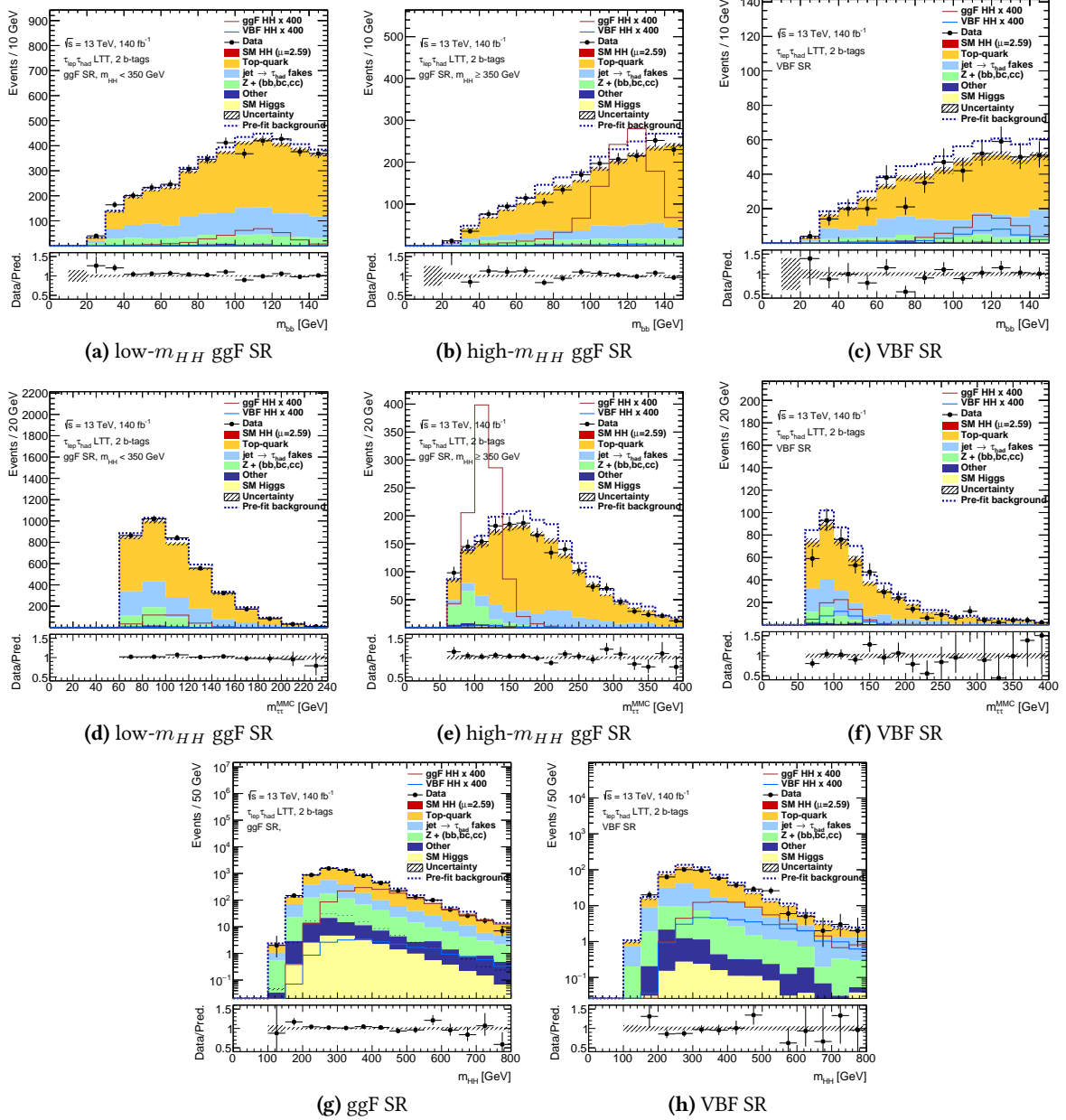


Figure 5.49: Post-fit data/MC distributions of key variables in the LTT signal regions. The results are obtained by applying the LTT fit results to the LTT signal region.

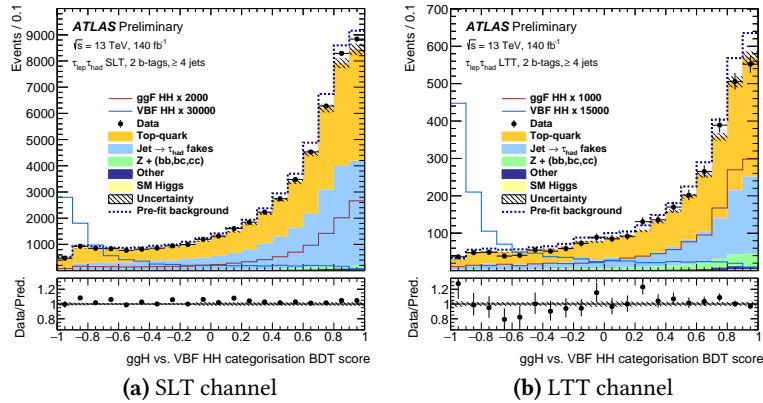


Figure 5.50: Post-fit data/MC distributions of the ggF/VBF classification BDT score in the $\tau_{\text{lep}}\tau_{\text{had}}$ channels. The categorisation BDT is only shown for events with at least four jets which represent a subset of the ggF SRs. It is shown on the left for the SLT region with the SLT fit result applied and on the right for the LTT regions with the LTT fit result applied.

5.6.1.3 Combined fit

The combined fit, incorporating all $\tau_{\text{had}}\tau_{\text{had}}$ and $\tau_{\text{lep}}\tau_{\text{had}}$ regions, is detailed in Table 5.22. Table 5.25 presents the derived signal strengths from this combined fit, applied to the data under various signal hypotheses. These results include the $\tau_{\text{had}}\tau_{\text{had}}$, $\tau_{\text{lep}}\tau_{\text{had}}$ channels, and their combination.

The inclusive signal strength hypothesis shows the best fit value of (2.16 ± 1.65) , which is a 1.4 standard deviation excess over the predictions of background-only hypothesis; this excess predominantly arises from the SLT channel in the $\tau_{\text{lep}}\tau_{\text{had}}$ analysis. The expected significance of this result is 0.76 standard deviations.

For the Vector Boson Fusion (VBF) production, the best-fit signal strength is found to be (21 ± 36) . The significance of this excess with respect to the background-only hypothesis is 0.61 standard deviations, driven by the VBF SR in the LTT analysis. The expected significance is of 0.03 standard deviations.

A detailed examination of the consistency of these results across channels is provided in section B.2.3.

Table 5.25: Observed signal strength when fitting data in the $\tau_{\text{had}}\tau_{\text{had}}$, $\tau_{\text{lep}}\tau_{\text{had}}$ and their combination. The uncertainty includes both statistical and systematic components. 1D indicates that only that parameter is considered, while 2D implies simultaneous fit of two signal strengths.

signal hypothesis	$\tau_{\text{had}}\tau_{\text{had}}$	$\tau_{\text{lep}}\tau_{\text{had}}$	comb.
μ_{HH}	-0.36 ± 1.35	7.7 ± 3.4	2.16 ± 1.65
μ_{ggH} 1D	-0.36 ± 1.35	7.6 ± 3.4	2.14 ± 1.66
μ_{VBF} 1D	-17 ± 35	85 ± 69	21 ± 36
μ_{ggH} 2D	-0.28 ± 1.38	7.1 ± 3.4	2.00 ± 1.68
μ_{VBF} 2D	-11 ± 37	54 ± 66	17 ± 36

Figure 5.51 shows the ranking of the NPs for the combined fit to the Asimov dataset and the observed data.

The primary uncertainties affecting signal strength determination are the uncertainty in single Higgs plus heavy flavour production, single top production, the combined HH cross-section uncertainty from the renormalization scheme and top-quark mass scheme, and the Monte Carlo statistical uncertainty in the highest BDT bins in the high m_{HH} region. Remarkably, these factors have a lesser impact than the statistical uncertainty of the data, expected to be 1.00.

Figures 5.52 to 5.55 illustrate the NP pulls comparisons for a fit to data assuming a signal strength of zero, for both the combined and the individual $\tau_{\text{had}}\tau_{\text{had}}$ and $\tau_{\text{lep}}\tau_{\text{had}}$ channels.

Specifically, Figure 5.54 highlights a channel-dependent pull in the $Z + HF$ generator comparison uncertainty, which is addressed in the decorrelation strategy for this parameter.

Figure 5.56 demonstrates the correlations for highly correlated NPs from the $\tau_{\text{lep}}\tau_{\text{had}}$ fit to both the Asimov dataset and data, excluding MC statistical uncertainty NPs. The level of NP correlation is consistent between the two fit configurations.

Finally, post-fit distributions of fitted variables in the 9 signal regions are depicted in Figure 5.57. In these plots, the signal is included in the histogram stack and ratio, with the uncertainty band only on the background stack.

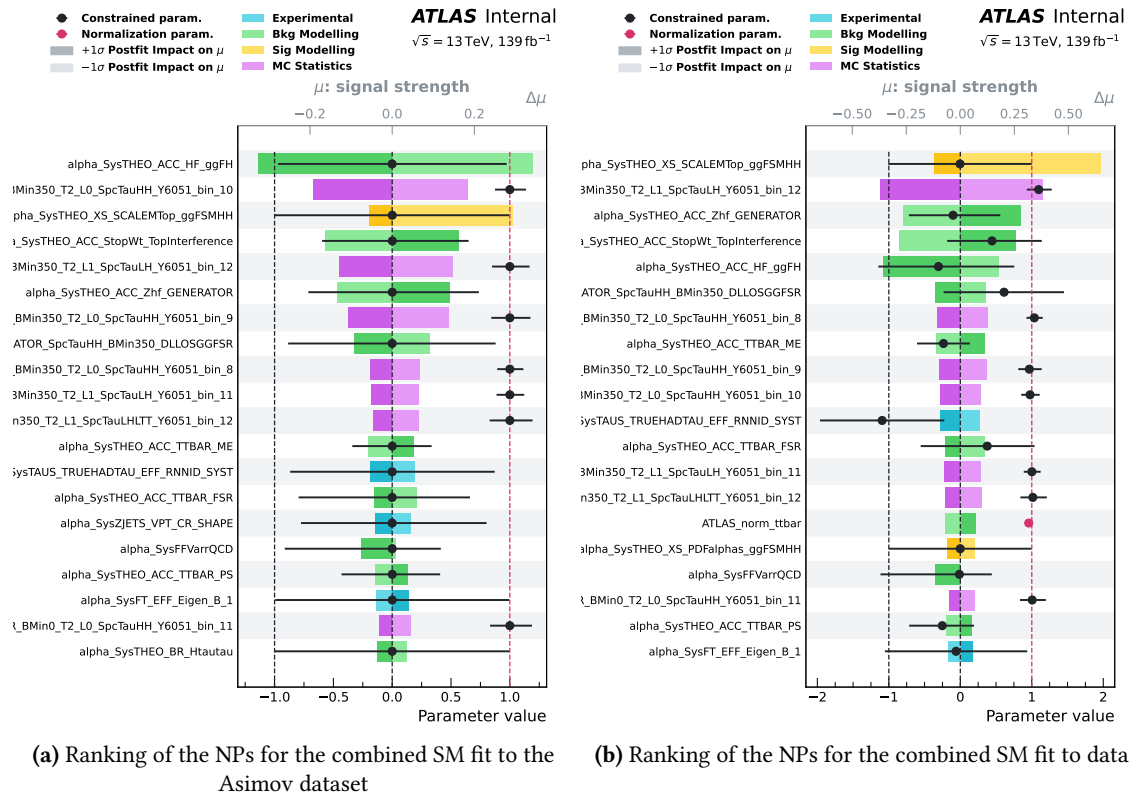


Figure 5.51: Ranking of the NPs for the combined SM fit to the Asimov dataset in Figure (a) and to data in Figure (b).

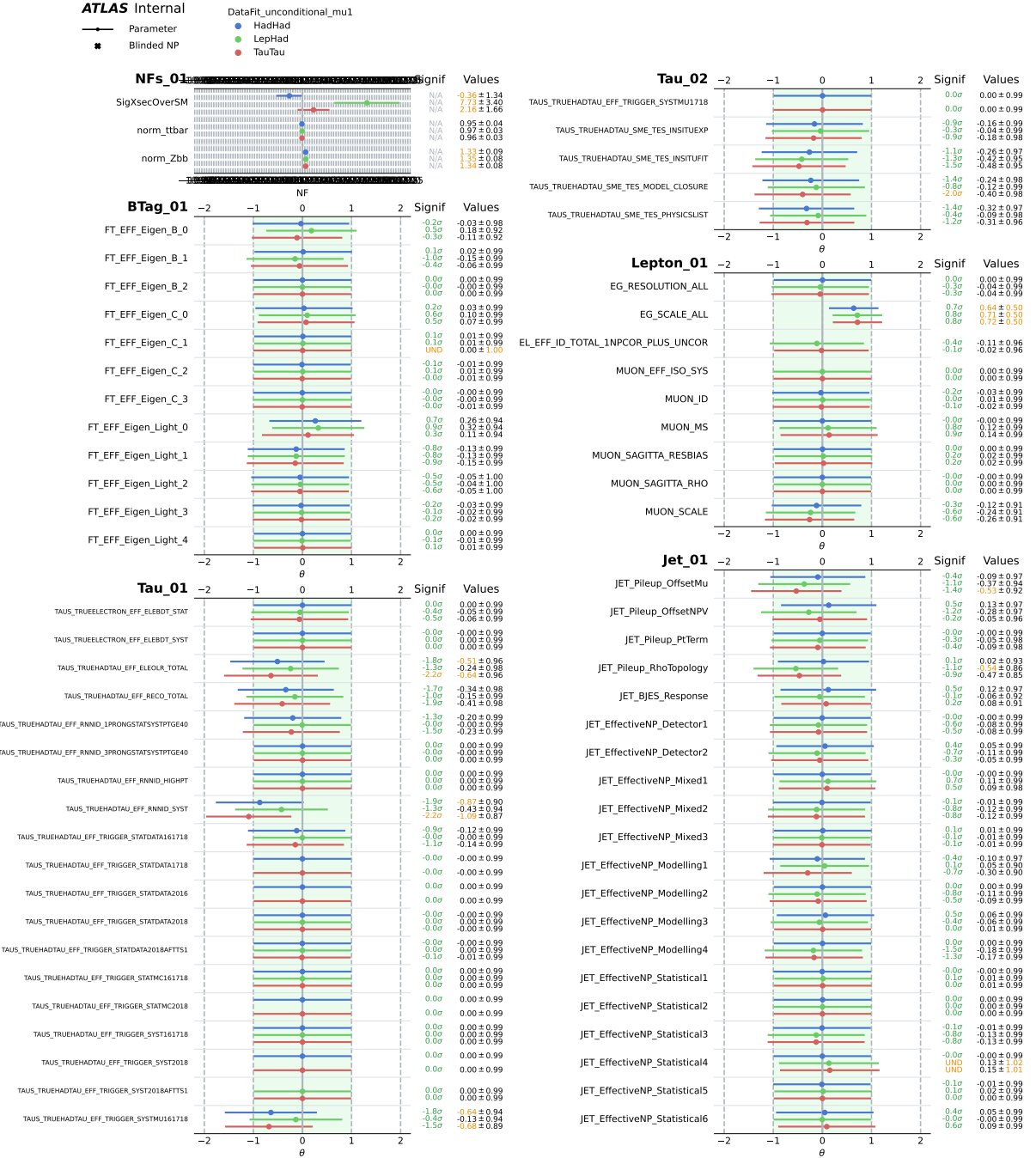


Figure 5.52: NP pulls comparison for the unconditional fit to data for the combination (red) and the $\tau_{\text{had}}\tau_{\text{had}}$ and $\tau_{\text{lep}}\tau_{\text{had}}$ channels individually.

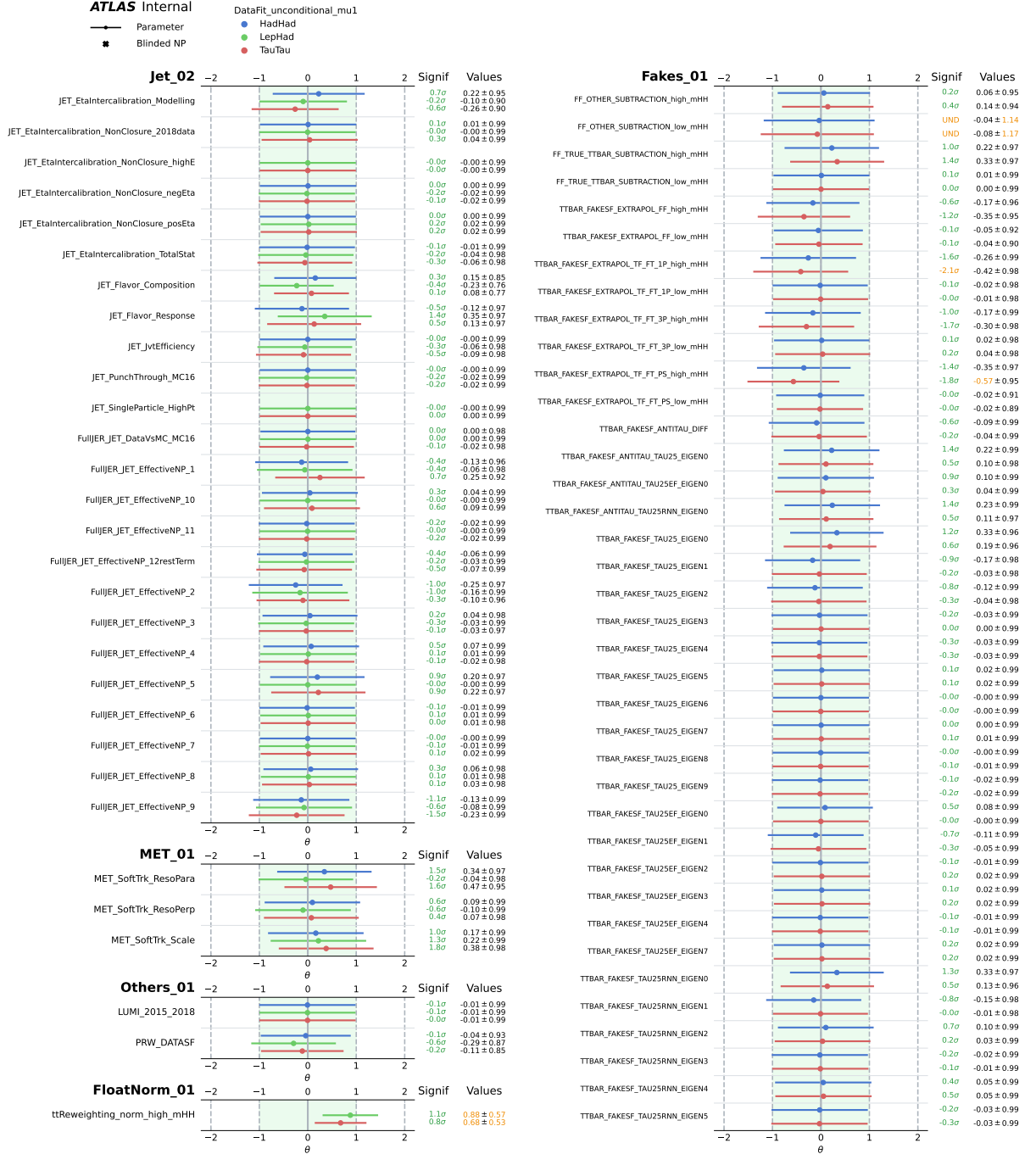


Figure 5.53: NP pulls comparison for the unconditional fit to data for the combination (red) and the $\tau_{\text{had}}\tau_{\text{had}}$ and $\tau_{\text{lep}}\tau_{\text{had}}$ channels individually.

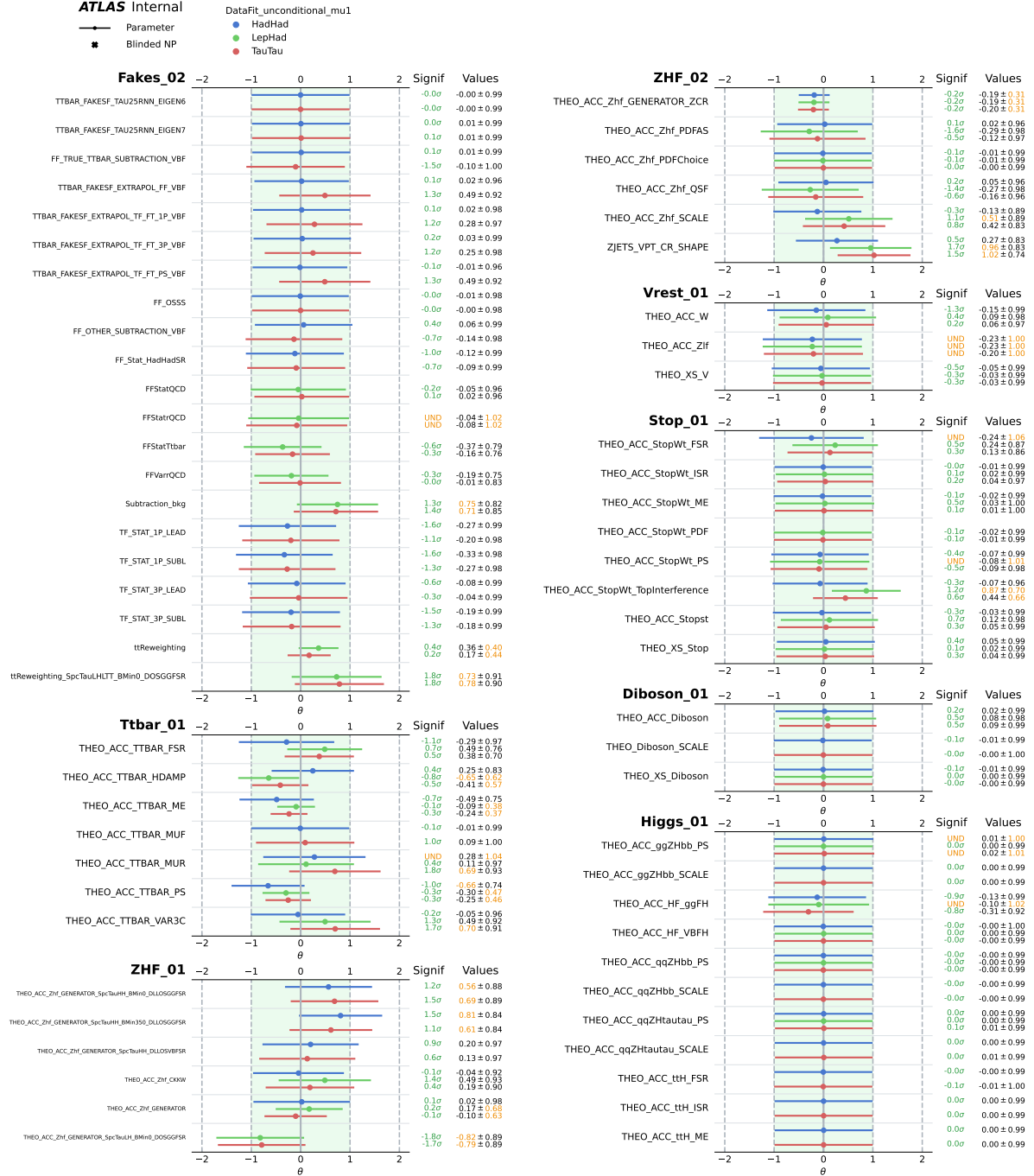


Figure 5.54: NP pulls comparison for the unconditional fit to data for the combination (red) and the $\tau_{\text{had}}\tau_{\text{had}}$ and $\tau_{\text{lep}}\tau_{\text{had}}$ channels individually.

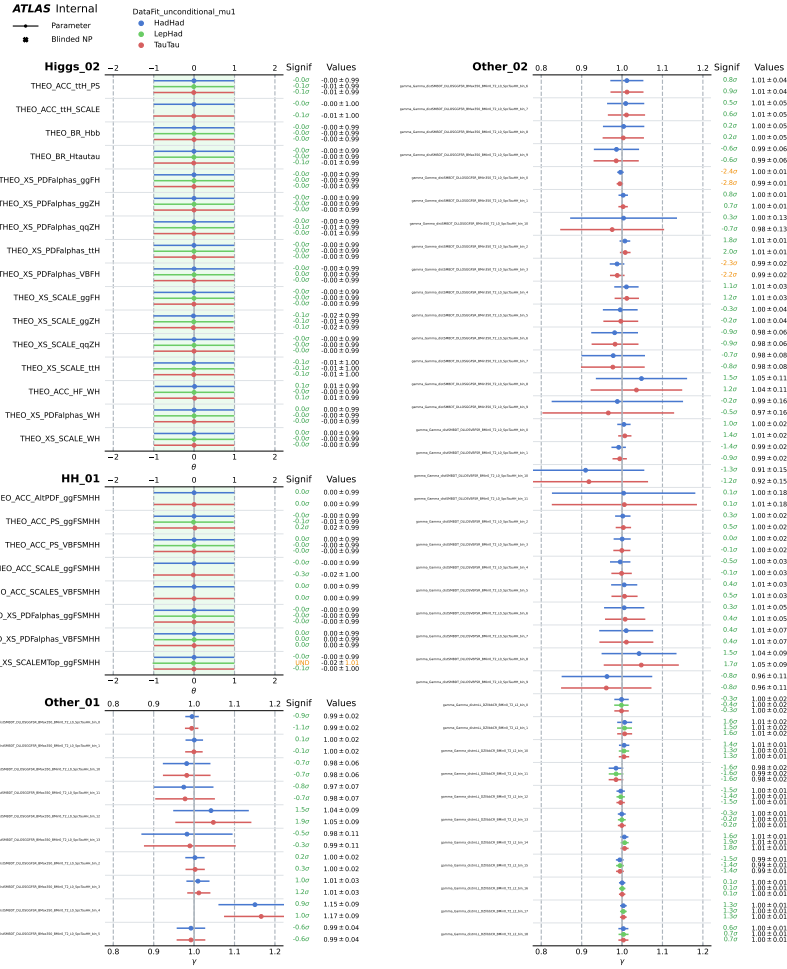


Figure 5.55: NP pulls comparison for the unconditional fit to data for the combination (red) and the $\tau_{had}\tau_{had}$ and $\tau_{lep}\tau_{had}$ channels individually.

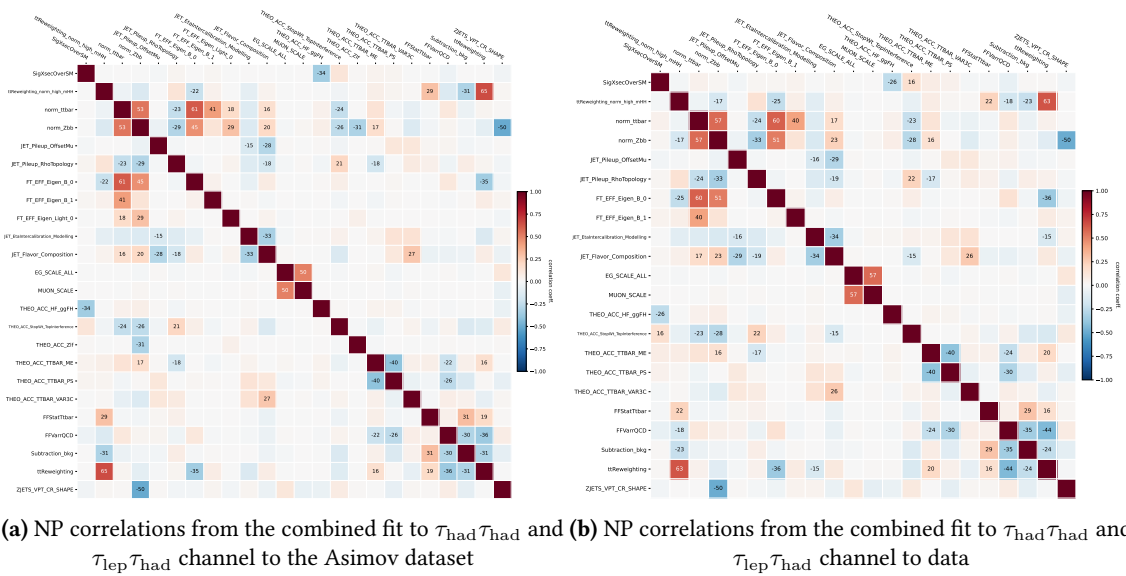
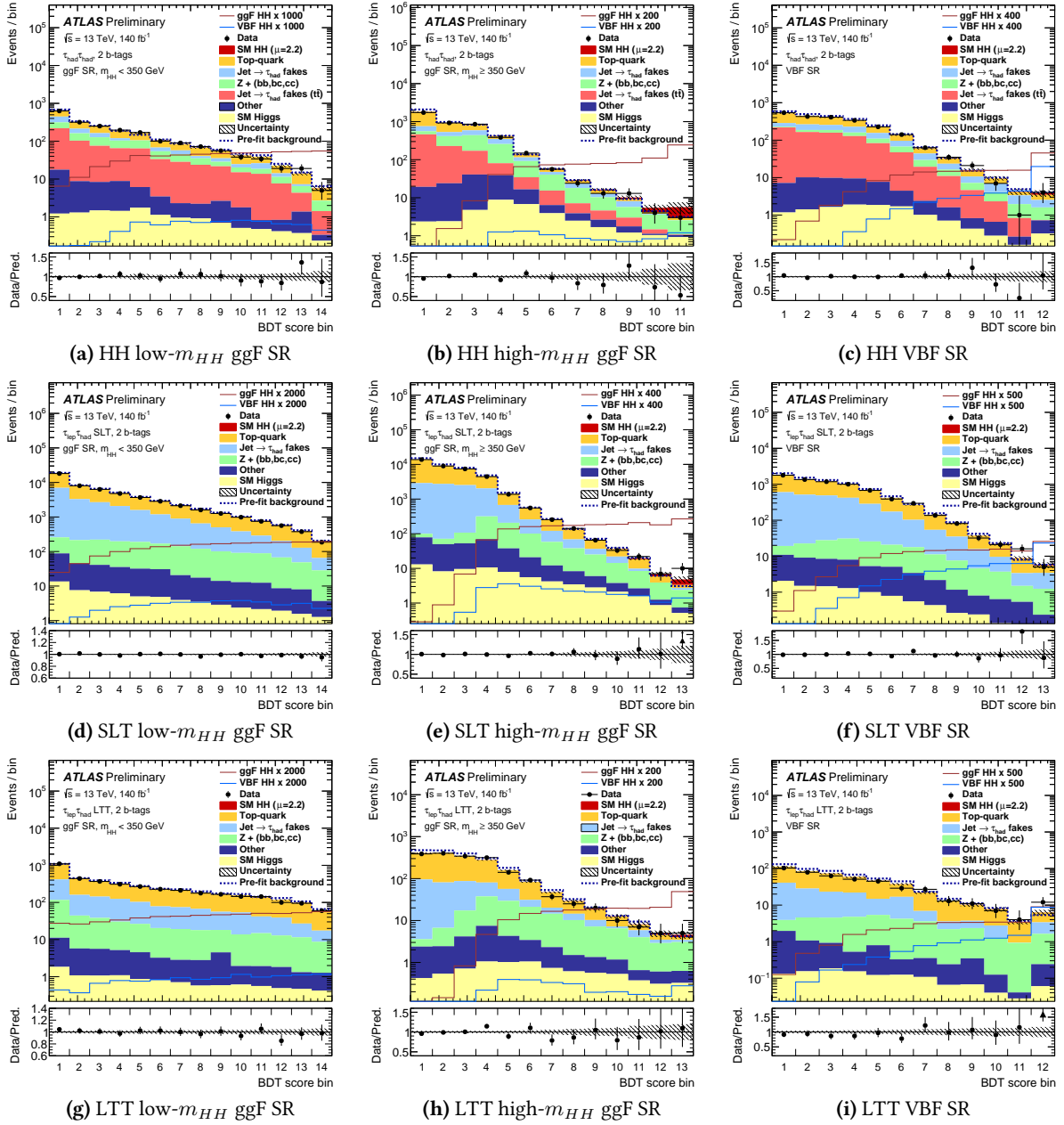


Figure 5.56: NP correlations from the combined fit to $\tau_{had}\tau_{had}$ and $\tau_{lep}\tau_{had}$ channel to the Asimov dataset in Figure (a) and to data in Figure (b). MC statistical uncertainties are not included in the correlations.

Figure 5.57: Post-fit BDT score distributions in the $\tau_{had}\tau_{had}$ and $\tau_{lep}\tau_{had}$ signal regions after the combined fit.

5.6.2 Limits and scans

5.6.2.1 $\tau_{\text{had}}\tau_{\text{had}}$

The upper limits at 95% confidence level (CL) for both observed and expected outcomes on the HH signal strength (ggF+VBF) are presented in Table 5.26, including individual production modes as well. These limits are derived from a one-dimensional fit of μ_{ggF} (μ_{VBF}) with the other signal strength fixed at 1, and a simultaneous two-dimensional fit of both μ_{ggF} and μ_{VBF} , where setting a limit on one allows the normalization factor of the other to fluctuate, in the $\tau_{\text{had}}\tau_{\text{had}}$ channel. Additionally, Table 5.27 delineates both observed and expected 95% CL intervals for κ_λ (κ_{2V}) values, determined via the negative log-likelihoods (NLL) as a function of κ_λ (κ_{2V}), under the assumption of the Standard Model (SM) HH production hypothesis.

Table 5.26: Observed and expected 95% CL limits on the HH signal strength (ggF+VBF) in the $\tau_{\text{had}}\tau_{\text{had}}$ channel, including individual production modes.

95% CL upper limits on	μ_{HH}	$\mu_{\text{ggF}}^{\text{1D}}$	$\mu_{\text{VBF}}^{\text{1D}}$	$\mu_{\text{ggF}}^{\text{2D}}$	$\mu_{\text{VBF}}^{\text{2D}}$
Observed	3.42	3.47	80	3.63	87
Expected	3.86	3.91	101	3.99	103

Table 5.27: 95% CL observed and expected intervals for κ_λ and κ_{2V} in the $\tau_{\text{had}}\tau_{\text{had}}$ channel.

	95% CI for κ_λ	95% CI for κ_{2V}
Observed	[-1.46, 7.97]	[-0.22, 2.40]
Expected	[-2.76, 9.44]	[-0.41, 2.59]

Figure 5.58 illustrates the likelihood scans for κ_λ and κ_{2V} parameters, both expected and observed. In these fittings, all other couplings influencing single-Higgs and di-Higgs productions are maintained at their SM predicted values, except for the parameter under consideration. Notably, for both κ_λ and κ_{2V} , the constraints are stronger than expected as a result of the negative signal strengths observed in data fittings. Specifically for κ_λ , the scan converges to the point with the minima cross-section given that the HH predictions cannot be zero for any value of the parameter.

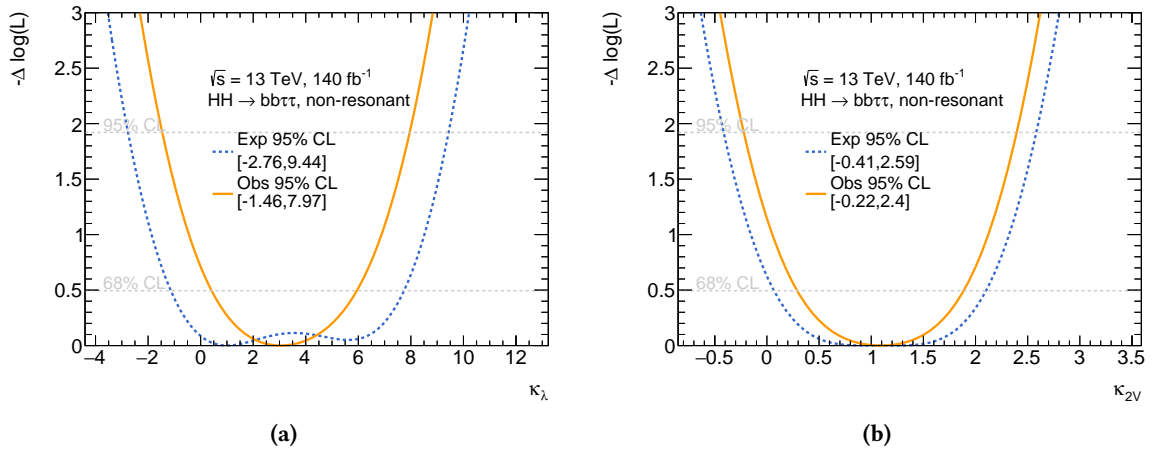


Figure 5.58: Negative log-likelihood ratio comparison for different κ_λ (a) and κ_{2V} (b) hypotheses, based on the fit to data and Asimov dataset constructed under the SM hypothesis in the $\tau_{\text{had}}\tau_{\text{had}}$ channel.

5.6.2.2 $\tau_{\text{lep}}\tau_{\text{had}}$

In Table 5.28, the upper limits at a 95% confidence level for both expected and observed results on the HH signal strength (ggF+VBF) are presented for the $\tau_{\text{lep}}\tau_{\text{had}}$ channels, including individual

production modes as well as their combination. Table 5.29 displays the 95% CL intervals for κ_λ (κ_{2V}) values, calculated using negative log-likelihoods (NLL) as a function of κ_λ (κ_{2V}), under the standard model (SM) hypothesis for HH production.

Table 5.28: 95% CL limits on the HH signal strength (ggF+VBF) in the $\tau_{\text{lep}}\tau_{\text{had}}$ channel, including individual production modes, both observed and expected.

95% CL upper limits on	μ_{HH}	$\mu_{\text{ggF}}^{1\text{D}}$	$\mu_{\text{VBF}}^{1\text{D}}$	$\mu_{\text{ggF}}^{2\text{D}}$	$\mu_{\text{VBF}}^{2\text{D}}$
Observed LTT	22.4	21.1	720	17.8	756
Observed SLT	16.4	16.7	155	16.9	133
Observed $\tau_{\text{lep}}\tau_{\text{had}}$	16.0	15.9	213	15.2	180
Expected LTT	19.7	20.2	317	21.1	322
Expected SLT	6.43	6.52	125	6.60	128
Expected $\tau_{\text{lep}}\tau_{\text{had}}$	5.98	6.04	112	6.14	115

Table 5.29: 95% CL intervals for κ_λ and κ_{2V} in the $\tau_{\text{lep}}\tau_{\text{had}}$ channel, both observed and expected.

	95% CI for κ_λ	95% CI for κ_{2V}
Observed LTT	[-9.04, 16.32]	[-4.88, 0.04], [2.27, 7.16]
Observed SLT	[-8.29, 0.90], [7.53, 14.37]	[-1.28, 3.47]
Observed $\tau_{\text{lep}}\tau_{\text{had}}$	[-7.87, 0.29], [8.01, 13.92]	[-1.54, 3.71]
Expected LTT	[-8.74, 15.82]	[-2.86, 5.14]
Expected SLT	[-5.01, 12.37]	[-0.67, 2.85]
Expected $\tau_{\text{lep}}\tau_{\text{had}}$	[-4.67, 11.87]	[-0.64, 2.83]

Figure 5.59 presents the NLL scans as a function of κ_λ and κ_{2V} , showcasing both expected and observed results for the $\tau_{\text{lep}}\tau_{\text{had}}$ channels, individually and combined. It is noted that the SLT channels primarily affect the sensitivity in terms of expected outcomes.

In the SLT channel, the observed κ_λ profile exhibits a minimum around -5, primarily affected by the excess in the high- m_{HH} region, indicating a preference for parameters that increase the signal contribution. Conversely, the lack of excess in the low- m_{HH} region disfavors the positive κ_λ value with an equivalent cross-section. The combined $\tau_{\text{lep}}\tau_{\text{had}}$ result for κ_λ is also notably affected by the SLT channel.

Regarding κ_{2V} , the LTT curve suggests a two-sigma level disfavor of the SM hypothesis because of the excess in the VBF SR. The absence of such excess in the SLT channel results in the best fit value aligning with the SM at approximately a one-sigma level.

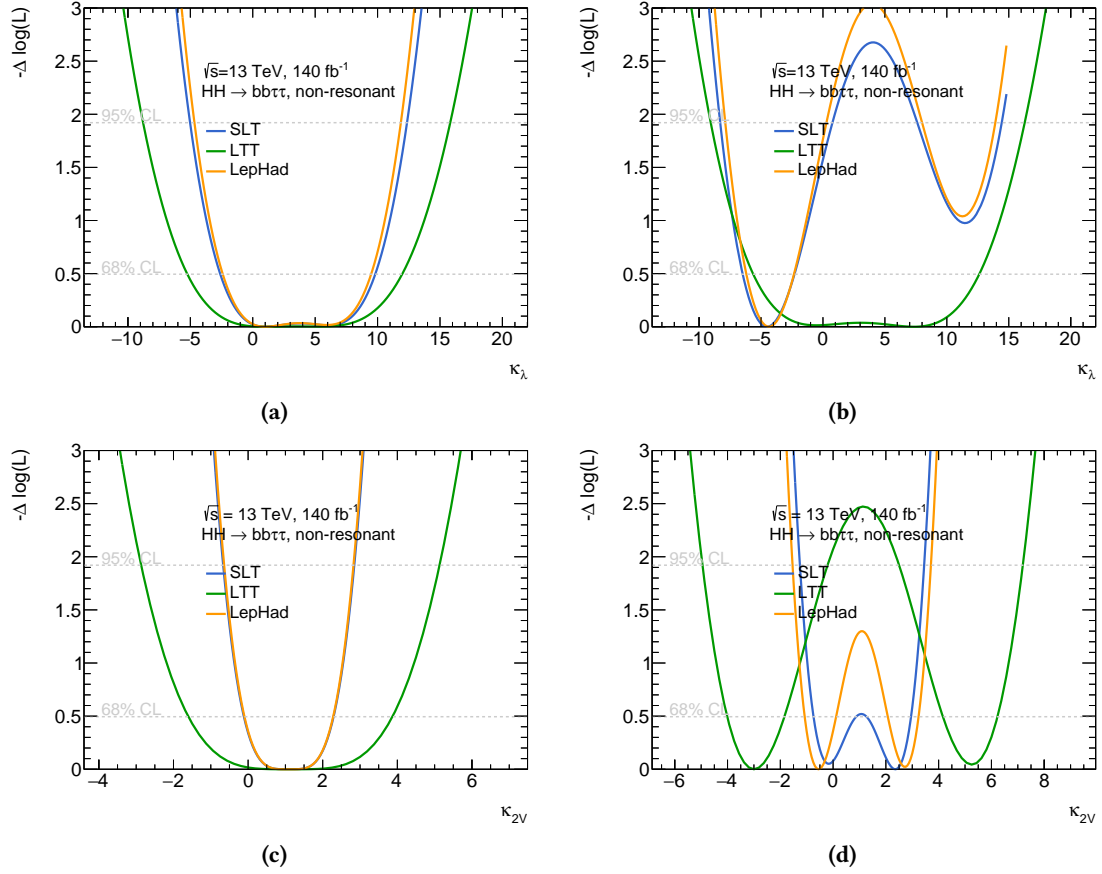


Figure 5.59: Negative logarithm of the likelihood ratio comparing different κ_λ (a) and κ_{2V} (c) hypotheses to an Asimov dataset (b) and data (d) in the $\tau_{\text{lep}}\tau_{\text{had}}$ channels, shown individually and combined.

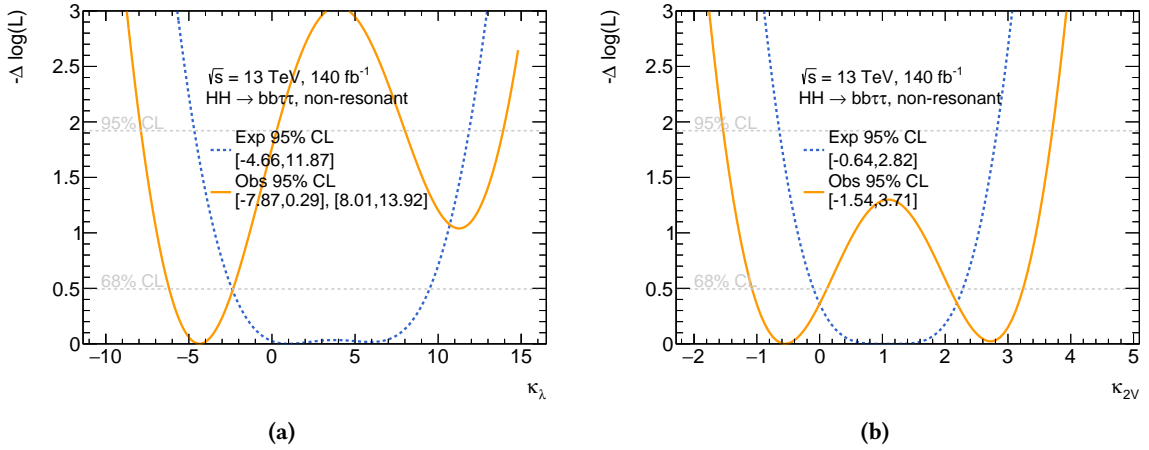


Figure 5.60: Negative logarithm of the likelihood ratio for different κ_λ (a) and κ_{2V} (b) hypotheses, based on fits to data and an Asimov dataset under the SM hypothesis in the $\tau_{\text{lep}}\tau_{\text{had}}$ channel.

5.6.2.3 Combined Limits

In Table 5.30, the observed and expected upper limits at the 95% confidence level (CL) are presented for the HH signal strength (ggF+VBF). This includes a breakdown for each production mode in both the $\tau_{\text{had}}\tau_{\text{had}}$ and $\tau_{\text{lep}}\tau_{\text{had}}$ channels, as well as their collective analysis. Table 5.31 illustrates the intervals at 95% CL for κ_λ (κ_{2V}) values, derived from the negative log-likelihoods (NLL) calculated as a function of κ_λ (κ_{2V}). These NLL scans were conducted under the assumption of the standard model (SM) hypothesis for HH production.

Table 5.30: Observed and expected 95% CL upper limits on μ_{HH} , μ_{ggF} and μ_{VBF} from the individual SR likelihood fits as well as the combined results. The μ_{ggF} and μ_{VBF} limits are quoted both from the results of the simultaneous fit of both signal strengths (central column), as well as from independent fits for the individual production modes, assuming the other to be SM-like. The uncertainties quoted on the combined expected upper limits correspond to the 1σ uncertainty band.

		μ_{HH}	μ_{ggF}	μ_{VBF}	$\mu_{ggF} (\mu_{VBF}=1)$	$\mu_{VBF} (\mu_{ggF}=1)$
$\tau_{had}\tau_{had}$	observed	3.4	3.6	87	3.5	80
	expected	3.9	4.0	103	3.9	101
$\tau_{lep}\tau_{had}$ SLT	observed	16	17	133	17	155
	expected	6.4	6.6	128	6.5	125
$\tau_{lep}\tau_{had}$ LTT	observed	22	18	767	21	731
	expected	20	21	323	20	317
Combined	observed	5.9	5.8	91	5.9	94
	expected	$3.1^{+1.3}_{-0.9}$	$3.2^{+1.7}_{-0.9}$	72^{+32}_{-20}	$3.2^{+1.7}_{-0.9}$	71^{+31}_{-20}

Summary plots of the observed and expected 95% CL upper limits on μ_{HH} from the individual SR likelihood fits as well as the combined results are shown in Figure 5.61.

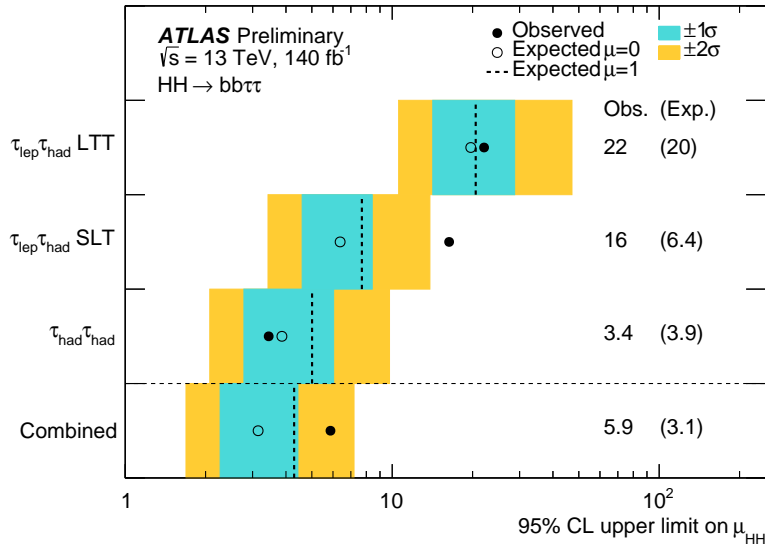


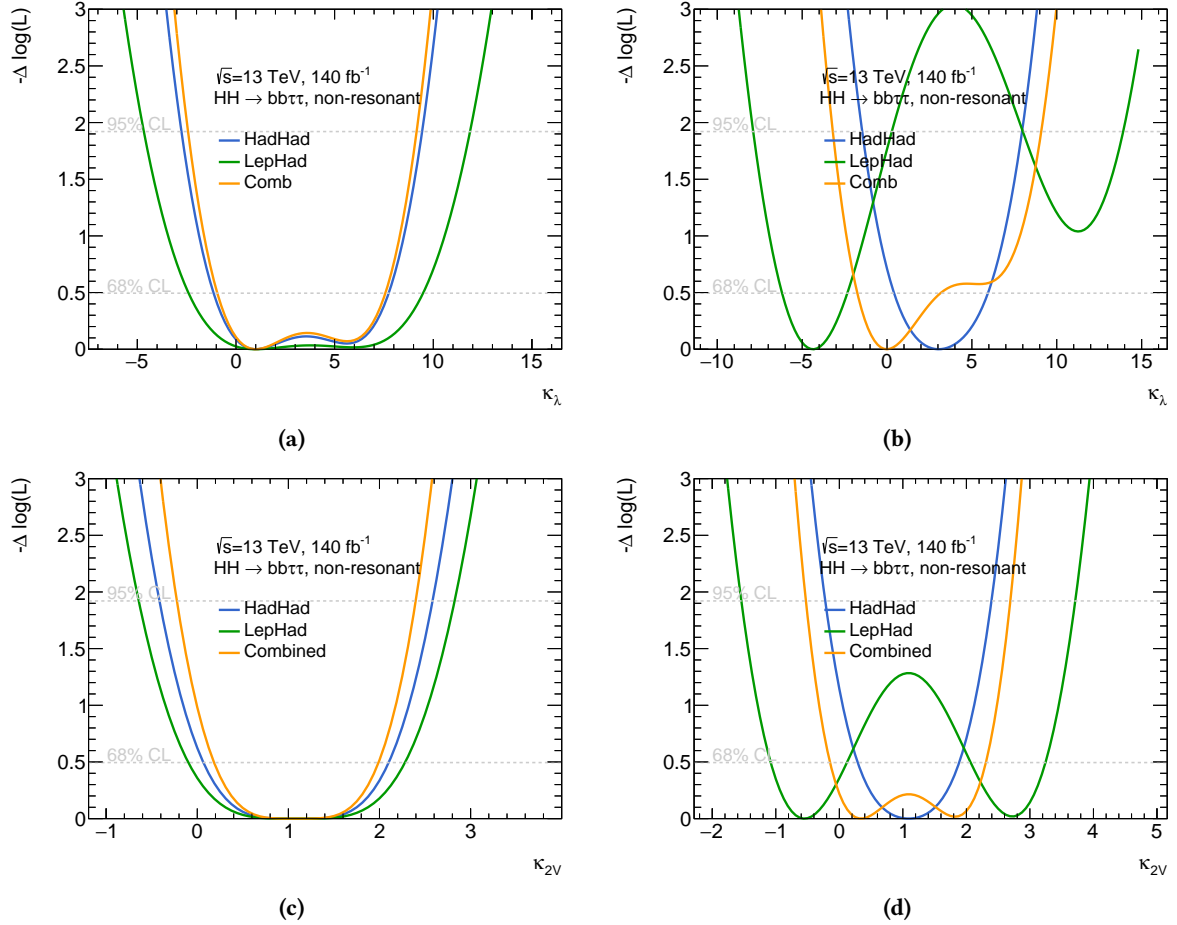
Figure 5.61: Summary of observed (filled circles) and expected (open circles) 95% CLs upper limits on μ_{HH} from the fit of each individual channel and the combined fit in the background-only ($\mu_{HH} = 0$) hypothesis. The dashed lines indicate the expected 95% CLs upper limits on μ_{HH} in the SM hypothesis ($\mu_{HH} = 1$). The cyan and yellow bands indicate the $\pm 1\sigma$ and $\pm 2\sigma$ variations on the expected limit with respect to the background-only hypothesis due to statistical and systematic uncertainties, respectively.

Table 5.31 shows the 95% CL intervals for κ_λ and κ_{2V} , as observed and expected in the $\tau_{lep}\tau_{had}$, $\tau_{had}\tau_{had}$ channels and their combination. A comparison of different channels and their combination is shown in Figure 5.62. Figure 5.63 shows the likelihood ratio's negative logarithm comparing various κ_λ and κ_{2V} hypotheses in the combined fit to data and an Asimov dataset formulated under the SM hypothesis.

Lastly, Figure 5.64 presents the 68% and 95% likelihood contours, both expected and observed,

Table 5.31: 95% CL intervals for κ_λ and κ_{2V} , as observed and expected in the $\tau_{\text{lep}}\tau_{\text{had}}$, $\tau_{\text{had}}\tau_{\text{had}}$ channels and their combination.

	95% CI for κ_λ	95% CI for κ_{2V}
Observed $\tau_{\text{lep}}\tau_{\text{had}}$	[-7.87, 0.29], [8.01, 13.92]	[-1.54, 3.71]
Observed $\tau_{\text{had}}\tau_{\text{had}}$	[-1.46, 7.97]	[-0.22, 2.40]
Observed Combined	[-3.19, 9.09]	[-0.53, 2.70]
Expected $\tau_{\text{lep}}\tau_{\text{had}}$	[-4.67, 11.87]	[-0.64, 2.83]
Expected $\tau_{\text{had}}\tau_{\text{had}}$	[-2.76, 9.44]	[-0.41, 2.59]
Expected Combined	[-2.43, 9.16]	[-0.22, 2.40]

**Figure 5.62:** Comparison of different κ_λ (a) and κ_{2V} (c) hypotheses against an Asimov dataset (b) and actual data (d), shown through the negative logarithm of the likelihood ratio. The curves represent both individual channels and their combined analysis.

for the simultaneous fit of κ_λ and κ_{2V} .

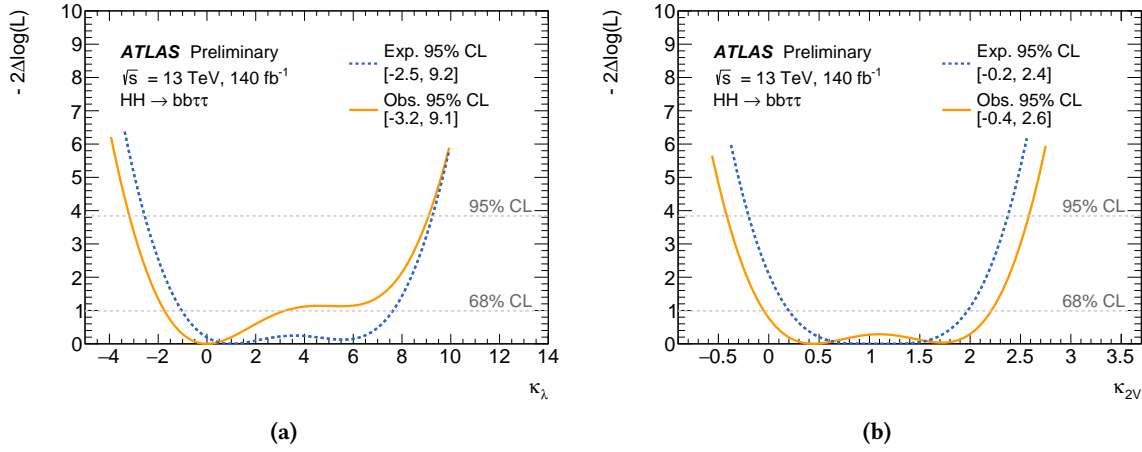


Figure 5.63: Likelihood ratio's negative logarithm comparing various κ_λ (a) and κ_{2V} (b) hypotheses in the combined fit to data and an Asimov dataset formulated under the SM hypothesis.

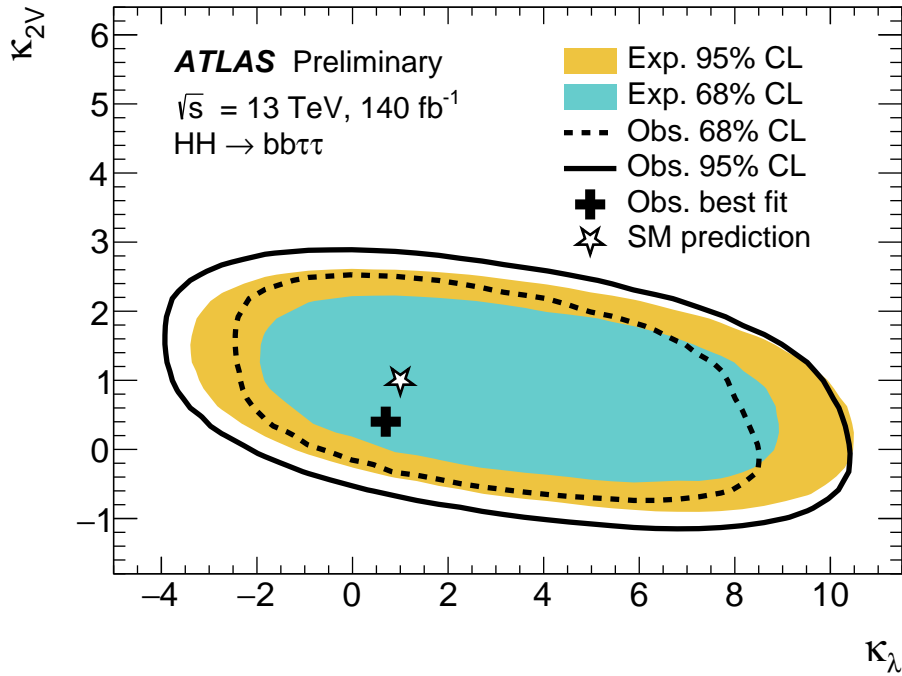


Figure 5.64: Simultaneous determination of κ_λ and κ_{2V} : 68% and 95% likelihood contours, both expected and observed, in the combined analysis. The SM prediction is indicated by the star, while the best-fit value is denoted by the black cross.

5.7 Conclusion

The analysis of non-resonant Higgs boson pair production in the $b\bar{b}\tau^+\tau^-$ final state has been updated in this study, utilizing the full Run 2 ATLAS dataset, which amounts to 140 fb^{-1} of proton-proton collisions at a centre-of-mass energy of 13 TeV. This analysis advances beyond the findings reported in a previous search (Ref. [4]) using the same dataset. Enhancements in the event classification have been implemented, primarily to improve sensitivity towards κ_λ and the Vector Boson Fusion (VBF) production mode. The employment of multivariate classifiers has improved the sensitivity to Standard Model HH production and to the coupling parameters κ_λ and κ_{2V} . The sensitivity of the analysis exhibits an improvement ranging from 10% to 20%, depending on the parameter of interest. Additionally, interpretations in the context of gluon-gluon Fusion (ggF) and VBF production modes have been incorporated, marking a significant extension over the findings

of Ref. [4]. Furthermore, the statistical methodology applied in interpreting the observed yields in terms of signal coupling modifiers has undergone refinement.

No conclusive evidence of the HH signal has been observed. The observed 95% confidence level (CL) upper limit for the HH production signal strength μ_{HH} is established at 5.9, contrasted with a predicted limit of 3.1 under the background-only hypothesis ($\mu_{HH} = 0$). This discrepancy between observed and expected limits is attributed to a slight excess observed in the $\tau_{\text{lep}}\tau_{\text{had}}$ SLT SR within the high- m_{HH} category. The 95% confidence intervals for κ_λ and κ_{2V} are observed (expected) to be $-3.2 < \kappa_\lambda < 9.1$ ($-2.5 < \kappa_\lambda < 9.2$) and $-0.4 < \kappa_{2V} < 2.6$ ($-0.2 < \kappa_{2V} < 2.4$) respectively.

Part III

Higgs Physics beyond LHC

The Future Circular Collider

6.1	Introduction of FCC project	192
6.1.1	Future Colliders	192
6.1.2	The Future Circular Collider	193
6.2	FCC Integrated program	194
6.2.1	FCC-ee	194
6.2.2	FCC-hh	194
6.3	Higgs Physics at Future Circular Colliders	194
6.3.1	Higgs-Electron Yukawa coupling	195
6.3.2	Trilinear Higgs self-coupling	195

This chapter provides a brief overview of the Future Circular Collider (FCC) project, a project spearheaded by the European Organization for Nuclear Research, commonly referred to as CERN.

The first official document outlining the FCC, the Conceptual Design Report (CDR), [9], [10], [11], and [12], was published in January 2019.

The FCC project, also known as the FCC Integrated program (FCC-Int), can be broken down into two main stages: the FCC Electron-Positron Collider (FCC-ee) and the FCC Hadron-Hadron Collider (FCC-hh).

The important step of studying the feasibility of the FCC began in 2021, and a mid-term review of this Feasibility Study is being done in this fall of 2023 [13]. This will serve as an important check point for the progress the project.

The arrangement of this chapter is as follows:

In Section 6.1, I present an Introduction of the Future Circular Collider (FCC) project. This sets the scene for a broader discourse on forthcoming collider projects, addressed in Subsection 6.1.1.

Section 6.1.2 delves into the nuances of the FCC, providing an in-depth exhibition of this leading-edge project.

Section 6.2 discuss the specifics of the FCC Integrated (FCC-Int)program. Within this section, the FCC-Int is divided into two major components: the FCC Electron-Positron Collider (FCC-ee) and the FCC Hadron-Hadron Collider (FCC-hh). These components are discussed in Section 6.2.1 and Section 6.2.2 respectively, facilitating a comprehension of the multiples aspects of the FCC project.

Finally, Section 6.3 provides a brief overview of the physics program of the FCC.

6.1 Introduction of FCC project

The Large Hadron Collider (LHC) is planning to stop in the year 2041, and the High-Luminosity LHC (HL-LHC) could be the last upgrade of the LHC. After the LHC, another accelerator is needed to continue the exploration of the high energy frontier, and understand better the Standard Model (SM) and the universe. There are still many unsolved mysteries in the SM, such as the origin of the matter-antimatter asymmetry, the nature of dark matter, the hierarchy problem, the neutrino mass, etc. For the Higgs model, if the second Higgs doublet exist.

The FCC program was proposed as a successor of the LHC and can re-use the existing infrastructure at CERN in particular the injector chain.

The CERN Council launched the FCC Feasibility Study in 2021, and the Feasibility-Study "mid-term review" is scheduled for autumn 2023 [13]. This Feasibility Study is designed to establish the necessary foundation for the initial stage of the FCC integrated project. This stage includes not only the construction of the tunnel and the development of technical infrastructure, but also the implementation of the electron-positron collider (FCC-ee). Furthermore, it involves creating suitable financial and organizational models. Alongside this, the study will ensure compatibility with a subsequent hadron collider (FCC-hh), while keeping the R&D directions defined and setting a time schedule for the creation of the high-field magnets required for this later stage.

6.1.1 Future Colliders

Two types of e^+e^- accelerators, a linear and a circular collider, have been proposed by the particle physics community. For linear colliders, the International Linear Collider (ILC) was proposed to be constructed in Japan, while the Compact Linear Collider (CLIC) was proposed by CERN. Both are electron-positron colliders working at different centre-of-mass (c.o.m.) energies (\sqrt{s}). For circular colliders, CERN proposes the Future Circular Collider (FCC), while the Chinese community proposes the Circular Electron-Positron Collider (CEPC). The designs of the FCC and CEPC are similar. Both of them will initially operate as electron-positron machines, then be upgraded to become hadron colliders.

This thesis will primarily concentrate on the feasibility study of the Future Circular Collider (FCC). Additional details and findings will be elaborated upon in subsequent sections.

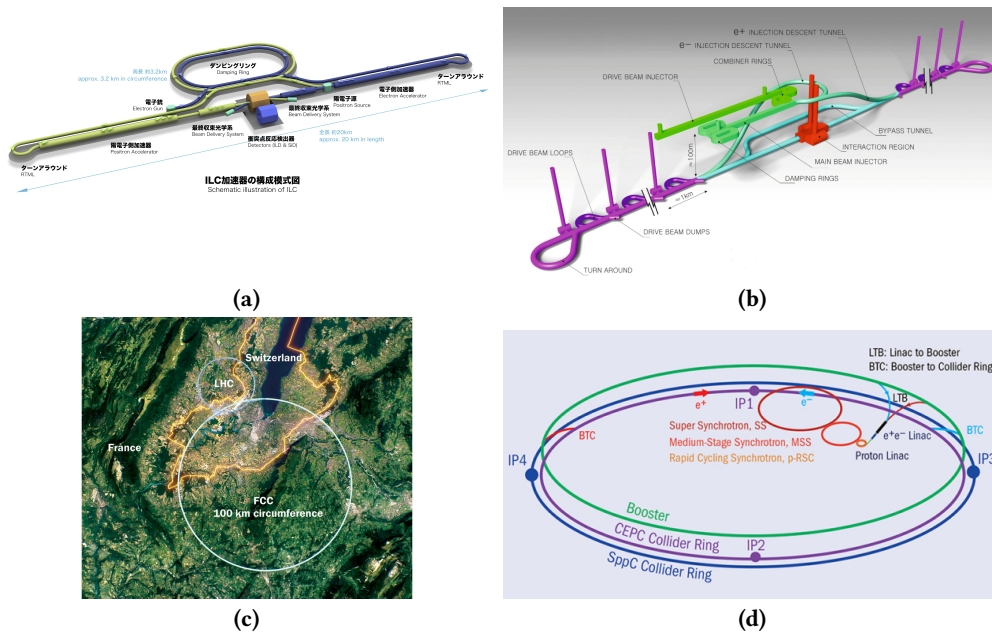


Figure 6.1: Comparison of different particle accelerator layouts: (a) International Linear Collider (ILC), (b) Compact Linear Collider (CLIC), (c) Future Circular Collider (FCC), and (d) Circular Electron Positron Collider (CEPC).

6.1.2 The Future Circular Collider

The current strategy for the Future Circular Collider (FCC), which was agreed upon in 2020, prioritizes the creation of an electron-positron Higgs boson factory as the most critical facility following the Large Hadron Collider (LHC). This strategy also includes investigating the technical and financial feasibility of such a Higgs boson factory. Additionally, plans have been outlined for a hadron collider, which would be placed in the same 90km-long tunnel.

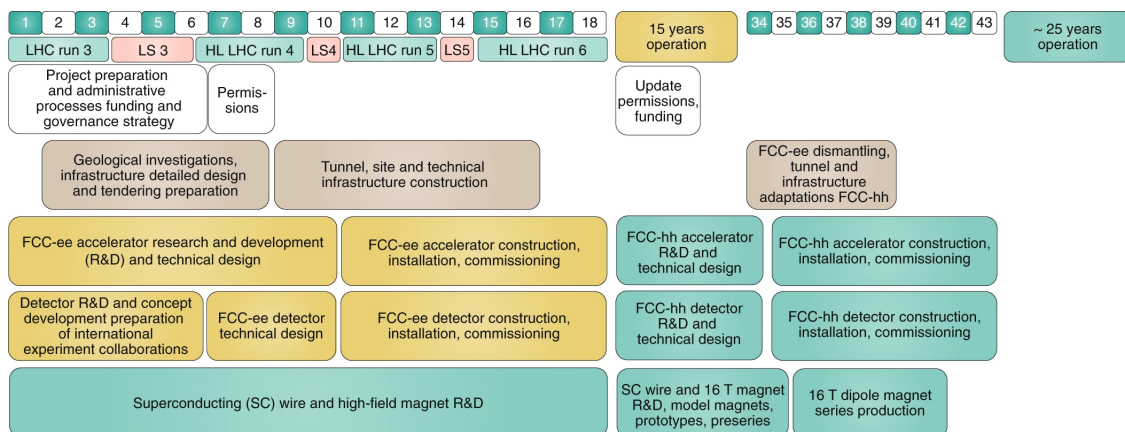


Figure 6.2: FCC Integrated Program from Ref. [181]

As per Ref. [181], the five-year feasibility studies for the Future Circular Collider (FCC) began in 2021, during the LHC-Run3, as part of an 18-year preparation phase. The next European Strategy meeting, which is set to take place around 2026, will decide whether to approve the project. If approved, civil engineering efforts, as well as the construction of accelerators and detectors, will commence. The entire FCC integrated program (FCC-INT) bears resemblance to the LEP-LHC program, where the Large Electron-Positron collider was followed by the LHC in the same tunnel. The first stage of FCC, operating as an electron-positron machine (FCC-ee), will run at different

centre-of-mass (c.o.m.) energy points for 15 years. Subsequently, there will be a 10-year long shut-down to upgrade the machine to an FCC hadron collider (FCC-hh), which will involve changing the magnets and detectors. Following this upgrade, FCC-hh will run for 25 years to acquire data.

6.2 FCC Integrated program

6.2.1 FCC-ee

The FCC will initially operate as an electron-positron collider, functioning at various center-of-mass energy levels, as outlined in Table 6.1. The collider is scheduled to run at the Z pole for a four-year period, during which it aims to accumulate 150 ab^{-1} of data. Subsequently, it will shift to the W^+W^- production threshold and operate for two years.

The FCC will run at the ZH threshold (240 GeV) for three years, with the goal of accumulating 7.2 ab^{-1} of data. This phase of operation will effectively transform the collider into a Higgs factory, enabling precise measurements of Higgs boson properties. Ultimately, the FCC will reach its highest energy level of 365 GeV to investigate the $t\bar{t}$ events, and also to investigate the Higgs width, Higgs self-coupling.

It may optionally run at the Higgs mass ($\sqrt{s} = 125 \text{ GeV}$) to directly measure the electron Yukawa coupling. Ref. [182]

Table 6.1: The baseline FCC-ee operation model with four interaction points, showing the centre-of-mass energies, instantaneous luminosities for each IP, integrated luminosity per year summed over 4 IPs corresponding to 185 days of physics per year and 75% efficiency.

	Z, years 1-2	Z, later	WW, years 1-2	WW, later	ZH	$t\bar{t}$
\sqrt{s} (GeV)	88, 91, 94		157, 163		240	340-350 365
Lumi/IP ($10^{34} \text{ cm}^{-2} \text{ s}^{-1}$)	70	140	10	20	5.0	0.75 1.20
Lumi/year (ab^{-1})	34	68	4.8	9.6	2.4	0.36 0.58
Run time (year)	2	2	2	0	3	1 4
Number of events	$6 \times 10^{12} \text{ Z}$		$2.4 \times 10^8 \text{ WW}$		$1.45 \times 10^6 \text{ HZ}$ $+4.5 \times 10^4 \text{ WW} \rightarrow \text{H}$	$1.9 \times 10^6 \text{ } t\bar{t}$ $+3.3 \times 10^5 \text{ HZ}$ $+8 \times 10^4 \text{ WW} \rightarrow \text{H}$

In this dissertation, we undertake a comprehensive investigation of the Higgs boson mass determination and the ZH cross-section measurement at the ZH production threshold, characterized by a center-of-mass energy of 240 GeV.

6.2.2 FCC-hh

After the electron-positron phase, the FCC will be upgraded into a proton-proton collider, referred as FCC-hh. It is expected to achieve the highest center-of-mass energy of 100 TeV, with the integrated luminosity of 30 ab^{-1} . It will offer a unique opportunity to explore the TeV scale, with large production rates of Higgs bosons at high transverse momentum for various production channels.

6.3 Higgs Physics at Future Circular Colliders

Beside the Higgs mass and ZH cross-section measurements, which will be detailed in the next Chapter 7, there are many other Higgs physics topics that is proposed to be studied at FCC.

6.3.1 Higgs-Electron Yukawa coupling

The electron Yukawa coupling measurement was studied in [182]. After achieving the MeV precision on the Higgs boson mass, the electron Yukawa coupling could be measured via the resonant s-channel $e^+e^- \rightarrow H$ by operating the FCC-ee at $\sqrt{s} = m_H$. So far, the Yukawa couplings have been measured only for top (t), bottom (b) quarks and τ lepton. At the end of the high luminosity LHC (HL-LHC) era, part of the Higgs boson Yukawa couplings to the second family fermions will be probed. But the Yukawa coupling to the first family fermion is difficult to probe since the Higgs boson branching ratio is proportional to the square of the mass of the fermion. The resonant Higgs boson production was considered so far only for a muon collider since the cross-section of $e^+e^- \rightarrow H$ is about 1.64 fb while for muon ($\mu^+\mu^- \rightarrow H$) the cross-section is 70 pb . There are several challenges for this measurement. First, we need a very accurate knowledge of the Higgs mass, which is expected to be achieved with the ZH recoil studies. Second, the ISR and BES needs to be known at about the MeV level. And finally, several backgrounds have to be known precisely. But this measurement has many fundamental physics motivations and implications. In particular, the Higgs mechanism for first family of fermions can be probed experimentally, and the existence of a particle that is quasi-degenerate with Higgs boson mass can be studied.

6.3.2 Trilinear Higgs self-coupling

The Higgs boson self-coupling measurement at FCC was studied in [183] and [184]. The self-coupling can be measured at FCC-ee using the loop-induced modifications to single-Higgs production. If we include all the FCC-ee running, a precision of 42% can be achieved on κ_λ . It will be reduced to 34% in combination with HL-LHC data, to 21% with 4 interaction points (IP). If we have four interaction points (IPs), the Higgs boson self-coupling could be discovered at FCC-ee. It would be reduced to 12% if only κ_λ is allowed to vary and the other parameters are taken at their SM values. The FCC-hh has the potential to reach a precision better than 5% on κ_λ from di-Higgs production in combination with the precise Higgs boson decay branching ratio measurements from the FCC-ee.

Higgs mass and cross-section measurements at the Future Circular Collider

7.1	Introduction to ZH recoil analysis	199
7.2	"Recoil mass" method	200
7.3	IDEA	202
7.3.1	Muon and electron performance	203
7.4	Monte-Carlo samples	203
7.4.1	Event generators	204
7.5	Event Selection	208
7.5.1	Preselection Requirements	208
7.5.2	Kinematic Requirements	208
7.5.3	Basic and Baseline selections	209
7.5.4	Event yields and requirement flow	209
7.6	Higgs mass measurement	212
7.6.1	Event categorization	212
7.6.2	Signal modeling	213
7.6.3	Background modeling	215
7.6.4	Results	215
7.6.5	Auxiliary fit configurations	217
7.7	ZH Cross-section measurement	219
7.7.1	Boosted Decision Tree	221
7.7.1.1	Training samples	221
7.7.1.2	Input variables	222
7.7.1.3	Hyper-parameters	223
7.7.1.4	BDT performance	223
7.7.2	Fitting Strategy	227
7.7.2.1	Fit on recoil mass distribution (m_{recoil})	227
7.7.2.2	Fit on BDT score distribution	229
7.7.3	Conclusion	231
7.8	Sources of systematic uncertainties	231
7.8.1	Beam Energy Spread (BES)	232
7.8.2	Initial State Radiation (ISR)	233
7.8.2.1	ISR treatment in WHIZARD	233
7.8.2.2	Comparison with KKMC	234
7.8.3	Center-of-mass (COM)	235
7.8.4	Lepton momentum scale (LEPSCALE)	236
7.8.5	Lepton momentum resolution (LEPRES)	237
7.8.6	Final State Radiation (FSR)	237
7.8.7	Signal modeling (SIGM)	237

7.8.8 Background modeling (BKGM)	237
7.9 Experimental requirements	237
7.10 Conclusion	238

In this chapter, I will present my contribution to the feasibility study of the Higgs boson mass and cross-section measurements at the Future Circular Collider (FCC). FCC, as described in the previous chapter, is a next-generation particle collider project proposed by the European Organization for Nuclear Research (CERN). The first Conceptual Design Report (CDR) of the FCC was published in January 2019 [9–12].

The Higgs mass and cross-section measurements are one of the most important physics feasibility study of the FCC, since it can determine the Higgs boson mass at MeV level precision, and measure the Higgs boson production cross-sections at per mille level precision. The Higgs width, with theoretical prediction is 4.1 MeV [14], can be determined at the percent level. The cross-section measurement can also be used to constrain the Higgs boson couplings to the Z boson (g_{HZZ}) as a standard "candle", then to determine other Higgs boson couplings.

Benefiting from the initial state information at the electron-positron collider, the recoil mass technique is used in this study, to calculate the mass of the system recoiling against the reconstructed Z boson, which ensure the measurements are independent of the Higgs information. Without making any assumptions on the Higgs boson decay modes, the ZH cross-section can be measured inclusively. Any discrepancy of the ZH cross-section measurement would indicate that the Higgs boson decay modes are not fully understood, or there are new physics beyond the Standard Model (SM).

The $Z \rightarrow \mu^+\mu^-$ and $Z \rightarrow e^+e^-$ final states are used in this study, since they have the cleanest experimental signature, and the best mass resolution.

This chapter is organized as following, then an overview of the Higgs boson physics at the FCC using Higgsstrahlung channels is given in Section 7.1. The recoil mass technique is introduced in Section 7.2, the Monte Carlo samples used in this study are described in Section 7.4, the event selection is described in Section 7.5. The Higgs boson mass measurement is presented in Section 7.6, and the ZH cross-section measurement is presented in Section 7.7. The systematic uncertainties are discussed in Section 7.8, and the conclusion is given in Section 7.10.

7.1 Introduction to ZH recoil analysis

The FCCee (Future Circular Collider in the Electron-Positron collision mode) is designed to operate at several center-of-mass energies \sqrt{s} , to develop a rich physics programme [10]. In particular, it will run at $\sqrt{s} = 240$ GeV, where it is expected to generate approximately 10^6 $e^+ + e^- \rightarrow ZH$ events in three years of data taking. Although $qq \rightarrow e^+ + e^- \rightarrow ZH$ events have been previously observed in the ATLAS detector [185] and CMS [186], the much smaller background at FCC-ee will enable unprecedented precision in the measurement of Higgs boson properties using $e^+e^- \rightarrow e^+ + e^- \rightarrow ZH$ events.

At $\sqrt{s} = 240$ GeV, the main Higgs production modes are the "Higgsstrahlung" process, $e^+ + e^- \rightarrow ZH$, and to a lesser extent, the WW fusion process, $e^+ + e^- \rightarrow \nu_e \bar{\nu}_e H$, as shown in Figure 7.1.

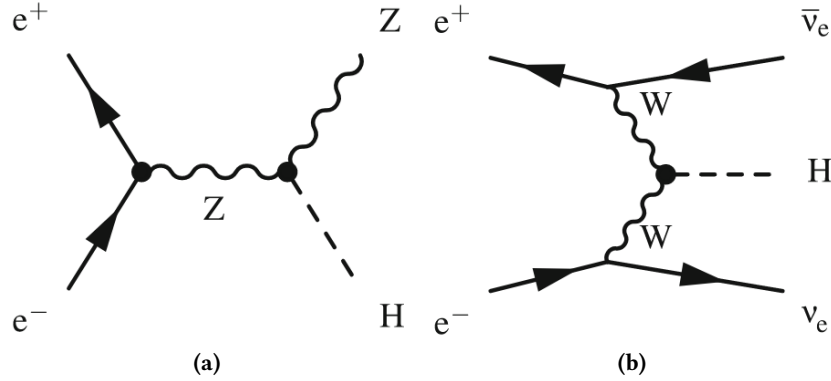


Figure 7.1: Main diagrams of the Higgs production modes at $\sqrt{s} = 240$ GeV: (a) represents the Higgsstrahlung process, (b) represents the WW fusion process, Adapted from Ref. [187]

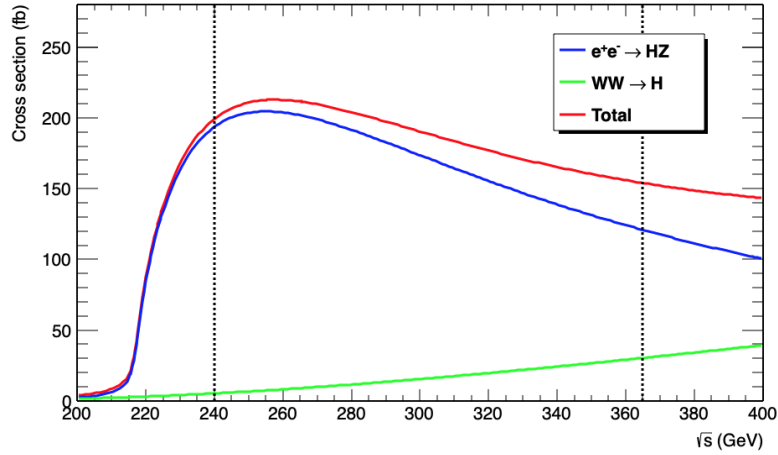


Figure 7.2: Improved-Born Higgs production cross-sections for the Higgsstrahlung process and the WW fusion process (see Figure 7.1), incorporating initial state radiation [188], are predicted by HZHA [189] as a function of center-of-mass energy with a Higgs boson mass m_h of 125 GeV. The minor interference term between the two diagrams in the final state is integrated into the WW fusion cross-section. Vertical dashed lines represent the anticipated \sqrt{s} values at the FCC-ee. Adapted from Ref. [187].

In comparison to hadron collisions, electron-positron collisions offer the unique advantage of knowing the precise center-of-mass energy for each event. In hadron colliders, the initial momentum of the interacting gluons or quarks remains unknown, necessitating the use of parton distribution functions. Conversely, electron-positron colliders involve collisions between elementary particles thereby eliminating the need for parton distribution functions and enabling a more accurate understanding of the initial conditions of the system. Consequently, lepton colliders serve as ideal candidates for conducting precise measurements in the realm of particle physics.

In Higgsstrahlung events, since the center-of-mass energy of the collision is known, we can acquire information on the recoiling Higgs boson, just by studying the associated Z boson, as detailed in Section 7.2. This boson comprises a pair of leptons ($\ell^+ \ell^-$) or quarks ($q \bar{q}$) and does not require prior knowledge of the Higgs information. Consequently, we can carry out a Higgs model-independent study.

By quantifying the number of events related to Higgsstrahlung and WW fusion processes, we can ascertain their respective inclusive cross-sections. Examining the distribution of the recoil mass (m_{rec}) allows us to extract the Higgs mass with uncertainty at the MeV level.

We can analyze various Higgs decay modes ($H \rightarrow X \bar{X}$). The cross-section times the branching ratio is proportional to the square of the respective coupling strengths. This relationship can be expressed as follows:

$$\sigma_{ZH} \times Br(H \rightarrow X \bar{X}) \propto \frac{g_{HZZ}^2 \times g_{HXX}^2}{\Gamma_H}, \quad (7.1.1)$$

$$\sigma_{H\nu_e \bar{\nu}_e} \times Br(H \rightarrow X \bar{X}) \propto \frac{g_{HWW}^2 \times g_{HXX}^2}{\Gamma_H}. \quad (7.1.2)$$

Here, σ_{ZH} and $\sigma_{H\nu_e \bar{\nu}_e}$ represent the inclusive cross-sections of the Higgsstrahlung and WW fusion processes, respectively. $Br(H \rightarrow X \bar{X})$ denotes the branching ratio of Higgs decays into an $X \bar{X}$ particle pair, which can be any known or unknown particle. g_{HXX} is the Higgs coupling constant, and Γ_H is the Higgs width. Equation 7.1.1 demonstrates the proportionality for the ZH production process, while Equation 7.1.2 illustrates the proportionality for the $\nu_e \bar{\nu}_e H$ production process.

By analyzing the Higgs boson decay to a pair of Z boson, $H \rightarrow ZZ$, we can extract the Higgs coupling to two Z bosons, denoted as g_{HZZ} . This coupling can be determined from Equation 7.1.1

$$\sigma_{ZH} \times Br(H \rightarrow ZZ) \propto \frac{g_{HZZ}^4}{\Gamma_H}.$$

Once obtained, g_{HZZ} serves as a "standard candle" to facilitate the study of other Higgs decay channels. This approach allows us to determine all the Higgs couplings, g_{HXX} , thereby providing a comprehensive understanding of the Higgs boson's properties and its interactions with other particles.

The Higgs mass is a fundamental parameter of the Standard Model (SM) and will be measured by the HL-LHC up to a precision of approximately 20 MeV [190]. Although radiative corrections to all other SM only depends logarithmically on m_H , to fully exploit the FCC-ee potential in measuring the cross-sections and branching fractions, the Higgs mass has to be known up to a 10 MeV level. Furthermore, a potential run at the Higgs resonance of $\sqrt{s} = 125$ GeV could probe the electron-Yukawa coupling via s-channel Higgs production and requires precision of the Higgs mass equal or better to its width, i.e. around 4 MeV [182].

Both the cross-section and mass measurements are challenging and put stringent requirements on the detector and machine parameters, which is the scope of this section. It extends the initial studies as described in Ref. [187], to a more complete analysis with a robust evaluation of the uncertainties.

7.2 "Recoil mass" method

In this section, we present the technical aspects of the recoil technique. The previous results with the Higgs boson recoil mass method have been documented in Reference [187].

In this dissertation, I extend the previous results with new techniques. I focus on the leptonic

decays of the Z boson ($Z \rightarrow \ell^+ \ell^-$, where $\ell = e$ or μ) for mass and cross-section measurements. This choice offers greater precision and enables inclusive and efficient selection of ZH events, regardless of the Higgs boson decay mode. As a result, this method effectively facilitates an almost entirely model-independent determination of the HZZ coupling (g_{HZZ}). However, the small Z di-electron and di-muon branching ratios, Table 7.1, reduce the statistical accuracy but allow for better resolution.

Table 7.1: Z Decay Modes Branching Ratios, adapted from [14]

Decay Mode	Branching Ratio
$Z \rightarrow e^+ e^-$	$3.3632 \pm 0.0042\%$
$Z \rightarrow \mu^+ \mu^-$	$3.3662 \pm 0.0066\%$
$Z \rightarrow \tau^+ \tau^-$	$3.3696 \pm 0.0083\%$
$Z \rightarrow l^+ l^-$	$3.3658 \pm 0.0023\%$
$Z \rightarrow \text{invisible}$	$20.000 \pm 0.055\%$
$Z \rightarrow \text{hadrons}$	$69.911 \pm 0.056\%$
$Z \rightarrow c\bar{c}$	$12.03 \pm 0.21\%$
$Z \rightarrow b\bar{b}$	$15.12 \pm 0.05\%$

The mass m_{recoil} recoiling against the lepton pair is calculated using total energy-momentum conservation, as represented in Equation 7.2.1 and illustrated in Figure 7.3 by computing the difference of the four-vector of center-of-mass energy and lepton pair system.

$$m_{\text{recoil}}^2 = (\sqrt{s} - E_{l^+ l^-})^2 - p_{l^+ l^-}^2 = s - 2E_{l^+ l^-} \sqrt{s} + m_{l^+ l^-}^2 \quad (7.2.1)$$

Here, \sqrt{s} represents the center-of-mass energy, $E_{l^+ l^-}$ denotes the energy of the di-lepton system, and $m_{l^+ l^-}$ refers to the invariant mass of the di-lepton system.

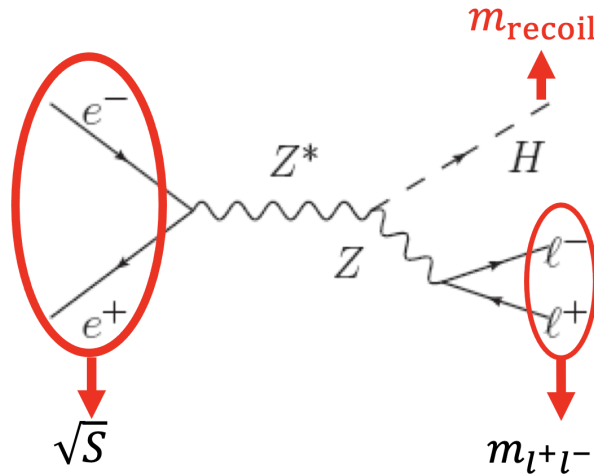


Figure 7.3: Feynman diagram illustrating the Higgsstrahlung process and the recoil mass (m_{recoil}) calculation. Adapted from [191].

Figure 7.3 provides a visual representation of the calculation using the leading order Feynman diagram of the ZH production process. Since it uses the center-of-mass energy, the recoil mass is sensitive to its precise knowledge, which can be affected by the Beam Energy Spread (BES) and Initial State Radiation (ISR) of the incoming leptons.

The main backgrounds come from the WW, ZZ, and Z/γ processes as can be seen from Figure 7.4, which displays the m_{rec} distribution of both signal and background events after a basic selection

described in Section 7.5, in the range 40 to 160 GeV. Two prominent peaks are visible: the largest one, around 91 GeV, is stemming from the ZZ process; the other one is around 125 GeV, and it originates from the $e^+ + e^- \rightarrow ZH$ process.

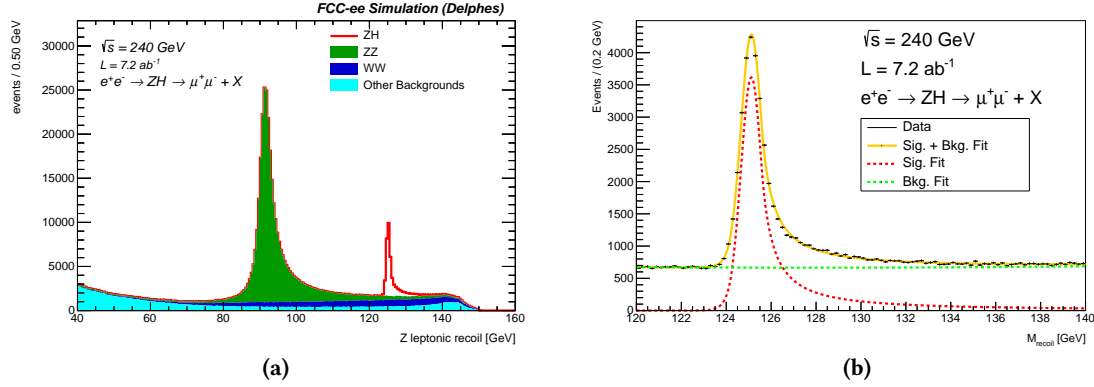


Figure 7.4: (a) displays the inclusive m_{rec} distribution for events where a Z boson decays into a $\mu^+ \mu^-$ pair, with energies ranging from 40 to 160 GeV, after the basic selection described in Section 7.5. The Z and Higgs mass peaks are clearly visible in this distribution. Reproduced according to [187]. (b) shows the zoomed-in view of the m_{rec} distribution in the vicinity of m_h . The ZH signal is fitted using a double-sided Crystal Ball function, while the simulated background is fitted with a second-order polynomial. Reproduced according to [187].

Figure 7.4a shows the m_{recoil} distribution of both signal and background events in the range of 40 to 160 GeV. Two prominent peaks are visible: one around 125 GeV, originating from the ZH process, and another around 91 GeV, stemming from the ZZ process.

Figure 7.4b illustrates an example of a combined signal and background fit. The signal modeling employs a Double-Sided Crystal Ball function, while the background representation utilizes a polynomial function.

The Double-Sided Crystal Ball function features a Gaussian core, accompanied by two tails characterized by exponential functions. More details on the fitting functions will be discussed in Section 7.6.2.

Ultimately [187], the σ_{ZH} accuracy and the Higgs boson mass are expected to achieve 0.5% and MeV level respectively. After measuring the ZH cross-section, the couplings of HZZ, g_{HZZ} and Higgs boson width (Γ_H) can be determined and are expected to achieve per mil precision.

7.3 IDEA

For this study, the Innovative Detector for an Electron-positron Accelerator (IDEA) was selected as the default detector model for the MC simulations. Its design consists of a 5-layered silicon pixel vertex detector surrounded by a very light tracking drift chamber with up to 112 sensitive layers leading to excellent tracking performances. Both tracking devices are inside a 2 T thin solenoid. A dual-readout calorimeter is placed outside the solenoid to identify and measure both the electromagnetic and hadronic particles. Finally, the detector is enclosed by μ -RWELL muon chambers, a technology based on Resistive Plate Chambers and Gas Electron Multiplier detectors. The key feature of IDEA is to have a large tracking volume with a small yoke for optimal track resolution. In this study, a slight variant of IDEA is used, where the electromagnetic calorimeter is replaced by a crystal ECAL, improving the electron resolution significantly.

7.3.1 Muon and electron performance

The IDEA drift chamber is very transparent, up to 5 % X_0 in the central region and 10 % X_0 in the forward region, as can be seen from Figure 7.5a. The corresponding muon momentum resolution as a function of the momentum and azimuthal angle θ is shown on the right of Figure 7.5b. Excellent performance is achieved with muon momentum resolutions better than 0.1 %.

Electrons are subject to Bremsstrahlung and therefore have degraded reconstructed performance. However, the Bremsstrahlung photons can be detected in the ECAL and part of the energy can be recovered. Especially with the crystal ECAL, the energy recovery is maximized. Full simulation studies have shown that the equivalent degradation of electron tracks in the IDEA+crystal detector amounts to a factor of 1.25 w.r.t. the muon track resolution. The factor 1.25 is applied to the DELPHES simulation for electrons.

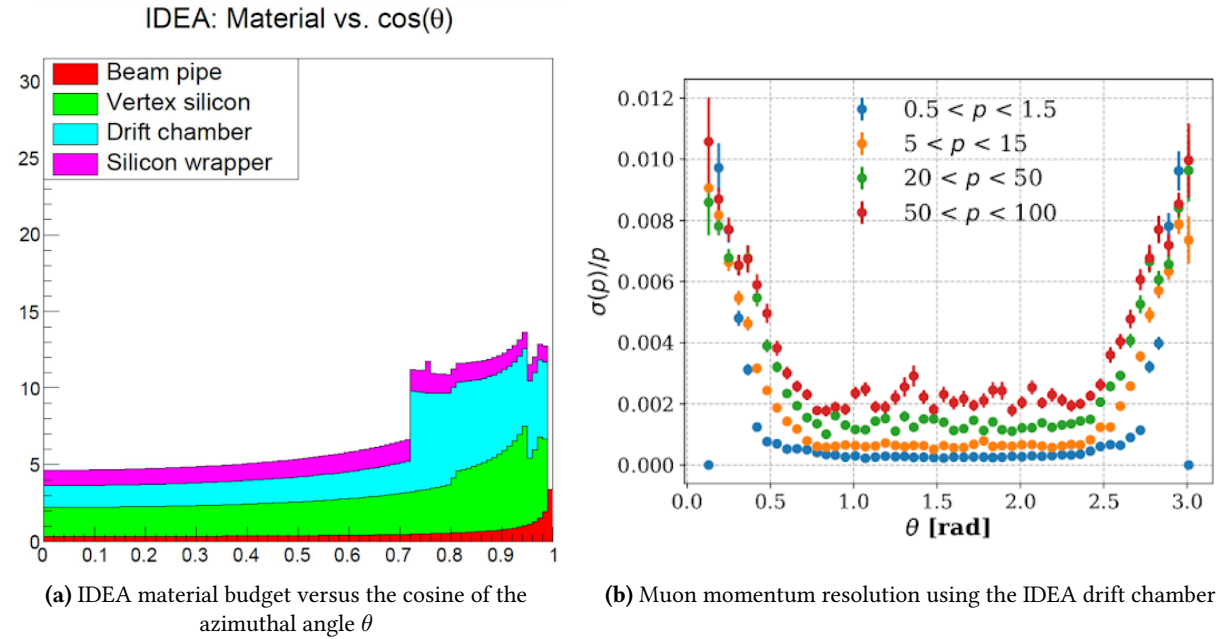


Figure 7.5: IDEA material budget versus the cosine of the azimuthal angle θ (a) and muon momentum resolution using the IDEA drift chamber (b).

7.4 Monte-Carlo samples

The FCC-ee is currently in the conceptual design phase, which is conducted by feasibility studies of the physics programs using Monte Carlo (MC) simulations. These simulations enable to predict and analyze the outcomes that can be expected once the accelerator and detectors are operational.

Events for different physical processes are generated using several generators, as described in Section 7.4.1. The detector simulation and reconstruction are performed by the fast simulation package DELPHES [192], which smears gen-level particles with a resolution formula and efficiency to mimic a more realistic detector. The entire chain of event generation, simulation, and reconstruction is embedded within the Key4HEP software framework. The official central samples "Winter2023" are used in this analysis.

In the initial phase of this study, all Monte Carlo (MC) samples were generated locally. Then, to address storage limitations and ensure that all feasibility study groups utilize identical and thoroughly verified samples, the FCC collaboration centrally produced the Monte Carlo samples.

The MC samples employed in this analysis were generated at a center-of-mass energy of 240 GeV

($\sqrt{s} = 240$ GeV) using either the PYTHIA or WHIZARD generator. The luminosity in the analysis was set to 7.2 ab^{-1} , corresponding to two interaction points. A beam energy spread of 0.185 % is applied to both incoming beams (corresponding to 222 MeV) and the vertex is smeared according to the realistic conditions, as described in the CDR [10]. The crossing angle of 30 mrad is not applied to the simulation.

7.4.1 Event generators

Event generation was conducted with WHIZARD [193], parton showering with PYTHIA 6 [194], and both event generation and parton showering with PYTHIA 8 [195]. MC samples using other generators, such as KKMC [196], were simulated to investigate systematic uncertainties. These samples are detailed in Table 7.2.

Table 7.2: Monte Carlo Samples used in this analysis. They are all produced at a center-of-mass energy of 240 GeV.

Sample Name	Processes	Generator	# of events	x-section(pb)
Higgs Processes				
wzp6_ee_mumuH	$e^+e^- \rightarrow \mu^+\mu^-H$	WHIZARD + PYTHIA 6	1,200,000	0.0067643
wzp6_ee_eeH	$e^+e^- \rightarrow e^+e^-H$	WHIZARD + PYTHIA 6	1,200,000	0.0071611
Diboson Processes				
p8_ee_ZZ_ecm240	$e^+e^- \rightarrow ZZ$	PYTHIA 8	56,162,093	1.35899
p8_ee_WW_ecm240	$e^+e^- \rightarrow WW$	PYTHIA 8	373,375,386	16.4385
Dilepton Processes				
wzp6_ee_mumu	$e^+e^- \rightarrow \mu^+\mu^-$	WHIZARD + PYTHIA 6	53,400,000	5.288
wzp6_ee_ee_Mee_30_150	$e^+e^- \rightarrow e^+e^-$	WHIZARD + PYTHIA 6	85,400,000	8.305
wzp6_ee_tautau	$e^+e^- \rightarrow \tau^+\tau^-$	WHIZARD + PYTHIA 6	52,400,000	4.668
Electron Photon Processes				
wzp6_egamma_eZ_Zmumu	$e^-\gamma \rightarrow e^-Z(\mu^+\mu^-)$	WHIZARD + PYTHIA 6	6,000,000	0.10368
wzp6_gammae_eZ_Zmumu	$e^+\gamma \rightarrow e^+Z(\mu^+\mu^-)$	WHIZARD + PYTHIA 6	5,600,000	0.10368
wzp6_egamma_eZ_Zee	$e^-\gamma \rightarrow e^-Z(e^+e^-)$	WHIZARD + PYTHIA 6	6,000,000	0.05198
wzp6_gammae_eZ_Zee	$e^+\gamma \rightarrow e^+Z(e^+e^-)$	WHIZARD + PYTHIA 6	6,000,000	0.05198
Photon Photon Processes				
wzp6_gaga_mumu_60	$\gamma\gamma \rightarrow \mu^+\mu^-$	WHIZARD + PYTHIA 6	33,900,000	1.5523
wzp6_gaga_ee_60	$\gamma\gamma \rightarrow e^+e^-$	WHIZARD + PYTHIA 6	22,500,000	0.873
wzp6_gaga_tautau_60	$\gamma\gamma \rightarrow \tau^+\tau^-$	WHIZARD + PYTHIA 6	33,700,000	0.836
Other Processes				
wzp6_ee_nuenueZ	$e^+e^- \rightarrow \nu_e\bar{\nu}_eZ$	WHIZARD + PYTHIA 6	2,000,000	0.033274

In this study, we consider the signal process $e^+e^- \rightarrow ZH \rightarrow \mu^+\mu^-H$ ($e^+e^- \rightarrow ZH \rightarrow e^+e^-H$) for the $\mu^+\mu^-$ (e^+e^-) final states, where the Z boson decays into a muon (electron) pair, and the Higgs boson (H) decays inclusively. The primary background sources are derived from $e^+e^- \rightarrow ZZ$, $e^+e^- \rightarrow WW$, and $e^+e^- \rightarrow \ell^+\ell^-$, with ℓ denoting either e or μ . However, final states featuring $\tau^+\tau^-$ are considered rare backgrounds due to the low τ decay ratio.

The Feynman diagrams for all signal MC sample productions can be found in Figure 7.6. It illustrates the s-channel Feynman diagram of the Higgsstrahlung process, wherein the Z boson decays into various leptons (e^+e^- , $\mu^+\mu^-$, or $\tau^+\tau^-$) while the Higgs boson decays inclusively. Notably, the electron final state simulations also encompass the ZZ fusion, where Z bosons are radiated from incoming electrons or positrons, as depicted in Figure 7.7.

The $e^+e^- \rightarrow ZZ$ process features only t-channel Feynman diagrams, as shown in Figure 7.8.

In the $e^+e^- \rightarrow W^+W^-$ simulations, both s- and t-channel Feynman diagrams are included, with W decaying inclusively, as shown in Figure 7.9.

The $e^+e^- \rightarrow \ell^+\ell^-$ processes are represented in Figure 7.10 for the s-channel, with the electron

final states also exhibiting a t-channel.

In a lepton collider, incoming leptons radiate photons, leading to potential interactions between the leptons and radiated photons or between the radiated photons themselves. The Feynman diagrams for electron-photon processes are displayed in Figure 7.11a, while the positron-photon processes can be found in Figure 7.11b. These processes are characterized by $e^-(e^+)\gamma \rightarrow e^-(e^+)Z$, followed by $Z \rightarrow \ell^+\ell^-$, where ℓ can be e, μ , or τ .

Photon collisions are illustrated in the Feynman diagram in Figure 7.12 through the t-channel, where ℓ can be e, μ , or τ . All processes involving photon initial states are simulated using the equivalent photon/electron approximation (EPA) [197].

Figure 7.14 represent the VBF production mode of the Higgs boson, where the Higgs boson is produced through the fusion of W bosons. The final states include neutrinos.

Figure 7.13 is included to comprehensively present the WW fusion processes.

The relative size of these backgrounds after a simple requirement on the leptons can be seen in Figure 7.15 for both $\mu^+\mu^-$ (Figure 7.15a) and e^+e^- channels (Figure 7.15b).

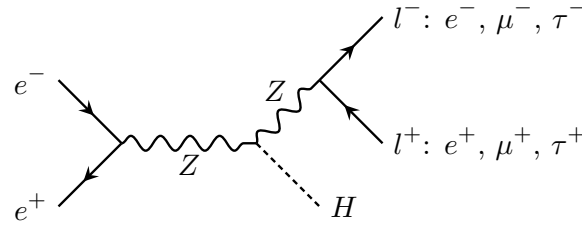


Figure 7.6: Feynman diagram for the process $e^+e^- \rightarrow Z(\ell^+\ell^-)H$ where ℓ can be e, μ or τ

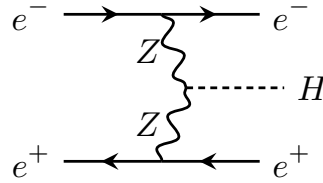


Figure 7.7: Feynman diagram illustrating the $e^+e^- \rightarrow e^+e^-H$ process, where a Higgs boson is produced through the fusion of Z bosons, which are radiated from an incoming electron and positron.

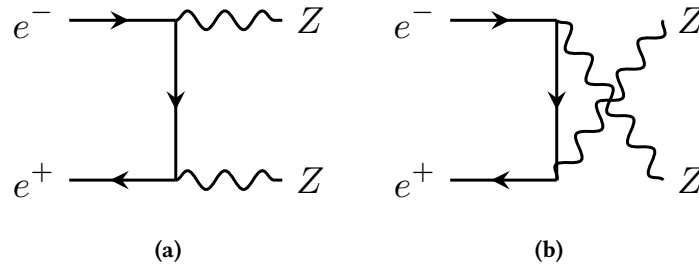


Figure 7.8: Feynman diagrams for the process $e^+e^- \rightarrow ZZ$. The left panel (a) shows the standard order, while the right panel (b) displays the swapping the final states. Both diagrams consider the Z decay inclusively.

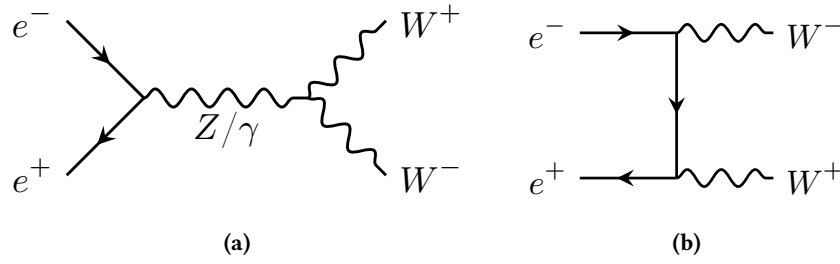


Figure 7.9: Feynman diagrams for the process $e^+e^- \rightarrow W^+W^-$. Both panels show the inclusive decays of W^+ and W^- . The left panel (a) displays the s-channel, while the right panel (b) presents the t-channel.

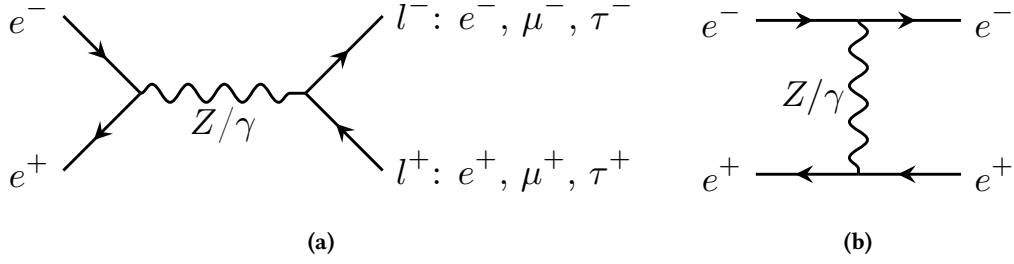


Figure 7.10: Feynman diagrams for the process $e^+e^- \rightarrow \ell^+\ell^-$ where ℓ can be e, μ , or τ . The left panel (a) displays the s-channel, while the right panel (b) presents the t-channel.

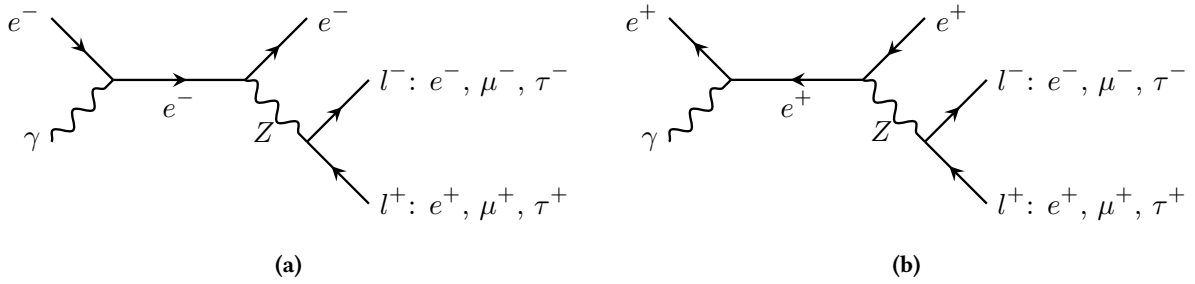


Figure 7.11: Feynman diagrams for the processes. Diagram (a) represents $e^-\gamma \rightarrow e^-Z(\ell^+\ell^-)$, while diagram (b) illustrates $e^+\gamma \rightarrow e^+Z(\ell^+\ell^-)$. In both cases, ℓ can be e, μ , or τ .

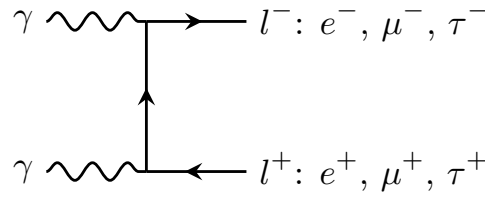


Figure 7.12: Feynman diagram for the process $\gamma\gamma \rightarrow \ell^+\ell^-$ where ℓ can be e, μ or τ .

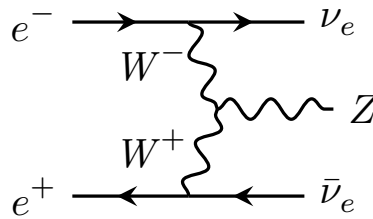


Figure 7.13: Feynman diagram for the process $e^+e^- \rightarrow \nu_e\bar{\nu}_e Z$ with W exchange.

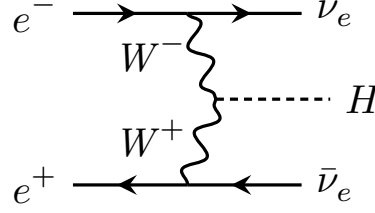


Figure 7.14: Feynman diagram for the VBF process $e^+e^- \rightarrow \nu_e \bar{\nu}_e H$ with W exchange.

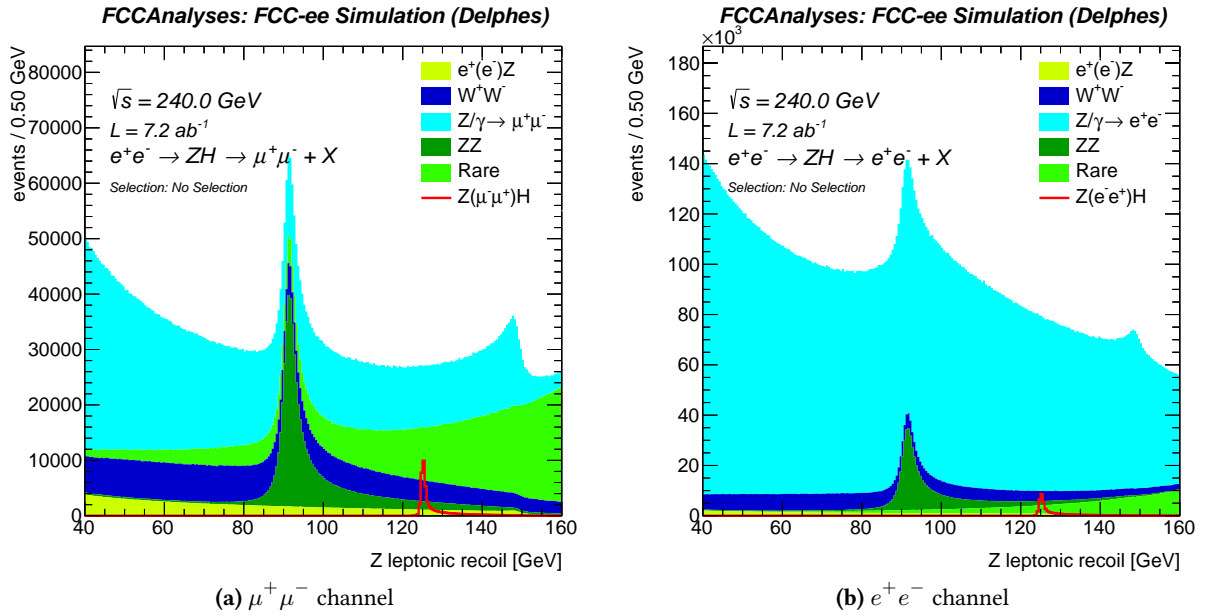


Figure 7.15: m_{rec} distribution without selection for $\mu^+\mu^-$ ((a)) and e^+e^- channels ((b)).

7.5 Event Selection

In this section, a basic and a baseline event selection are introduced, in order to focus on regions where the signal process is prominent and effectively suppresses background processes. The main backgrounds in this analysis are WW, ZZ, and Z/ γ , but other rare processes are included as well (see Section 7.4 for a complete list of samples). Only electrons and muons are used (referred to as leptons), which can be measured with high precision such that tight selection requirements can be applied.

The event selection is divided into two parts: preselection requirements (see Section 7.5.1), and kinematic requirements (see Section 7.5.2). An overview of all the selections and the event yields is presented in Section 7.5.4.

7.5.1 Preselection Requirements

Before applying kinematic requirements to focus on the signal region, a set of preselection requirements is applied to leptons in order to identify whether they are likely originating from the $e^+ + e^- \rightarrow \text{ZH}$ process or background processes. The selection for the leptons is as follows:

- **Selection of at least 2 leptons.** Ensure the event contains a minimum of two leptons. The leptons are directly taken from the ReconstructedParticles collection.
- **Requirement of at least one isolated lepton with $I_{\text{rel}} < 0.25$.** Reduce background contributions by requiring that at least one lepton be well-separated from other particles (mainly semi-leptonic flavor decays). For a given lepton, the relative cone isolation I_{rel} is defined as the sum of all the ReconstructedParticles momenta within a cone of radius $\Delta R < 0.5$, divided by the lepton momentum.
- **Momentum threshold $p > 20$ GeV.** Exclude low-energy leptons and minimize noise from soft radiation.
- **Opposite charge requirement.** Ensure that the leptons have opposite charges in order to enhance the signal and suppress background processes.

In case more than two leptons are present in the event, the lepton pair is selected that minimizes the following expression:

$$\chi^2 = 0.6 \times (m_{\ell\ell} - m_Z)^2 + 0.4 \times (m_{\text{rec}} - m_h)^2, \quad (7.5.1)$$

with $m_Z = 91.2$ GeV, $m_h = 125$ GeV, $m_{\ell\ell}$ the invariant mass of the lepton pair and m_{rec} the recoil. The fractions 0.6 and 0.4 have been approximately optimized to take into account the different resolutions of the two terms. The χ^2 encapsulates both the kinematic constraints on the Z and Higgs mass and therefore optimally selects the best lepton pair to originate from the radiating Z.

7.5.2 Kinematic Requirements

An additional set of kinematic requirements is applied to further reduce the background events and enhance signal purity. A set of plots motivating the selection requirements are given in Appendix C.1.

We primarily focus on the leptonic reconstruction of Z boson clusters, specifically examining the decay channels $Z \rightarrow \mu^+\mu^-$ and $Z \rightarrow e^+e^-$. Our kinematic requirements center on the invariant mass, denoted as $m_{\ell^+\ell^-}$, and the momentum, represented by p .

Contrasting with hadron colliders, where transverse momentum (p_T) is commonly used, because of the initial state is poorly known, we employ momentum p in our lepton collider analysis.

The requirements are only based on the lepton information, to retain the Higgs decay mode independence (see Section 7.7 for an explicit evaluation of the decay mode independence).

➤ **Invariant mass of the di-lepton pair:** $86 \text{ GeV} < m_{\ell\ell} < 96 \text{ GeV}$ (Fig. C.1);

➤ **Di-lepton momentum:** $20 \text{ GeV} < p_{\ell\ell} < 70 \text{ GeV}$ (Fig. C.2);

➤ **Recoil mass:** $120 \text{ GeV} < m_{\text{rec}} < 140 \text{ GeV}$ (Fig. C.3);

Both preselection and kinematic requirements rely solely on the lepton properties.

7.5.3 Basic and Baseline selections

The "**basic selection**" is defined as the set of preselection and kinematic requirements defined above. It is used for the model-independent ZH cross-section analysis.

For the Higgs mass analysis, an additional requirement is applied to further reduce Z/γ events, which typically contain hard ISR photons collinear to the beam and therefore left undetected, resulting in a peaking behavior of the direction of the missing momentum vector towards the forward regions, as can be seen in Fig. C.4. The following requirements are thus applied:

➤ **Cosine of missing momentum:** $|\cos(\theta_{\text{miss}})| < 0.98$ (Fig. C.4).

The "**baseline selection**" is thus defined as the basic selection complemented with this additional requirement. This additional requirement cannot be applied to the model-independent cross-section analysis since it is sensitive to Higgs decay mode containing invisible decays (see Section 7.7).

7.5.4 Event yields and requirement flow

Event requirement-flows, yields, and selection efficiencies for the muon and electron final states are shown in Fig. 7.16 and Table 7.3 respectively. It clearly indicates a strong background reduction while retaining the signal events to a good extent. Due to the additional t-channel production of $Z/\gamma \rightarrow e^+e^-$ events, this background is more abundant in the electron final state w.r.t. the muon final state.

The recoil distributions after the full event selection are shown in Fig. 7.17. A narrow distribution is obtained, as a direct result of the excellent resolution performance of the IDEA drift chamber. The electron channel is visibly degraded due to the 20% additional smearing w.r.t. the muons, as explained in Section 7.3.1. Additionally, the WHIZARD electron samples contain a small fraction of VBF events which also degrades the resolution. Combined with the higher backgrounds, the muon channel will dominate the uncertainty on the Higgs cross-section and mass.

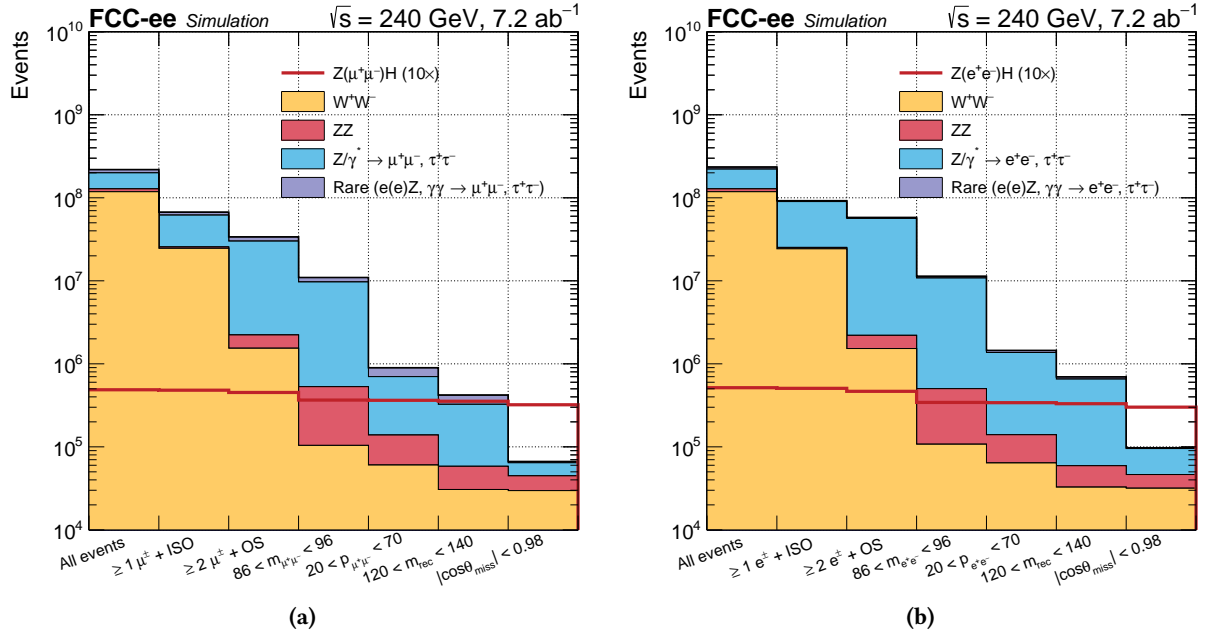


Figure 7.16: Event requirement flow plots for the muon ((a)) and electron ((b)) final states.

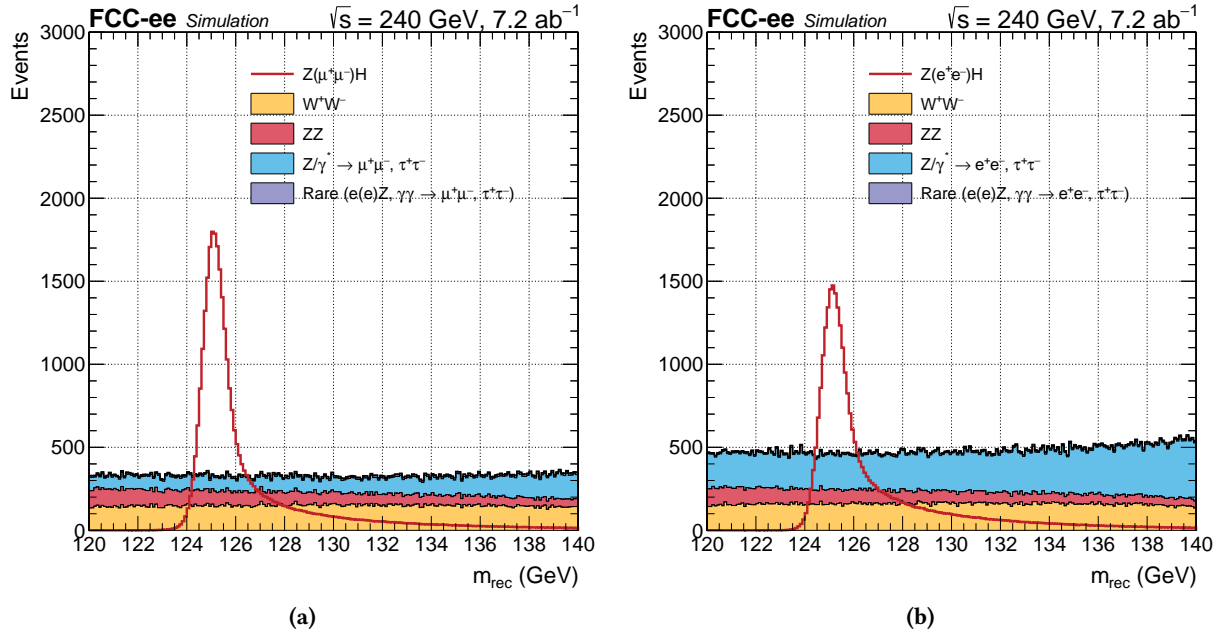


Figure 7.17: Recoil distributions after all requirements (including the $\cos(\theta_{\text{miss}})$ requirement) for the muon ((a)) and electron ((b)) final states.

Table 7.3: Cut flow and event yields for the muon (top) and electron (bottom) final states for an integrated luminosity of 7.2 ab^{-1} . The error reflects the uncertainty on the Monte Carlo event statistics.

Process	ZH	WW	ZZ	Z/ γ	Rare
Muon final state					
All events	$4.87\text{e}+04 \pm 3.44\text{e}+01$	$1.18\text{e}+08 \pm 6.13\text{e}+03$	$9.78\text{e}+06 \pm 1.31\text{e}+03$	$7.17\text{e}+07 \pm 6.98\text{e}+03$	$1.89\text{e}+07 \pm 2.23\text{e}+03$
$\geq 1\ell^{\pm} + \text{ISO}$	$4.81\text{e}+04 \pm 3.42\text{e}+01$	$2.46\text{e}+07 \pm 2.79\text{e}+03$	$9.61\text{e}+05 \pm 4.09\text{e}+02$	$3.63\text{e}+07 \pm 5.05\text{e}+03$	$5.27\text{e}+06 \pm 1.19\text{e}+03$
$\geq 2\ell^{\pm} + \text{OS}$	$4.52\text{e}+04 \pm 3.32\text{e}+01$	$1.54\text{e}+06 \pm 6.99\text{e}+02$	$6.88\text{e}+05 \pm 3.46\text{e}+02$	$2.78\text{e}+07 \pm 4.45\text{e}+03$	$3.76\text{e}+06 \pm 9.91\text{e}+02$
$86 < m_{\ell\ell} < 96 \text{ GeV}$	$3.66\text{e}+04 \pm 2.99\text{e}+01$	$1.04\text{e}+05 \pm 1.82\text{e}+02$	$4.27\text{e}+05 \pm 2.73\text{e}+02$	$9.16\text{e}+06 \pm 2.55\text{e}+03$	$1.28\text{e}+06 \pm 4.64\text{e}+02$
$20 < p_{\ell\ell} < 70 \text{ GeV}$	$3.64\text{e}+04 \pm 2.98\text{e}+01$	$6.04\text{e}+04 \pm 1.38\text{e}+02$	$7.84\text{e}+04 \pm 1.17\text{e}+02$	$5.62\text{e}+05 \pm 6.32\text{e}+02$	$1.96\text{e}+05 \pm 2.28\text{e}+02$
$120 < m_{\text{rec}} < 140 \text{ GeV}$	$3.54\text{e}+04 \pm 2.94\text{e}+01$	$3.06\text{e}+04 \pm 9.86\text{e}+01$	$2.76\text{e}+04 \pm 6.94\text{e}+01$	$2.67\text{e}+05 \pm 4.36\text{e}+02$	$9.52\text{e}+04 \pm 1.60\text{e}+02$
$ \cos(\theta_{\text{miss}}) < 0.98$	$3.21\text{e}+04 \pm 2.80\text{e}+01$	$2.97\text{e}+04 \pm 9.70\text{e}+01$	$1.50\text{e}+04 \pm 5.12\text{e}+01$	$1.95\text{e}+04 \pm 1.15\text{e}+02$	$2.34\text{e}+03 \pm 1.69\text{e}+01$
Efficiency (%)	6.60E+01	2.51E-02	1.53E-01	2.73E-02	1.24E-02
Electron final state					
All events	$5.16\text{e}+04 \pm 3.65\text{e}+01$	$1.18\text{e}+08 \pm 6.13\text{e}+03$	$9.78\text{e}+06 \pm 1.31\text{e}+03$	$9.34\text{e}+07 \pm 7.96\text{e}+03$	$1.33\text{e}+07 \pm 1.70\text{e}+03$
$\geq 1\ell^{\pm} + \text{ISO}$	$5.07\text{e}+04 \pm 3.62\text{e}+01$	$2.43\text{e}+07 \pm 2.77\text{e}+03$	$9.58\text{e}+05 \pm 4.08\text{e}+02$	$6.48\text{e}+07 \pm 6.71\text{e}+03$	$2.22\text{e}+06 \pm 6.62\text{e}+02$
$\geq 2\ell^{\pm} + \text{OS}$	$4.66\text{e}+04 \pm 3.47\text{e}+01$	$1.53\text{e}+06 \pm 6.96\text{e}+02$	$6.75\text{e}+05 \pm 3.43\text{e}+02$	$5.43\text{e}+07 \pm 6.16\text{e}+03$	$1.49\text{e}+06 \pm 5.25\text{e}+02$
$86 < m_{\ell\ell} < 96 \text{ GeV}$	$3.43\text{e}+04 \pm 2.98\text{e}+01$	$1.08\text{e}+05 \pm 1.85\text{e}+02$	$3.95\text{e}+05 \pm 2.62\text{e}+02$	$1.03\text{e}+07 \pm 2.69\text{e}+03$	$5.38\text{e}+05 \pm 2.29\text{e}+02$
$20 < p_{\ell\ell} < 70 \text{ GeV}$	$3.40\text{e}+04 \pm 2.96\text{e}+01$	$6.40\text{e}+04 \pm 1.42\text{e}+02$	$7.60\text{e}+04 \pm 1.15\text{e}+02$	$1.23\text{e}+06 \pm 9.27\text{e}+02$	$8.01\text{e}+04 \pm 1.23\text{e}+02$
$120 < m_{\text{rec}} < 140 \text{ GeV}$	$3.31\text{e}+04 \pm 2.92\text{e}+01$	$3.27\text{e}+04 \pm 1.02\text{e}+02$	$2.65\text{e}+04 \pm 6.80\text{e}+01$	$5.96\text{e}+05 \pm 6.45\text{e}+02$	$4.15\text{e}+04 \pm 9.07\text{e}+01$
$ \cos(\theta_{\text{miss}}) < 0.98$	$3.01\text{e}+04 \pm 2.79\text{e}+01$	$3.17\text{e}+04 \pm 1.00\text{e}+02$	$1.47\text{e}+04 \pm 5.05\text{e}+01$	$4.90\text{e}+04 \pm 1.84\text{e}+02$	$2.10\text{e}+03 \pm 1.59\text{e}+01$
Efficiency (%)	5.84E+01	2.68E-02	1.50E-01	5.24E-02	1.58E-02

7.6 Higgs mass measurement

In this section, the Higgs mass analysis is outlined, in order to estimate a realistic uncertainty with the dominant systematic effects included. The analysis uses $Z(\ell^+\ell^-)H$ events, where $\ell = e$ or μ . Indeed, a precise measurement of the Higgs mass relies on an accurate lepton momentum resolution in order to precisely predict the recoil mass distribution and infer the mass from it. With the IDEA drift chamber, excellent performances can be obtained for both muon and electrons, as explained in Section 7.3.1.

The Higgs mass measurement starts with an event selection to reduce the backgrounds while retaining as many signal events as possible. In order to further enhance the sensitivity on the Higgs mass uncertainty, the events are categorized according to their lepton polar angle, driven by the material differences. The effect on the resolutions and recoil distributions is explained in Section 7.6.1.

To infer the Higgs mass uncertainty, a maximum likelihood fit is deployed using the RooFit-based CMS Combine tool. For this, two steps are necessary:

- an analytic modeling of the signal and background shapes,
- fit the Higgs mass dependency on the analytic shapes to the MC data.

Both steps are explained in detail in Section 7.6.2. Similarly, the background modeling is described in Section 7.6.3. The analytic models are then used to construct the likelihood, which is minimized in the Asimov dataset in order to extract the uncertainty on the Higgs mass. Results are discussed in Section 7.6.4, whereas other fit configurations are discussed in Section 7.6.5.

7.6.1 Event categorization

Due to the material dependency in the central and forward regions of the detector, the events are classified into three distinct categories, based on whether the azimuthal angle θ of the lepton is central ($0.8 < \theta < 2.34$ rad) or forward (the complementary azimuthal space):

- Central-central (CC): both leptons are in the central region of the detector;
- Central-forward (CF): one lepton is central and the other lepton is forward;
- Forward-Forward (FF): both leptons are in the forward region of the detector.

In the end, a total of 6 categories are used in the final fit: 3 for the muon and 3 for the electron final states. The different recoil distributions for all categories are shown in Fig. 7.18. All the categories are fitted simultaneously in the final fit to retain the total statistical power of the selected events. The advantage of such categorization is that the different recoil resolutions are separated in the fit, leading to a higher sensitivity to the Higgs mass (see Section 7.6.4). Another advantage of the categorization is that it eases the parameterization of the signal shapes because different resolution components are decoupled.

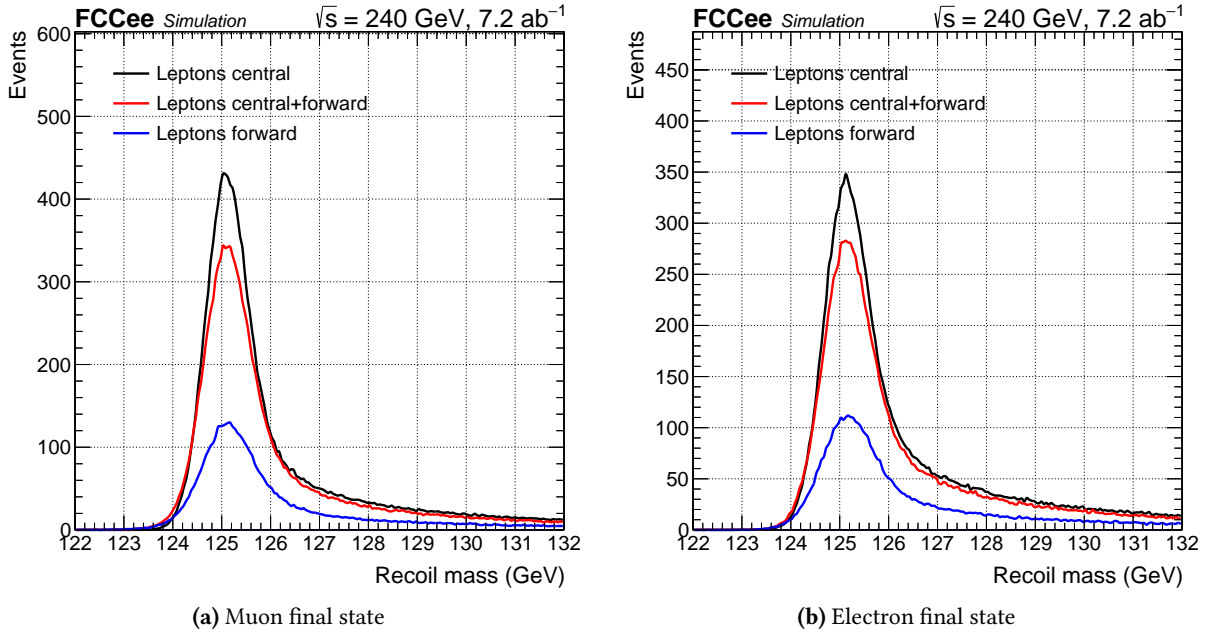


Figure 7.18: Categorized recoil distributions for the (a) muon and (b) electron final states.

7.6.2 Signal modeling

It is important to accurately model analytically the recoil signal shapes in the recoil mass range of $m_{\text{rec}} \in [120, 140]$ GeV. Both the peak and tails are important to capture all possible effects such as lepton resolution, initial state radiation, and beam energy spread. All processes and uncertainties leading to deviations in the distribution should be taken into account as systematic uncertainties.

In the current analysis, the signal shapes have to be modeled for each of the 6 categories. To be complete, also the inclusive muon and electron shapes are considered (i.e. without azimuthal categorization). Throughout this section, the inclusive muon category is used as an example, but the procedure is applied to the other categories. All the fits and plots are given in Appendix C.2.

Typically, recoil distributions are modeled using a (double) Crystal-Ball function (DSCB). This function has 7 degrees of freedom: the overall normalization, mean, width, and 2 parameters each describing the left and right-hand tails of the distribution. The result after fitting the 125 GeV sample to the DSCB is shown in Figure 7.19a (left). Both the peak and tails are not well modeled, and this cannot be solved by optimizing the initial fit parameters. Therefore a more appropriate description of the recoil distribution is needed having more degrees of freedom.

After various attempts, a combination of two single-sided (mirrored) Crystal-Ball functions plus a Gaussian was proven to model the signal sufficiently well (2CBG). Both Crystal-Ball functions share the same mean and width, though the offsets and tails are independent. The Gaussian is added to cope with the transition of the peak to the tails, therefore it has a separate mean and width. The total PDF is given by the following equation:

$$\text{pdf}_{\text{rec}} = cb_1 \text{CB}(\mu, \sigma, \alpha_1, n_1) + cb_2 \text{CB}(\mu, \sigma, \alpha_2, n_2) + \text{Gauss}(\mu_{gt}, \sigma_{gt}) \quad (7.6.1)$$

Two coefficients cb_1 and cb_2 regulate the normalization of the Crystall-Ball functions, whereas the normalization of the Gaussian is constrained to the unity normalization of the PDF. However, both Crystal-Ball functions are dominant in normalization ($\approx 85\%$) and the Gaussian term contributes only to $\approx 15\%$. In total, the p.d.f contains 10 degrees of freedom, sufficient to properly model the signal template, as shown in Fig. 7.19b. In Fig. 7.20a, the decomposition of the 3 terms in the

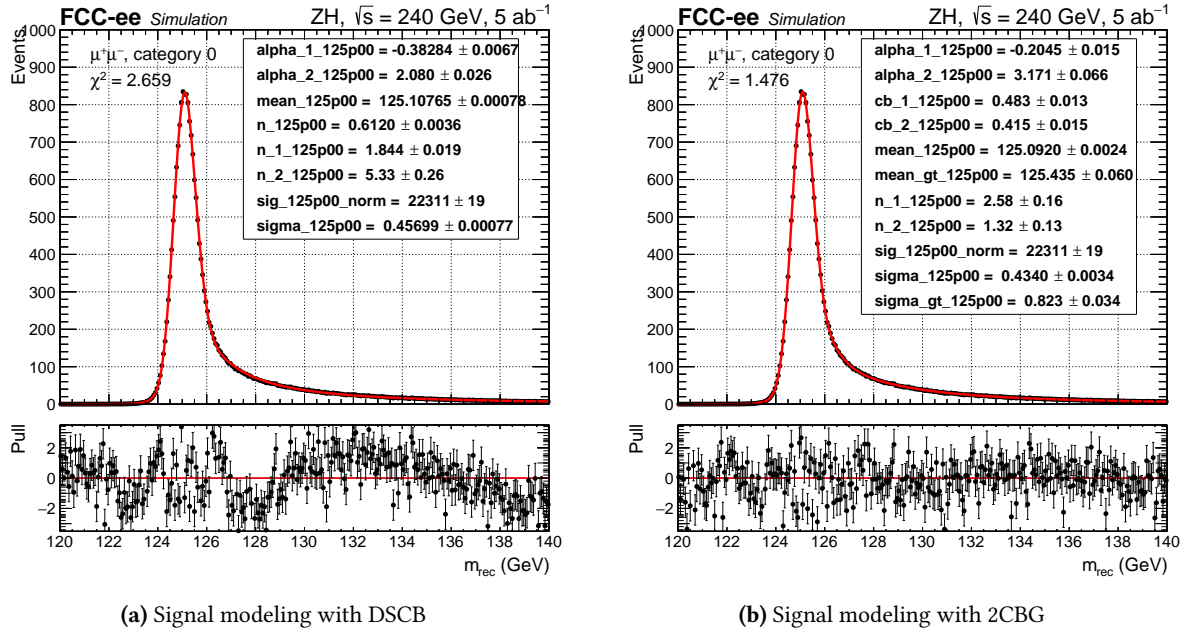


Figure 7.19: Fits for signal modeling using DSCB (a) and 2CBG (b).

recoil PDF for $m_h = 125$ GeV is shown, clearly indicating the contribution of each term.

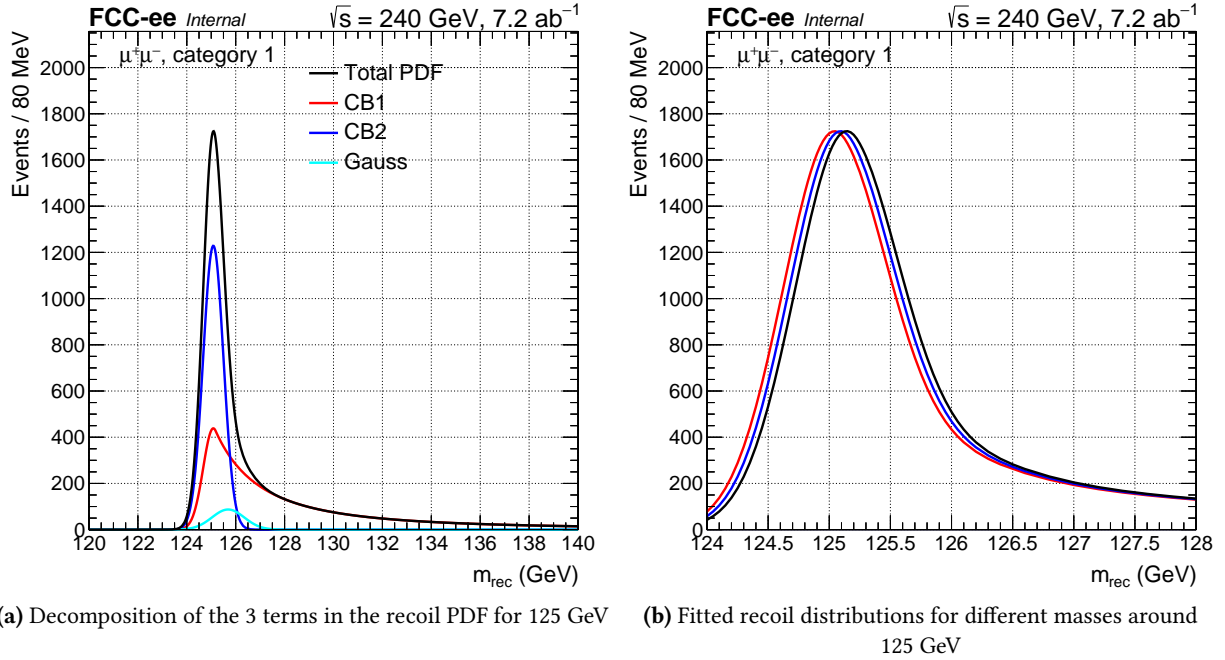


Figure 7.20: Visual representation of the (a) decomposition of the 3 terms in the recoil PDF for 125 GeV and (b) fitted recoil distributions for various masses around 125 GeV.

In order to know the impact of the Higgs mass on the recoil shape and the parameters of the 2CBG PDF, additional samples around the nominal mass sample of $m_h = 125$ GeV were generated (± 50 MeV and ± 100 MeV). Each mass sample is fitted to the 2CBG PDF and the parameters are extracted. No strong biases relative to the statistical uncertainties are observed for all the recoil mass fits.

The 10 fit parameters from the 2CBG PDF are then parameterized as a function of m_h , such that the entire signal model depends only on m_h and the functions used. It was found that only the means (both μ and μ_{gt}) and overall normalization (due to varying cross-section as a function of m_h) do depend significantly on the Higgs mass, whereas the other parameters are nearly constant.

This means that the shape is rather independent of the mass (in the vicinity of 125 GeV), but only a linear shift of the mean as a function of m_h . All the 10 parameters, whether constant or not, are interpolated using splines. As an example, in Fig. 7.21a, the mean (μ) spline as a function of m_h is shown. A good linear dependency is observed.

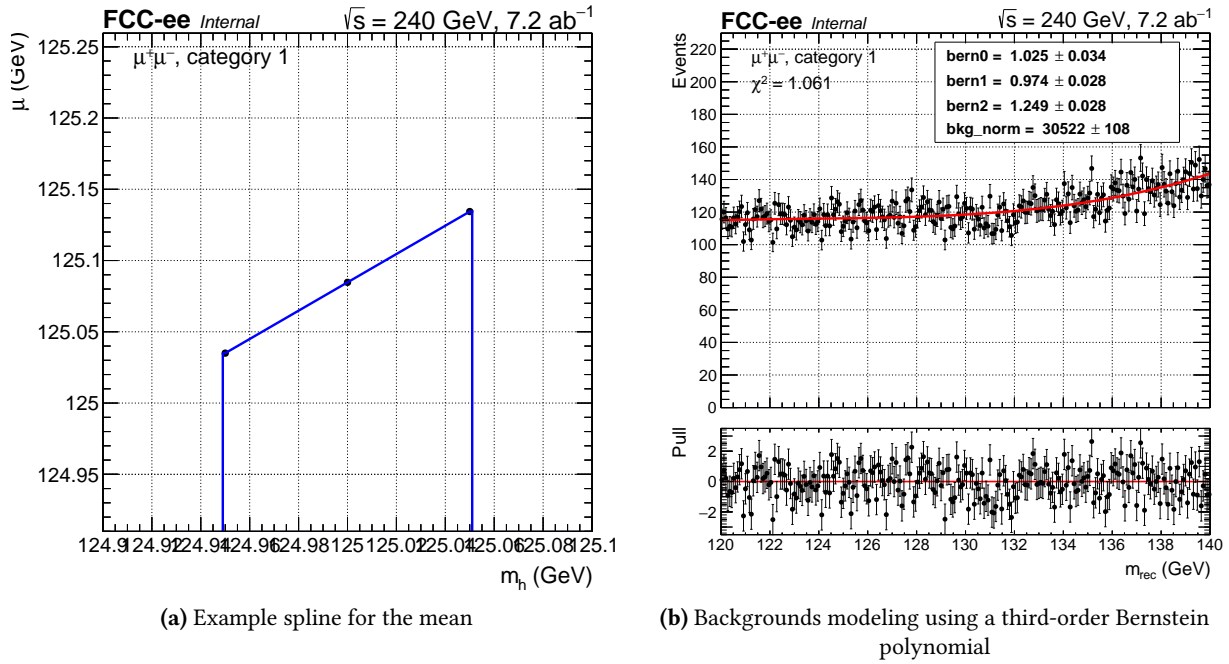


Figure 7.21: Visual representation of the (a) example spline for the mean and (b) background modeling using a third-order Bernstein polynomial.

7.6.3 Background modeling

The modeling of the background is easier due to its smooth behavior in the recoil mass range of $m_{\text{rec}} \in [120, 140]$ GeV. Because there is no constraint power for the individual backgrounds, all the backgrounds are merged together in a single process. The total background is modeled as a third-order polynomial, as shown in Figure 7.21b. Bernstein polynomials have been chosen which are positive-definite in the (re-scaled) range of $[0, 1]$ which enhances the stability during the fit. The three coefficients of the polynomial are kept constant, whereas the total normalization is kept floating.

7.6.4 Results

Statistical tests and fits are performed using the parameterized signal and background shapes, within the framework of Combine, the CMS statistical framework developed in the context of Higgs analyses. The signal and background analytical shapes are fitted to the pseudo-data Asimov dataset (i.e. randomized per-bin events with a mean equal to the sum of signal and background). As a reference, the 125 GeV signal sample has been chosen to construct the Asimov dataset. During the fit, the Higgs mass m_h and the background normalization are left floating, where the 2CBG is fully parameterized as a function of m_h using splines. A likelihood scan is performed to extract the Higgs mass with robust uncertainties.

Several systematic uncertainties are incorporated in the fit. An overview and discussion of the systematic sources are given in Section 7.8 (the nuisances are shared with the cross-section analysis). They all affect the shape of the recoil distribution and therefore the alternative shapes also need to

be parameterized using the 2CBG as PDF. Depending on the systematic type, the following parameters are perturbed: σ, σ_{gt} for beam energy spread, μ, μ_{gt} for the center-of-mass and lepton scale variation uncertainties. The parametric shape variations are incorporated in the Likelihood using a strength parameter ξ , where $\xi = \pm 1$ means the Up/Down variations and $\xi = 0$ the nominal value (there is one parameter per nuisance). This floating parameter enters the likelihood as a multiplicative Gaussian term. They act only on the signal parameters describing the 2CBG and were derived only for the 125 GeV signal sample. It is assumed their magnitude is equal for all the mass points around the vicinity of 125 GeV. The backgrounds are not taken into account by these nuisances, as it is assumed they only act on the normalization with a negligible shape effect. Therefore their potential normalization is absorbed by the overall background normalization. This can change when including control regions to constrain certain nuisances, but this is out of the scope of this study.

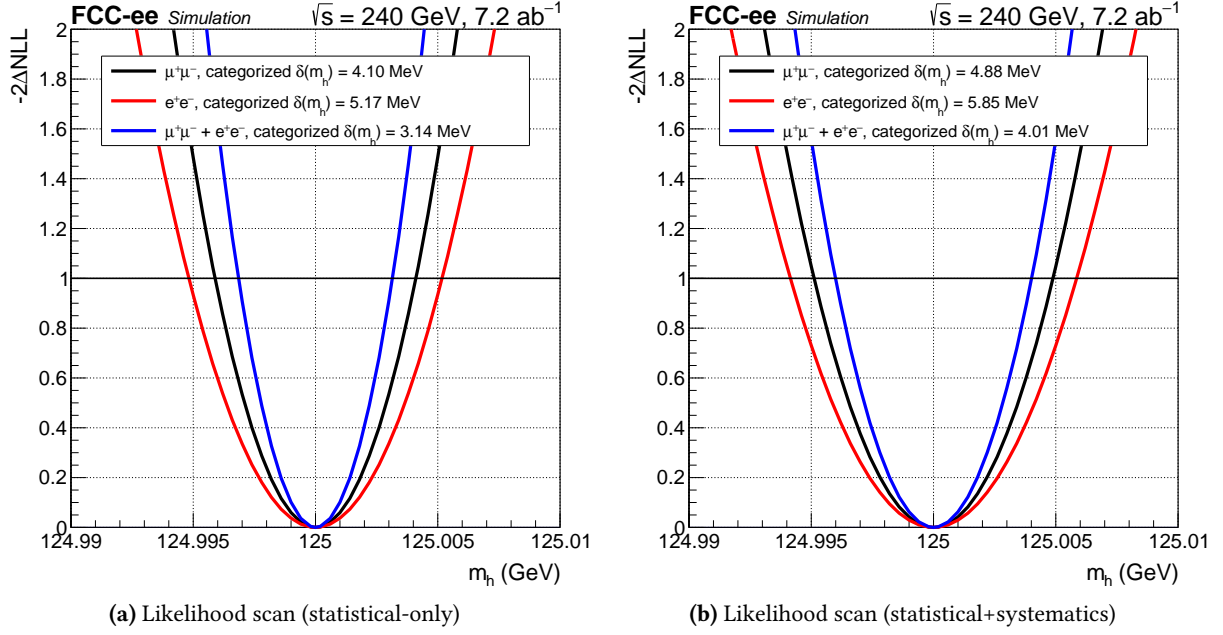


Figure 7.22: Likelihood scans for (a) statistical-only and (b) including systematics.

A likelihood scan is performed for the simultaneous fit, combining the 3 muon and 3 electron channels. The results are shown in Fig. 7.22. On the left plot, the statistical-only uncertainty scans are shown (i.e. without systematics). A combined result of 3.14 MeV is obtained at 68 % confidence level. The result is driven by the muon channel; the electron channel improves the result by 23 %. On the right plot, the statistics plus systematic likelihood scans are shown. A total uncertainty of 4.01 MeV is obtained at 68 %. Compared to the statistical-only result, the systematics degrade the result by 28 %, therefore the Higgs mass analysis is statistically dominated. The extracted Higgs mass is:

$$m_H = 125 \text{ GeV} \pm 3.14 \text{ MeV}(\text{stat.}) \pm 2.49 \text{ MeV}(\text{syst.}) = 125 \text{ GeV} \pm 4.01 \text{ MeV} \quad (7.6.2)$$

A breakdown of the nuisances and their impact is shown in Figure 7.23 (left). The dominant uncertainty is the center-of-mass energy, which is estimated to be 2 MeV and directly scales the uncertainty on the mass (see Section 7.8.3). The other nuisances impact the analysis with less than 1 MeV, in agreement with the simple calculations shown in Section 7.8. In Figure 7.23b, the equivalent breakdown is shown, but when using an uncertainty of 6 % of the beam energy spread (see next paragraph for a discussion).

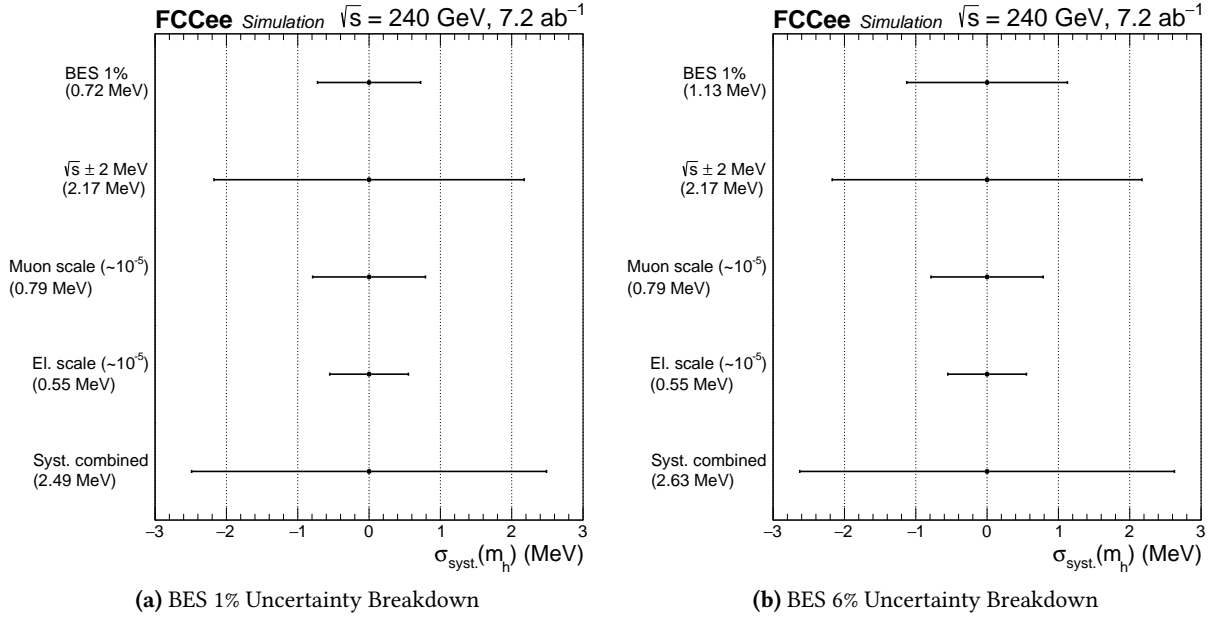


Figure 7.23: Uncertainty breakdown on the mass analysis for (a) the nominal fit with BES 1% and (b) BES 6%.

7.6.5 Auxiliary fit configurations

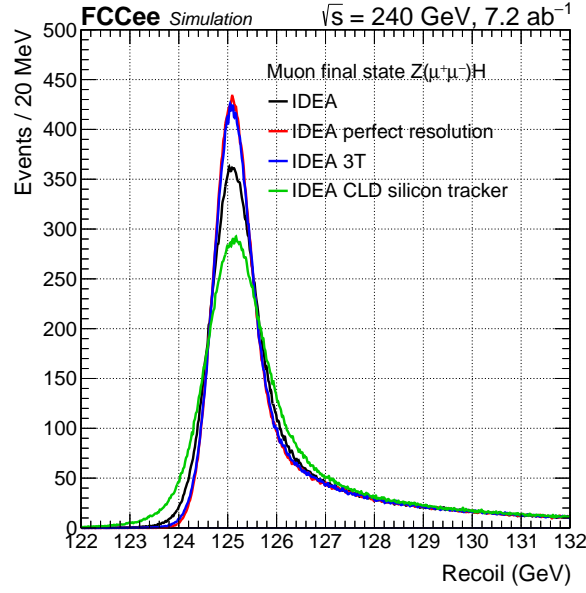
Several auxiliary fits in different (detector) configurations have been performed to check dependencies and impacts on the Higgs mass uncertainty. The studies and results are performed using the nominal categorized fit configuration unless stated otherwise. The list is given below (where by default the values are reported as statistical-only, values between brackets indicate the combined statistical and systematic uncertainty), and the uncertainties on the Higgs mass are tabulated in Table 7.4. In particular, the impact of interesting detector configurations related to tracking is shown in Fig. 7.24, for the muon final state only.

1. **Inclusive fits:** Instead of categorizing the events in 3 (or 6) angular categories, the fit is performed in a single category for the muon and electron final states. The uncertainty on the mass degrades by 20(12)% ($3.14(4.01) \rightarrow 3.75(4.50) \text{ MeV}$).
2. **Degrading electron resolution:** The current modified IDEA detector with a crystal calorimeter provides optimal EM energy resolution, whereas the default IDEA design relies on the Dual Readout calorimetry. Not having crystals would reduce the electron resolution performance due to the lack of Bremsstrahlung recovery. To assess such degradation, the electron resolution was smeared twice as much as the muons (instead of 1.25 using crystals). The electron-only sensitivity got reduced by 16(11)% ($5.17(5.85) \rightarrow 5.98(6.49) \text{ MeV}$), whereas the total statistical uncertainty (i.e. combining with the muon channel) got reduced by 6(2)% ($3.14(4.01) \rightarrow 3.32(4.11) \text{ MeV}$). The relative gain from the electrons on the combined Higgs mass is reduced from 23(22)% to 19(19)%.
3. **Magnetic field:** The magnetic field was increased from 2 to 3 Tesla, leading to a better momentum resolution (the resolution scales approximately with $\propto 1/B$). The uncertainty on the Higgs mass improved by 17(12)% ($3.14(4.01) \rightarrow 2.60(3.54) \text{ MeV}$). The rather limited improvement is due to the beam energy spread, which degrades the recoil distribution.
4. **Silicon tracker:** The drift chamber is replaced by a full silicon tracker. Due to the enhanced multiple scattering (more material), the resolution is expected to degrade, especially for low-momentum leptons (the resolution scales approximately with $\propto 1/\sqrt{X_0}$). Indeed, the uncertainty on the Higgs mass increased by 28(16)% ($3.14(4.01) \rightarrow 4.01(4.66) \text{ MeV}$).

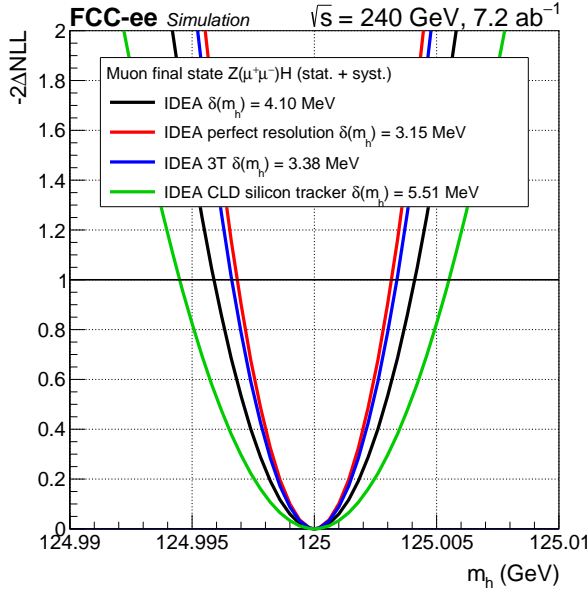
5. **Increased BES uncertainty:** In the nominal case, the BES is estimated to be accurate up to 1 %, based on radiative return events (see Section 7.8.1). An accuracy of 6 % is obtained from the accelerator bunch length monitoring only. This 6 % BES uncertainty was evaluated on the Higgs mass and the absolute impact on the BES increased from 0.7 MeV to 1.1 MeV (see Fig. 7.23). The resulting impact on the Higgs mass is (negligibly) degraded with 2 % ($4.01 \rightarrow 4.09$ MeV), as the dominant systematic uncertainty is the center-of-mass energy with 2 MeV.
6. **Switching off BES:** The beam energy spread of 0.185 % strongly contributes to the broadening of the recoil distribution. The effect has been studied by switching off entirely the beam energy spread in the analysis. The improvement in the Higgs mass uncertainty is 43(25)% ($3.14(4.01) \rightarrow 1.80(2.99)$ MeV).
7. **Ideal resolution:** After the event selection, the reconstructed muon kinematics is replaced by the generator-level kinematics, to mimic an ideal resolution (but still using realistic backgrounds and event selection). The improvement in the Higgs mass uncertainty was found to be 24(17)% ($3.14(4.01) \rightarrow 2.39(3.33)$ MeV).
8. **Freeze backgrounds:** Freezing the normalization of the background does not change the uncertainty on the Higgs mass, as both shapes are very distinct and operate orthogonally (the mass moves horizontally whereas the background normalization moves vertically).
9. **Remove backgrounds:** The effect on the backgrounds was evaluated by running the fit without backgrounds. For the combined fit, statistical only, the uncertainty on the Higgs mass is improved by 21(11)% ($3.14(4.01) \rightarrow 2.49(3.56)$ MeV).

Table 7.4: Statistical (stat+syst) uncertainty on the Higgs mass (MeV) for various fit configurations. Fits are performed using the nominal categorization unless stated otherwise. The values in brackets represent the statistical+systematic uncertainties. Values are normalized to an integrated luminosity of 7.2 ab^{-1} .

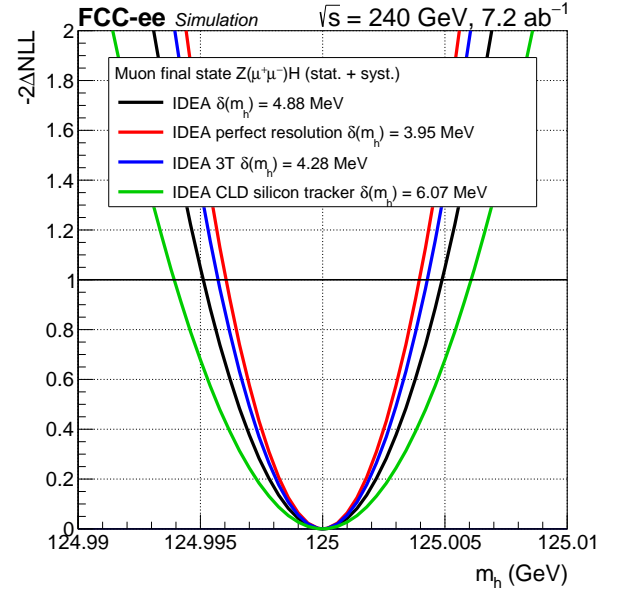
Fit configuration	$\mu^+\mu^-$ channel	e^+e^- channel	combination
Nominal	4.10 (4.88)	5.17 (5.85)	3.14 (4.01)
Inclusive	4.84 (5.53)	6.16 (6.73)	3.75 (4.50)
Degradation electron resolution ¹	4.10 (4.88)	5.98 (6.49)	3.32 (4.11)
Magnetic field 3T	3.38 (4.28)	4.30 (5.00)	2.60 (3.54)
CLD 2T (silicon tracker)	5.51 (6.07)	6.20 (6.70)	4.01 (4.66)
BES 6% uncertainty	4.10 (5.01)	5.17 (6.10)	3.14 (4.09)
No beam energy spread	2.27 (3.42)	3.11 (4.04)	1.80 (2.99)
Ideal resolution	2.89 (3.95)	3.89 (4.56)	2.39 (3.33)
Freeze backgrounds	4.10 (4.88)	5.17 (5.85)	3.14 (4.00)
Remove backgrounds	3.37 (4.34)	3.85 (4.80)	2.49 (3.56)



(a) Recoil Distribution for Different Detector Configurations



(b) Higgs Mass Uncertainty (Statistical Only) for Different Detector Configurations



(c) Higgs Mass Uncertainty (Statistical + Systematics) for Different Detector Configurations

Figure 7.24: Impact of different detector configurations related to tracking on the recoil distribution and uncertainty on the Higgs mass, for the muon final state only.

7.7 ZH Cross-section measurement

Unlike the mass measurement in Section 7.6, where strict selections can be applied to increase the signal significance, in the cross-section measurement model independence of the Higgs decay modes must be maintained.

The recoil mass technique, as detailed in Section 7.2, provides a unique opportunity to measure the cross-section of the $e^+ + e^- \rightarrow ZH$ production mode in a Higgs decay model-independent manner. Thus, any deviation from the Standard Model prediction would indicate the presence of new physics.

During the mass measurement, we applied the selection $|\cos(\theta_{\text{miss}})| < 0.98$ to reduce the $Z \rightarrow \ell^+ \ell^-$

events. However, this selection introduces a bias towards Higgs decays involving neutrinos (or any non-Standard Model invisible decays) which induce intrinsic missing momentum, causing these events to be rejected.

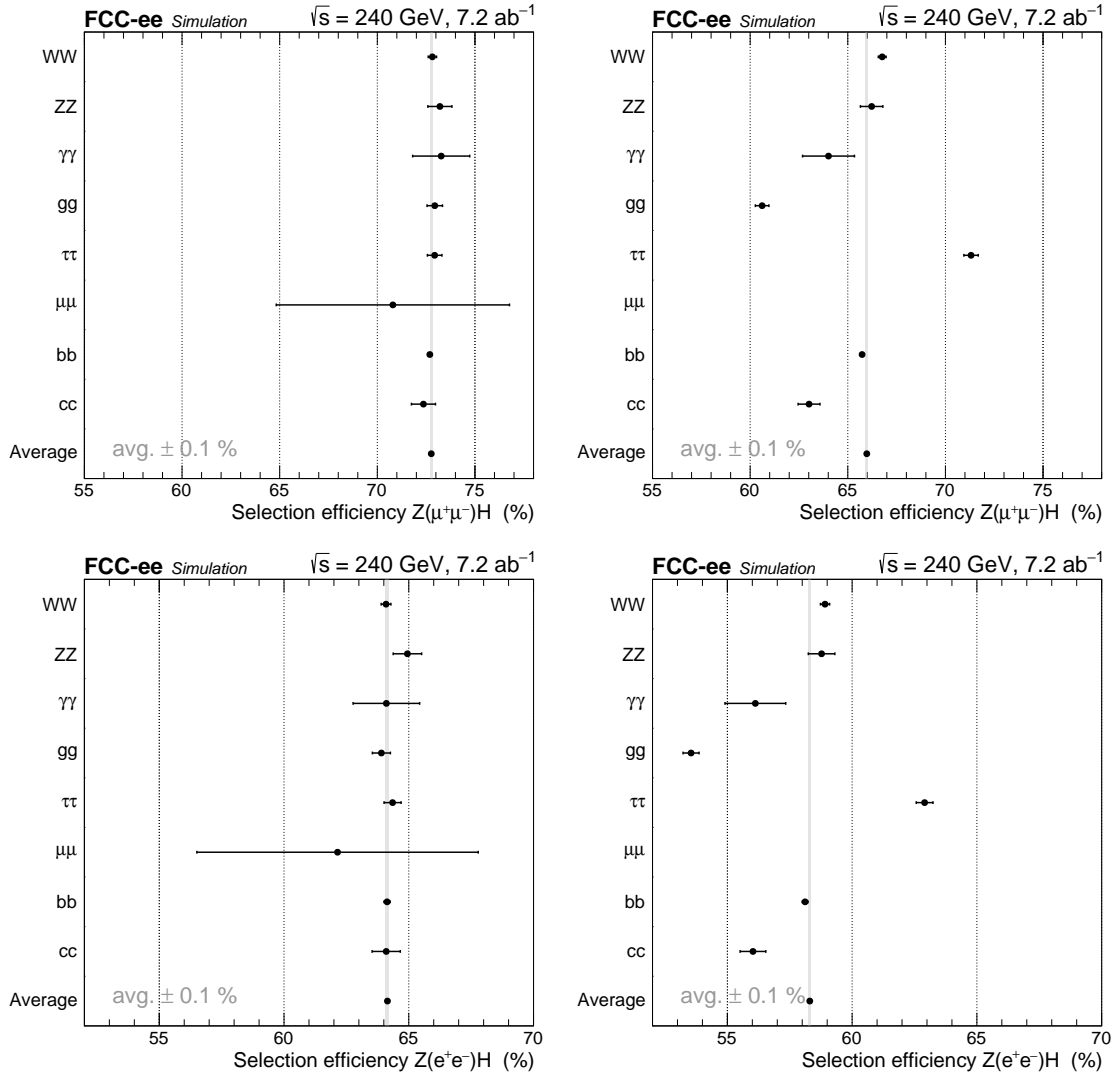


Figure 7.25: Selection efficiency of the different Higgs decay modes with $Z \rightarrow \mu^+ \mu^-$ (top row) and $Z \rightarrow e^+ e^-$ decay mode (bottom row). The left column shows the selection efficiency with the basic selection (without $\cos(\theta_{\text{miss}})$ requirement), and the right column shows selection efficiency with baseline selection (with $\cos(\theta_{\text{miss}})$ requirement).

The selection efficiency of the various Higgs decay modes for $Z \rightarrow \mu^+ \mu^-$ (top) and $Z \rightarrow e^+ e^-$ decay mode is examined in Figure 7.25. The left plots delineate the selection efficiency applying basic selection criteria, excluding the $\cos(\theta_{\text{miss}})$ requirement. In contrast, the plots on the right exhibit the selection efficiency when the baseline selection criteria are employed, inclusive of the $\cos(\theta_{\text{miss}})$ requirement, clearly indicating a violating of the Higgs decay mode-independency.

In the $e^+ e^- \rightarrow \text{ZH}$ cross-section measurement, after applying the basic selection criteria detailed in Section 7.5, we do not use the $\cos(\theta_{\text{miss}})$ requirement and replace it with a Boosted Decision Tree (BDT) approach to further reject the background. This alternative method provides a more accurate representation of the Higgs decay processes involving neutrinos while preserving model independence in the cross-section measurement.

7.7.1 Boosted Decision Tree

Several BDT implementations are available, XGBoost is a standalone package compatible with multiple programming languages and widely used in industry.

XGBoost is employed to perform the BDT study in this work. The TMVA implementation, on the other hand, was utilized in the Chapter 5.

No matter which implementation it is, the principle of the BDT is the same. A BDT uses a series of decision trees to classify events. The structure of the trees are defined by a set of hyperparameters that are optimized during the training process. For each decision tree, the training process starts from the root node, which contains all the training samples. Then sorted the events to the child nodes based on the value of a specific variable. The splitting process continues until the stopping criteria are met, which is defined by the maximum depth of the tree, the minimum number of events in the leaf nodes, or other criteria.

In the entire BDT process, three samples are used: training samples, validation samples and testing samples. The training samples are used to train the model, and the topology of the tree will be fixed once the training process is finished, while the validation samples are used to compare the BDT performance between training and validation samples, then choose the model. The testing samples are used to finally evaluate the performance of the model. These three samples should be orthogonal to make sure the BDT is not biased. In this analysis, a special set of samples are generated by the same setting as the final testing samples, but different seed to assure the orthogonality. The detail of the training and validation samples are detailed in Section 7.7.1.1.

7.7.1.1 Training samples

A distinct dataset, which is orthogonal to the dataset presented in Table 7.2, has been specifically generated for the purpose of BDT training. This approach is designed to ensure minimal bias and enhance the model's generalization capabilities.

In the case of the $\mu^+\mu^-$ (e^+e^-) channel, all signal events that meet the basic selection criteria, without $\cos(\theta_{\text{miss}})$ cut, are utilized for the training process. To maintain a balanced training and validation set, the total number of background training samples is set to match the total number of signal samples. Within the various background processes, the number of events allocated for training is determined based on a proportionality factor, which is the product of each process's cross-section and cut efficiency. By adhering to this proportional distribution, the training set can better represent the underlying characteristics of the different processes.

The training samples are equally separated into training and validation datasets, where the training dataset is used to train the BDT model while the validation dataset is used to verify the performance and generalization of the BDT model, which ensures an unbiased evaluation of the BDT model's performance and robustness. This partitioning strategy prevents over-fitting and allows for a more accurate estimation of the model's performance on unseen data.

The specific breakdown of signal and background events for both the $\mu^+\mu^-$ and e^+e^- channels is thoroughly documented in Table 7.5 and Table 7.6. By employing this carefully designed training strategy, along with the equal separation of training and testing datasets, the BDT model can achieve a more accurate and robust performance, ultimately contributing to a more reliable analysis in the context of the thesis.

Table 7.5: Training Samples for muon channel. They are all produced at a center-of-mass energy of 240 GeV.

Sample Name	Process	Generator	Training + Validation	cross-section (pb)
Higgs Processes				
wzp6_ee_mumuH	$e^+e^- \rightarrow \mu^+\mu^-H$	WHIZARD + PYTHIA 6	873007	0.0067643
Diboson Processes				
p8_ee_ZZ	$e^+e^- \rightarrow ZZ$	PYTHIA 8	59261	1.35899
p8_ee_WW_mumu	$e^+e^- \rightarrow WW \rightarrow \mu^+\nu_\mu\mu^-\bar{\nu}_\mu$	PYTHIA 8	62966	0.25792
Dilepton Processes				
wzp6_ee_mumu	$e^+e^- \rightarrow \mu^+\mu^-$	WHIZARD + PYTHIA 6	551655	5.288
Electron Photon Processes				
wzp6_egamma_eZ_Zmumu	$e^-\gamma \rightarrow e^-Z(\mu^+\mu^-)$	WHIZARD + PYTHIA 6	28662	0.10368
wzp6_gammae_eZ_Zmumu	$e^+\gamma \rightarrow e^+Z(\mu^+\mu^-)$	WHIZARD + PYTHIA 6	28512	0.10368
Photon Photon Processes				
wzp6_gaga_mumu_60	$\gamma\gamma \rightarrow \mu^+\mu^-$	WHIZARD + PYTHIA 6	141949	1.5523

Table 7.6: Training Samples for electron channel. They are all produced at a center-of-mass energy of 240 GeV.

Sample Name	Process	Generator	Training + Validation	cross-section (pb)
Higgs Processes				
wzp6_ee_eeH	$e^+e^- \rightarrow e^+e^-H$	WHIZARD + PYTHIA 6	769907	0.0067643
Diboson Processes				
p8_ee_ZZ	$e^+e^- \rightarrow ZZ$	PYTHIA 8	29894	1.35899
p8_ee_WW_ee	$e^+e^- \rightarrow WW \rightarrow e^+\nu_e e^-\bar{\nu}_e$	PYTHIA 8	34874	0.25792
Dilepton Processes				
wzp6_ee_ee_Mee_30_150	$e^+e^- \rightarrow e^+e^-$ (30-150 GeV)	WHIZARD + PYTHIA 6	660832	8.305
Electron Photon Processes				
wzp6_egamma_eZ_Zee	$e^-\gamma \rightarrow e^-Z(e^+e^-)$	WHIZARD + PYTHIA 6	7883	0.05198
wzp6_gammae_eZ_Zee	$e^+\gamma \rightarrow e^+Z(e^+e^-)$	WHIZARD + PYTHIA 6	7887	0.05198
Photon Photon Processes				
wzp6_gaga_ee_60	$\gamma\gamma \rightarrow e^+e^-$	WHIZARD + PYTHIA 6	28534	0.873

7.7.1.2 Input variables

In a general context, features are used to describe the characteristics of the data, while in the context of high energy physics, "input variables" are used instead of "features". In this study, a variety of input variables were selected for the Boosted Decision Tree (BDT) training, with a primary focus on lepton-related variables. Given that the fundamental selection criteria require the presence of a minimum of two leptons, information pertaining to both leptons was incorporated into the BDT training process. In addition to these lepton-related variables, Higgsstrahlung-related and polarization-related variables can also be considered for inclusion in the BDT training to further improve the classification performance.

To maintain consistency between the $\mu^+\mu^-$ and e^+e^- channels, the same set of variables was applied to both channels. The BDT input variables, along with their descriptions, are listed in Table 7.7. Plots of the input distributions are given in Appendix C.3.

The variables under consideration can be classified into three categories. The first category consists of $p_{\ell^+\ell^-}$, $\theta_{\ell^+\ell^-}$, and $m_{\ell^+\ell^-}$, which encapsulate the information pertaining to the lepton pair cluster. The second category is composed of $p_{l_{\text{leading}}}$, $\theta_{l_{\text{leading}}}$, $p_{l_{\text{subleading}}}$, and $\theta_{l_{\text{subleading}}}$, each of which contributes to the understanding of individual leptonic attributes. The third and final category is represented by $\pi - \Delta\phi_{\ell^+\ell^-}$ and $\Delta\theta_{\ell^+\ell^-}$, which elucidate the spatial relationship between the two leptons.

These variables serve as input features for the BDT, assisting the algorithm in distinguishing be-

Table 7.7: Input variables for BDT training. The leading or sub-leading lepton is sorted by the lepton momentum.

Variable	Description
$p_{\ell^+\ell^-}$	Lepton pair momentum
$\theta_{\ell^+\ell^-}$	Lepton pair polar angle
$m_{\ell^+\ell^-}$	Lepton pair invariant mass
$p_{l_{\text{leading}}}$	Momentum of the leading lepton
$\theta_{l_{\text{leading}}}$	Polar angle of the leading lepton
$p_{l_{\text{subleading}}}$	Momentum of the subleading lepton
$\theta_{l_{\text{subleading}}}$	Polar angle of the subleading lepton
$\pi - \Delta\phi_{\ell^+\ell^-}$	Acoplanarity of the lepton pair
$\Delta\theta_{\ell^+\ell^-}$	Acolinearity of the lepton pair

tween signal and background events in both the $\mu^+\mu^-$ and e^+e^- channels. With these variables, the BDT is able to achieve a high level of classification performance, improving the overall sensitivity of the analysis.

7.7.1.3 Hyper-parameters

Hyper-parameters serve a crucial role in the configuration of the BDT model.

The specific values of the hyper-parameters utilized for the BDT model in this study are listed in Table 7.8. The hyper-parameters not explicitly defined here are assigned their default values in the XGBoost framework.

Table 7.8: Values of the Hyper-parameters utilized for the BDT model training.

Parameter	Value
n_estimators	350
learning_rate	0.20
max_depth	3
subsample	0.5
gamma	3
min_child_weight	10
max_delta_step	0
colsample_bytree	0.5

7.7.1.4 BDT performance

The results from the BDT training are presented in this section. The performance of the BDT model is demonstrated by the distribution of BDT scores, feature importance of input variables, efficiency, and various performance metrics, including the ROC curve, area under the curve (AUC), error curve, and log loss curve.

Figure 7.26 shows the BDT score distributions for the $\mu^+\mu^-$ and e^+e^- channels, comparing the signal and background events from the training and validation datasets. The BDT model exhibits consistent performance for both channels, with signal events predominantly located in regions with

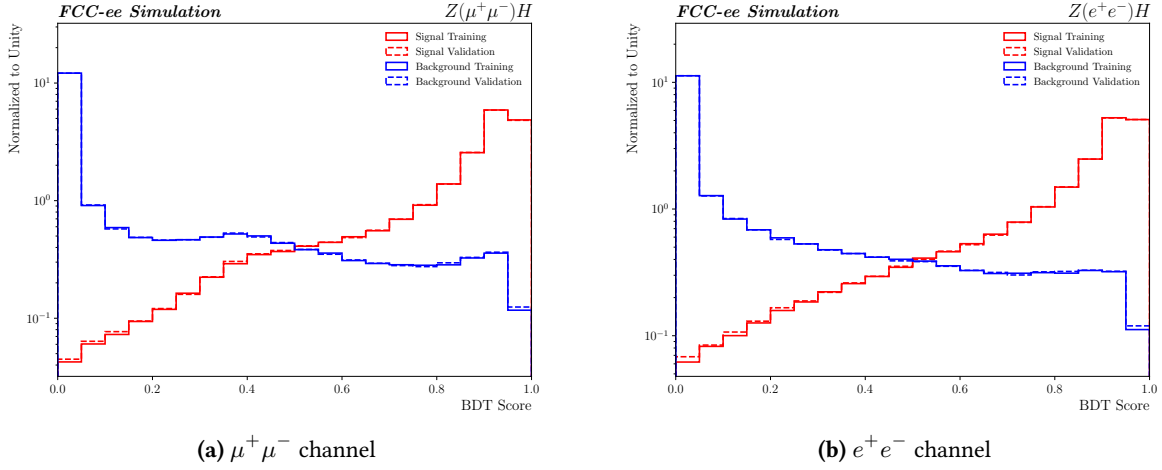


Figure 7.26: BDT distributions for $\mu^+\mu^-$ (a) and e^+e^- (b) channel signal and background events from the training (solid) and test (dashed) datasets. The BDT model demonstrates consistent performance for both channels, as signal events are predominantly found in regions with high BDT scores, while background events are concentrated at low BDT scores.

high BDT scores and background events concentrated at lower BDT scores.

Figure 7.27 presents the BDT efficiency curves for both $\mu^+\mu^-$ (left) and e^+e^- (right) channels. The curves illustrate the discrimination power of the BDT model, with the signal events showing higher efficiency compared to background events. This representation highlights the effectiveness of the BDT model in separating the signal and background. The relative importance of input variables for the $\mu^+\mu^-$ and e^+e^- channels is displayed in Figure 7.28. This representation highlights the contribution of each variable in the decision-making process of the BDT model.

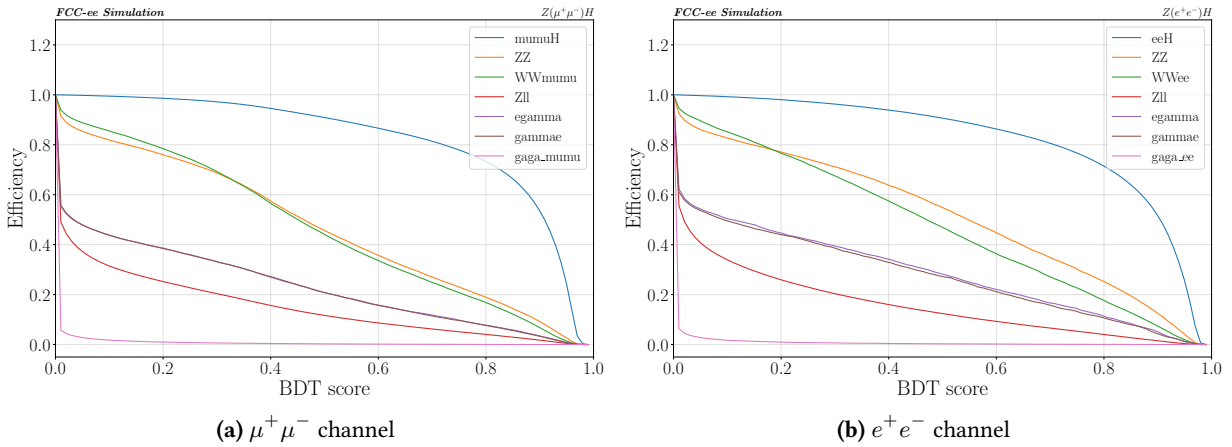
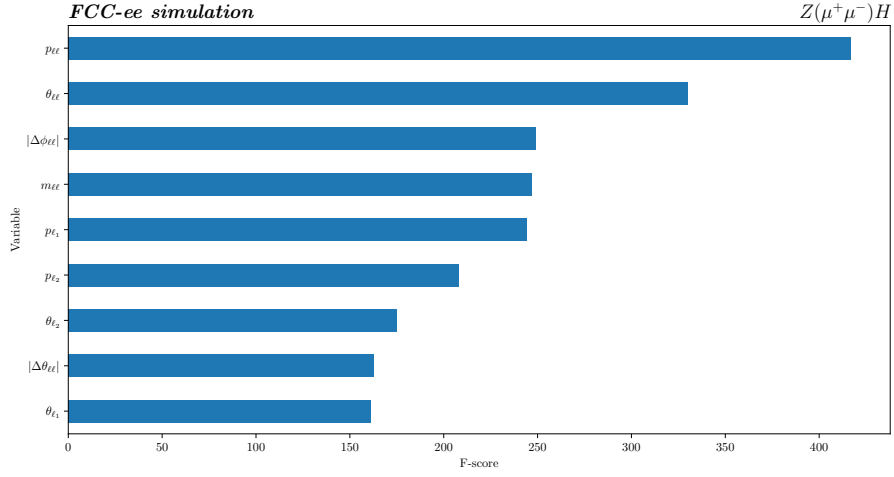
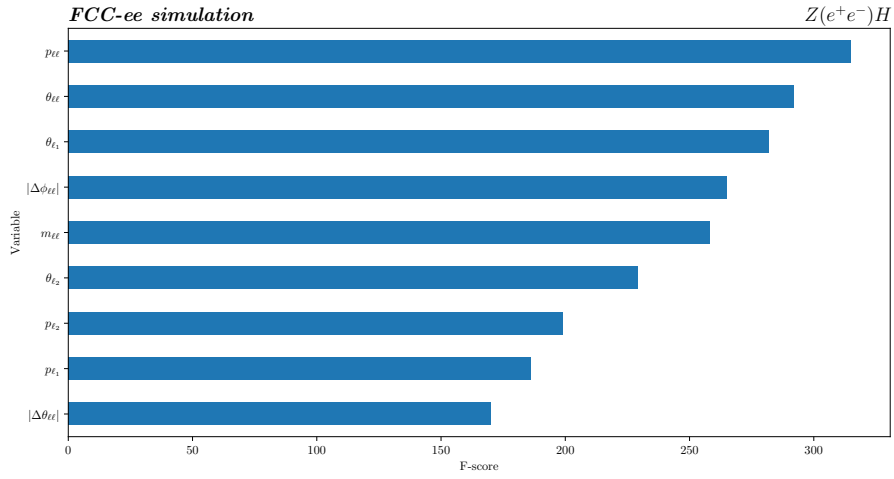
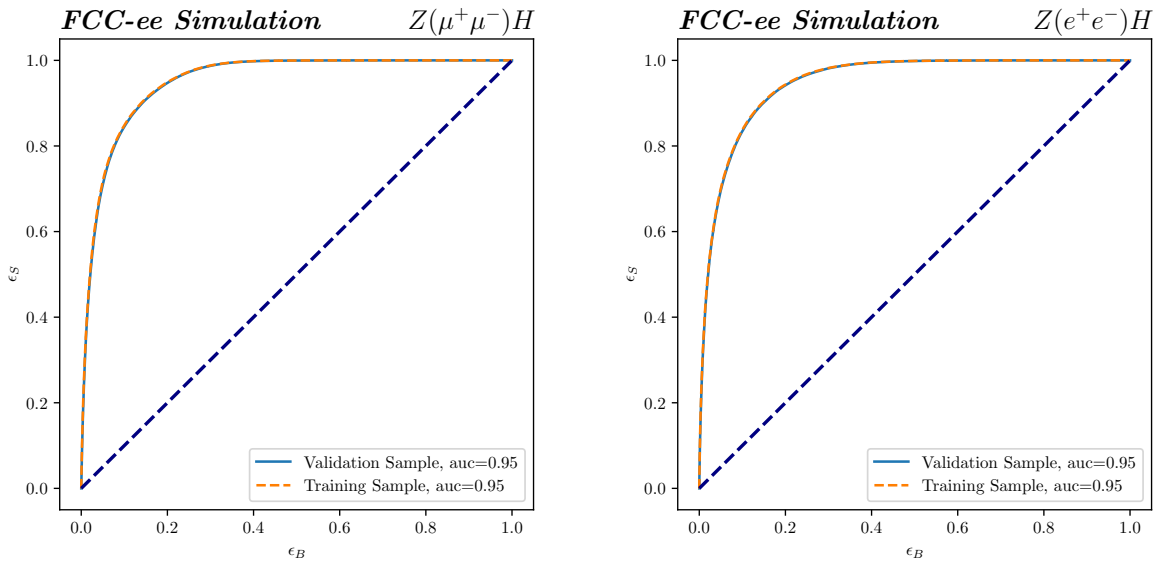


Figure 7.27: BDT efficiency curve for $\mu^+\mu^-$ (a) and e^+e^- (b).

Figure 7.29 shows the ROC curves for the $\mu^+\mu^-$ (a) and e^+e^- (b) channels. The x-axis represents the background efficiency, and the y-axis represents signal efficiency. Performance metrics such as the AUC (Figure 7.30), error curve (Figure 7.31), log loss curve (Figure 7.32), further illustrates the effectiveness of the BDT model for both the $\mu^+\mu^-$ and e^+e^- channels.

The good agreements between the curves of the training and validation dataset in Figure 7.29 reveal the model's ability to discriminate between signal and background events effectively, providing a comprehensive understanding of its generality. The rest plots shows the BDT model arrived at the optimal performance.

(a) $\mu^+\mu^-$ channel(b) e^+e^- channel**Figure 7.28:** Feature importance of the input variables for $\mu^+\mu^-$ (a) and e^+e^- (b).(a) $\mu^+\mu^-$ channel(b) e^+e^- channel**Figure 7.29:** ROC curve for $\mu^+\mu^-$ (a) and e^+e^- (b).

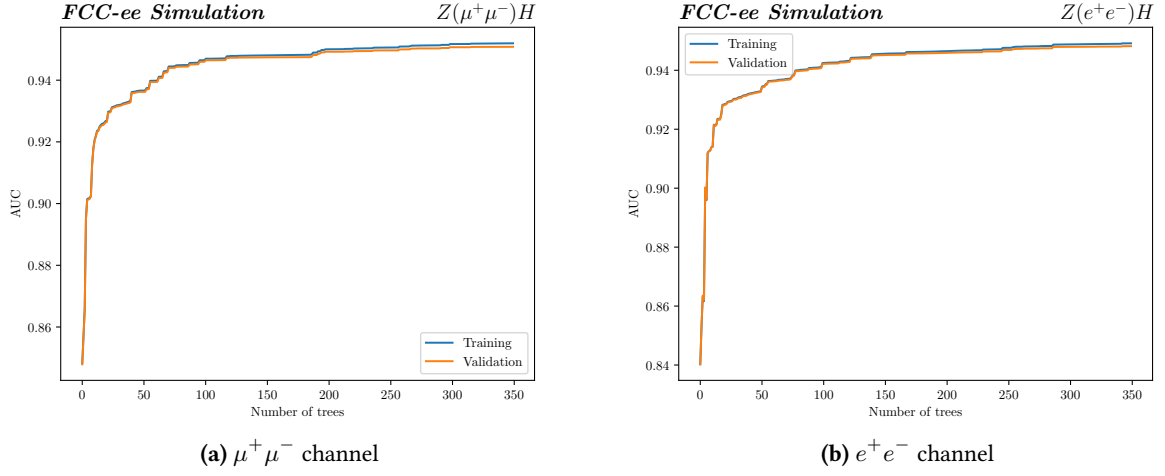


Figure 7.30: Area under the ROC curve (AUC) for $\mu^+\mu^-$ (a) and e^+e^- (b).

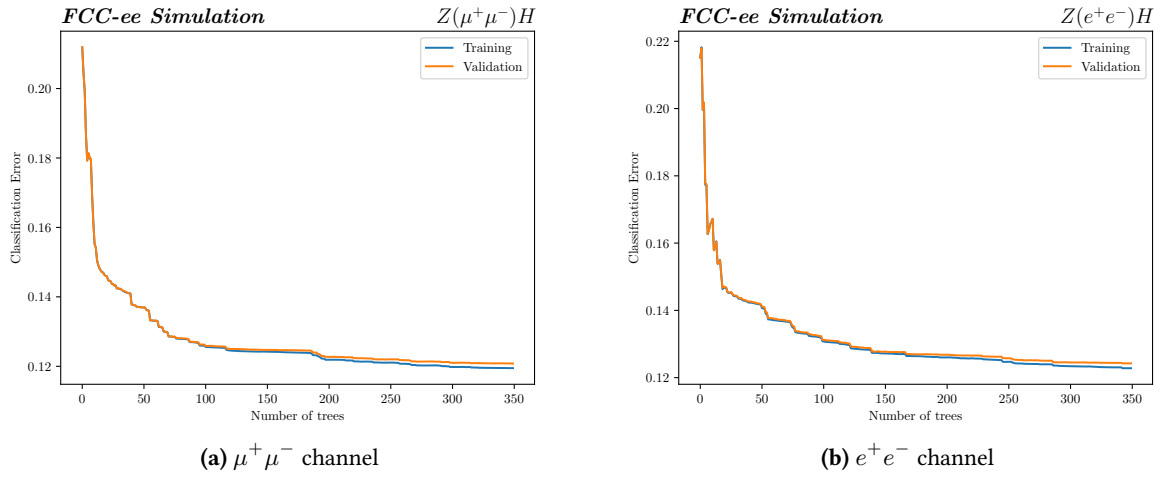


Figure 7.31: Classification error curves for $\mu^+\mu^-$ (a) and e^+e^- (b).

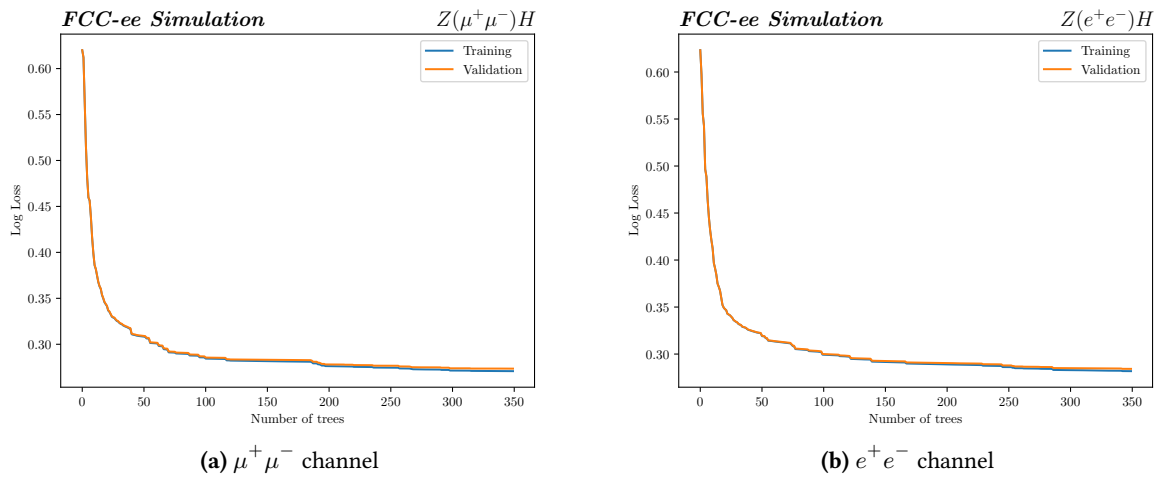


Figure 7.32: Log loss curve for $\mu^+\mu^-$ (a) and e^+e^- (b).

7.7.2 Fitting Strategy

The statistical analysis is performed using the Combine software [198], which is based on the RooFit and RooStats packages [199, 200].

To extract the signal yields, I tried to fit the m_{recoil} distribution, using both analytical shape and binned fit.

The m_{recoil} distribution is first used as the fitted shape to extract the signal yield, the same as the mass measurement in Section 7.6 but with a template fit (binned instead of parametric). After applying the BDT requirement on the score large then 0.3, the background shape is distorted, which introduce uncertainties on the background shape, as shown in Figure 7.33.

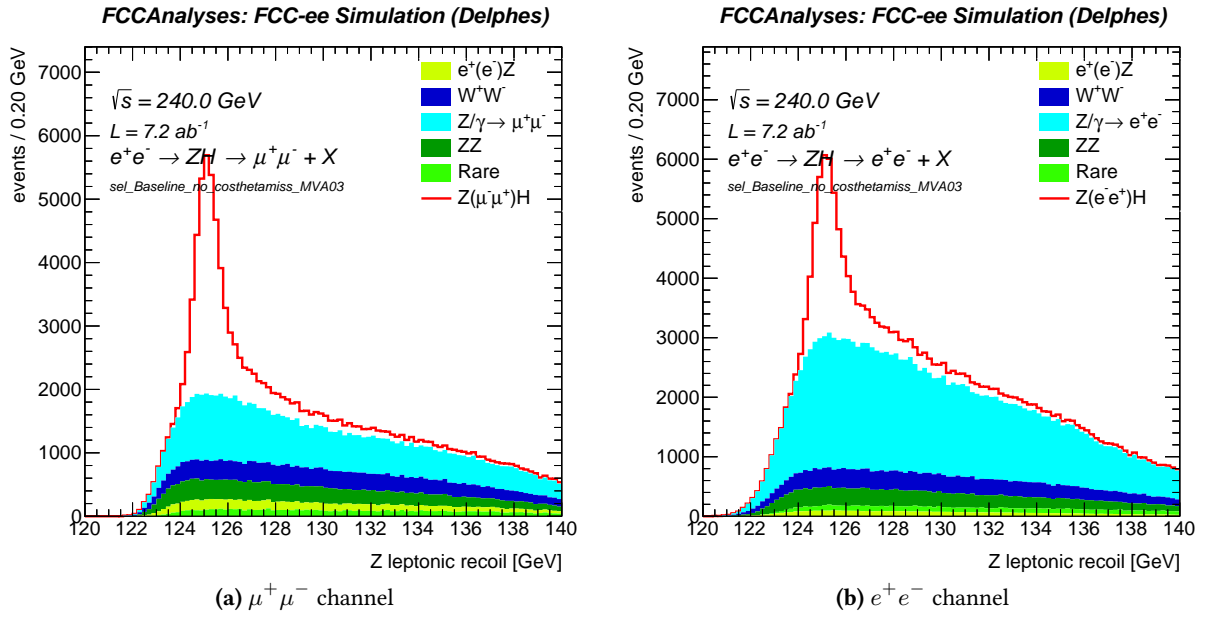


Figure 7.33: m_{rec} distribution for the $\mu^+\mu^-$ (a) and e^+e^- (b) channels in linear scale with basic selection, BDT score > 0.3 is applied, i.e. without the $\cos(\theta_{\text{miss}})$ requirement.

For the cross-section measurement, the signal yield is the only parameter of interest, thus the precise distribution of the signal shape is not required. Therefore, the binned fit method is introduced to avoid bias on the shapes. The model-independence after BDT requirements are also verified, but this prevents us to use a more powerful BDT model. With more powerful input variables used in the training, the BDT requirement will be more powerful but potentially break the model-independent requirement.

In Section 7.7.2.2, the BDT score shape is introduced as the fitted shape can avoid applying the BDT requirements, thus the model-independent requirement is always satisfied (due to the basic selection that was proven already to be model-independent).

A binned fit method was employed utilizing the m_{rec} in Section 7.7.2.1 or BDT response distribution in Section 7.7.2.2.

7.7.2.1 Fit on recoil mass distribution (m_{recoil})

The m_{rec} distribution is first used as the fitted shape to extract the signal yield, the same as the mass measurement in Section 7.6.

Figure 7.34 shows the m_{rec} distributions for the $\mu^+\mu^-$ and e^+e^- channels with baseline selection, i.e. basic selection with the additional $\cos(\theta_{\text{miss}})$ requirement. Figure 7.35 displays the m_{rec} distri-

butions for the $\mu^+\mu^-$ and e^+e^- channels with basic selection.

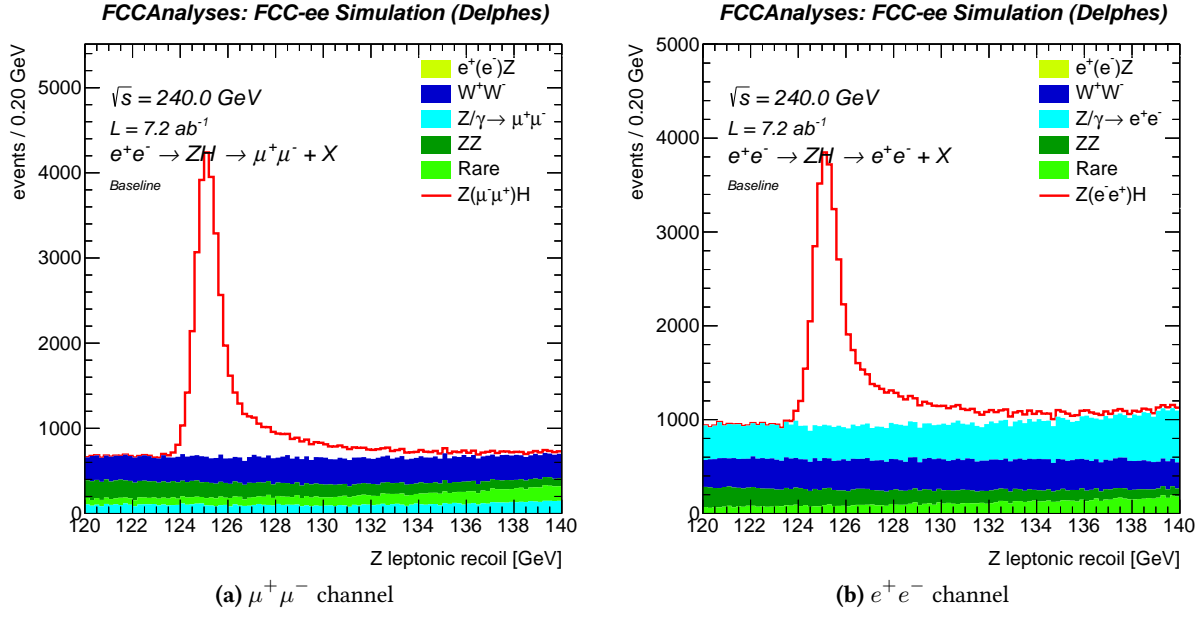


Figure 7.34: m_{rec} distribution for the $\mu^+\mu^-$ (a) and e^+e^- (b) channels in linear scale with baseline selection, i.e. with the $\cos\theta_{\text{missing}}$ requirement.

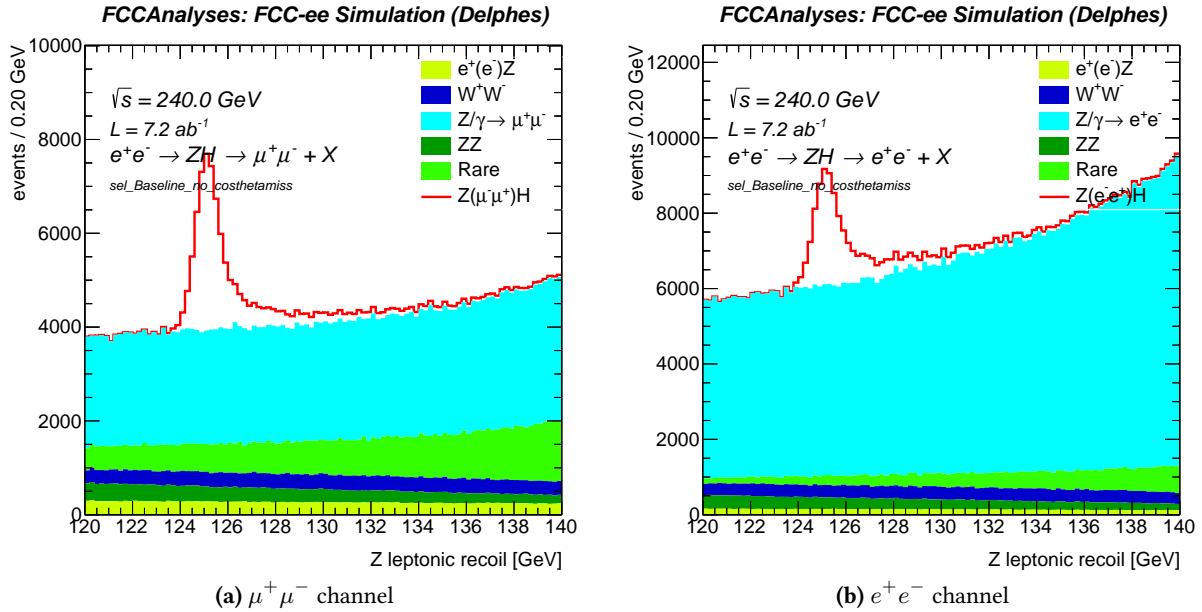


Figure 7.35: m_{rec} distribution for the $\mu^+\mu^-$ (a) and e^+e^- (b) channels in linear scale with basic selection.

The binned fit is applied on the m_{rec} distribution on both the baseline selection and baseline without $\cos(\theta_{\text{miss}})$ requirement.

The log-likelihood scans on baseline shape are depicted in Figure 7.36a. Fitting the baseline selection results in 0.82 % and 0.98 % uncertainty on the cross-section for $\mu^+\mu^-$ and e^+e^- respectively. The $\mu^+\mu^-$ and e^+e^- combined fit lower the uncertainty down to 0.63 %. The $\mu^+\mu^-$ channel is the dominant channel while e^+e^- improves the uncertainty by 23 %.

Removing the $\cos(\theta_{\text{miss}})$ requirement ensures model-independency but increases the cross-section uncertainty, from 0.63 % to 1.04 % (i.e. by 65 %), for the $\mu^+\mu^-$ plus e^+e^- channel combined result. The individual results are 1.28 % and 1.77 %, for the $\mu^+\mu^-$ and e^+e^- channels respectively.

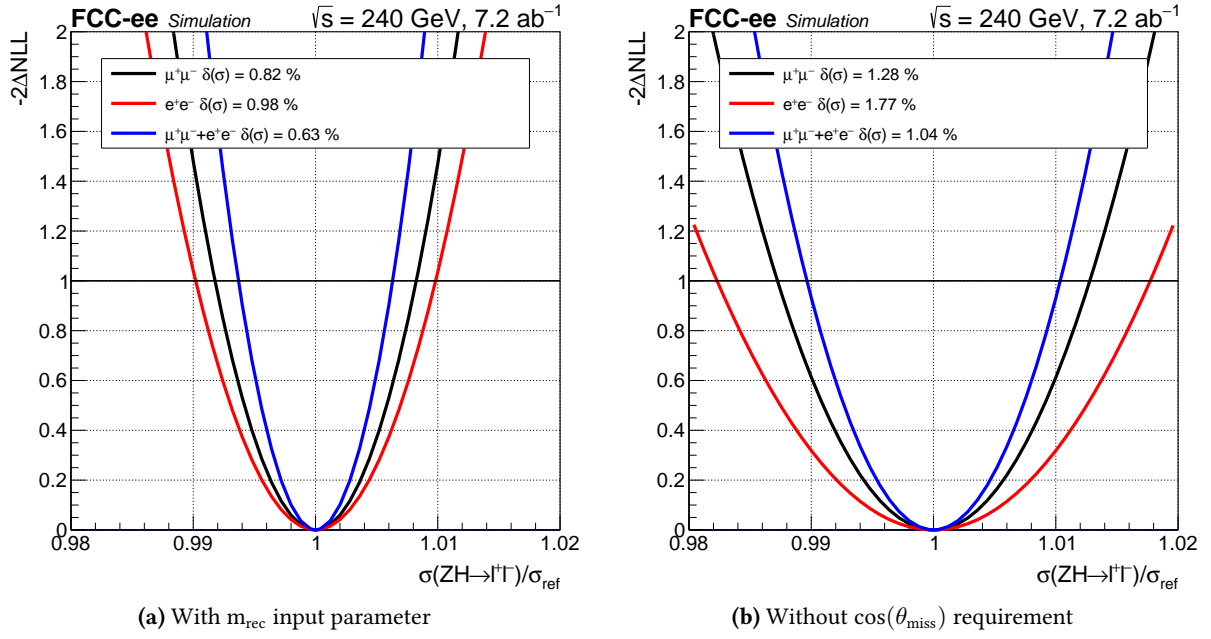


Figure 7.36: Fit results using m_{rec} as the input parameter. The differences in the fit profiles illustrate the impact of including or excluding the $\cos(\theta_{\text{miss}})$ requirement on the fitting process. (a) with baseline selection, while (b) without basic selection.

7.7.2.2 Fit on BDT score distribution

Since the cross-section is only related to the signal yield, it can be extracted by fitting on any variable. After training the BDT model, the BDT score became the most powerful variable to separate signal and background events. Therefore, the BDT score distribution is the best candidate for fitting among all the variables.

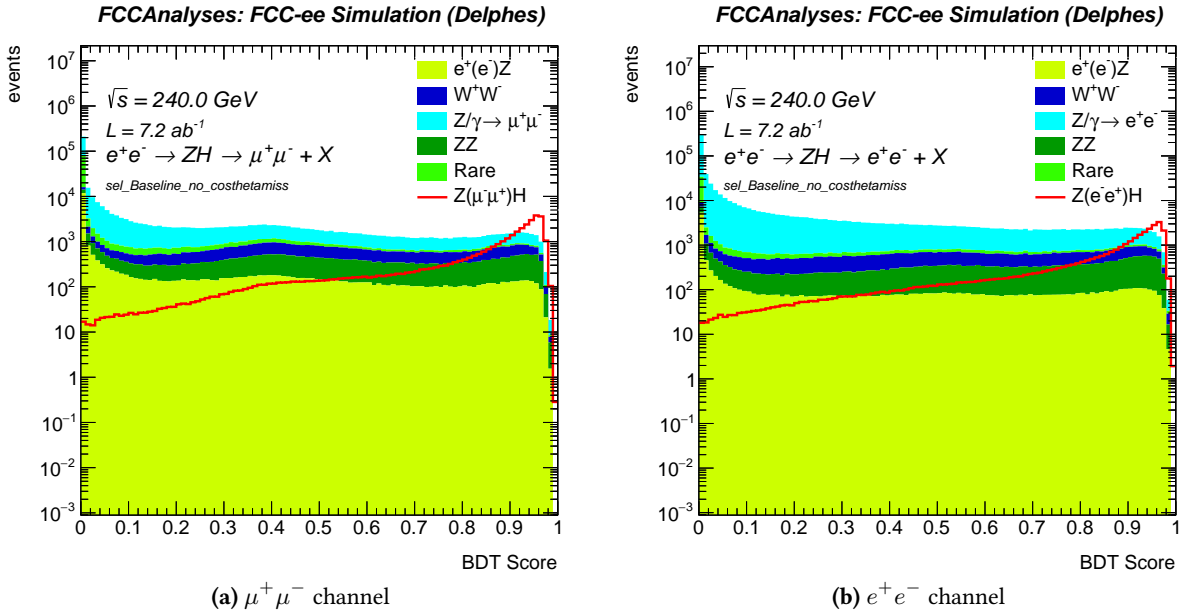


Figure 7.37: BDT score distributions for $\mu^+\mu^-$ (a) and e^+e^- (b) channels in log scale. The distributions demonstrate the BDT model's ability to effectively differentiate signal and background events, while the overlaid distribution represent the expected distributions used in the fitting process.

Figure 7.37 shows the BDT score distributions for both the $\mu^+\mu^-$ (Figure 7.37a) and e^+e^- (Figure 7.37b) channels in a logarithmic scale, after basic selection, highlighting the signal and back-

ground shapes used in the template fit. The events in these plots are normalized by the luminosity (7.2 ab^{-1}) and cross-section, which enables a direct comparison of the different distributions. In both panels, the signal events are represented by a red line, while the background events are shown as a stacked histogram.

The main purpose of these plots is to illustrate the distinct shapes of the signal and background distributions, which are crucial for the binned fitting procedure. The normalization by luminosity and cross-section ensures that the distributions are presented on a scale that reflects the events that could be collected in the detector, enabling the comparison of their shapes and the assessment of the binned fitting procedure's performance.

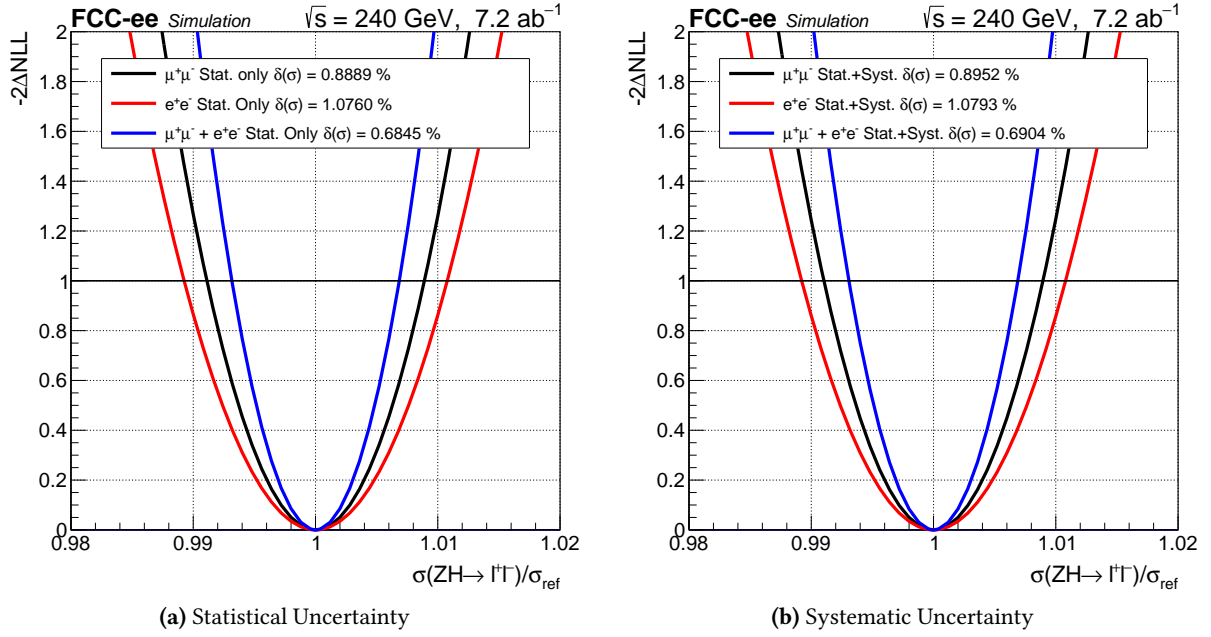


Figure 7.38: Log-likelihood fit results using the BDT score as the input parameter. The fit profile demonstrates the differences in the fitting process when employing an alternative input parameter. Statistical uncertainty (a) and statistic plus systematic uncertainties (including BES 1%, center-of-mass, lepton momentum scale) (b) are considered.

When fitting on the BDT score with the basic selection, the uncertainty for the $\mu^+\mu^-$ channel is 0.889 % and 1.076 % for the e^+e^- channel, while the combined uncertainty becomes 0.685 % (see Fig. 7.38). The $\mu^+\mu^-$ is here also the leading channel and e^+e^- improves the uncertainty by 23 %.

By employing the binned fit method using the BDT score, the analysis gains enhanced sensitivity and precision in estimating the signal yields for the $\mu^+\mu^-$ and e^+e^- channels in a model-independent way and have a sensitivity comparable to the model-dependent analysis which uses the $\cos(\theta_{\text{miss}})$ requirement (0.68 % vs. 0.63 %). Including the BES 1 %, center-of-mass, lepton momentum scale as systematic uncertainties increase the combined uncertainty to 0.690 % (0.685 % for statistical only). The BES is the leading systematic uncertainty which has about 0.09 % impact on the results. Center-of-mass, muon scale, and lepton scale are negligible (see Fig. 7.39 for the uncertainty breakdown).

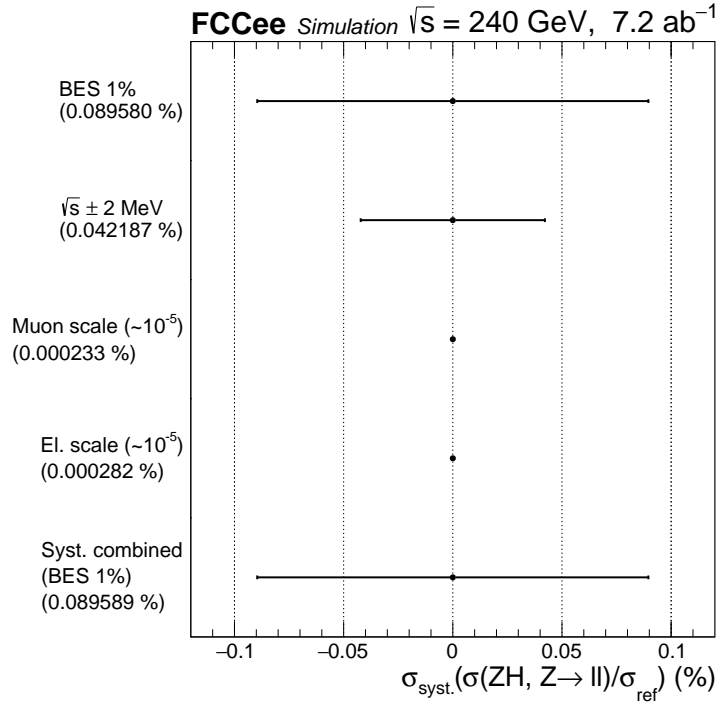


Figure 7.39: Uncertainty breakdown on the cross-section analysis.

7.7.3 Conclusion

A BDT approach has been introduced to replace the $\cos(\theta_{\text{miss}})$ requirement to ensure the model-independency of the ZH cross-section measurement. Binned fits are applied on both m_{rec} and BDT score distributions to obtain the uncertainties on the cross-section measurements.

Removing the $\cos(\theta_{\text{miss}})$ requirement increases the uncertainty on the ZH cross-section by 65 % (0.63 % to 1.04 %).

Changing the fit distribution from m_{rec} to the BDT score distribution, the uncertainty on the ZH cross-section is improved from 1.04 % to 0.68 %. It becomes comparable to the result obtained when fitting on m_{rec} with the model-dependent baseline selection (0.63 %), while the model independency is preserved.

The final result is predominantly due to the $\mu^+\mu^-$ channel, with the electron-electron channel contributing to a 23 % improvement.

7.8 Sources of systematic uncertainties

In this section, the main sources of systematic uncertainties are addressed, and their impact on both the cross-section and mass measurements is estimated. Several sources of systematic uncertainty must be taken into account when building the test statistic used to extract the proper uncertainties on the Higgs mass and cross-section. Such sources are modeled in the test statistic as nuisance parameters, with the effect of either changing the event rate of the considered signal and background processes (rate uncertainties) or changing the shape of the recoil mass template distributions (shape uncertainties). Depending on their type, experimental and theoretical uncertainties are propagated as shape or normalization uncertainties to the recoil mass and eventual other distributions such as control regions.

Nuisance parameters are propagated to the Likelihood by Gaussian constraint terms centered

around their zero-values (i.e. $\mu = 0$). The magnitude of the uncertainty, being the width σ that enters the Gaussian constraint term, is estimated by an educated guess or by additional studies. For each of the relevant systematics, their magnitude is estimated in this section. The impact of the nuisances and the breakdown are discussed in the relevant sections for the mass and cross-section.

Note that not all uncertainties are implemented yet in the fit. In particular, ISR, FSR, lepton resolution, signal and background modeling uncertainties have to be evaluated more precisely before being implemented in these analyses.

7.8.1 Beam Energy Spread (BES)

At a center-of-mass energy of $\sqrt{s} = 240$ GeV, the nominal (Gaussian) beam energy spread is equal $\pm 0.185\%$ per beam, or equivalently 222 MeV [10]. This energy spread is enabled in the WHIZARD and PYTHIA event generators as independent Gaussian smearing². The effect on the final recoil distribution is shown in Figure 7.40. A significant broadening of the mass peak is observed.

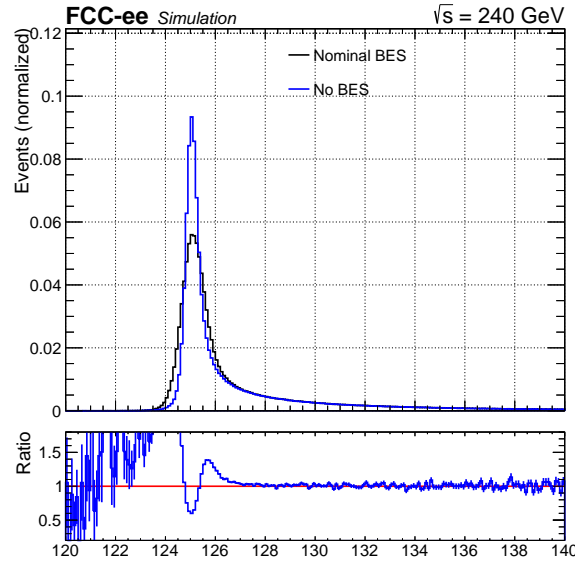


Figure 7.40: Effect of the beam energy spread (0 and 222 MeV) on the $Z(\mu, \mu)H$ recoil mass distribution.

The beam energy spread is subject to uncertainties related to the accelerator equipment (RF cavities and monitoring). As the BES has an impact on the recoil mass peak, it is important to quantify this effect and estimate the impact on the mass and cross-section measurements. We describe two methods to estimate the uncertainty of the BES:

1. Accelerator instrumentation: the bunch length can be monitored at the ps level or better, which is equivalent to $c \times 1 \text{ ps} = 0.3 \text{ mm}$. Since the bunch length at $\sqrt{s} = 240$ GeV is 5.3 mm, this corresponds to a beam energy spread uncertainty of about $0.3 / 5.3 = 6 \%$ (or better).
2. Data-driven: using $ee \rightarrow ff(\gamma)$ events by measuring the longitudinal imbalance of di-muon spectrum and/or Bhabha during the fill. This could constrain the BES uncertainty to 1 %.

In order to assess the impact of the BES uncertainties on the recoil mass distribution, two perturbed signals at the nominal Higgs mass value of 125 GeV were generated with $\pm 6 \%$ and $\pm 1 \%$ of BES uncertainty respectively w.r.t. the nominal BES value. The results and ratios w.r.t. the nominal are

²In PYTHIA 8.X.X, both beam smearing are varied simultaneously.

shown in Figure 7.41. For the $\pm 6\%$ variations, a shape effect of 1-2 % is observed near the mass peak, whereas the impact on the $\pm 1\%$ variations is reduced substantially.

The perturbed samples are fitted with the 2CBG PDF where the norm, CB μ , and CB σ are free parameters, keeping the other parameters as their nominal values derived from the central sample (nominal BES).

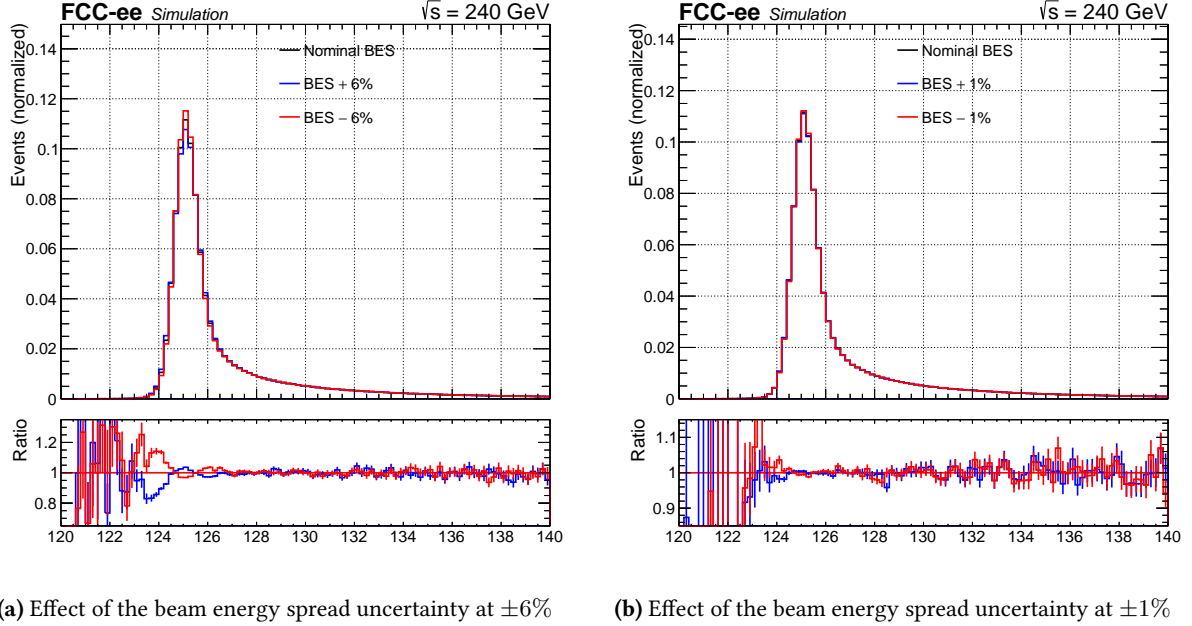


Figure 7.41: Effect of the beam energy spread uncertainty ($\pm 6\%$ left, $\pm 1\%$ right) on the $Z(\mu, \mu)H$ recoil mass distribution.

7.8.2 Initial State Radiation (ISR)

Initial State Radiation uncertainties arise from the mis-modelling of the ISR spectra in Monte-Carlo generators. It mainly affects the high-mass tails of the recoil mass distribution as can be seen from Figure 7.42a where the comparison has been made between switching ON and OFF the ISR uncertainty in WHIZARD. Apart from a small shift of the peak, the distribution broadens and the effect becomes more important in the high-mass tail of the distribution, as can be expected from the recoil mass formula.

The main goal is to derive a valid (shape) uncertainty for the ISR spectra, in order to evaluate its impact on the mass and cross-section measurements. Estimating the ISR uncertainty by taking the ISR OFF distribution is too drastic (cf. Figure 7.42) and will yield a large overestimation of the ISR uncertainty. Therefore, in the next paragraph, the ISR uncertainty with WHIZARD will be re-evaluated. Afterward, WHIZARD will be compared to the state-of-the-art KKMC Monte-Carlo generator.

As the WHIZARD ISR spectrum is quasi-identical to KKMC (see later) and there is a lack of handles to perturb the ISR in WHIZARD, currently ISR is not included as a systematic uncertainty.

7.8.2.1 ISR treatment in WHIZARD

There are two handles in WHIZARD to treat ISR uncertainty:

1. Order of the QED radiation approximation;

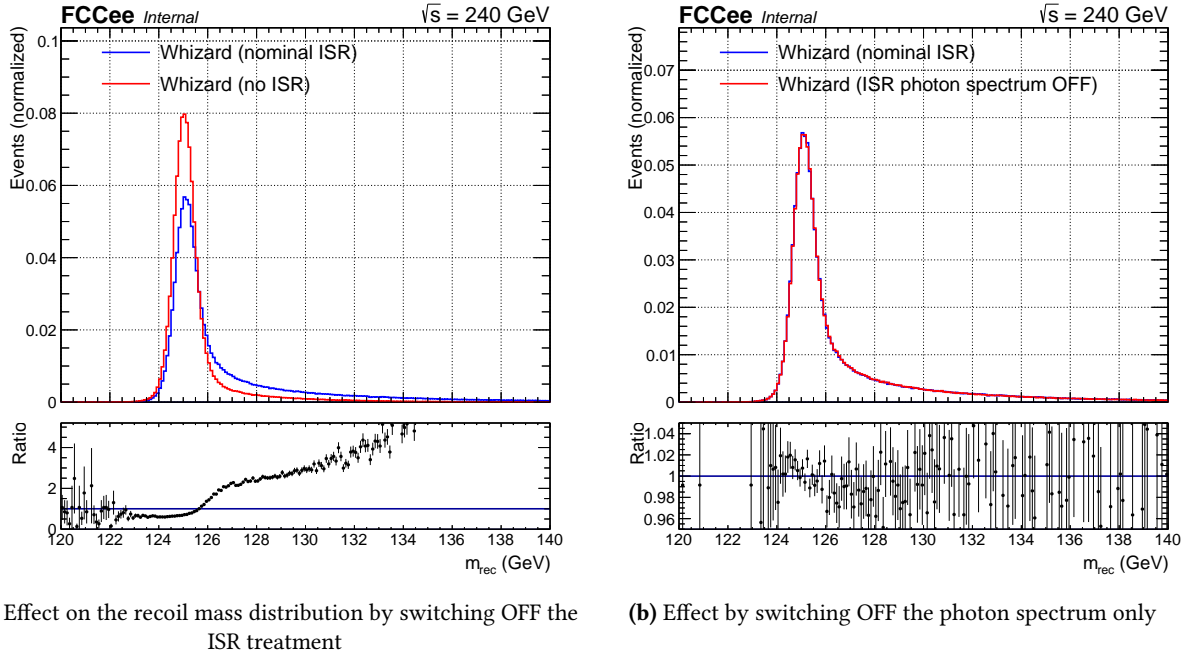


Figure 7.42: Effect on the recoil mass distribution by switching OFF the ISR treatment (a) and by switching OFF the photon spectrum only (b).

2. Binary flag related to giving a non-zero p_T spectrum to the photons (strict collinear approximation). An ad-hoc distribution for the photon spectrum is applied.

The effect on the latter, by switching OFF the photon p_T spectrum is shown in Figure 7.42b. A strong shape dependency is observed around the mass peak, but also on the tails despite being hardly visible due to the large statistical error bars.

This perturbed distribution was used to evaluate the impact of the ISR uncertainty on the mass and cross-section. The distribution is symmetrized around the central one (i.e. with nominal ISR). It was found that the impact is quite large due to its strong shape dependency, therefore this approach is very conservative. It is believed that the theoretical ISR uncertainties are much lower and more studies are to be performed to further reduce this uncertainty to a reasonable level.

7.8.2.2 Comparison with KKMC

KKMC is a state-of-the-art Monte-Carlo generator for $ee \rightarrow ff$ production, where the ISR treatment is known to be modeled properly, from previous comparison with data [201]. A comparison has been made between KKMC and WHIZARD in the $ee \rightarrow \mu\mu$ at $\sqrt{s} = 240$ GeV with ISR enabled but BES and FSR disabled, in order to assess only the ISR performance in WHIZARD (in this configuration all photons come from ISR).

In Figure 7.43, the sum of all the photon momenta and the di-muon momentum are shown, both of which are ISR-sensitive distributions, as a comparison between both event generators. Only the generator-level quantities are shown here. The requirements for these distributions are simple: exactly two opposite sign leptons with $m(\mu^+\mu^-) > 220$ GeV, to be in the same ISR-kinematical regime as the $e^+e^- \rightarrow ZH$ process. WHIZARD is producing distributions statistically compatible with the KKMC ones, therefore the ISR treatment in WHIZARD can be considered as accurate and valid. A slight trend in the high $p(\mu^+\mu^-)$ tail is observed, though within statistical uncertainty.

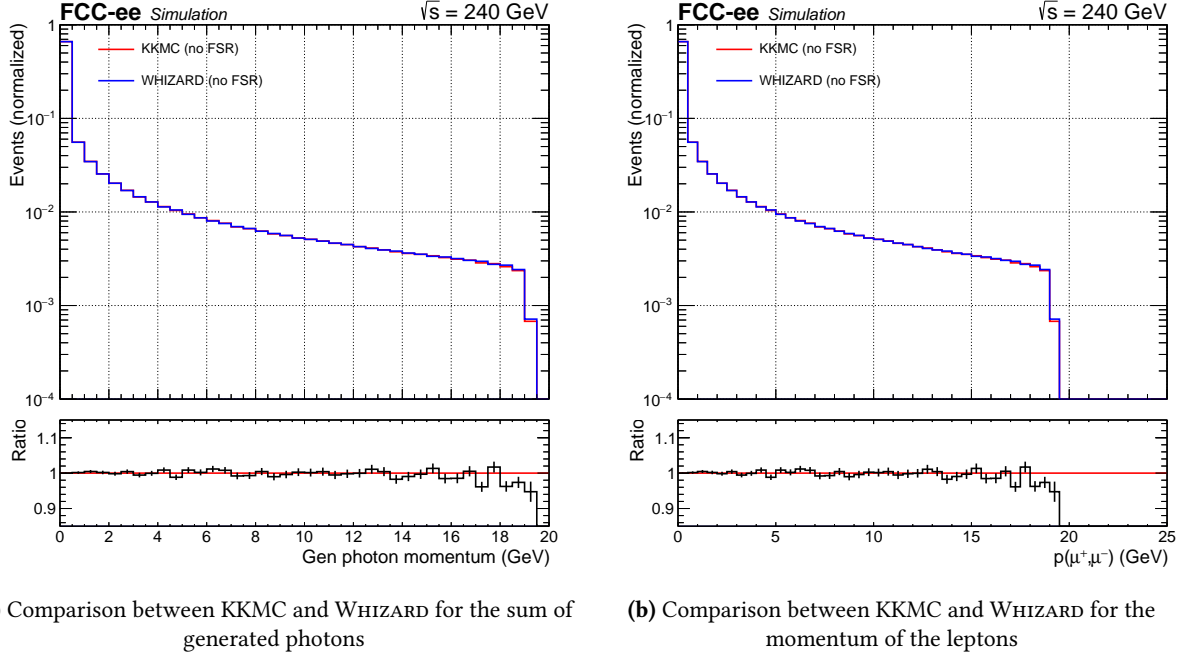


Figure 7.43: Comparison between KKMC and WHIZARD with ISR enabled but BES and FSR OFF. Exactly two opposite-sign leptons are required with $m(\mu^+\mu^-) > 220$ GeV.

7.8.3 Center-of-mass (COM)

The center-of-mass energy at $\sqrt{s} = 240$ GeV is expected to be known at the 2 MeV level or better. It will be measured precisely using radiative return events in the $Z \rightarrow \mu\mu$ or $Z \rightarrow jj$ channels. Radiative return is used to calibrate the center-of-mass energy in high-energy physics experiments by analyzing the energy of photons emitted by particles like electrons or positrons before collision, allowing precise determination of the energy at which particle interactions occur. As \sqrt{s} enters directly into the recoil mass definition, the impact of this uncertainty translates directly into a 2 MeV systematic uncertainty on the fitted mass. The change on the cross-section is expected to be negligible.

From the definition of the recoil mass (with E_i the energy of lepton i),

$$m_{rec}^2 = s - 2\sqrt{s}(E_1 + E_2) + m_{ll}^2 \quad (7.8.1)$$

and assuming $E_1 + E_2 = m_Z$ and $m_{rec} = m_H$ one obtains $E_1 + E_2 = (s + m_Z^2 - m_H^2)/(2\sqrt{s})$. If \sqrt{s} differs with an amount of δ , one has:

$$m_{rec}^2 = (\sqrt{s} + \delta)^2 - 2(\sqrt{s} + \delta)(s + m_Z^2 - m_H^2)/(2\sqrt{s}) + m_{ll}^2. \quad (7.8.2)$$

Taking the differential:

$$d(m_{rec}^2) = \delta(s - m_Z^2 + m_H^2)/(2\sqrt{s}), \quad (7.8.3)$$

which numerically yields $d(m_{rec}) = 1.08 * \delta * 125 \text{ GeV}/m_{rec}$ (note that 1.08 would be 1.0 if we were exactly at the threshold). Finally, if the center-of-mass is shifted by 2 MeV ($= \delta$), the corresponding variation on $d(m_{rec}) = 2.16$ MeV. This simple calculation assumes no shape variation

but rather a shift of the recoil mass peak. However, nearly all the statistics are within ± 1 GeV of the peak, such that the shift can be considered as constant within 1 %.

In Figure 7.44a, the perturbed samples are fitted with the 2CBG PDF where the norm, CB μ , and CB σ are free parameters, keeping the other parameters as their nominal values derived from the central sample (nominal BES).

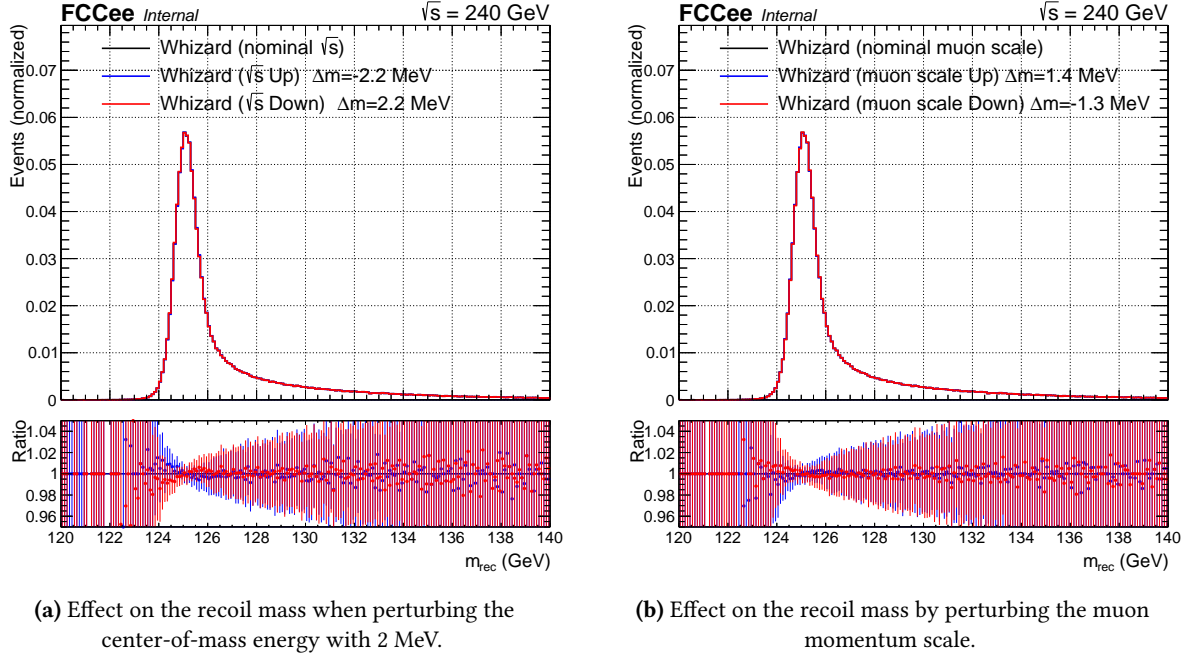


Figure 7.44: Effect on the recoil mass when perturbing the center-of-mass energy with 2 MeV (a) and the muon momentum scale (b). The quoted Δm values are the mean histogram values w.r.t. the nominal sample. Plots are done using the Spring2021 campaign.

7.8.4 Lepton momentum scale (LEPSCALE)

The lepton momentum scale can safely be assumed to be in the order of 10^{-5} due to the large statistical power of radiative return events which could constrain the lepton scale up to this precision.

Indeed, with 7.2 ab^{-1} of data at $\sqrt{s} = 240$ GeV, we will have about 100 M of Z bosons from the radiative return, hence 3 M (per lepton flavor) of $Z \rightarrow \ell\ell$ that can be used to calibrate the scale. The resolution on the $Z \rightarrow \ell\ell$ mass peak is about 150-200 MeV, hence an uncertainty on the peak position of $200 \text{ MeV} / \sqrt{3 \times 10^6} = 0.11 \text{ MeV}$. Hence, there is the statistical potential to determine in-situ the scale with a relative uncertainty of $0.11 \text{ MeV} / 90 \text{ GeV} = 10^{-6}$, comparable to the relative uncertainty on the Z mass. However, since it is not proven yet that the stability of the magnetic field can be controlled to the level of 10^{-6} or better, we can take 10^{-5} as a conservative estimate (NMR probes should allow monitoring of the field to that level). One may also want to check the (θ, ϕ) dependence of the scale, but the calibration runs at the Z peak will provide a high level of precision.

To understand the effect on the recoil mass, one needs to change the lepton energies by $\delta = 10^{-5} \times E$, with $E \approx 45$ GeV since the Z is nearly at rest. Writing that $m_{ll} \approx E_1 + E_2$, one obtains that $d(m_{rec}^2) = 4 * \delta * (\sqrt{s} - m_Z)$, which yields in the peak region $d(m_{rec}) = 2 * \delta * 150/125 = 1 \text{ MeV}$.

This simple error propagation gives a resulting uncertainty of 1 MeV on the mass. This is checked in the analysis by changing the lepton energy with a factor of 10^{-5} and checking the resulting recoil distribution. Indeed, the impact on the fit with the perturbed momentum scale results in an

uncertainty of approximately 1 MeV for both muons and electrons.

The lepton scale uncertainty for muons and for electrons are independent since they are measured in independent event phase spaces. Hence, the muon and electron momentum scales are decorrelated in the fit. An example of the effect of the muon momentum scale uncertainty is shown in Figure 7.44b.

The resulting varied scale profiles are used as shape uncertainties in the fit. The perturbed samples are fitted with the 2CBG PDF where the norm, CB μ , and CB σ are free parameters, keeping the other parameters as their nominal values derived from the central sample (nominal BES).

7.8.5 Lepton momentum resolution (LEPRES)

Uncertainty related to the muon momentum resolution must be taken into account. It directly affects the width of the recoil distribution, hence the precision of how the Higgs mass can be resolved. Resolution stability and uncertainties are extracted from $Z \rightarrow \ell\ell$ events, as discussed in the previous paragraph. The uncertainty has to be propagated to the analysis and the impact has to be estimated.

7.8.6 Final State Radiation (FSR)

By default, QED Final State Radiation (FSR) is performed by PYTHIA. However, the KKMC FSR implementation is more state-of-the-art as it has an implementation of PHOTOS which is fine-tuned mostly to LEP data. An uncertainty of the FSR spectra between KKMC and WHIZARD has to be implemented and propagated to the fit.

7.8.7 Signal modeling (SIGM)

A systematic uncertainty to take into account the signal modeling has to be implemented in the fit.

7.8.8 Background modeling (BKGM)

A systematic uncertainty to take into account the background modeling has to be implemented in the fit.

7.9 Experimental requirements

In this section, a summary of the detector requirements is given, which are mainly applicable to the mass analysis.

An ultimate precision on the Higgs mass measurement of 4.0 MeV is achievable with an integrated luminosity of 7.2 ab^{-1} and using the improved IDEA detector, consisting of a very light drift chamber and crystal electromagnetic calorimeter. It has been shown that the uncertainty on the Higgs mass is 3.1 MeV (stat. only) and increases to 4.0 MeV when systematics are taken into account. The impact on the experimental uncertainties is close to 30 %, dominated by the center-of-mass uncertainty of 2 MeV. In order to keep the systematic component as small as possible compared to the statistical uncertainty, strict experimental requirements are necessary and studied extensively.

The muon channel is dominant in the mass uncertainty, therefore an excellent tracking performance is a key detector requirement for this analysis. Thanks to the drift chamber, resolutions at the sub-percent level are achievable, depending on the momentum and position in the detector. As shown, when replacing the reconstructed muons and their uncertainties with the associated generator kinematics, the total uncertainty on the mass, dominated by the selection requirements and backgrounds, improves by 24 % (stat. only) and 17 % (stat. + syst.). When increasing the magnetic field from 2 T to 3 T, the uncertainty improves by 17 % (stat. only) and 12 % (stat. + syst.), and is limited by the beam energy spread which becomes dominant. Given the potential extra expected complications regarding the machine-detector interface and luminosity control upon increasing the magnetic field, such an option will need further studies to be included in the detector design. Categorization of the events in distinct polar angle regions decouples the different resolutions of the forward and central regions, leading to an improvement of 20 % (stat. only) and 12 % (stat. + syst.).

On the other hand, including the electron channel improves the uncertainty by 23 % (stat. only) and 22 % (stat. + syst.), which is less than the potential statistical improvement of 41 %. This is primarily due to the worse momentum resolution of the electrons, rather than the increase of the Z/γ t-channel background. Nevertheless, the crystal calorimeter has an excellent resolution for low energy photons, such that the Bremsstrahlung photons can be recovered, leading to a global electron momentum resolution that is "only" 25 % less performant than the one from muons. To see the impact of a degraded electron momentum resolution (e.g. by the usage of a less performant electromagnetic calorimeter), the analysis was repeated by using an electron momentum resolution with a factor of 2 worse than for muons (instead of the nominal factor of 1.25), leading to an overall degradation of the Higgs mass uncertainty of 6 % (stat. only) and 2 % (stat. + syst.) w.r.t. the nominal detector configuration.

The beam energy spread of 222 MeV contributes strongly to the broadening of the recoil distribution. The associated uncertainty, estimated by data-driven techniques, is 1 %, which amounts to a few MeV on the beam energy uncertainty. The resulting uncertainty of the BES-only uncertainty on the Higgs mass is less than 1 MeV. To assess the impact on the beam energy spread itself, a study has been performed by switching off entirely the beam energy spread, which translated in an improvement of about 43 % (stat. only) and 25 % (stat. + syst.) on the Higgs mass uncertainty.

A dominating systematic uncertainty originates from the precision of the center-of-mass energy \sqrt{s} , which directly enters the recoil mass definition. Data-driven estimates show that this can be controlled up to a 2 MeV level, but more rigorous studies have to be performed. After implementing such uncertainty in the fit, the impact on the center-of-mass only on the Higgs mass was found to be 2 MeV, as expected, which serves as a validation of the methods and fit strategies used.

7.10 Conclusion

In this chapter, the Higgs boson mass and the model-independent ZH cross-section measurements have been studied using di-muon and di-electron events, using the recoil mass method, with the FCC-ee simulated data at $\sqrt{s} = 240$ GeV. First, a basic event selection is applied to reduce the main backgrounds while retaining the signal yields. The cross-section measurement then proceeds using a dedicated Boosted Decision Tree to further separate the signal from backgrounds, with emphasis on Higgs decay mode independence. The di-electron and di-muon final states are fitted simultaneously to extract the ZH cross-section with a relative precision of 0.69 %. Instead of the BDT, the Higgs mass analysis uses an additional kinematic requirement to reduce the background: the Higgs mass is measured by fitting directly the recoil mass distribution, after imposing an additional selection on $\cos(\theta_{\text{miss}})$. The recoil mass distributions are modeled analytically using a custom PDF and are injected into a maximum likelihood fit to extract the mass uncertainty. By

categorizing the leptons based on their polar angle, the sensitivity is increased and a combined uncertainty of 4.0 MeV is obtained when including the dominant systematics. Several systematic uncertainties have been evaluated and found to be almost negligible for the cross-section measurement, but impacting the Higgs mass uncertainty at the 30 % level. An extensive set of experimental requirements have been discussed, both from the machine and detector point of view, and the conclusion is that the tracking performance and the center-of-mass energy determination are the most crucial elements. They must be controlled precisely to achieve the final precision that the statistics that will be delivered by FCC-ee is promising.

Conclusion

In this dissertation, contributions to the understanding of physics within the ATLAS experiment and the Future Circular Collider (FCC) project have been made. Through analysis and the application of advanced statistical and machine learning techniques, new insights have been gained and innovative methodologies have been developed and validated.

Within the ATLAS experiment, the first achievement was the successful implementation of the p_T^{rel} calibration method, utilizing the Run 2 dataset. This calibration was applied to the DL1r b -tagger for the first time in muon-in-jet events, with the extrapolation from semi-leptonic to inclusive events. A comparative analysis with the $t\bar{t}$ calibration, the primary calibration method at ATLAS, revealed agreement, affirming the efficacy of the p_T^{rel} calibration as a viable alternative or complementary approach.

The search for double Higgs production presented a focal point, with a detailed analysis combining both ggF and VBF production modes. Utilizing the full Run 2 LHC pp collision data at $\sqrt{s} = 13$ TeV collected with the ATLAS detector, with an integrated luminosity of 140fb^{-1} , the study examined Higgs boson decays into b -quarks and τ leptons. The analysis was divided into the $\tau_{\text{had}}\tau_{\text{had}}$ and $\tau_{\text{lep}}\tau_{\text{had}}$ channels, with the latter further subdivided based on the trigger used.

A set of dedicated classifier utilizing Boosted Decision Trees (BDTs) was employed to define ggF- and VBF-enriched signal regions. The ggF-enriched signal region is further divided into ggF-high m_{HH} and ggF-low m_{HH} regions to capture SM and BSM signal separately. Dedicated BDTs were trained on these signal regions to discriminate the signal and background and used to extract parameters such as signal strength μ_{HH} , and coupling parameters κ_λ and κ_{2V} . The sensitivity of the analysis exhibits an improvement ranging from 10% to 20%, depending on the parameter of interest.

No significant excess above the expected background from Standard Model processes is observed.

For this channel, the observed (expected) upper limit for the di-Higgs production cross-section obtained in our study is 5.9 (3.1) times the SM prediction at a 95% confidence level.

The Higgs self-coupling parameter, κ_λ , has an observed (expected) 95% confidential interval of $-3.2 < \kappa_\lambda < 9.1$ ($-2.5 < \kappa_\lambda < 9.2$). Moreover, the 95% confidential interval of di-Higgs to two weak bosons ($HHVV$) coupling parameter, κ_{2V} , is observed (expected) to be constrained between $-0.4 < \kappa_{2V} < 2.6$ ($-0.2 < \kappa_{2V} < 2.4$).

On the FCC feasibility studies, the focus was on Higgs mass and ZH cross-section measurements in the $ZH \rightarrow l^+l^-$ channel, where the Z boson decays into a pair of muons or electrons, with the FCC-ee simulated data at $\sqrt{s} = 240$ GeV.

The "recoil" technique is used to identify the Higgs candidates against the Z boson, using the energy-momentum conservation law. A customized PDF is used to model the recoil mass distributions, which are then injected into a maximum likelihood fit to extract the mass uncertainty. By categorizing the leptons based on their polar angle, the sensitivity is increased and a combined uncertainty of 4.0 MeV is obtained when including the dominant systematics.

A dedicated Boosted Decision Tree (BDT) is employed to remove the cut $\cos(\theta_{\text{miss}})$ which breaks the decay mode independence of the ZH cross-section measurement. The BDT response was used to extract the ZH cross-section uncertainty with a relative precision of 0.69 %.

The evaluation of several systematic uncertainties underscored their minimal impact on the cross-section measurement while impacting the Higgs mass uncertainty at the 30 % level.

A discussion on experimental requisites, from both machine and detector perspectives, emphasized the importance of precise control over tracking performance and center-of-mass energy determination to fully harness the statistical potential offered by FCC-ee.

The collective findings and methodological advancements within this dissertation not only enrich the existing body of knowledge but also provide a solid foundation for future explorations within the realms of the ATLAS experiment and the FCC project. The implications of this work extend through the broader scientific community, contributing towards the ongoing quest to unravel the fundamental intricacies of the universe.

Appendix

Spurious Signal Test for di-Higgs production in the $b\bar{b}\gamma\gamma$ final state

A.1	Smoothing the di-photon background	245
A.1.1	Gaussian Process Regression	246
A.1.1.1	1 GeV and 4 GeV binning result	246
A.1.2	4-to-1GeV refill method (or equivalently RGFR method)	246
A.1.2.1	Fit Function	246
A.1.2.2	Histogram refilling	250
A.1.2.3	Final RGFR (4-to-1 GeV) smoothing strategy	251
A.2	Spurious Signal Test	253
A.2.1	Test of Original Data	253
A.2.2	Test of the distribution obtained with the RGFR (4-to-1 GeV) method	253
A.3	Conclusion	257

A.1 Smoothing the di-photon background

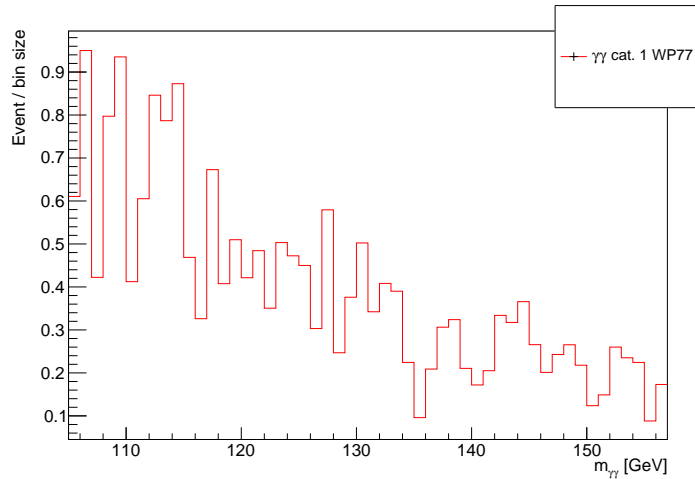


Figure A.1: Continuum $\gamma\gamma$ distribution of category 1

The knowledge of the background shape is essential to distinguish the small di-Higgs signal from the background. Unfortunately, for $HH \rightarrow b\bar{b}\gamma\gamma$ simulation, the number of $\gamma\gamma$ events after selection in Monte-Carlo is small and the H025 baseline selection also rejects numerous events. In the low statistic case, the statistical fluctuation becomes important. Figure A.1 shows the significant fluctuation of $\gamma\gamma$ distribution of category 1 (high mass tight BDT score). A smoothing method

is expected to reduce the statistical fluctuation and give better separation between the di-photon background and the di-Higgs signal.

A.1.1 Gaussian Process Regression

Gaussian Process Regression (GPR) [202] is a nonparametric approach to regression, which works well on small datasets [203]. Unlike many machine learning algorithms, GPR does not learn exact values for every parameter in a function. In this section, Gaussian Process Regression will be used to smooth the continuum $\gamma\gamma$ background. Monte-Carlo data are sorted into five categories following the H025 baseline selection.

A.1.1.1 1 GeV and 4 GeV binning result

Both 1 GeV binning and 4 GeV binning are studied in this part, therefore the range $105\text{GeV} < m_{\gamma\gamma} < 157\text{GeV}$ is chosen to have integer bin numbers for both 1 GeV and 4 GeV binning. The GPR smoothed results with 1 GeV binning are shown in figure A.2.

The original histograms are in red while the GPR smoothed results are in blue. For category 2 and 4, the GPR results are smooth and falling monotonically while category 1, 3 and VBF results are oscillating in the mass window ($m_{\gamma\gamma} \in [105, 157]$ GeV). It is the consequence of high fluctuation and low events in each bin. Therefore, the bin width is enlarged to 4 GeV in order to increase the statistic in each bin and reduce the fluctuation. In this case, 4 GeV binnings were used as the GPR input to obtain smooth and monotonic result.

In figure A.3, the 4 GeV binning GPR smoothed results are shown. After rebinning into 4 GeV, all the five categories display a smooth histogram.

A.1.2 4-to-1GeV refill method (or equivalently RGFR method)

Although the 4 GeV binning GPR smoothed result is satisfactory, it cannot be used directly since all the other channels, including the di-Higgs signal, will use 1 GeV binning. In order to reproduce 1 GeV binning histograms, the RGFR (Rebin-GPR-Fit-Refill) method is introduced.

Indeed, once the original distribution has been rebinned and the GPR algorithm has been applied, the RGFR (4-to-1 GeV) refill method needs two additional steps:

1. Fitting the 4 GeV binning GPR smoothed results,
2. Refilling 1 GeV histograms using this fit function.

The basic idea of this method is to use the most likely analytic function of the GPR smoothed histogram to do the fast function based Monte Carlo simulation. The refill function will be chosen in A.1.2.1 and the refill histograms will be checked in A.1.2.2

A.1.2.1 Fit Function

The fit function should be as close to the object distribution as possible. The χ^2/NDF is used to describe the difference between the fit function and the original or GPR smoothed histogram. Table A.1 shows the χ^2/NDF of the fit of original distributions, where the sum of all 5 categories are close for 3rd, 4th, 5th polynomial and exponential function.

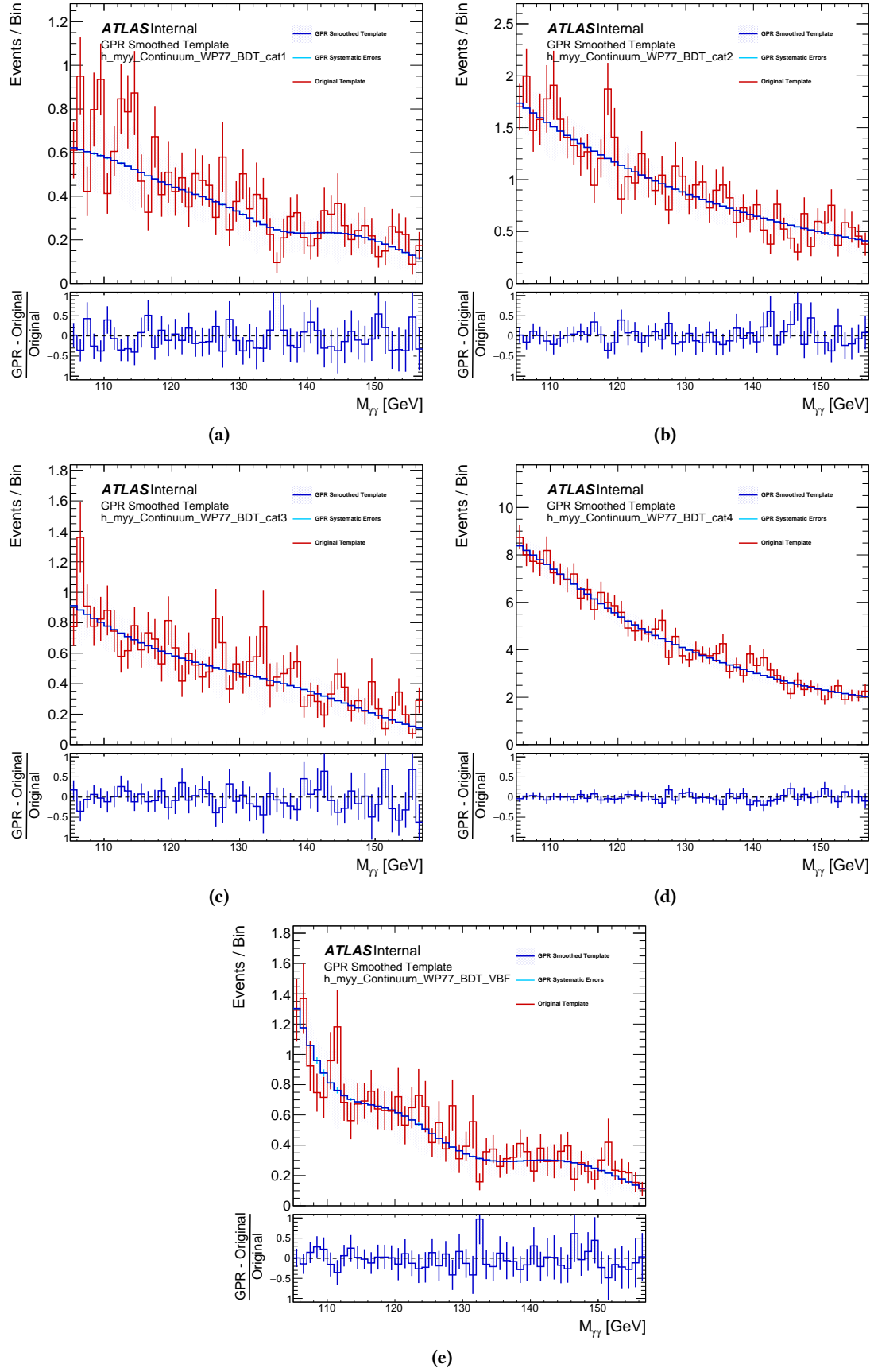


Figure A.2: 1 GeV binning GPR smoothing result of category 1, 2, 3, 4 and VBF based on H025 baseline selection

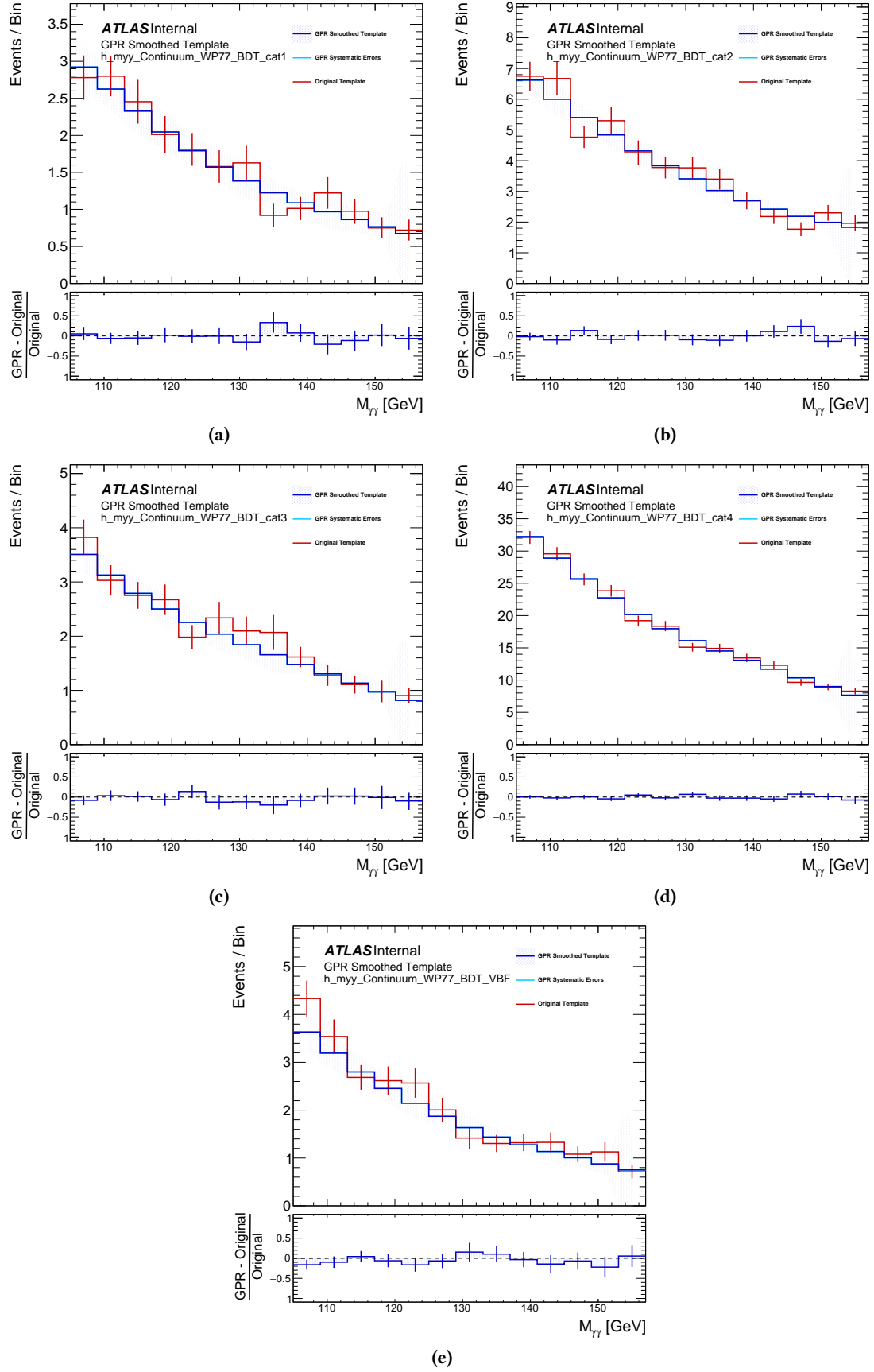


Figure A.3: 4 GeV binning GPR smoothing result of category 1, 2, 3, 4 and VBF based on H025 baseline

χ^2/NDF	Category 1	Category 2	Category 3	Category 4	VBF	Sum of 5 categories
Pol. 2	1.4510	1.2257	1.1915	1.0246	1.1432	6.0360
Pol. 3	1.4827	1.2496	1.1773	1.0259	1.0544	5.9900
Pol. 4	1.5113	1.2758	1.2046	1.0494	1.0698	6.1109
Pol. 5	1.5425	1.2516	1.2333	1.0749	1.0857	6.1880
Exp.	1.4300	1.2170	1.3262	0.9955	1.0933	6.0680

Table A.1: χ^2/NDF of original fitting with second, third, fourth, fifth order polynomial and exponential function.

In table A.2 which shows the χ^2/NDF of the 4 GeV binning GPR smoothed, one sees that the 4th and 5th order polynomial give the smallest χ^2/NDF , meaning they are good candidates to reproduce the 4 GeV binning GPR smoothed histogram. In average of both table A.1 and A.2, the 4th polynomial is best choice. The χ^2/NDF are abnormally small since the uncertainties are not corrected for the smoothing procedure.

χ^2/NDF	Category 1	Category 2	Category 3	Category 4	VBF	Sum of 5 categories
Pol. 2	0.0091	0.0010	0.0303	0.2755	0.0280	0.3440
Pol. 3	0.0194	0.0033	0.0456	0.0169	0.0498	0.1350
Pol. 4	0.0027	0.0011	0.0035	0.0142	0.0014	0.0229
Pol. 5	0.0024	0.0009	0.0055	0.0128	0.0009	0.0224
Exp.	0.0049	0.0201	0.0592	0.1130	0.0049	0.2022

Table A.2: χ^2/NDF of 4 GeV binning GPR smoothed fitting with second, third, fourth, fifth order polynomial and exponential function.

The 4th and 5th order polynomial give almost the same shape. Then their fit to the original histograms are studied in order to confirm that 4th order polynomial is the best fit function comparing to the 5th order polynomial.

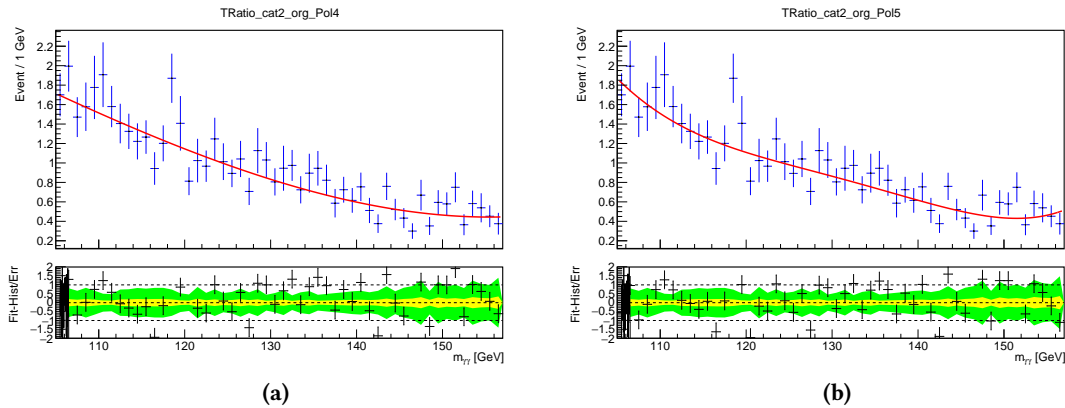


Figure A.4: Fit of category 2 original distribution with 4th (on the left) and 5th (on the right) order polynomial. Original distribution in blue while fit function in red.

In figure A.4, the 4th (left) and 5th (right) order polynomial fit of the original category 2 distribution are shown. For category 2, the 5th order polynomial is overfitted on the two edges, while 4th order does not have edge effect. In this case, 4th order polynomial is the best choice to fit the 4 GeV binning GRP smoothed result.

A.1.2.2 Histogram refilling

In this section, the 4^{th} order polynomial is used to refill the histogram using the same, 10 times and 100 times the number of entries as the original histogram for each category. After the refilling, χ^2/NDF are used to test the properties of the refilled histogram. The test results of the refilled histograms with 1 times, 10 times and 100 times the number of entries than the original are shown in table A.3, A.4 and A.5 respectively.

χ^2/NDF	Category 1	Category 2	Category 3	Category 4	VBF	Sum of 5 categories
1 times entries						
Pol. 3	1.1110	0.9161	0.8719	1.3611	0.9428	5.2028
Pol. 4	1.1250	0.9349	0.8907	1.3880	0.9553	5.2938
Pol. 5	1.1405	0.9546	0.9097	1.4152	0.9741	5.3941
Exp.	1.2180	0.8902	0.8489	1.3110	0.9074	5.1754

Table A.3: χ^2/NDF of fit of RGFR (4-to-1 GeV) refill histogram using 4^{th} order polynomial with the same numbers of entries as the original histogram

χ^2/NDF	Category 1	Category 2	Category 3	Category 4	VBF	Sum of 5 categories
10 times entries						
Pol. 3	0.7507	0.6842	0.9677	1.0968	0.6112	4.1107
Pol. 4	0.7654	0.6978	0.9941	1.1095	0.6236	4.1904
Pol. 5	0.7813	0.7115	1.0224	1.1263	0.6388	4.2803
Exp.	0.8073	0.7554	1.3534	1.3710	0.7139	5.0010

Table A.4: χ^2/NDF of fit of RGFR (4-to-1 GeV) refill histogram using 4^{th} order polynomial with 10 times the number entries compared to the original histogram

χ^2/NDF	Category 1	Category 2	Category 3	Category 4	VBF	Sum of 5 categories
100 times entries						
Pol. 3	0.8875	0.7414	1.1093	1.1434	0.9021	4.7837
Pol. 4	0.9020	0.7575	1.1263	1.0360	0.8946	4.7164
Pol. 5	0.9164	0.7760	1.1526	0.9834	0.8923	4.7207
Exp.	1.0583	1.1770	3.3048	5.1683	1.0144	11.7227

Table A.5: χ^2/NDF of fit of RGFR (4-to-1 GeV) refill histogram using 4^{th} order polynomial with 100 times the number entries compared to the original histogram

For the 3^{rd} , 4^{th} and 5^{th} order polynomial fit, χ^2/NDF is close to one for all 1, 10 and 100 times entries, meaning the uncertainties are also well reproduced. With the increase of entries, the χ^2/NDF of the fit using exponential function increase because the refilled histogram have the shape of 4^{th} order polynomial and the increased statistics underline the shape difference of the different functions compared to the 4^{th} order polynomial. 100 times the number of entries are chosen in order to reduce the statistical fluctuations.

A.1.2.3 Final RGFR (4-to-1 GeV) smoothing strategy

In the end, for this study, the final RGFR (4-to-1 GeV) smoothing strategy is as follows:

1. Rebinning original 1 GeV binning histogram to 4 GeV binning histogram,
2. Running GPR smoothing,
3. Fitting 4 GeV GPR smoothed histogram with 4^{th} order polynomial function and obtaining this fit function,
4. Refilling 1 GeV binning histogram using the fit function in the previous step with 100 times the number of entries than the original.

One could find the comparison of the di-Higgs and single Higgs distribution on top of original and RGFR (4-to-1 GeV) smoothed $\gamma\gamma$ distribution in figure A.5, where the left coloum shows the di-higgs, single higgs and original $\gamma\gamma$ distribution, which has important fluctuation, while the right with RGFR (4-to-1 GeV) refilled $\gamma\gamma$ distribution, which is smooth with significantly smaller fluctuations.

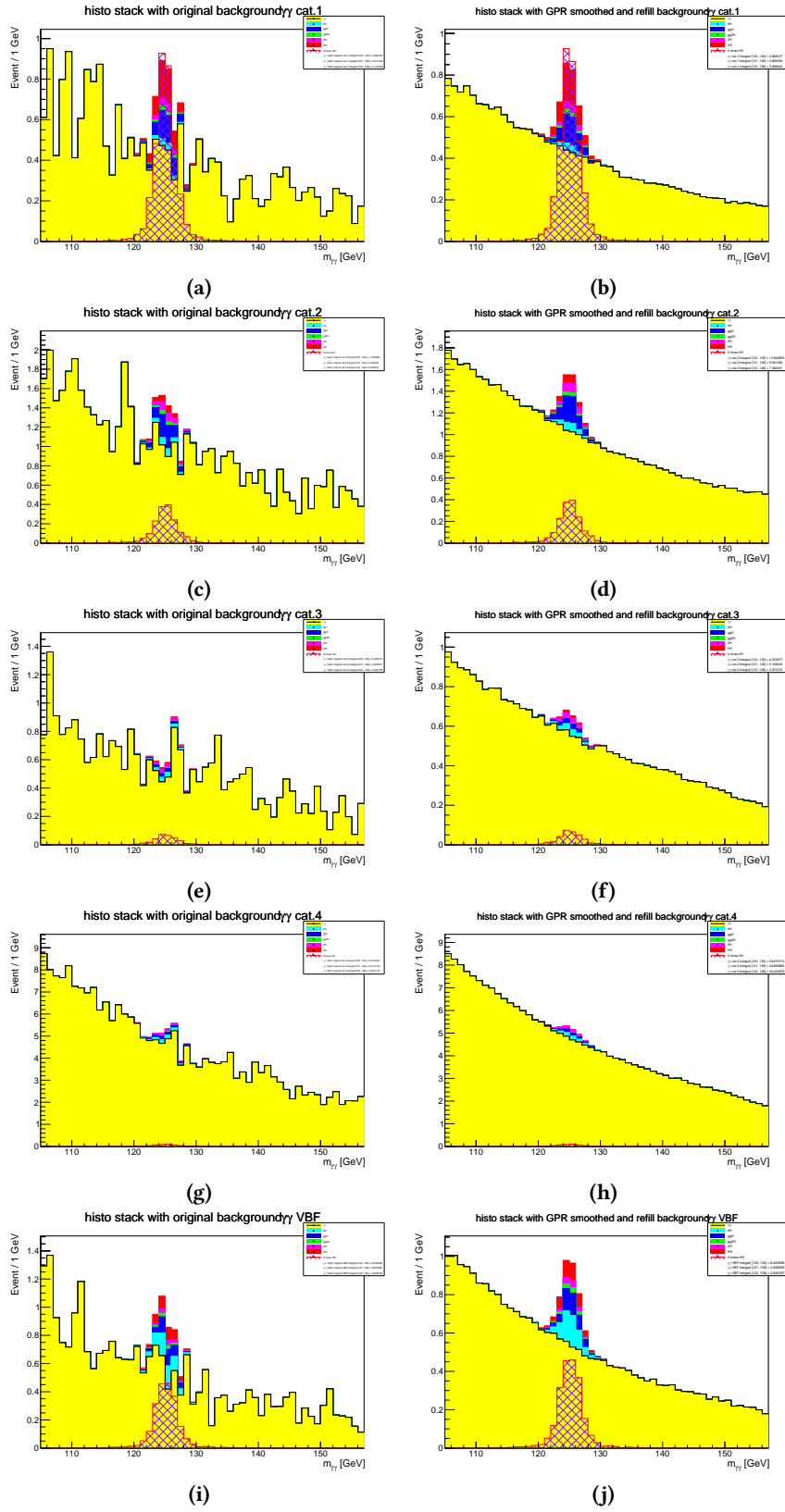


Figure A.5: comparison of the di-Higgs and single Higgs distribution on top of original and RGFR (4-to-1 GeV) smoothed $\gamma\gamma$ distribution. Original $\gamma\gamma$ distribution on the left while RGFR (4-to-1 GeV) method results on the right.

A.2 Spurious Signal Test

The spurious signal is the potential fake signal originating from the background, which may hide the real signal. A spurious signal test can estimate the number of spurious signal events and describe the capability to extra the real signal from the spurious one. The test is performed in the mass window $m_{\gamma\gamma} \in [121, 129]$, which gives the best di-Higgs sensitivity.

Usually, the spurious signal test requires the following criteria,

$$\begin{aligned} & |Max(N_{sp}/\sigma_{bkg})| < 20\% \\ \text{or } & |Max(|N_{sp}/N_{ref}|) < 10\%, \end{aligned}$$

where N_{sp} is the number of events of spurious signals, σ_{bkg} is the background uncertainty and N_{ref} is the reference number of events, where the reference is the di-Higgs signal in our case. Max refers to the maximum ratio, in absolute value, obtained in any bin.

For low statistics, the typical criteria may fail because of the large ratio of spurious signal, therefore loose criteria are introduced.

The $1 - \sigma$ criteria is as follows:

$$\begin{aligned} & |Max(|N_{sp,1-\sigma}/\sigma_{bkg}|) < 20\% \\ \text{or } & |Max(|N_{sp,1-\sigma}/N_{ref}|) < 10\%. \end{aligned}$$

The $1 - \sigma$ spurious signal criteria is defined as

$$N_{sp,1-\sigma} = \begin{cases} N_{sp} + \Delta_{MC} & \text{if } N_{sp} + \Delta_{MC} < 0 \\ N_{sp} - \Delta_{MC} & \text{if } N_{sp} - \Delta_{MC} > 0 \\ 0, & \text{otherwise} \end{cases} \quad (\text{A.2.1})$$

where Δ_{MC} is a local statistical fluctuation of the background template. $N_{sp,1-\sigma}$ should then pass the criteria as N_{sp} before.

A.2.1 Test of Original Data

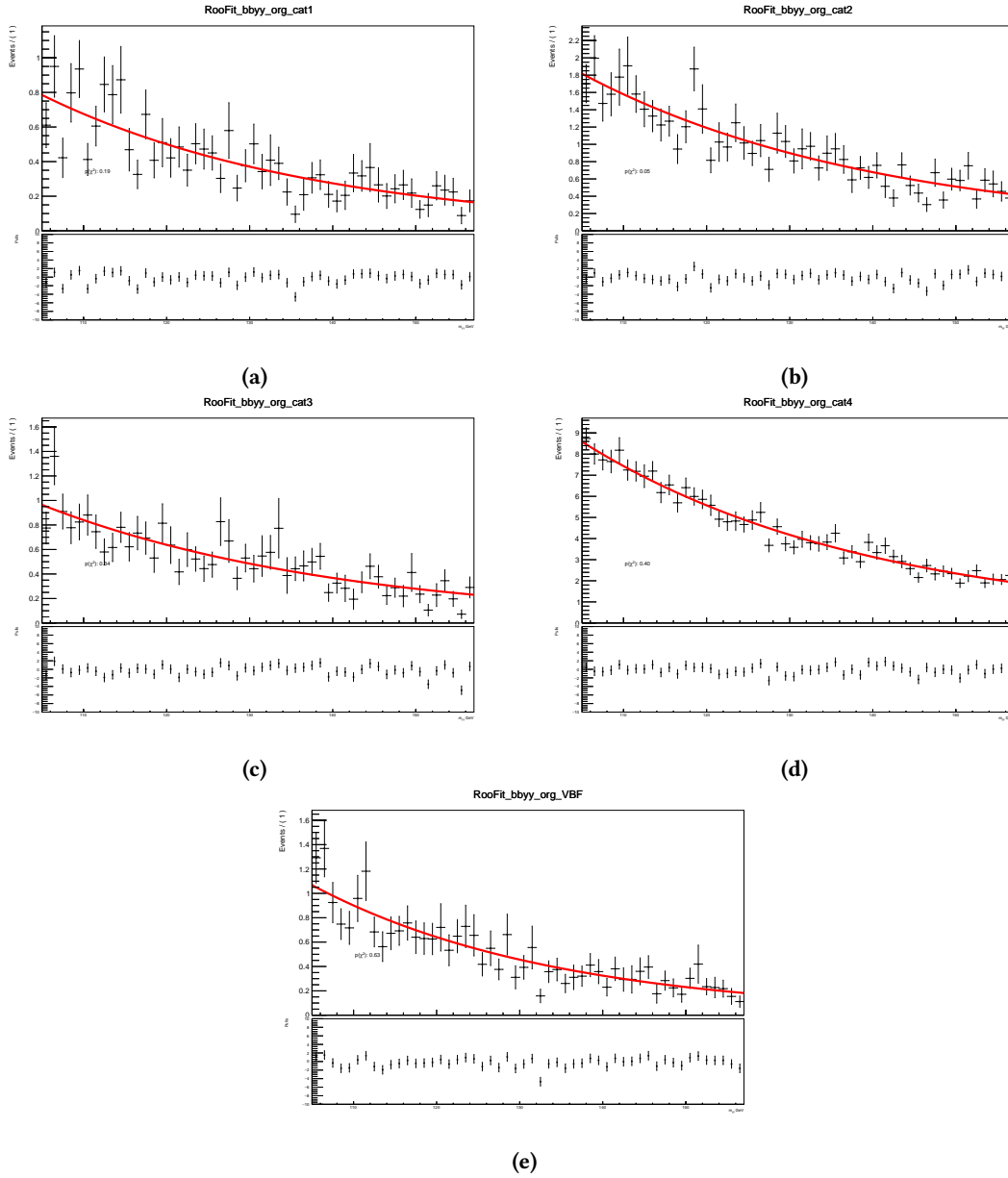
For the test of the original data, shown in table A.6, category 3 and 4 fail the criteria for the exponential function, but they pass the $1 - \sigma$ criteria. Using the $1 - \sigma$ criteria, the smoothing is not necessary.

A.2.2 Test of the distribution obtained with the RGFR (4-to-1 GeV) method

Although the smoothing is not necessary, it is still interesting to see how much the RGFR (4-to-1 GeV) smoothing strategy will contribute to the spurious signal reduction.

For the test of RGFR (4-to-1 GeV) method refilled distribution, shown in table A.7, all five categories pass the typical criteria. The RGFR (4-to-1 GeV) smoothing strategy reduces the number of

Category	Category 1	Category 2	Category 3	Category 4	VBF
Selected function	Exp.	Exp.	Exp.	Exp.	Exp.
$Max(N_{sp}/\sigma_{bkg}) [\%]$	-13.4	-17.2	20.2	-30.08	17.4
$Max(N_{sp,1-\sigma}/\sigma_{bkg}) [\%]$	0	0	-3.44	-13.9	0
$Max(N_{sp,2-\sigma}/\sigma_{bkg}) [\%]$	0	0	0	0	0
$Max(N_{sp}/N_{ref}) [\%]$	-34.1	-146	620	1.78×10^3	84
$Max(N_{sp,1-\sigma}/N_{ref}) [\%]$	0	0	-108	-815	0
$Max(N_{sp,2-\sigma}/N_{ref}) [\%]$	0	0	0	0	0
$Max(N_{sp})$	-0.238	-0.485	0.401	-1.65	0.36
χ^2/NDF	1.24	1.36	1.09	1.04	0.883
$Prob(\chi^2) [\%]$	19.3	4.71	34.2	40.4	62.7

Table A.6: Spurious Signal Test for the original H025 Monte-Carlo simulation with MC16a, MC16d and MC16e**Figure A.6:** Spurious signal test. Fit of original histograms for different categories

Category	Category 1	Category 2	Category 3	Category 4	VBF
Selected function	Exp.	Exp.	Exp.	Exp.	Exp.
$Max(N_{sp}/\sigma_{bkg})$ [%]	1.5	2.46	1.98	-4.97	-3.08
$Max(N_{sp,1-\sigma}/\sigma_{bkg})$ [%]	0.0128	0.991	0.583	-3.53	-1.64
$Max(N_{sp,2-\sigma}/\sigma_{bkg})$ [%]	0	0	0	-2.09	-0.208
$Max(N_{sp}/N_{ref})$ [%]	0.0172	0.0477	0.0275	-0.2	-0.0399
$Max(N_{sp,1-\sigma}/N_{ref})$ [%]	0.00104	0.023	0.0108	-0.15	-0.0232
$Max(N_{sp,2-\sigma}/N_{ref})$ [%]	0	0	0	-0.099	-0.00649
$Max(N_{sp})$	0.0281	0.0712	0.04	-0.297	-0.0571
χ^2/NDF	1.06	1.18	3.32	5.18	1.02
$Prob(\chi^2)$ [%]	36.1	18.2	0	0	44.2

Table A.7: Spurious Signal Test for RGFR (4-to-1 GeV) method results with 100 times the number of the entries of the original histograms

spurious signal by about 84%.

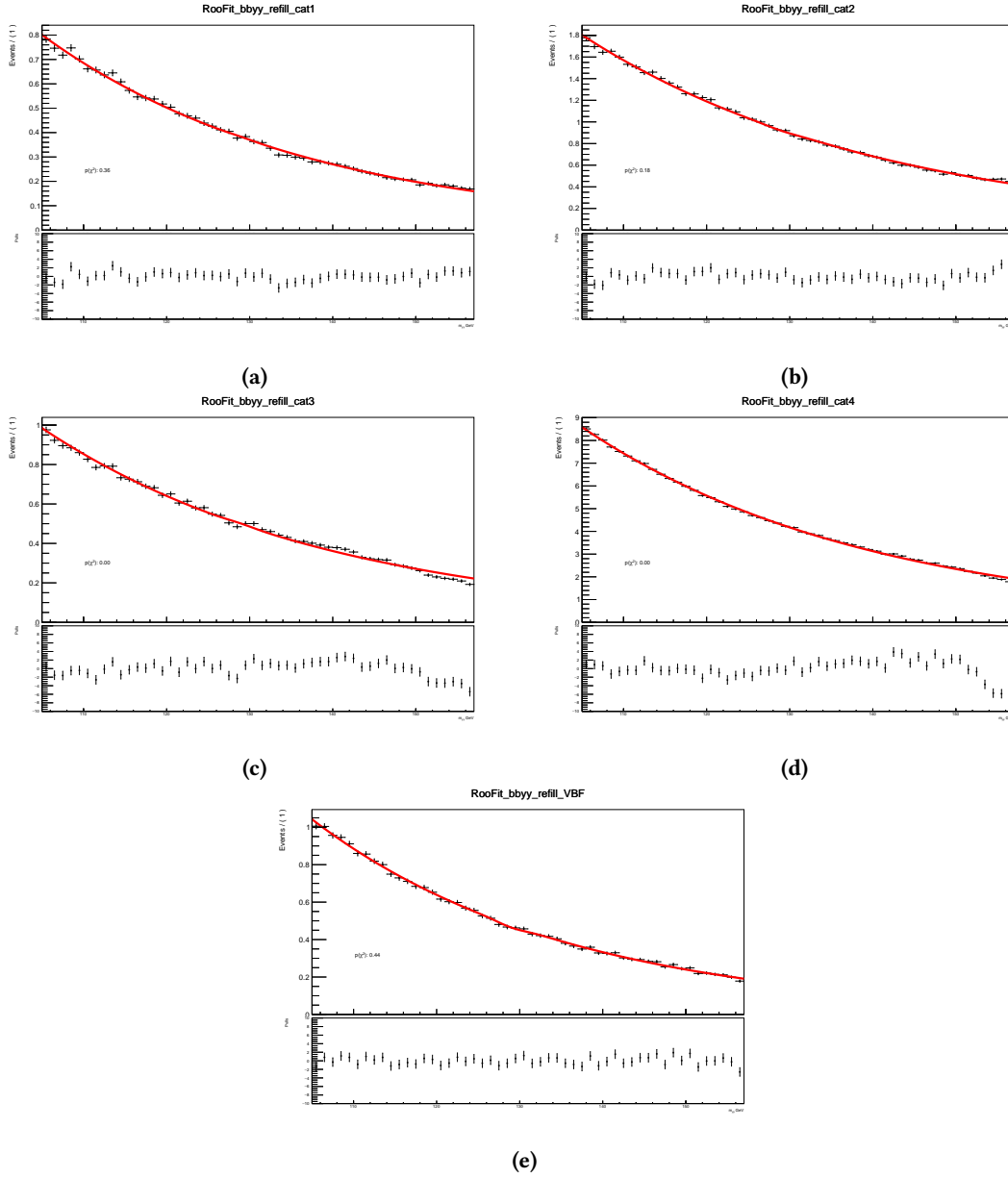


Figure A.7: Spurious signal test. Fit of RGFR (4-to-1 GeV) refilled result (100 times entries)

A.3 Conclusion

The RGFR (4-to-1 GeV) smoothing strategy in [A.1.2.3](#) helps to overcome oscillating shape when some categories have low statistic. Although the spurious signal test in [A.2.1](#) shows that smoothing is not necessary using the usual requirements, the new smoothing strategy can reduce the spurious signal by about 84%.

Background studies for di-Higgs production in the $b\bar{b}\tau^+\tau^-$ final state

B.1	Background modelling	259
B.1.1	Fake- τ backgrounds in the $\tau_{\text{lep}}\tau_{\text{had}}$ channel	259
B.1.2	Multijet with fake- τ in the $\tau_{\text{had}}\tau_{\text{had}}$ channel	266
B.1.3	$t\bar{t}$ with fake- τ_{had} in the $\tau_{\text{had}}\tau_{\text{had}}$ channel with scale-factor method	271
B.2	Complementary Results	272
B.2.1	Limits and scans compare with the previous results	272
B.2.1.1	$\tau_{\text{had}}\tau_{\text{had}}$: Comparison with previous analysis	272
B.2.1.2	$\tau_{\text{lep}}\tau_{\text{had}}$: Comparison with previous analysis	273
B.2.1.3	Combined: Comparison with previous analysis	274
B.2.2	Additional fit checks	275
B.2.2.1	Alternative post-fit plots for the HadHad channel	275
B.2.2.2	Alternative post-fit plots for the LepHad channel	279
B.2.2.3	Alternative post-fit plots for the Combined fit	280
B.2.3	Compatibility tests	280
B.2.3.1	Compatibility across different channels	281
B.2.3.2	Compatibility across different analysis regions and channels	281
B.2.3.3	Compatibility with previous Run-2 result	282

B.1 Background modelling

B.1.1 Fake- τ backgrounds in the $\tau_{\text{lep}}\tau_{\text{had}}$ channel

The fake- τ_{had} backgrounds estimation follows closely the internal note documentation [204] of the previous round of the analysis [4]. For this round, the method is validated with the inclusion of $t\bar{t}$ dilepton (DSID 410472) and V+jets SHERPA 2.2.11 samples following these guidelines:

1. check the purity of the desired backgrounds in $t\bar{t}$ and multi-jet control regions;
2. derive fake factors (FFs) as a function of τ_{had} η and p_T ;
3. evaluate the fakes in the validation region (0- b -tag region).

In the $\tau_{\text{lep}}\tau_{\text{had}}$ channel, a combined fake-factor method similar to that described in Ref. [HIGG-2016-16-withern] is used to estimate multi-jet and $t\bar{t}$ backgrounds with fake- $\tau_{\text{had-vis}}$. A schematic depiction of this method is shown in Figure B.1.

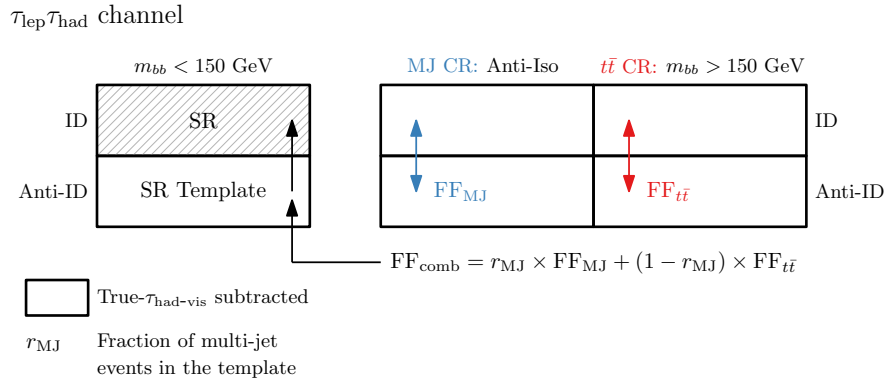


Figure B.1: Schematic depiction of the combined fake-factor method used to estimate multi-jet and $t\bar{t}$ backgrounds with fake- $\tau_{\text{had-vis}}$ in the $\tau_{\text{lep}}\tau_{\text{had}}$ channel. Backgrounds which are not from events with fake- $\tau_{\text{had-vis}}$ originating from jets are estimated from simulation and are subtracted from data in all control regions. Events in which an electron or a muon is misidentified as a $\tau_{\text{had-vis}}$ are also subtracted, but their contribution is very small. Both sources are indicated by ‘True- $\tau_{\text{had-vis}}$ subtracted’ in the legend.

This method employs events in two groups of regions. The events in the identification (ID) regions require one identified $\tau_{\text{had-vis}}$, whereas events in the anti-identification (anti-ID) regions contain one anti- $\tau_{\text{had-vis}}$ candidate.

If an event does not contain an identified $\tau_{\text{had-vis}}$, it is checked for reconstructed $\tau_{\text{had-vis}}$ candidates satisfying the anti- $\tau_{\text{had-vis}}$ requirements. If an event contains multiple anti- $\tau_{\text{had-vis}}$ candidates, one is chosen randomly. In the LTT category, however, only the anti- $\tau_{\text{had-vis}}$ candidate that is within $\Delta R = 0.2$ of the HLT $\tau_{\text{had-vis}}$ object is considered.

In order to define a fake- $\tau_{\text{had-vis}}$ background template, an anti-ID region is defined using event selection criteria equivalent to the SR selection, with one anti- $\tau_{\text{had-vis}}$ candidate instead of one identified $\tau_{\text{had-vis}}$. This region, which is enriched with fake- $\tau_{\text{had-vis}}$, is defined as the SR Template region. The template for estimating fake- $\tau_{\text{had-vis}}$ in the SR is obtained by subtracting from the data distribution in the SR Template region the distribution of simulated background events in which the $\tau_{\text{had-vis}}$ candidate is not a fake- $\tau_{\text{had-vis}}$ originating from jets. This subtraction is referred to as the true- $\tau_{\text{had-vis}}$ subtraction given that the number of events in which an electron or muon is misidentified as a $\tau_{\text{had-vis}}$, which are also subtracted, is very small. The data and simulated events that are used to build the template are scaled with event weights, referred to as fake-factors (FFs), to estimate the fake- $\tau_{\text{had-vis}}$ background in the SR.

The FFs are derived separately for multi-jet (FF_{MJ}) and $t\bar{t}$ ($\text{FF}_{t\bar{t}}$) events in dedicated control regions.

The multi-jet control regions (MJ CRs) and $t\bar{t}$ control regions ($t\bar{t}$ CRs) are defined separately for the ID and the anti-ID regions, depending on whether they contain one identified $\tau_{\text{had-vis}}$ or one anti- $\tau_{\text{had-vis}}$ candidate, respectively. Besides the $\tau_{\text{had-vis}}$ selection, the MJ CRs are defined using the SR selection with an inverted electron or muon isolation requirement (anti-Iso) and without the $m_{bb} < 150 \text{ GeV}$ requirement. The MJ CR’s purity in multi-jet production events varies between 65% and 90% depending on the trigger category type (SLT or LTT) and whether the MJ CR is in the ID or anti-ID region. Similarly, the $t\bar{t}$ CRs are defined using the SR selection with an inverted m_{bb} requirement ($m_{bb} > 150 \text{ GeV}$). The $t\bar{t}$ CR is about 95% pure in the events from $t\bar{t}$ production.

To demonstrate the purity of the desired backgrounds in the $t\bar{t}$ CR and MJ CR for the SLT and LTT categories, distributions of the τp_T for the control regions with the τ_{had} and anti- τ_{had} requirements, separately for 1-prong and 3-prong τ_{had} are included. These distributions can be seen in Figures B.2 and B.3 for $t\bar{t}$ CR, and Figures B.4 and B.5 for MJ CR, where the fake contribution is taken from Monte Carlo only. Thus, the gap between the Monte Carlo prediction and data in the MJ CR is attributed to multi-jet events, which are not simulated for this analysis.

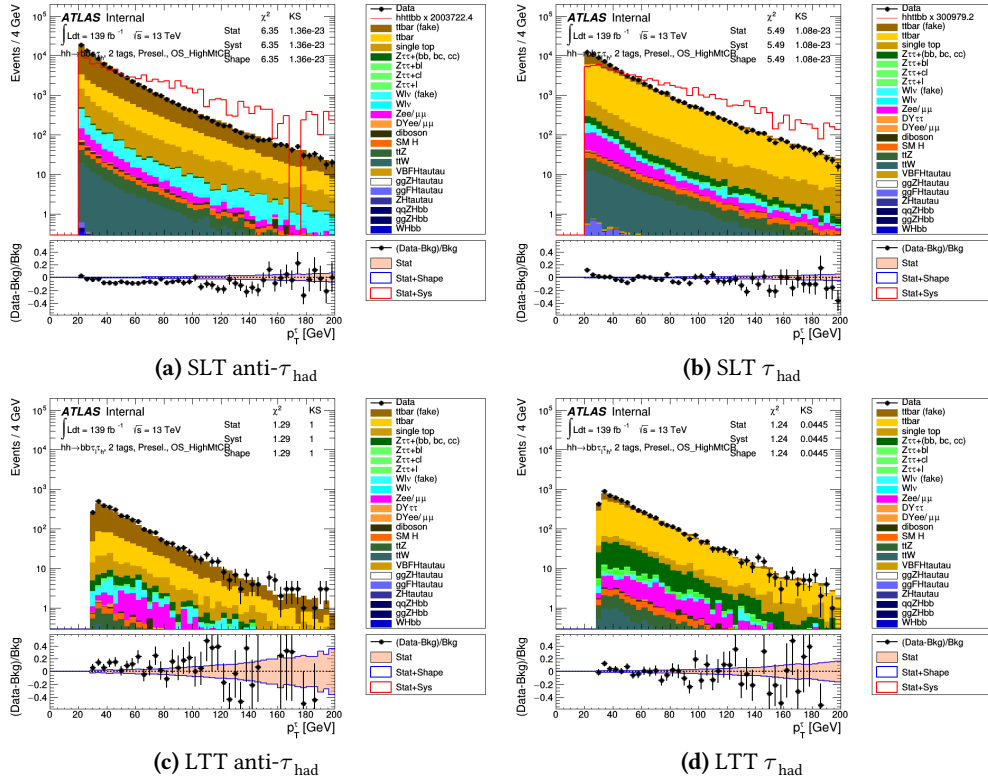


Figure B.2: Plots of the $\tau_{\text{had}} p_T$ distributions for the (left) anti- τ_{had} and (right) τ_{had} selection for SLT (top) and LTT (bottom) channels in the $t\bar{t}$ control region with 1-prong τ_{had} .

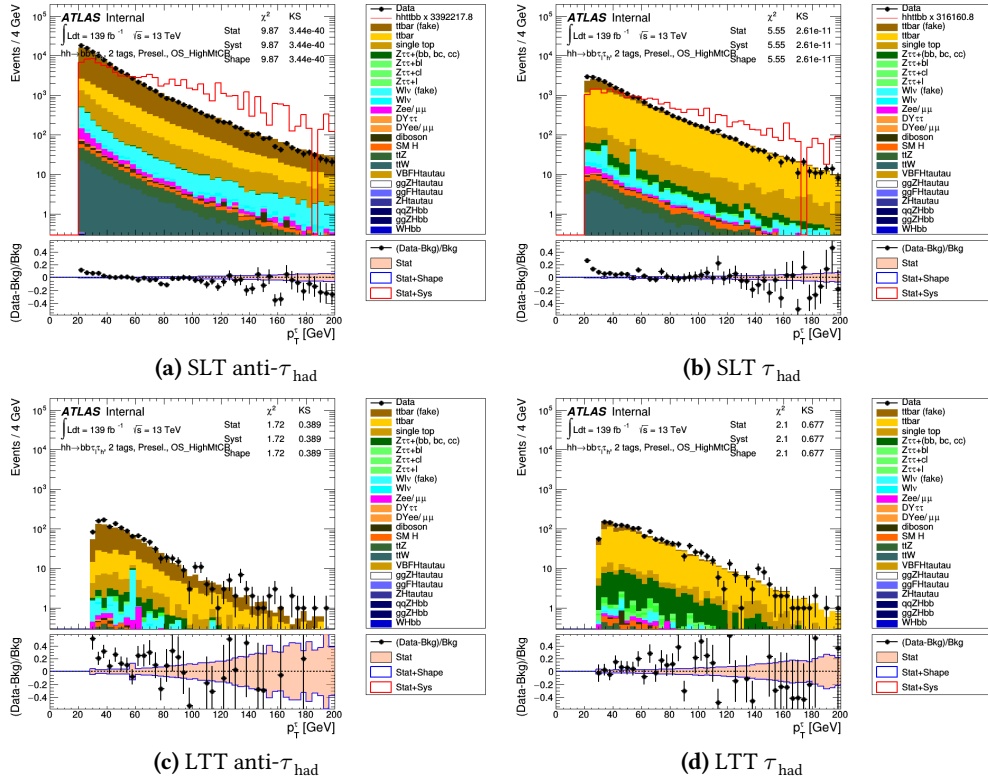


Figure B.3: Plots of the $\tau_{\text{had}} p_T$ distributions for the (left) anti- τ_{had} and (right) τ_{had} selection for SLT (top) and LTT (bottom) channels in the $t\bar{t}$ control region with 3-prong τ_{had} .

For backgrounds that do not originate from events with fake- $\tau_{\text{had-vis}}$ originating from jets, estimates are obtained through simulations. These estimates are then removed from the data distribution

Figures B.6 and B.7, FFs, when parameterized based on η , exhibit no consistent pattern. Therefore, they are parameterized solely based on the p_T of the $\tau_{\text{had-vis}}$. This is done independently for both 1-prong and 3-prong $\tau_{\text{had-vis}}$ categories. The terms '1-prong' and '3-prong' denote the count of tracks associated with a reconstructed $\tau_{\text{had-vis}}$. The parameterization is also carried out separately for the SLT and LTT categories. Individual fake factors for each process (multi-jet and $t\bar{t}$) are then used to provide a combined fake factor.

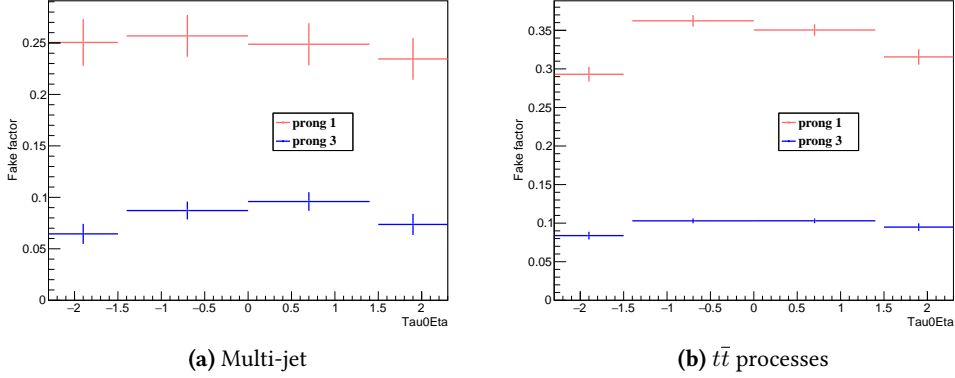


Figure B.6: Fake-factors as a function of η for 1-prong and 3-prong τ_{had} candidates for (a) multi-jet and (b) $t\bar{t}$ processes for the $\tau_{\text{lep}}\tau_{\text{had}}$ SLT category. No significant trend is observed.

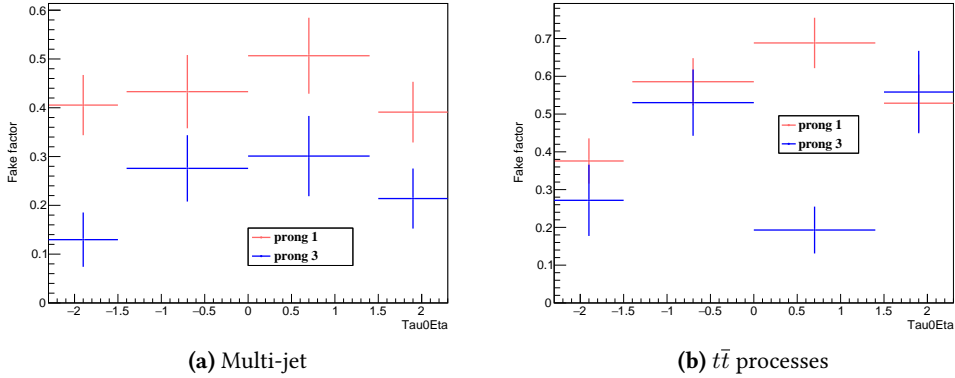


Figure B.7: Fake-factors as a function of η for 1-prong and 3-prong τ_{had} candidates for (a) multi-jet and (b) $t\bar{t}$ processes for the $\tau_{\text{lep}}\tau_{\text{had}}$ LTT category. No significant trend is observed.

Figures B.8 and B.9 display the fake-factors (FF) for both the SLT and LTT categories. These factors are computed separately for $t\bar{t}$ and multi-jet and are also broken down for 1 and 3-prong τ_{had} candidates. The parameterization is in relation to p_T (τ_{had}), with a necessity for opposite-sign lepton-tau pairs.

The FFs corresponding to the individual background processes are combined as

$$FF_{\text{comb}} = r_{\text{MJ}} \times FF_{\text{MJ}} + (1 - r_{\text{MJ}}) \times FF_{t\bar{t}},$$

where r_{MJ} is the expected fraction of multi-jet events in the SR Template. The number of multi-jet events in the SR Template is estimated by taking the number of data events in the SR Template and subtracting the expected number of non-multi-jet background events with both true- and fake- $\tau_{\text{had-vis}}$ as estimated from simulation. The non-multi-jet background events are dominated by $t\bar{t}$ production.

The r_{MJ} is parameterised as a function of the $\tau_{\text{had-vis}}$ p_T , and it is measured separately for the $\tau_e\tau_{\text{had}}$ and $\tau_\mu\tau_{\text{had}}$ events, for 1- and 3-prong $\tau_{\text{had-vis}}$ categories, and for the SLT and LTT categories. The FF_{comb} is used to scale the events used for the SR Template in order to obtain the fake- $\tau_{\text{had-vis}}$ background prediction in the SR.

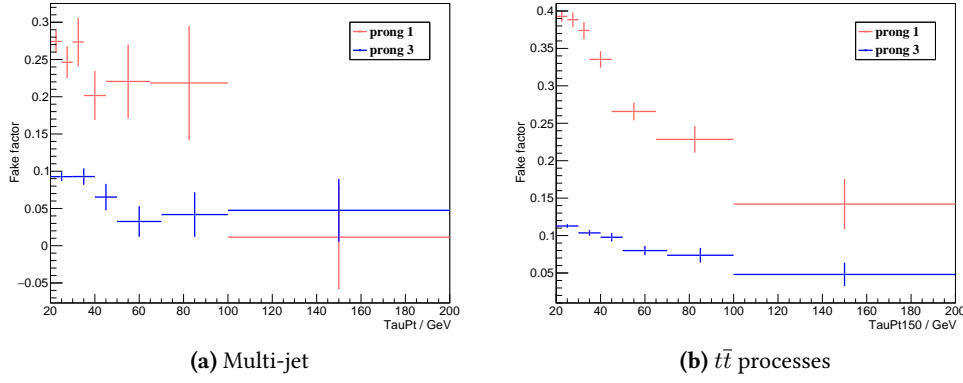


Figure B.8: Fake-factors for 1-prong and 3-prong τ_{had} candidates for (a) multi-jet and (b) $t\bar{t}$ processes for the $\tau_{\text{lep}}\tau_{\text{had}}$ SLT category.

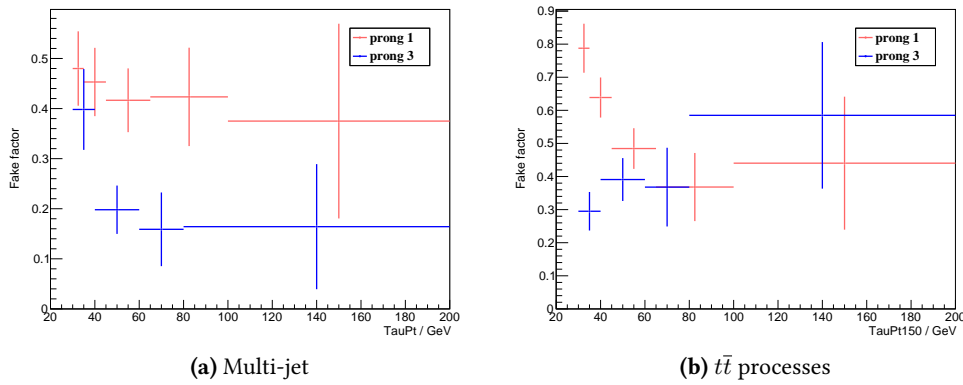


Figure B.9: Fake-factors for 1-prong and 3-prong τ_{had} candidates for (a) multi-jet and (b) $t\bar{t}$ processes for the $\tau_{\text{lep}}\tau_{\text{had}}$ LTT category.

The FFs for different background processes are combined using the equation:

$$\text{FF}_{\text{comb}} = r_{\text{MJ}} \times \text{FF}_{\text{MJ}} + (1 - r_{\text{MJ}}) \times \text{FF}_{t\bar{t}}.$$

In this expression, r_{MJ} denotes the anticipated proportion of multi-jet events present in the SR Template.

To estimate the number of multi-jet events in the SR Template, one must take the total data events in the SR Template and then subtract the projected number of non-multi-jet background events. These projections for both true- and fake- $\tau_{\text{had-vis}}$ are derived from simulations. It is important to note that the majority of non-multi-jet background events originate from $t\bar{t}$ production.

r_{MJ} is characterized in relation to the $\tau_{\text{had-vis}}$ p_{T} . Measurements for r_{MJ} are performed separately considering the $\tau_e\tau_{\text{had}}$ and $\tau_\mu\tau_{\text{had}}$ events, the 1-prong and 3-prong $\tau_{\text{had-vis}}$ categories, and finally the SLT and LTT categories.

The resultant FF_{comb} plays a pivotal role as it scales the events for the SR Template, facilitating the determination of the counterfeit $\tau_{\text{had-vis}}$ background forecast in the SR.

The process of determining the fake- $\tau_{\text{had-vis}}$ background through the combined FF methodology exhibits sensitivity to the modeling of $t\bar{t}$ simulated events that include true- $\tau_{\text{had-vis}}$. This is because $t\bar{t}$ represents the primary background that is deduced from the data during the derivation of both the FF and r_{MJ} , and also when the SR Template is procured. Moreover, the modeling of simulated $t\bar{t}$ events with fake- $\tau_{\text{had-vis}}$ affects the derivation of r_{MJ} .

To enhance the accuracy of predictions, simulated events originating from $t\bar{t}$ production are dif-

ferentially reweighted to match data distributions. This adjustment considers factors like jet multiplicity and the scalar sum of transverse momentum for all visible end-state elements in the event. The coefficients for this reweighting are sourced from a $t\bar{t}$ control region ($t\bar{t}$ CR2). This region has approximately 93% purity in events from $t\bar{t}$ production. The defining selection criteria for $t\bar{t}$ CR2 are identical to that of the SR selection. However, variations exist, such as an inverted m_{bb} requirement ($m_{bb} > 150$ GeV) and an added constraint of $m_T^W > 40$ GeV. Events in this control zone need a reconstructed $\tau_{\text{had-vis}}$ candidate, but this candidate is not obligated to satisfy the recurrent neural-network identification standards. The m_T^W requirement is introduced to curtail the potential influence of multi-jet events.

In the ensuing analysis, statistical uncertainties associated with $\text{FF}_{t\bar{t}}$, FF_{MJ} , and r_{MJ} are evaluated and propagated to the final determination.

The variation between the estimated fake- $\tau_{\text{had-vis}}$ background values, determined with and without the specified $t\bar{t}$ modeling correction, is considered as an uncertainty for the background prediction. A conservative modeling uncertainty of 30% is allocated to simulated non- $t\bar{t}$ backgrounds that are deducted from the data.

Given the significant reliance on the modeling of simulated $t\bar{t}$ events containing fake- $\tau_{\text{had-vis}}$, the computed r_{MJ} values are adjusted by a factor of ± 0.5 , ensuring the range $0 \leq r_{\text{MJ}} \leq 1$. Notably, the influence of such a conservative uncertainty estimation remains minimal since the FFs in both multi-jet and $t\bar{t}$ events exhibit similarity.

For the SLT category, the overarching uncertainty in the FF_{comb} value does not exceed 10%, while for the LTT category, it remains within a ceiling of 25%.

To validate the ability of the combined fake factor methodology in representing the MVA BDT shape for low- m_{HH} ggF, high- m_{HH} ggF, and VBF categories, plots were generated utilize the fake factor method to approximate the collective contributions of multi-jet and $t\bar{t}$ in distinct validation regions.

The efficacy of the combined FF method is initially examined for closure in the $t\bar{t}$ CR. Subsequently, it is validated within the 1- b -tagged region. This particular region is the same as the $\tau_{\text{lep}}\tau_{\text{had}}$ SR, with the exception being its strict requirement for precisely one b -tagged jet. Direct application of the combined fake factor methodology to the $t\bar{t}$ CR is illustrated in Figures B.10 and B.11.

Furthermore, Figures B.12 and B.13 present the BDT distributions for the low- m_{HH} ggF, high- m_{HH} ggF, and VBF categories within the 1- b -tag validation domain. These plots are different based on the SLT and LTT criteria. Notably, the anticipated background distributions agree well with the observed distributions in both the SLT and LTT validation segments.

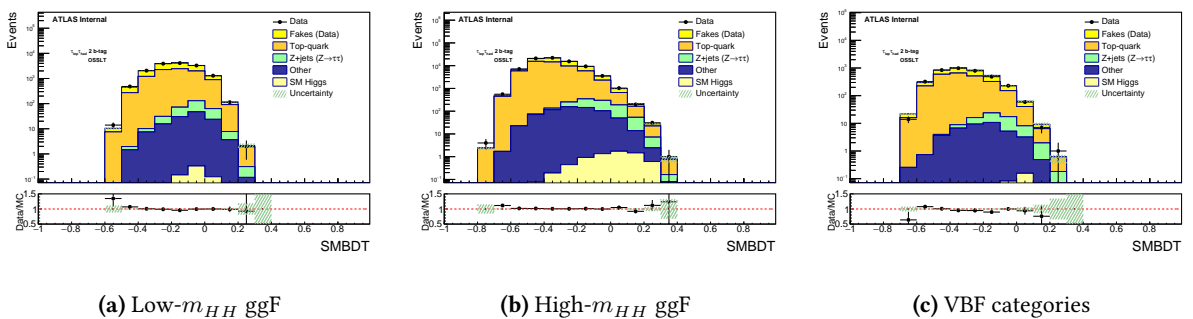


Figure B.10: The SLT BDT distributions for (a) low- m_{HH} ggF, (b) high- m_{HH} ggF, and (c) VBF categories in the signal-depleted $t\bar{t}$ CR where the $t\bar{t}$ FF are measured. This is a simple closure test.

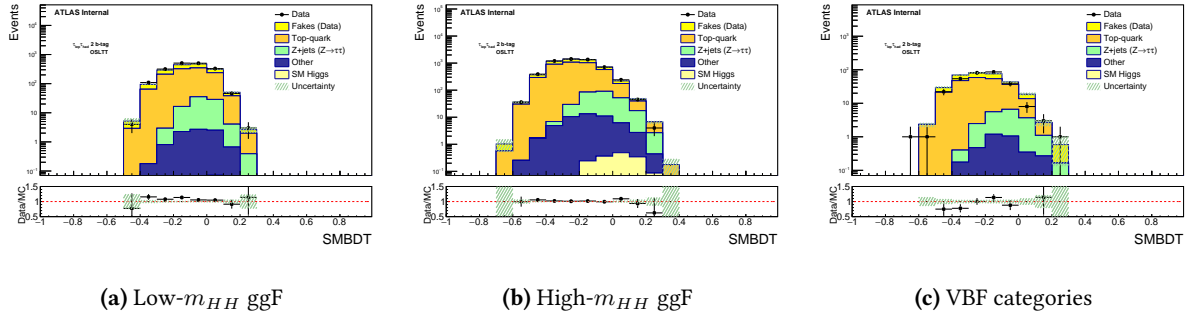


Figure B.11: The LTT BDT distributions for (a) low- m_{HH} ggF, (b) high- m_{HH} ggF, and (c) VBF categories in the signal-depleted $t\bar{t}$ CR where the $t\bar{t}$ FF are measured. This is a simple closure test.

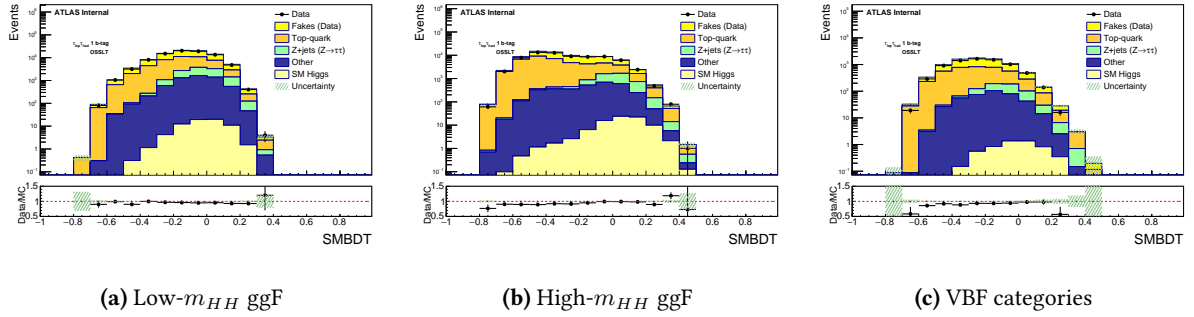


Figure B.12: The SLT BDT distributions for (a) low- m_{HH} ggF, (b) high- m_{HH} ggF, and (c) VBF categories in the 1- b -tag validation region.

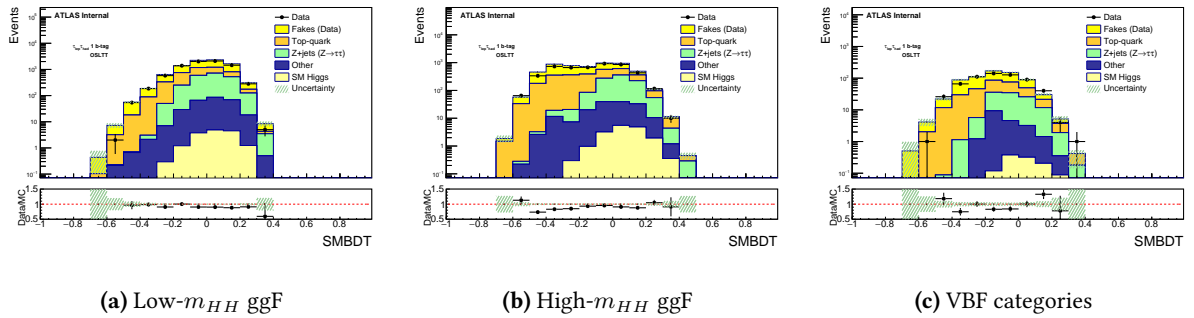


Figure B.13: The LTT BDT distributions for (a) low- m_{HH} ggF, (b) high- m_{HH} ggF, and (c) VBF categories in the 1- b -tag validation region.

B.1.2 Multijet with fake- τ in the $\tau_{\text{had}}\tau_{\text{had}}$ channel

In the $\tau_{\text{had}}\tau_{\text{had}}$ channel, the estimation of the multi-jet background relies on a data-driven fake-factor methodology. This is consistent with the approach applied in previous round of the $b\bar{b}\tau^+\tau^-$ analysis, as referenced in [4, 205]. The fake factors (FFs) previously identified in [4] are retained in this analysis iteration. This decision is informed by the observation that transitioning from the Monte Carlo configuration SHERPA 2.2.1 to SHERPA 2.2.11 for modeling the V+jets samples has no obvious effect on the multi-jet background estimation.

In Figures B.14 and B.15, the leading $\tau_{\text{had}} p_T$ distributions for each analysis category are depicted. These plots cover the 1-tag SS and the 1-tag OS regions and feature the V+jets SHERPA 2.2.11 and $t\bar{t}$ dilepton samples. They demonstrate that the modification in samples does not alter the multi-jet background estimation compared to the previous round of analysis.

Furthermore, Figure B.14 provides a closure examination of the fake factor estimation approach within the 1-tag SS region. This pertains to the low- m_{HH} ggF SR, high- m_{HH} ggF SR, and VBF

SR categories. Since this region informs the estimation of the fake factors, its primary function here is as a closure verification.

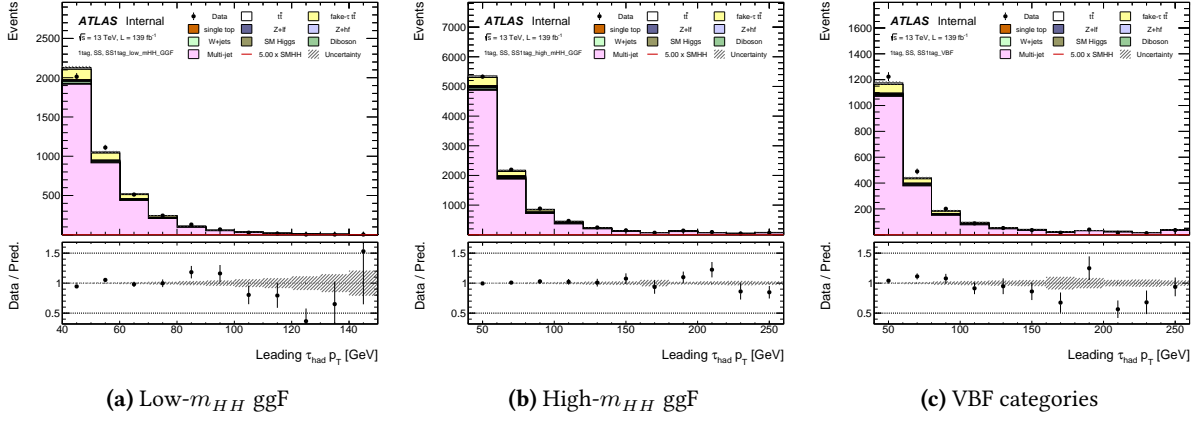


Figure B.14: Closure check of the fake factor method in 1-tag SS ID-region showing the leading $\tau_{\text{had}} p_T$ distributions for the (a) low- m_{HH} ggF, (b) high- m_{HH} ggF and (c) VBF categories in the $\tau_{\text{had}}\tau_{\text{had}}$ channel.

In Figure B.15, the multi-jet fake validation region (1-tag OS) is depicted for the analysis categories: low- m_{HH} ggF SR, high- m_{HH} ggF SR, and VBF SR. As this region is not employed during the formulation of the method, it serves as an independent validation area.

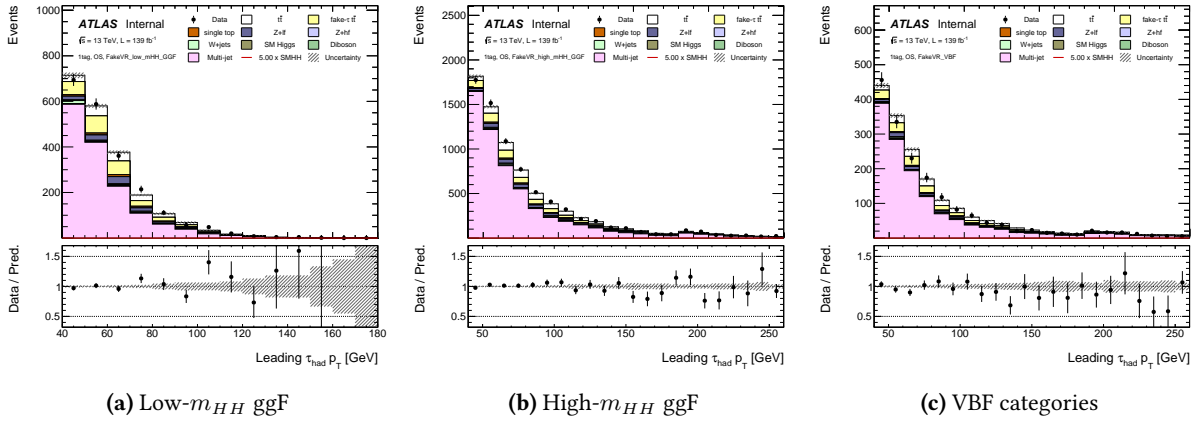


Figure B.15: Validation of the multi-jet estimate in the 1-tag OS multi-jet validation region showing the leading $\tau_{\text{had}} p_T$ distributions for the (a) low- m_{HH} ggF, (b) high- m_{HH} ggF and (c) VBF categories in the $\tau_{\text{had}}\tau_{\text{had}}$ channel.

In the following, the detailed method for deriving the fake factors (FF s) as employed in previous rounds of the $b\bar{b}\tau^+\tau^-$ analysis is outlined.

The derivation of Fake factors (FF s) is rooted in a control region containing events with two $\tau_{\text{had-vis}}$ and same-sign (SS) electric charges (known as the SS CR). These factors are calculated as ratios: specifically, the number of events featuring two loose τ_{had} over those with one loose and one anti- τ_{had} candidate. Notably, due to certain restrictions in the "HIGG4D3" derivations (required at least one loose τ_{had}), inverting the τ_{had} -ID is viable only for one of the τ_{had} . Events having one loose and one anti- τ_{had} candidate with opposite-sign (OS) electric charges then have these FF s applied to predict the number of OS multi-jet events with two loose τ_{had} .

In the derivation process, fake factors are distinctly determined for both 1- and 3-prong τ_{had} . This is carried out separately within the STT and DTT trigger categories, and also differentiated among the 0-, 1-, and 2- b -tag domains. Additionally, to accommodate varied τ_{had} identification in the HLT and the evolving trigger selection, fake factors are split by the year of data collection. Nonetheless, the 2- b -tag region, grappling with limited statistics in the SS domain, employs FF s from the 1- b -tag region. To ensure accuracy, transfer factors (TF s) correct the multi-jet normalization in the 2- b -tag

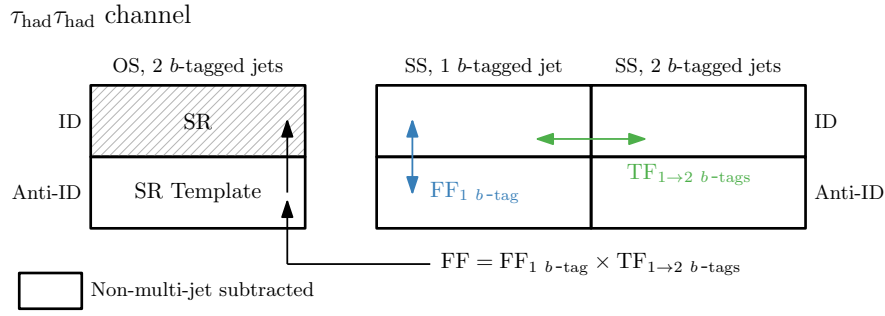


Figure B.16: Schematic depiction of the fake-factor method to estimate the multi-jet background with fake- $\tau_{\text{had-vis}}$ in the $\tau_{\text{had}}\tau_{\text{had}}$ channel. Backgrounds that are not from multi-jet events are simulated and subtracted from data in all the control regions. This is indicated by ‘Non-multi-jet subtracted’ in the legend

	1 b -tag SS ID	1 b -tag SS anti-ID	2 b -tags OS anti-ID
1-prong	12%	6.6%	54%
3-prongs	12%	6.8%	48%

Table B.1: Relative subtraction of non-multijet-fake backgrounds in the DTT control regions used for the multijet estimation.

region, further discussed below. The sole application of the 0- b -tag regions remains validation. A schematic representation of the regions utilized for multi-jet estimation is provided in Figure B.16.

Information regarding the composition of these regions is outlined in the internal note documentation from the previous round of the analysis. The tables Tables B.1 and B.2 display the proportionate subtraction of backgrounds not attributed to multijet-fakes within these specified regions.

Inverting only the τ_{had} -ID of the sub-leading p_T τ_{had} candidate results in the establishment of both anti-ID OS and SS CRs, from which multijet estimation can be derived. Likewise, inverting the τ_{had} -ID of the leading p_T τ_{had} candidate also yields a separate multijet estimation. To augment the number of events for modeling the multijet background, these two estimations are averaged. The background templates, to which the fake factors are applied, remain statistically independent. In cases with limited data within the STT category, FF s are evaluated inclusively with both τ_{had} p_T and η .

Within the DTT category, evidence indicates that the two sets of fake factors— FF_1 , which is binned in accordance with the p_T of the sub-leading τ_{had} (when only its ID is inverted), and FF_0 , binned based on both the p_T and η of the leading τ_{had} (upon inverting solely its ID)—demonstrate statistical congruence. This can be further corroborated by referring to the internal documentation from the previous analysis iteration. Given this statistical compatibility, both FF_0 and FF_1 are merged. This integration accounts for the statistical weight each holds within specific p_T bins. As an illustrative case, FF_0 is excluded from influencing the overarching fake-factor below a threshold of 40 GeV, in line with the 40 GeV cut imposed on the leading τ_{had} within the study. Consequently,

	1 b -tag SS ID	1 b -tag SS anti-ID	2 b -tags OS anti-ID
Leading τ_{had} fails (1-prong)	14%	3.8%	12%
SubLeading τ_{had} fails (1-prong)	16%	10%	33%
Leading τ_{had} fails (3-prongs)	20%	4.5%	18%
SubLeading τ_{had} fails (3-prongs)	14%	12%	32%

Table B.2: Relative subtraction of non-multijet-fake backgrounds in the STT control regions used for the multijet estimation.

for the DTT category, fake factors are calculated as:

$$FF_i(p_T \tau_{\text{had}}^i, \eta \tau_{\text{had}}^i, N_{\text{prong}} \tau_{\text{had}}^i, \dots) = \frac{N_{\text{data}}(\text{loose } \tau_{\text{had}}^i) - N_{\text{non-multijet MC}}(\text{loose } \tau_{\text{had}}^i)}{N_{\text{data}}(\text{anti-}\tau_{\text{had}}^i) - N_{\text{non-multijet MC}}(\text{anti-}\tau_{\text{had}}^i)}, \quad (\text{B.1.1})$$

where τ_{had}^i refers to the leading ($i = 0$) or subleading τ_{had} ($i = 1$). The term $N_{\text{data(non-multijet MC)}}$ signifies the number of τ_{had} candidates in data or simulated non-multijet events that belong to the designated FF bin.

To proceed, the pair of fake-factors, FF_0 and FF_1 , are averaged as follows:

$$FF_{\text{avg}}(p_T \tau_{\text{had}}, \eta \tau_{\text{had}}, N_{\text{prong}} \tau_{\text{had}}, \dots) = \frac{N_{\text{data}}(\text{loose } \tau_{\text{had}}) - N_{\text{non-multijet MC}}(\text{loose } \tau_{\text{had}})}{N_{\text{data}}(\text{anti-}\tau_{\text{had}}) - N_{\text{non-multijet MC}}(\text{anti-}\tau_{\text{had}})}, \quad (\text{B.1.2})$$

where $N_{\text{data(non-multijet MC)}}$ denotes the number of τ_{had} candidates in data (simulated non-multijet) events, without considering if the $\tau_{\text{had-vis}}$ candidate takes the position of leading or subleading in p_T . For each event, the numerator can encompass at most two loose τ_{had} (provided they belong to the same FF bin), while the denominator can have a maximum of one anti- τ_{had} . Defined in this manner, these fake factors serve as a means to average FF_0 and FF_1 , with the weights influenced by the relative number of events that impact a specific p_T and η bin. Events with a single anti- τ_{had} are influenced by these fake factors, based on its respective p_T and η . This holds true irrespective of the τ_{had} being a p_T -leading or sub-leading entity within the event¹. This methodology, when contrasted with the 2-dimensional fake-factor p_T -binning [205], permits a more detailed binning in the present strategy and facilitates a straightforward comparison of FF compatibility between the OS and SS regions, particularly when extracting systematic uncertainties. It's pertinent to mention that both methods yield results that are statistically in harmony. Moreover, there exists a commendable alignment between the multijet estimates derived from separate applications of FF_0 and FF_1 to their associated events, and the principal estimate sourced from FF_{avg} . The aforementioned evaluations are available in the internal note documentation from the previous rounds of the analysis [4].

In our discussions, we highlighted the use of transfer factors to adjust the normalization of the multijet prediction in the 2- b -tag region, especially when employing fake factors from the 1- b -tag region. Specifically, a transfer factor is defined as the ratio of the p_T/η -inclusive fake-factor within the 2- b -tag SS region relative to its counterpart in the 1- b -tag SS region. This is derived inclusively for both STT and DTT trigger categories. There are distinct transfer factors set up: two based on the number of prongs in τ_{had} (either 1 or 3), and two more depending on whether the τ_{had} is leading or sub-leading. The derived fake factors for STT and DTT, along with the four transfer factors, can be found in Figure B.17 and Figure B.18, in that order.

¹The subsequent multijet estimate is then scaled down by a factor of 1/2, essentially producing an average from events in which the leading τ_{had} and the subleading τ_{had} fail to be identified.

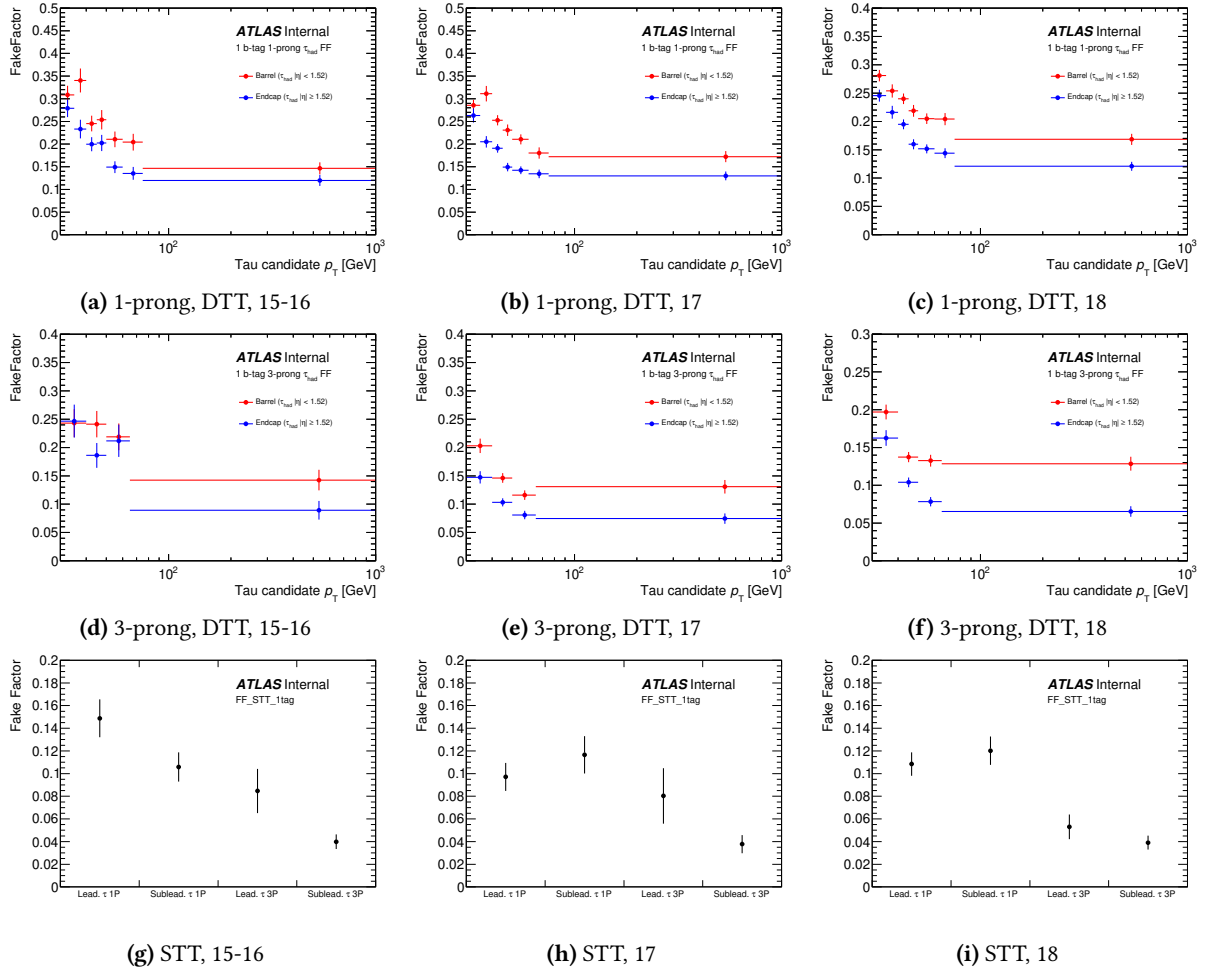


Figure B.17: Fake factors for 1-prong DTT ((a), (b), (c)), 3-prong DTT ((d), (e), (f)), and STT ((g), (h), (i)) for the data-taking periods 15-16, 17, and 18 for the di-Higgs $\tau_{\text{had}}\tau_{\text{had}}$ channel.

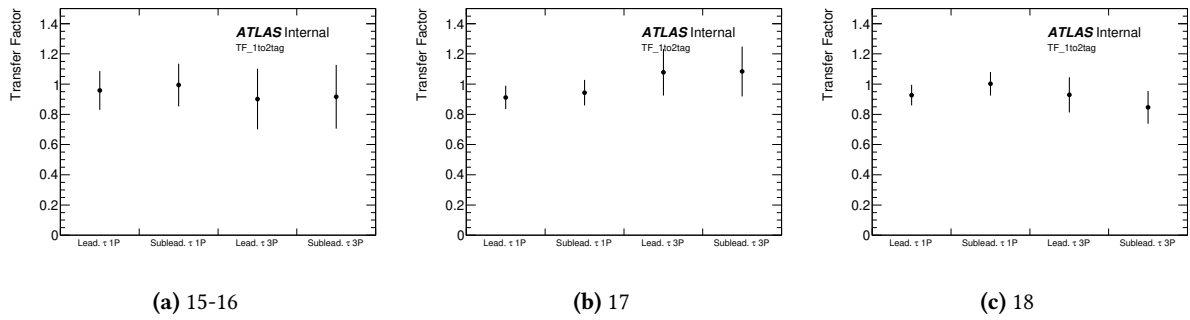


Figure B.18: Transfer factors for the data-taking periods (a) 15-16, (b) 17, and (c) 18 for the di-Higgs $\tau_{\text{had}}\tau_{\text{had}}$ channel.

B.1.3 $t\bar{t}$ with fake- τ_{had} in the $\tau_{\text{had}}\tau_{\text{had}}$ channel with scale-factor method

Background events originating from $t\bar{t}$ production in the $\tau_{\text{had}}\tau_{\text{had}}$ channel that contain fake- $\tau_{\text{had-vis}}$ are quantified using simulation. Nonetheless, to address the misidentification efficiencies of fake- $\tau_{\text{had-vis}}$, data-derived scale factors (SFs) are employed for corrections. A graphical representation detailing this approach can be found in Figure B.19.

The SFs are determined within the $t\bar{t}$ CR that is defined in the context of the $\tau_{\text{lep}}\tau_{\text{had}}$ SLT category, as elaborated in Section B.1.1. To ensure compatibility with the selection criteria of the $\tau_{\text{had}}\tau_{\text{had}}$ signal region (SR), modifications are made to the $t\bar{t}$ CR to specifically incorporate events where $\tau_{\text{had-vis}}$ satisfies $|\eta| < 2.5$.

Using a profile-likelihood fit, SFs are derived based on the fake- $\tau_{\text{had-vis}}$ p_T as a function, separately for 1- and 3-prong fake- $\tau_{\text{had-vis}}$ objects. This approach fits the m_T^W distribution of simulated events to data.

By fitting the m_T^W distribution, we can identify the contributions from the $t\bar{t}$ events that contain either true- or fake- $\tau_{\text{had-vis}}$. Additionally, the fit compensates for the shared modeling of the $t\bar{t}$ simulation across both contributions.

Different trigger categories are performed with separate fits.

Considering the 1-prong fake- $\tau_{\text{had-vis}}$, the SFs are approximately one for fake- $\tau_{\text{had-vis}}$ p_T under 40 GeV, but decrease to $\text{SF} \approx 0.6$ when fake- $\tau_{\text{had-vis}}$ p_T exceeds 70 GeV. Conversely, the 3-prong fake- $\tau_{\text{had-vis}}$ SFs are typically $\approx 20\%$ higher than those for the 1-prong counterparts.

For estimating the $t\bar{t}$ background with fake- $\tau_{\text{had-vis}}$ in the $\tau_{\text{had}}\tau_{\text{had}}$ SR, we rely on simulated events that meet the SR criteria. These events are then weighted using the corresponding SFs for each fake- $\tau_{\text{had-vis}}$ in the event.

In the process of deriving the SFs, we account for uncertainties both in the response of the detector and in modeling the $t\bar{t}$ events. Uncertainties associated with other minor processes are also considered.

The covariance matrix, which captures all measurement uncertainties, is then diagonalised. Subsequently, the emerging eigenvectors define individual nuisance parameters (NPs), which are integrated into the final signal extraction fit. Theoretical uncertainties in the simulated $t\bar{t}$ events, where SFs are implemented, and these too are incorporated into the final signal extraction fit.

Regarding the estimation of the fake- $\tau_{\text{had-vis}}$ background originating from multi-jet production via the fake-factor method (refer to Section B.1.2), it is essential to subtract a substantial portion of $t\bar{t}$ events with at least one fake- $\tau_{\text{had-vis}}$ from the data in the OS 2- b -tagged-jet anti-ID region (SR Template). This step is pivotal for projecting the multi-jet contribution in the $\tau_{\text{had}}\tau_{\text{had}}$ SR. The modeling of the simulated $t\bar{t}$ events with fake- $\tau_{\text{had-vis}}$ in this anti-ID region is adjusted using SFs derived through the previously mentioned method. The region for measuring these SFs resembles

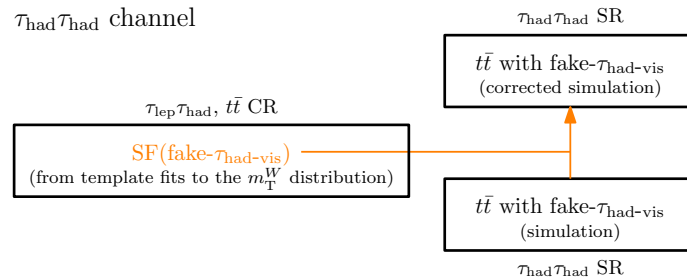


Figure B.19: Schematic depiction of the fake- $\tau_{\text{had-vis}}$ scale-factor method to estimate the $t\bar{t}$ background with fake- $\tau_{\text{had-vis}}$ in the $\tau_{\text{had}}\tau_{\text{had}}$ channel.

the $t\bar{t}$ control region (CR), but require that the $\tau_{\text{had-vis}}$ candidate fulfills the anti- $\tau_{\text{had-vis}}$ criteria.

In the anti-ID region, the measured SFs for the 1-prong fake- $\tau_{\text{had-vis}}$ stay close to one for fake- $\tau_{\text{had-vis}}$ p_T values below 40 GeV. These SFs exhibit a decreasing trend in value with an increase in the fake- $\tau_{\text{had-vis}}$ p_T , as the observations in the ID region. The SFs for the 3-prong fake- $\tau_{\text{had-vis}}$ are generally elevated by around 10%–20% in comparison to the 1-prong fake- $\tau_{\text{had-vis}}$ objects.

B.2 Complementary Results

B.2.1 Limits and scans compare with the previous results

B.2.1.1 $\tau_{\text{had}}\tau_{\text{had}}$: Comparison with previous analysis

The comparison of the upper limits between the old and new analysis is summarised in Table B.3. The inclusive signal strength fit produces a μ_{HH} of (0.70 ± 1.71) for the previous result and (-0.36 ± 1.35) in the current analysis. As the event selection did not change, the compatibility between the results of the two analyses can be obtained with a bootstrapping technique, which is estimated to one standard deviation, as documented in Section B.2.3.3.

Table B.3: Comparison between expected and observed quantities for the current and previous analysis round in the $\tau_{\text{had}}\tau_{\text{had}}$ channel.

analysis	95% CL UL on μ_{HH}	95% CI for κ_λ	95% CI for κ_{2V}
Current analysis (obs.)	3.42	[-1.46, 7.97]	[-0.22, 2.40]
Previous analysis (obs.)	4.95	[-2.72, 9.47]	[-0.63, 2.77]
Current analysis (exp.)	3.86	[-2.76, 9.4]	[-0.41, 2.59]
Previous analysis (exp.)	4.42	[-3.38, 10.4]	[-0.66, 2.79]

Finally, B.20 shows the comparison of the expected and observed likelihood ratio scans for κ_λ and κ_{2V} in the current and previous analysis.

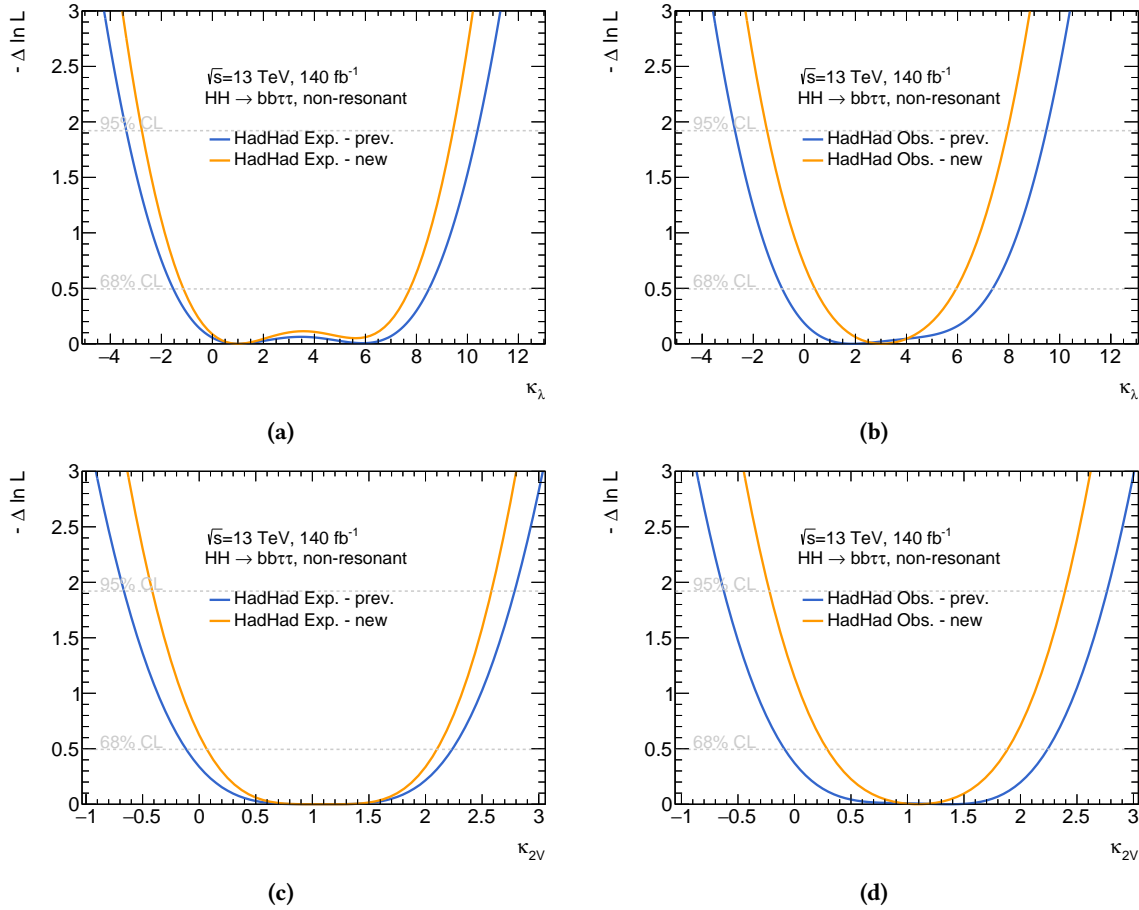


Figure B.20: Negative logarithm of the likelihood ratio comparing different κ_λ (top) and κ_{2V} (bottom) hypotheses for the fit to Asimov (left) and data (right) in the current and previous analysis for the $\tau_{\text{had}}\tau_{\text{had}}$ channel.

B.2.1.2 $\tau_{\text{lep}}\tau_{\text{had}}$: Comparison with previous analysis

The comparison between the old and new analysis results is summarised in Table B.4. The inclusive signal strengths fit in the SLT channel produces a μ_{HH} of (2.33 ± 3.59) for the previous result and (7.82 ± 3.61) in the current analysis. As the event selection did not change, the compatibility between the results of the two analyses can be obtained with a bootstrapping technique, which is estimated to 2.4 standard deviations, as documented in Section B.2.3.3.

Table B.4: Comparison between expected and observed quantities for the current and previous analysis round in the $\tau_{\text{lep}}\tau_{\text{had}}$ channel.

analysis	95% CL UL on μ_{HH}	95% CI for κ_λ	95% CI for κ_{2V}
Current analysis (obs.)	16.0	$[-7.84, 0.47], [7.92, 13.75]$	$[-1.54, 3.72]$
Previous analysis (obs.)	9.7	$[-7.00, 14.73]$	$[-1.49, 3.62]$
Current analysis (exp.)	5.98	$[-4.67, 11.87]$	$[-0.64, 2.83]$
Previous analysis (exp.)	7.8	$[-5.90, 13.49]$	$[-1.22, 3.36]$

Finally, B.21 shows the comparison of the expected and observed likelihood ratio scans for κ_λ and κ_{2V} in the current and previous analysis.

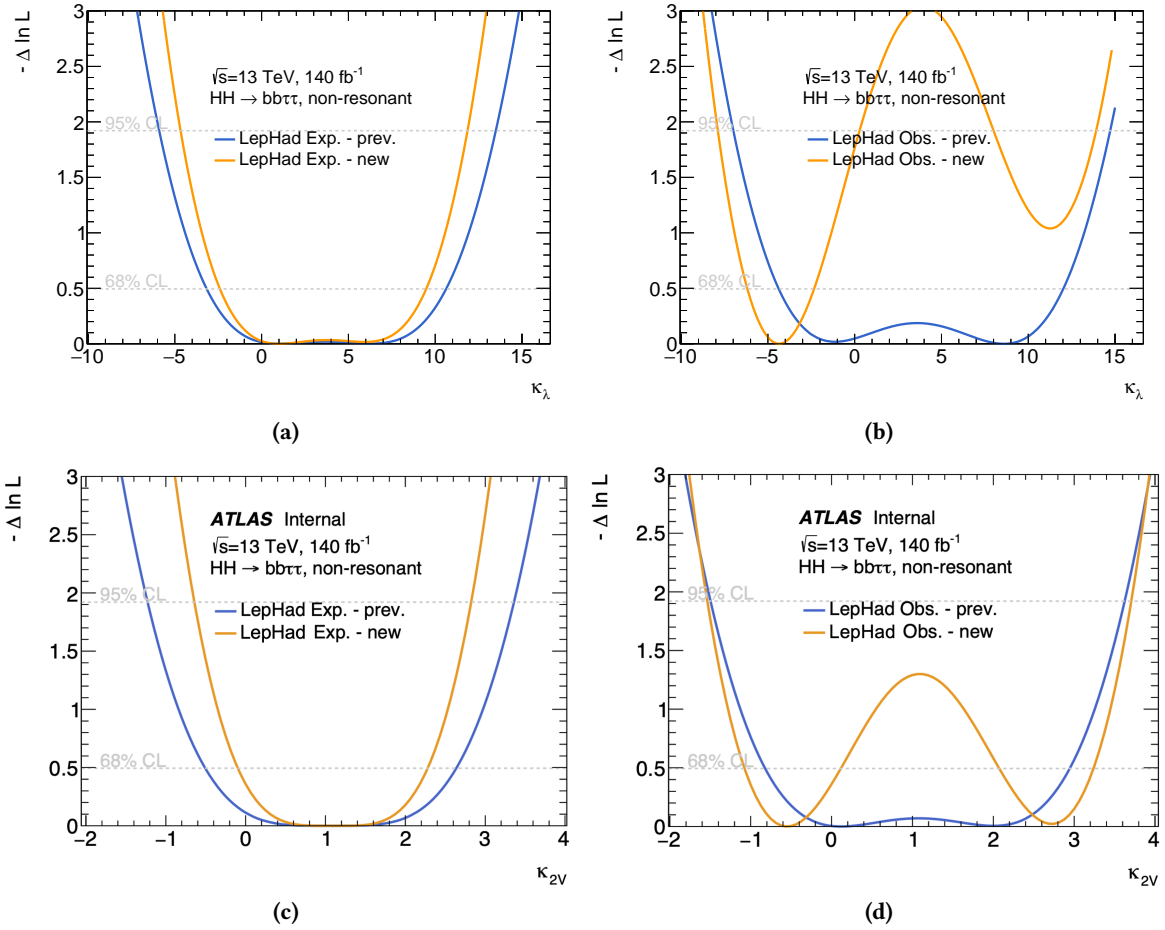


Figure B.21: Negative logarithm of the likelihood ratio comparing different κ_λ (top) and κ_{2V} (bottom) hypotheses for the fit to Asimov (left) and data (right) in the current and previous analysis for the $\tau_{\text{lep}}\tau_{\text{had}}$ channel.

B.2.1.3 Combined: Comparison with previous analysis

The comparison between the old and new analysis is summarised in Table B.5.

Table B.5: Comparison between expected and observed quantities for the current and previous analysis round in the combined analysis.

analysis	95% CL UL on μ_{HH}	95% CI for κ_λ	95% CI for κ_{2V}
Current analysis (obs.)	5.89	[-3.19, 9.09]	[-0.53, 2.70]
Previous analysis (obs.)	4.7	[-2.7, 9.5]	[-0.6, 2.7]
diff.	+25%	< 1%	-2%
Current analysis (exp.)	3.15	[-2.42, 9.16]	[-0.22, 2.40]
Previous analysis (exp.)	3.9	[-3.07, 10.20]	[-0.54, 2.67]
diff.	-20%	-11%	-19%

Finally, B.22 shows the comparison of the expected and observed likelihood ratio scans for κ_λ and κ_{2V} in the current and previous analysis.

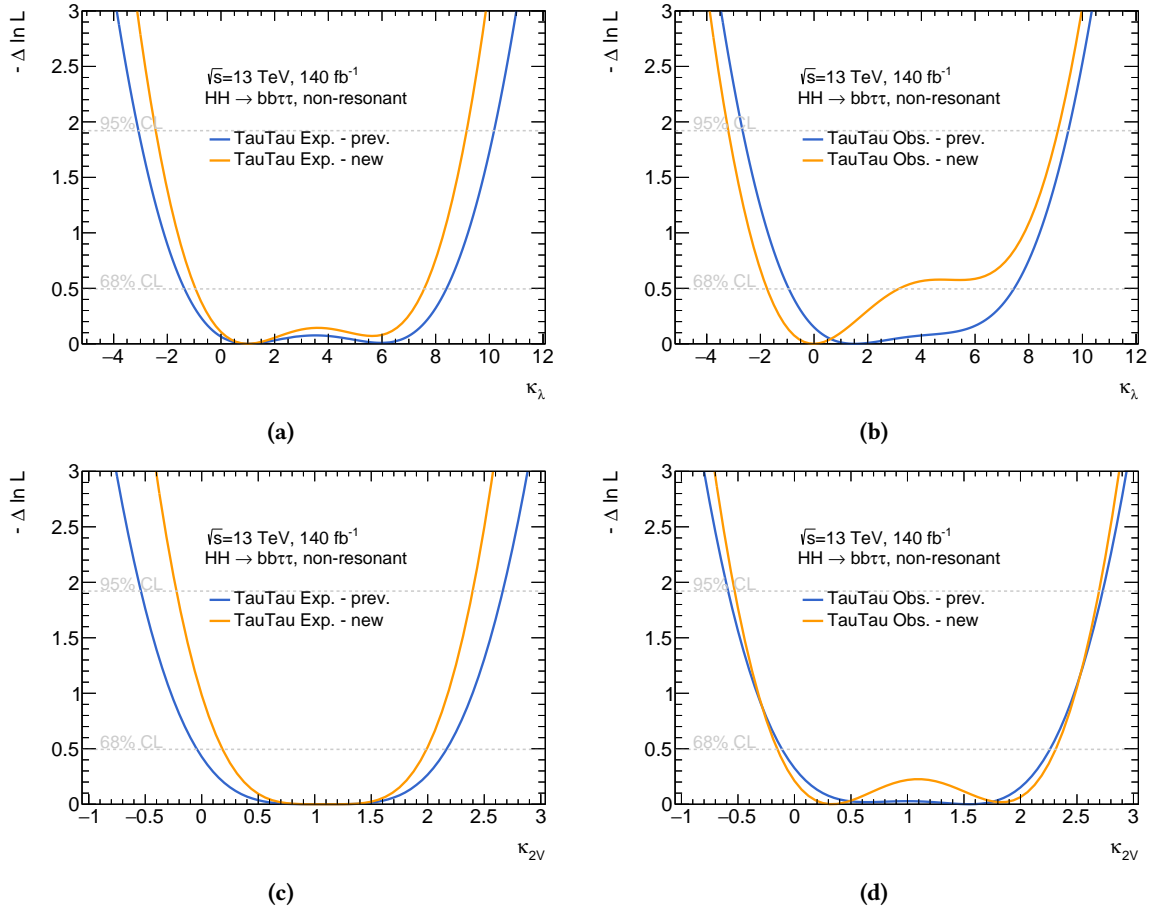


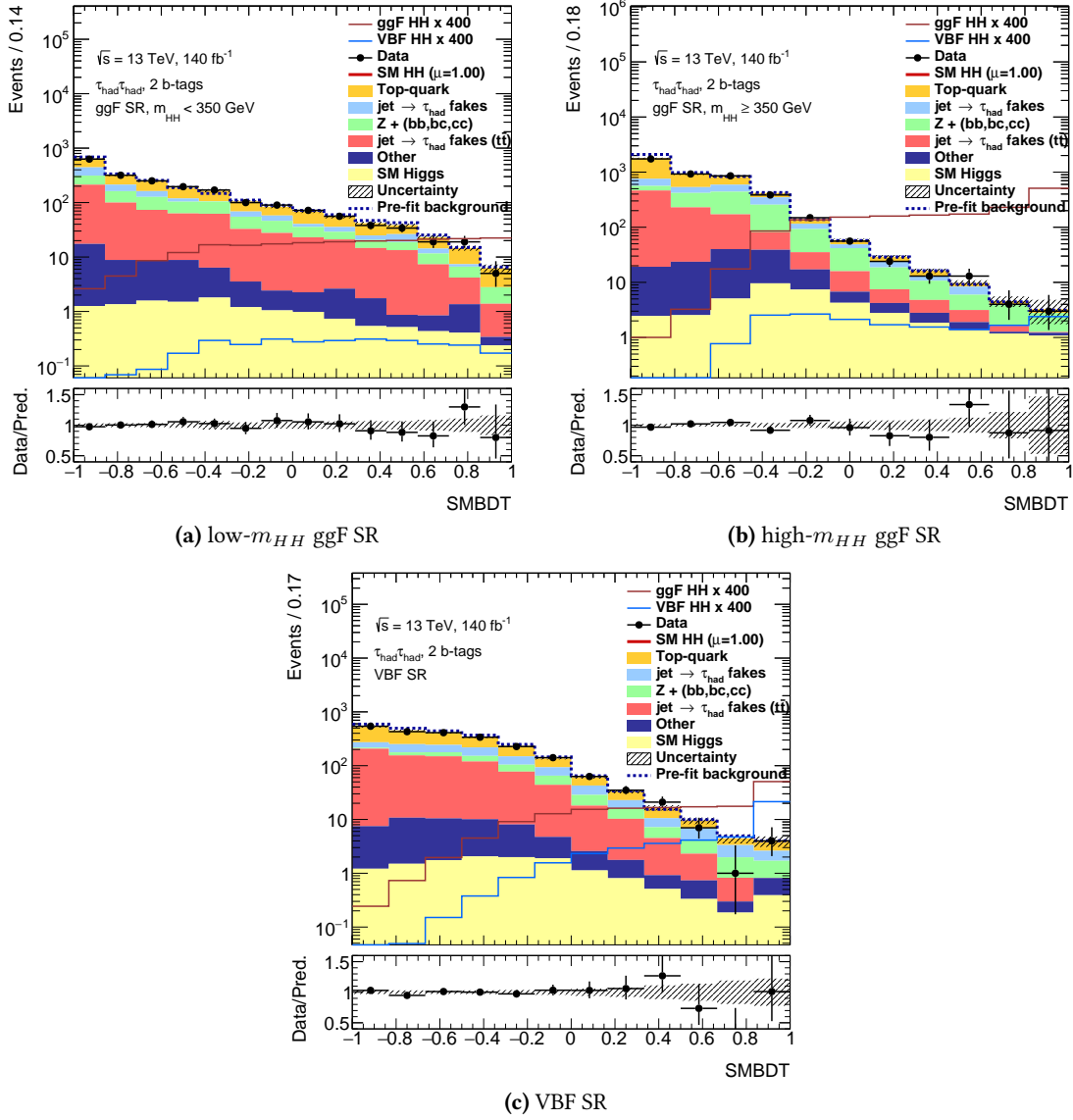
Figure B.22: Negative logarithm of the likelihood ratio comparing different κ_λ (top) and κ_{2V} (bottom) hypotheses for the fit to Asimov (left) and data (right) in the current and previous analysis for the combination.

B.2.2 Additional fit checks

B.2.2.1 Alternative post-fit plots for the HadHad channel

Post-fit distributions of the fitted variables in the 4 regions are shown in Figure B.23.

Post-fit distribution of other input variables are shown in Figures B.24 and B.25 ; the plots are obtained by extrapolating the nuisance parameters for the data fit excluding the gamma parameters.

Figure B.23: Post-fit BDT score distributions in the $\tau_{had}\tau_{had}$ signal regions.

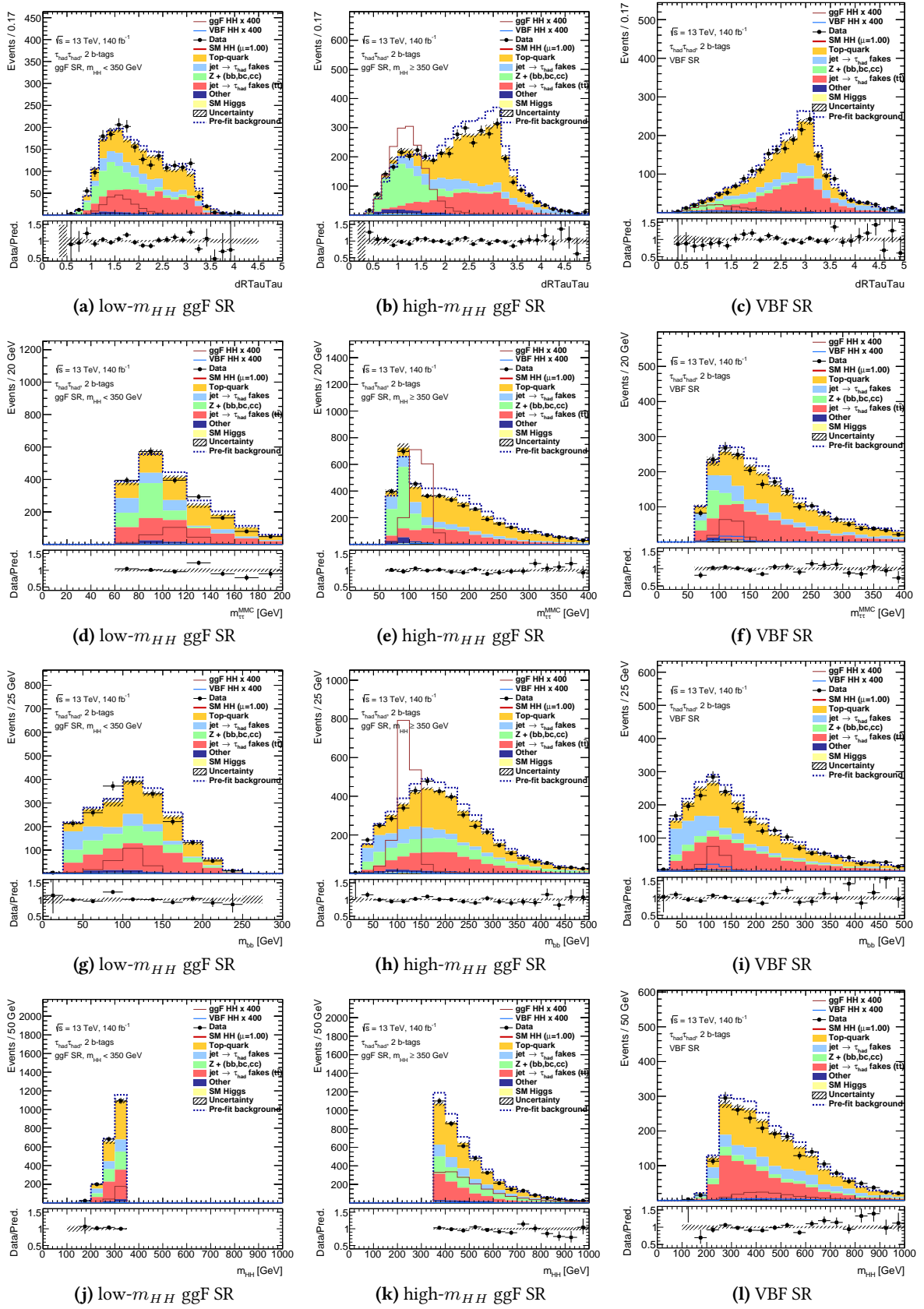


Figure B.24: Post-fit data/Mc distributions of key variables in the $\tau_{had}\tau_{had}$ channel signal regions.

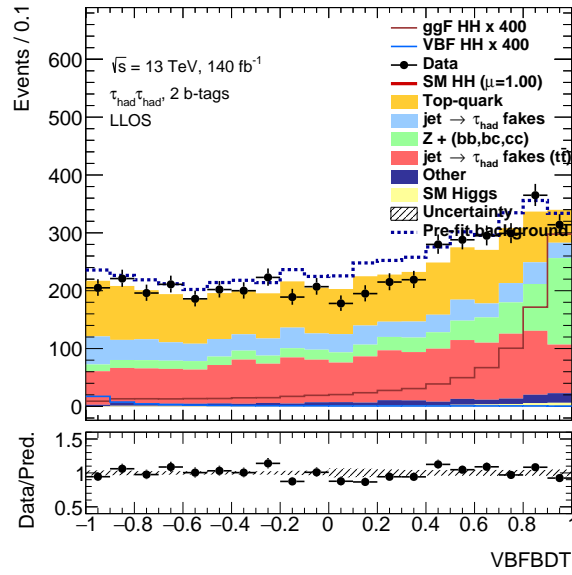


Figure B.25: Post-fit data/MC distribution of the ggF/VBF classification BDT score in the $\tau_{\text{had}}\tau_{\text{had}}$ channel. The categorisation BDT is only shown for events with at least four jets which represent a subset of the ggH SRs.

B.2.2.2 Alternative post-fit plots for the LepHad channel

Figure B.26 shows the data/prediction comparison for the post-fit BDT score distributions in the $\tau_{\text{lep}}\tau_{\text{had}}$ SRs. The choice of the binning is discussed in Section 5.5.3; In the post-fit plots, the signal is excluded from the stack of histograms and the ratio; the CR agreement is not shown, since this is identical to the one from the $\tau_{\text{had}}\tau_{\text{had}}$ standalone fit.

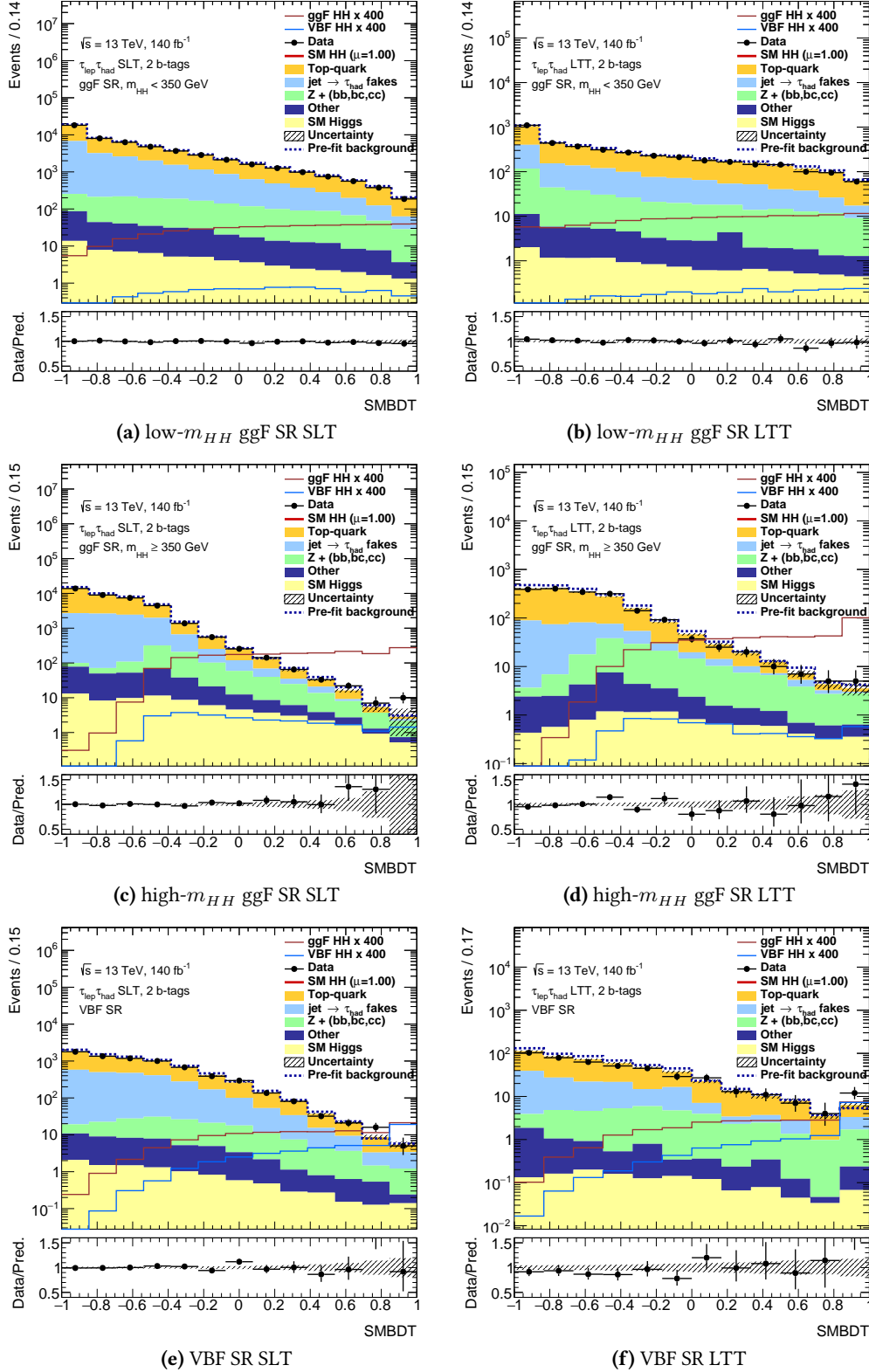


Figure B.26: Post-fit BDT score distributions in the $\tau_{\text{lep}}\tau_{\text{had}}$ signal regions. The result of the inclusive signal strength fit is used to produce these distributions.

B.2.2.3 Alternative post-fit plots for the Combined fit

Post-fit distributions of the fitted variables in the 9 signal regions are shown in Figure B.27². In the post-fit plots, the signal is excluded in the stack of histograms and the ratio, the uncertainty band is drawn on the background stack only.

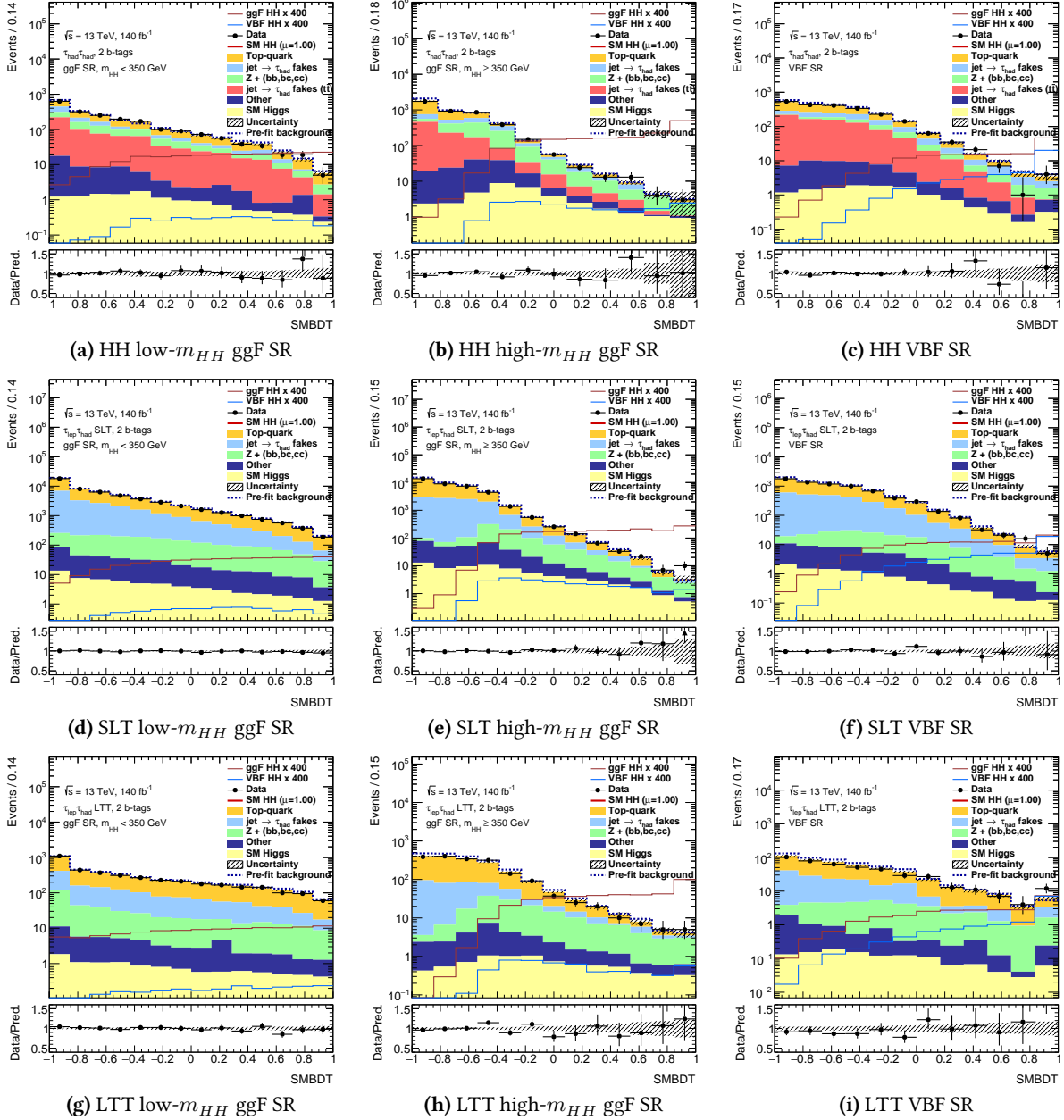


Figure B.27: Post-fit BDT score distributions in the $\tau_{\text{had}}\tau_{\text{had}}$ and $\tau_{\text{lep}}\tau_{\text{had}}$ signal regions after the combined fit.

B.2.3 Compatibility tests

To assess the self-consistency of the fit, we calculate the compatibility between two separate fit results: the nominal setup with a single signal strength parameter in all channels and analysis regions, and an alternative model with a separate signal strength for each channel (or for each analysis region). The difference in the best-fit negative-log likelihood between the two situations

²The CR post-fit is not shown since it is basically equivalent to the result of the CR-only fit.

then follows a χ^2 distribution with N degrees of freedom, where N is the difference in the number of signal strength parameters between the two fits.

In the following, we separately study the compatibility across different channels (nominal fit compared to a fit with a separate signal strength for each channel), and also across all analysis regions (nominal fit compared to a fit with a separate signal strength for each analysis region).

B.2.3.1 Compatibility across different channels

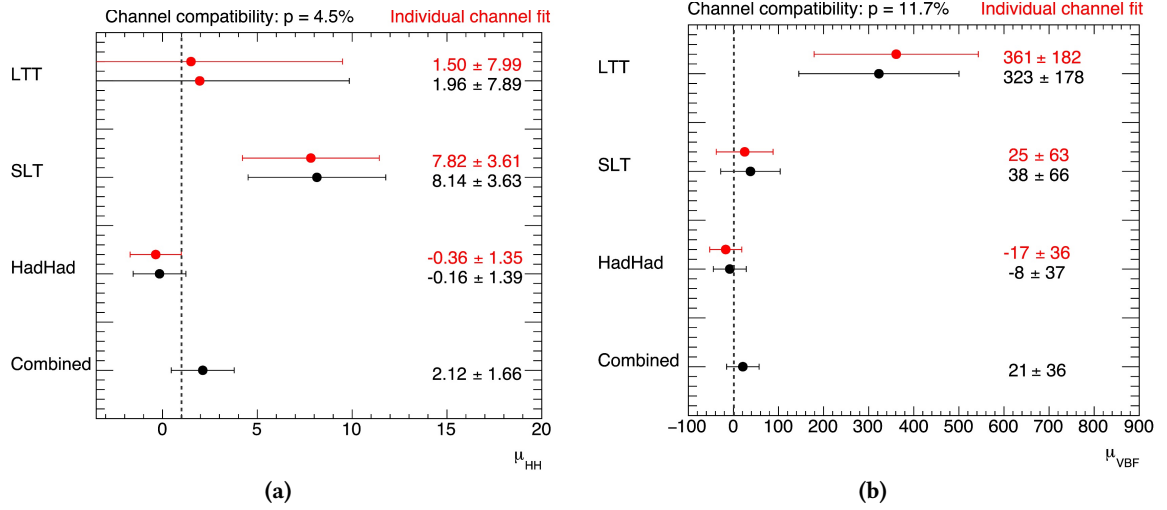


Figure B.28: Compatibility of the fit result across different analysis channels, for μ_{HH} in Figure (a) and μ_{VBF} in Figure (b). The black markers correspond to the combined fit with a single POI, and to a separate fit with one POI per channel. The results from separate fits to each analysis regions are additionally shown in red.

As Figure B.28 shows, the per-channel compatibility is 4.5% for μ_{HH} and 11.7% for μ_{VBF} . Good agreement is observed between a combined fit to all channels with separate signal strengths, and individual fits to each channel.

B.2.3.2 Compatibility across different analysis regions and channels

Table B.6: Compatibility of the fit result for μ_{HH} across different analysis channels and regions.

One global POI: $\mu_{HH} = 2.12 \pm 1.66$			
One POI per region:			
	Had-had	SLT	LTT
low-mHH	-3.85 ± 35.18	-292 ± 147	-234 ± 213
high-mHH	-0.15 ± 1.41	8.05 ± 3.70	134.8 ± 81.6
VBF	-0.55 ± 11.2	15.5 ± 28.9	0.087 ± 7.86
Compatibility: 4.6%			

The compatibility across all nine analysis regions is 4.6% for μ_{HH} (Table B.6) and 3.4% for μ_{VBF} (Table B.7).

Table B.7: Compatibility of the fit result for μ_{VBF} across different analysis channels and regions.

One global POI: $\mu_{\text{VBF}} = 21 \pm 36$			
One POI per region:			
	Had-had	SLT	LTT
low-mHH	-235 ± 3179	-20827 ± 9200	-13380 ± 10027
high-mHH	-222 ± 261	1041 ± 545	-546 ± 1085
VBF	-1.90 ± 38	16 ± 60	335 ± 187
Compatibility: 3.4%			

B.2.3.3 Compatibility with previous Run-2 result

The compatibility of this result with the previous Run-2 analysis is investigated through a bootstrapping technique. A number of resampled datasets are generated by Poisson-fluctuating around the observed data. The MC templates are not resampled. (Owing to the inclusion of the di-leptonic ttbar sample and the move to Sherpa 2.2.11 as the generator for the Z+jets background, this analysis shares only a fraction of MC events with the previous result.)

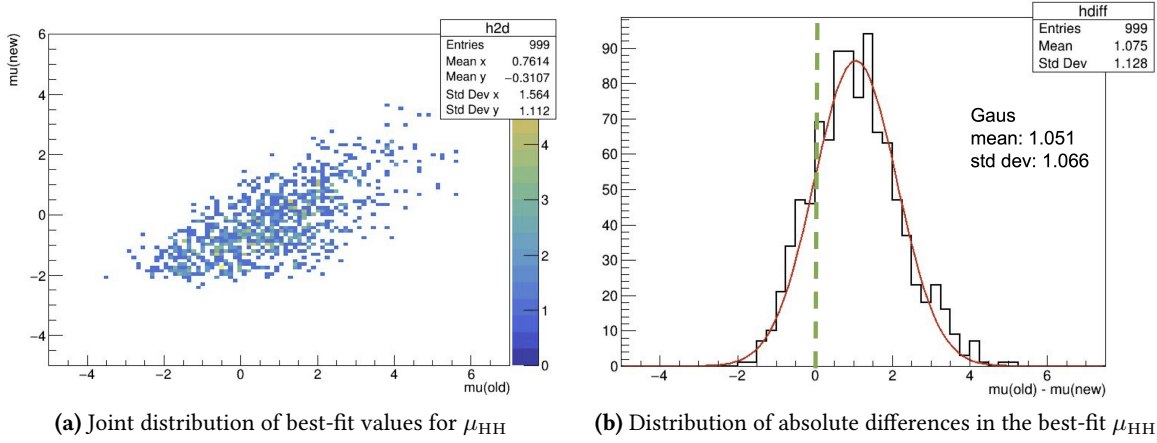


Figure B.29: Bootstrap result for the had-had channel. Figure (a): joint distribution of best-fit values for μ_{HH} obtained from the previous Run-2 analysis (horizontal axis) and the present analysis (vertical axis). The correlation coefficient is 70%. Figure (b): distribution of absolute differences in the best-fit μ_{HH} between the two results.

Figure B.29 shows the result of the bootstrap performed in the had-had channel, indicating compatibility at the 1σ -level. Figure B.30 illustrates the equivalent result for the SLT channel, where the compatibility is worse owing due to the presence of an excess in a signal-like discriminant bin. In this case, the compatibility with the previous Run 2 result stands at 2.4σ .

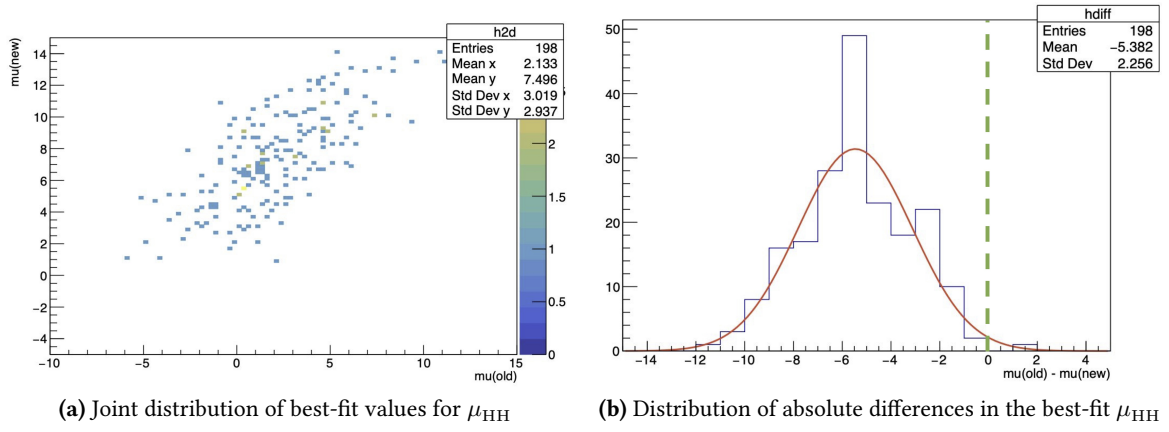


Figure B.30: Bootstrap result for the SLT channel. Figure (a): joint distribution of best-fit values for μ_{HH} obtained from the previous Run-2 analysis (horizontal axis) and the present analysis (vertical axis). The correlation coefficient is 72%. Figure (b): distribution of absolute differences in the best-fit μ_{HH} between the two results.

CHAPTER

Detailed points of the Higgs analyses at the Future Circular Collider

C.1 Event selection plots	285
C.2 Recoil mass fits	288
C.3 BDT input variables	289
C.4 BDT hyper-parameters	292

C.1 Event selection plots

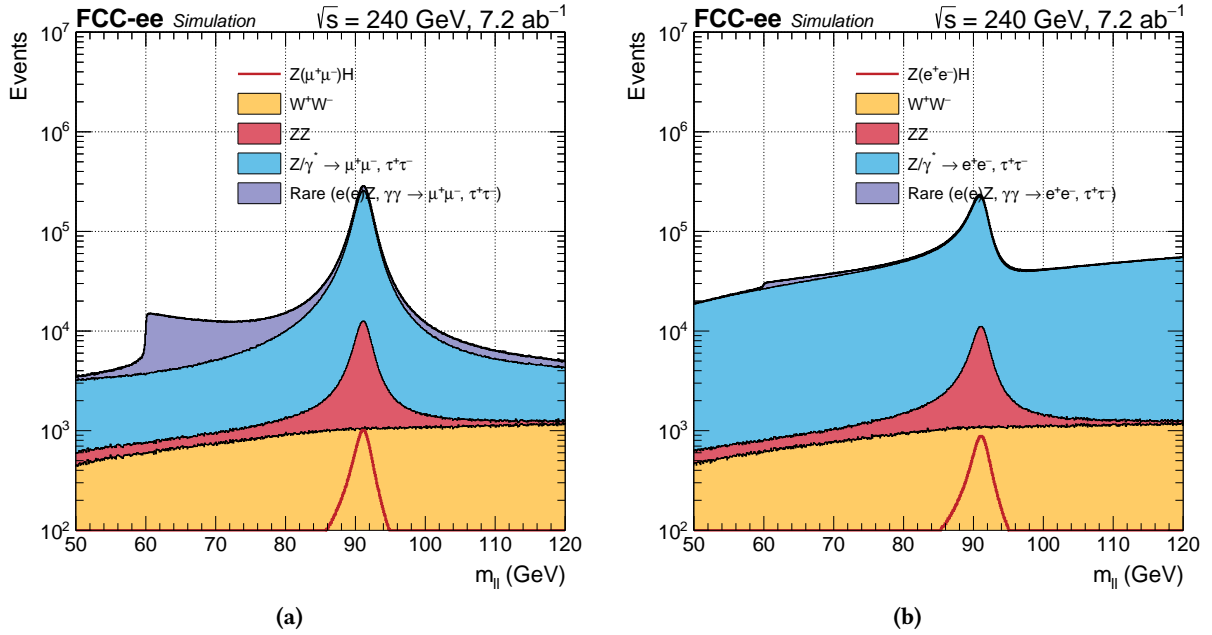


Figure C.1: $m_{\ell\ell}$ distribution after the muon selection criteria for the muon (a) and electron (b) final states.

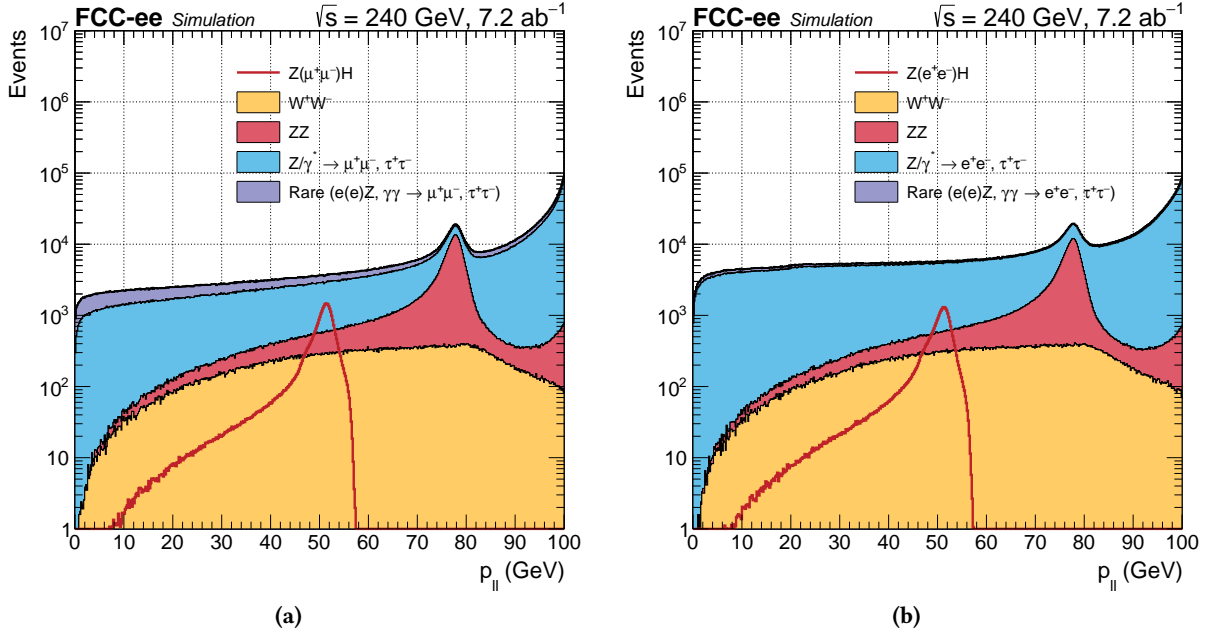


Figure C.2: $p_{\ell\ell}$ distribution after the $m_{\ell\ell}$ cut for the muon (a) and electron (b) final states.

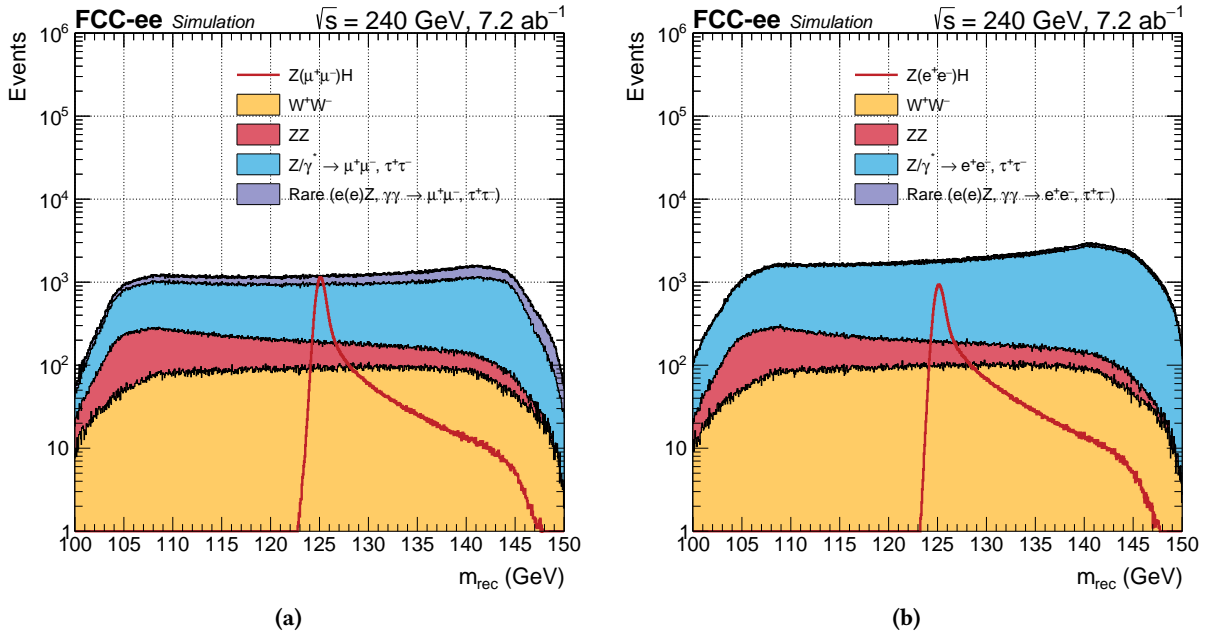


Figure C.3: m_{rec} distribution after the $p_{\ell\ell}$ cut for the muon (a) and electron (b) final states.

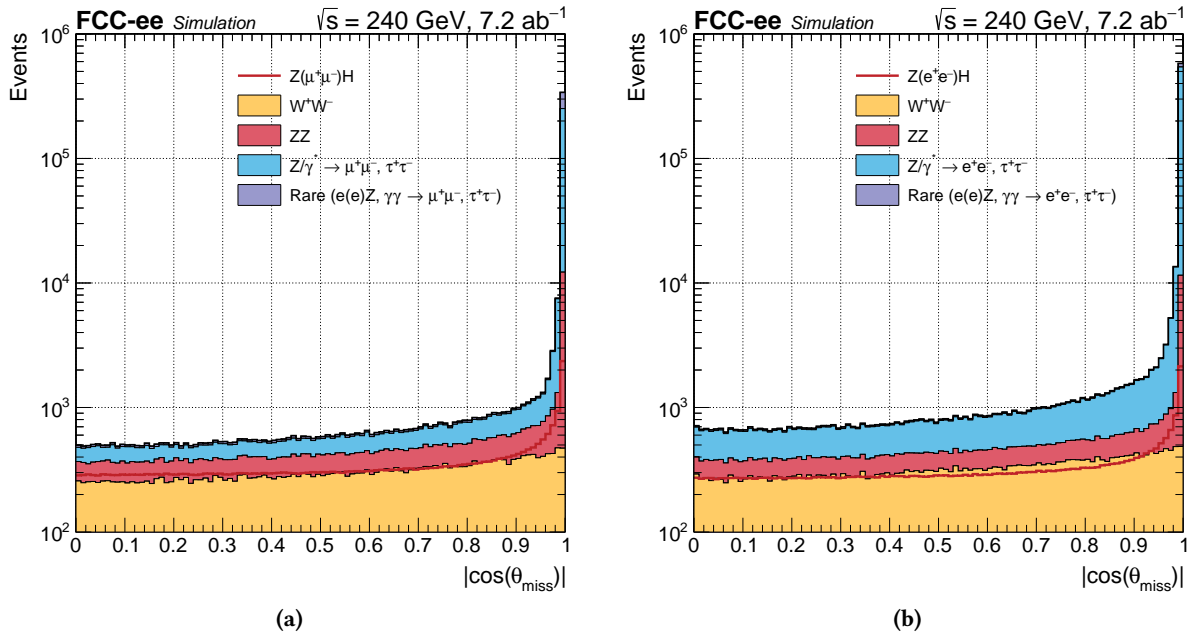


Figure C.4: $\cos(\theta_{\text{miss}})$ distribution after the m_{rec} cut for the muon (a) and electron (b) final states.

C.2 Recoil mass fits

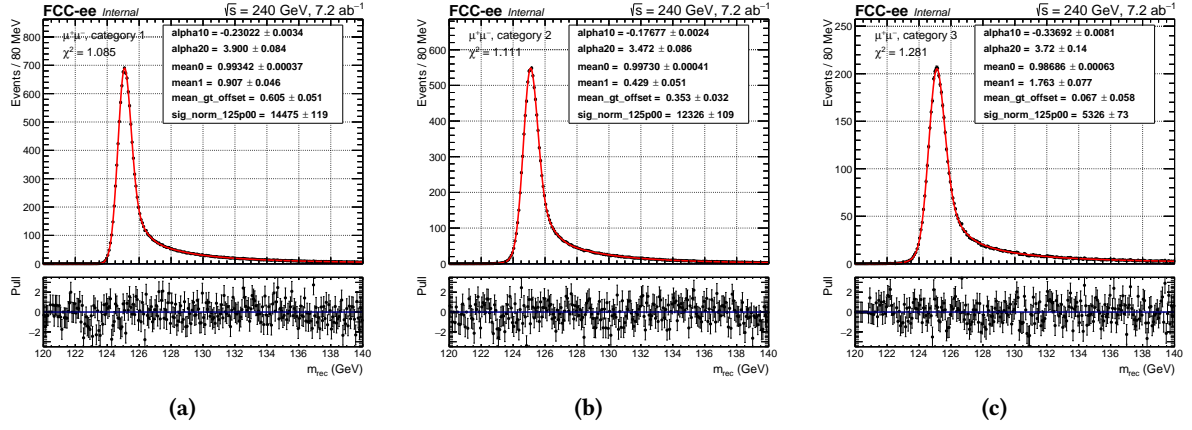


Figure C.5: Signal samples for 125 GeV muon channel: CC ((a)), CF ((b)) FF ((c)).

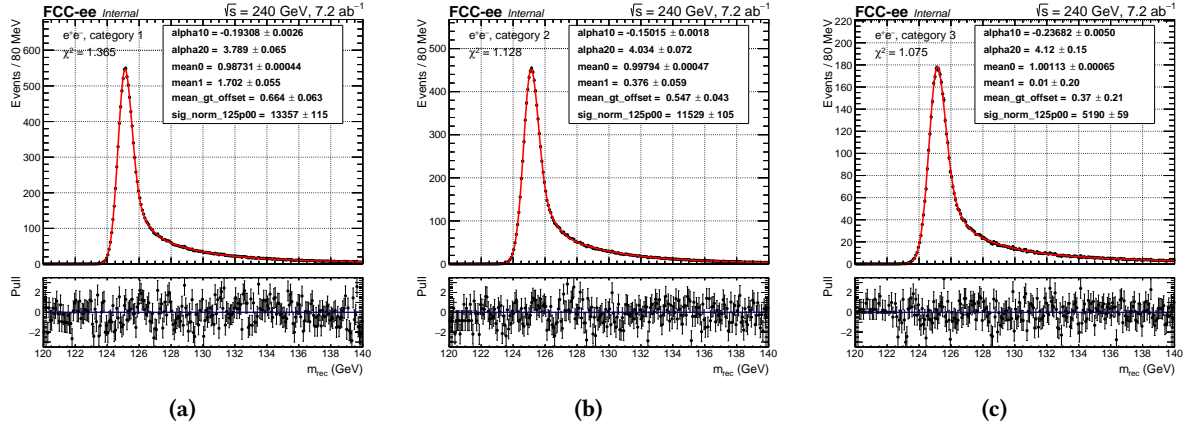


Figure C.6: Signal samples for 125 GeV electron channel: CC ((a)), CF ((b)) FF ((c)).

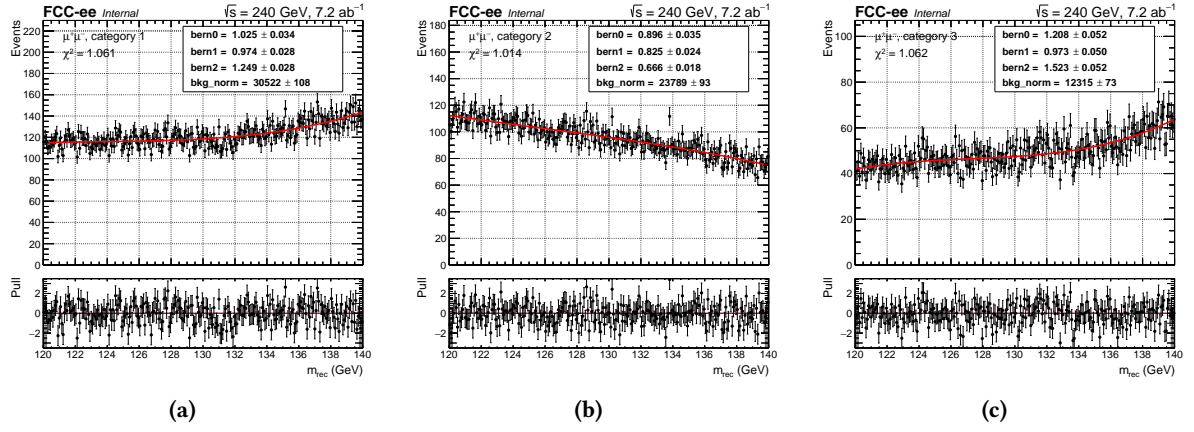


Figure C.7: Background distributions for the muon channel: CC ((a)), CF ((b)), FF ((c)).

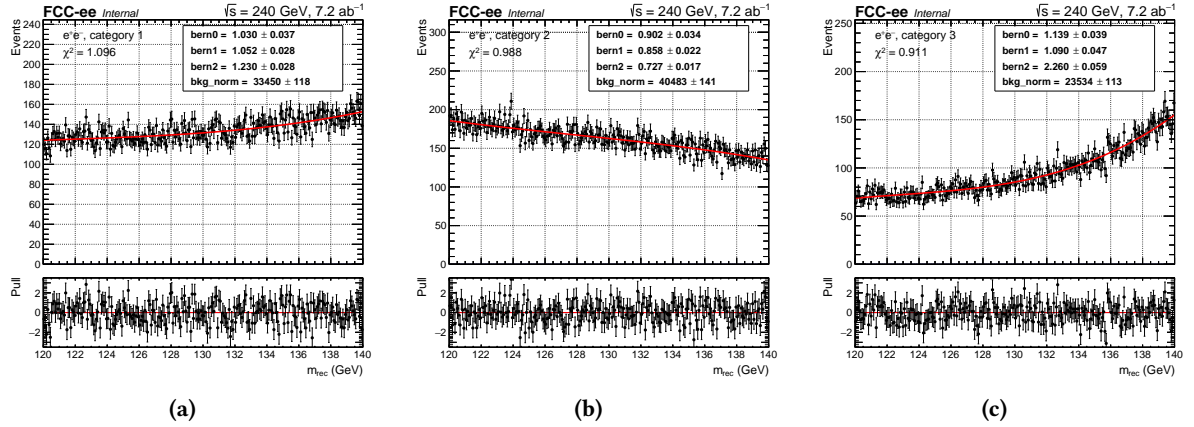
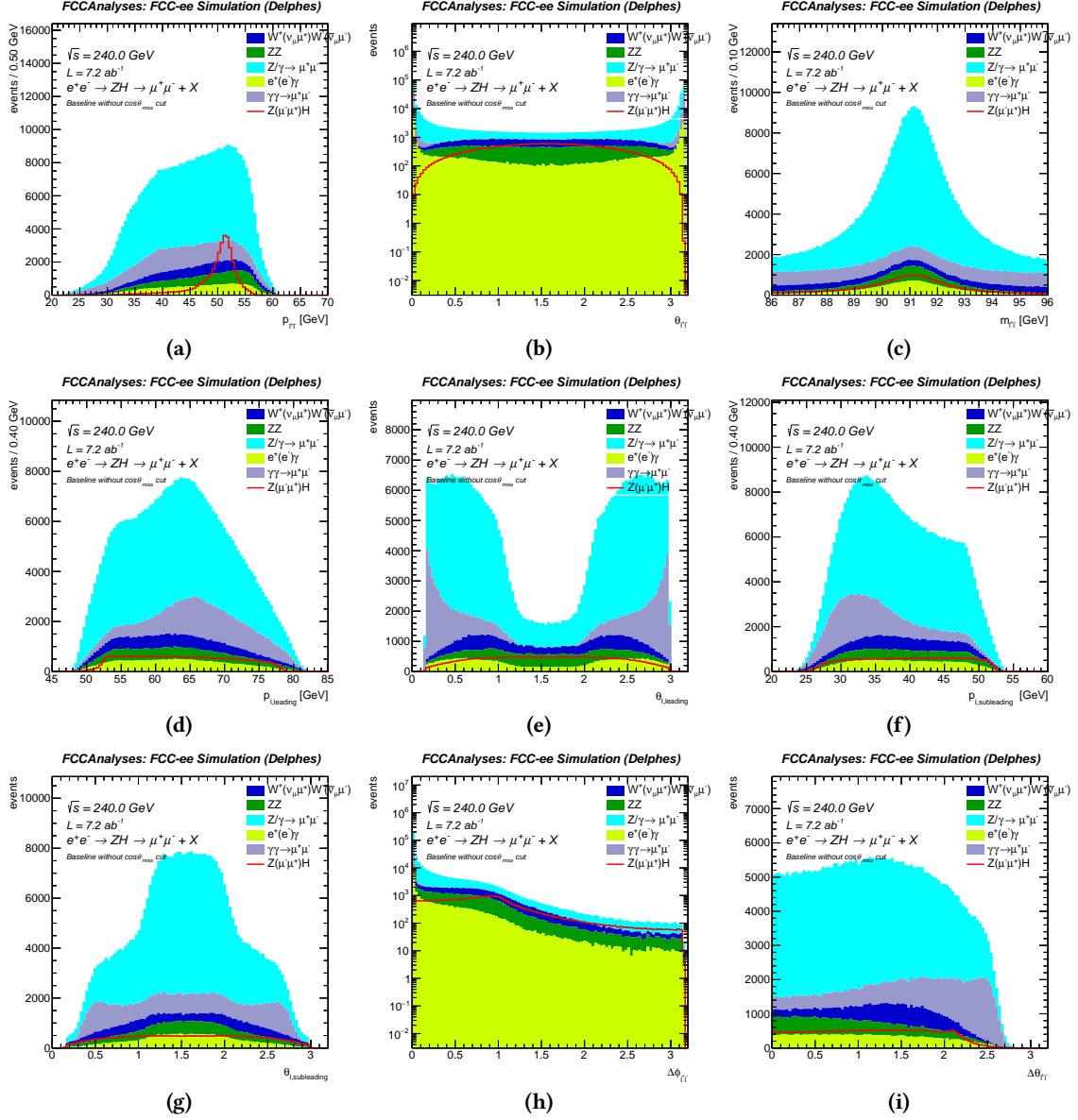
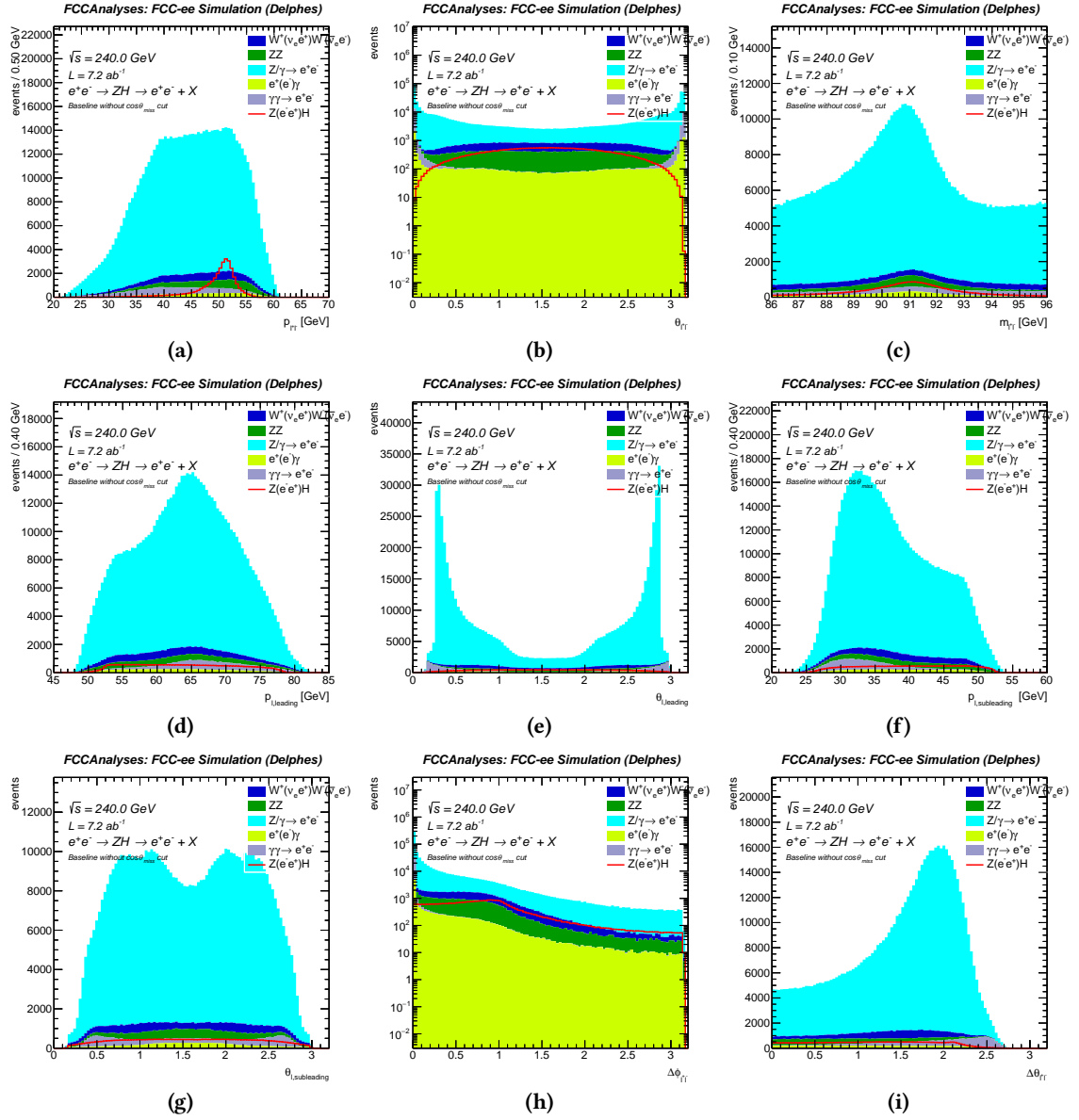


Figure C.8: Background distributions for the electron channel: CC ((a)), CF ((b)), FF ((c)).

C.3 BDT input variables

Figure C.9: Input variables for BDT training for the $\mu^+\mu^-$ channel.

Figure C.10: Input variables for BDT training for the e^+e^- channel.

C.4 BDT hyper-parameters

Each hyper-parameter and its respective value are defined as follows:

1. **n_estimators (350):** This parameter refers to the number of boosting rounds or the number of trees used in the model. A higher value typically results in better model performance but may also lead to over-fitting. In our case, we have found that 350 trees balance well model performance and computational efficiency.
2. **learning_rate (0.20):** The learning rate, also known as shrinkage, controls the contribution of each tree to the final model. A smaller learning rate typically requires more trees but reduces the risk of over-fitting. We have set the learning rate to 0.20, which provides a good balance between model performance and the number of trees needed.
3. **max_depth (3):** The maximum depth of each tree determines the number of layers in the tree. A larger depth increases the model's complexity and may result in better performance but also increases the risk of over-fitting. We have set the maximum depth to 3, which provides a reasonable trade-off between model complexity and the risk of over-fitting.
4. **subsample (0.5):** This parameter controls the fraction of the training data-set used to build each tree. A lower value introduces randomness and may help prevent over-fitting. In our case, we have set the sub-sample ratio to 0.5, meaning that each tree is built using a randomly selected 50% of the training data.
5. **gamma (3):** The gamma parameter, also known as the minimum loss reduction, specifies the minimum reduction in the loss function required to make a split at a leaf node. A higher gamma value makes the model more conservative, reducing the risk of over-fitting. We have set gamma to 3, which helps control the model's complexity while still allowing it to learn from the data.
6. **min_child_weight (10):** This parameter controls the minimum sum of instance weights (hesians) required in a child node. Larger values of min_child_weight result in a more conservative model by preventing over-fitting. We have set the min_child_weight value to 10 to control the model's complexity and avoid over-fitting.
7. **max_delta_step (0):** This parameter sets the maximum step size allowed for each tree's weight estimation. A value of 0 means that there is no constraint on the step size. In our case, we have set max_delta_step to 0, allowing the model to adjust the step size freely.
8. **colsample_bytree (0.5):** This parameter controls the fraction of features to be randomly selected for each tree. A smaller value can help prevent over-fitting by reducing the correlation between trees. We have set the colsample_bytree value to 0.5, meaning that each tree is built using a random 50% of the features.

Bibliography

- [1] ATLAS Collaboration. *Observation of a new particle in the search for the Standard Model Higgs boson with the ATLAS detector at the LHC*. In: *Phys. Lett. B* 716 (2012), p. 1. DOI: [10.1016/j.physletb.2012.08.020](https://doi.org/10.1016/j.physletb.2012.08.020). arXiv: [1207.7214](https://arxiv.org/abs/1207.7214) [hep-ex] (cit. on pp. 7, 17, 22).
- [2] CMS Collaboration. *Observation of a new boson at a mass of 125 GeV with the CMS experiment at the LHC*. In: *Phys. Lett. B* 716 (2012), p. 30. DOI: [10.1016/j.physletb.2012.08.021](https://doi.org/10.1016/j.physletb.2012.08.021). arXiv: [1207.7235](https://arxiv.org/abs/1207.7235) [hep-ex] (cit. on pp. 7, 17, 22).
- [3] ATLAS Collaboration. *Measurement of the b -jet identification efficiency with the p_T^{rel} method in multi-jet events using pp collisions at $\sqrt{s} = 13$ TeV with the ATLAS Detector*. ATL-PHYS-PUB-2022-025. 2022. URL: <https://cds.cern.ch/record/2809692> (cit. on pp. 8, 88, 89, 94, 95, 96, 105).
- [4] ATLAS Collaboration. *Search for resonant and non-resonant Higgs boson pair production in the $b\bar{b}\tau^+\tau^-$ decay channel using 13 TeV pp collision data from the ATLAS detector*. In: (2022). arXiv: [2209.10910](https://arxiv.org/abs/2209.10910) [hep-ex] (cit. on pp. 8, 35, 112, 118, 133, 186, 187, 259, 266, 269).
- [5] ATLAS Collaboration. *Constraining the Higgs boson self-coupling from single- and double-Higgs production with the ATLAS detector using pp collisions at $\sqrt{s} = 13$ TeV*. ATLAS-CONF-2022-050. 2022. URL: <https://cds.cern.ch/record/2816332> (cit. on pp. 8, 112).
- [6] ATLAS Collaboration. *Combination of searches for non-resonant and resonant Higgs boson pair production in the $b\bar{b}\gamma\gamma$, $b\bar{b}\tau^+\tau^-$ and $b\bar{b}b\bar{b}$ decay channels using pp collisions at $\sqrt{s} = 13$ TeV with the ATLAS detector*. ATLAS-CONF-2021-052. 2021. URL: <https://cds.cern.ch/record/2786865> (cit. on pp. 8, 112).
- [7] ATLAS Collaboration. *Differential $t\bar{t}$ cross-section measurements using boosted top quarks in the all-hadronic final state with 139 fb^{-1} of ATLAS data*. ATLAS-CONF-2021-050. 2021. URL: <https://cds.cern.ch/record/2782534> (cit. on pp. 8, 112).
- [8] ATLAS Collaboration. *HEFT interpretations of Higgs boson pair searches in $b\bar{b}\gamma\gamma$ and $b\bar{b}\tau^+\tau^-$ final states and of their combination in ATLAS*. ATL-PHYS-PUB-2022-019. 2022. URL: <https://cds.cern.ch/record/2806411> (cit. on pp. 8, 112).
- [9] M. Mangano et al. *FCC Physics Opportunities: Future Circular Collider Conceptual Design Report Volume 1. Future Circular Collider*. Tech. rep. 6. Geneva: CERN, 2019. DOI: [10.1140/epjc/s10052-019-6904-3](https://doi.org/10.1140/epjc/s10052-019-6904-3). URL: <https://cds.cern.ch/record/2651294> (cit. on pp. 9, 191, 198).
- [10] M. Benedikt et al. *FCC-ee: The Lepton Collider: Future Circular Collider Conceptual Design Report Volume 2. Future Circular Collider*. Tech. rep. 2. Geneva: CERN, 2019. DOI: [10.1140/epjst/e2019-900045-4](https://doi.org/10.1140/epjst/e2019-900045-4). URL: <https://cds.cern.ch/record/2651299> (cit. on pp. 9, 191, 198, 199, 204, 232).
- [11] M. Benedikt et al. *FCC-hh: The Hadron Collider: Future Circular Collider Conceptual Design Report Volume 3. Future Circular Collider*. Tech. rep. Geneva: CERN, 2019. DOI: [10.1140/epjst/e2019-900087-0](https://doi.org/10.1140/epjst/e2019-900087-0). URL: <https://cds.cern.ch/record/2651300> (cit. on pp. 9, 191, 198).
- [12] F. Zimmermann et al. *HE-LHC: The High-Energy Large Hadron Collider: Future Circular Collider Conceptual Design Report Volume 4. Future Circular Collider*. Tech. rep. Geneva: CERN, 2019. DOI: [10.1140/epjst/e2019-900088-6](https://doi.org/10.1140/epjst/e2019-900088-6). URL: <https://cds.cern.ch/record/2651305> (cit. on pp. 9, 191, 198).
- [13] F. Zimmermann. *FCC-ee Status and Overview*. Tech. rep. 2023. arXiv: [2305.06913](https://arxiv.org/abs/2305.06913). URL: <https://cds.cern.ch/record/2860289> (cit. on pp. 9, 191, 192).
- [14] R. L. Workman et al. *Review of Particle Physics*. In: *PTEP* 2022 (2022), p. 083C01. DOI: [10.1093/ptep/ptac097](https://doi.org/10.1093/ptep/ptac097) (cit. on pp. 9, 31, 32, 198, 201).
- [15] S. Weinberg. *A Model of Leptons*. In: *Phys. Rev. Lett.* 19 (1967), pp. 1264–1266. DOI: [10.1103/PhysRevLett.19.1264](https://doi.org/10.1103/PhysRevLett.19.1264) (cit. on pp. 22, 23).
- [16] V. E. Barnes et al. *Observation of a Hyperon with Strangeness Minus Three*. In: *Phys. Rev. Lett.* 12 (1964), pp. 204–206. DOI: [10.1103/PhysRevLett.12.204](https://doi.org/10.1103/PhysRevLett.12.204) (cit. on p. 22).
- [17] H. Fritzsch, M. Gell-Mann, and H. Leutwyler. *Advantages of the Color Octet Gluon Picture*. In: *Phys. Lett. B* 47 (1973), pp. 365–368. DOI: [10.1016/0370-2693\(73\)90625-4](https://doi.org/10.1016/0370-2693(73)90625-4) (cit. on p. 22).
- [18] P. W. Higgs. *Broken symmetries, massless particles and gauge fields*. In: *Phys. Lett.* 12 (1964), pp. 132–133. DOI: [10.1016/0031-9163\(64\)91136-9](https://doi.org/10.1016/0031-9163(64)91136-9) (cit. on pp. 22, 27).
- [19] P. W. Higgs. *Broken Symmetries and the Masses of Gauge Bosons*. In: *Phys. Rev. Lett.* 13 (1964). Ed. by J. C. Taylor, pp. 508–509. DOI: [10.1103/PhysRevLett.13.508](https://doi.org/10.1103/PhysRevLett.13.508) (cit. on pp. 22, 27).

- [20] F. Englert and R. Brout. *Broken Symmetry and the Mass of Gauge Vector Mesons*. In: *Phys. Rev. Lett.* 13 (1964). Ed. by J. C. Taylor, pp. 321–323. DOI: [10.1103/PhysRevLett.13.321](https://doi.org/10.1103/PhysRevLett.13.321) (cit. on pp. 22, 27).
- [21] G. S. Guralnik, C. R. Hagen, and T. W. B. Kibble. *Global Conservation Laws and Massless Particles*. In: *Phys. Rev. Lett.* 13 (1964). Ed. by J. C. Taylor, pp. 585–587. DOI: [10.1103/PhysRevLett.13.585](https://doi.org/10.1103/PhysRevLett.13.585) (cit. on pp. 22, 27).
- [22] T. W. B. Kibble. *Symmetry breaking in nonAbelian gauge theories*. In: *Phys. Rev.* 155 (1967). Ed. by J. C. Taylor, pp. 1554–1561. DOI: [10.1103/PhysRev.155.1554](https://doi.org/10.1103/PhysRev.155.1554) (cit. on pp. 22, 27).
- [23] S. L. Glashow. *Partial-symmetries of weak interactions*. In: *Nuclear Physics* 22.4 (1961), pp. 579–588. ISSN: 0029-5582. DOI: [https://doi.org/10.1016/0029-5582\(61\)90469-2](https://doi.org/10.1016/0029-5582(61)90469-2). URL: <https://www.sciencedirect.com/science/article/pii/0029558261904692> (cit. on p. 23).
- [24] A. Salam. *Weak and Electromagnetic Interactions*. In: *Conf. Proc. C* 680519 (1968), pp. 367–377. DOI: [10.1142/9789812795915_0034](https://doi.org/10.1142/9789812795915_0034) (cit. on p. 23).
- [25] N. Cabibbo. *Unitary Symmetry and Leptonic Decays*. In: *Phys. Rev. Lett.* 10 (1963), pp. 531–533. DOI: [10.1103/PhysRevLett.10.531](https://doi.org/10.1103/PhysRevLett.10.531) (cit. on p. 23).
- [26] M. Kobayashi and T. Maskawa. *CP Violation in the Renormalizable Theory of Weak Interaction*. In: *Prog. Theor. Phys.* 49 (1973), pp. 652–657. DOI: [10.1143/PTP.49.652](https://doi.org/10.1143/PTP.49.652) (cit. on p. 23).
- [27] Z. Maki, M. Nakagawa, and S. Sakata. *Remarks on the unified model of elementary particles*. In: *Prog. Theor. Phys.* 28 (1962), pp. 870–880. DOI: [10.1143/PTP.28.870](https://doi.org/10.1143/PTP.28.870) (cit. on p. 23).
- [28] B. Pontecorvo. *Mesonium and anti-mesonium*. In: *Sov. Phys. JETP* 6 (1957), p. 429 (cit. on p. 23).
- [29] B. Pontecorvo. *Neutrino Experiments and the Problem of Conservation of Leptonic Charge*. In: *Zh. Eksp. Teor. Fiz.* 53 (1967), pp. 1717–1725. URL: http://www.jetp.ras.ru/cgi-bin/dn/e_026_05_0984.pdf (cit. on p. 23).
- [30] S. L. Glashow, J. Iliopoulos, and L. Maiani. *Weak Interactions with Lepton-Hadron Symmetry*. In: *Phys. Rev. D* 2 (1970), pp. 1285–1292. DOI: [10.1103/PhysRevD.2.1285](https://doi.org/10.1103/PhysRevD.2.1285) (cit. on p. 24).
- [31] K. Nishijima. *Charge Independence Theory of V Particles**. In: *Progress of Theoretical Physics* 13.3 (Mar. 1955), pp. 285–304. ISSN: 0033-068X. DOI: [10.1143/PTP.13.285](https://doi.org/10.1143/PTP.13.285). eprint: <https://academic.oup.com/ptp/article-pdf/13/3/285/5425869/13-3-285.pdf>. URL: <https://doi.org/10.1143/PTP.13.285> (cit. on p. 24).
- [32] M. Gell-Mann. *The interpretation of the new particles as displaced charge multiplets*. In: *Nuovo Cim.* 4S2 (1956), pp. 848–866. DOI: [10.1007/BF02748000](https://doi.org/10.1007/BF02748000) (cit. on p. 24).
- [33] M. E. Peskin and D. V. Schroeder. *An introduction to quantum field theory*. Boulder, CO: Westview, 1995. URL: <https://cds.cern.ch/record/257493> (cit. on p. 24).
- [34] D. H. Perkins. *Introduction to High Energy Physics*. 4th ed. Cambridge University Press, 2000. DOI: [10.1017/CBO9780511809040](https://doi.org/10.1017/CBO9780511809040) (cit. on pp. 24, 25, 26).
- [35] Particle Data Group. *Electroweak Model and Constraints on New Physics*. 2020. URL: <https://pdg.lbl.gov/2020/reviews/rpp2020-rev-standard-model.pdf> (cit. on p. 25).
- [36] M. Thomson. *Modern Particle Physics*. Cambridge University Press, 2013. DOI: [10.1017/CBO9781139525367](https://doi.org/10.1017/CBO9781139525367) (cit. on p. 26).
- [37] I. Neutelings. URL: <https://tikz.net/author/izaak/> (cit. on pp. 28, 51, 52, 65).
- [38] J. Riebesell. URL: <https://tikz.net/author/janosh/> (cit. on p. 28).
- [39] Particle Data Group. *Status of Higgs Boson Physics*. 2020. URL: <https://pdg.lbl.gov/2020/reviews/rpp2020-rev-higgs-boson.pdf> (cit. on pp. 28, 29).
- [40] J. C. Romão and J. P. Silva. *A RESOURCE FOR SIGNS AND FEYNMAN DIAGRAMS OF THE STANDARD MODEL*. In: *International Journal of Modern Physics A* 27.26 (Oct. 2012), p. 1230025. DOI: [10.1142/s0217751x12300256](https://doi.org/10.1142/s0217751x12300256). URL: <https://doi.org/10.1142/s0217751x12300256> (cit. on p. 29).
- [41] LHC Higgs Cross Section Working Group. *Handbook of LHC Higgs Cross Sections: 3. Higgs Properties*. In: *CERN-2013-004* (CERN, Geneva, 2013). DOI: [10.5170/CERN-2013-004](https://doi.org/10.5170/CERN-2013-004). arXiv: [1307.1347 \[hep-ph\]](https://arxiv.org/abs/1307.1347) (cit. on pp. 30, 33).
- [42] D. de Florian et al. *Handbook of LHC Higgs Cross Sections: 4. Deciphering the Nature of the Higgs Sector*. In: (2016). DOI: [10.23731/CYRM-2017-002](https://doi.org/10.23731/CYRM-2017-002). arXiv: [1610.07922 \[hep-ph\]](https://arxiv.org/abs/1610.07922) (cit. on pp. 30, 33).
- [43] L. C. S. W. Group. *LHC Cross Section Working Group Twiki*. Feb. 2021. URL: <https://twiki.cern.ch/twiki/bin/view/LHCPhysics/LHCHXSWGHH> (cit. on p. 34).

- [44] J. Baglio et al. $gg \rightarrow HH$: Combined Uncertainties. In: *Phys. Rev. D* 103 (Aug. 2020), 056002. 5 p. DOI: [10.1103/PhysRevD.103.056002](https://doi.org/10.1103/PhysRevD.103.056002). arXiv: [2008.11626](https://arxiv.org/abs/2008.11626). URL: <https://cds.cern.ch/record/2729029> (cit. on p. 34).
- [45] D. de Florian et al. *Handbook of LHC Higgs Cross Sections: 4. Deciphering the Nature of the Higgs Sector*. CERN Yellow Reports: Monographs. Geneva: CERN, Oct. 2016. DOI: [10.23731/CYRM-2017-002](https://doi.org/10.23731/CYRM-2017-002). URL: <https://cds.cern.ch/record/2227475> (cit. on p. 34).
- [46] ATLAS Collaboration. *Search for Higgs boson pair production in the two bottom quarks plus two photons final state in pp collisions at $\sqrt{s} = 13$ TeV with the ATLAS detector*. In: *Phys. Rev. D* 106 (2021), p. 052001. DOI: [10.1103/PhysRevD.106.052001](https://doi.org/10.1103/PhysRevD.106.052001). arXiv: [2112.11876 \[hep-ex\]](https://arxiv.org/abs/2112.11876) (cit. on p. 35).
- [47] ATLAS Collaboration. *Reconstruction and identification of boosted $di\text{-}\tau$ systems in a search for Higgs boson pairs using 13 TeV proton–proton collision data in ATLAS*. In: *JHEP* 11 (2020), p. 163. DOI: [10.1007/JHEP11\(2020\)163](https://doi.org/10.1007/JHEP11(2020)163). arXiv: [2007.14811 \[hep-ex\]](https://arxiv.org/abs/2007.14811) (cit. on p. 35).
- [48] ATLAS Collaboration. *Search for the $HH \rightarrow b\bar{b}b\bar{b}$ process via vector-boson fusion production using proton–proton collisions at $\sqrt{s} = 13$ TeV with the ATLAS detector*. In: *JHEP* 07 (2020), p. 108. DOI: [10.1007/JHEP07\(2020\)108](https://doi.org/10.1007/JHEP07(2020)108). arXiv: [2001.05178 \[hep-ex\]](https://arxiv.org/abs/2001.05178) (cit. on p. 35). Erratum: in: *JHEP* 01 (2021), p. 145. DOI: [10.1007/JHEP01\(2021\)145](https://doi.org/10.1007/JHEP01(2021)145).
- [49] ATLAS Collaboration. *Search for resonant pair production of Higgs bosons in the $b\bar{b}b\bar{b}$ final state using pp collisions at $\sqrt{s} = 13$ TeV with the ATLAS detector*. In: *Phys. Rev. D* 105 (2022), p. 092002. DOI: [10.1103/PhysRevD.105.092002](https://doi.org/10.1103/PhysRevD.105.092002). arXiv: [2202.07288 \[hep-ex\]](https://arxiv.org/abs/2202.07288) (cit. on p. 35).
- [50] ATLAS Collaboration. *Search for nonresonant pair production of Higgs bosons in the $b\bar{b}b\bar{b}$ final state in pp collisions at $\sqrt{s} = 13$ TeV with the ATLAS detector*. In: (2023). arXiv: [2301.03212 \[hep-ex\]](https://arxiv.org/abs/2301.03212) (cit. on p. 35).
- [51] F. Bishara, R. Contino, and J. Rojo. *Higgs pair production in vector-boson fusion at the LHC and beyond*. In: *Eur. Phys. J. C* 77.7 (2017), p. 481. DOI: [10.1140/epjc/s10052-017-5037-9](https://doi.org/10.1140/epjc/s10052-017-5037-9). arXiv: [1611.03860 \[hep-ph\]](https://arxiv.org/abs/1611.03860) (cit. on pp. 36, 115).
- [52] *LHC Higgs Cross Section HH Sub-group*. URL: <https://twiki.cern.ch/twiki/bin/view/LHCPhysics/LHCHWGH?redirectedfrom=LHCPhysics.LHCHXSWGHH> (cit. on pp. 37, 114, 117).
- [53] D. Abbott et al. *Supporting Document: The Search for Non-Resonant ggF and VBF HH Production Decaying to the $4b$ Final State Using the Full Run-2 Data*. Tech. rep. Geneva: CERN, 2021. URL: <https://cds.cern.ch/record/2780536> (cit. on p. 39).
- [54] L. R. Evans and P. Bryant. *LHC Machine*. In: *JINST* 3 (2008), S08001. 164 p. DOI: [10.1088/1748-0221/3/08/S08001](https://doi.org/10.1088/1748-0221/3/08/S08001). URL: <https://cds.cern.ch/record/1129806> (cit. on p. 44).
- [55] A. Breskin and R. Voss. *The CERN Large Hadron Collider: Accelerator and Experiments*. Geneva: CERN, 2009. URL: <https://cds.cern.ch/record/1244506> (cit. on p. 44).
- [56] A. Lopes and M. L. Perrey. *FAQ-LHC The guide*. Jan. 2022. URL: <https://cds.cern.ch/record/2809109> (cit. on pp. 44, 47).
- [57] CERN website. URL: <https://home.cern/> (cit. on p. 44).
- [58] E. Mobs. *The CERN accelerator complex - August 2018. Complexe des accélérateurs du CERN - Août 2018*. In: (Aug. 2018). URL: <https://cds.cern.ch/record/2636343> (cit. on p. 44).
- [59] O. S. Brüning et al. *LHC Design Report*. CERN Yellow Reports: Monographs. Geneva: CERN, 2004. DOI: [10.5170/CERN-2004-003-V-1](https://doi.org/10.5170/CERN-2004-003-V-1). URL: <https://cds.cern.ch/record/782076> (cit. on pp. 45, 46).
- [60] R. Steerenberg. *Batch Compression Merging and Splitting (BCMS)*. *Batch Compression Merging and Splitting (BCMS)*. In: (Apr. 2017). URL: <https://cds.cern.ch/record/2259071> (cit. on p. 45).
- [61] R. Steerenberg. *LHC report: full house for the LHC*. In: (July 2017). URL: <https://cds.cern.ch/record/2272573> (cit. on p. 45).
- [62] A. A. Gorzawski. *Luminosity control and beam orbit stability with beta star leveling at LHC and HL-LHC*. 2016. DOI: [10.5075/epfl-thesis-7338](https://doi.org/10.5075/epfl-thesis-7338). URL: <https://cds.cern.ch/record/2238309> (cit. on p. 45).
- [63] ATLAS Collaboration. *ATLAS data quality operations and performance for 2015–2018 data-taking*. In: *JINST* 15 (2020), P04003. DOI: [10.1088/1748-0221/15/04/P04003](https://doi.org/10.1088/1748-0221/15/04/P04003). arXiv: [1911.04632 \[physics.ins-det\]](https://arxiv.org/abs/1911.04632) (cit. on pp. 46, 47).

- [64] ATLAS Collaboration. *Measurement of the Inelastic Proton–Proton Cross Section at $\sqrt{s} = 13$ TeV with the ATLAS Detector at the LHC*. In: *Phys. Rev. Lett.* 117 (2016), p. 182002. DOI: [10.1103/PhysRevLett.117.182002](https://doi.org/10.1103/PhysRevLett.117.182002). arXiv: [1606.02625 \[hep-ex\]](https://arxiv.org/abs/1606.02625) (cit. on p. 46).
- [65] S. Karppinen et al. *Design of Beampipes for LHC Experiments*. In: *Vacuum* 64 (July 2003), 476–473. 12 p. URL: <https://cds.cern.ch/record/631307> (cit. on p. 47).
- [66] H. Wiedemann. *Particle Accelerator Physics II, Nonlinear and Higher-Order Beam Dynamics*. Springer Berlin, Heidelberg. DOI: doi.org/10.1007/978-3-642-97550-9 (cit. on p. 48).
- [67] K. Wille. *Synchrotron Radiation (lecture)*. URL: <https://indico.cern.ch/event/218284/contributions/1520454/> (cit. on p. 48).
- [68] ATLAS Collaboration. *The ATLAS Experiment at the CERN Large Hadron Collider*. In: *JINST* 3 (2008), S08003. DOI: [10.1088/1748-0221/3/08/S08003](https://doi.org/10.1088/1748-0221/3/08/S08003) (cit. on pp. 48, 49, 52, 53, 54, 56, 57, 58, 59, 60).
- [69] ATLAS Collaboration. *ATLAS: letter of intent for a general-purpose pp experiment at the large hadron collider at CERN*. In: (1992). URL: <http://cds.cern.ch/record/291061> (cit. on pp. 48, 49).
- [70] The ATLAS experiment website. URL: <https://atlas.cern/> (cit. on pp. 48, 49).
- [71] CMS Collaboration. *The CMS Experiment at the CERN LHC*. In: *JINST* 3 (2008), S08004. DOI: [10.1088/1748-0221/3/08/S08004](https://doi.org/10.1088/1748-0221/3/08/S08004) (cit. on p. 48).
- [72] CMS Collaboration. *CMS: letter of intent by the CMS Collaboration for a general purpose detector at LHC*. Tech. rep. Geneva: CERN, 1992. URL: <https://cds.cern.ch/record/290808> (cit. on p. 48).
- [73] The CMS experiment website. URL: <https://cms.cern/> (cit. on p. 48).
- [74] LHCb Collaboration. *The LHCb Detector at the LHC*. In: *JINST* 3 (2008), S08005. DOI: [10.1088/1748-0221/3/08/S08005](https://doi.org/10.1088/1748-0221/3/08/S08005). URL: <https://cds.cern.ch/record/1129809> (cit. on p. 49).
- [75] H. Dijkstra et al. *LHCb Letter of Intent, LHCb Collaboration*. Tech. rep. Geneva: CERN, Jan. 1995. URL: <http://cds.cern.ch/record/691698> (cit. on p. 49).
- [76] The LHCb experiment website. URL: <https://lhcb-outreach.web.cern.ch/> (cit. on p. 49).
- [77] Alice Collaboration. *The ALICE experiment at the CERN LHC. A Large Ion Collider Experiment*. In: *JINST* 3 (2008), S08002. 259 p. DOI: [10.1088/1748-0221/3/08/S08002](https://doi.org/10.1088/1748-0221/3/08/S08002). URL: <https://cds.cern.ch/record/1129812> (cit. on p. 49).
- [78] Alice Collaboration. *Letter of Intent for A Large Ion Collider Experiment [ALICE]*. Tech. rep. Geneva: CERN, 1993. URL: <http://cds.cern.ch/record/290825> (cit. on p. 49).
- [79] The ALICE experiment website. URL: <https://alice-collaboration.web.cern.ch/> (cit. on p. 49).
- [80] J. Pequeno. *Computer generated image of the whole ATLAS detector*. Mar. 2008. URL: <https://cds.cern.ch/record/1095924> (cit. on pp. 49, 50).
- [81] J. Pequeno and P. Schaffner. *How ATLAS detects particles: diagram of particle paths in the detector*. Jan. 2013. URL: <https://cds.cern.ch/record/1505342> (cit. on pp. 49, 50).
- [82] Quantum Diaries. URL: <https://www.quantumdiaries.org/wp-content/uploads/2011/05/exp-magnets.png> (cit. on p. 53).
- [83] A. M. Rodriguez Vera and J. Antunes Pequeno. *ATLAS Detector Magnet System*. May 2021. URL: <https://cds.cern.ch/record/2770604> (cit. on p. 53).
- [84] ATLAS Collaboration. *ATLAS inner detector: Technical Design Report, 1*. Technical design report. ATLAS. Geneva: CERN, 1997. URL: <https://cds.cern.ch/record/331063> (cit. on pp. 53, 54).
- [85] N. C. Benekos et al. *ATLAS Inner Detector Performance*. Tech. rep. Geneva: CERN, Dec. 2003. URL: <https://cds.cern.ch/record/688762> (cit. on p. 54).
- [86] J. Pequeno. *Computer generated image of the ATLAS inner detector*. Mar. 2008. URL: <https://cds.cern.ch/record/1095926> (cit. on p. 54).
- [87] ATLAS Collaboration. *Experiment Briefing: Keeping the ATLAS Inner Detector in perfect alignment*. July 2020. URL: <https://cds.cern.ch/record/2723878> (cit. on pp. 54, 64).
- [88] M. Capeans et al. *ATLAS Insertable B-Layer Technical Design Report*. Tech. rep. Sept. 2010. URL: <https://cds.cern.ch/record/1291633> (cit. on pp. 55, 56).
- [89] ATLAS Collaboration. *Modelling radiation damage to pixel sensors in the ATLAS detector*. In: *JINST* 14 (2019), P06012. DOI: [10.1088/1748-0221/14/06/P06012](https://doi.org/10.1088/1748-0221/14/06/P06012). arXiv: [1905.03739 \[hep-ex\]](https://arxiv.org/abs/1905.03739) (cit. on p. 55).

- [90] C. Goessling et al. *Planar n+-in-n silicon pixel sensors for the ATLAS IBL upgrade*. In: *Nuclear Instruments and Methods in Physics Research Section A: Accelerators, Spectrometers, Detectors and Associated Equipment* 650.1 (2011), pp. 198–201. ISSN: 0168-9002. DOI: <https://doi.org/10.1016/j.nima.2010.11.186>. URL: <https://www.sciencedirect.com/science/article/pii/S016890021002735X> (cit. on p. 55).
- [91] C. Da Via et al. *3D silicon sensors: Design, large area production and quality assurance for the ATLAS IBL pixel detector upgrade*. In: *Nuclear Instruments and Methods in Physics Research Section A: Accelerators, Spectrometers, Detectors and Associated Equipment* 694 (2012), pp. 321–330. ISSN: 0168-9002. DOI: <https://doi.org/10.1016/j.nima.2012.07.058>. URL: <https://www.sciencedirect.com/science/article/pii/S0168900212008509> (cit. on p. 55).
- [92] ATLAS Collaboration. *Operation and performance of the ATLAS semiconductor tracker in LHC Run 2*. In: *JINST* 17 (2021), P01013. DOI: [10.1088/1748-0221/17/01/P01013](https://doi.org/10.1088/1748-0221/17/01/P01013). arXiv: [2109.02591](https://arxiv.org/abs/2109.02591) [[physics.ins-det](#)] (cit. on p. 56).
- [93] ATLAS Collaboration. *Performance of the ATLAS Transition Radiation Tracker in Run 1 of the LHC: tracker properties*. In: *JINST* 12 (2017), P05002. DOI: [10.1088/1748-0221/12/05/P05002](https://doi.org/10.1088/1748-0221/12/05/P05002). arXiv: [1702.06473](https://arxiv.org/abs/1702.06473) [[hep-ex](#)] (cit. on p. 56).
- [94] A. Vogel. *ATLAS Transition Radiation Tracker (TRT): Straw Tube Gaseous Detectors at High Rates*. Tech. rep. Geneva: CERN, Apr. 2013. URL: <https://cds.cern.ch/record/1537991> (cit. on p. 56).
- [95] J. Pequenaio. *Computer Generated image of the ATLAS calorimeter*. Mar. 2008. URL: <https://cds.cern.ch/record/1095927> (cit. on p. 57).
- [96] ATLAS Collaboration. *ATLAS liquid-argon calorimeter: Technical Design Report*. Technical design report. ATLAS. Geneva: CERN, 1996. DOI: [10.17181/CERN.FWRW.FOOQ](https://doi.org/10.17181/CERN.FWRW.FOOQ). URL: <https://cds.cern.ch/record/331061> (cit. on p. 57).
- [97] ATLAS Collaboration. *Electron and photon energy calibration with the ATLAS detector using LHC Run 1 data*. In: *Eur. Phys. J. C* 74 (2014), p. 3071. DOI: [10.1140/epjc/s10052-014-3071-4](https://doi.org/10.1140/epjc/s10052-014-3071-4). arXiv: [1407.5063](https://arxiv.org/abs/1407.5063) [[hep-ex](#)] (cit. on p. 58).
- [98] J. Pequenaio. *Computer generated image of the ATLAS Muons subsystem*. Mar. 2008. URL: <https://cds.cern.ch/record/1095929> (cit. on p. 60).
- [99] A. M. Rodriguez Vera et al. *Trigger and Data Acquisition - ATLAS Fact Sheet*. In: (July 2021). URL: <https://cds.cern.ch/record/2775198> (cit. on p. 60).
- [100] ATLAS Collaboration. *ATLAS High-Level Trigger, Data Acquisition and Controls: Technical Design Report*. ATLAS-TDR-16; CERN-LHCC-2003-022. 2003. URL: <https://cds.cern.ch/record/616089> (cit. on p. 61).
- [101] ATLAS Collaboration. *ATLAS Approved Plots DAQ*. URL: <https://twiki.cern.ch/twiki/bin/view/AtlasPublic/ApprovedPlotsDAQ> (cit. on pp. 61, 62).
- [102] ATLAS Collaboration. *Electron reconstruction and identification in the ATLAS experiment using the 2015 and 2016 LHC proton–proton collision data at $\sqrt{s} = 13$ TeV*. In: *Eur. Phys. J. C* 79 (2019), p. 639. DOI: [10.1140/epjc/s10052-019-7140-6](https://doi.org/10.1140/epjc/s10052-019-7140-6). arXiv: [1902.04655](https://arxiv.org/abs/1902.04655) [[hep-ex](#)] (cit. on p. 64).
- [103] ATLAS Collaboration. *Performance of the ATLAS track reconstruction algorithms in dense environments in LHC Run 2*. In: *Eur. Phys. J. C* 77 (2017), p. 673. DOI: [10.1140/epjc/s10052-017-5225-7](https://doi.org/10.1140/epjc/s10052-017-5225-7). arXiv: [1704.07983](https://arxiv.org/abs/1704.07983) [[hep-ex](#)] (cit. on pp. 65, 67).
- [104] ATLAS Collaboration. *ATLAS Tracking Software Tutorial*. Aug. 2022. URL: <https://atlassoftwaredocs.web.cern.ch/trackingTutorial/index.html> (cit. on p. 65).
- [105] Y. Amhis et al. *Averages of b-hadron, c-hadron, and τ -lepton properties as of 2021*. Tech. rep. June 2022. arXiv: [2206.07501](https://arxiv.org/abs/2206.07501). URL: <https://cds.cern.ch/record/2815545> (cit. on p. 65).
- [106] T. G. Cornelissen et al. *Updates of the ATLAS Tracking Event Data Model (Release 13)*. Tech. rep. Geneva: CERN, June 2007. URL: <https://cds.cern.ch/record/1038095> (cit. on p. 65).
- [107] R. Frühwirth. *Application of Kalman filtering to track and vertex fitting*. In: *Nuclear Instruments and Methods in Physics Research Section A: Accelerators, Spectrometers, Detectors and Associated Equipment* 262.2 (1987), pp. 444–450. ISSN: 0168-9002. DOI: [https://doi.org/10.1016/0168-9002\(87\)90887-4](https://doi.org/10.1016/0168-9002(87)90887-4). URL: <https://www.sciencedirect.com/science/article/pii/0168900287908874> (cit. on p. 66).
- [108] ATLAS Collaboration. *Impact Parameter Resolution*. URL: <https://atlas.web.cern.ch/Atlas/GROUPS/PHYSICS/PLOTS/IDTR-2015-007/> (cit. on p. 67).

- [109] ATLAS Collaboration. *Electron and photon performance measurements with the ATLAS detector using the 2015–2017 LHC proton–proton collision data*. In: *JINST* 14 (2019), P12006. DOI: [10.1088/1748-0221/14/12/P12006](https://doi.org/10.1088/1748-0221/14/12/P12006). arXiv: [1908.00005 \[hep-ex\]](https://arxiv.org/abs/1908.00005) (cit. on pp. 68, 69, 70, 71, 72, 73).
- [110] ATLAS Collaboration. *Electron and photon reconstruction and performance in ATLAS using a dynamical, topological cell clustering-based approach*. ATL-PHYS-PUB-2017-022. 2017. URL: <https://cds.cern.ch/record/2298955> (cit. on pp. 68, 70, 72).
- [111] ATLAS Collaboration. *Electron and photon energy calibration with the ATLAS detector using 2015–2016 LHC proton–proton collision data*. In: *JINST* 14 (2019), P03017. DOI: [10.1088/1748-0221/14/03/P03017](https://doi.org/10.1088/1748-0221/14/03/P03017). arXiv: [1812.03848 \[hep-ex\]](https://arxiv.org/abs/1812.03848) (cit. on pp. 68, 70, 72).
- [112] W. Lampl et al. *Calorimeter Clustering Algorithms: Description and Performance*. Tech. rep. Geneva: CERN, Apr. 2008. URL: <https://cds.cern.ch/record/1099735> (cit. on p. 68).
- [113] ATLAS Collaboration. *Topological cell clustering in the ATLAS calorimeters and its performance in LHC Run 1*. In: *Eur. Phys. J. C* 77 (2017), p. 490. DOI: [10.1140/epjc/s10052-017-5004-5](https://doi.org/10.1140/epjc/s10052-017-5004-5). arXiv: [1603.02934 \[hep-ex\]](https://arxiv.org/abs/1603.02934) (cit. on pp. 68, 69).
- [114] ATLAS Collaboration. *Muon reconstruction and identification efficiency in ATLAS using the full Run 2 pp collision data set at $\sqrt{s} = 13$ TeV*. In: *Eur. Phys. J. C* 81 (2021), p. 578. DOI: [10.1140/epjc/s10052-021-09233-2](https://doi.org/10.1140/epjc/s10052-021-09233-2). arXiv: [2012.00578 \[hep-ex\]](https://arxiv.org/abs/2012.00578) (cit. on pp. 73, 75, 76, 77).
- [115] ATLAS Collaboration. *Muon reconstruction performance of the ATLAS detector in proton–proton collision data at $\sqrt{s} = 13$ TeV*. In: *Eur. Phys. J. C* 76 (2016), p. 292. DOI: [10.1140/epjc/s10052-016-4120-y](https://doi.org/10.1140/epjc/s10052-016-4120-y). arXiv: [1603.05598 \[hep-ex\]](https://arxiv.org/abs/1603.05598) (cit. on pp. 73, 75).
- [116] J. Illingworth and J. Kittler. *A survey of the hough transform*. In: *Computer Vision, Graphics, and Image Processing* 44.1 (1988), pp. 87–116. ISSN: 0734-189X. DOI: [https://doi.org/10.1016/S0734-189X\(88\)80033-1](https://doi.org/10.1016/S0734-189X(88)80033-1). URL: <https://www.sciencedirect.com/science/article/pii/S0734189X88800331> (cit. on p. 74).
- [117] M. Tanabashi et al. *Review of Particle Physics*. In: *Phys. Rev. D* 98 (3 Aug. 2018). DOI: [10.1103/PhysRevD.98.030001](https://doi.org/10.1103/PhysRevD.98.030001). URL: <https://link.aps.org/doi/10.1103/PhysRevD.98.030001> (cit. on p. 77).
- [118] ATLAS Collaboration. *Measurement of the tau lepton reconstruction and identification performance in the ATLAS experiment using pp collisions at $\sqrt{s} = 13$ TeV*. ATL-CONF-2017-029. 2017. URL: <https://cds.cern.ch/record/2261772> (cit. on p. 78).
- [119] ATLAS Collaboration. *Reconstruction, Energy Calibration, and Identification of Hadronically Decaying Tau Leptons in the ATLAS Experiment for Run-2 of the LHC*. ATL-PHYS-PUB-2015-045. 2015. URL: <https://cds.cern.ch/record/2064383> (cit. on p. 78).
- [120] ATLAS Collaboration. *Identification of hadronic tau lepton decays using neural networks in the ATLAS experiment*. ATL-PHYS-PUB-2019-033. 2019. URL: <https://cds.cern.ch/record/2688062> (cit. on p. 78).
- [121] M. Cacciari, G. P. Salam, and G. Soyez. *The anti- k_t jet clustering algorithm*. In: *JHEP* 04 (2008), p. 063. DOI: [10.1088/1126-6708/2008/04/063](https://doi.org/10.1088/1126-6708/2008/04/063). arXiv: [0802.1189 \[hep-ph\]](https://arxiv.org/abs/0802.1189) (cit. on pp. 78, 79).
- [122] ATLAS Collaboration. *Jet reconstruction and performance using particle flow with the ATLAS Detector*. In: *Eur. Phys. J. C* 77 (2017), p. 466. DOI: [10.1140/epjc/s10052-017-5031-2](https://doi.org/10.1140/epjc/s10052-017-5031-2). arXiv: [1703.10485 \[hep-ex\]](https://arxiv.org/abs/1703.10485) (cit. on p. 80).
- [123] ATLAS Collaboration. *Jet energy scale and resolution measured in proton–proton collisions at $\sqrt{s} = 13$ TeV with the ATLAS detector*. In: *Eur. Phys. J. C* 81 (2020), p. 689. DOI: [10.1140/epjc/s10052-021-09402-3](https://doi.org/10.1140/epjc/s10052-021-09402-3). arXiv: [2007.02645 \[hep-ex\]](https://arxiv.org/abs/2007.02645) (cit. on p. 80).
- [124] ATLAS Collaboration. *E_T^{miss} performance in the ATLAS detector using 2015–2016 LHC pp collisions*. ATL-CONF-2018-023. 2018. URL: <https://cds.cern.ch/record/2625233> (cit. on pp. 80, 84, 85).
- [125] W. Lampl et al. *Calorimeter Clustering Algorithms: Description and Performance*. ATL-LARG-PUB-2008-002. 2008. URL: <https://cds.cern.ch/record/1099735> (cit. on p. 80).
- [126] A. Hoecker et al. *TMVA - Toolkit for Multivariate Data Analysis*. 2007. arXiv: [physics/0703039 \[physics.data-an\]](https://arxiv.org/abs/physics/0703039) (cit. on p. 81).
- [127] ATLAS Collaboration. *Optimisation and performance studies of the ATLAS b-tagging algorithms for the 2017–18 LHC run*. ATL-PHYS-PUB-2017-013. 2017. URL: <https://cds.cern.ch/record/2273281> (cit. on p. 81).
- [128] ATLAS Collaboration. *ATLAS b-jet identification performance and efficiency measurement with $t\bar{t}$ events in pp collisions at $\sqrt{s} = 13$ TeV*. In: *Eur. Phys. J. C* 79 (2019), p. 970. DOI: [10.1140/epjc/s10052-019-7450-8](https://doi.org/10.1140/epjc/s10052-019-7450-8). arXiv: [1907.05120 \[hep-ex\]](https://arxiv.org/abs/1907.05120) (cit. on pp. 81, 83).

- [129] P. J. Windischhofer. *Heavy-flavour jet tagging in ATLAS*. In: (Jan. 2020). URL: <https://cds.cern.ch/record/2706702> (cit. on pp. 81, 82).
- [130] ATLAS Collaboration. *Expected performance of the 2019 ATLAS b-taggers*. URL: <http://atlas.web.cern.ch/Atlas/GROUPS/PHYSICS/PLOTS/FTAG-2019-005> (cit. on pp. 81, 82).
- [131] ATLAS Collaboration. *Performance of 2019 recommendations of ATLAS Flavor Tagging algorithms with Variable Radius track jets*. URL: <http://atlas.web.cern.ch/Atlas/GROUPS/PHYSICS/PLOTS/FTAG-2019-006> (cit. on pp. 81, 82).
- [132] ATLAS Collaboration. *Measurement of the c-jet mistagging efficiency in $t\bar{t}$ events using pp collision data at $\sqrt{s} = 13$ TeV collected with the ATLAS detector*. In: *Eur. Phys. J. C* 82 (2022), p. 95. DOI: [10.1140/epjc/s10052-021-09843-w](https://doi.org/10.1140/epjc/s10052-021-09843-w). arXiv: [2109.10627](https://arxiv.org/abs/2109.10627) [hep-ex] (cit. on p. 81).
- [133] ATLAS Collaboration. *Identification of Boosted Higgs Bosons Decaying Into $b\bar{b}$ With Neural Networks and Variable Radius Subjets in ATLAS*. ATL-PHYS-PUB-2020-019. 2020. URL: <https://cds.cern.ch/record/2724739> (cit. on p. 81).
- [134] ATLAS Collaboration. *Secondary vertex finding for jet flavour identification with the ATLAS detector*. ATL-PHYS-PUB-2017-011. 2017. URL: <https://cds.cern.ch/record/2270366> (cit. on p. 81).
- [135] ATLAS Collaboration. *Topological b-hadron decay reconstruction and identification of b-jets with the JetFitter package in the ATLAS experiment at the LHC*. ATL-PHYS-PUB-2018-025. 2018. URL: <https://cds.cern.ch/record/2645405> (cit. on p. 81).
- [136] ATLAS Collaboration. *Identification of Jets Containing b-Hadrons with Recurrent Neural Networks at the ATLAS Experiment*. ATL-PHYS-PUB-2017-003. 2017. URL: <https://cds.cern.ch/record/2255226> (cit. on p. 81).
- [137] ATLAS Collaboration. *Performance of missing transverse momentum reconstruction with the ATLAS detector using proton–proton collisions at $\sqrt{s} = 13$ TeV*. In: *Eur. Phys. J. C* 78 (2018), p. 903. DOI: [10.1140/epjc/s10052-018-6288-9](https://doi.org/10.1140/epjc/s10052-018-6288-9). arXiv: [1802.08168](https://arxiv.org/abs/1802.08168) [hep-ex] (cit. on p. 84).
- [138] ATLAS Collaboration. *Performance of missing transverse momentum reconstruction with the ATLAS detector in the first proton–proton collisions at $\sqrt{s} = 13$ TeV*. ATL-PHYS-PUB-2015-027. 2015. URL: <https://cds.cern.ch/record/2037904> (cit. on p. 84).
- [139] ATLAS Collaboration. *Measurement of the top quark mass in the $t\bar{t} \rightarrow$ dilepton channel from $\sqrt{s} = 8$ TeV ATLAS data*. In: *Phys. Lett. B* 761 (2016), pp. 350–371. DOI: [10.1016/j.physletb.2016.08.042](https://doi.org/10.1016/j.physletb.2016.08.042). arXiv: [1606.02179](https://arxiv.org/abs/1606.02179) [hep-ex] (cit. on p. 89).
- [140] ATLAS Collaboration. *Search for the Standard Model Higgs boson produced in association with a vector boson and decaying to a $b\bar{b}$ pair in pp collisions at 13 TeV using the ATLAS detector*. ATLAS-CONF-2016-091. 2016. URL: <https://cds.cern.ch/record/2206813> (cit. on p. 89).
- [141] ATLAS Collaboration. *Performance of b-Jet Identification in the ATLAS Experiment*. In: *JINST* 11.04 (2016), P04008. DOI: [10.1088/1748-0221/11/04/P04008](https://doi.org/10.1088/1748-0221/11/04/P04008). arXiv: [1512.01094](https://arxiv.org/abs/1512.01094) [hep-ex] (cit. on pp. 89, 98, 104).
- [142] ATLAS Collaboration. *ATLAS b-jet identification performance and efficiency measurement with $t\bar{t}$ events in pp collisions at $\sqrt{s}=13$ TeV*. In: *The European Physical Journal C* 79.11 (2019), p. 970. DOI: [10.1140/epjc/s10052-019-7450-8](https://doi.org/10.1140/epjc/s10052-019-7450-8). URL: <https://doi.org/10.1140/epjc/s10052-019-7450-8> (cit. on p. 89).
- [143] A. Buckley. *ATLAS Pythia 8 tunes to 7 TeV data*. Tech. rep. ATL-PHYS-PROC-2014-273. Geneva: CERN, Dec. 2014. URL: <https://cds.cern.ch/record/1974411> (cit. on p. 92).
- [144] NNPDF Collaboration, R. D. Ball, et al. *Parton distributions with LHC data*. In: *Nucl. Phys. B* 867 (2013), p. 244. DOI: [10.1016/j.nuclphysb.2012.10.003](https://doi.org/10.1016/j.nuclphysb.2012.10.003). arXiv: [1207.1303](https://arxiv.org/abs/1207.1303) [hep-ph] (cit. on pp. 92, 113).
- [145] D. J. Lange. *The EvtGen particle decay simulation package*. In: *Nucl. Instrum. Meth. A* 462 (2001), p. 152. DOI: [10.1016/S0168-9002\(01\)00089-4](https://doi.org/10.1016/S0168-9002(01)00089-4) (cit. on pp. 92, 113).
- [146] S. Agostinelli et al. *GEANT4 – a simulation toolkit*. In: *Nucl. Instrum. Meth. A* 506 (2003), p. 250. DOI: [10.1016/S0168-9002\(03\)01368-8](https://doi.org/10.1016/S0168-9002(03)01368-8) (cit. on pp. 92, 113).
- [147] ATLAS Collaboration. *Properties of jets and inputs to jet reconstruction and calibration with the ATLAS detector using proton–proton collisions at $\sqrt{s} = 13$ TeV*. ATL-PHYS-PUB-2015-036. 2015. URL: <https://cds.cern.ch/record/2044564> (cit. on p. 92).
- [148] ATLAS Collaboration. *Performance of pile-up mitigation techniques for jets in pp collisions at $\sqrt{s} = 8$ TeV using the ATLAS detector*. In: *Eur. Phys. J. C* 76 (2016), p. 581. DOI: [10.1140/epjc/s10052-016-4395-z](https://doi.org/10.1140/epjc/s10052-016-4395-z). arXiv: [1510.03823](https://arxiv.org/abs/1510.03823) [hep-ex] (cit. on p. 92).

- [149] ATLAS Collaboration. *Electron efficiency measurements with the ATLAS detector using the 2015 LHC proton–proton collision data*. ATLAS-CONF-2016-024. 2016. URL: <https://cds.cern.ch/record/2157687> (cit. on p. 103).
- [150] ATLAS Collaboration. *Muon reconstruction performance of the ATLAS detector in proton–proton collision data at $\sqrt{s} = 13$ TeV*. In: *Eur. Phys. J. C* 76.5 (2016), p. 292. DOI: [10.1140/epjc/s10052-016-4120-y](https://doi.org/10.1140/epjc/s10052-016-4120-y). arXiv: [1603.05598](https://arxiv.org/abs/1603.05598) [hep-ex] (cit. on p. 103).
- [151] ATLAS Collaboration. *Electron and photon energy calibration with the ATLAS detector using data collected in 2015 at $\sqrt{s} = 13$ TeV*. ATL-PHYS-PUB-2016-015. 2016. URL: <https://cds.cern.ch/record/2203514> (cit. on p. 103).
- [152] ATLAS Collaboration. *Tagging and suppression of pileup jets with the ATLAS detector*. ATLAS-CONF-2014-018. 2014. URL: <https://cds.cern.ch/record/1700870> (cit. on p. 103).
- [153] A. Collaboration. *Jet energy scale measurements and their systematic uncertainties in proton–proton collisions at $\sqrt{s} = 13$ TeV with the ATLAS detector*. In: *Phys. Rev. D* 96 (7 Oct. 2017), p. 072002. DOI: [10.1103/PhysRevD.96.072002](https://doi.org/10.1103/PhysRevD.96.072002). URL: <https://link.aps.org/doi/10.1103/PhysRevD.96.072002> (cit. on p. 103).
- [154] G. Aad et al. *Jet energy measurement with the ATLAS detector in proton–proton collisions at $\sqrt{s} = 7$ TeV*. In: *Eur. Phys. J. C* 73.3 (2013), p. 2304. DOI: [10.1140/epjc/s10052-013-2304-2](https://doi.org/10.1140/epjc/s10052-013-2304-2). arXiv: [1112.6426](https://arxiv.org/abs/1112.6426) [hep-ex] (cit. on p. 104).
- [155] K. Nakamura et al. (Particle Data Group). *Review of Particle Physics*. In: *J. Phys. G* 37 (2010) (cit. on pp. 104, 106).
- [156] DELPHI Collaboration. *Determination of heavy quark non-perturbative parameters from spectral moments in semileptonic B decays*. In: *Eur. Phys. J. C* 45 (2006), pp. 35–59. DOI: [10.1140/epjc/s2005-02406-7](https://doi.org/10.1140/epjc/s2005-02406-7). arXiv: [hep-ex/0510024](https://arxiv.org/abs/hep-ex/0510024) [hep-ex] (cit. on pp. 104, 105).
- [157] Y. Amhis et al. *Averages of b-hadron, c-hadron, and τ -lepton properties as of summer 2014*. In: (2014). arXiv: [1412.7515](https://arxiv.org/abs/1412.7515) [hep-ex] (cit. on p. 106).
- [158] CDF Collaboration. *Measurement of Ratios of Fragmentation Fractions for Bottom Hadrons in $p\bar{p}$ Collisions at $\sqrt{s} = 1.96$ -TeV*. In: *Phys. Rev. D* 77.072003 (2008). DOI: [10.1103/PhysRevD.77.072003](https://doi.org/10.1103/PhysRevD.77.072003). arXiv: [0801.4375](https://arxiv.org/abs/0801.4375) [hep-ex] (cit. on p. 106).
- [159] ATLAS Collaboration. *Luminosity determination in pp collisions at $\sqrt{s} = 13$ TeV using the ATLAS detector at the LHC*. In: (2022). arXiv: [2212.09379](https://arxiv.org/abs/2212.09379) [hep-ex] (cit. on p. 113).
- [160] ATLAS Collaboration. *The ATLAS Simulation Infrastructure*. In: *Eur. Phys. J. C* 70 (2010), p. 823. DOI: [10.1140/epjc/s10052-010-1429-9](https://doi.org/10.1140/epjc/s10052-010-1429-9). arXiv: [1005.4568](https://arxiv.org/abs/1005.4568) [physics.ins-det] (cit. on p. 113).
- [161] T. Sjöstrand, S. Mrenna, and P. Skands. *A brief introduction to PYTHIA 8.1*. In: *Comput. Phys. Commun.* 178 (2008), pp. 852–867. DOI: [10.1016/j.cpc.2008.01.036](https://doi.org/10.1016/j.cpc.2008.01.036). arXiv: [0710.3820](https://arxiv.org/abs/0710.3820) [hep-ph] (cit. on pp. 113, 114).
- [162] ATLAS Collaboration. *The Pythia 8 A3 tune description of ATLAS minimum bias and inelastic measurements incorporating the Donnachie–Landshoff diffractive model*. ATL-PHYS-PUB-2016-017. 2016. URL: <https://cds.cern.ch/record/2206965> (cit. on p. 113).
- [163] E. Bothmann et al. *Event generation with Sherpa 2.2*. In: *SciPost Phys.* 7.3 (2019), p. 034. DOI: [10.21468/SciPostPhys.7.3.034](https://doi.org/10.21468/SciPostPhys.7.3.034). arXiv: [1905.09127](https://arxiv.org/abs/1905.09127) [hep-ph] (cit. on p. 113).
- [164] S. Alioli et al. *A general framework for implementing NLO calculations in shower Monte Carlo programs: the POWHEG BOX*. In: *JHEP* 06 (2010), p. 043. DOI: [10.1007/JHEP06\(2010\)043](https://doi.org/10.1007/JHEP06(2010)043). arXiv: [1002.2581](https://arxiv.org/abs/1002.2581) [hep-ph] (cit. on pp. 114, 115).
- [165] A. Buckley et al. *LHAPDF6: parton density access in the LHC precision era*. In: *Eur. Phys. J. C* 75 (2015), p. 132. DOI: [10.1140/epjc/s10052-015-3318-8](https://doi.org/10.1140/epjc/s10052-015-3318-8). arXiv: [1412.7420](https://arxiv.org/abs/1412.7420) [hep-ph] (cit. on p. 114).
- [166] J. Butterworth et al. *PDF4LHC recommendations for LHC Run II*. In: *J. Phys. G* 43 (2016), p. 023001. DOI: [10.1088/0954-3899/43/2/023001](https://doi.org/10.1088/0954-3899/43/2/023001). arXiv: [1510.03865](https://arxiv.org/abs/1510.03865) [hep-ph] (cit. on p. 114).
- [167] ATLAS Collaboration. *ATLAS Pythia 8 tunes to 7 TeV data*. ATL-PHYS-PUB-2014-021. 2014. URL: <https://cds.cern.ch/record/1966419> (cit. on p. 114).
- [168] ATLAS Collaboration. *Summary of ATLAS Pythia 8 tunes*. ATL-PHYS-PUB-2012-003. 2012. URL: <https://cds.cern.ch/record/1474107> (cit. on p. 114).
- [169] M. Grazzini et al. *Higgs boson pair production at NNLO with top quark mass effects*. In: *JHEP* 05 (2018), p. 059. DOI: [10.1007/JHEP05\(2018\)059](https://doi.org/10.1007/JHEP05(2018)059). arXiv: [1803.02463](https://arxiv.org/abs/1803.02463) [hep-ph] (cit. on p. 114).

- [170] M. Bähr et al. *Herwig++ physics and manual*. In: *Eur. Phys. J. C* 58 (2008), p. 639. DOI: [10.1140/epjc/s10052-008-0798-9](https://doi.org/10.1140/epjc/s10052-008-0798-9). arXiv: [0803.0883 \[hep-ph\]](https://arxiv.org/abs/0803.0883) (cit. on pp. 115, 118).
- [171] J. Bellm et al. *Herwig 7.0/Herwig++ 3.0 release note*. In: *Eur. Phys. J. C* 76.4 (2016), p. 196. DOI: [10.1140/epjc/s10052-016-4018-8](https://doi.org/10.1140/epjc/s10052-016-4018-8). arXiv: [1512.01178 \[hep-ph\]](https://arxiv.org/abs/1512.01178) (cit. on pp. 115, 118).
- [172] J. Alwall et al. *The automated computation of tree-level and next-to-leading order differential cross sections, and their matching to parton shower simulations*. In: *JHEP* 07 (2014), p. 079. DOI: [10.1007/JHEP07\(2014\)079](https://doi.org/10.1007/JHEP07(2014)079). arXiv: [1405.0301 \[hep-ph\]](https://arxiv.org/abs/1405.0301) (cit. on pp. 115, 117).
- [173] The NNPDF Collaboration, R. D. Ball, et al. *Parton distributions for the LHC run II*. In: *JHEP* 04 (2015), p. 040. DOI: [10.1007/JHEP04\(2015\)040](https://doi.org/10.1007/JHEP04(2015)040). arXiv: [1410.8849 \[hep-ph\]](https://arxiv.org/abs/1410.8849) (cit. on pp. 115, 117).
- [174] F. A. Dreyer and A. Karlberg. *Vector-boson fusion Higgs pair production at N3LO*. In: *Physical Review D* 98.11 (Dec. 2018). ISSN: 2470-0029. DOI: [10.1103/physrevd.98.114016](https://doi.org/10.1103/physrevd.98.114016). URL: <http://dx.doi.org/10.1103/PhysRevD.98.114016> (cit. on p. 117).
- [175] A. Elagin et al. *A New Mass Reconstruction Technique for Resonances Decaying to di-tau*. In: *Nucl. Instrum. Meth. A* 654 (2011), pp. 481–489. DOI: [10.1016/j.nima.2011.07.009](https://doi.org/10.1016/j.nima.2011.07.009). arXiv: [1012.4686 \[hep-ex\]](https://arxiv.org/abs/1012.4686) (cit. on pp. 121, 122).
- [176] B. P. Roe et al. *Boosted decision trees, an alternative to artificial neural networks*. In: *Nucl. Instrum. Meth. A* 543.2-3 (2005), pp. 577–584. DOI: [10.1016/j.nima.2004.12.018](https://doi.org/10.1016/j.nima.2004.12.018). arXiv: [physics/0408124](https://arxiv.org/abs/physics/0408124) (cit. on p. 133).
- [177] A. Hocker et al. *TMVA - Toolkit for Multivariate Data Analysis*. In: (Mar. 2007). arXiv: [physics/0703039](https://arxiv.org/abs/physics/0703039) (cit. on p. 133).
- [178] C. Bernaciak et al. *Fox-Wolfgram moments in Higgs physics*. In: *Physical Review D* 87.7 (Apr. 2013). DOI: [10.1103/physrevd.87.073014](https://doi.org/10.1103/physrevd.87.073014). URL: <https://doi.org/10.1103/PhysRevD.87.073014> (cit. on p. 136).
- [179] D. Buscher. *Search for Higgs bosons with b-jets in the final state in proton-proton collisions with the ATLAS experiment*. Freiburg U., 2016. URL: <https://cds.cern.ch/record/2232472> (cit. on p. 137).
- [180] J. H. Kim et al. *Probing the Triple Higgs Self-Interaction at the Large Hadron Collider*. In: *Phys. Rev. Lett.* 122.9 (2019), p. 091801. DOI: [10.1103/PhysRevLett.122.091801](https://doi.org/10.1103/PhysRevLett.122.091801). arXiv: [1807.11498 \[hep-ph\]](https://arxiv.org/abs/1807.11498) (cit. on pp. 146, 147).
- [181] M. Benedikt et al. *Future Circular Colliders succeeding the LHC*. In: *Nature Phys.* 16.4 (2020), pp. 402–407. DOI: [10.1038/s41567-020-0856-2](https://doi.org/10.1038/s41567-020-0856-2). URL: <https://cds.cern.ch/record/2715354> (cit. on p. 193).
- [182] D. d’Enterria, A. Poldaru, and G. Wojcik. *Measuring the electron Yukawa coupling via resonant s-channel Higgs production at FCC-ee*. In: *Eur. Phys. J. Plus* 137.2 (2022), p. 201. DOI: [10.1140/epjp/s13360-021-02204-2](https://doi.org/10.1140/epjp/s13360-021-02204-2). arXiv: [2107.02686 \[hep-ex\]](https://arxiv.org/abs/2107.02686) (cit. on pp. 194, 195, 200).
- [183] M. McCullough. *An Indirect Model-Dependent Probe of the Higgs Self-Coupling*. In: *Phys. Rev. D* 90.1 (2014), p. 015001. DOI: [10.1103/PhysRevD.90.015001](https://doi.org/10.1103/PhysRevD.90.015001). arXiv: [1312.3322 \[hep-ph\]](https://arxiv.org/abs/1312.3322) (cit. on p. 195).
- [184] A. Blondel and P. Janot. *Future strategies for the discovery and the precise measurement of the Higgs self coupling*. In: (Sept. 2018). arXiv: [1809.10041 \[hep-ph\]](https://arxiv.org/abs/1809.10041) (cit. on p. 195).
- [185] M. Aaboud et al. *Observation of $H \rightarrow b\bar{b}$ decays and VH production with the ATLAS detector*. In: *Phys. Lett. B* 786 (2018), pp. 59–86. DOI: [10.1016/j.physletb.2018.09.013](https://doi.org/10.1016/j.physletb.2018.09.013). arXiv: [1808.08238 \[hep-ex\]](https://arxiv.org/abs/1808.08238) (cit. on p. 199).
- [186] A. M. Sirunyan et al. *Observation of Higgs boson decay to bottom quarks*. In: *Phys. Rev. Lett.* 121.12 (2018), p. 121801. DOI: [10.1103/PhysRevLett.121.121801](https://doi.org/10.1103/PhysRevLett.121.121801). arXiv: [1808.08242 \[hep-ex\]](https://arxiv.org/abs/1808.08242) (cit. on p. 199).
- [187] P. Azzurri et al. *A special Higgs challenge: measuring the mass and production cross section with ultimate precision at FCC-ee*. In: *Eur. Phys. J. Plus* 137.1 (2022), p. 23. DOI: [10.1140/epjp/s13360-021-02202-4](https://doi.org/10.1140/epjp/s13360-021-02202-4). arXiv: [2106.15438 \[hep-ex\]](https://arxiv.org/abs/2106.15438) (cit. on pp. 199, 200, 202).
- [188] F. A. Berends and R. Kleiss. *Initial State Radiation at LEP Energies and the Corrections to Higgs Boson Production*. In: *Nucl. Phys. B* 260 (1985), pp. 32–60. DOI: [10.1016/0550-3213\(85\)90309-8](https://doi.org/10.1016/0550-3213(85)90309-8) (cit. on p. 199).
- [189] G. Altarelli, T. Sjostrand, and F. Zwirner, eds. *Physics at LEP2: Vol. 1*. CERN Yellow Reports: Conference Proceedings. Feb. 1996. DOI: [10.5170/CERN-1996-001-V-1](https://doi.org/10.5170/CERN-1996-001-V-1) (cit. on p. 199).
- [190] M. Cepeda et al. *Report from Working Group 2: Higgs Physics at the HL-LHC and HE-LHC*. In: *CERN Yellow Rep. Monogr.* 7 (2019). Ed. by A. Dainese et al., pp. 221–584. DOI: [10.23731/CYRM-2019-007.221](https://doi.org/10.23731/CYRM-2019-007.221). arXiv: [1902.00134 \[hep-ph\]](https://arxiv.org/abs/1902.00134) (cit. on p. 200).

- [191] A. Li. *Perspectives for Higgs measurements at Future Circular Colliders*. In: *PoS PANIC2021* (2022), p. 420. DOI: [10.22323/1.380.0420](https://doi.org/10.22323/1.380.0420) (cit. on p. 201).
- [192] J. de Favereau et al. *DELPHES 3, A modular framework for fast simulation of a generic collider experiment*. In: *JHEP* 02 (2014), p. 057. DOI: [10.1007/JHEP02\(2014\)057](https://doi.org/10.1007/JHEP02(2014)057). arXiv: [1307.6346 \[hep-ex\]](https://arxiv.org/abs/1307.6346) (cit. on p. 203).
- [193] W. Kilian, T. Ohl, and J. Reuter. *WHIZARD: Simulating Multi-Particle Processes at LHC and ILC*. In: *Eur. Phys. J. C* 71 (2011), p. 1742. DOI: [10.1140/epjc/s10052-011-1742-y](https://doi.org/10.1140/epjc/s10052-011-1742-y). arXiv: [0708.4233 \[hep-ph\]](https://arxiv.org/abs/0708.4233) (cit. on p. 204).
- [194] T. Sjöstrand, S. Mrenna, and P. Z. Skands. *PYTHIA 6.4 physics and manual*. In: *JHEP* 05 (2006), p. 026. DOI: [10.1088/1126-6708/2006/05/026](https://doi.org/10.1088/1126-6708/2006/05/026). arXiv: [hep-ph/0603175](https://arxiv.org/abs/hep-ph/0603175) (cit. on p. 204).
- [195] T. Sjöstrand et al. *An introduction to PYTHIA 8.2*. In: *Comput. Phys. Commun.* 191 (2015), p. 159. DOI: [10.1016/j.cpc.2015.01.024](https://doi.org/10.1016/j.cpc.2015.01.024). arXiv: [1410.3012 \[hep-ph\]](https://arxiv.org/abs/1410.3012) (cit. on p. 204).
- [196] S. Jadach et al. *Multi-photon Monte Carlo event generator KKMcee for lepton and quark pair production in lepton colliders*. In: *Comput. Phys. Commun.* 283 (2023), p. 108556. DOI: [10.1016/j.cpc.2022.108556](https://doi.org/10.1016/j.cpc.2022.108556). arXiv: [2204.11949 \[hep-ph\]](https://arxiv.org/abs/2204.11949) (cit. on p. 204).
- [197] K. Hagiwara et al. *Single weak boson production at TeV e^+e^- colliders*. In: *Nucl. Phys. B* 365 (1991), pp. 544–596. DOI: [10.1016/0550-3213\(91\)90442-Z](https://doi.org/10.1016/0550-3213(91)90442-Z) (cit. on p. 205).
- [198] *Procedure for the LHC Higgs boson search combination in Summer 2011*. In: (Aug. 2011) (cit. on p. 227).
- [199] W. Verkerke and D. P. Kirkby. *The RooFit toolkit for data modeling*. In: *eConf C0303241* (2003). Ed. by L. Lyons and M. Karagoz, MOLT007. arXiv: [physics/0306116](https://arxiv.org/abs/physics/0306116) (cit. on p. 227).
- [200] L. Moneta et al. *The RooStats Project*. In: *PoS ACAT2010* (2010). Ed. by T. Speer et al., p. 057. DOI: [10.22323/1.093.0057](https://doi.org/10.22323/1.093.0057). arXiv: [1009.1003 \[physics.data-an\]](https://arxiv.org/abs/1009.1003) (cit. on p. 227).
- [201] S. Jadach, B. Ward, and Z. Was. *Coherent Exclusive Exponentiation For Precision Monte Carlo Calculations*. In: *Phys. Rev. D* 63.11 (2001), pp. 113009/1–65. DOI: [10.1103/PhysRevD.63.113009](https://doi.org/10.1103/PhysRevD.63.113009). URL: <https://cds.cern.ch/record/445628> (cit. on p. 234).
- [202] F. Pedregosa et al. *Scikit-learn: Machine Learning in Python*. In: *Journal of Machine Learning Research* 12 (2011), pp. 2825–2830 (cit. on p. 246).
- [203] R. J. Hyneman. *Measuring Higgs Boson Couplings, including to the Top Quark, in the Diphoton Decay Channel with Run 2 Data Collected by the ATLAS Detector*. 2020. URL: <http://cds.cern.ch/record/2712576> (cit. on p. 246).
- [204] A. Betti et al. *Searches for Higgs boson pair production in the $b\bar{b}\tau^+\tau^-$ final state with 139 fb^{-1} of pp collision data with the ATLAS detector*. Tech. rep. Geneva: CERN, 2020. URL: <https://cds.cern.ch/record/2743097> (cit. on p. 259).
- [205] ATLAS Collaboration. *A search for resonant and non-resonant Higgs boson pair production in the $b\bar{b}\tau^+\tau^-$ decay channel in pp collisions at $\sqrt{s} = 13$ TeV with the ATLAS detector*. In: *Phys. Rev. Lett.* 121 (2018), p. 191801. DOI: [10.1103/PhysRevLett.121.191801](https://doi.org/10.1103/PhysRevLett.121.191801). arXiv: [1808.00336 \[hep-ex\]](https://arxiv.org/abs/1808.00336) (cit. on pp. 266, 269). Erratum: in: *Phys. Rev. Lett.* 122 (2019), p. 089901. DOI: [10.1103/PhysRevLett.122.089901](https://doi.org/10.1103/PhysRevLett.122.089901).

List of Figures

1.1	Standard Model from: texample.net/tikz/examples/model-physics/	23
1.2	Higgs potential $V(\phi) = \mu^2 \phi ^2 + \lambda \phi ^4$ with $\lambda > 0$ and either (a) $\mu^2 \geq 0$ or (b) $\mu^2 < 0$ (Adapted from Refs. [37, 38]).	28
1.3	Depictions of the leading order interaction vertices of the Higgs as predicted by the Brout-Englert-Higgs mechanism. (a) Trilinear and (b) quartic Higgs self-coupling respectively as predicted by the h^3 and h^4 terms of the \mathcal{L}_H Lagrangian. (c) and (d) delineate the Higgs interaction with the vector boson ($V = W, Z$) in the \mathcal{L}_{VVH} and \mathcal{L}_{VVHH} Lagrangians. The coupling factors values (displayed in red) are derived from the Lagrangians themselves, while their signs are referenced from Ref. [40].	29
1.4	Leading order fermion couplings to the Higgs and interaction vertex factor as predicted by the Yukawa theory.	30
1.5	Higgs boson production cross-sections as a function of the centre-of-mass-energy (\sqrt{s}) for a Higgs mass $m_H = 125$ GeV. The tH production cross-section accounts for t -channel and s -channel only (no tWH production).(Adapted from Refs. [41, 42]).	30
1.6	Leading order Feynman diagrams contribution to the Higgs boson production at LHC. Different Higgs boson production modes at the Large Hadron Collider (LHC) for a Higgs mass $m_H = 125$ GeV: (a) gluon fusion (ggF), (b) Vector Boson Fusion (VBF), (c) Higgs production associated with a vector boson (VH), (d) Higgs production associated with $t\bar{t}$ (ttH), (e) Higgs production associated with single t	31
1.7	Feynman diagrams representing various decay modes of the Higgs boson: (a) Higgs decay into a pair of b quarks, (b) Higgs decay into a pair of leptons, (c) Higgs decay into a pair of gauge bosons, (d) Higgs decay into two photons via fermion loop, (e) Higgs decay into two photons via boson loop.	32
1.8	Higgs boson branching ratios and their uncertainties for different mass ranges around 125 GeV (Adapted from Refs. [41, 42]).	33
1.9	Leading-order Feynman diagrams of the ggF Higgs boson pair production in the Standard Model through the Higgs-top quark Yukawa interactions parameter, defined as $k_t \equiv y_t/y_t^{\text{SM}}$ (a) and the Higgs boson self-coupling parameter, defined as $\kappa_\lambda \equiv \lambda_{HHH}/\lambda_{HHH}^{\text{SM}}$ (b).	34
1.10	Tree-level Feynman diagrams for the VBF HH production mode. The vertices denoted by κ_{2V} , κ_V and κ_λ represent the $VVHH$, VVH and HHH couplings, respectively.	34
1.11	Di-Higgs decay branching ratios.	35
2.1	Schematic representation of the LHC's configuration. Notably, the physical proximity between the ALICE, ATLAS, and LHCb detectors is closer than illustrated in this diagram (adapted from Ref. [58]).	44
2.2	The LHC and ATLAS integrated luminosity evolution over time for the full Run 2 (taken from Ref. [63]).	46
2.3	ATLAS luminosity-weighted distribution of the mean number (μ) of interactions per bunch crossing for the full Run 2 (taken from Ref. [63]).	47
2.4	(a) Schematic of the ATLAS detector and (b) Transverse cut-away view of the detector. The bending of the trajectories for charged particles is a result of the magnetic field within the ATLAS (Referenced from [80, 81]).	50
2.5	An illustration of the coordinate system of the LHC and the ATLAS detector. Adapted from Ref. [37].	51

2.6	The correlation between pseudorapidity η and specific values of the polar angle θ . Adapted from Ref. [37].	52
2.7	(a) Illustrations of the solenoid, barrel, and endcap toroid magnets. (b) The generated magnetic field lines: the solenoid induces a field parallel to the beam axis within the tracker (depicted by the straight green lines), whereas the toroidal magnets produce the rotating field (blue lines). The barrel toroid magnets account for the broader central field lines, and the smaller outer ones result from the combined influence of the endcap magnet field and the barrel toroid. (Adapted from Refs. [82, 83]).	53
2.8	Dependence of the radial (B_r) and axial (B_z) magnetic field components on radial (R) and longitudinal (z) coordinates within the inner detector cavity (source: Ref. [68]).	53
2.9	(a) The three-dimensional structure of the ATLAS inner detector. (b) Transverse and (c) longitudinal representations of the ATLAS inner detector. The Insertable B-Layer (IBL) is displayed only in the transverse view (referenced from Refs. [68, 86, 87]).	54
2.10	Variation of radiation length (X_0) with η for the distinct components of the inner detector (adapted from Ref. [88]).	55
2.11	Illustrative depiction of the ATLAS calorimeter delineating both the electromagnetic and hadronic calorimeters (sourced from Refs. [68, 95]).	57
2.12	Illustration of a barrel module. The granularity in η and ϕ of the cells across the three layers, in conjunction with the trigger towers, is displayed (source: Ref. [68]).	58
2.13	A schematic of the hadronic tile calorimeter module, showcasing the components of the optical readout, including tiles, fibers, and photomultipliers. Adapted from Ref. [68].	59
2.14	Representation of the Muon Spectrometer (Source: Ref. [98]).	60
2.15	The Trigger and Data Acquisition (TDAQ) mechanism employed by ATLAS during Run 2. (a) displays anticipated peak rates and bandwidths across each component, whereas (b) shows into the intricacies of the Level 1 (L1) trigger system (sourced from Ref. [101]).	62
3.1	(a) A diagram showing the path of an electron (depicted by the red solid line) through the ATLAS detector, including its passage through the tracking system and the electromagnetic calorimeter where it releases its energy. The dashed red line portrays the path of a photon generated by the interaction of electron with the tracking system material. (b) An illustration of a charged particle traversing sub-detector planes, with red stars marking hit measurements in the layers, black arrows for fitted tracks, green dots for reconstructed track intersections, and blue lines for the distance between each layer's track and hit (Adapted from Refs. [87, 102]).	64
3.2	(a) Schematic representation of the track helix parameters ATLAS utilizes for comprehensive track description. (b) Comparative schematic of Light- and b -jet tracks. Light-jets originate at the primary vertex (PV) while b -hadrons generate a secondary vertex (SV) distanced from the primary vertex. Tracks associated with b -jets are typified by pronounced longitudinal (z_0) and transverse (d_0) impact parameters. (c) Depiction of the longitudinal and transverse impact parameters related to two varied tracks (blue and green) from a b -jet (sourced from Refs. [37, 106]).	65
3.3	Efficiency of track reconstruction for charged primary particles within jets having $ \eta < 1.2$ ($ \eta > 1.2$) plotted against the production radius in simulated dijet MC events (sourced from Ref. [103]).	67

3.4	Spatial resolution (σ) comparison for the transverse (d_0) and longitudinal (z_0) impact parameters between Run 1 (2012, $\sqrt{s} = 8$ TeV) and Run 2 (2015, $\sqrt{s} = 13$ TeV) datasets, plotted as a function of (a), (c) p_T within $0 < \eta < 0.2$, and (b), (d) η for the range $0.4 < p_T < 0.5$ GeV. The observed improvements can be associated with the Run 2 integration of the Insertable B-Layer (IBL) in the inner detector (source: Ref. [108]).	67
3.5	(a) Distribution of the EM fraction (f_{EM}) and (b) reconstruction efficiency as a function of the f_{EM} selection requirement for simulated true electron (black) and pile-up (red) clusters (taken from Ref. [109]).	69
3.6	Reconstruction efficiencies for cluster, track, cluster and track, and electron as a function of the generated electron E_T (taken from Ref. [109]).	70
3.7	Electron identification efficiency in $Z \rightarrow e^+e^-$ events in data as a function of (a) E_T and (b) η for the Loose, Medium and Tight operating points. For both plots, the bottom panel shows the data-to-simulation ratios (taken from Ref. [109]).	71
3.8	Efficiency of the different isolation working points for electrons passing the Medium identification criterion in inclusive $Z \rightarrow e^+e^-$ events as a function (a) E_T and (b) η . The bottom panel shows the ratio of the efficiencies measured in data and in MC simulations (taken from Ref. [109]).	72
3.9	(a) Depiction of energy scale factors, α , and (b) the additional constant term, c , as functions of η . The shaded areas represent statistical uncertainties. For (a) and (b), the bottom panels demonstrate the disparities between values measured during a particular data-acquisition period and those measured using 2017 data. (c) This contrasts the invariant mass distribution, m_{ee} , of the selected $Z \rightarrow e^+e^-$ candidates between data and simulation after applying calibration and resolution corrections to the data and simulation, respectively. The total event count in the simulation is scaled to match the data. The uncertainty band in the bottom plot indicates the impact of variations in the calibration and resolution correction factors (adapted from Ref. [109]).	73
3.10	Efficiency functions based on (a) p_T and (b) for the Loose, Medium, and Tight identification WP in simulated $t\bar{t}$ events for tracks with $p_T > 10$ GeV, differentiated between prompt muons and muons from hadron decays (source: Ref. [114]).	76
3.11	Depending on the genuine $\tau_{had-vis}$ efficiency, this showcases the rejection of quark and gluon jets falsely identified as hadronic τ -decays (designated as fake $\tau_{had-vis}$). The RNN-based (solid line) and BDT-based (dotted line) identification techniques are represented by the 1-prong (in red) and 3-prong (in blue) ROC curves. The markers align with the four pre-established working points: <i>Tight</i> , <i>Medium</i> , <i>Loose</i> , and <i>Very loose</i> , which sequentially depict increased signal selection efficiencies (sourced from Ref. [120]).	78
3.12	Reconstruction of Large-R jets ($R = 1.0$) using the anti- k_t algorithm, displaying circular cones in the η - ϕ plane (sourced from Ref. [121]).	79
3.13	$H \rightarrow b\bar{b}$ decay depictions: (a) shows resolved topology and (b) showcases boosted topology. Events are either reconstructed with small-R jets ($R = 0.4$) or a large-R jet ($R = 1.0$). The angular separation between the b -hadrons is given by: $\Delta R(b, b) \approx \frac{2m_H}{p_T^H}$	80
3.14	Low level taggers used by the MV2, DL1 and DL1r tagger (taken from Ref. [129]).	82
3.15	Comparison of ROC curves for the 2018 recommended versions of MV2 and DL1, the 2019 DL1r optimization, evaluated on a simulated dataset of $t\bar{t}$ events. The MV2c10 and DL1 algorithms do not use the RNNIP input variables, while the DL1r algorithm does. (a),(b): Performance on PFlow small-R jets with $20 < p_T < 250$ GeV and $ \eta < 2.5$. The shaded bands represent statistical uncertainty (Adapted from Refs. [130, 131]).	82

3.16	(a) Illustration of the E_T^{miss} distributions for $Z \rightarrow \mu^+ \mu^-$ simulations using a specialized event selection and the Loose E_T^{miss} working point with EMTopo and PFlow jets. The RMS resolution derived from combined distributions of E_x^{miss} and E_y^{miss} is presented in relation to (b) the count of inelastic collisions per bunch crossing (μ) and (c) the primary vertex count per bunch crossing (N_{PV}). Analysis conducted using the Loose E_T^{miss} working point for datasets comprising EMTopo jets (circular marker) and PFlow jets (triangular marker) as well as MC simulation with EMTopo jets (square marker) in the $Z \rightarrow e^+ e^-$ event selection (Adapted from Ref. [124]).	85
4.1	A diagrammatic representation depicting a jet cone (in black) with an embedded b -hadron decaying semi-leptonically at a secondary vertex (in green). The resulting muon and its momentum, projected transverse to the jet+muon axis, is illustrated as the p_T^{rel} . (Taken from Ref. [3].)	89
4.2	(a) Displays the b -jet distributions for three distinctive p_T^{jet} bins. (b) contrasts the b -jet distributions for four distinct MV2 OPs. (From Ref. [3])	94
4.3	(a) p_T^{rel} distributions for muons originating from direct bottom hadron decays across three separate jet p_T^{jet} bins. (b) p_T^{rel} distributions for muons originating from cascade bottom hadron decays across three separate jet p_T^{jet} bins. (From Ref. [3])	95
4.4	Spectra of Muon p_T^{rel} for the b -, c - and light-jet templates are depicted in yellow, blue, and red colors, respectively. Simulations generate the heavy flavour templates, while a data-driven method extracts the light-jet template. (From Ref. [3])	96
4.5	(a) The pre-fit distribution is b -tagged by DL1r at $\varepsilon_b^{\text{nom}} = 70\%$. (b) The pre-fit distribution presents jets failed the tagging criterion. Data is in black, and templates appear as a stack. Both systematic and statistical uncertainties are included in the uncertainty band.	97
4.6	(a) The post-fit distribution is b -tagged by DL1r at $\varepsilon_b^{\text{nom}} = 70\%$. (b) The post-fit distribution of jets that did not meet the tagging criterion. Black represents data, with templates forming a stack. The band of uncertainty includes both systematic and statistical uncertainties.	98
4.7	A comparative analysis of simulated b -tagging efficiency as a function of jet transverse momentum (p_T). The efficiency for jets containing muons is depicted by the red curve, while the green curve represents jets devoid of muons. The black curve illustrates the ratio of these efficiencies. The plot on the right incorporates a semileptonic correction to the jet momentum.	99
4.8	Comparative analysis of b -tagging efficiency, both in data and simulation, as a function of jet transverse momentum (p_T). The left plot illustrates efficiency for jets that contain muons, while the right plot focuses on jets that are devoid of muons.	101
4.9	Ratio between the b -tagging efficiency scale factor of jet with and without muons for the 60, 70, 77 and 85% working point as function of jet p_T bins.	102
4.10	Comparison of the p^* spectrum between the ATLAS simulated data and results from DELPHI [156]. (From Ref. [3])	105
4.11	Jet p_T dependent efficiencies (left) and scale factors (right) determined through the p_T^{rel} technique for the DL1r algorithm at nominal efficiencies of $\varepsilon_b^{\text{nom}} = 60\%, 70\%, 77\%$, and 85% in sequence from top to bottom. The MC predictions are displayed in red, with data symbolized by black dots. The green bands convey both statistical and systematic uncertainties.	108
4.12	Comparative analysis between p_T^{rel} b -tagging efficiency scale factors (represented by a black marker and accompanied by a green uncertainty band) and $t\bar{t}$ likelihood-based method scale factors (shown in red).	109
5.1	Parton level invariant mass distribution of the HH system m_{HH} , for the nominal ggF HH signal samples in the $\tau_{\text{had}}\tau_{\text{had}}$ channel with varied $\kappa_\lambda = 1, 10$ values overlaid.	115

5.2	Parton-level distributions of the nominal VBF HH signal sample showing (top row) the invariant mass and (bottom row) the pseudo-rapidity separation of the VBF jet system in the $\tau_{\text{had}}\tau_{\text{had}}$ channel. Each plot varies one coupling (κ_λ , κ_{2V} , or κ_V) according to the settings detailed in Table 5.2, while the other two couplings are fixed to their Standard Model values. Distributions have been normalized to unity.	116
5.3	Parton level plots for the nominal VBF HH signal sample showing the invariant mass distribution and the pseudo-rapidity separation of the VBF jets system in the $\tau_{\text{lep}}\tau_{\text{had}}$ channel. For each plot κ_λ , κ_{2V} and κ_V are varied respectively as shown in Table 5.2 while the other two couplings are set to their SM prediction. The distributions are normalised to unity.	117
5.4	Nominal VBF HH signal sample plots for various κ_{2V} values at parton level. m_{HH} distributions are shown in the $\tau_{\text{had}}\tau_{\text{had}}$ (Figure 5.4a) and $\tau_{\text{lep}}\tau_{\text{had}}$ (Figure 5.4b) channels. For each plot κ_λ , κ_{2V} , and κ_V are varied respectively as shown in Table 5.2 while the other two couplings are set to their SM prediction. The distributions are normalised to unity.	117
5.5	Sketch depicting the analysis strategy starting with the triggers and event selection for the $b\bar{b}$ $\tau_{\text{had}}\tau_{\text{had}}$ and $b\bar{b}$ $\tau_{\text{lep}}\tau_{\text{had}}$ sub-channels, followed by a BDT approach defining the orthogonality between ggF and VBF signal regions. The ggF signal region is subsequently split based on a m_{HH} requirement of 350 GeV to improve the sensitivity of enhanced κ_λ . Furthermore, a control region ($Z + HF$) is defined based on various single- and di-lepton triggers and event selection with the $m_{\ell\ell}$ shape used as parameter of interest.	119
5.6	Event categorisation into low- m_{HH} ggF, high- m_{HH} ggF and VBF signal regions.	123
5.7	Selection efficiency for the ggF HH signal across various analysis categories. The efficiency is plotted against the coupling parameter κ_λ for the channels: $\tau_{\text{had}}\tau_{\text{had}}$ (a), $\tau_{\text{lep}}\tau_{\text{had}}$ SLT (b), and $\tau_{\text{lep}}\tau_{\text{had}}$ LTT (c).	125
5.8	Selection efficiency for the VBF HH signal across various analysis categories. The efficiency is plotted against the coupling parameter κ_λ for the channels: $\tau_{\text{had}}\tau_{\text{had}}$ (a), $\tau_{\text{lep}}\tau_{\text{had}}$ SLT (b), and $\tau_{\text{lep}}\tau_{\text{had}}$ LTT (c).	125
5.9	Selection efficiency for the VBF HH signal across various analysis categories. The efficiency is depicted in relation to the coupling parameter κ_{2V} for channels: $\tau_{\text{had}}\tau_{\text{had}}$ (a), $\tau_{\text{lep}}\tau_{\text{had}}$ SLT (b), and $\tau_{\text{lep}}\tau_{\text{had}}$ LTT (c).	125
5.10	Comparisons of the m_{HH} shape for the VBF HH process across various κ_λ values in the $\tau_{\text{had}}\tau_{\text{had}}$ (a) and $\tau_{\text{lep}}\tau_{\text{had}}$ ggF SRs (c). Furthermore, the distributions of the ggF/VBF BDT scores for the VBF HH process across different κ_λ values in the inclusive SR are shown for $\tau_{\text{had}}\tau_{\text{had}}$ (b) and $\tau_{\text{lep}}\tau_{\text{had}}$ (d). The nominal values for the event categorization in ggF/VBF are set at -0.11 and -0.13 for $\tau_{\text{had}}\tau_{\text{had}}$ and $\tau_{\text{lep}}\tau_{\text{had}}$ channels, respectively.	126
5.11	Comparisons of the m_{HH} shape for the ggF HH process at various κ_λ values near the interference maximum. This is observed in the $\tau_{\text{had}}\tau_{\text{had}}$ channel (a) for the ggF low- and high- m_{HH} SRs, (b) the VBF SR, and (c) the inclusive SR.	127
5.12	Comparison of V p_T shapes between the various SRs and the Z CR for both $\tau_{\text{had}}\tau_{\text{had}}$ (a) and $\tau_{\text{lep}}\tau_{\text{had}}$ (b) channels.	130
5.13	$Z + HF$ CR Data/MC comparison. Each subfigure shows different variable.	131
5.14	Investigations on the Vp_T shape uncertainty in the Z CR.	132
5.15	Input variables optimisation strategy.	135
5.16	Hyperparameters optimisation strategy.	136
5.17	Level of improvement of the trafo6 [179] binned significance obtained by adding one variable after another, where m_{jj}^{VBF} and $\Delta\eta_{jj}^{\text{VBF}}$ are considered as baseline.	137

5.18	Distributions of ggF/VBF BDT input variables in the $\tau_{\text{lep}}\tau_{\text{had}}$ SLT channel showing the separation between the ggF HH events (in green) and the SM VBF HH events (in red). BSM VBF HH processes are also included in these plots although they are not used in the training.	138
5.19	Pre-fit distributions input MVA variables in the $\tau_{\text{lep}}\tau_{\text{had}}$ SLT channel for the ggF/VBF BDT in the low- m_{HH} ggF SR (a)-(b), high- m_{HH} ggF SR (c)-(d), and VBF SR (e)-(f) regions.	139
5.20	Representative set of pre-fit MVA input variable distributions in the $\tau_{\text{lep}}\tau_{\text{had}}$ SLT SRs.	140
5.21	Representative set of pre-fit MVA input variable distributions in the $\tau_{\text{lep}}\tau_{\text{had}}$ SLT SRs.	141
5.22	Categorisation BDT variable distributions in the $\tau_{\text{lep}}\tau_{\text{had}}$ SLT SRs.	141
5.23	Hyperparameters optimisation for the ggF/VBF BDT in the $\tau_{\text{lep}}\tau_{\text{had}}$ SLT channel. The optimal point is found at textttNTrees = 126 and MaxDepth = 4.	142
5.24	ggF/VBF BDT scores for training, validation and test samples and output scores in the $\tau_{\text{lep}}\tau_{\text{had}}$ SLT channel	142
5.25	Constraints on κ_{2V} , κ_{λ} as well as the limits on μ_{HH} , μ_{VBF} and μ_{ggF} as a function of the ggF-VBF separation BDT working point. The same signal vs. sum of backgrounds BDT has been used to evaluate the performance for each of the scan points.	144
5.26	BDT hyperparameter optimisation in the $\tau_{\text{lep}}\tau_{\text{had}}$ SLT channel. Dependence of the validation significance on the number of trees (NTrees) and the maximum allowed depth of each tree (MaxDepth).	145
5.27	Evolution of the validation significance of the discriminant in the two ggF SRs as additional observables are added to the list of baseline quantities, consisting of the variables m_{HH} , m_{bb} , $m_{\tau\tau}^{\text{MMC}}$, $\Delta R(b, b)$, and $\Delta R(\tau, \tau)$. For the high- m_{HH} plot (b), the blue curve shows the binned significance computed on a binning generated with the trafo60 algorithm requiring at least 5.0 expected background events per bin, while the black curve is more aggressive and requires at least 1.0 expected background event per bin.	148
5.28	Evolution of the validation significance of the discriminant in the VBF SRs as additional observables are added to the list of baseline quantities, consisting of the variables m_{HH} , m_{bb} , $m_{\tau\tau}^{\text{MMC}}$, $\Delta R(b, b)$, and $\Delta R(\tau, \tau)$. The blue curve shows the binned significance computed on a binning generated with the trafo60 algorithm requiring at least 5.0 expected background events per bin, while the black curve is more aggressive and requires at least 1.0 expected background event per bin.	149
5.29	Binned distributions of the trained BDT discriminants in each $\tau_{\text{lep}}\tau_{\text{had}}$ signal region, shown for the signal used during training (red) and the sum of all SM backgrounds (blue). The distributions are shown separately for the training, validation, and test data sets.	150
5.30	Pre-fit BDT score distributions in the $\tau_{\text{lep}}\tau_{\text{had}}$ SLT regions ((a)-(c)) and pre-fit m_{ll} distribution in the $Z + HF$ control region ((d)).	151
5.31	Pre-fit distributions of the input variables used in the $\tau_{\text{lep}}\tau_{\text{had}}$ SLT channel for the low- m_{HH} ggF SR ((a)-(b)), high- m_{HH} ggF SR ((c)-(d)), and VBF SR ((e)-(f)) regions.	152
5.32	Comparison of NP pulls between conditional and unconditional data fits for the inclusive signal strength in the $\tau_{\text{had}}\tau_{\text{had}}$ channel.	158
5.33	Comparison of NP pulls between conditional and unconditional data fits for the inclusive signal strength in the $\tau_{\text{had}}\tau_{\text{had}}$ channel.	159
5.34	Comparison of NP pulls between conditional and unconditional data fits for the inclusive signal strength in the $\tau_{\text{had}}\tau_{\text{had}}$ channel.	160

5.35	Comparison of NP pulls between conditional and unconditional data fits for the inclusive signal strength in the $\tau_{\text{had}}\tau_{\text{had}}$ channel.	161
5.36	NP ranking for the $\tau_{\text{had}}\tau_{\text{had}}$ SM fit (μ_{HH} hypothesis) to the Asimov dataset (Figure (a)) and to actual data (Figure (b)).	161
5.37	NP correlations from the $\tau_{\text{had}}\tau_{\text{had}}$ SM fit to the Asimov dataset in Figure (a) and to actual data in Figure (b). MC statistical uncertainties are not included in the correlations.	162
5.38	Post-fit BDT score distributions in the $\tau_{\text{had}}\tau_{\text{had}}$ signal regions. Due to the negative signal strength, the signal templates are not shown. The definition of the uncertainty band needs clarification.	162
5.39	Post-fit distributions of key variables in the $\tau_{\text{had}}\tau_{\text{had}}$ channel signal regions. Due to the negative signal strength, the signal templates are not shown.	163
5.40	Post-fit distribution of the ggF/VBF classification BDT score in the $\tau_{\text{had}}\tau_{\text{had}}$ channel. The categorisation BDT is only shown for events with at least four jets, representing a subset of the ggH SRs. Due to the negative signal strength, the signal templates are not shown.	164
5.41	NP pulls comparison for the unconditional fit to data for the $\tau_{\text{lep}}\tau_{\text{had}}$ channel and the SLT and LTT channels individually.	166
5.42	NP pulls comparison for the unconditional fit to data for the $\tau_{\text{lep}}\tau_{\text{had}}$ channel and the SLT and LTT channels individually.	167
5.43	NP pulls comparison for the unconditional fit to data for the $\tau_{\text{lep}}\tau_{\text{had}}$ channel and the SLT and LTT channels individually.	168
5.44	NP pulls comparison for the unconditional fit to data for the $\tau_{\text{lep}}\tau_{\text{had}}$ channel and the SLT and LTT channels individually.	169
5.45	Ranking of the NPs for the $\tau_{\text{lep}}\tau_{\text{had}}$ SM fit (μ_{HH} hypothesis) to the Asimov dataset in Figure (a) and to data in Figure (b).	170
5.46	NP correlations from the $\tau_{\text{lep}}\tau_{\text{had}}$ SM fit to the Asimov dataset in Figure (a) and to data in Figure (b). MC statistical uncertainties are not included in the correlations.	170
5.47	Post-fit BDT score distributions in the $\tau_{\text{lep}}\tau_{\text{had}}$ signal regions. The result of the inclusive signal strength fit is used to produce these distributions.	171
5.48	Post-fit data/MC distributions of key variables in the SLT signal regions. The results are obtained by applying the SLT fit results to the SLT signal region.	172
5.49	Post-fit data/MC distributions of key variables in the LTT signal regions. The results are obtained by applying the LTT fit results to the LTT signal region.	173
5.50	Post-fit data/MC distributions of the ggF/VBF classification BDT score in the $\tau_{\text{lep}}\tau_{\text{had}}$ channels. The categorisation BDT is only shown for events with at least four jets which represent a subset of the ggF SRs. It is shown on the left for the SLT region with the SLT fit result applied and on the right for the LTT regions with the LTT fit result applied.	173
5.51	Ranking of the NPs for the combined SM fit to the Asimov dataset in Figure (a) and to data in Figure (b).	175
5.52	NP pulls comparison for the unconditional fit to data for the combination (red) and the $\tau_{\text{had}}\tau_{\text{had}}$ and $\tau_{\text{lep}}\tau_{\text{had}}$ channels individually.	176
5.53	NP pulls comparison for the unconditional fit to data for the combination (red) and the $\tau_{\text{had}}\tau_{\text{had}}$ and $\tau_{\text{lep}}\tau_{\text{had}}$ channels individually.	177
5.54	NP pulls comparison for the unconditional fit to data for the combination (red) and the $\tau_{\text{had}}\tau_{\text{had}}$ and $\tau_{\text{lep}}\tau_{\text{had}}$ channels individually.	178
5.55	NP pulls comparison for the unconditional fit to data for the combination (red) and the $\tau_{\text{had}}\tau_{\text{had}}$ and $\tau_{\text{lep}}\tau_{\text{had}}$ channels individually.	179
5.56	NP correlations from the combined fit to $\tau_{\text{had}}\tau_{\text{had}}$ and $\tau_{\text{lep}}\tau_{\text{had}}$ channel to the Asimov dataset in Figure (a) and to data in Figure (b). MC statistical uncertainties are not included in the correlations.	179

5.57	Post-fit BDT score distributions in the $\tau_{\text{had}}\tau_{\text{had}}$ and $\tau_{\text{lep}}\tau_{\text{had}}$ signal regions after the combined fit.	180
5.58	Negative log-likelihood ratio comparison for different κ_λ (a) and κ_{2V} (b) hypotheses, based on the fit to data and Asimov dataset constructed under the SM hypothesis in the $\tau_{\text{had}}\tau_{\text{had}}$ channel.	181
5.59	Negative logarithm of the likelihood ratio comparing different κ_λ (a) and κ_{2V} (c) hypotheses to an Asimov dataset (b) and data (d) in the $\tau_{\text{lep}}\tau_{\text{had}}$ channels, shown individually and combined.	183
5.60	Negative logarithm of the likelihood ratio for different κ_λ (a) and κ_{2V} (b) hypotheses, based on fits to data and an Asimov dataset under the SM hypothesis in the $\tau_{\text{lep}}\tau_{\text{had}}$ channel.	183
5.61	Summary of observed (filled circles) and expected (open circles) 95% CLs upper limits on μ_{HH} from the fit of each individual channel and the combined fit in the background-only ($\mu_{HH} = 0$) hypothesis. The dashed lines indicate the expected 95% CLs upper limits on μ_{HH} in the SM hypothesis ($\mu_{HH} = 1$). The cyan and yellow bands indicate the $\pm 1\sigma$ and $\pm 2\sigma$ variations on the expected limit with respect to the background-only hypothesis due to statistical and systematic uncertainties, respectively.	184
5.62	Comparison of different κ_λ (a) and κ_{2V} (c) hypotheses against an Asimov dataset (b) and actual data (d), shown through the negative logarithm of the likelihood ratio. The curves represent both individual channels and their combined analysis.	185
5.63	Likelihood ratio's negative logarithm comparing various κ_λ (a) and κ_{2V} (b) hypotheses in the combined fit to data and an Asimov dataset formulated under the SM hypothesis.	186
5.64	Simultaneous determination of κ_λ and κ_{2V} : 68% and 95% likelihood contours, both expected and observed, in the combined analysis. The SM prediction is indicated by the star, while the best-fit value is denoted by the black cross.	186
6.1	Comparison of different particle accelerator layouts: (a) International Linear Collider (ILC), (b) Compact Linear Collider (CLIC), (c) Future Circular Collider (FCC), and (d) Circular Electron Positron Collider (CEPC).	193
6.2	FCC Integrated Program from Ref. [181]	193
7.1	Main diagrams of the Higgs production modes at $\sqrt{s} = 240\text{GeV}$: (a) represents the Higgsstrahlung process, (b) represents the WW fusion process, Adapted from Ref. [187]	199
7.2	Improved-Born Higgs production cross-sections for the Higgsstrahlung process and the WW fusion process (see Figure 7.1), incorporating initial state radiation [188], are predicted by HZHA [189] as a function of center-of-mass energy with a Higgs boson mass m_h of 125 GeV. The minor interference term between the two diagrams in the final state is integrated into the WW fusion cross-section. Vertical dashed lines represent the anticipated \sqrt{s} values at the FCC-ee. Adapted from Ref. [187].	199
7.3	Feynman diagram illustrating the Higgsstrahlung process and the recoil mass (m_{recoil}) calculation. Adapted from [191].	201
7.4	(a) displays the inclusive m_{rec} distribution for events where a Z boson decays into a $\mu^+\mu^-$ pair, with energies ranging from 40 to 160 GeV, after the basic selection described in Section 7.5. The Z and Higgs mass peaks are clearly visible in this distribution. Reproduced according to [187]. (b) shows the zoomed-in view of the m_{rec} distribution in the vicinity of m_h . The ZH signal is fitted using a double-sided Crystal Ball function, while the simulated background is fitted with a second-order polynomial. Reproduced according to [187].	202

7.5	IDEA material budget versus the cosine of the azimuthal angle θ (a) and muon momentum resolution using the IDEA drift chamber (b).	203
7.6	Feynman diagram for the process $e^+e^- \rightarrow Z(\ell^+\ell^-)H$ where ℓ can be e, μ or τ	205
7.7	Feynman diagram illustrating the $e^+e^- \rightarrow e^+e^-H$ process, where a Higgs boson is produced through the fusion of Z bosons, which are radiated from an incoming electron and positron.	205
7.8	Feynman diagrams for the process $e^+e^- \rightarrow ZZ$. The left panel (a) shows the standard order, while the right panel (b) displays the swapping the final states. Both diagrams consider the Z decay inclusively.	205
7.9	Feynman diagrams for the process $e^+e^- \rightarrow W^+W^-$. Both panels show the inclusive decays of W^+ and W^- . The left panel (a) displays the s-channel, while the right panel (b) presents the t-channel.	206
7.10	Feynman diagrams for the process $e^+e^- \rightarrow \ell^+\ell^-$ where ℓ can be e, μ , or τ . The left panel (a) displays the s-channel, while the right panel (b) presents the t-channel.	206
7.11	Feynman diagrams for the processes. Diagram (a) represents $e^-\gamma \rightarrow e^-Z(\ell^+\ell^-)$, while diagram (b) illustrates $e^+\gamma \rightarrow e^+Z(\ell^+\ell^-)$. In both cases, ℓ can be e, μ , or τ	206
7.12	Feynman diagram for the process $\gamma\gamma \rightarrow \ell^+\ell^-$ where ℓ can be e, μ or τ	206
7.13	Feynman diagram for the process $e^+e^- \rightarrow \nu_e\bar{\nu}_eZ$ with W exchange.	206
7.14	Feynman diagram for the VBF process $e^+e^- \rightarrow \nu_e\bar{\nu}_eH$ with W exchange.	207
7.15	m_{rec} distribution without selection for $\mu^+\mu^-$ ((a)) and e^+e^- channels ((b)).	207
7.16	Event requirement flow plots for the muon ((a)) and electron ((b)) final states.	210
7.17	Recoil distributions after all requirements (including the $\cos(\theta_{\text{miss}})$ requirement) for the muon ((a)) and electron ((b)) final states.	210
7.18	Categorized recoil distributions for the (a) muon and (b) electron final states.	213
7.19	Fits for signal modeling using DSCB (a) and 2CBG (b).	214
7.20	Visual representation of the (a) decomposition of the 3 terms in the recoil PDF for 125 GeV and (b) fitted recoil distributions for various masses around 125 GeV.	214
7.21	Visual representation of the (a) example spline for the mean and (b) background modeling using a third-order Bernstein polynomial.	215
7.22	Likelihood scans for (a) statistical-only and (b) including systematics.	216
7.23	Uncertainty breakdown on the mass analysis for (a) the nominal fit with BES 1% and (b) BES 6%.	217
7.24	Impact of different detector configurations related to tracking on the recoil distribution and uncertainty on the Higgs mass, for the muon final state only.	219
7.25	Selection efficiency of the different Higgs decay modes with $Z \rightarrow \mu^+\mu^-$ (top row) and $Z \rightarrow e^+e^-$ decay mode (bottom row). The left column shows the selection efficiency with the basic selection (without $\cos(\theta_{\text{miss}})$ requirement), and the right column shows selection efficiency with baseline selection (with $\cos(\theta_{\text{miss}})$ requirement).	220
7.26	BDT distributions for $\mu^+\mu^-$ (a) and e^+e^- (b) channel signal and background events from the training (solid) and test (dashed) datasets. The BDT model demonstrates consistent performance for both channels, as signal events are predominantly found in regions with high BDT scores, while background events are concentrated at low BDT scores.	224
7.27	BDT efficiency curve for $\mu^+\mu^-$ (a) and e^+e^- (b).	224
7.28	Feature importance of the input variables for $\mu^+\mu^-$ (a) and e^+e^- (b).	225
7.29	ROC curve for $\mu^+\mu^-$ (a) and e^+e^- (b).	225
7.30	Area under the ROC curve (AUC) for $\mu^+\mu^-$ (a) and e^+e^- (b).	226
7.31	Classification error curves for $\mu^+\mu^-$ (a) and e^+e^- (b).	226
7.32	Log loss curve for $\mu^+\mu^-$ (a) and e^+e^- (b).	226
7.33	m_{rec} distribution for the $\mu^+\mu^-$ (a) and e^+e^- (b) channels in linear scale with basic selection, BDT score > 0.3 is applied, i.e. without the $\cos(\theta_{\text{miss}})$ requirement.	227

7.34	m_{rec} distribution for the $\mu^+\mu^-$ (a) and e^+e^- (b) channels in linear scale with baseline selection, i.e. with the $\cos\theta_{\text{missing}}$ requirement.	228
7.35	m_{rec} distribution for the $\mu^+\mu^-$ (a) and e^+e^- (b) channels in linear scale with basic selection.	228
7.36	Fit results using m_{rec} as the input parameter, The differences in the fit profiles illustrate the impact of including or excluding the $\cos(\theta_{\text{miss}})$ requirement on the fitting process. (a) with baseline selection, while (b) without basic selection. . . .	229
7.37	BDT score distributions for $\mu^+\mu^-$ (a) and e^+e^- (b) channels in log scale. The distributions demonstrate the BDT model's ability to effectively differentiate signal and background events, while the overlaid distribution represent the expected distributions used in the fitting process.	229
7.38	Log-likelihood fit results using the BDT score as the input parameter. The fit profile demonstrates the differences in the fitting process when employing an alternative input parameter. Statistical uncertainty (a) and statistic plus systematic uncertainties (including BES 1%, center-of-mass, lepton momentum scale) (b) are considered.	230
7.39	Uncertainty breakdown on the cross-section analysis.	231
7.40	Effect of the beam energy spread (0 and 222 MeV) on the $Z(\mu, \mu)H$ recoil mass distribution.	232
7.41	Effect of the beam energy spread uncertainty ($\pm 6\%$ left, $\pm 1\%$ right) on the $Z(\mu, \mu)H$ recoil mass distribution.	233
7.42	Effect on the recoil mass distribution by switching OFF the ISR treatment (a) and by switching OFF the photon spectrum only (b).	234
7.43	Comparison between KKMC and WHIZARD with ISR enabled but BES and FSR OFF. Exactly two opposite-sign leptons are required with $m(\mu^+\mu^-) > 220$ GeV. . .	235
7.44	Effect on the recoil mass when perturbing the center-of-mass energy with 2 MeV (a) and the muon momentum scale (b). The quoted Δm values are the mean histogram values w.r.t. the nominal sample. Plots are done using the Spring2021 campaign.	236
A.1	Continuum $\gamma\gamma$ distribution of category 1	245
A.2	1 GeV binning GPR smoothing result of category 1, 2, 3, 4 and VBF based on H025 baseline selection	247
A.3	4 GeV binning GPR smoothing result of category 1, 2, 3, 4 and VBF based on H025 baseline	248
A.4	Fit of category 2 original distribution with 4^{th} (on the left) and 5^{th} (on the right) order polynomial. Original distribution in blue while fit function in red.	249
A.5	comparison of the di-Higgs and single Higgs distribution on top of original and RGFR (4-to-1 GeV) smoothed $\gamma\gamma$ distribution. Original $\gamma\gamma$ distribution on the left while RGFR (4-to-1 GeV) method results on the right.	252
A.6	Spurious signal test. Fit of original histograms for different categories	254
A.7	Spurious signal test. Fit of RGFR (4-to-1 GeV) refilled result (100 times entries) . .	256
B.1	Schematic depiction of the combined fake-factor method used to estimate multi-jet and $t\bar{t}$ backgrounds with fake- $\tau_{\text{had-vis}}$ in the $\tau_{\text{lep}}\tau_{\text{had}}$ channel. Backgrounds which are not from events with fake- $\tau_{\text{had-vis}}$ originating from jets are estimated from simulation and are subtracted from data in all control regions. Events in which an electron or a muon is misidentified as a $\tau_{\text{had-vis}}$ are also subtracted, but their contribution is very small. Both sources are indicated by 'True- $\tau_{\text{had-vis}}$ subtracted' in the legend. . .	260
B.2	Plots of the τ_{had} p_T distributions for the (left) anti- τ_{had} and (right) τ_{had} selection for SLT (top) and LTT (bottom) channels in the $t\bar{t}$ control region with 1-prong τ_{had} . .	261
B.3	Plots of the τ_{had} p_T distributions for the (left) anti- τ_{had} and (right) τ_{had} selection for SLT (top) and LTT (bottom) channels in the $t\bar{t}$ control region with 3-prong τ_{had} . .	261

B.4	Plots of the $\tau_{\text{had}} p_T$ distributions for the (left) anti- τ_{had} and (right) τ_{had} selection for SLT (top) and LTT (bottom) channels in the multi-jet control region with 1-prong τ_{had} .	262
B.5	Plots of the $\tau_{\text{had}} p_T$ distributions for the (left) anti- τ_{had} and (right) τ_{had} selection for SLT (top) and LTT (bottom) channels in the multi-jet control region with 3-prong τ_{had} .	262
B.6	Fake-factors as a function of η for 1-prong and 3-prong τ_{had} candidates for (a) multi-jet and (b) $t\bar{t}$ processes for the $\tau_{\text{lep}}\tau_{\text{had}}$ SLT category. No significant trend is observed.	263
B.7	Fake-factors as a function of η for 1-prong and 3-prong τ_{had} candidates for (a) multi-jet and (b) $t\bar{t}$ processes for the $\tau_{\text{lep}}\tau_{\text{had}}$ LTT category. No significant trend is observed.	263
B.8	Fake-factors for 1-prong and 3-prong τ_{had} candidates for (a) multi-jet and (b) $t\bar{t}$ processes for the $\tau_{\text{lep}}\tau_{\text{had}}$ SLT category.	264
B.9	Fake-factors for 1-prong and 3-prong τ_{had} candidates for (a) multi-jet and (b) $t\bar{t}$ processes for the $\tau_{\text{lep}}\tau_{\text{had}}$ LTT category.	264
B.10	The SLT BDT distributions for (a) low- m_{HH} ggF, (b) high- m_{HH} ggF, and (c) VBF categories in the signal-depleted $t\bar{t}$ CR where the $t\bar{t}$ FF are measured. This is a simple closure test.	265
B.11	The LTT BDT distributions for (a) low- m_{HH} ggF, (b) high- m_{HH} ggF, and (c) VBF categories in the signal-depleted $t\bar{t}$ CR where the $t\bar{t}$ FF are measured. This is a simple closure test.	266
B.12	The SLT BDT distributions for (a) low- m_{HH} ggF, (b) high- m_{HH} ggF, and (c) VBF categories in the 1- b -tag validation region.	266
B.13	The LTT BDT distributions for (a) low- m_{HH} ggF, (b) high- m_{HH} ggF, and (c) VBF categories in the 1- b -tag validation region.	266
B.14	Closure check of the fake factor method in 1-tag SS ID-region showing the leading $\tau_{\text{had}} p_T$ distributions for the (a) low- m_{HH} ggF, (b) high- m_{HH} ggF and (c) VBF categories in the $\tau_{\text{had}}\tau_{\text{had}}$ channel.	267
B.15	Validation of the multi-jet estimate in the 1-tag OS multi-jet validation region showing the leading $\tau_{\text{had}} p_T$ distributions for the (a) low- m_{HH} ggF, (b) high- m_{HH} ggF and (c) VBF categories in the $\tau_{\text{had}}\tau_{\text{had}}$ channel.	267
B.16	Schematic depiction of the fake-factor method to estimate the multi-jet background with fake- $\tau_{\text{had-vis}}$ in the $\tau_{\text{had}}\tau_{\text{had}}$ channel. Backgrounds that are not from multi-jet events are simulated and subtracted from data in all the control regions. This is indicated by ‘Non-multi-jet subtracted’ in the legend	268
B.17	Fake factors for 1-prong DTT ((a), (b), (c)), 3-prong DTT ((d), (e), (f)), and STT ((g), (h), (i)) for the data-taking periods 15-16, 17, and 18 for the di-Higgs $\tau_{\text{had}}\tau_{\text{had}}$ channel.	270
B.18	Transfer factors for the data-taking periods (a) 15-16, (b) 17, and (c) 18 for the di-Higgs $\tau_{\text{had}}\tau_{\text{had}}$ channel.	270
B.19	Schematic depiction of the fake- $\tau_{\text{had-vis}}$ scale-factor method to estimate the $t\bar{t}$ background with fake- $\tau_{\text{had-vis}}$ in the $\tau_{\text{had}}\tau_{\text{had}}$ channel.	271
B.20	Negative logarithm of the likelihood ratio comparing different κ_λ (top) and κ_{2V} (bottom) hypotheses for the fit to Asimov (left) and data (right) in the current and previous analysis for the $\tau_{\text{had}}\tau_{\text{had}}$ channel.	273
B.21	Negative logarithm of the likelihood ratio comparing different κ_λ (top) and κ_{2V} (bottom) hypotheses for the fit to Asimov (left) and data (right) in the current and previous analysis for the $\tau_{\text{lep}}\tau_{\text{had}}$ channel.	274
B.22	Negative logarithm of the likelihood ratio comparing different κ_λ (top) and κ_{2V} (bottom) hypotheses for the fit to Asimov (left) and data (right) in the current and previous analysis for the combination.	275

B.23	Post-fit BDT score distributions in the $\tau_{\text{had}}\tau_{\text{had}}$ signal regions.	276
B.24	Post-fit data/Mc distributions of key variables in the $\tau_{\text{had}}\tau_{\text{had}}$ channel signal regions.	277
B.25	Post-fit data/MC distribution of the ggF/VBF classification BDT score in the $\tau_{\text{had}}\tau_{\text{had}}$ channel. The categorisation BDT is only shown for events with at least four jets which represent a subset of the ggH SRs.	278
B.26	Post-fit BDT score distributions in the $\tau_{\text{lep}}\tau_{\text{had}}$ signal regions. The result of the inclusive signal strength fit is used to produce these distributions.	279
B.27	Post-fit BDT score distributions in the $\tau_{\text{had}}\tau_{\text{had}}$ and $\tau_{\text{lep}}\tau_{\text{had}}$ signal regions after the combined fit.	280
B.28	Compatibility of the fit result across different analysis channels, for μ_{HH} in Figure (a) and μ_{VBF} in Figure (b). The black markers correspond to the combined fit with a single POI, and to a separate fit with one POI per channel. The results from separate fits to each analysis regions are additionally shown in red.	281
B.29	Bootstrap result for the had-had channel. Figure (a): joint distribution of best-fit values for μ_{HH} obtained from the previous Run-2 analysis (horizontal axis) and the present analysis (vertical axis). The correlation coefficient is 70%. Figure (b): distribution of absolute differences in the best-fit μ_{HH} between the two results.	282
B.30	Bootstrap result for the SLT channel. Figure (a): joint distribution of best-fit values for μ_{HH} obtained from the previous Run-2 analysis (horizontal axis) and the present analysis (vertical axis). The correlation coefficient is 72%. Figure (b): distribution of absolute differences in the best-fit μ_{HH} between the two results.	283
C.1	$m_{\ell\ell}$ distribution after the muon selection criteria for the muon (a) and electron (b) final states.	285
C.2	$p_{\ell\ell}$ distribution after the $m_{\ell\ell}$ cut for the muon (a) and electron (b) final states.	286
C.3	m_{rec} distribution after the $p_{\ell\ell}$ cut for the muon (a) and electron (b) final states.	286
C.4	$\cos(\theta_{\text{miss}})$ distribution after the m_{rec} cut for the muon (a) and electron (b) final states.	287
C.5	Signal samples for 125 GeV muon channel: CC ((a)), CF ((b)) FF ((c)).	288
C.6	Signal samples for 125 GeV electron channel: CC ((a)), CF ((b)) FF ((c)).	288
C.7	Background distributions for the muon channel: CC ((a)), CF ((b)) FF ((c)).	289
C.8	Background distributions for the electron channel: CC ((a)), CF ((b)) FF ((c)).	289
C.9	Input variables for BDT training for the $\mu^+\mu^-$ channel.	290
C.10	Input variables for BDT training for the e^+e^- channel.	291

List of Tables

1.1	The Standard Model Higgs boson production cross-sections for $m_H = 125$ GeV in pp collisions at $\sqrt{s} = 13$ TeV. Adapted from Ref. [14].	31
1.2	The branching ratios and the relative uncertainty for an SM Higgs boson with $m_H = 125$ GeV, Adapted from Reference [14].	32
3.1	Electron isolation working points and isolation efficiency ε definitions. In the Gradient working point definition, the unit of p_T is GeV. For all working points, a cone size of $\Delta R = 0.2$ for calorimeter and $\Delta R_{\max} = 0.2$ for track isolations has been used. The HighPtCaloOnly WP is only based on calorimeter isolation while the other WPs require both calorimeter and tracks isolation criteria. (taken from Ref. [109]).	71
3.2	Prompt-muon efficiencies (ε_μ) and light-hadron misidentification rates (ε_{had}) for different identification working points, assessed on a $t\bar{t}$ MC sample across various p_T -regions within $ \eta < 2.5$. The Tight working point inherently does not select muons with $p_T < 4$ GeV, evident in the $3 < p_T < 5$ GeV region. The provided statistical uncertainties are substantially smaller than the reported final digit (adapted from Ref. [114]).	76
3.3	Muon isolation working point definitions. The utilized criteria are listed in the second column, while the third column presents the minimum track p_T requirement. The working points indicated with “*” are available in two versions: one using $p_T^{\text{varcone30}}$ (i.e., variable ΔR cone) and the other utilizing p_T^{cone20} (i.e., fixed ΔR cone) for $p_T > 50$ GeV (based on Ref. [114]).	77
3.4	Isolation working point efficiencies for prompt muons (ε_μ) and muons originating from bottom and charm semileptonic decays (ε_{HF}) assessed in a $t\bar{t}$ MC sample for tracks within different p_T -regions that satisfy the Medium identification and vertex association criteria. The studied isolation working points pertain to variants with a constant cone size of $\Delta R = 0.2$ for $p_T > 50$ GeV. The statistical uncertainties are notably smaller than the last reported digit (adapted from Ref. [114]).	77
3.5	Input variables for the MV2c10 and DL1r algorithms. Only the DL1r algorithm uses the JETFITTER c -tagging and RNNIP variables (adapted from Ref. [128]). . .	83
4.1	List of trigger identifiers used in this research for each year alongside their respective jet p_T thresholds.	91
4.2	Details of p_T^{jet} bins and relevant thresholds for triggers during 2016 and 2017. . . .	91
4.3	Details of p_T^{jet} bins and relevant thresholds for triggers during 2018.	91
4.4	Selection parameters for muon-jet samples.	93
4.5	Mass, mean lifetime, and decay rate into $l\nu_l + X$ decay of the different b -hadrons as cited in Ref. [155].	106
4.6	Fractions of b -hadrons as generated in simulated Z^0 -decays, inclusive assessments executed at CDF [158], Compared to the mean value proposed by the HFAG [157] (CDF, LHCb and LEP). The concluding column reveals values derived using the ATLAS muon filtered di-jets simulation, using DL1r tagger.	106

5.1	Generators used to simulate the signal and background processes. If not otherwise specified, the order of the cross-section calculation refers to the expansion in the strong coupling constant (α_s). The acronyms ME, PS and UE are used for matrix element, parton shower and underlying event, respectively. Details of the simulation of the signal and background samples are described in the text. (†) The NNLO(QCD)+NLO(EW) cross-section calculation for the $pp \rightarrow ZH$ process already includes the $gg \rightarrow ZH$ contribution. The $qq \rightarrow ZH$ process is normalised to the NNLO(QCD)+NLO(EW) cross-section for the $pp \rightarrow ZH$ process, after subtracting the $gg \rightarrow ZH$ contribution.	114
5.2	κ_λ , κ_{2V} and κ_V coupling parameter values considered for the nominal VBF HH samples generation.	116
5.3	κ_λ , κ_{2V} and κ_V coupling parameter values considered for the alternative VBF HH samples generation.	118
5.4	SLTs used in the $\tau_{\text{lep}}\tau_{\text{had}}$ sub-channel, along with the trigger-dependent offline p_T thresholds, for each year/period.	120
5.5	LTTs used in the $\tau_{\text{lep}}\tau_{\text{had}}$ sub-channel, along with the trigger-dependent offline p_T thresholds, for each year/period. These triggers are checked when the event fails the SLTs. When an OR of multiple triggers is used in the electron channel, the 4J12 trigger is prioritized due to lower jet p_T thresholds. This means that other triggers are checked if and only if 4J12 doesn't fire. The offline selection is adjusted accordingly. For 2017 and 2018, different MTTs are used for two different regions defined by $30 \text{ GeV} < p_T^\tau \leq 40 \text{ GeV}$ and $p_T^\tau > 40 \text{ GeV}$	120
5.6	Triggers used for data taking in the $\tau_{\text{had}}\tau_{\text{had}}$ channel.	121
5.7	Summary of the event selections, shown separately for events that are selected by different triggers. In cases where pairs of reconstructed objects of the same type are required, thresholds for the (sub-)leading p_T object are given outside (within) parentheses where different event selection thresholds are applied. When the selection depends on the year of data-taking, the possible values of the requirements are separated by commas, except for the jet selection in the LTT and DTT triggers, which use multiple selection criteria as described in Section 5.2. The trigger p_T thresholds shown are applied to the offline physics objects that are matched to the corresponding trigger objects.	122
5.8	Pre-fit event yields in the $b\bar{b} \tau_{\text{had}}\tau_{\text{had}}$ signal regions. Here, Zttjj represents the processes as $Z \rightarrow \tau\tau + jj$, whereas Zjj represents $Z \rightarrow ee/\mu\mu + jj$. Inclusive SR refers to inclusiveness in m_{HH}	124
5.9	Acceptance times efficiency of the SM ggF and VBF HH signals in all analysis categories.	125
5.10	Pre-fit event yields in the di-Higgs $bb\tau_{\text{lep}}\tau_{\text{had}}$ SLT signal region for the data, background and signal. Here, Zttjj represents the processes as $Z \rightarrow \tau\tau + jj$, whereas Zjj represents $Z \rightarrow ee/\mu\mu + jj$. Inclusive SR refers to inclusiveness in m_{HH}	128
5.11	Pre-fit event yields in the di-Higgs $bb\tau_{\text{lep}}\tau_{\text{had}}$ LTT signal region for signal, data and background. Here, Zttjj represents the processes as $Z \rightarrow \tau\tau + jj$, whereas Zjj represents $Z \rightarrow ee/\mu\mu + jj$. Inclusive SR means inclusiveness in m_{HH}	129
5.12	Pre-fit event yields obtained from the $Z + HF$ control region. Only contributions > 0.1 are shown.	132
5.13	Training hyperparameters that are fixed during training.	135
5.14	Input variables used for the ggF-VBF BDT training in the $\tau_{\text{lep}}\tau_{\text{had}}$ SLT channel.	137
5.15	Training hyperparameters chosen for the ggF/VBF BDT in the $\tau_{\text{lep}}\tau_{\text{had}}$ SLT channel.	140
5.16	κ_{2V} , κ_λ as well as the limits on μ_{HH} , μ_{VBF} and μ_{ggF} values for various parameters across different WP points. The fit is performed on the validation dataset to avoid biasing the results.	143

5.17	κ_{2V} , κ_λ as well as the limits on μ_{HH} , μ_{VBF} and μ_{ggF} values for various parameters across different WP points. The fit is performed on the validation dataset to avoid biasing the results. Inclusive: SR BDT trained on events without ggF/VBF categorisation. Region: SR BDT trained on events with ggF/VBF categorisation.	145
5.18	Training hyperparameters chosen for the BDTs used in the three $\tau_{lep}\tau_{had}$ analysis categories.	146
5.19	Input variables used for the low- m_{HH} ggF BDT training in the $\tau_{lep}\tau_{had}$ SLT channel.	146
5.20	Input variables used for the high- m_{HH} ggF BDT training in the $\tau_{lep}\tau_{had}$ SLT channel.	147
5.21	Input variables used for the VBF BDT training in the $\tau_{lep}\tau_{had}$ SLT channel.	147
5.22	Regions entering the fit and fitted observable in each analysis region and channel.	154
5.23	Signal strengths observed from data fitting in the $\tau_{had}\tau_{had}$ channel under varied signal hypotheses. The uncertainties encompass both statistical and systematic aspects. The designation 1D indicates a single parameter consideration, whereas 2D denotes a simultaneous fit of two signal strengths.	157
5.24	Observed signal strength when fitting data in the SLT, LTT and $\tau_{lep}\tau_{had}$ channel under different signal hypothesis. The uncertainty includes both statistical and systematic components. 1D indicates that only that parameter is considered, while 2D implies simultaneous fit of two signal strengths.	165
5.25	Observed signal strength when fitting data in the $\tau_{had}\tau_{had}$, $\tau_{lep}\tau_{had}$ and their combination. The uncertainty includes both statistical and systematic components. 1D indicates that only that parameter is considered, while 2D implies simultaneous fit of two signal strengths.	174
5.26	Observed and expected 95% CL limits on the HH signal strength (ggF+VBF) in the $\tau_{had}\tau_{had}$ channel, including individual production modes.	181
5.27	95% CL observed and expected intervals for κ_λ and κ_{2V} in the $\tau_{had}\tau_{had}$ channel.	181
5.28	95% CL limits on the HH signal strength (ggF+VBF) in the $\tau_{lep}\tau_{had}$ channel, including individual production modes, both observed and expected.	182
5.29	95% CL intervals for κ_λ and κ_{2V} in the $\tau_{lep}\tau_{had}$ channel, both observed and expected.	182
5.30	Observed and expected 95% CL upper limits on μ_{HH} , μ_{ggF} and μ_{VBF} from the individual SR likelihood fits as well as the combined results. The μ_{ggF} and μ_{VBF} limits are quoted both from the results of the simultaneous fit of both signal strengths (central column), as well as from independent fits for the individual production modes, assuming the other to be SM-like. The uncertainties quoted on the combined expected upper limits correspond to the 1σ uncertainty band.	184
5.31	95% CL intervals for κ_λ and κ_{2V} , as observed and expected in the $\tau_{lep}\tau_{had}$, $\tau_{had}\tau_{had}$ channels and their combination.	185
6.1	The baseline FCC-ee operation model with four interaction points, showing the centre-of-mass energies, instantaneous luminosities for each IP, integrated luminosity per year summed over 4 IPs corresponding to 185 days of physics per year and 75% efficiency.	194
7.1	Z Decay Modes Branching Ratios, adapted from [14]	201
7.2	Monte Carlo Samples used in this analysis. They are all produced at a center-of-mass energy of 240 GeV.	204
7.3	Cut flow and event yields for the muon (top) and electron (bottom) final states for an integrated luminosity of 7.2 ab^{-1} . The error reflects the uncertainty on the Monte Carlo event statistics.	211
7.4	Statistical (stat+syst) uncertainty on the Higgs mass (MeV) for various fit configurations. Fits are performed using the nominal categorization unless stated otherwise. The values in brackets represent the statistical+systematic uncertainties. Values are normalized to an integrated luminosity of 7.2 ab^{-1}	218

7.5	Training Samples for muon channel. They are all produced at a center-of-mass energy of 240 GeV.	222
7.6	Training Samples for electron channel. They are all produced at a center-of-mass energy of 240 GeV.	222
7.7	Input variables for BDT training. The leading or sub-leading lepton is sorted by the lepton momentum.	223
7.8	Values of the Hyper-parameters utilized for the BDT model training.	223
A.1	χ^2/NDF of original fitting with second, third, fourth, fifth order polynomial and exponential function.	249
A.2	χ^2/NDF of 4 GeV binning GPR smoothed fitting with second, third, fourth, fifth order polynomial and exponential function.	249
A.3	χ^2/NDF of fit of RGFR (4-to-1 GeV) refill histogram using 4 th order polynomial with the same numbers of entries as the original histogram	250
A.4	χ^2/NDF of fit of RGFR (4-to-1 GeV) refill histogram using 4 th order polynomial with 10 times the number entries compared to the original histogram	250
A.5	χ^2/NDF of fit of RGFR (4-to-1 GeV) refill histogram using 4 th order polynomial with 100 times the number entries compared to the original histogram	250
A.6	Spurious Signal Test for the original H025 Monte-Carlo simulation with MC16a, MC16d and MC16e	254
A.7	Spurious Signal Test for RGFR (4-to-1 GeV) method results with 100 times the number of the entries of the original histograms	255
B.1	Relative subtraction of non-multijet-fake backgrounds in the DTT control regions used for the multijet estimation.	268
B.2	Relative subtraction of non-multijet-fake backgrounds in the STT control regions used for the multijet estimation.	268
B.3	Comparison between expected and observed quantities for the current and previous analysis round in the $\tau_{\text{had}}\tau_{\text{had}}$ channel.	272
B.4	Comparison between expected and observed quantities for the current and previous analysis round in the $\tau_{\text{lep}}\tau_{\text{had}}$ channel.	273
B.5	Comparison between expected and observed quantities for the current and previous analysis round in the combined analysis.	274
B.6	Compatibility of the fit result for μ_{HH} across different analysis channels and regions.	281
B.7	Compatibility of the fit result for μ_{VBF} across different analysis channels and regions.	282

Acknowledgement

I would like to extend my heartfelt gratitude to my supervisor, Gregorio Bernardi, for his invaluable guidance and support throughout my Ph.D. journey. His patience in our many discussions, his passion for physics, and his professionalism in explaining complex concepts have been profoundly inspiring. He stands as a role model whom I aspire to emulate in my future career.

My sincere thanks also go to Stefan Hohenegger, Cédric Lorcé, and Claude Charlot, who welcomed me into the fascinating world of physics during my Bachelor and Master internships. Their mentorship has been instrumental in shaping my academic path.

I am grateful to the members of my thesis monitoring committee ("Committee de suivi de thèse"), David Franco and Antoine Letessier-Selvon, for their constructive feedback and for monitoring my progress over the last three years.

A special acknowledgment is due to the jury members of my thesis defense: Emmanuel Perez, Alessandra Tonazzo, Elisabeth Petit, and particularly Jean-Baptiste de Vivie de Regie and Roberto Salerno, for their critical roles as referees of my thesis.

My appreciation extends to the entire APC ATLAS group, Giovanni Marchiori, Marco Bomben, and Ph.D. students and post-docs, both past and present, Romain Bouquet, Keerthi Nakkalil, Qiuping Shen, Yulei Zhang, Alexis Maloizel, Giulia Di Gregorio, and Tong Li have been pillars of my Ph.D. experience.

I am thankful to the administrative staff at the Laboratoire Astroparticule et Cosmologie (APC), Sabine Tesson, Olivier Lelong, and Kevin Velaidomestry, for their assistance with the paperwork and administrative duties throughout my studies.

I would also like to express my gratitude to Université Paris Cité, the Ecole Doctorale STEP'UP (ED560) and the French National Centre for Scientific Research (Centre national de la recherche scientifique, CNRS) for their financial support during my doctoral research.

Acknowledgment is also due to the people I met at the Laboratoire de Physique Nucléaire et des Hautes Énergies (LPNHE), Yufeng Wang, Yajun He, Tou Da Yu, and the administrative staff, who provided much-needed support during the initial months of my Ph.D.

Additionally, my thanks to the p_T^{rel} and FTag group for their assistance and support with the p_T^{rel} calibration work.

I am thankful for the $HH \rightarrow b\bar{b}\tau^+\tau^-$ analysis team, notably Brian Moser, Carlo Pandini, Valerio Dao. Especially Jem Guhit, with whom I closely collaborated in the $\tau_{\text{lep}}\tau_{\text{had}}$ channel to derive our physics results.

I also wish to express my gratitude to Valentina Cairo for her guidance since the beginning of my Ph.D. since the $HH \rightarrow b\bar{b}\gamma\gamma$ analysis and later as di-Higgs convener during my $HH \rightarrow b\bar{b}\tau^+\tau^-$ analysis work.

I extend my appreciation to the Future Circular Collider program, especially to Emmanuel Perez, Patrizia Azzi, and Jan Eysermans, the latter with whom I had the pleasure of working closely on the FCC-ee Higgs mass and ZH cross-section measurement analysis.

A heartfelt thank you to my friends Qier Wu, Silun ZHANG for the joyful memories created in Paris, and to Chenhao Jin, Hao Huang, Hao Wei, Long Hu and Jinyang Feng for the enduring friendship that began during our Bachelor's program.

To my girlfriend, Zhuoran Yu, your presence in my life has been a source of joy and strength.

Your understanding and support, especially during those late night and early morning hours spent debugging and submitting analysis jobs, have been nothing short of extraordinary. I am grateful for your love and companionship to help me through this journey.

Lastly, I owe an immeasurable debt of gratitude to my family. To my parents, whose unwavering support has been my foundation; to my grandparents, for their love and care; and to all my relatives, for their support and understanding of my choices.